EXTERNAL FORCING ON VOLCANOES AND VOLCANIC PROCESSES: OBSERVATIONS, ANALYSIS AND IMPLICATIONS

EDITED BY: Stéphanie Dumont, Nathalie Feuillet, Simona Petrosino and David M. Pyle

PUBLISHED IN: Frontiers in Earth Science

frontiers Research Topics

ISSN 1664-8714
ISBN 978-2-83250-080-4
DOI 10.3389/978-2-83250-080-4

About Frontiers

Frontiers is more than just an open-access publisher of scholarly articles: it is a pioneering approach to the world of academia, radically improving the way scholarly research is managed. The grand vision of Frontiers is a world where all people have an equal opportunity to seek, share and generate knowledge. Frontiers provides immediate and permanent online open access to all its publications, but this alone is not enough to realize our grand goals.

Frontiers Journal Series

The Frontiers Journal Series is a multi-tier and interdisciplinary set of open-access, online journals, promising a paradigm shift from the current review, selection and dissemination processes in academic publishing. All Frontiers journals are driven by researchers for researchers; therefore, they constitute a service to the scholarly community. At the same time, the Frontiers Journal Series operates on a revolutionary invention, the tiered publishing system, initially addressing specific communities of scholars, and gradually climbing up to broader public understanding, thus serving the interests of the lay society, too.

Dedication to Quality

Each Frontiers article is a landmark of the highest quality, thanks to genuinely collaborative interactions between authors and review editors, who include some of the world's best academicians. Research must be certified by peers before entering a stream of knowledge that may eventually reach the public - and shape society; therefore, Frontiers only applies the most rigorous and unbiased reviews.
Frontiers revolutionizes research publishing by freely delivering the most outstanding research, evaluated with no bias from both the academic and social point of view. By applying the most advanced information technologies, Frontiers is catapulting scholarly publishing into a new generation.

What are Frontiers Research Topics?

Frontiers Research Topics are very popular trademarks of the Frontiers Journals Series: they are collections of at least ten articles, all centered on a particular subject. With their unique mix of varied contributions from Original Research to Review Articles, Frontiers Research Topics unify the most influential researchers, the latest key findings and historical advances in a hot research area! Find out more on how to host your own Frontiers Research Topic or contribute to one as an author by contacting the Frontiers Editorial Office: frontiersin.org/about/contact

EXTERNAL FORCING ON VOLCANOES AND VOLCANIC PROCESSES: OBSERVATIONS, ANALYSIS AND IMPLICATIONS

Topic Editors:
Stéphanie Dumont, University of Beira Interior, Portugal
Nathalie Feuillet, UMR7154 Institut de Physique du Globe de Paris (IPGP), France
Simona Petrosino, Sezione di Napoli - Osservatorio Vesuviano, Italy
David M. Pyle, University of Oxford, United Kingdom

Citation: Dumont, S., Feuillet, N., Petrosino, S., Pyle, D. M., eds. (2022). External Forcing on Volcanoes and Volcanic Processes: Observations, Analysis and Implications. Lausanne: Frontiers Media SA. doi: 10.3389/978-2-83250-080-4

Table of Contents

frontiers | Frontiers in Earth Science

TYPE Editorial
PUBLISHED 24 August 2022
DOI 10.3389/feart.2022.999214

OPEN ACCESS

EDITED AND REVIEWED BY
Valerio Acocella,
Roma Tre University, Italy

*CORRESPONDENCE
Stéphanie Dumont,
sdumont@segal.ubi.pt

SPECIALTY SECTION
This article was submitted to Volcanology, a section of the journal Frontiers in Earth Science

RECEIVED 20 July 2022
ACCEPTED 22 July 2022
PUBLISHED 24 August 2022

CITATION
Dumont S, Petrosino S, Pyle D and Feuillet N (2022), Editorial: External forcing on volcanoes and volcanic processes: Observations, analysis and implications.
Front. Earth Sci. 10:999214.
doi: 10.3389/feart.2022.999214

Editorial: External forcing on volcanoes and volcanic processes: Observations, analysis and implications

Stéphanie Dumont[1,2]*, Simona Petrosino[3], David Pyle[4] and Nathalie Feuillet[5]

[1]Instituto Dom Luiz (IDL), Universidade da Beira Interior, Covilhã, Portugal, [2]Instituto Dom Luiz (IDL), Faculdade de Ciências, Universidade de Lisboa, Lisboa, Portugal, [3]Istituto Nazionale di Geofisica e Vulcanologia, Sezione di Napoli—Osservatorio Vesuviano, Naples, Italy, [4]Department of Earth Sciences, University of Oxford, Oxford, United Kingdom, [5]Paris University, Institut de Physique du Globe de Paris, Paris, France

KEYWORDS

external forcing, modulation of volcanic processes, eruption triggering, periodic variations and behaviors, short and long time scales

Editorial on the Research Topic
External forcing on volcanoes and volcanic processes: Observations, analysis and implications

Volcanoes are complex systems that evolve in space and time as a result of their internal dynamics. These internal dynamics span both long and short time scales, reflecting the different steps for the magma to form, accumulate and evolve before being eventually erupted. All of these stages may be influenced by processes external to the volcano, although most of the evidence that has been gathered on this has considered influences on the magmatic fluids stored at crustal depths, or emerging at surface. External forcing acts either through the stress or gravitational fields that may accelerate or slow down the transfer of magma towards the surface. Changing tectonic stresses and Earth tides may induce changes in the dynamical state of volcanoes, ultimately providing the triggers that may lead to eruption. Water, which is ubiquitous on Earth, and present in its different fluid and solid envelopes, appears to play a key role, acting on volcanic systems from pore- to global-scale in various ways (hydrological modulation, ice cap loading), due to its physico-chemical properties.

This Research Topic brings together contributions, which provide new constraints and lines of evidence on the nature and variety of external processes influencing activity at quiet, restless and erupting volcanoes.

Seasonal hydrological variations can influence the evolution of volcanic systems, as suggested by Petrosino et al. who compare the behaviour of Vesuvius and Campi Flegrei (Italy). They find that part of the ground deformation reflects the seasonality of the hydrological cycles at both volcanoes, whereas part of the seismicity shows a seasonal

pattern only at Campi Flegrei. The authors conclude that rainfall patterns, through the combined action of water loading, diffusion processes in a fractured medium and interaction with the shallow hydrothermal fluids, play a role in modulating the dynamics of metastable volcanoes experiencing unrest, like Campi Flegrei.

Volcanoes with shallow hydrothermal systems may be subject to sudden increases in surface steam emission in response to external forcing, such as sudden decrease of atmospheric pressure or variation of meteoric water input. Bremond d'Ars and Gibert analyze the temperature fluctuations measured with 1 s resolution in the fumaroles at La Soufrière volcano (Guadeloupe, France). The authors observe temperature variations of more than 10°C with remarkable periodic patterns and compare them to rainfall measurements, finding a correlation between the two data sets.

In a study on the same volcanic system, Moune et al. synthesise the long term (5 years) high resolution dataset on volcanic gas compositions and fluxes from the hydrothermal systems of La Soufrière. They show how the influence of the inputs from the magmatic system at depth can be deconvolved from the processes acting within the shallow hydrothermal system, once the external influence of the tropical environment is accounted for.

Rowell et al. provide new insights on how water controls the evolution of explosive eruptions and especially the release of SO_2 into the stratosphere by a new model based on the coupling of one-dimensional models of conduit flow and atmospheric column rise. The comprehensive approach of the authors demonstrates that the predominant control factor of the jet behavior is the efficiency by which the water is incorporated into it and that hydrovolcanic eruptions have a rather reduced effect on climate forcing. This study also suggests that climate variations may impact the relative global frequency of hydrovolcanic eruptions on longer time scales.

More generally, the cryospheric environment has specific signatures on volcanic activity, as shown by Edwards et al. who provide a framework for understanding the impact of the cryosphere on glaciovolcanic systems, landforms and deposits. Their study, based on both observational data and numerical modeling, provides evidence for the modulations in eruptive style as well as rate and timing of eruptions in many volcanoes worldwide.

The investigation of the stability conditions of glacier-covered systems provides further insights on stress-related interactions at volcanoes. Lucas et al. study Westdahl Peak, a subglacial volcano on Unimak Island (Aleutian Arc, USA). The authors use thermomechanical finite element models to evaluate how the stability of a glaciated volcano is impacted by variations in ice cap thickness, magma chamber depth, geometry, magma flux rate, and seasonal changes in ice cover thickness. The results of the numerical experiments indicate that the presence of an ice cap increases the stability of the magma system. In addition, magma flux rates influence the timing of eruptions when the system is experiencing seasonal variations in ice thickness.

At a simple level, volcano-tectonic interactions are related to stress variations in the surrounding crust. Hedger and Gottsmann investigate stress transfer between the Akhisar-Kiliç fault segment (AKFS) in the Central Anatolian Volcanic Province and the active Hasan Dağ volcanic complex (Turkey). Using 3D finite element modelling, the authors show that progressive stress accumulation, quantified using the Coulomb Failure Stress change, promotes conditions favourable to failure and magma rising in the crust.

The stress field of volcanoes may also be altered by large scale processes such ocean loading, as suggested by Dumont et al. who investigated the existence of a possible link between the global eruptive activity and the global mean sea-level by analyzing the time-series of both data sets between 1880 and 2009. The authors found common decadal periodicities, ranging between ~20 and ~90 years, that have been also identified in the polar motion. By linking global processes and the worldwide eruptions, the authors provide a new angle to tackle external forcing on volcanoes acting on decadal scales.

Periodic signals have also been encountered in different geophysical parameters recorded at volcanoes on shorter time-scales, revealing variations of the volcano's gravitational field mainly related to lunisolar tides. Thus, seismic tremor generated by the hydrothermal activity at the two volcanoes of Ischia and Campi Flegrei (Italy) analyzed by Petrosino and Dumont using a time-series analysis technique, appears to be composed of periodic variations coinciding with those of long lunisolar Earth tides, ranging from ~5 to ~29 days. By extracting these tidal components, the authors suggest that the response of the hydrothermal system to this forcing depends on the source of the seismic tremor and the degree of hydrothermal alteration of the surrounding medium.

Sottili et al. present a wide-ranging historical perspective on the Research Topic, highlighting the development of ideas around oscillations of the fluid envelopes of the planet from their origins in Greek and Roman philosophy, to their re-emergence in arguments around different planetary-scale processes in the 19th and 20th centuries. Their essay highlights the interconnections between physical processes that act at different time scales, and links astronomical, climatic and geological phenomena, with a focus on volcanic activity.

Theoretical modeling offers a way to investigate the interplay between external forcing and internal dynamics at volcanoes which may favour transitions from stable to unstable regimes. From continuous deformation measurements at Akutan, Okmok (Aleutian arc, USA) and Piton de la Fournaise (La Reunion, France) volcanoes, Walwer et al. extract the temporal patterns by applying a data-adaptive statistical methodology which provides information on the underlying dynamics without *a priori* assumption on the physical mechanisms. Then, using phase portrait reconstructions, the authors formulate data-based mathematical models which concur to the definition of the

dynamical state of the volcanic systems and may help in distinguishing between stable/unstable conditions.

In summary, the works collected in the present Research Topic cover a wide range of methodologies mainly based on purely theoretical approaches and data analysis or both, providing new evidences on the influence and diversity of external processes acting on volcanic systems at different temporal and spatial scales.

Author contributions

All authors listed have made a substantial, direct, and intellectual contribution to the work and approved it for publication.

Funding

The editorial activity of SD was made as part of her postdoctoral fellowship (SFRH/BPD/117714/2016) funded by the Portuguese Fundação para a Ciência e a Tecnologia (FCT) and the European Union, co-financed by the Ministério da Ciência, Tecnologia e Ensino Superior (MCTES), Fundo Social Europeu (FSE), and Programa Operacional Regional Centro (POR-Centro, Centro 2020); and research projects funded by the FCT, I.P./MCTES through national funds (PIDDAC and CEEC)—UIDB/50019/2020- IDL, PTDC/CTA-GEF/6674/2020—RESTLESS and 2021.00876.CEECIND).

Acknowledgments

We thank the Editor in chief and Frontiers Team for their help at different stages of preparing this collection as well as the reviewers.

Conflict of interest

The authors declare that the research was conducted in the absence of any commercial or financial relationships that could be construed as a potential conflict of interest.

Publisher's note

frontiers in Earth Science

BRIEF RESEARCH REPORT
published: 02 November 2021
doi: 10.3389/feart.2021.758602

Modulation of Ground Deformation and Earthquakes by Rainfall at Vesuvius and Campi Flegrei (Italy)

Simona Petrosino, Ciro Ricco and Ida Aquino*

Istituto Nazionale di Geofisica e Vulcanologia, Sezione di Napoli-Osservatorio Vesuviano, Naples, Italy

Volcanoes are complex systems whose dynamics is the result of the interplay between endogenous and exogenous processes. External forcing on volcanic activity by seasonal hydrological variations can influence the evolution of a volcanic system; yet the underlying mechanisms remain poorly understood. In the present study, we analyse ground tilt, seismicity rates and rainfall amount recorded over 6 years (2015–2021) at Vesuvius and Campi Flegrei, two volcanic areas located in the south of Italy. The results indicate that at both volcanoes the ground deformation reflects the seasonality of the hydrological cycles, whereas seismicity shows a seasonal pattern only at Campi Flegrei. A correlation analysis on shorter time scales (days) indicates that at Vesuvius rain and ground tilt are poorly correlated, whereas rain and earthquakes are almost uncorrelated. Instead, at Campi Flegrei precipitations can affect not only ground deformation but also earthquake rate, through the combined action of water loading and diffusion processes in a fractured medium, likely fostered by the interaction with the shallow hydrothermal fluids. Our observations indicate a different behavior between the two volcanic systems: at Vesuvius, rain-induced hydrological variations poorly affect the normal background activity. On the contrary, such variations play a role in modulating the dynamics of those metastable volcanoes with significant hydrothermal system experiencing unrest, like Campi Flegrei.

Keywords: Vesuvius, Campi Flegrei, ground tilt, earthquakes, rainfall

OPEN ACCESS

Edited by:
Roberto Sulpizio,
University of Bari Aldo Moro, Italy

Reviewed by:
Stephen R. McNutt,
University of South Florida, United States
Micol Todesco,
Istituto Nazionale di Geofisica e Vulcanologia (INGV), Italy

****Correspondence:***
Simona Petrosino
simona.petrosino@ingv.it

Specialty section:
This article was submitted to Volcanology, a section of the journal Frontiers in Earth Science

Received: *14 August 2021*
Accepted: *11 October 2021*
Published: *02 November 2021*

Citation:
Petrosino S, Ricco C and Aquino I (2021) Modulation of Ground Deformation and Earthquakes by Rainfall at Vesuvius and Campi Flegrei (Italy). Front. Earth Sci. 9:758602. doi: 10.3389/feart.2021.758602

INTRODUCTION

In the recent years an increasing number of observations has been showing how rainfall-induced stress variations play a role in modulating ground deformation and seismic activity. Meteoric water storage and load can produce surface deformation, inducing crustal stresses and modulating seismicity (Craig et al., 2017). In addition, variations of the pore-fluid pressures induced by rainfall can promote both ground deformation (Kümpel et al., 2001; Dal Moro and Zadro, 1998; Westerhaus and Welle, 2002; Lesparre et al., 2017) and earthquake nucleation, often with seasonal patterns well correlated with precipitations (Muço, 1999; Heinzl et al., 2006).

The modulation of ground deformation and seismicity by rainfall assumes a critical role in volcanic environments because it superimposes on the endogenous processes and may influence the volcano dynamics. In particular, for those volcanoes in magmatic/hydrothermal unrest or prone to eruption, meteoric input can act as a trigger for volcanic activity. This interaction occurs on typical time scales going from hours, to days and months. As an example, the effect of meteoric water load and the subsequent interaction with groundwater at Nevado del Ruiz (Colombia) possibly caused

deformation events and triggered phreatic explosions and seismicity occurred through 1985–1988 (Banks et al., 1990). The study of the seasonal pattern of eruptions over more than 150 years of available records at Piton de la Fournaise (La Réunion) suggested to explore the possible link with rainfall, by modelling the volumetric ground deformation in response to a water loading/unloading mechanism (Violette et al., 2001). At Soufrière Hills volcano (Montserrat, Lesser Antilles), the response of seismic activity to intense precipitations observed over 3 years (2001–2003) of monitoring has been attributed to both shallow and deeper fluid/solid interactions occurring at different time scales (from hours to days) and related to the percolation of water into cracks (Matthews et al., 2002, 2009). The authors conclude that the rainfall modulates existing, internal processes, rather than generating new events itself. Extreme rainfall is supposed to have triggered the 2018 rift eruption at Kīlauea volcano (Hawaii), by increasing the pore pressure at depths of 1–3 km and promoting the mechanical failure of the volcanic edifice (Farquharson and Amelung, 2020). It is noteworthy that the eruption was not caused by the forceful intrusion of new magma into the rift zone, but by a dyke propagation prompted by meteoric water infiltration. Also the statistical analysis of the occurrence of historical eruptions at Kīlauea strongly suggests a correlation between rainfall and volcanic activity (Farquharson and Amelung, 2020).

In the present paper we investigate and compare the possible links among rainfall, ground deformation and seismicity at two of volcanoes currently characterized by different activity: Vesuvius, which is in a quiescent state, and Campi Flegrei, a caldera experiencing unrest.

Vesuvius and Campi Flegrei are potentially dangerous volcanoes located in the area of Naples (Southern Italy). Vesuvius is a stratovolcano which experienced its last eruption in 1944 (Sbrana et al., 2020). It is characterized by a great variability in eruptive style: highly explosive, sub-Plinian and Plinian eruptions alternating with periods of Strombolian and effusive open-conduit activity, that typically followed long periods of quiescence (Cioni et al., 2008 and references therein). After the last subplinian eruption, in 1631, Vesuvius was marked by open-conduit activity, which ended with the eruption of 1944. The alternating activity of Vesuvius resulted in different deposits including lavas and pyroclastic products. The ground deformation inferred from more than 20 years of tiltmeter signals shows a common subsidence pattern of the southern part of the volcanic edifice, related to joint effects of gravitational sliding and extensional tectonic stress (Ricco et al., 2013, 2021). This background tilt showed gradual or abrupt interruptions in both trend and amplitude during phases of high seismic activity (Ricco et al., 2021), resulting in more complex deformation patterns and indicating a close link between ground tilt and seismicity. The most significant episodes related to variations of internal dynamics occurred in 2017–2019 (Ricco et al., 2021). Vesuvius seismicity consists mainly of volcano-tectonic (VT) earthquakes of low-to-moderate magnitudes (up to 3.6) and mainly located along the crater axis, up to a depth of 6 km below sea level (bsl) (Madonia et al., 2008). The source mechanisms are related to the interaction of the regional and local stress fields, as well as to fluid-driven rock fracturing triggered by pressure variations in the shallow hydrothermal system. Since 2003, low-frequency (LF) and long-period (LP) earthquakes have been observed and associated with mechanisms of brittle slow failure of dry rocks, and resonance of pre-existing fluid-filled cracks, respectively (Bianco et al., 2005; Petrosino et al., 2020a). At Vesuvius a correlation between rainfall and seismicity has not yet been observed; modulation of seismic activity on short (daily) time scales has been interpreted to be linked to a number of possible mechanisms related with the cooling/warming diurnal cycle of the volcanic edifice and/or with the daily oscillation of the geomagnetic field (Mazzarella and Scafetta, 2016). On long time scales (decades) it has been hypothesized that sea level changes could modulate the eruptive cycles (Bragato, 2015).

Campi Flegrei is a caldera generated by at least two major collapses, related to the Campanian Ignimbrite (~39 ka), and the Neapolitan Yellow Tuff eruptions (~15 ka). The caldera experiences slow subsidence alternating with fast ground uplift accompanied by seismicity. After the last eruption of Monte Nuovo in 1538, Campi Flegrei experienced a phase of subsidence, followed by episodes of uplift between 1950–1952 (about 0.75 m), 1969–1972 (1.77 m), and 1982–1984 (1.79 m). Since 1985, the area has undergone a further phase of subsidence, with only brief uplift events recorded in 1989, 1994, and 2000. A new episode of ground uplift started in 2005 and it is still ongoing with accelerated rate during 2011–2013 and subsequently since September 2020; to date the overall vertical deformation is about 0.8 m. Uplift episodes are likely related to the pressurization of hot fluids (CO_2 and H_2O) exsolving from a deep magmatic body towards a shallow hydrothermal system where they mix with meteoric components (Gresse et al., 2017). Hydrothermal fluids and gases are released at the surface of Solfatara crater and Pisciarelli fumarolic field, the most thermally active sites of the caldera (Caputo et al., 2020; Cusano et al., 2021). Uplifts are accompanied by seismicity consisting of both sequences of VT earthquakes and LP events. The most remarkable LP swarm occurred in October 2006 (Saccorotti et al., 2007; Falanga and Petrosino, 2012; De Lauro et al., 2012) and it was located at depths of about 500 m bsl beneath the Solfatara crater. The LP generation mechanism is related to the acoustic resonance of a crack filled by a water-gas mixture of hydrothermal origin (Cusano et al., 2008). The VT activity is characterized by the alternation of swarms lasting a few hours, and phases of low seismicity rate (Petrosino et al., 2018; Bellucci Sessa et al., 2021). Since 2018 the activity is increasing and the most relevant earthquakes (Md 3.1 and 3.3) occurred on December 6th, 2019 and April 26th, 2020. The earthquakes are mainly located beneath the Solfatara-Pozzuoli area, at depths up to 4 km bsl, with the highest concentration between 1–2 km bsl (Bellucci Sessa et al., 2021). The source mechanism is a brittle shear failure induced by the pressurization of the hydrothermal system and the consequent fluid flow towards the surface (Saccorotti et al., 2007). As shown in recent works, there is evidence that the volcanic system responds the to the rainfall both in term of ground deformation and seismic activity. In particular, diffusive processes into the highly fractured rocks,

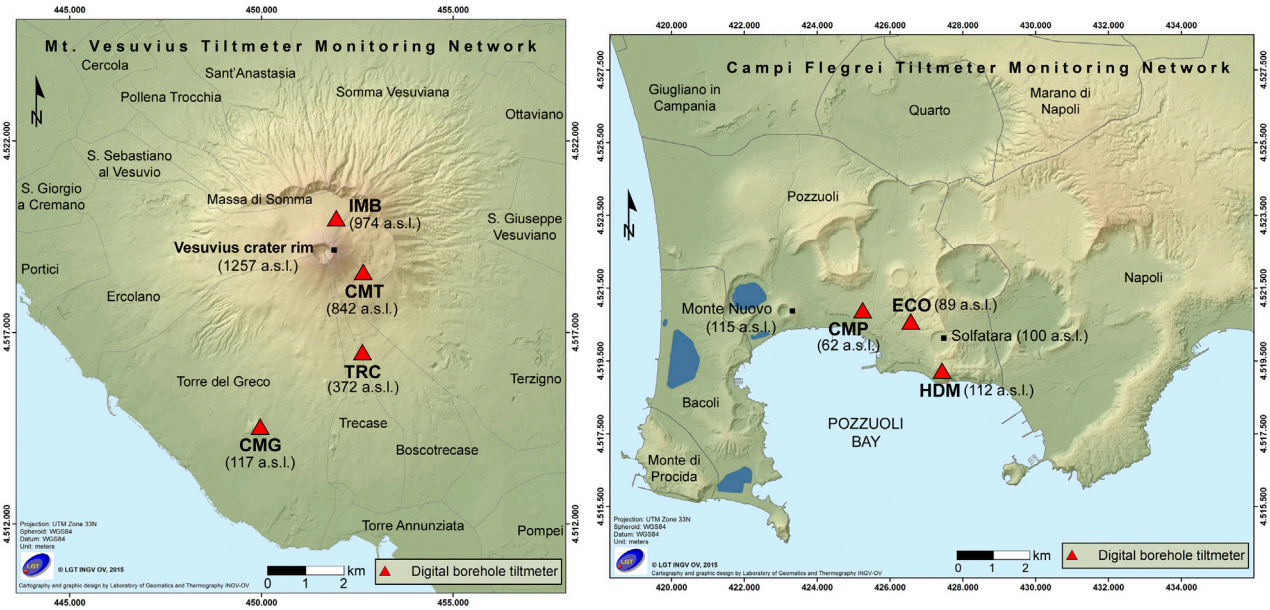

FIGURE 1 | Map of Vesuvius **(A)** and Campi Flegrei **(B)** with the location of the borehole tiltmeters. The base maps were created by the INGV-OV Laboratory of Geomatics and Thermography, © LGT INGV OV, 2015.

pore pressure and permeability variations have been advocated to explain the correlation between rain and ground tilt (Ricco et al., 2019; Petrosino et al., 2020b), as well as rain and seismicity (Petrosino et al., 2018, Scafetta and Mazzarella 2021).

In continuity with the previous studies, in the present work we perform a statistical correlation analysis of the time series of ground tilt, seismicity rates and rainfall amount recorded over 6 years (2015–2021). The results indicate that, although at both Vesuvius and Campi Flegrei ground deformation is sensitive to the input of meteoric water, the two volcanic systems respond in a different way to rain-induced hydrological variations. In particular, at a stressed caldera like Campi Flegrei the rainfall can modulate not only ground deformation on different time scales but also earthquake rate. These observations suggest that the Campi Flegrei dynamics is the result of a complex interplay between endogenous and exogenous processes.

DATA AND METHODS

The borehole tiltmeter network at Vesuvius is currently composed of four instruments (TRC, IMB, CMG and CMT) which started to operate contemporaneously since September 2016 (**Figure 1**). At Campi Flegrei the network consists of three borehole tiltmeters (CMP, ECO and HDM) working since 2015 (**Figure 1**). Both networks are managed by Istituto Nazionale di Geofisica e Vulcanologia, Sezione di Napoli–Osservatorio Vesuviano (INGV-OV). The tiltmeter stations consist of digital sensors model "Lily Self-Leveling Borehole Tiltmeter" equipped with a self-leveling bubble electrolyte with a dynamic range of ±330 μradians and a resolution less than 5 nradians. The tiltmeter package includes a magnetic compass and a temperature sensor. Ground tilt variations are measured along two orthogonal directions NS and EW; they are recorded with a sampling rate of 1 sample per minute. The depths of the bore hole installations range from 20 to 28 m (Ricco et al., 2018).

We used tiltmeter data from October 1st 2016 to March 31st 2021 for Vesuvius, and from April 1st 2015 to March 31st 2021 for Campi Flegrei. The number of VT earthquakes for the same time intervals was obtained by the INGV-OV seismic catalogue, available at the url (https://www.ov.ingv.it/index.php/cataloghi-sismici-vulcani-napoletani?category[0]=73&category_children=1&own=0, last access 2021/04/30). Rainfall amount data sampled at 1 day for Pozzuoli and Torre del Greco towns were downloaded by the historical archive of the website https://www.3bmeteo.com/meteo/ora/storico (last access 2021/04/30).

Borehole tilt signals contain several components: trend (which is often related to the dynamics of the area and consists of net movement), seasonal and tidal deformation, and a residual which is related to isolated events (such as earthquakes), rainfall-induced deformation and short period (less than a few days) fluctuations (Kümpel et al., 2001; Garcia et al., 2010; De Lauro et al., 2018). The typical representation of tilt data (cumulative deformation over a certain time interval; **Supplementary Figure S1**) highlights the long period trend, minimizing short period noise which is often considered as a disturbance to discard. An equivalent way to represent data is by differencing the time series (Chatfield, 2013): in this case data will reveal short term variations, with the trend being removed. Thus, considering the time derivative of the tiltmeter signals is a useful approach to compare the ground deformation with rainfall amount (Breitenberger, 1999; Dal Moro and Zadro, 1998).

For our analyses, we used the differenced ground tilt and calculated the root mean square (RMS) according to:

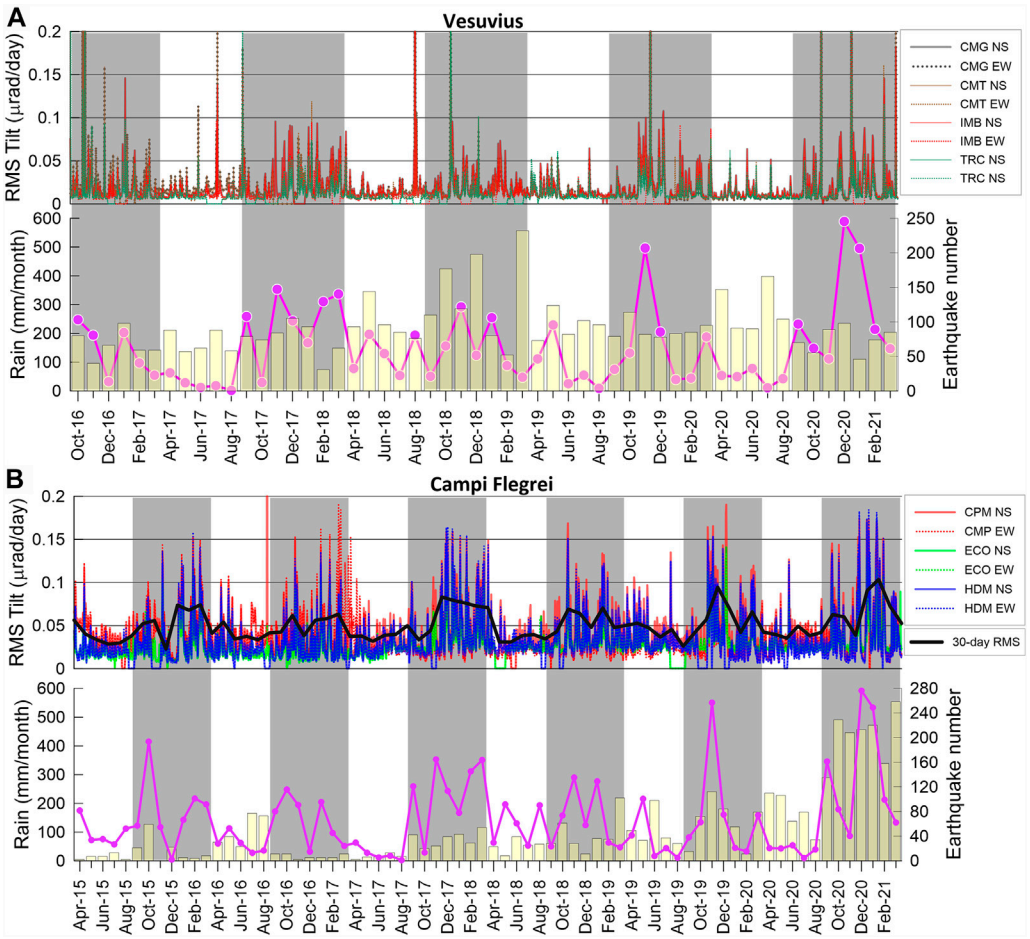

FIGURE 2 | Daily RMS tilt and monthly distribution of rainfall **(purple line)** and earthquakes **(yellow bars)** at Vesuvius **(A)** and Campi Flegrei **(B)**. The light-grey boxes in the background mark the wet season of the hydrological year. For Campi Flegrei, the RMS tilt calculated over a 30-day time window and averaged over the components of all instruments is also shown **(black line)**.

$$x_{rms} = \sqrt{\frac{1}{N}\sum_{i=1}^{N} x_i^2}$$

where x represents the time series and N is the number of samples in the selected time window. After having tried several durations between 1 and 30 days, we chose a 1-day time interval, long enough to stabilize fast ground tilt fluctuations/oscillations, nevertheless still suitable to show evidence of ground deformation at short time scales. This is a good compromise between too much detail and a too generalized overview. Thus, the obtained RMS represents an estimate of the daily average ground tilt.

We estimated the cross-correlation among RMS tilt, rainfall amount and earthquake number in order to obtain an indication of the similarity of the time series as a function of the time lag (Chatfield, 2013). The normalized cross-correlation function is defined as:

$$C_{xy}(k) = \frac{1}{N\sqrt{C_{xx}(0)}\sqrt{C_{yy}(0)}}\sum_{i=1}^{N-k}(x_i - \mu_x)(y_{i+k} - \mu_y)$$

where N is the number of samples, (μ_x, μ_y) and $(\sqrt{C_{xx}(0)}, \sqrt{C_{yy}(0)})$ denote the mean and the zero lag autocorrelation of the time series, and $k < N$ are positive integer values. The maxima (or minima if the signals are negatively correlated) of the cross-correlation function correspond to the points in time where the signals are best aligned. It is important to remark that correlation tests a relationship between two variables, but it does not imply causation.

RESULTS

A generalized overview of the temporal pattern of ground deformation, earthquakes and rainfall throughout the entire time interval of analysis is shown in **Figure 2**, in which we compare the daily RMS of both the components of the ground tilt, and the monthly distributions of VTs and rainfall amount. A simple visual inspection shows the seasonality of the RMS tilt at both Vesuvius and Campi Flegrei areas, reflecting the pattern of

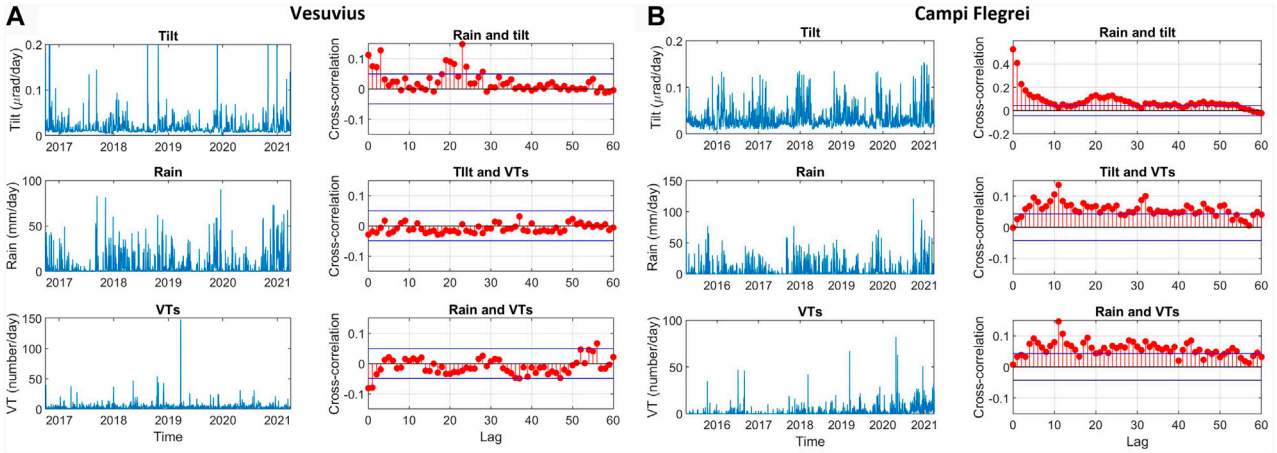

FIGURE 3 | (A) On the left, daily values of RMS tilt, rainfall and earthquake number for Vesuvius. On the right, cross-correlation functions among the three time series (lag = 1 corresponds to 1 day). The blue horizontal lines mark the confidence limits (95%), above which the correlation between the time-series is considered significant. **(B)** On the left, daily values of RMS tilt, rainfall and earthquake number for Campi Flegrei. On the right, cross-correlation functions among the three time series.

the hydrological year (Petrosino et al., 2018). The comparison among the time series indicates a possible correlation among the three physical observables (especially between tilt and rainfall), which appear more evident at Campi Flegrei. The patterns of the RMS tilt (nearly overlapped in **Figure 2**) are almost independent of the site, as confirmed by the estimates of the cross-correlation matrix among the different tilt components and sensors (**Supplementary Figure S2**). Such analysis provides correlation coefficients greater than 0.75 for the tiltmeters installed at both areas (except for TRC site, which has a slight lower value), suggesting a common origin of the observed daily average tilt.

A further observation regards the RMS values of the tilt at Campi Flegrei which are higher than those recorded at Vesuvius: with the exception of few peaks, RMS is far below <0.05 μrad/day in the dry season and <0.1 μrad/day at Vesuvius, while at Campi Flegrei these thresholds are often exceeded. This behavior suggests that the daily induced ground response to rainfall is more prominent at Campi Flegrei.

The cross-correlation analysis of the daily sampled time series provides further insights. In order to have a mean spatial estimate of the cross-correlation functions, at Campi Flegrei we averaged the RMS of the tilt over all the components and instruments. At Vesuvius we excluded the time series recorded at TRC site from the average estimate, considering its lower correlation with the signals acquired at the other three instruments. Moreover, at Campi Flegrei we extracted from the seismic catalogue only earthquakes with inter-event times less than 1 day because it has been inferred that this clustered seismicity (often grouped in intense seismic swarms) is closely related with exogenous processes, while the background seismicity (inter-event times >1 day) accounts for endogenous dynamics (Petrosino et al., 2018).

The results are shown in **Figure 3**. In general, at Vesuvius the correlations among the time series are low ($C(k) < 0.2$). Maxima values of correlation between tilt and rain occur at lags [0–4] and [19–24]. Tilt and VTs as well as rain and VTs are almost uncorrelated at least at the daily time scale (**Figure 3A**). A similar analysis performed only on the ground tilt recorded at TRC site confirms the low degree of correlation among tilt, rain and VTs (**Supplementary Figure S3**).

The cross-correlation among rainfall, ground tilt and earthquakes at Campi Flegrei shows a different pattern. From **Figure 3B**, the maximum value (0.53) of cross-correlation between RMS tilt and the rainfall daily time series is at zero lag (within the 1-day uncertainty which corresponds to the sampling rate of the available rainfall data) suggesting a nearly instantaneous response of the ground deformation to meteoric input. Then, the cross-correlation function smoothly decreases during the first 10 days, indicating a persistent relationship between the two observables. Moreover, although seismicity and tilt, as well as seismicity and rainfall, appear poorly correlated, the corresponding cross-correlation functions have both a maximum value (above the 95% significance level) at a time lag of 11 days.

In order to take into account the eventual delay related to meteoric water diffusion into the ground, at Campi Flegrei data were further analysed by considering the RMS tilt, rainfall amount and VT number calculated over a time window of 30 days. Then we estimated the cross-correlation coefficients from the linear regression between rain and tilt as well as rain and earthquakes (**Figure 4A**). We observed an increase in both the cross-correlation values (0.77 rain and tilt, 0.36 rain and VTs) on 30 days, compared with the daily values. The obtained regression relationship between tilt and rain is:

$$y = 0.026 + 0.000086x$$

The equation provides an intercept value (0.026 μrad) which is consistent with the 30-day RMS tilt observed during dry seasons (black line in **Figure 2B**). In addition, referring to the time interval of 30 days, the regression law predicts an increase of 0.01 μrad/mm of the ground tilt for each increase of 120 mm of rain (which is the median values of the 6-year distribution of the

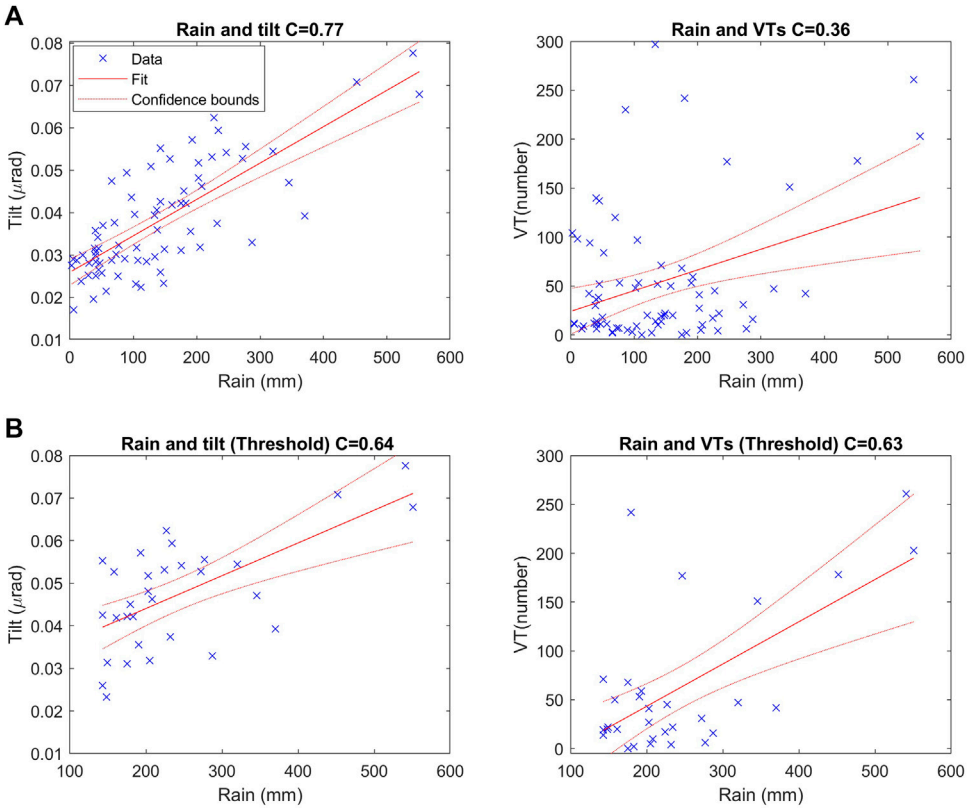

FIGURE 4 | Results of the regression analysis at Campi Flegrei. **(A)** On the left, linear regression between rainfall amount and RMS tilt. On the right, linear regression between rainfall amount and VT number. The red dotted lines mark the 95% confidence interval. All the variables have been estimated over a 30-day moving window. **(B)** On the left, linear regression between rainfall amount and RMS tilt, considering only rainfall values exceeding the 60th percentile of the 6-years distribution. On the right, linear regression between rainfall amount and VT number using the same rain threshold. The red dotted lines mark the 95% confidence interval. All the variables have been estimated over 30-day moving windows.

30-day precipitation amounts; **Supplementary Figure S4**). Such an increase is about two orders of magnitude lower that the monthly variations of the tilt rates related to the volcanic uplift (**Supplementary Figure S1**; https://www.ov.ingv.it/index.php/monitoraggio-e-infrastrutture/bollettini-tutti/bollett-mensili-cf).

We also investigated the possibility of a threshold effect related to heavy and/or long-lasting precipitations. Because the average rainfall amount lies between the 45th and 55th percentiles of the total distribution (Knapp et al., 2015), we extracted only those RMS tilt and earthquake data corresponding to rainfall exceeding the 60th percentile (143 mm in 30 days) of the distribution calculated over 6 years (**Supplementary Figure S4**). In this case, the regression of the 30-day-average data provides correlation coefficients of 0.64 and 0.63 for rain and tilt and rain and VTs, respectively (**Figure 4B**). While the rain and VT cross-correlation increases considering the rainfall threshold, the rain and tilt cross-correlation is slightly higher when no threshold is applied. It is likely that the threshold introduction acts as a cut off for the nearly-instantaneous induced deformation effect and accounts mainly for the contribution related to a diffusive process.

DISCUSSION

Rainfall-induced ground deformations have been observed in many areas, especially for very shallow borehole instrument installations (Goulty, N. R., et al., 1979; Sakata and Sato, 1986; Roeloffs et al., 1989; Westerhaus and Welle, 2002; Kümpel et al., 2001; Lesparre et al., 2017). In our study cases, we notice a different behavior of the two volcanic areas of Vesuvius and Campi Flegrei. At Vesuvius a relationship between rainfall and ground deformation appears on seasonal time scale, as the RMS tilt shows amplitude variations which reflect the pattern of wet and dry seasons of the hydrological year (**Figure 2A**). On the daily time scale, the correlation between rainfall and ground tilt seems low. Moreover, no correlation with earthquakes is further observed at any of the investigated time scales.

At Campi Flegrei both the seasonal patterns of ground tilt (**Figure 2B**) and earthquake rates (**Figure 2B** and **Supplementary Figure S5**) have a striking similarity with the hydrological cycles, as the RMS tilt and VT number are systematically higher during the wet season. Here the seasonal tilt variations are more pronounced compared with those of Vesuvius. In addition, an evident correlation among rainfall,

ground tilt and earthquakes also arises on the time scale of days. In particular, seismicity correlates with both rainfall and tilt (**Figure 3B**), with a delayed response which is focused at best when considering cumulative 30-days values and precipitation threshold (**Figure 4**). This suggests that a complex interplay among the three observables exists and that rainfall could have an impact on the dynamics of the system, as already pointed out in recent papers (Petrosino et al., 2018; Ricco et al., 2019; Petrosino et al., 2020b).

Several mechanisms have been proposed to take into account the possible hydromechanical coupling between rain and ground deformation observed in both tectonic and volcanic environments: among them, the most relevant are: 1) water loading essentially due to the ground compression by the added water mass, and 2) infiltration and diffusion processes which are able to modify the pore pressure of the medium (Kümpel et al., 2001; Westerhaus and Welle, 2002; Lesparre et al., 2017). The theory of poroelasticity (Wang, 2017; Wang and Kumpel, 2003) is able to explain the physical process at the origin of ground deformation related to water infiltration. According to this model, the tilt amplitude is proportional to the pore pressure gradient and depends on the rock poroelastic parameters. In the framework of the poroelasticity theory, variations of the pore-fluid pressure also play an important role in the generation of earthquakes, especially in hydrothermal/volcanic environments (Madonia et al., 2008; Savage et al., 2015; Ricco et al., 2021). Triggering of fluid-induced seismicity can be activated by diffusive processes related to pore pressure and permeability changes in porous and/or fractured saturated rocks (Shapiro et al., 2003; Andajani et al., 2020).

At Campi Flegrei such a mechanism has been invoked to explain the rainfall triggering of VT earthquakes (Scafetta and Mazzarella, 2021). The authors suggest that rainfall water percolates into the highly fractured and water-saturated rocks, mixing with deeper hot hydrothermal fluids, thus inducing pressure and permeability changes. By using a time-delayed rain function to model the diffusion process inside the soil, a delay of some days to 1–2 weeks is estimated so that water percolation affects seismicity in the depth range of 0–2.5 km. In addition, statistical results indicate that time-delayed models, compared to rapid seismic response to water infiltration, provide the highest correlations between the rainfall and seismic events at Campi Flegrei and thus represent the most probable scenario (Scafetta and Mazzarella, 2021).

From our analyses of geophysical time series recorded at Campi Flegrei, both a nearly prompt response to rainfall and a delayed one arise. As inferred in past studies the effect of the rain on ground tilt can be both immediate and delayed (Wyatt and Berger, 1980; Westernhaus and Welle, 2002; Garcia et al., 2010; Lesparre et al., 2017). Recently, Meurers et al. (2021) show that water accumulation on the terrain surface causes short-term (a few hours) tilt and gravity changes, while long-term (>a few days/weeks) variations occur frequently after long-lasting and/or heavy rain. On the other hand, seismic activity often appears as a lagged feedback to precipitations (Muço, 1999; Heinzl et al., 2006; Craig et al., 2017; Scafetta and Mazzarella, 2021). Therefore, on the basis of the existing mechanisms of hydrological response, we hypothesize a combined action of water loading (which is almost instantaneous) mainly effective on the ground deformation, and a diffusion process (on the time scale of 10–30 days), which also affect (besides the tilt) the seismicity. Indeed, the delay of 11 days of earthquake occurrence with respect to rain and ground deformation could likely be related to the time of the percolation of the shallow meteoric fluid in the fracture system of the medium. This is supported by the increase of the cross-correlation values cumulated on 30 days. We also have to consider an additional possible effect of the ground deformation which under the water loading and diffusive process generates itself elastic stress on the rocks, in turn favoring the occurrence of VTs.

Interestingly, the introduction of a threshold for the precipitation amount further increases the correlation between rain and VT number, suggesting that below a certain rainfall rate the diffusion process is only weakly effective in triggering earthquakes. This is consistent with the results of Scafetta and Mazzarella (2021) who found that seismic swarms are more likely to occur during wet days rather than in dry ones (see also **Supplementary Figure S5**). On the other hand, the correlation between rain and tilt slightly decreases when considering a minimum value for the precipitation amount, likely because the threshold could act as a cut off for the nearly instantaneous water loading effect of light rain on the ground deformation.

The results of the present paper provide the ground for systematical investigation of the link among tilt, seismicity and rain, identifying the RMS of instantaneous tilt on short/medium time scale (days, weeks) as a suitable observable which can better highlight (at least at the first-order) ground response to rainfall. Moreover, we have shown how the RMS pattern can enhance the seasonal behavior of the ground tilt time series; therefore it can be used as a quick indicator of seasonality in ground deformation data.

Interesting inferences can be obtained by cross-correlating the rainfall, RMS tilt and earthquake rates. Despite the assumption of a simple linear model to describe the ground response to rain (Garcia et al., 2010), we were able to highlight basic differences between Vesuvius and Campi Flegrei. The clearer response observed at Campi Flegrei, compared to Vesuvius, could be likely related to differences in the fracture density of the medium as well as in rock porosity and permeability (Zollo et al., 2006; Andajani et al., 2020; Ricco et al., 2021). Moreover, at Campi Flegrei the presence of a shallower aquifer, water saturated rocks and geothermal fluids (Gresse et al., 2017) can amplify the rain-induced ground response (Kümpel et al., 2001). The temperatures associated with the hydrothermal system (de Lorenzo et al., 2001; Zollo et al., 2006) and the presence of pressurized gases discharging at Solfatara affect the infiltration and propagation of meteoric water through porous rock and fractures, in turn influencing the poroelastic response of the volcanic system. As a result, Campi Flegrei caldera, differently from Vesuvius, is prone to respond to the stress variations related to pore-fluid pressure changes.

Finally, besides the medium properties and the presence of an active shallow hydrothermal system, a further factor which can control the response to rain-induced hydrological variations is

the state of the volcano. Vesuvius is characterized by a low-level background activity, poorly influenced by external forcing. On the contrary, at Campi Flegrei endogenous processes related to the ongoing unrest likely drive the system towards metastable conditions. Although the rain-induced deformation is two orders of magnitude lower than that related to the volcanic uplift, we can reasonably infer that rainfall can have an impact in modulating the dynamics of such a metastable system, which is more sensitive to exogenous triggering (Petrosino et al., 2018).

The present outcomes are the first steps for the future development of a finer modeling of water load and diffusive processes related to rainfall phenomena. Additional factors such as duration and intensity of the precipitations, pre-rainfall moisture conditions of the soil, rock physical parameters (fracture density, porosity, permeability) and threshold non linear mechanisms (Yamauchi 1987; Dal Moro and Zadro, 1998) should be eventually taken into account with the ultimate goal to determine a more accurate as possible transfer function between rainfall and ground response and seismicity.

DATA AVAILABILITY STATEMENT

The dataset of the daily RMS of the ground tilt at Vesuvius and Campi Flegrei can be found in the Zenodo repository https://doi.org/10.5281/zenodo.5196688. The INGV-OV seismic catalogue is available at the https://www.ov.ingv.it/index.php/cataloghi-sismici-vulcani-napoletani?category[0]=73&category_children=1&own=0. Rainfall amount data were downloaded by the historical archive of the website https://www.3bmeteo.com/meteo/ora/storico.

AUTHOR CONTRIBUTIONS

SP and CR conceived the research study, analyzed data and interpreted the results. IA handled the processing of raw tiltmeter data and drew **Figure 1**. SP wrote the first draft; all the authors read, corrected and approved the final article.

FUNDING

This work is part of the INGV research project LAST: Linked Analysis of Seismic and Tiltmeter observables (Ricerca Libera 2019 - Funding n. 53/2020). Publication fee has been supported by the "Institutional Funding for Editorial Activity" of INGV, Sezione di Napoli - Osservatorio Vesuviano.

ACKNOWLEDGMENTS

We acknowledged the INGV-OV Seismic Laboratory for having compiled the earthquake catalogue, and the INGV-OV Laboratory of Geomatics and Thermography (LGT) for having provided the base maps of **Figure 1**. We wish to thank Vincenzo Augusti for providing regular maintenance of the tiltmeter networks. Two reviewers are acknowledged for their suggestions, which improved the clarity of the article.

SUPPLEMENTARY MATERIAL

The Supplementary Material for this article can be found online at: https://www.frontiersin.org/articles/10.3389/feart.2021.758602/full#supplementary-material

REFERENCES

Andajani, R. D., Tsuji, T., Snieder, R., and Ikeda, T. (2020). Spatial and Temporal Influence of Rainfall on Crustal Pore Pressure Based on Seismic Velocity Monitoring. *Earth, Planets and Space* 72 (1), 1–17. doi:10.1186/s40623-020-01311-1

A. Zollo, P. Capuano, and M. Corciulo (Editors) (2006). *Geophysical Exploration of the Campi Flegrei (Southern Italy) Caldera'Interiors: Data, Methods and Results* (Napoli: GNV (National Group of Vulcanology), Doppiavoce Editore).

Banks, N. G., Carvajal, C., Mora, H., and Tryggvason, E. (1990). Deformation Monitoring at Nevado del Ruiz, Colombia-October 1985-March 1988. *J. Volcanol. Geotherm. Res.* 41 (1–4), 269–295. doi:10.1016/0377-0273(90)90092-T

Bellucci Sessa, E., Castellano, M., and Ricciolino, P. (2021). GIS Applications in Volcano Monitoring: the Study of Seismic Swarms at the Campi Flegrei Volcanic Complex, Italy. *Adv. Geosci.* 52, 131–144. doi:10.5194/adgeo-52-131-2021

Bianco, F., Cusano, P., Petrosino, S., Castellano, M., Buonocunto, C., Capello, M., et al. (2005). Small-aperture Array for Seismic Monitoring of Mt. Vesuvius. *Seismological Res. Lett.* 76 (3), 344–355. doi:10.1785/gssrl.76.3.344

Bragato, P. L. (2015). Italian Seismicity and Vesuvius' Eruptions Synchronize on a Quasi 60 year Oscillation. *Earth Space Sci.* 2 (5), 134–143. doi:10.1002/2014EA000030

Braitenberg, C. (1999). The Hydrologic Induced Strain-Tilt Signal: a Review. *Bull. D'inf. Marées Terrestres* 131 (10), 171–210.

Caputo, T., Cusano, P., Petrosino, S., Sansivero, F., and Vilardo, G. (2020). Spectral Analysis of Ground thermal Image Temperatures: what We Are Learning at Solfatara Volcano (Italy). *Adv. Geosci.* 52, 55–65. doi:10.5194/adgeo-52-55-2020

Chatfield, C. (2013). *The Analysis of Time Series: Theory and Practice*. New York: Springer.

Cioni, R., Bertagnini, A., Santacroce, R., and Andronico, D. (2008). Explosive Activity and Eruption Scenarios at Somma-Vesuvius (Italy): towards a New Classification Scheme. *J. Volcanology Geothermal Res.* 178 (3), 331–346. doi:10.1016/j.jvolgeores.2008.04.024

Craig, T. J., Chanard, K., and Calais, E. (2017). Hydrologically-Driven Crustal Stresses and Seismicity in the New Madrid Seismic Zone. *Nat. Commun.* 8 (1), 1–11. doi:10.1038/s41467-017-01696-w

Cusano, P., Caputo, T., De Lauro, E., Falanga, M., Petrosino, S., Sansivero, F., et al. (2021). Tracking the Endogenous Dynamics of the Solfatara Volcano (Campi Flegrei, Italy) through the Analysis of Ground Thermal Image Temperatures. *Atmosphere* 12 (8), 940. doi:10.3390/atmos12080940

Cusano, P., Petrosino, S., and Saccorotti, G. (2008). Hydrothermal Origin for Sustained Long-Period (LP) Activity at Campi Flegrei Volcanic Complex, Italy. *J. Volcanology Geothermal Res.* 177 (4), 1035–1044. doi:10.1016/j.jvolgeores.2008.07.019

Dal Moro, G., and Zadro, M. (1998). Subsurface Deformations Induced by Rainfall and Atmospheric Pressure: Tilt/strain Measurements in the NE-Italy Seismic Area. *Earth Planet. Sci. Lett.* 164 (1-2), 193–203. doi:10.1016/s0012-821x(98)00203-9

De Lauro, E., Falanga, M., and Petrosino, S. (2012). Study on the Long-Period Source Mechanism at Campi Flegrei (Italy) by a Multi-Parametric Analysis. *Phys. Earth Planet. Interiors* 206-207, 16–30. doi:10.1016/j.pepi.2012.06.006

De Lauro, E., Petrosino, S., Ricco, C., Aquino, I., and Falanga, M. (2018). Medium and Long Period Ground Oscillatory Pattern Inferred by Borehole Tiltmetric Data: New Perspectives for the Campi Flegrei Caldera Crustal Dynamics. *Earth Planet. Sci. Lett.* 504, 21–29. doi:10.1016/j.epsl.2018.09.039

de Lorenzo, S., Gasparini, P., Mongelli, F., and Zollo, A. (2001). Thermal State of the Campi Flegrei Caldera Inferred from Seismic Attenuation Tomography. *J. geodynamics* 32 (4-5), 467–486. doi:10.1016/s0264-3707(01)00044-8

Falanga, M., and Petrosino, S. (2012). Inferences on the Source of Long-Period Seismicity at Campi Flegrei from Polarization Analysis and Reconstruction of the Asymptotic Dynamics. *Bull. Volcanol* 74 (6), 1537–1551. doi:10.1007/s00445-012-0612-2

Farquharson, J. I., and Amelung, F. (2020). Extreme Rainfall Triggered the 2018 Rift Eruption at Kīlauea Volcano. *Nature* 580 (7804), 491–495. doi:10.1038/s41586-020-2172-5

García, A., Hördt, A., and Fabian, M. (2010). Landslide Monitoring with High Resolution Tilt Measurements at the Dollendorfer Hardt Landslide, Germany. *Geomorphology* 120 (1-2), 16–25. doi:10.1016/j.geomorph.2009.09.011

Goulty, N. R., Davis, P. M., Gilman, R., and Motta, N. (1979). Meteorological Noise in Wire Strainmeter Data from Parkfield, California. *Bull. Seismological Soc. America* 69 (6), 1983–1988. doi:10.1785/bssa0690061983

Gresse, M., Vandemeulebrouck, J., Byrdina, S., Chiodini, G., Revil, A., Johnson, T. C., et al. (2017). Three-Dimensional Electrical Resistivity Tomography of the Solfatara Crater (Italy): Implication for the Multiphase Flow Structure of the Shallow Hydrothermal System. *J. Geophys. Res. Solid Earth* 122 (11), 8749–8768. doi:10.1002/2017jb014389

Hainzl, S., Kraft, T., Wassermann, J., Igel, H., and Schmedes, E. (2006). Evidence for Rainfall-triggered Earthquake Activity. *Geophys. Res. Lett.* 33 (19). doi:10.1029/2006gl027642

Knapp, A. K., Hoover, D. L., Wilcox, K. R., Avolio, M. L., Koerner, S. E., La Pierre, K. J., et al. (2015). Characterizing Differences in Precipitation Regimes of Extreme Wet and Dry Years: Implications for Climate Change Experiments. *Glob. Change Biol.* 21 (7), 2624–2633. doi:10.1111/gcb.12888

Kümpel, H.-J., Lehmann, K., Fabian, M., and Mentes, G. (2001). Point Stability at Shallow Depths: Experience from Tilt Measurements in the Lower Rhine Embayment, Germany, and Implications for High-Resolution GPS and Gravity Recordings. *Geophys. J. Int.* 146 (3), 699–713. doi:10.1046/j.1365-246x.2001.00494.x

Lesparre, N., Boudin, F., Champollion, C., Chéry, J., Danquigny, C., Seat, H. C., et al. (2017). New insights on fractures deformation from tiltmeter data measured inside the Fontaine de Vaucluse karst system. *Geophys. J. Int.* 208 (3), 1389–1402. doi:10.1093/gji/ggw446

Madonia, P., Federico, C., Cusano, P., Petrosino, S., Aiuppa, A., and Gurrieri, S. (2008). Crustal Dynamics of Mount Vesuvius from 1998 to 2005: Effects on Seismicity and Fluid Circulation. *J. Geophys. Res. Solid Earth* 113 (B5). doi:10.1029/2007jb005210

Matthews, A. J., Barclay, J., Carn, S., Thompson, G., Alexander, J., Herd, R., et al. (2002). Rainfall-induced Volcanic Activity on Montserrat. *Geophys. Res. Lett.* 29 (13), 22–31. doi:10.1029/2002gl014863

Matthews, A. J., Barclay, J., and Johnstone, J. E. (2009). The Fast Response of Volcano-Seismic Activity to Intense Precipitation: Triggering of Primary Volcanic Activity by Rainfall at Soufrière Hills Volcano, Montserrat. *J. volcanology geothermal Res.* 184 (3-4), 405–415. doi:10.1016/j.jvolgeores.2009.05.010

Mazzarella, A., and Scafetta, N. (2016). Evidences for Higher Nocturnal Seismic Activity at the Mt. Vesuvius. *J. Volcanology Geothermal Res.* 321, 102–113. doi:10.1016/j.jvolgeores.2016.04.026

Meurers, B., Papp, G., Ruotsalainen, H., Benedek, J., and Leonhardt, R. (2021). Hydrological Signals in Tilt and Gravity Residuals at Conrad Observatory (Austria). *Hydrol. Earth Syst. Sci.* 25 (1), 217–236. doi:10.5194/hess-25-217-2021

Muço, B. (1999). Statistical Investigation on Possible Seasonality of Seismic Activity and Rainfall-Induced Earthquakes in Balkan Area. *Phys. earth Planet. interiors* 114 (3-4), 119–127. doi:10.1016/s0031-9201(99)00051-5

Petrosino, S., Cusano, P., and Madonia, P. (2018). Tidal and Hydrological Periodicities of Seismicity Reveal New Risk Scenarios at Campi Flegrei Caldera. *Sci. Rep.* 8 (1), 13808–13812. doi:10.1038/s41598-018-31760-4

Petrosino, S., and Cusano, P. (2020a). Low Frequency Seismic Source Investigation in Volcanic Environment: the Mt. Vesuvius Atypical Case. *Adv. Geosci.* 52, 29–39. doi:10.5194/adgeo-52-29-2020

Petrosino, S., Ricco, C., De Lauro, E., Aquino, I., and Falanga, M. (2020b). Time Evolution of Medium and Long-Period Ground Tilting at Campi Flegrei Caldera. *Adv. Geosci.* 52, 9–17. doi:10.5194/adgeo-52-9-2020

Ricco, C., Petrosino, S., Aquino, I., Cusano, P., and Madonia, P. (2021). Tracking the Recent Dynamics of Mt. Vesuvius from Joint Investigations of Ground Deformation, Seismicity and Geofluid Circulation. *Sci. Rep.* 11 (1), 965–1014. doi:10.1038/s41598-020-79636-w

Ricco, C., Aquino, I., Augusti, V., D'auria, L., Del Gaudio, C., and Scarpato, G. (2018). Improvement and Development of the Tiltmetric Monitoring Networks of Neapolitan Volcanoes. *Ann. Geophys.* 61 (1). doi:10.4401/ag-7496

Ricco, C., Aquino, I., Borgstrom, S. E. P., and Del Gaudio, C. (2013). 19 Years of Tilt Data on Mt. Vesuvius: State of the Art and Future Perspectives. *Ann. Geophys.* 56 (4), S0453. doi:10.4401/ag-6459

Ricco, C., Petrosino, S., Aquino, I., Del Gaudio, C., and Falanga, M. (2019). Some Investigations on a Possible Relationship between Ground Deformation and Seismic Activity at Campi Flegrei and Ischia Volcanic Areas (Southern Italy). *Geosciences* 9 (5), 222. doi:10.3390/geosciences9050222

Roeloffs, E. A., Burford, S. S., Riley, F. S., and Records, A. W. (1989). Hydrologic Effects on Water Level Changes Associated with Episodic Fault Creep Near Parkfield, California. *J. Geophys. Res.* 94 (B9), 12387–12402. doi:10.1029/jb094ib09p12387

Saccorotti, G., Petrosino, S., Bianco, F., Castellano, M., Galluzzo, D., La Rocca, M., et al. (2007). Seismicity Associated with the 2004–2006 Renewed Ground Uplift at Campi Flegrei Caldera, Italy. *Phys. Earth Planet. Interiors* 165 (1-2), 14–24. doi:10.1016/j.pepi.2007.07.006

Sakata, S., and Sato, H. (1986). Borehole-type Tiltmeter and Three-Component Strainmeter for Earthquake Prediction. *J,Phys,Earth* 34 (Suppl. ment), S129–S140. doi:10.4294/jpe1952.34.supplement_s129

Savage, M. K., Ferrazzini, V., Peltier, A., Rivemale, E., Mayor, J., Schmid, A., Massin, F., Got, J.-L., Battaglia, J., DiMuro, A., Staudacher, T., Rivet, D., Taisne, B., and Shelley, A. (2015). Seismic anisotropy and its precursory change before eruptions at Piton de la Fournaise volcano, La Réunion. *J. Geophys. Res. Solid Earth* 120 (5), 3430–3458. doi:10.1002/2014jb011665

Sbrana, A., Cioni, R., Marianelli, P., Sulpizio, R., Andronico, D., and Pasquini, G. (2020). Volcanic Evolution of the Somma-Vesuvius Complex (Italy). *J. Maps* 16 (2), 137–147. doi:10.1080/17445647.2019.1706653

Scafetta, N., and Mazzarella, A. (2021). On the Rainfall Triggering of Phlegraean Fields Volcanic Tremors. *Water* 13 (2), 154. doi:10.3390/w13020154

Shapiro, S. A., Patzig, R., Rothert, E., and Rindschwentner, J. (2003). Triggering of Seismicity by Pore-Pressure Perturbations: Permeability-Related Signatures of the Phenomenon. in" *Thermo-Hydro-Mechanical Coupling in Fractured Rock*. Basel: Birkhäuser, 1051–1066. doi:10.1007/978-3-0348-8083-1_16

Violette, S., de Marsily, G., Carbonnel, J. P., Goblet, P., Ledoux, E., Tijani, S. M., et al. (2001). Can rainfall trigger volcanic eruptions? A mechanical stress model of an active volcano: 'Piton de la Fournaise', Reunion Island. *Terra Nova* 13 (1), 18–24. doi:10.1046/j.1365-3121.2001.00297.x

Wang, H. F. (2017). *Theory of Linear Poroelasticity with Applications to Geomechanics and Hydrogeology*. Princeton: Princeton University Press.

Wang, R., and Kümpel, H. J. (2003). Poroelasticity: Efficient Modeling of Strongly Coupled, Slow Deformation Processes in a Multilayered Half-Space. *Geophysics* 68 (2), 705–717. doi:10.1190/1.1567241

Westerhaus, M., and Welle, W. (2002). Environmental Effects on Tilt Measurements at Merapi Volcano. *Bull. Inf. Marees Terr* 137, 10917–10926.

Wyatt, F., and Berger, J. (1980). Investigations of Tilt Measurements Using Shallow Borehole Tiltmeters. *J. Geophys. Res.* 85 (B8), 4351–4362. doi:10.1029/jb085ib08p04351

Yamauchi, T. (1987). Anomalous Strain Response to Rainfall in Relation to Earthquake Occurrence in the Tokai Area, Japan. *J,Phys,Earth* 35 (1), 19–36. doi:10.4294/jpe1952.35.19

Conflict of Interest: The authors declare that the research was conducted in the absence of any commercial or financial relationships that could be construed as a potential conflict of interest.

Publisher's Note: All claims expressed in this article are solely those of the authors and do not necessarily represent those of their affiliated organizations, or those of the publisher, the editors and the reviewers. Any product that may be evaluated in this article, or claim that may be made by its manufacturer, is not guaranteed or endorsed by the publisher.

frontiers in Earth Science

REVIEW
published: 14 December 2021
doi: 10.3389/feart.2021.777548

Tides and Volcanoes: A Historical Perspective

Gianluca Sottili[1]*, *Sebastien Lambert*[2] and *Danilo Mauro Palladino*[1]

[1]Dipartimento di Scienze Della Terra, Sapienza-Università di Roma, Rome, Italy, [2]SYRTE, Observatoire de Paris, Université PSL, CNRS, Sorbonne Université, LNE, Paris, France

In this paper, we examine the origins and the history of the hypothesis for an influence of tidal forces on volcanic activity. We believe that exploring this subject through a historical perspective may help geoscientists gain new insights in a field of research so closely connected with the contemporary scientific debate and often erroneously considered as a totally separated niche topic. The idea of an influence of the Moon and Sun on magmatic processes dates back to the Hellenistic world. However, it was only since the late 19th century, with the establishment of volcano observatories at Mt. Etna and Vesuvius allowing a systematic collection of observations with modern methods, that the "tidal controversy" opened one of the longest and most important debates in Earth Science. At the beginning of the 20th century, the controversy assumed a much more general significance, as the debate around the tidal influence on volcanism developed around the formulation of the first modern theories on the origins of volcanism, the structure of the Earth's interior and the mechanisms for continental drift. During the same period, the first experimental evidence for the existence of the Earth tides by Hecker (Beobachtungen an Horizontalpendeln über die Deformation des Erdkörpers unter dem Einfluss von Sonne und MondVeröffentlichung des Königl, 1907, 32), and the Chamberlin–Moulton planetesimal hypothesis (proposed in 1905 by geologist Thomas Chrowder Chamberlin and astronomer Forest Ray Moulton) about the "tidal" origin of the Solar System, influenced and stimulated new researches on volcano-tides interactions, such as the first description of the "lava tide" at the Kilauea volcano by Thomas Augustus Jaggar in 1924. Surprisingly, this phase of gradual acceptance of the tidal hypothesis was followed by a period of lapse between 1930 to late 1960. A new era of stimulating and interesting speculations opened at the beginning of the seventies of the 20th century thanks to the discovery of the moonquakes revealed by the Apollo Lunar Surface Experiment Package. A few years later, in 1979, the intense volcanism on the Jupiter's moon Io, discovered by the Voyager 1 mission, was explained by the tidal heating produced by the Io's orbital eccentricity. In the last part of the paper, we discuss the major advances over the last decades and the new frontiers of this research topic, which traditionally bears on interdisciplinary contributions (e.g., from geosciences, physics, astronomy). We conclude that the present-day debate around the environmental crisis, characterized by a large collection of interconnected variables, stimulated a new field of research around the complex mechanisms of mutual interactions among orbital factors, Milankovitch Cycles, climate changes and volcanism.

Keywords: volcanic eruptions, orbital forcing, history of tides, Tidal forces, orbital (Milankovitch) cycles

OPEN ACCESS

Edited by:
David M. Pyle,
University of Oxford, United Kingdom

Reviewed by:
Raffaello Cioni,
University of Florence, Italy
Tushar Mittal,
Massachusetts Institute of Technology, United States

***Correspondence:**
Gianluca Sottili
gianluca.sottili@uniroma1.it

Specialty section:
This article was submitted to Volcanology, a section of the journal Frontiers in Earth Science

Received: *15 September 2021*
Accepted: *29 November 2021*
Published: *14 December 2021*

Citation:
Sottili G, Lambert S and Palladino DM (2021) Tides and Volcanoes: A Historical Perspective. Front. Earth Sci. 9:777548. doi: 10.3389/feart.2021.777548

A PNEUMATIC ORIGIN: TIDES, VOLCANOES AND THE DEEP BREATH OF THE EARTH

In the present review, we will see how the tidal controversy reflected not only the level of contemporary scientific debate but it also stimulated interest and new perspectives on a variety of fields of research including geosciences, climatology, physics and astronomy. In fact, since the beginning, arguments either in favor or against an influence of tidal forces on volcanism were intertwined with important scientific "revolutions", which greatly influenced man's view about the origin of the Earth and of the Solar System. In ancient times, during the VI century BC, Greek philosophers from the Ionian school, beyond the mythological and religious beliefs of their times, attempted a more rational interpretation of natural phenomena, including tides and volcanic eruptions. Under the influence of Anaxagoras (V century BC), Plato in his dialogue Phaedo (IV century BC) hypothesized the existence of great fire rivers and streams of mud under the Earth, flowing together with hot and cold water (Bluck, 2014). It is likely that the Plato's idea of a network of subterranean channels feeding eruptions of mud and fire raised from the direct observation of an eruption at Mount Etna during his first travel in Sicily, in 388-387 BC. Interestingly, he recognized in the fluid nature of "the rivers of mud that flow before the lava in Sicily, and the lava itself" an explanation for a common sensitivity to "a kind of oscillation within the Earth moving all these up and down". Here, the word "oscillation" (gr. Αἰώρα, aiòra; Bluck, 2014) can be translated into "like a twist", thus evidencing the periodic nature of the fluids motion. This is likely the first documented attempt of relating volcanic phenomena to tidal motions, thus assuming a common tidal "sensitivity" for both the hydrosphere and volcanoes. Plato's idea was further reconsidered by Aristotle, who proposed that the periodic oscillation of subterranean fire and water may produce the compaction and the violent movement of air within subterranean channels, causing tremors, eruptions and earthquakes (a translation of Aristotle Meteorologica in Lee, 1952). The idea for a pneumatic origin of earthquakes and volcanic eruptions, due to the sea that enters and moves within hot caves, causing wind storms (Williams, 2006), was later on revised by Lucretius (I century BC) in his De rerum natura (Hine, 2002). Lucretius explained the eruptions of Mount Etna as follows: "First, the mountain's nature is all under-hollow, propped about with caverns of basaltic piers. In all its grottos be there wind and air [. . .] When this air is heated through and through, and, raging round, hath made the earth and all the rocks it touches horribly hot, and hath struck off from them fierce fire of swiftest flame, it lifts itself and hurtles thus straight upwards through its throat into high heaven, and thus bears on afar its burning blasts and scattereth afar its ashes, and rolls a smoke of pitchy murk and heaveth the while boulders of wondrous weight- Leaving no doubt in thee that "tis the air"st tumultuous power. Besides [. . .] the sea there at the roots of that same mount breaks its old billows and sucks back its surf." (translation of *De rerum natura*, VI 680–702 in Godwin, 1991). Later on, after a destructive earthquake occurred in the Mt. Vesuvius area in 62 or 63 CE (Hine, 1984), Seneca in his Natural Questions (for translation see e.g., Hine, 2010) interpreted the observation of "*sudden tidal waves*" inundating settlements and lands after earthquakes—a tsunamis event?- as an evidence for the periodic movements of a subterranean sea; the subterranean, periodic movements of this sea would cause violent movements of unhealthy air, plague, inundations, thus reaffirming the pneumatic origin of seismicity and eruptions. In support of this hypothesis, Seneca interpreted the dead of "hundreds of sheeps [. . .] in the Pompeii area" as an evidence for the fact "that a plague commonly occurs after major earthquakes, and this is not surprising. For many causes of death are lurking deep below: the air itself can be unhealthy for those who breathe it, either through a defect in the earth, or because the air is stagnating inertly in perpetual darkness, or because of contamination by the corrupting effects of subterranean fires". Certainly, to our modern scientific eyes, the "pneumatic" hypothesis for the origin of earthquakes and volcanic eruptions appears eccentric and deeply inadequate. However, the idea of a twisting subterranean world, where the movements of fire and water, and the related expansion of the vapor, may produce hot and unhealthy winds, earthquakes and rumbling volcanic eruptions was one of the most influencing and long-lasting views at least since the second half of the 18th century. In fact, the atmospheric and environmental effects of the Icelandic 1783–1784 Laki flood lava, which emitted ~122 megatons of SO_2 into the atmosphere and maintained a sulfuric aerosol veil that hung over the Northern Hemisphere for >5 months (Thordarson and Self, 2003), was attributed to the exhalations following the destructive Calabrian (South Italy) seismic sequences occurred in 1783 (Hamilton, 1783). Sir William Hamilton, in 1783, wrote: "Several fishermen assured me, that during the earthquake of the 5th of February at night, the sand near the sea was hot, and that they saw fire issue from the earth in many parts. The circumstance has been often repeated to me in the plain; and my idea is, that exhalations which issued during the violent commotions of the earth were full of electrical fire, just as the smoke of volcanoes is constantly observed to be during volcanic eruptions; for I saw no mark, in any part of my journey, of any volcanic matter having issued from the fissures of the earth; and I am convinced, that the whole damage has been done by exhalations and vapours only." Yet, in the early 19th century, the Plato's idea of subterranean fire rivers and hot currents communicating with the exterior of the globe was reported by Alexander von Humboldt (von Humboldt, 1866). However, the beginning of the 19th century was also marked by important changes in the interpretations of volcanism and seismicity. The debate between physicians, early geologists and natural philosophers about the internal state of the Earth will be fed by observations made on Vesuvius, as the early 19th century eruption was "not so small as to be contemptible

not so great as to be unapproachable", as remarked by Humphry Davy in the correspondence with Michael Faraday in 1819 (James, 1991).

In a few years, the dispute about the influence of tides on the molten interior of the Earth will be at the centre of the concomitant debate on the origin of volcanoes. The origin of this dispute will be the subject of the next paragraph.

TIDES AND VOLCANOES DURING THE 19TH CENTURY: BETWEEN SOLIDISM AND FLUIDISM

During the 19th century, the debate around the inner structure of the Earth was fed by conflicting arguments proposed by physicians, geologists and astronomers (*Brush, 1979*). Within this debate, the mainstream idea for the origin of volcanic 'fire' and igneous rocks by combustion of coal or sulphur contrasted with the early experiments of lava remelting conducted by Lazzaro Spallanzani around 1780 (Spallanzani, 1795) who also argued that water vapor is the dominant magmatic gas causing explosions (Sigurdsson, 1999).

The idea of a burning subterranean environment appeared now inadequate, as the origin of the internal heat of the Earth required new hypotheses (Brush, 1979). These include:

- a chemical cause, produced by the reaction of oxidation of metals at depth,
- a solar origin, as the earth's central fire would represent an ejectum from the solar furnace,
- an effect of the compression of materials by the huge pressures at the center of the Earth,
- the transit of the Earth through a hotter region of the space.

Whatever the origin of the Earth's internal heat, the dispute during the 19th century opened two main positions as fluidists, primarily geologists, argued for a fluid interior of the Earth, whilst solidists believed that the Earth is completely solid (Brush, 1979). In this dispute, investigating the influence of tidal forces on volcanism will be of central importance to provide evidence against or in favor of the fluidist theory. André-Marie Ampère, in 1833, evidenced how tidal forces exerted by the Moon on the Earth's enormous liquid interior would render the surface unstable (Brush, 2014):

"Those who assume the liquidity of the interior nucleus of the Earth seem to have forgotten the action which the moon would exert on this enormous liquid mass, an action which would result in tides similar to those of our oceans but much worse, as much by their extent as by the density of the liquid. It is hard to imagine how the envelope of the earth could resist the incessant beating by a kind of hydraulic lever 1,400 leagues in length."

In 1841, the foundation of the world's first volcano observatory at Mt. Vesuvius by King Ferdinand II of Bourbon allowed the collection of systematic observations on volcanic eruptions, which opened a new era in the scientific debate between solidism and fluidism. In 1854, Luigi Palmieri, a physicist and meteorologist, was appointed as the second Director of the Vesuvian Observatory where he developed the first model of electro-magnetic seismograph. During the 1872 eruption at Mt. Vesuvius, Palmieri observed that "precursory signals of eruptions" registered by his seismograph before and during the onset of lava flow episodes, often occurred at sygyzies (Palmieri, 1873). Interestingly, the report of the "Eruption of Vesuvius in 1872" by Palmieri is introduced by an overview on "The present state of knowledge of terrestrial volcanicity" by the fluidist Robert Mallet. In his introduction, Mallet proposes the existence, below a fifteen miles thick solid and cooled crust, of a "universal ocean of liquid material" feeding volcanoes. Also, Mallet contests the solidists' argument (e.g., by William *Hopkins, 1837*) that the claimed internal fluidity of the Earth would be inconsistent with the observed precessional motion and nutation of its axis of rotation due to the combined gravitational attractions of the Moon and the Sun (Brush, 1979). Kelvin hypothesized that Earth started to cool from its original molten state, and based on the Second Law of Thermodynamics, he calculated the age of the birth of the Earth at no more than 400 million years (Burchfield, 2009). Interestingly, Kelvin added a term due to the effects of tidal friction to its thermodynamic balance of the Earth's heat (Burchfield, 2009). On their side, solidists, by rejecting the "central fire" fluidists' hypothesis, opposed a new paradigm: Hopkins, hypothesized the existence of "isolated lakes of liquid rock, existing at comparatively small depths beneath the Earth's surface within the solid and relatively cold crust, each supplying its own volcano" (Palmieri, 1873). By the end of the 19th century, ancient and emerging theories about the feeding mechanisms of volcanoes, i.e., whether the result of communication between the interior and exterior of the globe or the consequence of the drainage of isolated lakes of molten material, will be tested on the grounds of systematic observations of eruptions. In 1892, Annibale Riccò, astronomer and first director of the Astronomic Observatory in Catania (Sicily), noticed a certain synchronism in the main eruptive crises at Stromboli and Etna volcanoes and hypothesized a common cause in the lunisolar action (Riccò and Arcidiacono, 1904). This hypothesis for a common feeding system shared by the two volcanoes was rejected by Giuseppe Mercalli, who also noticed nearly synchronous eruptive crises at Stromboli and Etna in 1865, 1874, 1879, and 1883, although he attributed this phenomenon to the action of a common, endogenous cause (Mercalli, 1892). Later on, in 1907, Mercalli in "The volcanoes of the Earth" confirmed his skepticism about the existence of the "central fire", as the persistence of volcanism in a given location for "only" thousands of years suggests the progressive depletion of local feeding systems (Mercalli, 1907). The 20th century opened new perspectives, as the debate among geoscientists around the origin of volcanism will be fed by innovative monitoring techniques of active volcanoes and will be influenced by new hypothesis on the origins of Earth and Solar System. In the next paragraph, we will see how the debate around the influence of tides on volcanism will benefit from the interdisciplinary contributions of geosciences, astronomy and experimental physics.

THE EARLY 20TH CENTURY: THE DEBATE BETWEEN "FIXISTS" AND "MOBILISTS" AND THE BIRTH OF NEW THEORIES ON TIDES AND VOLCANOES

The 20th century opened with the exposition of new theories on the origin of the Solar System with implications on the hypotheses about the formation and the inner structure of the Earth. In 1906, the geologist T. C. Chamberlin and the astronomer F. R. Moulton published the "planetesimal" or "eruptotidal" hypothesis, according to which the formation of the planets was explained by the gravitational effects of a close encounter of the Sun with another star (Brush, 1978). The new hypothesis by Chamberlin and Moulton, by replacing the nebular hypothesis for the origin of Solar System proposed, among others, by Lord Kelvin, had also a major impact in geosciences. In fact, the birth and growth of Earth was attributed by Chamberlin and Moulton to a slow process of accretion, thus explaining the terrestrial internal heat in terms of a slow "gravitational contraction". The time-scale for Earth's cooling hypothesized by Chamberlin, relatively longer than that predicted by the competing theories, was compatible with the presence of a fluid layer below the crust. Among other inferences on the structure of the Earth, Chamberlin hypothesized a differential motion of parts of the crust, leading, for example, to the building of mountain chains (Brush, 1978). The Chamberlin's model was rejected by physicists like Lord Kelvin, who argued that "the average substance of the Earth is more rigid than steel" and the tidal effects on a fluid layer would have been much higher than those observed (Thomson, 1863).

From a theoretical point of view, the planetesimal theory by Chamberlin and Moulton required quantitative data on the elasticity and plasticity of the Earth to support their hypothesis with convincing arguments against the nebular hypothesis. In this perspective, Chamberlin also proposed an experimental approach to acquire new data about the elasticity of the Earth: these include the experimental determination of the Earth's elastic properties and investigations about the effects of Earth tides on volcanism and seismicity (Gale, 1914). Interestingly, in the same period, Oskar Hecker, a German geodesist and seismologist, presented the first systematic Earth tides observations by means of a horizontal pendulum, thus determining the effective shear modulus for the Earth by direct instrumental observations (Hecker, 1907). Concerning the hypothesized effects of Earth tides on volcanism, the theory of Chamberlin and Moulton intertwined with the formation -and influenced the activity of-the volcanologist Thomas Augustus Jaggar. In 1902, Jaggar was sent by the US government to study the effects of the worst volcanic disasters of the 20th century at Soufrière and Mont Pelée. In his biography, Jaggar annotated "As I look back on the Martinique experience I know what a crucial point in my life it was....I realized that the killing of thousands of persons by subterranean machinery totally unknown to geologists...was worthy of a life work" (Jaggar, 1956). The Jaggar's life worthy work will be the construction of the Hawaiian Volcano Observatory (HVO) where, in 1912, he started systematical measurements of the oscillations of the Kilauea lava lake. The results of the analysis of the lava lake oscillations were published in 1924 (Jaggar, 1924). Jaggar opened the introduction of his manuscript as follows: "Chamberlin has written "pronounced tidal movements might be expected in the necks of volcanoes, if they were connected with large reservoirs of lava below…", thus acknowledging the influence of the contemporaneous scientific debate in astronomy and astrophysics on his work. Jaggar also provided a quantitative evidence for the existence of 'lava tides' (i.e., semidiurnal fluctuation of the Kilauea lava lake level of 2–7 feet) by the direct measurement of the fluctuation of the lava lake surface trough a telescopic alidade (Jaggar, 1924).

In the same period, since the early 1920s, the debate within the Earth Sciences was dominated by the hypotheses on the structure and motion of the Earth's outer surface and by the controversy about the mechanism of continental drift. A comprehensive treatment of the wide scientific debate around the development of the mobilist theory (see e.g., Frankel, 2012) is beyond the aim of the present paper. For our purposes, it is worth attention that one of the main criticisms by the "fixists" to the Wegener's hypothesis on the continental drift was actually focused on the weakness of the causal mechanism. In fact, Wegener postulated that the extensive horizontal displacements of continents can be explained by tidal forces (Frankel, 2012). Surprisingly, one of the strongest objections to Wegener's theory was moved by a non-fixist like Chamberlin, as he stated that tidal forces are too weak to cause continental drift (Chamberlin, 1928).

Mobilists like Van der Gracht, Daly, Joly, and Holmes replied to these objections by modifying Wegener's mechanism of continental drift or by replacing it. Among them, Daly (1911) in his "The Nature of Volcanic Action" wrote: "...if the volcanic mechanism is nicely balanced, a minute effect, like tidal strain, may pull the trigger and renew activity, for which the essential conditions have been long preparing." Here, for the first time, Daly formulated the idea of a "trigger" mechanism by tidal forces on the activity of volcanoes. However, the search for an endogenous mechanism of continental drift seemed to exile definitively the role of tides on volcanism to a background theme. The 1930–1970 was a period of remarkable lapse in the scientific debate around the tidal effects on terrestrial volcanism, with a very few exceptions as, for example, studies about the effects of Earth tides on Atlantic volcanoes (Hekla, La Palma, Fogo, Tristan da Cunha, Askja, Surtsey and San Jorge) by Machado (1967), where tidal forces are described in terms of "a mere trigger-force".

In the next paragraph, we will illustrate how the exploration of the Moon, with the first landing in 1969, and the Voyager missions in the outer Solar System opened a new era of stimulating debate among geoscientists, astronomers and physicists and how it fed interesting speculations around the role of gravitational forces on terrestrial and extra-terrestrial volcanism.

THE SEVENTIES AND THE SPACE EXPLORATION: THE DISCOVER OF MOONQUAKES AND A NEW PARADIGM FROM JUPITER'S MOON IO

After the 1930–1970 lapse, many papers, between 1970 and 1975, focused on the effects of tidal stresses on seismicity and eruptive activity, both at individual volcanoes e.g., at Galapagos (Filson et al., 1973), Stromboli (Johnston and Mauk, 1972), St. Augustine (Mauk and Kienle, 1973), Mt. Ngauruhoe (Michael and Christoffel, 1975) and Kilauea (Shimozuru, 1975) and at a global scale (Hamilton, 1973; Mauk and Johnston, 1973). Interestingly, the early studies by Jaggar (1924) on "lava tides" at Kilauea, apparently forgotten in the previous decades, were acknowledged in the new scientific literature and reinterpreted in light of new data, as for example the Kilauea 1968 eruption (Shimozuru, 1975). This renewed interest on tides and volcanoes emerged during the Moon race which offered both a broad range of advanced space and technology developments and a period of exceptionally stimulating debate around the origin of seismicity and volcanism on planets without plate tectonics. In particular, between 1969 and 1972, during the missions Apollo 11, 12, 14, 15, and 16, a network of seismic stations were installed by astronauts within the ALSEP (Apollo Lunar Surface Experiment Package) and recorded lunar seismicity until September 1977. The early results were published in November 1971 as the seismic network recorded episodes of frequent, small moonquakes (Latham et al., 1971). The seismic energy release, with a few exceptions caused by man-made and meteoroid impacts, appeared modulated by the lunar tidal cycle, with the main peaks occurring at monthly intervals near the time of perigee and a secondary peak near apogee. The exploration of the Moon and the discovery of moonquakes stimulated new hypothesis on the present dynamics of the lunar interior and re-opened a fruitful discussion about the role of tidal stresses on terrestrial seismicity and volcanism.

Overall, it appears that this renewed debate about the role of tides on volcanism is hinged around the idea of a tidal "trigger" mechanism acting on volcanic systems close to a critical state, as already formulated by Daly (1911). To note, among the new hypotheses to explain the trigger mechanism by Earth tides, Mauk and Kienle (1973) explained the tidal modulation of seismicity at St. Augustine volcano in terms of interaction between the orientation of tidal stresses -including the horizontal components- and the stress field of stress related to local structural and geological settings. This new approach will be largely adopted and implemented in the following years, both in terms of structural and geological field studies and theoretical modeling on active volcanoes (Patanè et al., 1994; Jentzsch et al., 2001; Sottili et al., 2007).

A second important discover, stimulating and feeding interesting speculations, occurred in March 1979, when an image captured during the Voyager 1 flyby revealed an eruption on the surface of the Jupiter's moon Io, the most volcanically active body in the Solar System. A few months later, the Voyager 2 provided a new set of images revealing the existence of hundreds of active volcanoes on the Io's surface. This unexpected discovery required the formulation of new hypotheses as, unlike Earth, Io's source of internal heat cannot been explained by radioactive isotope decay. A new model evidenced how the tides induced by Jupiter, enhanced by Io's orbital eccentricity and resonance with Europa and Ganymede, may lead to tidal dissipation and melting of a hypothetical liquid mantle (*Peale et al., 1979*): the volcanism on Io was the first documented example of volcanism exclusively caused by tidal forces.

In the following years, the tidal heating in subsurface oceans of icy satellites of the outer Solar System (i.e., Enceladus and Europa) has been proposed as a long-term energy source generating geysers of water vapor, seismicity (icequakes) and tectonic processes (Crawford and Stevenson, 1988; Greenberg et al., 1998; Hoppa et al., 1999). Once again, new models developed in astrophysics during the seventies influenced and stimulated–up to the present times-the debate around the relationship between tides, volcanism and seismicity within the Moon-Earth system. For example, recently, the tidally modulated icequakes on icy satellites has been modeled by investigating as analog the effects of tidal stresses on icequakes of the Ross Ice Shelf, Antarctica (Olsen et al., 2021). Also, the tidal heating during the early evolution of the Earth-Moon system has been modeled in light of evidence from the tidally generated Io's volcanism; in fact, the tidal heating, partly enhanced by a period of large lunar eccentricity, has been proposed as a potential heat source for the early lunar magma ocean (Touma and Wisdom, 1998).

The following decade opened with the May 1980 Mt St. Helens eruption, the first catastrophic eruption investigated by geoscientists using modern volcanology. The occurrence of the eruption underscored the importance of monitoring precursory activities as a tool to decipher unrest phenomena and eruptive crisis. In this context, the study of geophysical signals jump-started interest in monitoring active volcanoes to improve early warning systems. McNutt and Beavan (1984), noticed that "…the pattern of stress release at Mount St. Helens prior to May 18 was for the most part too rapid to be significantly affected by the Earth tides.". For the first time, the time-varying sensitivity of seismic activity to tidal stresses, as evidenced by volcanic unrest monitoring, was interpreted as indicator of "changing magma movement in the shallow crust beneath the volcano." In the last few decades, many studies focused on the role of tidal stresses in influencing volcanic activity (e.g., Kasahara et al., 2001; Custodio et al., 2003; Sottili et al., 2007; Cigolini et al., 2009; van Manen et al., 2010; Sottili and Palladino, 2012; Bredemeyer and Hansteen, 2014; De Lauro et al., 2018; Girona et al., 2018; Petrosino et al., 2018; Dinger et al., 2019; Pering et al., 2019; Caputo et al., 2020; Dumont et al., 2020; Dumont et al., 2021). On the other hand, the optimism about the interpretation of the time-varying sensitivity of seismic and volcanic activity to tidal stresses as a monitoring tool was partly mediated by critical and skeptical positions (e.g., Sparks, 1981; Hurwitz et al., 2014). Concerning the possible mechanisms of interaction between tidal forces and volcanism, recent works focused on phases of caldera unrest, when the quasi-diurnal and semi-diurnal tidal modulation of long-period seismicity and degassing rates has been explained in terms of fluid charge/discharge in the fractures of hydrothermal systems and/or by tidally induced changes in crustal permeability (e.g., at the Campi Flegrei caldera, Petrosino et al.,2018). Other studies focused on effusive activity, as the modulation of the growth rate of lava

fields by Earth tides has been associated with the effects of tidal stresses on the movements of magmatic fluids - gas, melt and lava - from the upper crust to the Earth's surface, e.g., during the 2014 eruption of Holuhraun, central Iceland (Dumont et al., 2020) and during the 2014–2015 eruption of Fogo volcano, Cape Verde (Dumont et al., 2021). Also, persistent open-conduit phases of explosive volcanic activity modulated by the fortnightly tides have been explained by cycles of compression–decompression of wall rocks influencing the escape of magmatic volatiles and promoting fluid-driven cracking of the country rocks, e.g., at Stromboli volcano, (Sottili and Palladino, 2012) and at Mount Etna (Sottili et al., 2007).

In summary, since the beginning of eighties, a lot of studies contributed to further investigate the influence of tidal forces on volcanic activity and, as in the past two centuries, the new models bear on interdisciplinary contributions from geosciences, physics and astronomy. A full review of the recent literature on this rapidly evolving subject is beyond the aim of the present historical overview. For an exhaustive, critical review of the present state-of-the art see for example Dumont et al. (2022). In the conclusive section we will see how the present-day debate around the environmental crisis, characterized by a large collection of interconnected variables, stimulated a new field of research around the complex mechanisms of mutual interactions among orbital factors, Milankovitch cycles, climate changes and volcanism.

FUTURE RESEARCH DIRECTION: CLIMATE CHANGES, ORBITAL FORCING AND VOLCANISM

Since its beginning, the attention of the scientific community around the tidal controversy appears remarkably influenced by the course of other disputes, as for example the early development of the continental drift theory and the lack of a convincing hypothesis for its causal mechanisms (Chamberlin, 1928). Investigating the origin of tides and their effects on the present state of the Earth influenced the mankind's general understanding of his origin and place in the Universe, either as the result of a series of catastrophic events or, as Kelvin postulated in light of the 2nd Law of Thermodynamics, as a consequence of a slow cooling where the action and intensity of geological forces must decrease with time (Burchfield, 2009). On the other hand, after long periods of lapse, the renewed interest in studying the effects of tidal forcing on volcanism was inspired by new explorations and discoveries from apparently distant fields of research, as astronomy and astrophysics.

Overall, it appears that the tidal controversy was continuously influenced and greatly stimulated by the contemporary scientific debate. The present-day new frontier of the research around the tidal controversy does not represent an exception. In fact, the ongoing environmental crisis, ruled by a complex interconnection of many variables, emphasizes the importance of evaluating quantitatively the contribution of either natural or anthropogenic factors to climate changes. Many studies dealing with palaeoenvironmental and palaeoclimatic reconstructions reveal millennial to million-year timescales of variability due to orbital forcing, based on high-resolution chronologies of sedimentary successions through tephrochronology (Albert et al., 2018; Giaccio et al., 2019; Leicher et al., 2019; Wulf et al., 2020). From a regional to a global scale, increasing evidence for common cycles in the volcanological, biological and astronomical-orbital events includes a remarkable synchronism with Milankovitch cycles, which strongly influenced the Earth's climatic patterns (Kutterolf et al., 2013; Kutterolf et al., 2019; Puetz et al., 2014). On a broader perspective, beyond the high-frequency (from semi-diurnal to fortnightly) tidal forcing of volcanic and seismic activities, low-frequency rotational tides (i.e., pole tide and fluctuations in the Length of Day, LOD) are claimed as major controlling factors for a variety of tectonic and volcanic processes acting both at a local (Lambert and Sottili, 2019) and at a global scale (Palladino and Sottili, 2014; Sottili et al., 2015). Specifically, a recent field of research is devoted to understanding how long-period rotational tide (i.e, monthly to multiyear pole tides and LOD changes) acts on volcanoes, as short-periodic (commonly semi-diurnal to fortnightly tides) forcing influences shallow volatile-saturated magma reservoir or hydrothermal environments (Sottili et al., 2007; Sottili and Palladino, 2012; Petrosino et al., 2018) whilst low-frequency, rotational tidal oscillations are compatible with the resonance time of the lithosphere (Zaccagnino et al., 2020) and with differential stress changes on wall rocks of magma chambers located within the shallow 20 km of the Earth's crust (Sottili et al., 2015; Lambert and Sottili, 2019). Moreover, over the last years, the detection of Milankovitch periodicities in volcanic explosive activity through the Pleistocene-Holocene (Kutterolf et al., 2013, 2019; Praetorius et al., 2016) led to the formulation of a variety of hypotheses on the possible cause-and-effect relationships among orbital forcing, climate changes and volcanism. For instance, the glacio-eustatism hypothesis links the observed Milankovitch periodicities in volcanic activity to crustal stress changes associated with ice age mass redistribution and sea level changes (Rampino and Self, 1993; Ryan et al., 2004; Watt et al., 2013; Praetorius et al., 2016; Rawson et al., 2016). This hypothesis seems to be corroborated by evidence for a subaerial volcanism increase during the last deglaciation phase (Huybers and Langmuir, 2009; Jull and Mc Kenzie, 1996) and during the Messinian salinity crisis in the Mediterranean area (Sternai et al., 2017) whilst the impact of Milankovitch cycle-caused sea level fluctuations on the volcanic construction process at mid-ocean ridges remains an area of active research (e.g., Olive et al., 2015; Goff, 2020).

An alternative hypothesis focuses on the role of crustal stress changes due to orbital oscillations of the inclination of the Earth causing a periodic increase in explosive volcanic activity (Jegen-Kulcsar et al., 2010; Bezverkhnii, 2017) and a perturbation in greenhouse gas emissions from the mantle (Bezverkhnii, 2014; Gilabert et al., 2021). On its turn, the orbital forcing of volcanism and volcanic gas output would play a significant role in determining the 41,000 years variations of the ocean water temperature (Bezverkhnii, 2019). This hypothesis also tries reconciling several difficulties related to the Milankovitch theory in explaining the 100 kyr cycles, since glacial–interglacial oscillations during the pre-mid-Pleistocene

transition are significantly asymmetric, thus contradicting a straightforward linear Milankovitch explanation (e.g., Ashkenazy and Tziperman, 2004).

In conclusion, the article collection in the present volume highlights the enduring interest in external processes interacting at various timescales with volcanic systems. Although progresses in specific instrumental developments and physical modeling have improved our capability to detect tidal signals in volcanic records, the new frontier of the tidal controversy appears -as already occurred in the past- greatly influenced by the contemporary scientific debate across a wide spectrum of research fields including geosciences, climatology, physics and astronomy Auer et al., 2015, Lirer et al., 2009.

AUTHOR CONTRIBUTIONS

All authors listed have made a substantial, direct, and intellectual contribution to the work and approved it for publication.

ACKNOWLEDGMENTS

we thank R. Cioni, T. Mittal and the Editors DP and Valerio Acocella for their helpful suggestions. This review was partly developed within the Tidal Interplate Lithospheric Deformation of Earth (TILDE) project, funded by ESA.

REFERENCES

Albert, P. G., Smith, V. C., Suzuki, T., Tomlinson, E. L., Nakagawa, T., McLean, D., et al. (2018). Constraints on the Frequency and Dispersal of Explosive Eruptions at Sambe and Daisen Volcanoes (South-West Japan Arc) from the Distal Lake Suigetsu Record (SG06 Core). *Earth-Science Rev.* 185, 1004–1028. doi:10.1016/j.earscirev.2018.07.003

Ashkenazy, Y., and Tziperman, E. (2004). Are the 41kyr Glacial Oscillations a Linear Response to Milankovitch Forcing. *Quat. Sci. Rev.* 23, 1879–1890. doi:10.1016/j.quascirev.2004.04.008

Auer, G., Piller, W. E., Reuter, M., and Harzhauser, M. (2015). Correlating Carbon and Oxygen Isotope Events in Early to Middle Miocene Shallow marine Carbonates in the Mediterranean Region Using Orbitally Tuned Chemostratigraphy and Lithostratigraphy. *Paleoceanography* 30, 332–352. doi:10.1002/2014PA002716

Bay, R. C., Bramall, N., and Price, P. B. (2004). Bipolar Correlation of Volcanism with Millennial Climate Change. *Proc. Natl. Acad. Sci.* 101 (17), 6341–6345. doi:10.1073/pnas.0400323101

Bezverkhnii, V. A. (2014). Correlation between 41000-year Rhythms in Variations in the Inclination of Earth, Violent Volcanic Eruptions, and Temperature of Deep Ocean Waters. *Izv. Atmos. Ocean. Phys.* 50 (6), 657–659. doi:10.1134/S0001433814040124

Bezverkhnii, V. A. (2017). Earth's Obliquity Oscillations Can Influence Climate Change by Driving Global Volcanic Activity. *Geosci. Res.* 2 (1), 22–26. doi:10.22606/gr.2017.21004

Bezverkhnii, V. A. (2019). On the 100 000-Year Rhythmicity in Geodynamics and the Paleoclimate. *Izv., Phys. Solid Earth* 55, 488–495. doi:10.1134/s1069351319030017

Bluck, R. S. (2014). *Plato's Phaedo: A Translation of Plato's Phaedo*. London and New York: Taylor and Francis Group. Routledge.

Bredemeyer, S., and Hansteen, T. H. (2014). Synchronous Degassing Patterns of the Neighbouring Volcanoes Llaima and Villarrica in South-central Chile: the Influence of Tidal Forces. *Int. J. Earth Sci. (Geol Rundsch)* 103 (7), 1999–2012. doi:10.1007/s00531-014-1029-2

Brush, S. G. (2014). *A History of Modern Planetary Physics*, 7. Cambridge, United Kingdom: Cambridge University Press.

Brush, S. G. (19781978). A Geologist Among Astronomers: The Rise and Fall of the Chamberlin-Moulton Cosmogony, Part 1. *J. Hist. Astron.* 9 (1), 1–41. doi:10.1177/002182867800900101

Brush, S. G. (1979). Nineteenth-century Debates about the inside of the Earth: Solid, Liquid or Gas. *Ann. Sci.* 36, 225–254. doi:10.1080/00033797900200231

Burchfield, J. D. (2009). *Lord Kelvin and the Age of the Earth*. Chicago: University of Chicago Press. doi:10.7208/9780226080260

Caputo, T., Cusano, P., Petrosino, S., Sansivero, F., and Vilardo, G. (2020). Spectral Analysis of Ground thermal Image Temperatures: what We Are Learning at Solfatara Volcano (Italy). *Adv. Geosci.* 52, 55–65. doi:10.5194/adgeo-52-55-2020

Chamberlin, R. T. (1928). "Some of the Objections to Wegener's Theory," in *Theory of Continental Drift: A Symposium on the Origin and Movement of Land Masses Both Inter-continental and Intracontinental, as Proposed by Alfred Wegener*. Editor W. van Waterschoot van der Gracht (Tulsa: American Association of Petroleum Geologists), 83–87. doi:10.1306/sv2329c3

Cigolini, C., Poggi, P., Ripepe, M., Laiolo, M., Ciamberlini, C., Delle Donne, D., et al. (2009). Radon Surveys and Real-Time Monitoring at Stromboli Volcano: Influence of Soil Temperature, Atmospheric Pressure and Tidal Forces on 222Rn Degassing. *J. Volcanology Geothermal Res.* 184 (3–4), 381–388. doi:10.1016/j.jvolgeores.2009.04.019

Crawford, G. D., and Stevenson, D. J. (1988). Gas-driven Water Volcanism and the Resurfacing of Europa. *Icarus* 73 (1), 66–79. doi:10.1016/0019-1035(88)90085-1

Custodio, S. I., Fonseca, J. F., d'Oreye, N. F., Faria, B. V., and Bandomo, Z. (2003). Tidal Modulation of Seismic Noise and Volcanic Tremor. *Geophys. Res. Lett.* 30 (15), 1816. doi:10.1029/2003gl016991

Daly, R. A. (1911). The Nature of Volcanic Action. *Proc. Am. Acad. Arts Sci.* 47, 48–119. doi:10.2307/20022712

De Lauro, E., Petrosino, S., Ricco, C., Aquino, I., and Falanga, M. (2018). Medium and Long Period Ground Oscillatory Pattern Inferred by Borehole Tiltmetric Data: New Perspectives for the Campi Flegrei Caldera Crustal Dynamics. *Earth Planet. Sci. Lett.* 504, 21–29. doi:10.1016/j.epsl.2018.09.039

Dinger, F., Bredemeyer, S., Arellano, S., Bobrowski, N., Platt, U., and Wagner, T. (2019). On the Link between Earth Tides and Volcanic Degassing. *Solid Earth* 10, 725–740. doi:10.5194/se-10-725-2019

Dumont, S., Custódio, S., Petrosino, S., Thomas, A., and Sottili, G. (2022). "Tides, Earthquakes and Volcanic Eruptions," in *A Tidal Journey through Earth's History*. Editors M. Green and J. C. Duarte (Elsevier).

Dumont, S., Le Mouël, J. L., Courtillot, V., Lopes, F., Sigmundsson, F., Coppola, D., et al. (2020). The Dynamics of a Long-Lasting Effusive Eruption Modulated by Earth Tides. *Earth Planet. Sci. Lett.* 536, 116145. doi:10.1016/j.epsl.2020.116145

Dumont, S., Silveira, G., Custódio, S., Lopes, F., Le Mouël, J.-L., Gouhier, M., et al. (2021). Response of Fogo Volcano (Cape Verde) to Lunisolar Gravitational Forces during the 2014-2015 Eruption. *Phys. Earth Planet. Interiors* 312, 106659. doi:10.1016/j.pepi.2021.106659

Filson, J., Simkin, T., and Leu, L.-k. (1973). Seismicity of a Caldera Collapse: Galapagos Islands 1968. *J. Geophys. Res.* 78, 8591–8622. doi:10.1029/jb078i035p08591

Frankel, H. R. (2012). *The Continental Drift Controversy*. New York: Columbia Univ. Press.

Gale, H. G. (1914). On an Experimental Determination of the Earth's Elastic Properties. *Science* 39 (1017), 927–933. doi:10.1126/science.39.1017.927

Giaccio, B., Leicher, N., Mannella, G., Monaco, L., Regattieri, E., Wagner, B., et al. (2019). Extending the Tephra and Palaeoenvironmental Record of the Central Mediterranean Back to 430 Ka: A New Core from Fucino Basin, central Italy. *Quat. Sci. Rev.* 225, 106003. doi:10.1016/j.quascirev.2019.106003

Gilabert, V., Batenburg, S. J., Arenillas, I., and Arz, J. A. (2021). Contribution of Orbital Forcing and Deccan Volcanism to Global Climatic and Biotic Changes across the Cretaceous-Paleogene Boundary at Zumaia, Spain. *Geology* 2021, 15. doi:10.1130/G49214.1

Girona, T., Huber, C., and Caudron, C. (20182018). Sensitivity to Lunar Cycles Prior to the 2007 Eruption of Ruapehu Volcano. *Sci. Rep.* 8, 1476. doi:10.1038/s41598-018-19307-z

Godwin, J. (1991). "De Rerum Natura IV with An Introduction, Translation and Commentary by John Godwin, " in *Aris & Phillips Classical Texts* (Liverpool University Press). doi:10.2307/j.ctv10tq4r7

Goff, J. A. (2020). "Empirical Prewhitening" Spectral Analysis Detects Periodic but Inconsistent Signals in Abyssal hill Morphology at the Southern East Pacific Rise. *Geochem. Geophys. Geosyst.* 21, e2020GC009261. doi:10.1029/2020GC009261

Greenberg, R., Geissler, P., Hoppa, G., Tufts, B. R., Durda, D. D., Pappalardo, R., et al. (1998). Tectonic Processes on Europa: Tidal Stresses, Mechanical Response, and Visible Features. *Icarus* 135, 64–78. doi:10.1006/icar.1998.5986

Hamilton, W. (1783). *An Account of the Earthquakes in Calabria, Sicily, &c.* London: As Communicated to the Royal Society. Colchester: J. Fenno. doi:10.1098/rstl.1783.0012

Hamilton, W. L. (1973). Tidal Cycles of Volcanic Eruptions: Fortnightly to 19 yearly Periods. *J. Geophys. Res.* 78, 3363–3375. doi:10.1029/jb078i017p03363

Hecker, O. (1907). *Beobachtungen an Horizontalpendeln über die Deformation des Erdkörpers unter dem Einfluss von Sonne und MondVeröffentlichung des Königl*, 32. Berlin: Preuszischen Geodätischen Institutes.

Hine, H. M. (2002) Seismology and Vulcanology in Antiquity? in C. J. Tuplin and T. E. Rihll (eds), *Science and Mathematics in Ancient Greek Culture*, 64–65.

Hine, H. M. (2010). *Seneca. Natural Questions*. University of Chicago Press.

Hine, H. M. (1984). The Date of the Campanian Earthquake. A.D. 62 or A.D. 63 or Both. *L'antiquité classique* 53, 266–269. doi:10.3406/antiq.1984.2130

Hoppa, G., Randall Tufts, B., Greenberg, R., and Geissler, P. (1999). Strike-Slip Faults on Europa: Global Shear Patterns Driven by Tidal Stress. *Icarus* 141 (2), 287–298. doi:10.1006/icar.1999.6185

Hurwitz, S., Sohn, R. A., Luttrell, K., and Manga, M. (2014). Triggering and Modulation of Geyser Eruptions in Yellowstone National Park by Earthquakes, Earth Tides, and Weather. *J. Geophys. Res. Solid Earth* 119, 1718–1737. doi:10.1002/2013JB010803

Jaggar, T. A., Finch, R. H., and Emerson, O. H. (1924). The Lava Tide, Seasonal Tilt and the Volcanic Cycle. *Month. Weather Rev.* 52, 142–145. doi:10.1175/1520-0493(1924)52<142:tltsta>2.0.co;2

Jaggar, T. A. (1956). *My Experiments with Volcanoes*. Honolulu: Hawaiian Volcano Research Association.

James, F. A. J. L. (1991). *The Correspondence of Michael Faraday*, Vol. 1. London: Institution of Electrical Engineers - Engineering and Technology. 1811 to December 1831. Letters 1 to 524.

Jegen-Kulcsar, M., Kutterolf, S., Kwasnitschka, T., and Freundt, A. (2010). *Cyclic Volcanism at Convergent Margins: Linked to Earth Orbital Parameters or Climate Changes*. Vienna: EGU General Assembly, 13373.

Jentzsch, G., Haase, O., Kroner, C., and Winter, U. (2001). Mayon Volcano, Philippines: Some Insights into Stress Balance. *J. Volcanology Geothermal Res.* 109, 205–217. doi:10.1016/s0377-0273(00)00312-7

Johnston, M. J. S., and Mauk, F. J. (1972). Earth Tides and the Triggering of Eruptions from Mt Stromboli, Italy. *Nature* 239, 266–267. doi:10.1038/239266b0

Kasahara, J., Nakao, S., and Koketsu, K. (2001). Tidal Influence on the 2000 Miyake Jima Eruption and its Implications for Hydrothermal Activity and Volcanism. *Proc. Jpn. Acad. Ser. B: Phys. Biol. Sci.* 77 (6), 98–103. doi:10.2183/pjab.77.98

Kutterolf, S., Jegen, M., Mitrovica, J. X., Kwasnitschka, T., Freundt, A., and Huybers, P. J. (2013). A Detection of Milankovitch Frequencies in Global Volcanic Activity. *Geology* 41 (2), 227–230. doi:10.1130/G33419.1

Kutterolf, S., Schindlbeck, J. C., Jegen, M., Freundt, A., and Straub, S. M. (2019). Milankovitch Frequencies in Tephra Records at Volcanic Arcs: The Relation of Kyr-Scale Cyclic Variations in Volcanism to Global Climate Changes. *Quat. Sci. Rev.* 204, 1–16. doi:10.1016/j.quascirev.2018.11.004

Lambert, S., and Sottili, G. (2019). Is There an Influence of the Pole Tide on Volcanism? Insights from Mount Etna Recent Activity. *Geophys. Res. Lett.* 46, 13730–13736. doi:10.1029/2019GL085525

Latham, G., Ewing, M., Dorman, J., Lammlein, D., Press, F., Toksoz, N., et al. (1971). Moonquakes. *Science* 174, 687–692. doi:10.1126/science.174.4010.687

Lee, H. D. P. (1952). *Aristotle. Meteorologica (With an English Translation by H.D.P.Lee)*. Cambridge, Mass. & London: Harvard University Press & Heinemann. (reprinted 1978).

Leicher, N., Giaccio, B., Zanchetta, G., Wagner, B., Francke, A., Palladino, D. M., et al. (2019). Central Mediterranean Explosive Volcanism and Tephrochronology during the Last 630 Ka Based on the Sediment Record from Lake Ohrid. *Quat. Sci. Rev.* 226, 106021. doi:10.1016/j.quascirev.2019.106021

Lirer, F., Harzhauser, M., Pelosi, N., Piller, W. E., Schmid, H. P., and Sprovieri, M. (2009). Astronomically Forced Teleconnection between Paratethyan and Mediterranean Sediments during the Middle and Late Miocene. *Palaeogeogr. Palaeoclimatol. Palaeoecol.* 275 (1-4), 1–13. doi:10.1016/j.palaeo.2009.01.006

Machado, F. (1967). Activity of the Atlantic Volcanoes, 1947-1965. *Bull. Volcanol.* 30, 29–34. doi:10.1007/bf02597652

Mauk, F. J., and Johnston, M. J. S. (1973). On the Triggering of Volcanic Eruptions by Earth Tides. *J. Geophys. Res.* 78, 3356–3362. doi:10.1029/jb078i017p03356

Mauk, F. J., and Kienle, J. (1973). Microearthquakes at St. Augustine Volcano, Alaska, Triggered by Earth Tides. *Science* 182, 386–389. doi:10.1126/science.182.4110.386

McNutt, S. R., and Beavan, R. J. (1984). Patterns of Earthquakes and the Effect of Solid Earth and Ocean Load Tides at Mount St. Helens Prior to the May 18, 1980, Eruption. *J. Geophys. Res.* 89 (B5), 3075–3086. doi:10.1029/jb089ib05p03075

Mercalli, G. (1907). *I Vulcani Attivi Della Terra*. Milano: Ulrico Hoepli.

Mercalli, G. (1892). *Sopra 1'eruzione dell'Etna cominciata il 9 luglio 1892 Atti della Società italiana di Scienze Naturali*. Milano.

Michael, M. O., and Christoffel, D. A. (1975). Triggering of Eruptions of Mt Ngauruhoe by Fortnightly Earth Tide Maxima, January 1972-June 1974. *New Zealand J. Geology. Geophys.* 18, 273–277. doi:10.1080/00288306.1975.10418198

Olive, J.-A., Behn, M. D., Ito, G., Buck, W. R., Escartín, J., and Howell, S. (2015). Sensitivity of Seafloor Bathymetry to Climate-Driven Fluctuations in Mid-ocean ridge Magma Supply. *Science* 350, 310–313. doi:10.1126/science.aad0715

Olsen, K. G., Hurford, T. A., Schmerr, N. C., Huang, M. H., Brunt, K. M., Zipparo, S., et al. (2021). Projected Seismic Activity at the Tiger Stripe Fractures on Enceladus, Saturn, from an Analog Study of Tidally Modulated Icequakes within the Ross Ice Shelf, Antarctica. *J. Geophys. Res. Planets* 126, e2021JE006862. doi:10.1029/2021JE006862

Palladino, D. M., and Sottili, G. (2014). Earth's Spin and Volcanic Eruptions: Evidence for Mutual Cause-And-Effect Interactions. *Terra Nova* 26, 78–84. doi:10.1111/ter.12073

Palmieri, L. (1873). in *The Eruption of Vesuvius in 1872. With Notes and an Introductory Sketch, &c.* Editor F. R. Robert Mallet (.S, (London: Asher and Co.).

Patanè, G., Frasca, A., Agodi, A., and Imposa, S. (1994). Earth Tides and Etnean Volcanic Eruptions: an Attempt at Correlation of the Two Phenomena during the 1983, 1985 and 1986 Eruptions. *Phys. Earth Planet. Interiors* 87, 123–135. doi:10.1016/0031-9201(94)90026-4

Peale, S. J., Cassen, P., and Reynolds, R. T. (1979). Melting of Io by Tidal Dissipation. *Science* 203, 892–894. doi:10.1126/science.203.4383.892

Pering, T. D., Ilanko, T., and Liu, E. J. (2019). Periodicity in Volcanic Gas Plumes: A Review and Analysis. *Geosciences* 9 (9), 394. doi:10.3390/geosciences9090394

Petrosino, S., Cusano, P., and Madonia, P. (2018). Tidal and Hydrological Periodicities of Seismicity Reveal New Risk Scenarios at Campi Flegrei Caldera. *Sci. Rep.* 8 (1), 13808–13812. doi:10.1038/s41598-018-31760-4

Praetorius, S., Mix, A., Jensen, B., Froese, D., Milne, G., Wolhowe, M., et al. (2016). Interaction between Climate, Volcanism, and Isostatic Rebound in Southeast Alaska during the Last Deglaciation. *Earth Planet. Sci. Lett.* 452, 79–89. doi:10.1016/j.epsl.2016.07.033

Puetz, S. J., Prokoph, A., Borchardt, G., and Mason, E. W. (2014). Evidence of Synchronous, Decadal to Billion Year Cycles in Geological, Genetic, and Astronomical Events. *Chaos, Solitons & Fractals* 62-63, 55–75. doi:10.1016/j.chaos.2014.04.001

Rampino, M. R., and Self, S. (1993). Climate-Volcanism Feedback and the Toba Eruption of ~74,000 Years Ago. *Quat. Res.* 40 (3), 269–280. doi:10.1006/qres.1993.1081

Rawson, H., Pyle, D. M., Mather, T. A., Smith, V. C., Fontijn, K., Lachowycz, S. M., et al. (2016). The Magmatic and Eruptive Response of Arc Volcanoes to Deglaciation: Insights from Southern Chile. *Geology* 44, 251–254. doi:10.1130/G37504.1

Riccò, A., and Arcidiacono, S. (1904). L'eruzione Dell'Etna Nel 1892. *Atti Acc. Gioenia Sc. Nat. Catania* 416 (15), 17.

Shimozuru, D. (1975). Lava lake Oscillations and the Magma Reservoir beneath a Volcano. *Bull. Volcanol.* 39, 570–580. doi:10.1007/bf02596977

Sigurdsson, H. (1999). *Melting the Earth; the Evolution of Ideas about Volcanic Eruptions*. New York: Oxford University Press, 250.

Sottili, G., Martino, S., Palladino, D. M., Paciello, A., and Bozzano, F. (2007). Effects of Tidal Stresses on Volcanic Activity at Mount Etna, Italy. *Geophys. Res. Lett.* 34, L01311. doi:10.1029/2006GL028190

Sottili, G., Palladino, D. M., Cuffaro, M., and Doglioni, C. (2015). Earth's Rotation Variability Triggers Explosive Eruptions in Subduction Zones. *Earth Planet. Sp* 67, 208. doi:10.1186/s40623-015-0375-z

Sottili, G., and Palladino, D. M. (2012). Tidal Modulation of Eruptive Activity at Open-Vent Volcanoes: Evidence from Stromboli, Italy. *Terra Nova* 24 (3), 233–237. doi:10.1111/j.1365-3121.2012.01059.x

Spallanzani, L. (1795). *Viaggi alle Due Sicilie e in alcune parti dell'Appennino*. Pavia.

Sparks, R. S. J. (1981). Triggering of Volcanic Eruptions by Earth Tides. *Nature* 290, 448. doi:10.1038/290448a0

Sternai, P., Caricchi, L., Garcia-Castellanos, D., Jolivet, L., Sheldrake, T. E., and Castelltort, S. (2017). Magmatic Pulse Driven by Sea-Level Changes Associated with the Messinian Salinity Crisis. *Nat. Geosci* 10, 783–787. doi:10.1038/ngeo3032

Thomson, W. (1863). *On the Rigidity of the Earth*, 153. London: Philosophical Transactions of the Royal Society.

Thordarson, T., and Self, S. (2003). Atmospheric and Environmental Effects of the 1783-1784 Laki Eruption: A Review and Reassessment. *J. Geophys. Res.* 108 (D1), 4011. doi:10.1029/2001JD002042

Touma, J., and Wisdom, J. (1998). Resonances in the Early Evolution of the Earth-Moon System. *Astron. J.* 115, 1653–1663. doi:10.1086/300312

van Manen, S. M., Kervyn, M., Blake, S., and Ernst, G. G. J. (2010). Apparent Tidal Influence on Magmatic Activity at Oldoinyo Lengai Volcano, Tanzania, as Observed in Moderate Resolution Imaging Spectroradiometer (MODIS) Data. *J. Volcanology Geothermal Res.* 189 (1-2), 151–157. doi:10.1016/j.jvolgeores.2009.11.003

von Humboldt, A. (1866). *Cosmos: Sketch of a Physical Description of the Universe*. New York: Harper & Brothers.

Watt, S. F. L., Pyle, D. M., and Mather, T. A. (2013). The Volcanic Response to Deglaciation: Evidence from Glaciated Arcs and a Reassessment of Global Eruption Records. *Earth-Science Rev.* 122, 77–102. doi:10.1016/j.earscirev.2013.03.007

Williams, G. D. (2006). Greco-Roman Seismology and Seneca on Earthquakes in Natural Questions 6. *J. Rom. Stud.* 96, 124–146. doi:10.3815/000000006784016206

Wulf, S., Keller, J., Satow, C., Gertisser, R., Kraml, M., Grant, K. M., et al. (2020). Advancing Santorini's Tephrostratigraphy: New Glass Geochemical Data and Improved marine-terrestrial Tephra Correlations for the Past ~360 Kyrs. *Earth-Science Rev.* 200, 102964. doi:10.1016/j.earscirev.2019.102964

Zaccagnino, D., Vespe, F., and Doglioni, C. (2020). Tidal Modulation of Plate Motions. *Earth-Science Rev.* 205, 103179. doi:10.1016/j.earscirev.2020.103179

Conflict of Interest: The authors declare that the research was conducted in the absence of any commercial or financial relationships that could be construed as a potential conflict of interest.

Publisher's Note: All claims expressed in this article are solely those of the authors and do not necessarily represent those of their affiliated organizations, or those of the publisher, the editors and the reviewers. Any product that may be evaluated in this article, or claim that may be made by its manufacturer, is not guaranteed or endorsed by the publisher.

frontiers in Earth Science

ORIGINAL RESEARCH
published: 12 January 2022
doi: 10.3389/feart.2021.772176

Low-Temperature Hydrothermal Systems Response to Rainfall Forcing: An Example From Temperature Time Series of Fumaroles at La Soufrière de Guadeloupe Volcano

Jean de Bremond d'Ars[1]* *and Dominique Gibert*[2]

[1]Univ Rennes, CNRS, Géosciences Rennes - UMR 6118, Rennes, France, [2]LGL-TPE, Univ Lyon, Univ Lyon 1, ENSL, CNRS, UMR 5276, 69622, Villeurbanne, France

OPEN ACCESS

Edited by:
Simona Petrosino,
Istituto Nazionale di Geofisica e Vulcanologia, Italy

Reviewed by:
Paolo Madonia,
Istituto Nazionale di Geofisica e Vulcanologia (INGV), Italy
Micol Todesco,
Istituto Nazionale di Geofisica e Vulcanologia (INGV), Italy

***Correspondence:**
Jean de Bremond d'Ars
bremond@univ-rennes1.fr

Specialty section:
This article was submitted to Volcanology, a section of the journal Frontiers in Earth Science

Received: 07 September 2021
Accepted: 17 December 2021
Published: 12 January 2022

Citation:
de Bremond d'Ars J and Gibert D (2022) Low-Temperature Hydrothermal Systems Response to Rainfall Forcing: An Example From Temperature Time Series of Fumaroles at La Soufrière de Guadeloupe Volcano. Front. Earth Sci. 9:772176. doi: 10.3389/feart.2021.772176

Volcanoes with highly-developed and shallow hydrothermal systems may be subject to sudden increases of their surface steam emission at vents in response to either deep forcing (e.g. increase of heat flux coming from the magma chamber) or external forcing (e.g. sudden decrease of atmospheric pressure or variation of meteoric water input). Because the vent plumbing has a limited heat and mass transfer capacity, the rise of steam pressure accompanying the increase of flux may destabilize the system in order to augment its net transfer capacity. This reorganization may, for instance, take the form of an enlargement of existing conduits and vents or to the creation of new ones. In such a case, local and extremely dangerous blast phenomena are likely to occur with devastating consequences several hundreds of meters around. Even volcanoes with a moderate activity and considered safe by the local population are exposed to such abrupt and dangerous events. The detection of early warning signals through temperature monitoring in the vents is of a primary importance and a main difficulty is to correctly interpret temperature jumps in order to reduce false alarms. We analyze time series of the temperature measured in three fumaroles located at the top of La Soufrière volcano in Guadeloupe, which are characterized by their relatively low temperature around 99°C, slightly above the boiling temperature of water at this altitude. Thanks to the long duration of the records from January to August 2017 and to their short 1-s sampling interval, a multiscale analysis can be performed over several orders of magnitude. We show that, despite their complex and sometimes erratic appearance, the temperature variations observed in the vents contain components highly correlated with rain input variations. Some remarkable patterns recurrently appear at different periods and we show that the main temperature variations of more than 10°C are related to the rainfall intensity. Our results illustrate the importance of external forcing on the otherwise complex and possibly chaotic dynamics of the shallow hydrothermal system of La Soufrière. They also reveal that a careful analysis of rainfall forcing must be done to be able to draw any conclusion concerning changes caused by the underlying hydrothermal system.

Keywords: Soufrière volcano, Guadeloupe, rainfall, fumarole temperature, external forcing, hydrothermal system, multiscale analysis, model

INTRODUCTION

A volcano acts as a conveyor of heat and mass from the Earth's interior to the atmosphere, and because of its location at the top part of the magmatic-hydrothermal system, it is prone to important reactions in response to variations of the atmospheric boundary conditions. Beside variations caused by its own dynamics, the atmosphere is subject to external forcing like seasonal variations of the solar radiance and tidal effects. Such a variety of causes results in a wide range of time constants observed in the variations of atmospheric forcing producing more or less important changes in the dynamics of the volcano, depending on its dynamical time constants. Like wind collapsing a bridge when resonance occurs, it is possible that resonance between external forcing and volcano dynamics may affect the volcano behavior. For volcanic areas located in oceanic domains where ocean-atmosphere interaction produces huge atmospheric phenomena like hurricanes, sudden jump of atmospheric pressure and heavy rain may dramatically destabilize volcanoes (Mastin, 1993; Violette et al., 2001; Farquharson and Amelung, 2020; Vittecoq et al., 2020; Scafetta and Mazzarella, 2021). The influence of rainfall on the dynamics of hydrothermal zones is well documented in many areas (e.g. Connor et al., 1993; Richter et al., 2004; Pearson et al., 2008; Diliberto, 2011; Diliberto, 2013; Madonia et al., 2013; Gaudin et al., 2017; Zimmer et al., 2017; Della Seta et al., 2021) most of them considering high-temperature systems, over 300°C. We will focus here on a lower-temperature hydrothermal system where fumaroles release gases around 99 °C, slightly above the boiling point of water.

La Soufrière de Guadeloupe volcano possesses a highly-developed hydrothermal system, subject to heavy rain input, where heat and mass transfers are ensured by hot hydrothermal fluids emitted by springs and fumaroles (Komorowski et al., 2005; Jessop et al., 2020). It can be considered as belonging to the volcanic subclass of "wet volcanoes" (Gunawan et al., 2017) offering monitoring challenges and research monitoring opportunities. Fumaroles can be seen as the ultimate end-part of the fracture network draining the thermal energy from deep under the lava dome toward the surface and, because of the relatively small number of outlets compared to the supposed size of the drained volume, it is likely that the fracture network has an arborescent structure with many deep-seated cracks converging toward the fumaroles (Jacob et al., 2005; Tamburello et al., 2019). Such a structure has a transport capacity limited by the upper end-part of the network which is particularly exposed to external atmospheric forcing, particularly rain inputs. Massive rainfall occurring during a short time period could provoke sudden steam collapse in the shallower part of the hydrothermal system accompanied by important pressure jumps able to initiate strong hammer water phenomena. Although not documented for volcanoes, this type of hazard is well-known in industrial applications (e.g. Urban and Schlüter, 2014; Mahmoudi et al., 2018) and could contribute to the mechanical weakening of a volcano.

Hydrothermal explosions occurring on "wet" active volcanoes represent a major risk if located nearby populated areas or tourists attracting sites (Rouwet et al., 2014; Erfurt-Cooper, 2018). The event of September 2014 on the Ontake volcano (Japan) where 63 persons were killed (data from EM-DAT, CRED/UCLouvain, Brussels, Belgium – www.emdat.be) illustrates the dangerousness of these highly explosive events that often occur without clear warning (Kaneko et al., 2016; Sandri et al., 2017). As recently stated in a US National Academy of Science report (National Academies of Sciences Engineering and Medicine, 2017), most unrest episodes of volcanoes start in hydrothermal systems and many phreatic eruptions occur without warning during periods of repose (Cyranoski, 2014; Fritz, 2014; Williams, 2014). As emphasized in a recent issue of Advances in Volcanology (Fearnley et al., 2018), understanding the dynamics of hydrothermal systems is an important challenge to win to predict dangerous events of hydrothermal origin (Erfurt-Cooper, 2018; Stix and de Moor, 2018). This appeals for an improvement of monitoring methods to follow temporal variations of fluid movements and pressure build-up susceptible to cause sudden and potentially deadly destabilization of hydrothermal systems. A better anticipation would be possible if reliable information concerning the dynamics and the state of the deep parts of the hydrothermal system may be extracted from the complex signals obtained with the monitoring set-up. In particular, it is of a primary importance to understand the effects of external forcing and remove variations imputable to forcing from the data time series in order to isolate information related to internal changes. Sudden external events (e.g. heavy rains, atmospheric pressure drop due to hurricanes) constitute short-time and intense forcing signals able to reveal impulse response of the volcano system. For instance, such events may be used to infer the typical time-scale of return to equilibrium. For complex systems like volcanoes, long time-constant may be due to the appearance of the so-called critical slowing down phenomenon which, in many instances may indicate that the system state is approaching a tipping point. In such a situation, the system becomes unstable and highly sensitive to small perturbations that can cause significant changes in its dynamics (Dakos et al., 2008; Scheffer et al., 2012).

In the present paper, we study in detail the influence of rain forcing on the temperature variations measured in three nearby fumaroles located in the South crater of la Soufrière de Guadeloupe volcano. We show that rain events produce signals at very different time-scales in the temperature time series, making the interpretation of the observed temperature variations in the vents particularly delicate. To isolate signal components related to changes in the dynamics of the deep parts of the hydrothermal system, it is necessary to carefully account for the rainfall history during the preceding days, weeks and months. Because of the specificity of each vent and near-surface hydrothermal system, some training of the analysis procedure is necessary before being able to identify warning signal indicating that thermodynamic conditions

changed underground. It is then necessary to implement monitoring systems sufficiently early in order to acquire a training data set.

La Soufrière de Guadeloupe is an andesite volcano located in the French West Indies (**Figure 1**) and is amongst the most active and potentially dangerous volcanoes of the Lesser Antilles Arc (Komorowski et al., 2005). Its phreatic last eruptions occurred in 1975-1977 (Feuillard et al., 1983) and since then an intense fumarolic activity is widespread at the summit of the dome with the emergence of new high flux fumaroles in recent years (Jessop et al., 2020; Moretti et al., 2020). Located in a tropical area, the hydrothermal system is fed by heavy rains, with an average annual cumulated rainfall over 7,000 mm/yr (Météo France data, http://pluiesextremes.meteo.fr, February 23, 2016 edition). Amongst all the active vents showing an important fumarolic activity on top of the dome (Jessop et al., 2020), we selected the South Crater area (SC) where three vents are instrumented, namely the northern (NSC), centre (CSC) and southern (SSC) fumaroles (**Figure 1**).

MEASUREMENT METHODS

The data were acquired with a Gantner Instruments Qstation connected to 24 bits A/D A107 Qbloxx modules *via* a RS485 bus. The Qstation is equipped with a GPS receiver providing a common time base to all modules. The sampling rate is 1 s and the data are transmitted to the Guadeloupe Volcano Observatory (OVSG) through a long-range Wi-Fi link. Platinum Pt1000 probes are used to measure the temperature in the fumarole vents. Because of the harsh environmental conditions, the Pt1000 are coated in a sealed Fluorinated Ethylene Propylene (FEP) tube. The inner diameter of the FEP tube is chosen to tightly fit the Pt1000 probe and ensure a good thermal conduction. This enables a fast time-response of the probe to abrupt temperature change. As it can be seen in **Figure 2**, the time constant of the response is less than 2 min. In the present study, the original 1-s time series are averaged over a 1-min sampling interval. Depending on the local configuration, the Pt1000 are inserted between 0.5 and 1 m in the fumarole conduit in order to minimize exterior perturbations like direct Sun or rain exposure. The meteorological data (wind, rain, pressure, atmospheric temperature) come from the weather station maintained by the OVSG, located at the northern peak (**Figure 1**), about 200 m north of the South Crater and at about the same altitude around 1,411 m.

Multiscale Forcing of Shallow Hydrothermal Activity by Rain Input

The three temperature time-series for the South crater vents from January to August 2017 are shown in **Figure 3**. Depending on the considered period, the time series are variably correlated and synchronized at short time scales. However, all curves share an identical and in-phase long-period appearance consisting in repeated patterns with a progressive temperature rise followed by a sharper temperature decrease. Despite its huge complexity, the CSC temperature curve has an upper envelope identical to the NSC curve.

Long-Period (months) Correlation Between Rain and NSC Temperature Time Series

Among the three temperature curves of **Figure 3**, the NSC temperature time series $T_{NSC}(t)$ is the most continuous and we shall focus on this data set to study the long-period forcing caused by rain input. We first look for a possible long-term forcing of the fumarole activity by meteoric water input. For this purpose, causal cumulative time series $RC_{\Delta t}(t)$ of rainfall are constructed for different duration Δt of rain accumulation:

$$RC_{\Delta t}(t) = \int_{t-\Delta t}^{t} R(\tau)\, d\tau \qquad (1)$$

$R(t)$ is the instantaneous rain and $RC_{\Delta t}(t)$ represents the amount of rainfall during a time period of Δt days preceding time t.

The cross-correlation between $RC_{\Delta t}(t)$ and $T_{NSC}(t)$ is computed for each value of the integration period Δt (**Figure 4A**), and we find that $RC_{\Delta t}(t)$ and $T_{NSC}(t)$ are maximally anti-correlated for Δt = 18 days (**Figures 4A, B**). A visual comparison between $RC_{\Delta t=18}(t)$ and $T_{NSC}(t)$ (**Figures 4C, D**) suggests that, although globally achieved, the anti-correlation is not constant over the considered time period. This is quantitatively assessed with the sliding linear correlation curve of **Figure 4E** where the size of the sliding window equals 18 days. The variations of correlation are moderate in January and February before vanishing in March with a very good anti-correlation near -1 during the whole month. April is characterized by a restart of the correlation variations whose amplitude increases in the second half of the month. The May to August period is characterized by large amplitude variations of the correlation with a pseudo period of roughly 1 month, i.e. nearby to the monthly modulation of the luni-solar tide. We emphasize that the variation pattern of the sliding correlation of **Figure 4E** follows the recognized seasonal modulation of the Guadeloupe climate: monthly rainfall are 830, 600, 680, 970, 1,340, 1,080, 1,300 and 1,690 mm/month respectively from January to August .[1]

Medium-Period (weeks) Forcing of Rain Input

At intermediate time-scales, and neglecting the short-time variations discussed below, the temperature time series at NSC (**Figure 4C**) appears as a piece-wise linearly segmented curve, indicating that the temperature roughly increases, decreases or remains constant during time periods of one or 2 weeks. This may be explained by the fact that rain events bring cold water

[1]https://donneespubliques.meteofrance.fr/?fond=donnee_libre&prefixe=BCA&extension=pdf&station=971&date=2017)

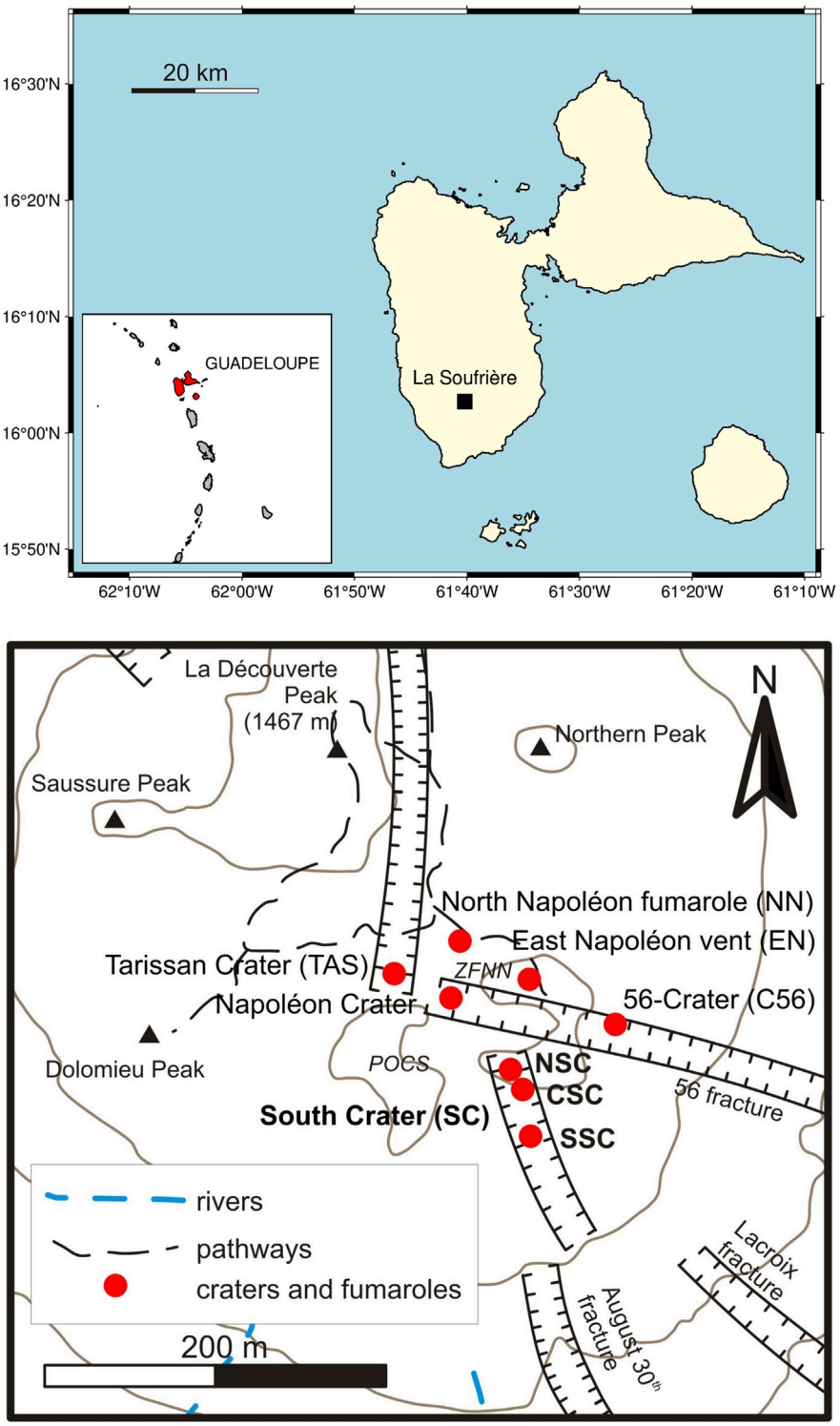

FIGURE 1 | Top: location map of Guadeloupe Island in the West Indies archipelago and of La Soufrière on Guadeloupe. Bottom: detailed map of the summit area of La Soufrière lava dome. The three active vents within the South Crater (SC) are the northern (NSC), center (CSC) and southern (SSC) craters.

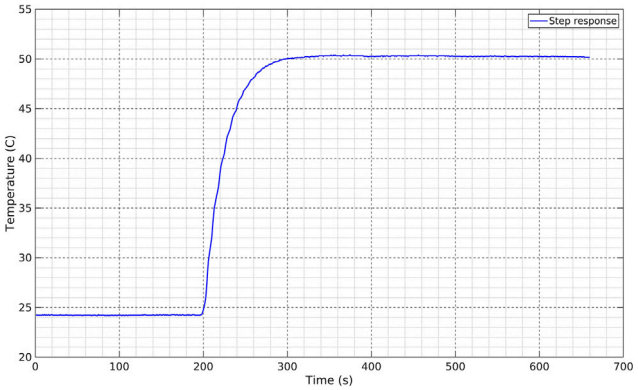

FIGURE 2 | time response of Pt1000 temperature probe obtained by suddenly immersing the probe in hot water.

underground, and depending on the balance between the amount of meteoric water supplied to the system and the energy flux coming from below, the fumarole temperature will either increase, decrease or remain constant.

We used the Shape Language Modeling tool (D'Errico, 2017) to perform a linear piece-wise decomposition of the temperature curve at NSC (**Figure 5A**). Each linear segment represents a situation where the temperature variation is steady, i.e. the temperature steadily decreases, remains constant or increases. The slope of each linear segment represents the temperature variation rate (°C day^{-1}) during the considered time interval. In order to document the influence of rain input on the temperature variation rate, we computed the rainfall rate [mm day^{-1}] for each time period of linear segment in **Figure 5A**. As it can be observed, the temperature variation rate is linearly correlated with the average rainfall rate (**Figure 5B**). Most data points (in red) are well aligned with a maximum likelihood bootstrapped slope of -0.021 ± 0.002 (°C day^{-1})/(mm day^{-1}) (**Figure 5C**). The bootstrapped linear regressions allow to compute the histogram (**Figure 5D**) of the intercepts of the fitted straight lines with the horizontal axis of **Figure 5B**. The maximum likelihood intercept equals 25 ± 0.6 mm day^{-1} and represents the rain rate necessary to maintain a steady fumarole temperature. The significance of the negative slope is established with a bootstrapping procedure that allows to determine the likelihood curve of each parameter, namely the slope and the intercept with the horizontal axis (**Figure 5B**). The slope probability curve (**Figure 5C**) is entirely supported in the negative part of the axis and rules out the possibility of a null or positive slope.

Short-Period (days) Correlation Between Rain and NSC Temperature Time Series

A close inspection of the temperature curve at NSC (**Figure 4C**) shows that the temperature variations have a short time-scale saw-tooth appearance with sharp decreases followed by regular temperature increases. These saw-tooth patterns are of variable duration and amplitude. In order to document the relationship

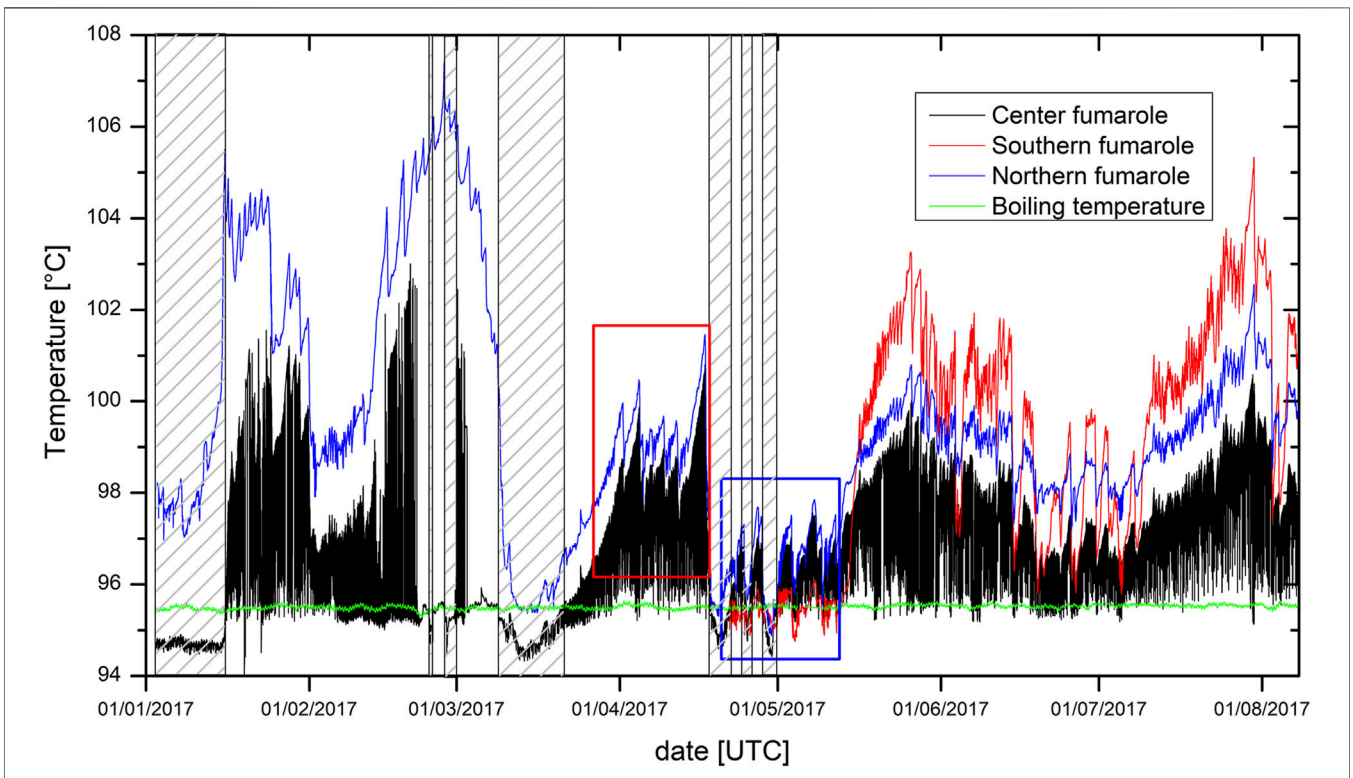

FIGURE 3 | Temperatures in the center, southern and northern fumaroles of the South Crater. Boxes with hatched pattern are when the Center fumarole temperature is below the boiling temperature of water (see part 3.4). Red and blue boxes are "hot" and "cold" periods of the northern fumarole discussed in part 4.2.

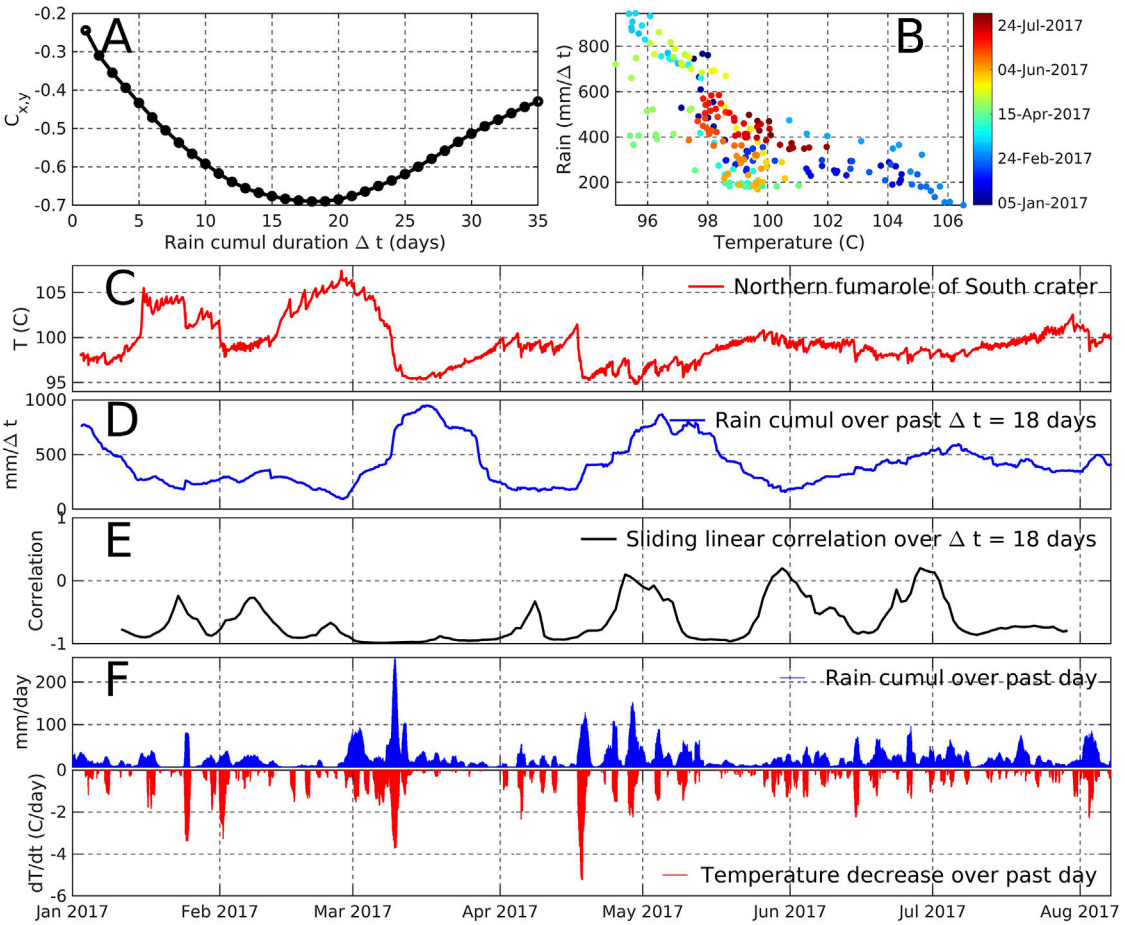

FIGURE 4 | Long- and short-term correlation between rain and temperature at NSC **(A)** Best correlation value obtained for different durations of rain accumulation. The best anti-correlation is for Δt = 18 days **(Eq. 1) (B)** Scatter plot of cumulated rain data for Δt = 18 days and NSC temperature **(C)** NSC temperature time series **(D)** Cumulated rain for Δt = 18 days **(E)** Linear correlation coefficient between cumulated rain and NSC temperature derived for a sliding window of 18 days **(F)** Mirror plot of cumulated rain for Δt = 1 day and of 1-day temperature difference at NSC **(Eq. 2)**.

between the onset of saw-tooth events in the NSC temperature curve and rain events, we compute the finite-difference time-derivative,

$$\Delta T_{NSC}(t) = \frac{T_{NSC}(t) - T_{NSC}(t - \Delta t)}{\Delta t} \qquad (2)$$

where Δt = 1 day. The negative part of $\Delta T_{NSC}(t)$ corresponds to temperature decreases and takes large values at occurrences of the sharp decreases in the saw-tooth patterns. When plotted against $RC_{\Delta t}(t)$ for Δt = 1 day (**Figure 4F**), we observe that all sharp decreases of the temperature fall in front of rain inputs.

The data analysis presented in **Figure 4** shows the existence of a good correlation between the long-term variations of the temperature at NSC and rain input. However, we observe that the long-term variations of $T_{NSC}(t)$ are actually composed of sequences of successive saw-tooth like features whose initial sharp jumps are triggered by short-term rain inputs (**Figure 4C**). We may conclude that long-term temperature variations mainly result from clustering of rain events occurring at short time-scale. This behavior is also observed in the CSC and SSC temperature curves indicating that rain inputs, even of small amplitude, perturb the shallow hydrothermal system at all the three fumaroles of the South crater.

Periodicity in CSC Time Series

The centre fumarole temperature T_{CSC} shows a particular behaviour (**Figure 3**) which is not observed in the other vents and thus deserves specific consideration. It oscillates between a high-temperature end-member, whose long-term variations are similar to the NSC temperature, and a low temperature end-member, close to the boiling temperature of water. This boiling temperature T_{boil} was estimated from measured pressure data P at the top of the dome, (ranging between 852 and 862 hPa, with an average value of 858 hPa) using the formula deduced from standard steam properties tables between 600 and 1,600 hPa

$$T_{\text{boil}} = 129.73521 - 77.45346 \exp\left(-9.5149\, 10^{-4} P\right) \qquad (3)$$

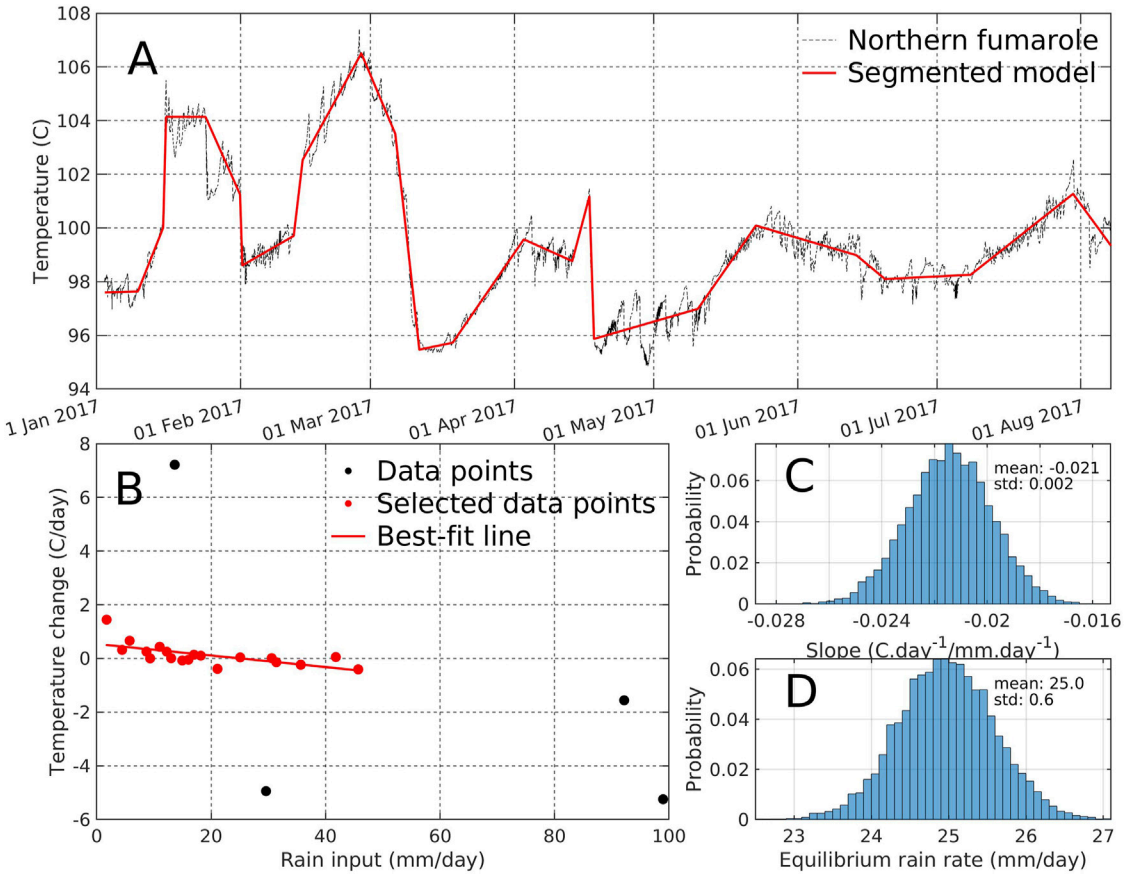

FIGURE 5 | Correlation between long-period temperature variations at the NSC vent and the input of meteoric water **(A)** Temperature time series at NSC (thin black line) and its segmented optimal approximation (red solid line) **(B)** Correlation between the mean rain input during each linear segment of the red line in **(A)** and the temperature drift (i.e. slope of the linear segment). Outliers in black are not taken into account for calculating the best-fit line **(C)** Probability distribution of the bootstrapped slope of the best-fit line in B **(D)** Probability distribution of the bootstrapped intercept of the best-fit line in B with the horizontal axis. This "equilibrium rain rate" corresponds to the amount of meteoric water input required to obtain a constant steam temperature at the fumaroles.

The T_{CSC} variations show periodic fluctuations with varying period along time which we studied by measuring the periodicity between times when T_{CSC} (the 1-Hz raw data being processed by a median filter to eliminate outliers) decreases by more than 0.1°C. This periodicity was averaged over a 24-h period and the results are shown in **Figure 6**. The red columns correspond to times where T_{CSC} is less than T_{boil} which are also shown as hatched boxes in **Figure 3**. We clearly see that this corresponds to longer time-periods. The inset of **Figure 6** shows that when T_{CSC} is greater than T_{boil} (black symbols), the time-period is less than 3 h and that the oscillations are roughly correlated with T_{CSC}. This observation is consistent with the experimental results obtained by Chen et al. (2015) (see their Fig. 17) who observed that the higher the heat flux supplied to a geysering system, the shorter its eruptive period. In our case, rain input temporarily captures a part of the heat flux coming from the deep hydrothermal reservoir, leaving the geysering system with less thermal energy to rebuild the steam pressure necessary to eject a pulse of hotter steam in the centre vent (also see Fig. 11 in Namiki et al., 2016).

NUMERICAL MODEL OF HEAT AND MASS TRANSFER BUDGET

Model Design

The linear dependence of the vent temperature variation with respect to the rate of meteoric water supplied to the system (**Figure 5B**) resembles a classical mixing between two reservoirs with different temperature. However, in the present instance, we must account for both phase change from liquid to vapor, and heating due to the deep hydrothermal system.

The fact that a rain rate of 25 ± 0.6 mm.day^{-1} maintains a constant vent temperature (**Figure 5D**) indicates that some regulation process is required to stop the increase of the steam pressure underground. This may be represented by a simple model where a reservoir of boiling liquid is connected to a high-permeability outlet representing the fumarole conduit and to an inlet formed by a low-permeability distributed fracture network draining the meteoric water (**Figure 7**). We assume that the temperature variations measured in the vents are due to

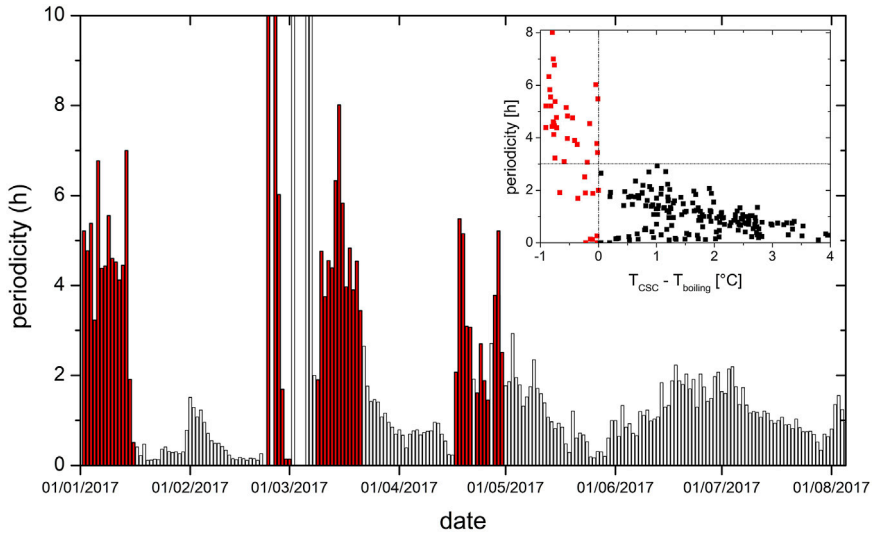

FIGURE 6 | Time periodicity of the Centre fumarole temperature (CSC). Red columns correspond to periods when the centre fumarole temperature (T_{CSC}) is less than the boiling temperature ($T_{boiling}$) **(**see **Figure 3)**. Inset: periodicity vs overheating of the Centre fumarole.

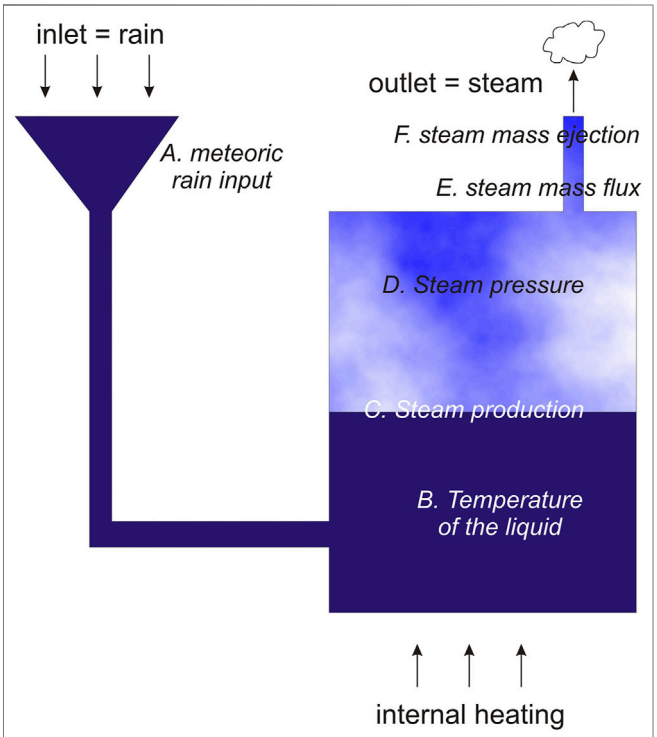

FIGURE 7 | Main parts of the shallow hydrothermal system connected to the South Crater vents with indication of the main parameters of the numerical model whose results are shown in **Figure 8**.

changes of the steam pressure *p* which depends on the amount of steam production in the upper part of the reservoir (**Figure 7**).

The steam production depends on the balance between the energy necessary to warm-up the liquid receiving fresh meteoric water and the remaining energy available to produce steam. Clearly, this balance directly depends on the amount of meteoric water supplied to the reservoir. For high-level steam production, the pressure increase in the reservoir induces a rise of the boiling temperature and a reduction of the steam production follows. Meanwhile, the steam ejected at the outlet reduces the reservoir pressure and the boiling temperature decreases. Thus the steam production and the steam ejection respectively play the role of a negative and of a positive feedback able to induce sustained oscillations.

We constructed a simple numerical model comprising the elements of **Figure 7** to illustrate the phenomenology associated with the processes described above and not to represent the real situation (i.e. thermal power, volume, etc.). The model is not made to represent the reality of the shallow hydrothermal system but aims at reproducing the main processes observed in the data, namely the forcing of rainfall on the fumarolic activity. The pressure and temperature dependence of latent heat are taken into account as well as the volume variation of the upper part of the reservoir in response to rain input and water evaporation. The simulation starts with a given amount of boiling liquid (1,000 kg) and the upper part of the reservoir (1 m^3) filled with steam under pressure (1.05 bar). The atmospheric pressure is taken constant at 0.8 bar and the thermal power equals 10 kW. The mass and energy budget (i.e. meteoric water input, steam production, steam ejection, boiling energy, heating energy) is updated at each 1-s time step during which a small amount of meteoric water may be introduced into the reservoir. The fumarole vent is represented as a pipe for which the steam mass flux is proportional to the square root of the pressure difference at both ends (Menon, 2004).

Model Results

Figure 8 shows the output of the model for a sequence of six successive input rates of meteoric water labeled from one to six in

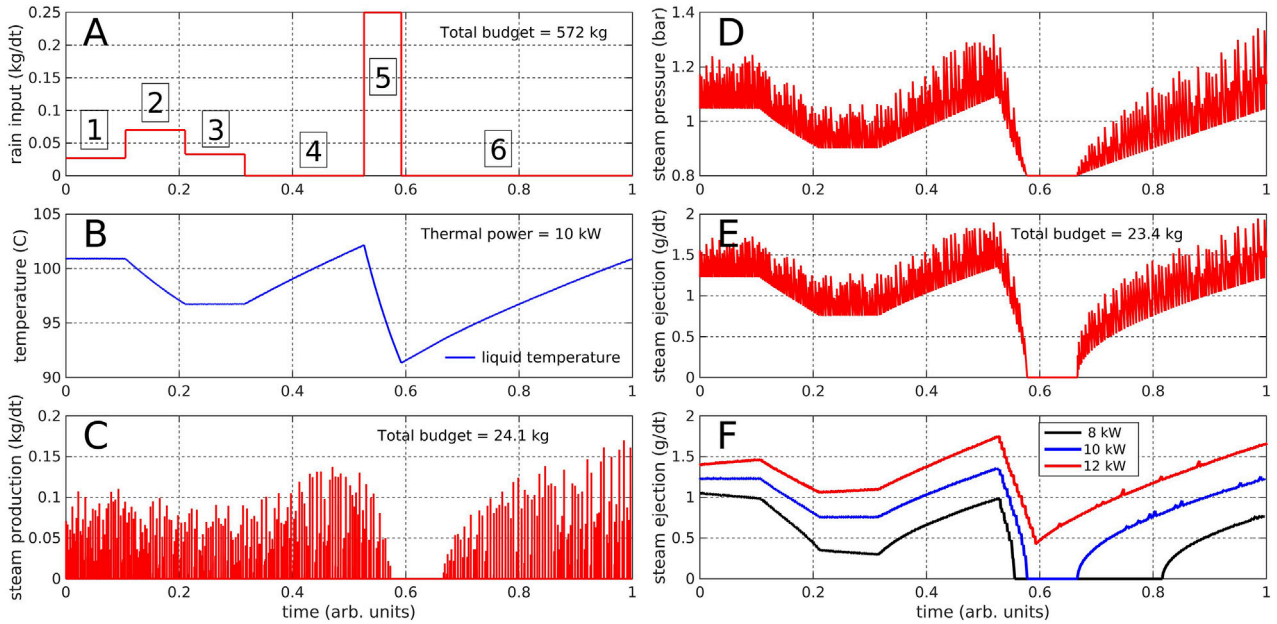

FIGURE 8 | Results of the numerical model corresponding to **Figure 7**. **(A)** Meteoric rain input **(B)** Temperature of the liquid contained in the reservoir **(C)** Steam production in the reservoir **(D)** Steam pressure in the reservoir **(E)** Steam mass flux at the vent **(F)** Steam mass ejection. See text for a detailed discussion.

Figure 8A. The adjustable parameters of the model are the heating power, the meteoric water input, the reservoir volume, the initial volume of liquid in the reservoir and the vent conduit diameter and length. Tens of trials were performed with different values of these parameters. In all cases, the models reached an equilibrium functioning point but, depending on the values chosen for the parameters, not all possible phenomena were observed. For instance, if the vent conduit diameter is too large, no increase of the steam pressure in the reservoir is observed. In the example we show here, we chose to only vary the rain input and keep the conduit geometry, the reservoir volume and the heating power constant in order to mimic the most probable situation on La Soufrière. The other plots of **Figure 8** represent the liquid temperature (**Figure 8B**), and steam production (**Figure 8C**), pressure (**Figure 8D**), mass ejection (**Figure 8E**). Observe that the liquid temperature varies smoothly while, as expected, the steam properties strongly oscillate due to the interplay of the negative and positive feedback quoted above. We now briefly discuss the phenomenology observed for each meteoric water input:

1 Equilibrium inputs (labels one and 3): Points exist where steam production and ejection exactly compensate. In such cases, the liquid temperature, the steam pressure and the steam ejection are constant. The equilibrium state is stable provided the rain rate does not vary. Observe that the value of the equilibrium rate depends on the steam pressure: more water input is needed when the pressure is lower because the boiling temperature is lower and the steam production higher.
2 Moderate water input above the equilibrium rate (label 2): The liquid temperature gently decreases, inducing a decrease of steam production, pressure and ejection rate. For some rate values, an equilibrium state similar to those shown in **Eq. 1**, **3** may be reached.
3 No water input (label 4): The liquid temperature increases (**Figure 8B**) while steam is produced (**Figure 8C**) and the pressure in the reservoir increases steadily (**Figure 8D**). Because the transport capacity of the outlet is proportional to the square root of the pressure difference at its ends, the increase of steam ejection slightly slows down (**Figure 8E**). Because of the unbalance between steam production and steam ejection, the reservoir pressure increases and may reach high values able to break the reservoir structure. This is typically what occurs during steam blasts.
4 High water input (label 5): The thermal power supplied to the reservoir is unable to maintain the liquid temperature above the boiling temperature. After a sharp decrease that begins with the rain input, the steam production ceases and the pressure falls down to the atmospheric pressure.
5 No water input (label 6): After the end of the strong rain episode, the liquid temperature begins to augment until the boiling temperature is reached and the steam production restarts while the pressure linearly builds up. Because of the square root dependence of the steam ejection with respect to the pressure gradient, the steam ejection sharply increases at the very beginning of the boiling and progressively slows down as the steam pressure increases.

On **Figure 8F** we observe different concavities of the curve of the steam ejection, which depend on the steam temperature. This is particularly noticeable at t around 0.7, which corresponds to re-heating of the system after the important

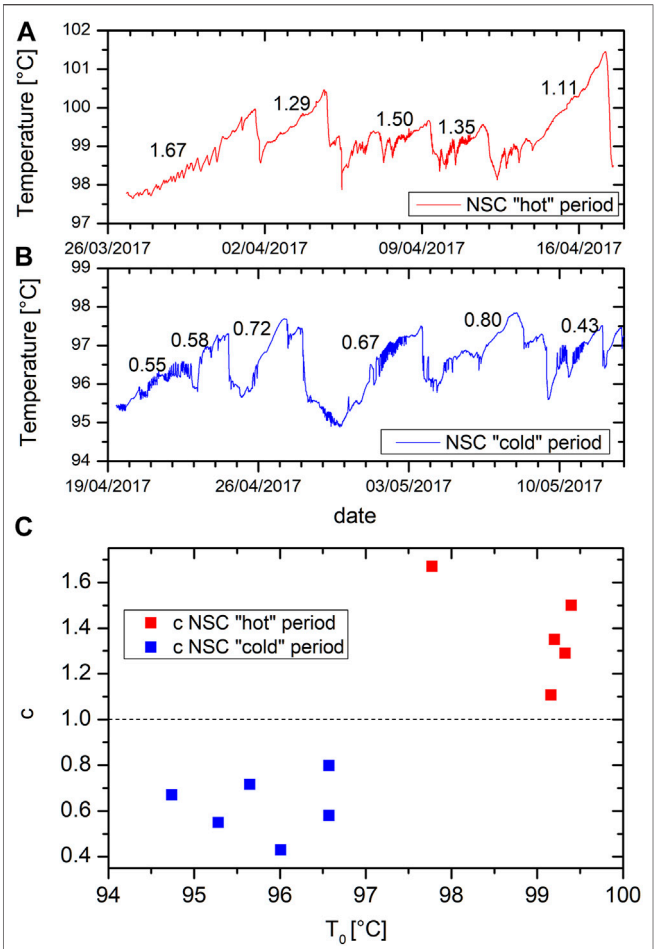

FIGURE 9 | Contrasted shape of hot (**(A)**, red box in **Figure 3**) vs cold periods (**(B)**, blue box in **Figure 3**) in the northern fumarole. Numbers are the exponent of a polynomial fit quantifying the concavity (c > 1) or the convexity (c < 1) **(C)** influence of the fumarole temperature on the concavity.

rain event labelled five in **Figure 8A** and where the liquid temperature is low and the steam ejection curves are strongly convex, in contrast with earlier times. Such a difference can also be observed in the northern fumarole temperatures. We selected two contrasted periods, a "hot" one (red box in **Figure 3**) and a "cold" one (blue box in **Figure 3**), both lasting about 23 days and separated by an important rainfall around the 18th of april (see blue curve on **Figure 4F**). Both periods are characterized by cyclic variations of the temperature with a period about 50 h on average (**Figures 9A, B**) and with contrasted concavity or convexity. We quantified this effect by fitting the temperature data with a polynomial function:

$$T = T_0 + \alpha t^c$$

where the exponent c describes the concavity. During hot periods (**Figure 9A**) the temperature curves of the cycles are concave with exponents c greater than 1, whereas during "cold" periods (**Figure 9B**) the curves are convex with exponents less than 1. On **Figure 9C** we compare these concavity exponents with the initial temperatures of the segments (T_0) and it clearly appears that the concavity is related with the temperature, in agreement with the results of the theoretical model.

DISCUSSION

A first important result obtained in the present study is the good correlation found between long-period temperature variations measured in the vents and the rainfall cumulated over 18 days (**Figure 5**). The existence of such a correlation shows that forcing by meteoric water input may explain the main temperature variations observed in the Southern crater fumaroles (**Figure 5**). Consequently, and on the sole observation of temperature curves, it is difficult to interpret temperature changes in term of variations of state of the hydrothermal system like, for instance, variation of input heat power or progressive sealing driven by mineral deposition (Stix and de Moor, 2018), or changes in the pore pressure within the dome. To reach such an objective, it is necessary to jointly analyze rainfall and temperature variations to detect slope changes in the linear correlation of **Figure 5B**. This requires collecting data during a sufficiently long period of time with a wide range of rain intensity. In practice, depending on the season, the observation period may reach up to 6 months.

In most situations, a quantitative estimate of the amount of meteoric water entering the hydrothermal system is unavailable, and it is therefore impossible to determine the heating power coming from below. Despite these limitations, it remains possible to obtain a qualitative view – i.e. increase, decrease, stability – of the liquid mass versus heating power balance by analyzing the speed of both reheating and pressure build-up following a heavy-rain event able to decrease the temperature below the boiling point. Recall that in such a situation, the steam production ceases until a sufficient amount of thermal energy is supplied to the reservoir to restart boiling. Obviously, the time necessary to produce steam again depends on the energy, i.e. heat flux, coming from below. **Figure 8F** shows the time-variation of steam production at the vent for a given rain input history (**Figure 8A**) and different heating powers. As expected, the main differences between the different heating powers occur when the liquid temperature falls near or below the boiling temperature. It is observed that the lower the heating power, the longer the quiescent period during which no steam is produced and the faster the restart of steam ejection. In order to detect these changes, a careful analysis of the rain history during the preceding months must be performed to remove the forcing effects from the data. This may be accomplished by using long short-term memory (LSTM) models and will be the subject of a forthcoming study.

Short-time variations of the fumarole temperature may be more informative about the dynamics of the hydrothermal system. Such is the case of short-period oscillations of temperature analyzed by Le Gonidec et al. (2019) where temperature oscillations strongly correlate with seismic noise produced by a resonator located in the shallow hydrothermal system. In the context of rain forcing, sudden transient rainfall may act as impulse perturbations of the hydrothermal system whose response can be considered as

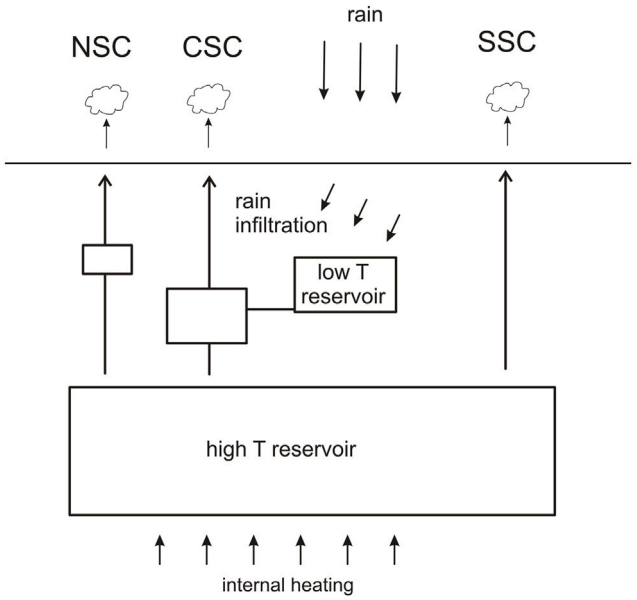

FIGURE 10 | Conceptual model of the hydrothermal system beneath the South Crater area (see text for details.).

some kind of "impulse responses". In such cases, the temperature recovery brings information about the thermal power capacity and the pressure build-up of the system.

The temperature data (**Figure 3**) allow to propose a conceptual model for the hydrothermal system beneath the South Crater (**Figure 10**). The similar global envelope of the three fumaroles (**Figure 3**) suggests that they are all fed at depth by a common high-temperature reservoir mainly responding to the internal forcing caused by the magmatic system. SSC being the hottest, could mean that it is more directly connected to the high-T reservoir. Conversely, the lower average temperature of NSC, which could imply a lower pressure at the vent, could be explained by the presence of an intermediate reservoir, or a longer or more tortuous superficial feeding system. The case of CSC is different as the complexity of its oscillations between two states with different periodicities suggests a geyser-like behaviour (Hurwitz and Manga, 2017). This kind of fluctuations is frequently observed in the field (e.g. Munoz-Saez et al., 2015; Kiryukhin and Karpov, 2020) and has been reproduced in laboratory experiments (e.g. Vandemeulebrouck et al., 2005; Adelstein et al., 2014). We thus suggest that the CSC sub-system may be functioning like a bubble-trap (Rudolph et al., 2018) where an intermediate reservoir between the high-T source and the surface is periodically connected to a low-T reservoir fed by meteoric water. The connection of these two reservoirs may explain the periodic fluctuations of the CSC temperature. This model, where the three fumaroles of the southern crater, although separated by no more than about 25 m exhibit very different behaviors, is in good agreement with the conclusions of Namiki et al. (2016) who demonstrate that differences in subsurface plumbing geometry can lead to contrasted eruption style even for similar heat and water supplies. This could also help to interpret other hydrothermal fields where different fumaroles, although not far from each other, may show contrasted behaviors such as, for instance Mt Etna in Italy (Madonia et al., 2013), Lastarria volcano in Chile (Zimmer et al., 2017) or Mt Epomeo on Ischia Island, Italy (Della Seta et al., 2021).

CONCLUSION

We perform here an analysis of temperature fluctuations in the three fumaroles of the South Crater at various time scales. During the January to August 2017 period considered here, the seismic activity was calm (Moretti et al., 2020); nevertheless a sustained hydrothermal activity was noticeable on the field (Le Gonidec et al., 2019; Jessop et al., 2020) and important temperature fluctuations in a range of more than 10°C, around an average value of about 99°C have been observed. We compare the temperature data to rainfall measurements during the same period and find a strong correlation between the two sets with important rainfall corresponding to lowering of the temperature.

As suggested by Gaudin et al. (2015) amongst others, the activity of the superficial hydrothermal system can be modified by the meteorological conditions, in particular the rainfalls, and most of the important variations in the fumaroles temperatures can be due to external forcing. A close and careful examination of these conditions is required to avoid erroneous estimations of the state of the volcanological system as even large temperature variations in fumaroles may be due to rain alone.

DATA AVAILABILITY STATEMENT

The raw data supporting the conclusions of this article will be made available by the authors, without undue reservation.

AUTHOR CONTRIBUTIONS

All authors listed have made a substantial, direct, and intellectual contribution to the work and approved it for publication.

FUNDING

This study is funded by the French Agence Nationale de la Recherche through the DIAPHANE (ANR-14-CE-04-0001) and MEGaMu (ANR-19-CE05-0033) projects.

ACKNOWLEDGMENTS

We are grateful to people at the Guadeloupe Volcano Observatory (OVSG) for assistance in the field and for providing meteorological data. We thank two reviewers, the guest associate editor SP and the chief editor Valerio Acocella for their comments that helped to improve the manuscript.

REFERENCES

Adelstein, E., Tran, A., Saez, C. M., Shteinberg, A., and Manga, M. (2014). Geyser Preplay and Eruption in a Laboratory Model with a Bubble Trap. *J. Volcanology Geothermal Res.* 285, 129–135. doi:10.1016/j.jvolgeores.2014.08.005

Chen, J., Yang, S., Liao, S., and Cao, X. (2015). Experimental Investigation of Effective Parameters on Geyser Periodicity in a Vertical Heated System. *Exp. Therm. Fluid Sci.* 68, 163–176. doi:10.1016/j.expthermflusci.2015.04.005

Connor, C. B., Clement, B. M., Song, X., Lane, S. B., and West-Thomas, J. (1993). Continuous Monitoring of High-Temperature Fumaroles on an Active Lava Dome, Volcán Colima, Mexico: Evidence of Mass Flow Variation in Response to Atmospheric Forcing. *J. Geophys. Res.* 98, 19713–19722. doi:10.1029/93JB02169

Cyranoski, D. (2014). Why Japan Missed Volcano's Warning Signs. *Nature*. doi:10.1038/nature.2014.16022

Dakos, V., Scheffer, M., van Nes, E. H., Brovkin, V., Petoukhov, V., Held, H., et al. (2008). Slowing Down as an Early Warning Signal for Abrupt Climate Change. *Proc. Natl. Acad. Sci.* 105, 14308–14312. doi:10.1073/pnas.0802430105

Della Seta, M., Esposito, C., Fiorucci, M., Marmoni, G. M., Martino, S., Sottili, G., et al. (2021). Thermal Monitoring to Infer Possible Interactions between Shallow Hydrothermal System and Slope-Scale Gravitational Deformation of Mt Epomeo (Ischia Island, Italy). *Geol. Soc. Lond. Spec. Publications* 519, 131. doi:10.1144/sp519-2020-131

D'Errico, J. (2017). SLM - Shape Language Modelling. *MATLAB Cent. File Exch.* Available at: https://www.mathworks.com/matlabcentral/fileexchange/24443-slm-shape-language-modeling.

Diliberto, I. S. (2013). Time Series Analysis of High Temperature Fumaroles Monitored on the Island of Vulcano (Aeolian Archipelago, Italy). *J. Volcanology Geothermal Res.* 264, 150–163. doi:10.1016/j.jvolgeores.2013.08.003

Erfurt-Cooper, P. (2017). "Active Hydrothermal Features as Tourist Attractions," in *Observing the Volcano World: Volcano Crisis Communication*. Editors C. J. Fearnley, D. K. Bird, K. Haynes, W. J. McGuire, and G. Jolly (Cham: Springer International Publishing), 85–105. doi:10.1007/11157_2016_33

Farquharson, J. I., and Amelung, F. (2020). Extreme Rainfall Triggered the 2018 Rift Eruption at Kīlauea Volcano. *Nature* 580, 491–495. doi:10.1038/s41586-020-2172-5

Fearnley, C. J., Bird, D. K., Haynes, K., McGuire, W. J., and Jolly, G. (2018). "Observing the Volcano World," in *Observing the Volcano World*. Editors C. J. Fearnley, D. K. Bird, K. Haynes, W. J. McGuire, and G. Jolly (Cham: Springer International Publishing). doi:10.1007/978-3-319-44097-2

Feuillard, M., Allegre, C. J., Brandeis, G., Gaulon, R., Le Mouel, J. L., Mercier, J. C., et al. (1983). The 1975-1977 crisis of la Soufriere de Guadeloupe (F.W.I): A still-born magmatic eruption. *J. Volcanology Geothermal Res.* 16, 317–334. doi:10.1016/0377-0273(83)90036-7

Fritz, A. (2014). Lack of Warning in Japan's Mt. Ontake Volcano Eruption Raises Questions. *Wash. Post* 2014, 9–10. https://www.washingtonpost.com/news/capital-weather-gang/wp/2014/09/30/lack-of-warning-in-japans-mt-ontake-volcano-eruption-raises-questions/

Gaudin, D., Finizola, A., Delcher, E., Beauducel, F., Allemand, P., Delacourt, C., et al. (2015). Influence of Rainfalls on Heat and Steam Fluxes of Fumarolic Zones: Six Months Records along the Ty Fault (Soufrière of Guadeloupe, Lesser Antilles). *J. Volcanology Geothermal Res.* 302, 273–285. doi:10.1016/j.jvolgeores.2015.06.015

Gaudin, D., Ricci, T., Finizola, A., Delcher, E., Alparone, S., Barde-Cabusson, S., et al. (2017). Heat flux-based strategies for the thermal monitoring of sub-fumarolic areas: Examples from Vulcano and La Soufrière de Guadeloupe. *J. Volcanology Geothermal Res.* 343, 122–134. doi:10.1016/j.jvolgeores.2017.06.021

Gunawan, H., Caudron, C., Pallister, J., Primulyana, S., Christenson, B., Mccausland, W., et al. (2017). New Insights into Kawah Ijen's Volcanic System from the Wet Volcano Workshop experiment. *Geol. Soc. Lond. Spec. Publications* 437, 35–56. doi:10.1144/SP437.7

Hurwitz, S., and Manga, M. (2017). The Fascinating and Complex Dynamics of Geyser Eruptions. *Annu. Rev. Earth Planet. Sci.* 45, 31–59. doi:10.1146/annurev-earth-063016-015605

Iole Serena, I. S. (2011). Long-term Variations of Fumarole Temperatures on Vulcano Island (Italy). *Ann. Geophys.* 54, 175–185. doi:10.4401/ag-5183

Jacob, T., Beauducel, F., David, J., Komorowski, J.-C., and Hammouya, G. (2005). "Ten Years of Extensometry at Soufrière of Guadeloupe: New Constranints on the Hydrothermal System." in Soufrière Hills Volcano - Ten Years On International Workshop, July 24-30 2005, (Kingston, Jamaica: Seismic Research Unit, University of West Indies).

Jessop, D. E., Moune, S., Moretti, R., Gibert, D., Komorowski, J.-C., Robert, V., et al. (2021). A multi-decadal view of the heat and mass budget of a volcano in unrest: La Soufrière de Guadeloupe (French West Indies). *Bull. Volcanol.* 83, 16. doi:10.1007/s00445-021-01439-2

Kaneko, T., Maeno, F., and Nakada, S. (2016). 2014 Mount Ontake Eruption: Characteristics of the Phreatic Eruption as Inferred from Aerial Observations. *Earth Planet. Sp* 68, 1–11. doi:10.1186/s40623-016-0452-y

Kiryukhin, A. V., and Karpov, G. (2020). A CO2-Driven Gas Lift Mechanism in Geyser Cycling (Uzon Caldera, Kamchatka). *Geosciences* 10, 180. doi:10.3390/geosciences10050180

Komorowski, J.-C., Boudon, G., Semet, M., Beauducel, F., Anténor-Habazac, C., Bazin, S., et al. (2005). "Guadeloupe," in *Volcanic Hazard Atlas of the Lesser Antilles*. Editors J. Lindsay, R. Robertson, J. Shepherd, and S. Ali, 65–102.

Le Gonidec, Y., Rosas-Carbajal, M., Bremond d'Ars, J. d., Carlus, B., Ianigro, J.-C., Kergosien, B., et al. (2019). Abrupt Changes of Hydrothermal Activity in a Lava Dome Detected by Combined Seismic and Muon Monitoring. *Sci. Rep.* 9, 3079. doi:10.1038/s41598-019-39606-3

Madonia, P., Rizzo, A. L., Diliberto, I. S., and Favara, R. (2013). Continuous Monitoring of Fumarole Temperatures at Mount Etna (Italy). *J. Volcanology Geothermal Res.* 257, 12–20. doi:10.1016/j.jvolgeores.2013.03.001

Mahmoudi, M., Fattahpour, V., Roostaei, M., Kotb, O., Wang, C., Nouri, A., et al. (2018). "An Experimental Investigation into Sand Control Failure Due to Steam Breakthrough in SAGD Wells," in SPE Canada Heavy Oil Technical Conference, Calgary, Alberta, Canada. doi:10.2118/189769-MS

Mastin, L. G. (1993). Can Rain Cause Volcanic Eruptions. U.S. Geol. Surv. Open-File Rep. 1993-0445. Available at: https://pubs.usgs.gov/of/1993/0445/.

Menon, E. S. (2004). *Piping Calculations Manual*. NY, United States. McGraw-Hill Education.

Moretti, R., Komorowski, J.-C., Ucciani, G., Moune, S., Jessop, D., de Chabalier, J.-B., et al. (2020). The 2018 Unrest Phase at La Soufrière of Guadeloupe (French West Indies) Andesitic Volcano: Scrutiny of a Failed but Prodromal Phreatic Eruption. *J. Volcanology Geothermal Res.* 393, 106769. doi:10.1016/j.jvolgeores.2020.106769

Munoz-Saez, C., Manga, M., Hurwitz, S., Rudolph, M. L., Namiki, A., and Wang, C.-Y. (2015). Dynamics within Geyser Conduits, and Sensitivity to Environmental Perturbations: Insights from a Periodic Geyser in the El Tatio Geyser Field, Atacama Desert, Chile. *J. Volcanology Geothermal Res.* 292, 41–55. doi:10.1016/j.jvolgeores.2015.01.002

Namiki, A., Ueno, Y., Hurwitz, S., Manga, M., Munoz-Saez, C., and Murphy, F. (2016). An Experimental Study of the Role of Subsurface Plumbing on Geothermal Discharge. *Geochem. Geophys. Geosyst.* 17, 3691–3716. doi:10.1002/2016GC006472

National Academies of Sciences Engineering and Medicine (2017). "Volcanic Eruptions and Their Repose, Unrest, Precursors, and Timing," in *National Academies of Siences Engineering and Medicine* (Washington, D.C.: National Academies Press). doi:10.17226/24650

Pearson, S. C. P., Connor, C. B., and Sanford, W. E. (2008). Rapid Response of a Hydrologic System to Volcanic Activity: Masaya Volcano, Nicaragua. *Geol* 36, 951–954. doi:10.1130/G25210A.1

Richter, G., Wassermann, J., Zimmer, M., and Ohrnberger, M. (2004). Correlation of Seismic Activity and Fumarole Temperature at the Mt. Merapi Volcano (Indonesia) in 2000. *J. Volcanology Geothermal Res.* 135, 331–342. doi:10.1016/j.volgeores.2004.03.006

Rouwet, D., Sandri, L., Marzocchi, W., Gottsmann, J., Selva, J., Tonini, R., et al. (2014). Recognizing and Tracking Volcanic Hazards Related to Non-magmatic Unrest: a Review. *J. Appl. Volcanol.* 3, 17. doi:10.1186/s13617-014-0017-3

Rudolph, M. L., Sohn, R. A., and Lev, E. (2018). Fluid Oscillations in a Laboratory Geyser with a Bubble Trap. *J. Volcanology Geothermal Res.* 368, 100–110. doi:10.1016/j.jvolgeores.2018.11.003

Sandri, L., Tonini, R., Rouwet, D., Constantinescu, R., Mendoza-rosas, A. T., Andrade, D., et al. (2017). "The Need to Quantify Hazard Related to Non-magmatic Unrest: From BET_EF to BET_UNREST," in *Volcanic Unrest*.

Editors J. Gottsmann, J. Neuberg, and B. Scheu (Berlin, Germany: Springer), 63–82. doi:10.1007/11157_2017_9

Scafetta, N., and Mazzarella, A. (2021). On the Rainfall Triggering of Phlegraean Fields Volcanic Tremors. *Water* 13, 154. doi:10.3390/w13020154

Scheffer, M., Carpenter, S. R., Lenton, T. M., Bascompte, J., Brock, W., Dakos, V., et al. (2012). Anticipating Critical Transitions. *Science* 80, 338. doi:10.1126/science.1225244

Stix, J., and de Moor, J. M. (2018). Understanding and Forecasting Phreatic Eruptions Driven by Magmatic Degassing. *Earth Planets Space* 70, 83. doi:10.1186/s40623-018-0855-z

Tamburello, G., Moune, S., Allard, P., Venugopal, S., Robert, V., Rosas-Carbajal, M., et al. (2019). Spatio-Temporal Relationships between Fumarolic Activity, Hydrothermal Fluid Circulation and Geophysical Signals at an Arc Volcano in Degassing Unrest: La Soufrière of Guadeloupe (French West Indies). *Geosciences* 9, 480. doi:10.3390/geosciences9110480

Urban, C., and Schlüter, M. (2014). Investigations on the Stochastic Nature of Condensation Induced Water Hammer. *Int. J. Multiphase Flow* 67, 1–9. doi:10.1016/j.ijmultiphaseflow.2014.08.001

Vandemeulebrouck, J., Stemmelen, D., Hurst, T., and Grangeon, J. (2005). Analogue Modeling of Instabilities in Crater lake Hydrothermal Systems. *J. Geophys. Res.* 110, 1–9. doi:10.1029/2003JB002794

Violette, S., de Marsily, G., Carbonnel, J. P., Goblet, P., Ledoux, E., Tijani, S. M., et al. (2001). Can rainfall trigger volcanic eruptions? A mechanical stress model of an active volcano: 'Piton de la Fournaise', Reunion Island. *Terra Nova* 13, 18–24. doi:10.1046/j.1365-3121.2001.00297.x

Vittecoq, B., Fortin, J., Maury, J., and Violette, S. (2020). Earthquakes and Extreme Rainfall Induce Long Term Permeability Enhancement of Volcanic Island Hydrogeological Systems. *Sci. Rep.* 10, 20231. doi:10.1038/s41598-020-76954-x

Williams, R. (2014). Why Japan's Deadly Ontake Eruption Could Not Be Predicted. *Conversat* 30, 7–9.

Zimmer, M., Walter, T. R., Kujawa, C., Gaete, A., and Franco-Marin, L. (2017). Thermal and Gas Dynamic Investigations at Lastarria Volcano, Northern Chile. The Influence of Precipitation and Atmospheric Pressure on the Fumarole Temperature and the Gas Velocity. *J. Volcanology Geothermal Res.* 346, 134–140. doi:10.1016/j.jvolgeores.2017.03.013

Conflict of Interest: The authors declare that the research was conducted in the absence of any commercial or financial relationships that could be construed as a potential conflict of interest.

Publisher's Note: All claims expressed in this article are solely those of the authors and do not necessarily represent those of their affiliated organizations, or those of the publisher, the editors and the reviewers. Any product that may be evaluated in this article, or claim that may be made by its manufacturer, is not guaranteed or endorsed by the publisher.

frontiers in Earth Science

ORIGINAL RESEARCH
published: 21 January 2022
doi: 10.3389/feart.2021.732696

Investigating Stress Transfer Between the Tuz Gölü Fault Zone and Hasan Dağ Volcano (Turkey)

Emily Hedger [1] *and Jo Gottsmann* [1,2]*

[1]School of Earth Sciences, University of Bristol, Bristol, United Kingdom, [2]Cabot Institute for the Environment, University of Bristol, Bristol, United Kingdom

Faulting, magmatism and volcanism are intrinsically linked by plate tectonics. Fault slip imparts stress changes to the surrounding crust and other faults and fractures. Volcano-tectonic hazard assessment in areas with long recurrence intervals of volcanic and tectonic activity requires an assessment of current stress levels. Here we investigate stress transfer between the Akhisar-Kiliç fault segment (AKFS) of the seismically active Tuz Gölü fault zone in the Central Anatolian Volcanic Province and the active Hasan Dağ volcanic complex. Current stress accumulation by protracted gradual slip on the AKFS since its most recent rupture (5.45 ka±0.16 BP) is quantified using the Coulomb Failure Stress change (ΔCFS). We calculate currently accrued ΔCFS magnitudes of between 2.5±0.2 and 15±0.5 MPa on the fault plane for published lower and upper-bound estimates of right-lateral slip rates, respectively. These changes are sufficient to promote failure of the segment. The M5.1 September 20, 2020 earthquake SW of Hasan Dağ occurred in a volume predicted by this study to have undergone fault unclamping by gradual slip along the AKFS. We also show that gradual slip of the AKFS contributes to the progressive unclamping of fractures and transtensional opening of potential magma pathways oriented perpendicularly to the AKFS both above and below Hasan Dağ's magma reservoir, while pathways oriented parallel to the AKFS are being clamped. Earthquake moment magnitudes of between M_w5.94 and M_w6.76 due to hypothetical partial or complete rupture of the segment exacerbate these trends. The spatial pattern of Coulomb failure stress changes on Hasan Dağ's magma reservoir is predominantly controlled by the location of rupture relative to the reservoir with the magnitude of the earthquake playing a subordinate role. We explore implications of our findings for the assessment of interconnected seismo-volcanic hazards and associated risks.

Keywords: volcano-tectonics, coulomb stress transfer, fault, volcano, Hasan Dag, Turkey

OPEN ACCESS

Edited by:
Simona Petrosino, Istituto Nazionale di Geofisica e Vulcanologia, Italy

Reviewed by:
Agust Gudmundsson, Royal Holloway, University of London, United Kingdom
Bruno Massa, University of Sannio, Italy

***Correspondence:**
Jo Gottsmann
j.gottsmann@bristol.ac.uk

Specialty section:
This article was submitted to Volcanology, a section of the journal Frontiers in Earth Science

Received: *29 June 2021*
Accepted: *09 December 2021*
Published: *21 January 2022*

Citation:
Hedger E and Gottsmann J (2022) Investigating Stress Transfer Between the Tuz Gölü Fault Zone and Hasan Dağ Volcano (Turkey). Front. Earth Sci. 9:732696. doi: 10.3389/feart.2021.732696

1 INTRODUCTION

At local scales, the temporal and spatial patterns of volcanic and seismic events are stochastic, statistically unrelated to one another (Hill et al., 2002). However, faulting and magmatic processes are intrinsically linked by plate tectonics (e.g., Perfit and Davidson, 2000; Karaoğlu et al., 2017) and there are several examples of stress transfer between tectonic and magmatic systems where fault rupture led to volcanic activity (**Table 1**). The inflation or voiding of magma reservoirs before and after eruptions causes local stresses to rotate, bringing optimally orientated faults in areas of increased

TABLE 1 | Selected examples of Coulomb failure stress transfer to magmatic systems causing the triggering (or partial triggering) of eruptions. Three modes are proposed: 1) unclamping of magma conduits above reservoir, 2) unclamping of magma conduits below reservoir, 3) direct clamping of the magma reservoir due to displacement on fault planes. Moment magnitude of earthquake (M_w), horizontal distance (D) distance between earthquake epicenter and volcanic system.

Year	M_w	Faulting regime	D	Volcano	Delay Time	Mode	Study
Since 1400	> 6	Normal	50–60 km	Vesuvius	< 10 years	3	Nostro et al. (1998)
Since 1841	> 6	Strike-slip	< 40 km	Mauna Loa	1-670 days	1 and 2	Walter and Amelung (2006)
Since 1906	≥8	Strike-slip, thrust	≤520 km	Southern Volcanic Zone (Andes)	< 5 years	1 and 2	Bonali et al. (2013)
1999	7	—	143 km	Popoxatépetl	8 h	1 and 2	De la Cruz-Reyna et al. (2010)
2003	4.5	—	34.5 km	Tungurahua	5 days	1 and 2	De la Cruz-Reyna et al. (2010)
2004–2005	9.3 and 8.7	Thrust	< 1200 km	Barren Island and Talang	12–60 days	1 and 2	Walter and Amelung (2007)
2010	8.8	Reverse	257 km	Copahue	< 3 years	2	Bonali (2013)
2015	6.4	Thrust	10 km	Ambrym	30 h	1 and 2	Hamling and Kilgour (2020)

stress closer to failure (Fukuyama et al., 2001; Roman et al., 2004; Ruppert et al., 2011). Conversely, stress released via slip on faults can encourage failure of a magma reservoir (Gudmundsson and Brenner, 2003; Walter and Amelung, 2007; Walter et al., 2007; Bonali et al., 2013). A positive feedback loop between the two phenomena has been noted by Nostro et al. (1998). Often both phenomena are only linked in hindsight.

Reservoir failure and transport of magma from a reservoir to the surface are prerequisites for a volcanic eruption. Reservoir failure occurs when excess magmatic pressure above lithostatic exceeds the surrounding rock's tensile strength (Wilson, 1980; Gudmundsson, 1988). Changes in magma reservoir volume typically lead to pressure variations on the reservoir wall (Blake, 1981). Equally, stress changes on a magma reservoir may produce volumetric fluctuations if the magnitude of stress change is great enough (Stein, 1999). Stress variations can lead to the clamping or unclamping of fractures around a reservoir which may promote or inhibit the propagation of magma towards the surface. Here, we investigate stress transfer between a major strike-slip fault system (the Tuz Gölü fault zone) and the active Hasan Dağ volcanic complex of the Central Anatolian Volcanic Province. A seismic swarm culminating in a M5.1 to M5.2 earthquake on September 20, 2020 occurred within 10 km of the summit of Hasan Dağ and within 20 km from the Tuz Gölü fault zone, in a volume with no recorded historic seismicity (Aydar et al., 2021). This raises questions about possible stress transfer from the major fault zone to the surrounding crust and secondary fault systems. We show that the currently accrued stress along the Tuz Gölü fault zone forces the magma-tectonic system towards failure and discuss resulting hazards.

2 BACKGROUND

2.1 Central Anatolian Tectonics

Central Anatolia is a region of lithospheric thinning (e.g., Piromallo and Morelli, 2003; Fichtner et al., 2013) hosted between the Western Anatolia Extentional Province and the Eastern Anatolia Shortening Province (e.g., Göğüş et al., 2017, and references therein) (**Figure 1**). The tectonics of Central Anatolia are dominated by two active NW-SE trending strike-slip fault systems: 1) the left-lateral Ecemiş fault zone and 2) the transtensive dextral Tuz Gölü fault zone (TGFZ) (Toprak and Göncöoğlu, 1993). In addition, sets of older normal faults with a NE-SW trend have been identified buried beneath Pleistocene volcanic products (Toprak and Göncöoğlu, 1993; Kürçer and Gökten, 2014). The 200 km long (Kürçer and Gökten, 2014) TGFZ marks the western border of the Central Anatolian Volcanic Province (CAVP). Seismicity along the fault is common, with an average earthquake focal depth of 10 km, and a moment magnitude $M_w \leq 5.2$ (Kürçer and Gökten, 2014). Block modelling across Central Anatolia by Aktuğ et al. (2013) indicates a normal component of the slip rate along the TGFZ of about 1 mm yr^{-1}, in addition to a right-lateral slip rate of about 5 mm yr^{-1} along the middle and/or southern part of the TGFZ (Aktuğ et al., 2013).

The TGFZ is composed of fault segments with lengths of between 4 and 33 km (Kürçer and Gökten, 2012). With a length of 27 km, the NW-SE trending Akhisar-Kiliç fault segment (AKFS) is one of the most important segments of the TGFZ due to its length and morphotectonic features which indicate a total vertical displacement of 268 m since the lower Pliocene (Kürçer and Gökten, 2012).

2.2 Hasan Dağ Volcano

Hasan Dağ is a polygenetic, twin peaked stratovolcano in the CAVP (Kuscu and Geneli, 2010) composed of Big Mount Hasan (BMH) at 3252 m a.s.l. and Small Mount Hasan (SMH) at 3069 m a.s.l. (**Figure 1**). Edifice formation occurred on the site of the extinct Keçikalesi volcano by three, distinctive evolutionary phases (Paleo-, Meso-, Neo-Hasan Dağ; < 7.21 ± 0.9 Ma, 1-0.1 Ma, and < 0.1 Ma, respectively) (Aydar, 1992; Aydar and Gourgaud, 1998). All evolutionary phases have temporal patterns synonymous with ignimbrite volcanism: dome lava extrusion preceding extensive volcanoclastic deposits and structural failure of the vent leading to caldera formation (Deniel et al., 1998). Magmas at Hasan Dağ have evolved from tholeiitic to calc-alkaline but are consistently dominated by andesites and rhyolites with subordinate basalts (Deniel et al., 1998).

Hasan Dağ's edifice is composed of pyroclastic deposits, lava flows and lava domes (Friedrichs et al., 2020), with the most recent pumice-forming eruption dated at 8.98 ± 0.64 ka (Schmitt et al., 2014) and a lava dome dated at < 6 ka (Aydar and Gourgaud, 1998). A long-term eruptive flux for Hasan Dağ is estimated at between 0.1 and 0.3 km^3 ka^{-1} (Friedrichs et al., 2020). Elevated levels of H_2S and CO_2 gas at the volcano's summit

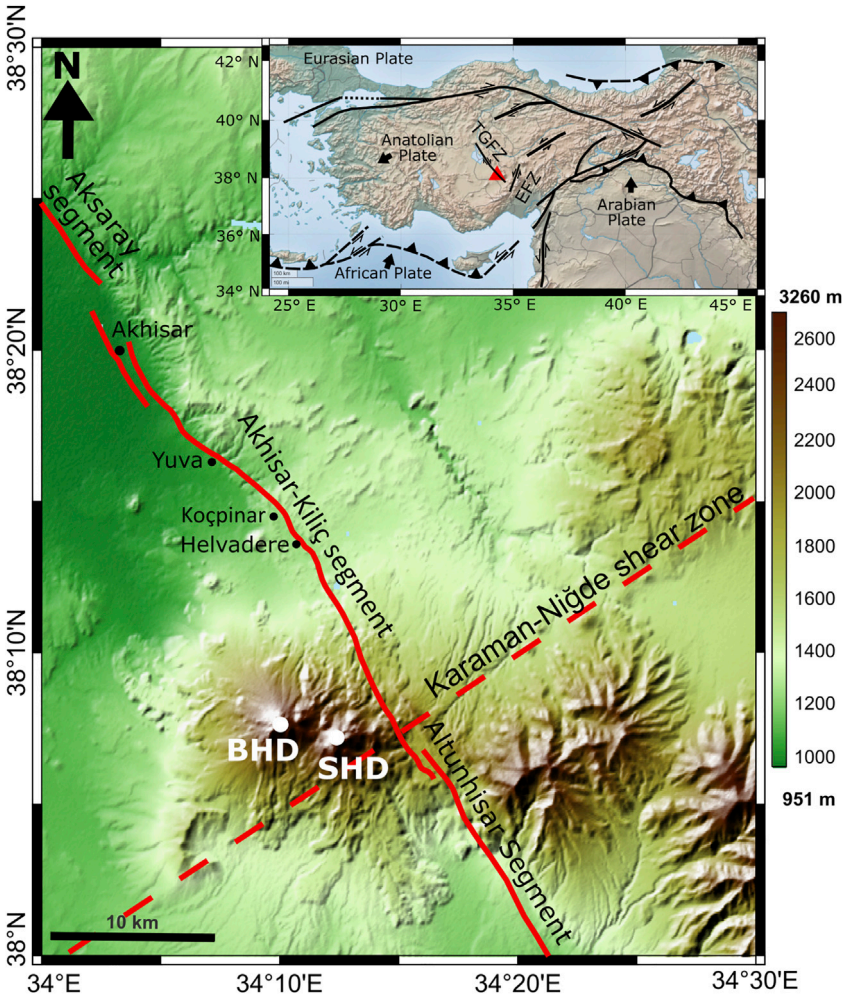

FIGURE 1 | Maps of the study area. Inset: Map of tectonic setting of the Anatolian microplate bound by the Eurasian plate to the north and African and Arabian plates to the south. Large arrows next to plate labels show the overall direction of plate movement. Black lines represent fault zones (EFZ: Ecemiş fault zone; TGFZ: Tuz Gölü fault zone). The red triangle shows the location of Hasan Dağ volcano. Fault locations and plate directions are from Tosun et al. (2007). Main panel: solid red line: Akhisar-Kiliç fault segment of the TGFZ; dashed red line: approximation of the Karaman-Niğde shear zone; BHD: Big Hasan Dağ; SHD: Small Hasan Dağ.

and fumarolic degassing on its western flank with temperatures of up to 68.7°C and CO_2 levels ~10,000 ppm are indicative of the presence of an active magmatic system (Dİker et al., 2018; Ulusoy et al., 2020; Aydar et al., 2021).

Mid-crustal low-seismic velocity layers beneath the volcanic province may represent magma reservoirs feeding active surface volcanism (Abgarmi et al., 2017). The electrical conductivity structure beneath Hasan Dağ highlights a conductive zone centred at 5 km depth beneath the plateau and is interpreted to represent the volcano's upper-crustal magma reservoir (Tank and Karaş, 2020).

2.3 Volcano-Tectonics of Hasan Dağ

The fault segment (AKFS) transects the north-eastern flank of the Hasan Dağ volcanic complex (Kürçer and Gökten, 2014) and intersects the sinistral, NE-SW trending Karaman-Niğde shear zone (KNSZ) (Aydar and Gourgaud, 1998; Şengör and Zabcı, 2019) (**Figure 1**). Quaternary volcanics of Hasan Dağ have been cut by faulting along the AKFS (Kürçer and Gökten, 2014). The segment has an average Quaternary vertical slip rate of 0.05 mm yr^{-1} (Kürçer and Gökten, 2012). Dextral offsets of Hasan Dağ lavas permit deducing average right-lateral slip rates of 0.58–3.35 mm yr^{-1} over the past 2 Ma (Krystopowicz et al., 2020). Paleoseismic and geochronological evidence (Kürçer and Gökten, 2012) of two Holocene earthquakes on the AKFS at 10 ± 0.41 ka BP and 5.450 ka±0.16 BP provide a recurrence interval of 4.55 ± 0.45 ka. Elevated footwall uplift rates towards the south-eastern end of the TGFZ may pertain to interactions between the fault zone and the Hasan Dağ magmatic system (Krystopowicz et al., 2020). Seismicity in proximity to Hasan Dağ includes hypocentral depths that are deeper (> 10 km) than common for the region (Aydar et al., 2021), and may perhaps be indicative of a volcanogenic origin (Kürçer and Gökten, 2014).

TABLE 2 | Abbreviations, units and definitions.

Symbol	SI Unit	Definition
TGFZ	—	Tuz Gölü fault zone
AKFS	—	Akhisar-Kiliçc fault segment
KNSZ	—	Karaman-Nığde shear zone
ΔCFS	Pa	Coulomb Failure Stress
$\Delta\tau$	Pa	Shear stress change
$\Delta\sigma_n$	Pa	Normal stress change
μ	—	Coefficient of friction
μ'	—	Effective coefficient of friction
P	Pa	Pore fluid pressure
B	—	Skempton's coefficient
σ_{kk}	Pa	Trace of stress tensor
M_w	—	Moment magnitude of earthquake
M_o	N m	Seismic moment of earthquake
SRL	km	Surface rupture length
RA	m^2	Fault rupture area
RW	m	Fault rupture width
AD	m	Average fault displacement
ρ	kg m^{-3}	Density
ν	—	Poisson's ratio
E_d	Pa	Dynamic Young's modulus
E_s	Pa	Static Young's modulus
V_p	m s^{-1}	P-wave velocity
V_s	m s^{-1}	S-wave velocity

3 METHODS

Slip on a fault occurs when shear stress overcomes static friction across the fault plane (Wang et al., 2014). This principle underlies the Coulomb Failure Criterion, which predicts the occurrence of slip when the Coulomb failure stress change (ΔCFS) on a fault overcomes a given value, defined as (King et al., 1994):

$$\Delta CFS = \Delta\tau + \mu(\Delta\sigma_n + \Delta P) \quad (1)$$

where $\Delta\tau$ is the change in shear stress, μ is the coefficient of friction, $\Delta\sigma_n$ is the change in normal stress, and Δ P is the change in pore fluid pressure. Symbols and abbreviations used throughout this paper are summarised in **Table 2**. The conventions employed in this study are 1) shear stress change on a fault is positive in the direction of slip and 2) normal stress change is extensional and thus positive if a fault or fracture is unclamped. Failure is encouraged if ΔCFS is positive and discouraged if negative; both increased shear and unclamping of faults promote failure.

Assuming rocks are undrained during the coseismic phase the change in pore pressure is defined by (Cocco and Rice, 2002):

$$\Delta\sigma_p = -B(\Delta\sigma_{kk})/3 \quad (2)$$

where B is Skempton's coefficient and σ_{kk} is the trace of the stress tensor (Harris, 1998). Assuming that the ductility of the interior fault material is greater than that of the surrounding materials gives $\sigma_{xx} = \sigma_{yy} = \sigma_{zz}$, and $(\Delta\sigma_{kk})/3 = \Delta\sigma$ (Harris, 1998). These assumptions cause the simplification of **Eq. 1** to:

$$\Delta CFS = \Delta\tau - \mu'\Delta\sigma \quad (3)$$

where is the effective coefficient of friction (King et al., 1994):

$$\mu' = \mu(1 - B) \quad (4)$$

In this study $\mu' = 0.4$, in line with volcano-tectonic studies of similar sized fault systems (Nostro et al., 1998).

3.1 Model Set-Up

To investigate volcano-tectonic linkages between the Tuz Gölü fault segment and Hasan Dağ we numerically solve for stresses imparted by slip on the fault segment (the source) to the surrounding crust and faults/fractures (the receivers) using Finite Element Analysis (COMSOL Multiphysics v5.4). The 3D model (**Figure 2**) is set up such that horizontal distances were −45 km ≤ x ≤ 45 km and −75 km ≤ y ≤ 75 km, while the model extends to a depth z of 36 km reflecting the depth of the Moho beneath the plateau surrounding Hasan Dağ (Tezel et al., 2013). The plateau sits at 1000 m above sea level with Hasan Dağ's edifice protruding above to a maximum prominence of 2253 m. Geospatial data of the region were obtained from a Digital Elevation Model (Aktuğ et al., 2013) based on the 3 arc-seconds NASA Shuttle Radar Topographic Mission (SRTM) data (Version 2; https://www2.jpl.nasa.gov/srtm/).

Model boundary condition are: 1) a free surface boundary constraint applied to the upper surface of the model, 2) a fixed constrained applied to the lower boundary, and 3) roller constraints at the lateral surfaces. The TGFZ and KNSZ are implemented as a set of identity pairs with continuity constraints applied and have either slip velocities or finite displacements prescribed depending on the nature of the study. The KNSZ has a no-slip boundary condition attributed to it. Both fault zones were modelled as straight, continuous features running through the entire modelling domain. While the TGFZ is modelled as a subvertical right-lateral fault trending 34°NW and dipping 68°SW from the horizontal, the KNSZ is modelled as vertical and trending at 55°NE (Kürçer and Gökten, 2014).

Using the upper-crustal high electrical conductivity anomaly beneath the volcano as a proxy (Tank and Karaş, 2020), we implement the volcano's magma reservoir by an oblate ellipsoid with a semi-minor axis of 1 km and semi-major axes of 1.8 km. The modelled reservoir contains six (a–f) point probes (**Figure 2**). a is at the upper most point on the reservoir while b is at the lower-most point. Both are 1 km from the reservoir's centre. Points a and b have tangents that are in the xy plane. c, d, e and f are on the side of the magma reservoir at greatest distance from the centre (1.8 km). Points c and d have tangents that are parallel to the fault plane of the AKFS while e and f have tangents that are perpendicular to it. The magma reservoir is located towards the south-eastern end of the fault plane.

A typical model contains a structured mesh with ~ 2.5 $\times 10^5$ elements solving for ~10^6 degrees of freedom. The mesh coarsens with distance from the fault plane, magma reservoir, and edifice.

Surface rupture lengths of 5, 10, 15, 20, 25, and 27 km were used to parameterise the partial or complete failure of the AKFS. To derive the moment magnitude M_w of the consequential earthquakes, we use the empirical relationship defined by Wells and Coppersmith (1994):

$$M_w = a + b\ log(SRL) \quad (5)$$

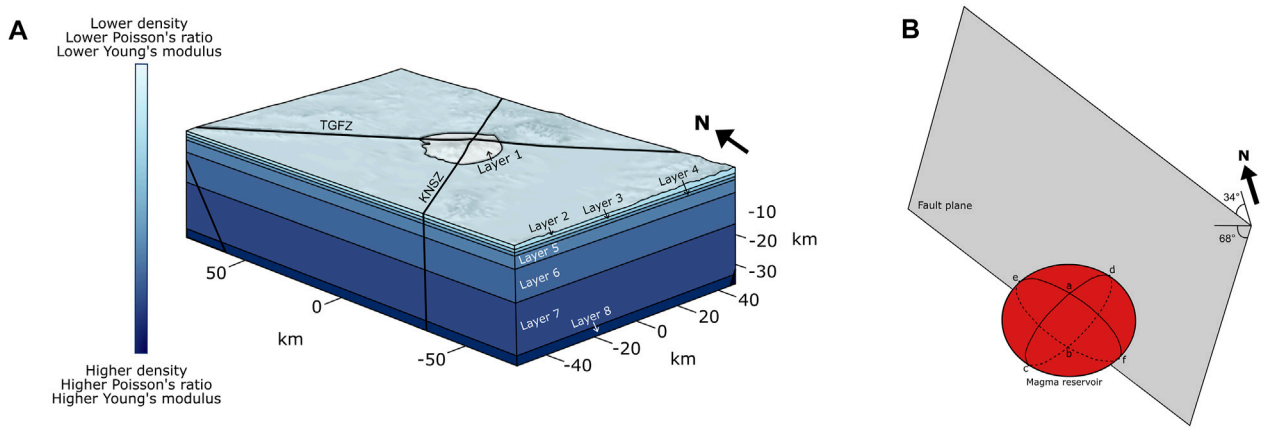

FIGURE 2 | Set up of the 3D finite element model. **(A)** Layered crustal mechanical heterogeneities are represented by subdomains with properties defined in **Table 3**. The modelled subsurface architecture shows an increase in mechanical rigidity and density with depth. TGFZ: Tuz Gölü fault zone; KNSZ: Karaman-Niğde shear zone. An oblate cavity [shown in **(B)**] centred at [0, 0, –5000], but not shown for clarity represents the magma reservoir of Hasan Dağ. **(B)** Schematic (not to scale) of the modeled relationship between the AKFS's fault plane and Hasan Dağ's magma reservoir. The magma reservoir is located towards the south-eastern end of the fault plane.

where SRL is the surface rupture length in km. a and b are 5.16±0.13 and 1.12±0.08, respectively, for strike-slip faulting, and 4.86±0.34 and 1.32±0.26, respectively for normal slip.

The fault rupture area (RA) is calculated from:

$$log\,(RA) = a + bM_w \tag{6}$$

If the faulting regime is strike-slip then a and b are −3.42±0.18 and 0.9±0.03, respectively, while for normal slip they are −2.87±0.50 and 0.82±0.08, respectively (Wells and Coppersmith, 1994).

Fault rupture widths (RW; in km) in down-dip direction for given M_w were derived from:

$$log\,(RW) = a + bM_w \tag{7}$$

where a and b are −0.76±0.12 and 0.27±0.02, respectively, for strike-slip faulting, and 1.14±0.28 and 0.35±0.05, respectively for normal slip (Wells and Coppersmith, 1994).

See **Table 5** for the full parameterisation.

3.2 Benchmarking

We benchmarked the numerical solutions of Coulomb failure stress changes against analytical solutions from the Coulomb 3.4 code (Toda et al., 2011) for the case of an elastic and mechanically homogeneous medium. Coulomb 3.4 outputs ΔCFS in 2D space, while our models solve in 3D. The simplest way to benchmark the 2D and 3D solutions is to solve for ΔCFS in the xy, xz and yz planes in our models and to identify the plane of both maximum and minimum principal stresses and hence of maximum shear stresses. Due to the dominance of right-lateral displacement along the sub-vertical AKFS, the Coulomb failure stress changes calculated in the xy plane in our 3D models provided the best fit to the Coulomb 3.4 stress solutions. As a result, all ΔCFS solutions from our numerical models are reported in the xy plane such that $\Delta CFS = \Delta CFF_{xy}$. See **Supplementary Material** for further details on model benchmarking.

3.3 Crustal Heterogeneity

The mechanical structure of the crust is parameterised from seismic p-wave velocity data. Data from Salah et al. (2014) are used for depths > 3 km, while in the absence of reliable shallow (< 3 km depth) crustal data for the CAVP and Hasan Dağ, the upper 3 km of the crust are parameterised using data from the Cascades. We chose seismic velocity data from Mt. St. Helens Volcano Kiser et al. (2016) due to close similarities in eruption style, eruptive products and edifice formation at both volcanoes and very similar upper-crustal seismic velocities (e.g., at 3 km depth V_p and V_p/V_s data in Central Anatolia are only 1.5% larger than in the Cascades). Note that the derived Coulomb Failure stress changes reported in this study for depth > 4 km are insensitive to the implemented mechanical structure < 3 km depth. The crustal density (ρ) distribution was obtained from p-wave velocities *via* the following polynomial regression fit (Brocher, 2005):

$$\rho = 1.6\,612V_p - 0.4\,721V_p^2 + 0.0\,671V_p^3 - 0.0\,043V_p^4 + 0.000\,106V_p^5 \tag{8}$$

Poisson's ratio (ν) was calculated as a function of the p- and s-wave velocity ratios:

$$\nu = \left(\left[V_p/V_s\right]^2 - 2\right)/\left(\left[V_p/V_s\right]^2 - 1\right) \tag{9}$$

Finally, the dynamic Young's modulus (E) was calculated from:

$$E_d = \left(V_p^2\nu(1+\nu)(1-2\nu)\right)/(1-\nu) \tag{10}$$

TABLE 3 | Mechanical properties assigned to each subdomain in the model. The plateau surrounding Hasan Dağ is set to z = 0 m in the model, thus the edifice extends to a height of z = 2532 m. See **Eq. 8** and **Supplementary Table S1** for further information on the derivation of the values.

Layer	Depth below plateau (km)	ν	E_d (GPa)
1	Edifice	0.25	5
2	0–1	0.18	17.4
3	1–2	0.17	25.0
4	2–3	0.22	33.0
5	3–7	0.27	37.3
6	7–17	0.28	38.2
7	17–33	0.25	47.1
8	33–36	0.25	81.6

An empirical correction is applied to convert the dynamic modulus E_d to static modulus E_s. Following (Gudmundsson, 1988) the ratio of E_s/E_d used in this study is 0.5. Elastic properties attributed to Hasan Dağ's edifice were taken from Montserrat (Young and Gottsmann, 2015) due to a lack of local data and broadly similar eruptive products of andesite volcanism at both volcanoes. See **Table 3** for mechanical properties assigned to all model domains.

3.4 Stress Drop of Earthquakes

The moment magnitude (M_w) is dimensionless, but can be linked to the seismic moment (M_o) of an earthquake (Hanks and Kanamori, 1979):

$$M_w = 2/3\, log\,(M_o) - 10.7 \tag{11}$$

The above equation gives seismic moment in 10^{-7} Nm. The seismic moment is a function of the stress drop $\Delta\sigma$ experienced by the fault during an earthquake (Kanamori and Anderson, 1975):

$$\Delta\sigma = (2M_o)/(\pi RW^2 SRL) \tag{12}$$

Here we assume that the stress drop equates to the magnitude of stress required for the fault to slip; i.e., rupture occurs at $\Delta CFS \geq \Delta\sigma$, and is further assumed to occur in the middle of the fault segment propagating outwards. We thus model the fault segment as transcurrent.

3.5 Time-Dependent Model

The cumulative displacement along a fault is a function of time (t), thus a time-dependent study is added to the model, whereby t = 0 is immediately after the most recent earthquake when the stress on the AKFS was at its minimum. This enables the interrogation of the temporal evolution of stress accumulation along fault segments with lengths equalling hypothetical future surface rupture lengths with a view to determine the timing of failure for given fault kinematics.

3.6 Coulomb Failure Stress Change on Receiver Faults

Changes in Coulomb failure stresses are modeled by 1) slip of the AKFS since its most recent earthquake (termed gradual slip hereafter) and 2) by a hypothetical earthquake caused by rupture of the AKFS. Quaternary (gradual) slip rates of 0.05 mm yr^{-1} normal slip, and 0.58–3.35 mm yr^{-1} right-lateral slip are applied to the AKFS until the calculated stress drop magnitude $\Delta\sigma$ is reached. Instantaneous displacements vectors were then applied to the fault segment to model the resultant Coulomb failure stress change on receiver faults from the hypothetical earthquake. See also **Supplementary Material** for the parameterisation of Coulomb failure stress changes.

3.7 Average Displacement by Faulting

The average fault displacement AD due to each earthquake was calculated via

$$log\,(AD) = a + bM_w \tag{13}$$

where M in the moment magnitude of each slip event, a and b are constants equalling −6.32±0.61 and 0.9±0.09, respectively (Wells and Coppersmith, 1994). Slip as a result of the hypothetical earthquakes follows the rake of the gradual slip. Earthquakes following normal slip displacement of 0.053 6 mm yr^{-1} and right-lateral slip of 0.58 mm yr^{-1} events have a rake of −175°. Earthquakes following normal slip displacement of 0.053 6 mm yr^{-1} and right-lateral slip of 3.35 mm yr^{-1} events have a rake of −179°. The derived average displacements and slip components are given in **Table 4**.

3.8 Coulomb Failure Stress Change on Hasan Dağ's Magma Reservoir

The Coulomb failure stress change on Hasan Dağ's magma reservoir is calculated for three different modes of crustal clamping and unclamping: 1) unclamping or clamping of magma pathways above the reservoir, 2) clamping or unclamping of pathways below the reservoir, 3) direct clamping of the reservoir walls. Six point probes on the magma reservoir are chosen to derive the stress change (**Figure 2B**). At these points, Coulomb failure stress change is quantified on the tangential plane to the reservoir or fracture surface (see **Supplementary Material**). Scenario 1 is calculated at point a both parallel and perpendicular to the strike of fault plane. Scenario 2 is calculated at point b also parallel and perpendicular to the strike of the fault. In both scenarios fractures are assumed vertical, dipping 90° from the horizontal. Scenario 3 is calculated at points c, d, e, and f. The temporal evolution of stress changes on the reservoir is calculated from the most recent earthquake up to just before each hypothetical earthquake. The resultant stress change due to each earthquake was quantified by the prescribed slip on the fault plane.

4 RESULTS

4.1 Fault Parameters

Table 5 shows the moment magnitudes (M_w) of the hypothetical earthquakes along the AKFS, and their associated dimensions for either strike-slip or normal slip kinematics. The fault kinematics

TABLE 4 | Values of average displacement (AD) (1σ errors in parentheses) across the Akhisar-Kiliç fault segment for given surface rupture length (SRL) derived from **Eq. 13**. Strike-slip and normal slip components are calculated based on the ratio between dextral slip and normal slip components of gradual annual slip on the segment over the past 2 Ma for given lower 1) and upper 2) bound slip rates as reported in Krystopowicz et al. (2020).

SRL (km)	AD (m)	dextral slip (m)	Normal slip (m)
(i) For lower-bound dextral slip of 0.58 mm yr^{-1} and normal slip 0.053 6 mm yr^{-1}			
5	0.11 (0.03)	0.097 (0.03)	0.009 (0.002)
10	0.21 (0.04)	0.20 (0.04)	0.018 (0.003)
15	0.33 (0.04)	0.30 (0.04)	0.028 (0.003)
20	0.43 (0.03)	0.40 (0.03)	0.037 (0.003)
25	0.55 (0.02)	0.50 (0.02)	0.046 (0.002)
27	0.58 (0.02)	0.53 (0.02)	0.049 (0.02)
(ii) For upper-bound dextral slip of 3.35 mm yr^{-1} and normal slip 0.053 6 mm yr^{-1}			
5	0.11 (0.03)	0.10 (0.03)	0.001 7 (0.000 5)
10	0.21 (0.04)	0.21 (0.04)	0.003 4 (0.007)
15	0.33 (0.04)	0.32 (0.03)	0.005 1 (0.006)
20	0.43 (0.03)	0.43 (0.03)	0.006 8 (0.000 5)
25	0.55 (0.02)	0.54 (0.02)	0.008 6 (0.000 3)
27	0.58 (0.02)	0.57 (0.02)	0.009 1 (0.000 3)

TABLE 5 | Values of maximum moment magnitude M_w for each earthquake for selected surface rupture lengths (SRL), the associated rupture areas (RA) and rupture widths (RW) as given by **Eqs 5**, **6**. 1σ errors are reported in parentheses. * gives values for fault segment with pure strike-slip kinematics; ** gives values for fault segment with pure normal slip kinematics.

	M_w	RA (km^2)	RW (km)
SRL* (km)			
5	5.94 (0.06)	84.8 (10.9)	7.0 (0.3)
10	6.28 (0.04)	170.6 (11.7)	8.6 (0.1)
15	6.48 (0.03)	256.7 (3.1)	10.6 (0.1)
20	6.62 (0.02)	343.1 (3.1)	10.6 (0.1)
25	6.73 (0.01)	429.7 (4.4)	11.4 (0.2)
27	6.76 (0.01)	464.3 (7.8)	11.6 (0.2)
Average			9.81 (1.62)
SRL** (km)			
5	5.78 (0.13)	74.4 (23.3)	7.7 (0.7)
10	6.18 (0.07)	157.6 (20.9)	10.5 (0.6)
15	6.41 (0.03)	244.5 (6.9)	12.7 (0.7)
20	6.58 (0.02)	333.8 (15.5)	14.5 (1.3)
25	6.71 (0.02)	424.9 (44.9)	16.1 (1.9)
27	6.75 (0.03)	461.9 (58.3)	16.7 (2.2)
Average			13.0 (3.16)

TABLE 6 | Values of stress drop $\Delta\sigma$ corresponding the moment magnitudes M_w of earthquakes from **Table 5**. * for fault segment with pure strike-slip kinematics. ** for fault segment with pure normal slip kinematics. The seismic moment M_o was derived from the moment magnitude M_w of each earthquake via **Eq. 11** (Hanks and Kanamori, 1979) which gives seismic moment in dyn cm, converted to MPa (1 dyn cm = 1×10^{-7} MPa) and substituted into **Eq. 12**. 1σ errors are reported in parentheses.

	$M_o \times 10^{19}$ (MPa)	$\Delta\sigma$ (MPa)
M_w*		
5.94 (0.06)	0.09 (0.02)	2.4 (0.6)
6.28 (0.07)	0.30 (0.04)	2.5 (0.4)
6.48 (0.03)	0.58 (0.06)	2.6 (0.3)
6.62 (0.02)	0.95 (0.07)	2.7 (0.2)
6.73 (0.02)	1.38 (0.07)	2.7 (0.2)
6.76 (0.03)	1.57 (0.07)	2.7 (0.2)
M_w**		
5.78 (0.13)	0.05 (0.03)	1.2 (0.7)
6.18 (0.07)	0.21 (0.05)	1.2 (0.3)
6.41 (0.03)	0.47 (0.05)	1.2 (0.2)
6.58 (0.01)	0.82 (0.01)	1.2 (0.2)
6.71 (0.02)	1.28 (0.08)	1.3 (0.3)
6.75 (0.03)	1.49 (0.14)	1.3 (0.4)

have little effect on the moment magnitudes for equivalent surface rupture lengths (SRLs). Moment magnitudes of strike-slip faulting match those by normal slip faulting for SRLs ≥10 km. The difference in M_w for SRL = 5 km is <3%. For strike-slip faults $5.94\pm0.06 \leq M_w \leq 6.76\pm0.01$, while for normal slip faults $5.78\pm0.13 \leq M_w \leq 6.75\pm0.03$. Uncertainties in calculated fault areas and fault widths are generally smaller for strike-slip faulting compared to normal slip faulting. Except for the shortest SRL considered, rupture width are greater for strike-slip kinematics compared to normal slip.

Table 6 reports the stress drops along the AKFS for given earthquake moment magnitudes (**Eq. 12**). As expected, the magnitude of the stress drop does not change significantly with increasing moment magnitude and we derive an average stress drop of 2.6±0.2 MPa for the range of magnitudes considered.

4.2 Coulomb Failure Stress Changes on Akhisar-Kiliç Fault Segment

Coulomb failure stress change accumulation due to gradual slip of the AKFS as function of time since its most recent earthquake (5.450 ka±0.16 BP) is summarised in **Figure 3**. We calculate a stress accumulation rate of 450±10 Pa yr^{-1} for the lower-bound estimate of the right-lateral slip rate (0.58 mm yr^{-1}). In this case a ΔCFS (equivalent to the stress drop calculated in **Eq. 13** and reported in **Table 6**) of 2.6±0.2 MPa is reached nowadays. The calculated stress accumulation for the upper-bound value of the right-lateral

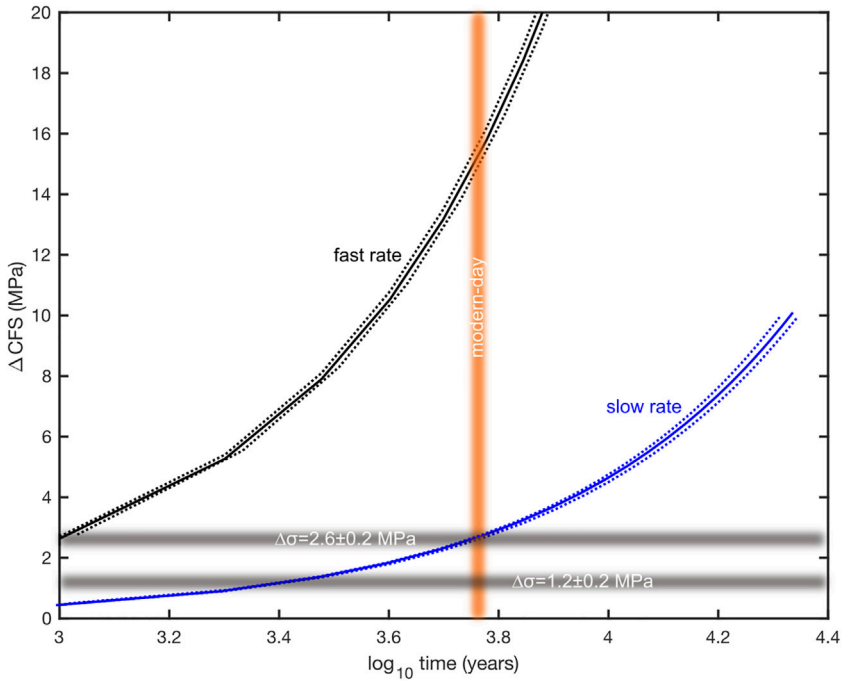

FIGURE 3 | Modeled Coulomb failure stress change accumulation ΔCFS (**Eq. 3**) by gradual slip on the Akhisar-Kiliçc fault segment (AKFS) for the range of transtensional slip velocities reported by Krystopowicz et al. (2020) as a function of time elapsed since the most recent earthquake [5450 ± 160; using data from Kürçer and Gökten (2012)]. The vertical shaded area represents modern-day including data uncertainty and the horizontal shaded areas indicates stress drops $\Delta\sigma$ of 2.6±0.2 MPa and 1.2±0.2 MPa calculated for the range of moment magnitudes M_w of earthquakes reported in **Table 5**. The solid blue line shows the stress accumulation on the AKFS for a dextral slip rate of 0.58 mm yr^{-1} (labeled slow rate) with a gradient of 450±10 Pa yr^{-1}. The solid black line shows the stress accumulation for a dextral slip rate of 3.35 mm yr^{-1} (labeled fast rate) and a resultant gradient of 2700 ± 67 Pa yr^{-1}. Both scenarios have a normal slip rate of 0.05 mm yr^{-1}. Uncertainties are expressed by dotted lines.

slip (3.35 mm yr^{-1}) is 2700±67 Pa yr^{-1}. As a result, the ΔCFS for fault rupture would have been attained ~1 ka after the most recent earthquake and thus around ~4.5 ka ago. The ΔCFS for pure normal rupture (**Table 6**) would have been reached at the greater rate of strike-slip within 500 years after the most recent earthquake, and thus ~2.5 ka ago at the smaller rate of strike-slip. The accuracy and precision of these results are subject to the accuracy of geochronological and palaeoseismological data reported by Kürçer and Gökten (2012) to estimate the timing of the most recent earthquake on the fault segment. Between 2.5±0.2 and 15±0.5 MPa of stress has accumulated on the fault since then, if both the timing and the range of right-lateral slip rates are taken as true.

4.3 Coulomb Failure Stress Change on Hasan Dağ's Magma Reservoir and Feeder Systems

Coulomb failure stress changes on fractures and hence potential magma pathways above the magma reservoir are summarised in **Figures 4A–D**. gradual slip on the fault segment in general causes unclamping of fractures perpendicular to the strike of the fault plane, but clamping parallel to it. The magnitude of ΔCFS has been increasing as a function of time since the last earthquake for both slip distributions and the magnitude of clamping of fractures is fractionally greater for the smaller dextral gradual slip rate (<2.5% difference for all magnitudes of future earthquakes). For fractures perpendicular to the strike of the fault, the rate of unclamping is 4.0×10^{-4} MPa yr^{-1} for the smaller rate of right-lateral slip, and 2.3×10^{-3} MPa yr^{-1} for the greater. Clamping of fractures parallel to the strike of the fault plane occurs at a rate of 3.1×10^{-4} MPa yr^{-1} for the smaller rate of right-lateral slip, and 2.1×10^{-3} MPa yr^{-1} for the greater.

Coulomb failure stress changes associated with the hypothetical fault ruptures exacerbate the trend of unclamping of fractures perpendicular to the strike of the fault, and clamping of fractures parallel to it. Again, there is little difference in results between the two rates of strike-slip kinematics (<0.05 MPa). The magnitude of ΔCFS largely increases with magnitude of the hypothetical earthquake event. An earthquake with an SRL of 10 km (M_w ~6.28) anomalously produces a smaller degree of clamping on fractures parallel to the strike of the fault plane than an earthquake with SRL of 5 km (M_w ~5.94).

Earthquakes with magnitudes $6.48 \leq M_w \leq 6.76$ significantly exacerbate the trends predicted by gradual Coulomb failure stress changes before fault rupture, whereby fractures perpendicular to the AKFS continue to be unclamped while fractures parallel to the AKFS being further clamped.

Figures 4E–H depict the Coulomb failure stress changes on fractures below Hasan Dağ's magma reservoir due to gradual slip

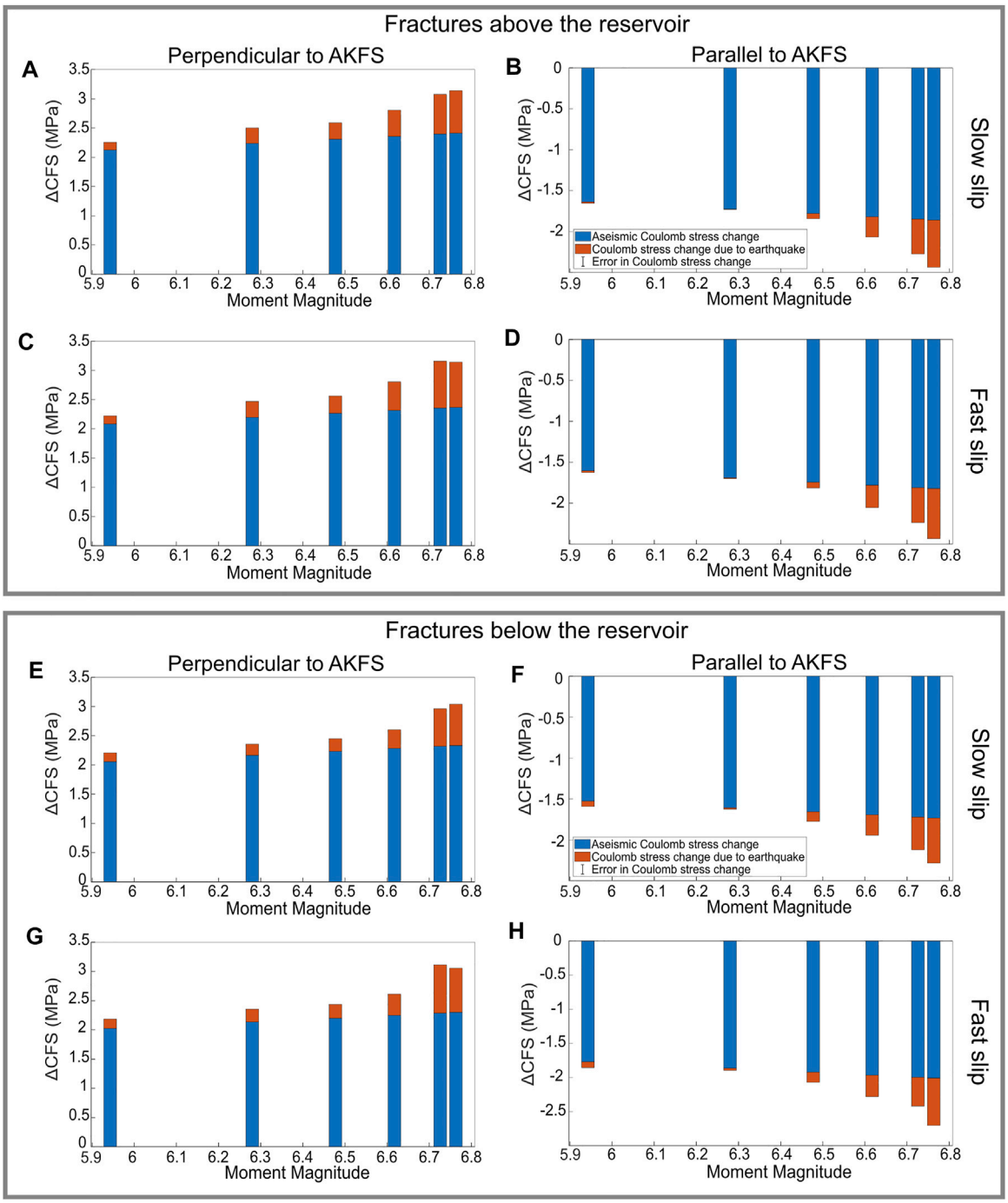

FIGURE 4 | Bar graphs of modeled changes in Coulomb failure stress on vertical fractures above **(A–D)** and below **(E–H)** Hasan Dağ's magma reservoir (extending from and to point probes a and b, respectively, in **Figure 2B**). The blue bars represent the change in Coulomb failure stress due to gradual slip along the Akhisar-Kiliçc fault segment (AKFS) since its most recent rupture (5450 ± 160 ka) and prior to hypothetical earthquakes with given moment magnitude (M_w). Orange segments show the Coulomb failure stress change as a result of the hypothetical earthquakes. **(A,B,E,F)** show results for a rate of 0.58 mm yr^{-1} right-lateral slip and a rate of 0.053 6 mm yr^{-1} of normal slip on the fault segment (labeled slow slip), while **(C,D,G,H)** show Coulomb failure stress change due to right-lateral slip of 3.35 mm y^{-1} and 0.053 6 mm yr^{-1} of normal slip (labeled fast slip). Positive stress changes represent unclamping of fractures, while negative stress changes indicate clamping. **(A,C,E,G)** show stress changes perpendicular to the strike of the AKFS. **(B,D,F,H)** show stress changes in a direction that is parallel to the strike of the AKFS.

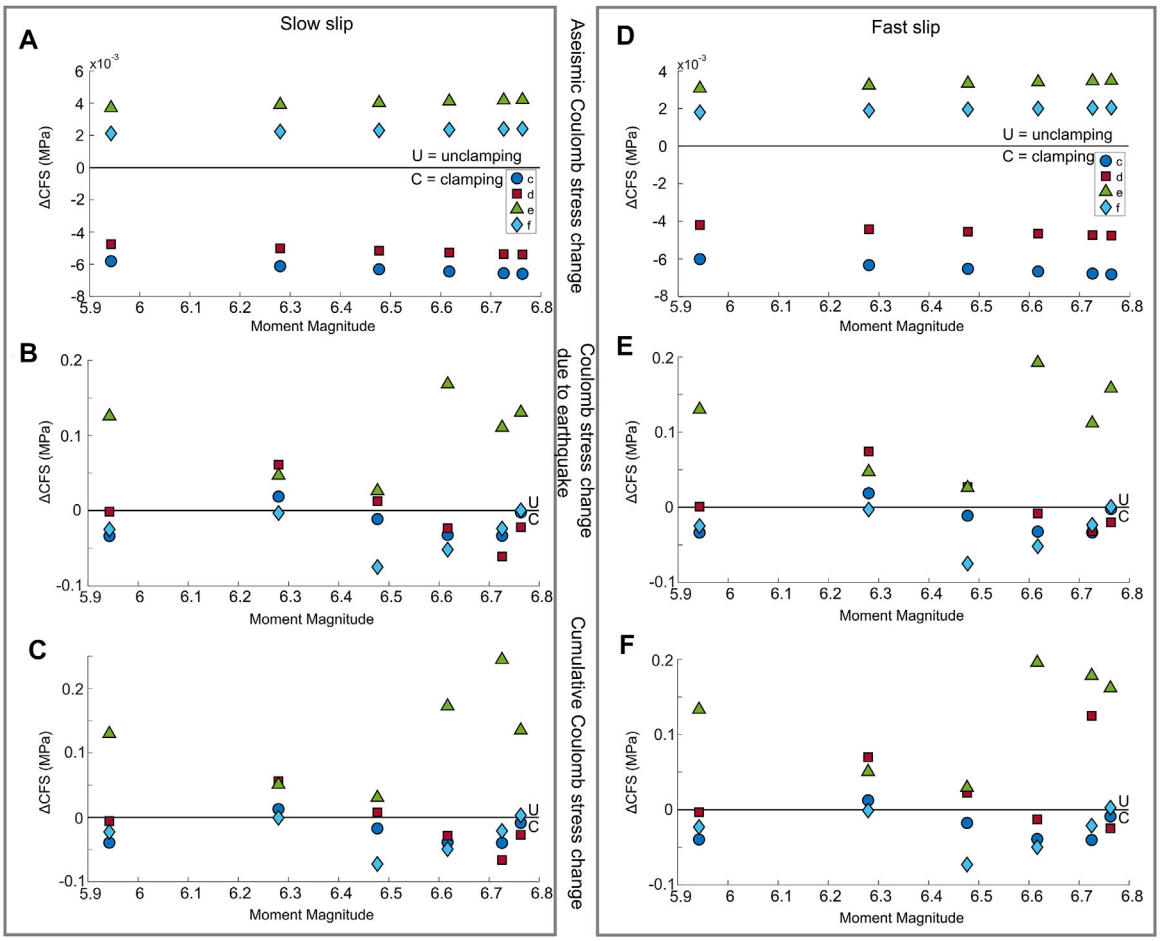

FIGURE 5 | Same as **Figure 4** but for modeled Coulomb failure stress changes on point probes c, d, e and f on Hasan Dağ's magma reservoir (see also **Figure 2B**). Tangents of c and d are parallel to the AKFS while tangents on e and f are perpendicular to it. **(A,D)** show the Coulomb failure stress changes on the points due to the gradual stress accumulation prior to hypothetical earthquakes with given moment magnitude. **(B,E)** show the Coulomb failure stress changes as a result of hypothetical earthquakes with given SRL. **(C,F)** show the cumulative Coulomb failure stress changes. **(A–C)** for 0.58 mm yr^{-1} right-lateral slip and 0.053 6 mm yr^{-1} of normal slip (labeled slow slip). **(D–F)** for 3.35 mm yr^{-1} right-lateral slip and 0.053 6 mm yr^{-1} of normal slip (labeled fast slip).

along the fault segment. Again, fractures are in general unclamped in a direction perpendicular to the fault plane but clamped parallel to it. There is <0.05 MPa difference in accrued stresses for the two slip rates for corresponding SRLs. Unclamping of fractures below the reservoir follows the same temporal pattern as predicted for fractures above the reservoir. The smaller slip-rate unclamps fractures perpendicular to the fault plane at a rate of 3.9×10^{-4} MPa yr^{-1}, while the greater slip-rate unclamps at a rate of 2.2×10^{-3} MPa yr^{-1}. Clamping of fractures parallel to the strike of the fault plane and below the reservoir occurs at a rate of 9.2×10^{-5} MPa yr^{-1} for the smaller component of right-lateral slip, and 1.6×10^{-3} MPa yr^{-1} for the greater.

All hypothetical earthquakes produce positive values of Coulomb failure stress changes on fractures in a direction perpendicular to the fault and hence result in further unclamping of potential magma pathways. This magnitude of clamping increases with magnitude of earthquake. All hypothetical earthquakes also exacerbate the trend of clamping on the fractures parallel to the strike of the fault plane. Matching the trend for fractures above the chamber, earthquakes with an SRL of 10 km produce a smaller magnitude of Coulomb failure stress change than earthquakes with an SRL of 5 km. Earthquakes with a SRL greater than 10 km produce increasing changes in Coulomb failure stress with increasing magnitude. Variations in the amount of modeled dextral slip on the fault segment have limited effects on the spatial and temporal evolution of Coulomb failure stress change on magma pathways below the reservoir.

The two rates of gradual slip produce very similar magnitudes of clamping of fractures along the reservoir wall; however, they are between one and two orders of magnitude smaller than the Coulomb failure stress change of fractures above and below the chamber (**Figure 5**). Point probes *c* and *d* (i.e., with tangents parallel to the fault plane) are both predicted to undergo clamping during gradual slip and prior to all hypothesised earthquake events. Point probes *e* and *f* (i.e., with tangents perpendicular to the fault plane) undergo unclamping during gradual slip.

The pattern of Coulomb failure stress change produced on fractures parallel to the reservoir produced by the hypothetical

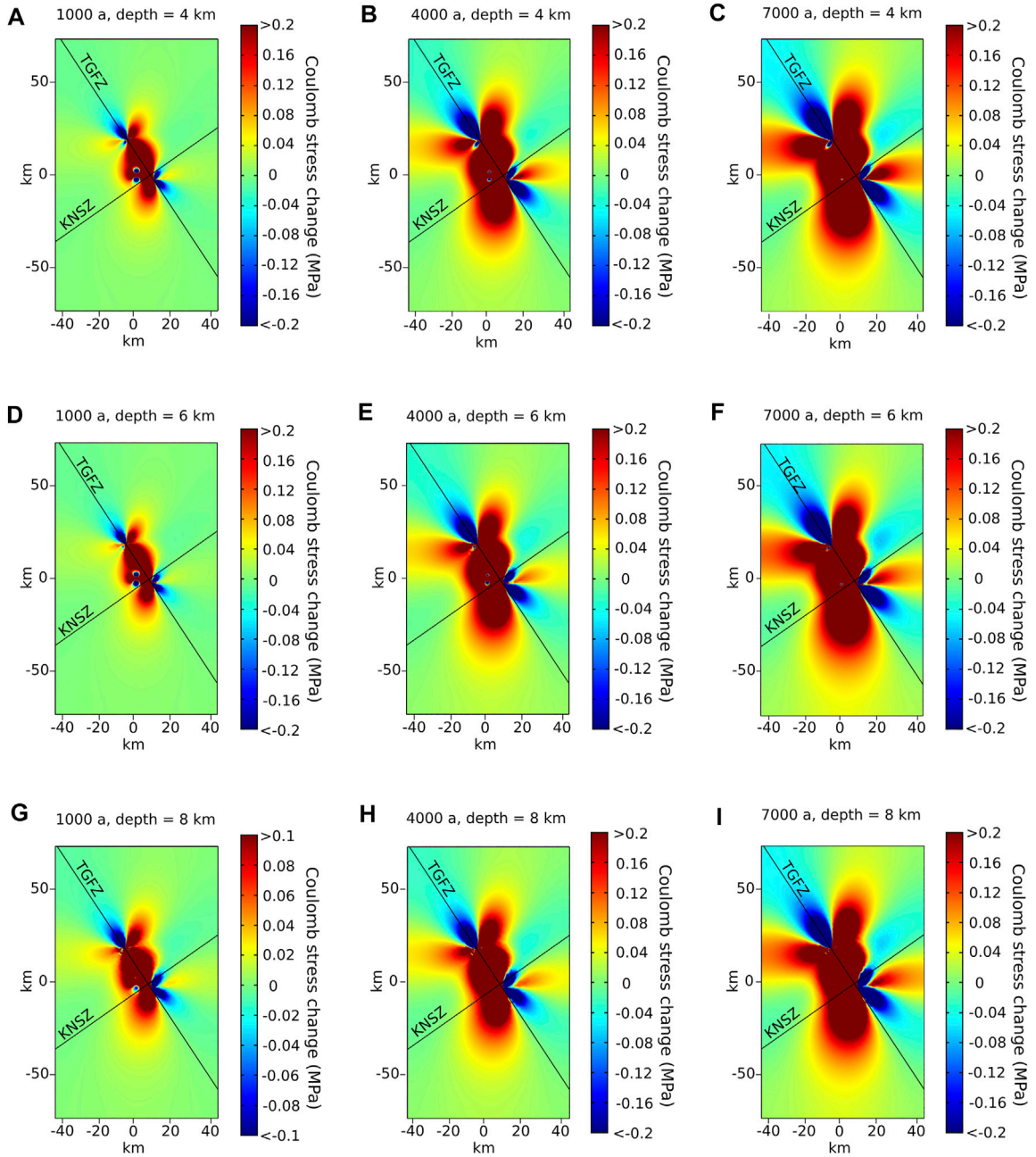

FIGURE 6 | Modeled gradual Coulomb failure stress changes at selected depths on vertical planes parallel to the Karaman-Niğde shear zone (trending 55° NE) after 1000, 4000 and 7000 years since the most recent earthquake on the AKFS. Changes are calculated for the more plausible slow gradual slip rate of 0.58 mm yr^{-1} right-lateral and 0.053 6 mm yr^{-1} normal slip. Coulomb failure stress changes at 4 km depth **(A–C)**, 6 km depth **(D–F)** and 8 km depth **(G–I)**. Note the reduction in scale in panel **(G)**.

earthquakes is more complex. While both slip rates produce very similar magnitudes of Coulomb failure stress change (<0.03 MPa), earthquakes with SRL = 5, 20, 25 and 27 km (M_w = 5.94, 6.62, 6.73 and 6.76) cause clamping at *c*, *d*, and *f*. An earthquakes with a SRL of 15 km (M_w = 6.48) clamps *c* and *f*, while an earthquake with SRL = 10 km (M_w = 6.62) only clamps *f*. The magnitude of Coulomb failure stress change as a result of hypothetical earthquakes is much greater than that due to gradual slip on the fault. Therefore the spatial pattern of stress changes produced by seismic slip of the fault dominates the cumulative Coulomb failure stress changes at each point probe on the reservoir.

4.4 Coulomb Failure Stress Changes on Receiver Faults of the KNSZ

Figure 6 shows the stress change on the KNSZ at different times (1, 4 and 7 ka since the most recent earthquake) and depths (4, 6

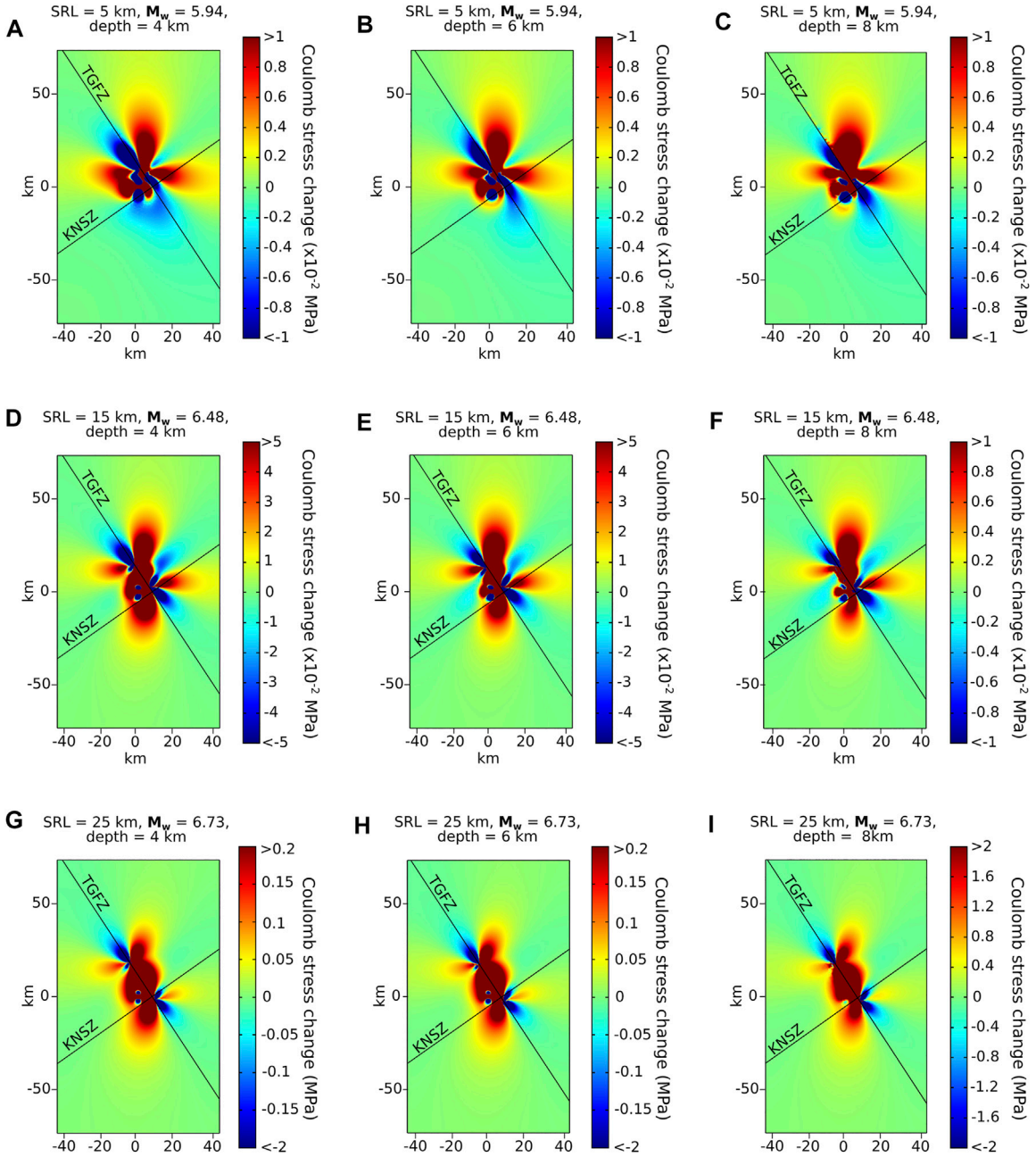

FIGURE 7 | Modeled Coulomb failure stress changes at selected depths on vertical planes parallel to the Karaman-Niğde shear zone (trending 55° NE) as a result of hypothetical earthquakes along the AKFS with a rake of −175° commensurate with the gradual slip distribution of 0.58 mm yr^{-1} right-lateral slip, and 0.053 6 mm yr^{-1} normal slip. **(A–C)** Coulomb failure stress change due to a M_w = 5.94 earthquake with surface rupture length (SRL) of 5 km. **(D–F)** for M_w = 6.48 and SRL = 15 km. **(G–I)** for M_w = 6.73 and SRL = 25 km. Note the change in scales as magnitude and depth increase.

and 8 km) due to gradual slip on the AKFS. Due to its greater plausibility, we only used the smaller estimate of right-lateral slip on the AKFS in the calculations. Unclamping of the KNSZ is predicted to propagate from the intersection with the AKFS to the southwest as a function of time. To the southeast of the intersection, the shear zone is clamped. While the distributions of ΔCFS show little variation with depth, the magnitude of ΔCFS decreases with distance from the AKFS and Hasan Dağ's magma reservoir.

Coulomb failure stress changes on the KNSZ and vertical receiver faults parallel to it as a result of hypothesised seismic slip on the AKFS are shown in **Figure 7**. Coulomb failure stress changes are shown for depths of 4, 6, and 8 km by three earthquakes with SRLs of 5, 15, and 25 km, respectively.

Overall, magnitudes of Coulomb failure stress change increase as a function of SRL. At all depths considered, interactions with the pressurised magma reservoir distort the pattern of Coulomb failure stress change, though this interaction becomes less prevalent with increasing magnitude of the earthquake. As a result of an M5.94 earthquake and a SRL of 5 km, the shear zone is predominantly unclamped to the west of the intersection with the TGFZ at all depths. At 4 km depth stress interactions are most significant and while the shear zone is broadly clamped to the southwest of the intersection up to ~20 km distance, localised unclamping is predicted in the vicinity of the magma reservoir. These complexities also persist at greater depth.

The spatial patterns of Coulomb change for earthquakes of magnitudes 6.48 and 6.73 with SRLs of 15 and 25 km, respectively, show large similarities to each other. Clamping of the shear zone occurs to the southeast of the intersection (for an SRL = 15 km also to the northeast), and unclamping occurs to the southwest.

5 DISCUSSION

5.1 Fault Parameters

Earthquake magnitudes, fault dimensions and surface rupture lengths of hypothetical earthquakes along the AKFS were calculated from the Wells and Coppersmith (1994) empirical formulae. That study used a substantial number of intraplate source parameters giving statistically significant relationships (more than 95% probability level) between most faulting characteristics. The faulting kinematics (normal, reverse, strike-slip) proves insignificant for the resultant moment magnitude of potential earthquakes along the AKFS (< 5% difference in results). However, it does prove significant for rupture areas associated with surface rupture lengths (SRLs) of 20 km and less. Given that the right-lateral component of slip along the fault segment is dominant over the normal slip, the empirical formulae for strike-slip faulting were deemed suitable to parameterise the fault dimensions. Calculating fault dimensions with the assumption of pure normal slip produces consistently smaller values. Omission of the normal slip component is likely to have caused a slight overestimation of the fault dimensions attributed to hypothetical earthquakes on the AKFS. In all models, we assumed rupturing to occur to the surface, reflecting rupture conditions caused by previous earthquakes studied by Kürçer and Gökten (2012).

Changes in Coulomb failure stress are static changes as changes in the off-fault stress field predicted by our models due to rupture of the AKFS are modeled instantaneous and permanent. Static stress change amplitudes diminish with $1/R^3$, where R is the distance from the earthquake's epicentre (Walter and Amelung, 2007). The proximity of the volcano's magma reservoir to the AKFS implies that seismic slip will be a dominant driver of stress changes in the reservoir as also demonstrated by results shown in panels B and E of **Figure 5**.

5.2 Rupture of the Akhisar-Kiliç Fault Segment

The two values of gradual right-lateral slip rates on the AKFS explored in the models cover the range of published values Kürçer and Gökten (2012). For the upper-bound estimate of right-lateral displacement (3.35 mm yr^{-1}) the models predict a seismic event of any plausible magnitude should have already occurred on the AKFS. If all model parameters are taken as exact representations of the geodynamic setting around Hasan Dağ, then this right-lateral component of slip for the AKFS must be regarded an overestimation. Our analysis indicates that the smaller component of right-lateral slip (0.58 mm yr^{-1}) likely provides more plausible estimate of the fault's kinematics. In this case stress accumulation on the fault plane since the most recent earthquake (~5.5 ka B.P.) is at least 2.5± 0.20 MPa and sufficient to promote failure of the segment (**Figure 3**).

Kürçer and Gökten (2012) propose a recurrence interval of 4660 ± 410 years for the AKFS. A greater quantity of time has elapsed since the last earthquake, even accounting for the upper boundary of error. Such a disparity in results may be due to a sparse data set available to the authors, but also due the authors' assumption that the fault segment is dominated by normal slip with a minor right-lateral component. This contrasts the assumptions of fault kinematics behind our study based on the findings of Aktuğ et al. (2013) and Krystopowicz et al. (2020). Furthermore the discrepancy in findings can be explained by the evolution of Hasan Dağ's magmatic system since its most recent eruption ~9 ka B.P (Schmitt et al., 2014). With the longevity of the Hasan Dağ magmatic system, it is not unreasonable to assume steady-state replenishment of the magma reservoir matching that of the Holocene eruption rate predicted by Friedrichs et al. (2020) (0.1 km^3 ka^{-1}). Pressurisation of the magma reservoir over this period would increase the normal stress on the AKFS, and thus discouraging slip.

5.3 Coulomb Failure Stress Change on Hasan Dağ's Magma Reservoir

In our model, Hasan Dağ's magma reservoir is kept at constant (lithostatic) pressure (i.e., no pressure changes over time are invoked. Exact quantification of the current state of pressurisation of Hasan Dağ's magma reservoir is beyond the scope of this study and possible variations in reservoir pressure due to magma influx and rejuvenation or volatile loss are hence neglected. Although InSAR data from the European Space Agency Sentinel-1 mission between 2014 and 2020 show annual ground displacement velocities at Hasan Dağ below the detectabilty limit of 1 cm yr^{-1} (Biggs et al., 2021), the volcano's high prominence and crustal mechanics of the CAVP could contribute to significant volumes of stealth magma accumulation at depth (Males and Gottsmann, 2021) at the geodetic detectability limit.

Hasan Dağ's magma reservoir is sufficiently close to the fault segment to permit stress interactions between the two. Globally, there is statistical significance between earthquakes of $M \geq 5$ and near field (within a few tens of km) volcanic unrest (Lemarchand and Grasso, 2007). Concurrency between earthquakes and eruptions is very high if $M > 6$ and eruptions are voluminous (Walter and Amelung, 2006). All point probes on the magma reservoir wall show linear increases, or decreases, of Coulomb failure stress as a result of protracted gradual slip on the fault

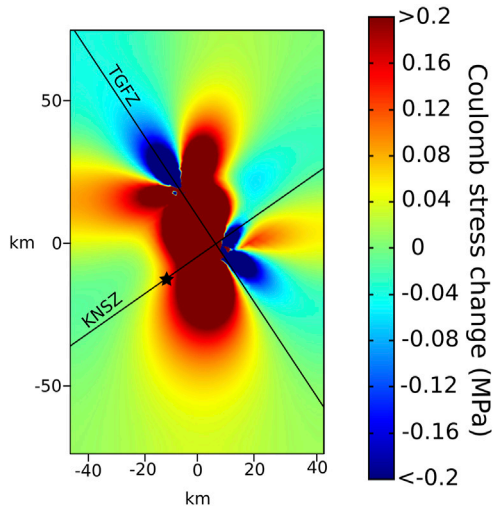

FIGURE 8 | Modeled present-day accumulation of Coulomb failure stress change on vertical faults parallel to the Karaman-Niğde shear zone (KNSZ) at a depth of 8 km due to right-lateral gradual slip of 0.58 mm yr^{-1} along the TGFZ. The black star marks the epicentral location (from the USGS earthquake catalogue) of the 20th of September 2020 M5.1 earthquake. The earthquake occurred in an volume of predicted positive Coulomb failure stress change where the shear zone would have undergone unclamping, thus encouraging rupture.

segment before the occurrence of any hypothetical earthquake. All modeled earthquakes cause a continuation of these trends at the point probes, either exacerbating conditions for reservoir failure and potential eruption or dampening them. Prior to all hypothetical earthquakes and independent of slip rate, magma pathways above the reservoir are unclamped in a direction perpendicular to the fault plane. When only strike-slip movement is considered along the fault (with a trend of 34°NW) then the magma reservoir sits in the tensional stress quadrant since the reservoir is located towards the south-eastern edge of the fault segment and within the western fault block where faulting would be encouraged (see **Figures 7**, **8** and also **Section 5.4**). Clamping on the same magma pathways occurs parallel to the fault plane due to the normal slip component of faulting.

Exacerbation of conditions allowing for magma propagation towards the surface does, however, not guarantee a volcanic eruption. Gudmundsson and Philipp (2006) concluded that for magma propagation to reach the surface the stress field around the pathways must be homogenised and favour extension fracture formation. At Hasan Dağ, the stability of tensional stresses parallel to the AKFS prior to all hypothetical earthquakes is favourable to magma propagation towards the surface, thus promoting conditions for eruption. The magnitude of gradual unclamping perpendicular to the AKFS is greater than gradual clamping orthogonal to it. The earthquake magnitudes considered here predicted to cause further unclamping of pathways above the reservoir and perpendicular to the AKFS thus continuing the encouragement of a future eruption. If the reservoir were close to critical failure, small changes in stress (±0.01 MPa) could trigger an eruption (Nostro et al., 1998; Kriswati et al., 2019). The magnitude of unclamping by the modeled earthquakes is predicated to be > 0.13 MPa and therefore significant.

Gradual slip along the fault segment also causes unclamping of fractures below the reservoir. All hypothetical earthquakes further exacerbate this, irrespective of the magnitude of right-lateral slip with unclamping magnitudes > 0.115 MPa and therefore significant. Unclamping of fractures beneath Hasan Dağ's magma reservoir (predicted to occur perpendicular to the AKFS) may already be evidenced by earthquakes with hypocentral depths > 10 km and thus below the average penetration depth of the TGFZ) (Kürçer and Gökten, 2014). Dilation of fractures below the reservoir may facilitate the formation of feeder dykes from depth and may encourage reservoir failure and eruption by the thermal and volumetric effects of injecting deeper-sourced mafic magma into an upper-crustal reservoir (Sparks et al., 1977). Mineralogical variations in ignimbrites at Hasan Dağ evidence such magma mixing prior to previous explosive eruptions (Aydar and Gourgaud, 1998).

Calculated Coulomb failure stress changes on the reservoir walls by gradual slip of the AKFS show a systematic pattern of clamping of fractures perpendicular to the AKFS and unclamping parallel to it. However, the spatial pattern of Coulomb failure stress change due to future hypothetical earthquakes does not show discernible trends at the lateral point probes. No model predicts wholesale encouragement or discouragement of lateral reservoir failure from predicted stress changes accompanying fault rupture. Lateral expulsion of magma from the reservoir is plausible if unclamping of the reservoir walls overcome the tensile strength of the country rock. Sill injection into country rock reduces the tensile stresses within the vicinity of the reservoir (Gudmundsson, 2000) moving the system further from critical failure. Direct squeezing of the reservoir is debated as to its actual effectiveness at encouraging eruptions due to the possible inadequacy of the volume of magma mobilised during clamping (Eggert and Walter, 2009).

Coulomb failure stress changes on the reservoir walls predicted by our models are a function of static stress transfer. This is not a true reflection of the stress perturbations occurring in the near field immediately after an earthquake. Earthquakes are accompanied by the release of energy in the form of seismic waves. The propagation of these waves causes short-lived, yet high amplitude, dynamic stress changes (Walter and Amelung, 2007). In addition to the static Coulomb failure stress changes that might encourage eruption, dynamic stress transfer can exacerbate the conditions for an eruption by causing expansion of the gaseous phase within a reservoir (Walter et al., 2007) or wholesale disruption of a magma mush (Davis et al., 2007; Gottsmann et al., 2009). Walter et al. (2007) concluded that dynamic stress transfer was at least as critical as static Coulomb failure stress transfer in triggering the Mt. Merapi eruption in 2006. Consequences of dynamic stress transfer for Hasan Dağ's magma reservoir are a topic for further research.

5.4 The September 20, 2020 Karaman-Niğde Earthquake

On the September 20, 2020, a M5.1 earthquake located 35 km to the southwest of Hasan Dağ's summit at a depth of ~8 km reactivated a

segment of the previously thought inactive Karaman-Niğde shear zone (KNSZ) (Aydar et al., 2021). The earthquake and subsequent aftershocks occurred in a volume predicted by this study to have undergone unclamping due to gradual slip along the AKFS (**Figure 8**). This supports the results of our modelling.

Our study does not model changes in Coulomb failure stress on the magma reservoir and fault segment due to slip events along the KNSZ. Further exploration is needed to quantify the mid to long-term effects of these earthquakes. An earthquake occurring on the AKFS would cause rotations of the stress field encompassing the KNSZ and would therefore encourage, or discourage further earthquakes there. However, the orientation of the shear zone relative to the fault segment's Coulomb failure stress change pattern means any seismic event along that segment only transfers a significant magnitude of Coulomb failure stress up to a distance ~20–30 km from the intercept of the two features.

5.5 Implications for Natural Hazard and Risk Assessment

An empirical formula (Wang et al., 2006) links earthquake magnitude with maximum distance of liquefaction R_{max}

$$log\,(R_{max}) = 2.05 + 0.45M_w \quad (14)$$

Taking the largest possible earthquake that could occur along the AKFS ($M_w \sim 6.76$), the equation predicts an R_{max} of ~120 km. This radius encompasses the towns of Aksaray, Nevşehir and Niğde amongst other settlements. These cities alone have a combined population of over 1,000,000. Furthermore, over a third of the city of Aksaray has been deemed to have a moderate to very high potential for liquefaction (Yalcin et al., 2008). Detailed estimations on liquefaction potential for the rest of the region is lacking.

Hasan Dağ is not the only volcanic centre that could be affected by seismic activity along the AKFS. Delle Donne et al. (2010) link earthquake magnitude to the greatest distance seismic energy released by that earthquake can trigger volcanic unrest:

$$M_w = -6.4 + 2.17log\,(R) \quad (15)$$

where R is the maximum distance of unrest. For the greatest earthquake magnitude predicted for the fault segment (M_w = 6.76), R is ~ 1160 km. This encompasses the Quaternary volcanic centres of Acigöl-Nevsehir, Göllü Dag, Erciyes Dağ, Karadağ and the Karapinar volcanic field.

At Hasan Dağ, future eruptions are likely to follow the historic pattern of volcanic activity. This could express itself in two ways. Lava dome extrusions as a continuation of recent activity (Aydar and Gourgaud, 1998; Schmitt et al., 2014; Friedrichs et al., 2020) or a fourth catastrophic ignimbrite eruption capable of reaching Aksaray (Aydar and Gourgaud, 1998). Late Pleistocene and Quaternary dome formations indicate eruptive volumes of up to 0.37 km^3 (Friedrichs et al., 2020) with pyroclastic flows extending up to 9 km from Hasan Dağ's summit (Aydar and Gourgaud, 1998).

In summary, significant seismic and volcano-tectonic hazards exist along the AKFS and we recommend local risk assessment include scenarios explored in this study.

6 CONCLUSION

Using 3D finite element modelling, this study shows that protracted gradual slip along the Akhisar-Kiliç fault segment (AKFS) of the Tuz Gölü fault zone forces the fault segment and Hasan Dağ's magma reservoir towards failure. The current accrual of Coulomb failure stress changes along the fault segment progressively unclamps magma pathways both above and below the magma reservoir. For the upper-bound estimate of Coulomb failure stress change accumulation of ~ 2700±67 Pa yr^{-1} strike-slip failure conditions were reached ~4.5 ka B.P. For the lower-bound estimate of 450±10 Pa yr^{-1} the conditions are currently met for strike-slip failure and were met ~2.5 ka ago for normal slip failure. Our findings imply that the lower-bound of published right-lateral slip rates (0.58 mm yr^{-1}) (Krystopowicz et al., 2020) might be a more plausible estimate of the slip distribution and stress accumulation along the fault segment. Its rupture could result in an earthquake of $5.78\pm0.13 \leq M_w \leq 6.76\pm0.03$ in the future.

Notwithstanding fault rupture, the current stress transfer from the AKFS to Hasan Dağ's magma reservoir by gradual slip of the segment alone is moving the reservoir towards failure with potential for renewed eruptive activity.

The criticality of Hasan Dağ's magmatic system is unknown, but fumarolic degassing and mid-crustal seismicity anomalies are suggestive of active magmatic feeder systems beneath the volcano. These observations in combination with our findings highlight a multi-hazard scenario that is ideally considered in interconnected natural risk analysis and disaster risk reduction (Pescaroli and Alexander, 2018). Finally, our findings have implications for quantifying volcano-tectonic interactions in systems with a long paucity in tectonic and eruptive activity.

DATA AVAILABILITY STATEMENT

The datasets presented in this study can be found in online repositories. The names of the repository/repositories and accession number(s) can be found below: https://doi.org/10.5281/zenodo.5036587.

AUTHOR CONTRIBUTIONS

JG conceived and coordinated the research underpinning this paper. EH developed the models, analyses and initial interpretation as part of an undergraduate project and thesis at the University of Bristol under the supervision of JG. Both authors drafted, read and approved the final manuscript.

FUNDING

JG acknowledges support from the Newton Fund TurkVolc project, NE/P008437/1 and NERC grant NE/S008845/1.

ACKNOWLEDGMENTS

JG expresses his gratitude to TurkVolc project team members Gökhan Atıcı and Mehmet Çobankaya for stimulating discussions whilst climbing Hasan Dağ volcano that inspired the study.

SUPPLEMENTARY MATERIAL

The Supplementary Material for this article can be found online at: https://www.frontiersin.org/articles/10.3389/feart.2021.732696/full#supplementary-material

REFERENCES

Abgarmi, B., Delph, J. R., Ozacar, A. A., Beck, S. L., Zandt, G., Sandvol, E., et al. (2017). Structure of the Crust and African Slab beneath the Central Anatolian Plateau from Receiver Functions: New Insights on Isostatic Compensation and Slab Dynamics. *Geosphere* 13, 1774–1787. doi:10.1130/GES01509.1

Aktuğ, B., Parmaksız, E., Kurt, M., Lenk, O., Kılıçoğlu, A., Gürdal, M. A., et al. (2013). Deformation of Central Anatolia: Gps Implications. *J. Geodyn.* 67, 78–96. doi:10.1016/j.jog.2012.05.008

Aydar, E., and Gourgaud, A. (1998). The Geology of Mount Hasan Stratovolcano, Central Anatolia, Turkey. *J. Volcanol. Geotherm. Res.* 85, 129–152. doi:10.1016/S0377-0273(98)00053-5

Aydar, E., Diker, C., Ulusoy, İ., and Şen, E. (2021). Volcanic Unrest Possibilities in Response to Recent Obruk Seismic Swarm on and Around Hasandağ Stratovolcano (Central Anatolia, Turkey). *Comptes RendusGéosci.* 353, 1–18. doi:10.5802/crgeos.46

Aydar, E. (1992). *Etude volcano-structurale et magmatologique du strato-volcan Hasan Dagi (Anatolie Centrale-Turquie)*. Clermont-Ferrand, France: Université Blaise Pascal. Thesis.

Biggs, J., Dogru, F., Dagliyar, A., Albino, F., Yip, S., Brown, S., et al. (2021). Baseline Monitoring of Volcanic Regions with Little Recent Activity: Application of Sentinel-1 InSAR to Turkish Volcanoes. *J. Appl. Volcanol.* 10, 1–14. doi:10.1186/s13617-021-00102-x

Blake, S. (1981). Volcanism and the Dynamics of Open Magma chambers. *Nature* 289, 783–785. doi:10.1038/289783a0

Bonali, F. L., Tibaldi, A., Corazzato, C., Tormey, D. R., and Lara, L. E. (2013). Quantifying the Effect of Large Earthquakes in Promoting Eruptions Due to Stress Changes on Magma Pathway: the Chile Case. *Tectonophysics* 583, 54–67. doi:10.1016/j.tecto.2012.10.025

Bonali, F. L. (2013). Earthquake-induced Static Stress Change on Magma Pathway in Promoting the 2012 Copahue Eruption. *Tectonophysics* 608, 127–137. doi:10.1016/j.tecto.2013.10.006

Brocher, T. M. (2005). Empirical Relations between Elastic Wavespeeds and Density in the Earth's Crust. *Bull. Seismol. Soc. Am.* 95, 2081–2092. doi:10.1785/0120050077

Cocco, M., and Rice, J. R. (2002). Pore Pressure and Poroelasticity Effects in Coulomb Stress Analysis of Earthquake Interactions. *J. Geophys. Res.* 107, ESE 2–1–ESE 2–17. doi:10.1029/2000JB000138

Davis, M., Koenders, M. A., and Petford, N. (2007). Vibro-agitation of Chambered Magma. *J. Volcanol. Geotherm. Res.* 167, 24–36. doi:10.1016/j.jvolgeores.2007.07.012

De la Cruz-Reyna, S., Tárraga, M., Ortiz, R., and Martínez-Bringas, A. (2010). Tectonic Earthquakes Triggering Volcanic Seismicity and Eruptions. Case Studies at Tungurahua and Popocatépetl Volcanoes. *J. Volcanol. Geotherm. Res.* 193, 37–48. doi:10.1016/j.jvolgeores.2010.03.005

Delle Donne, D., Harris, A. J. L., Ripepe, M., and Wright, R. (2010). Earthquake-induced thermal Anomalies at Active Volcanoes. *Geology* 38, 771–774. doi:10.1130/G30984.1

Deniel, C., Aydar, E., and Gourgaud, A. (1998). The Hasan Dagi Stratovolcano (Central Anatolia, Turkey): Evolution from Calc-Alkaline to Alkaline Magmatism in a Collision Zone. *J. Volcanol. Geotherm. Res.* 87, 275–302. doi:10.1016/S0377-0273(98)00097-3

Dİker, C., Ulusoy, I., Akkaş, E., Şen, E., Çubukçu, H., Gümüş, E., et al. (2018). "Self-potential, Surface Temperature, CO_2 Measurements and Related Structural Discontinuities on Mount Hasan, Turkey," in *Cities On Volcanoes 10 (INGV)*.

Eggert, S., and Walter, T. R. (2009). Volcanic Activity before and after Large Tectonic Earthquakes: Observations and Statistical Significance. *Tectonophysics* 471, 14–26. doi:10.1016/j.tecto.2008.10.003

Fichtner, A., Saygin, E., Taymaz, T., Cupillard, P., Capdeville, Y., and Trampert, J. (2013). The Deep Structure of the North Anatolian Fault Zone. *Earth Planet. Sci. Lett.* 373, 109–117. doi:10.1016/j.epsl.2013.04.027

Friedrichs, B., Atıcı, G., Danišík, M., Atakay, E., Çobankaya, M., Harvey, J. C., et al. (2020). Late Pleistocene Eruptive Recurrence in the post-collisional Mt. Hasan Stratovolcanic Complex (Central Anatolia) Revealed by Zircon Double-Dating. *J. Volcanol. Geotherm. Res.* 404, 107007. doi:10.1016/j.jvolgeores.2020.107007

Fukuyama, E., Kubo, A., Kawai, H., and Nonomura, K. i. (2001). Seismic Remote Monitoring of Stress Field. *Earth Planet. Sp* 53, 1021–1026. doi:10.1186/BF03351699

Göğüş, O. H., Pysklywec, R. N., Şengör, A. M. C., and Gün, E. (2017). Drip Tectonics and the Enigmatic Uplift of the Central Anatolian Plateau. *Nat. Commun.* 8, 1–9. doi:10.1038/s41467-017-01611-3

Gottsmann, J., Lavallée, Y., Martí, J., and Aguirre-Díaz, G. (2009). Magma-tectonic Interaction and the Eruption of Silicic Batholiths. *Earth Planet. Sci. Lett.* 284, 426–434. doi:10.1016/J.Epsl.2009.05.008

Gudmundsson, A., and Brenner, S. L. (2003). Loading of a Seismic Zone to Failure Deforms Nearby Volcanoes: a New Earthquake Precursor. *Terra Nova* 15, 187–193. doi:10.1046/j.1365-3121.2003.00481.x

Gudmundsson, A., and Philipp, S. L. (2006). How Local Stress Fields Prevent Volcanic Eruptions. *J. Volcanol. Geotherm. Res.* 158, 257–268. doi:10.1016/j.jvolgeores.2006.06.005

Gudmundsson, A. (1988). Effect of Tensile Stress Concentration Around Magma chambers on Intrusion and Extrusion Frequencies. *J. Volcanol. Geotherm. Res.* 35, 179–194. doi:10.1016/0377-0273(88)90015-7

Gudmundsson, A. (2000). Dynamics of Volcanic Systems in Iceland: Example of Tectonism and Volcanism at Juxtaposed Hot Spot and Mid-ocean ridge Systems. *Annu. Rev. Earth Planet. Sci.* 28, 107–140. doi:10.1146/annurev.earth.28.1.107

Hamling, I. J., and Kilgour, G. (2020). Goldilocks Conditions Required for Earthquakes to Trigger Basaltic Eruptions: Evidence from the 2015 Ambrym Eruption. *Sci. Adv.* 6, eaaz5261. doi:10.1126/sciadv.aaz5261

Hanks, T. C., and Kanamori, H. (1979). A Moment Magnitude Scale. *J. Geophys. Res.* 84, 2348–2350. doi:10.1029/JB084iB05p02348

Harris, R. A. (1998). Introduction to Special Section: Stress Triggers, Stress Shadows, and Implications for Seismic hazard. *J. Geophys. Res.* 103, 24347–24358. doi:10.1029/98JB01576

Hill, D. P., Pollitz, F., and Newhall, C. (2002). Earthquake-Volcano Interactions. *Phys. Today* 55, 41–47. doi:10.1063/1.1535006

Kanamori, H., and Anderson, D. L. (1975). Theoretical Basis of Some Empirical Relations in Seismology. *Bull. Seismol. Soc. Am.* 65, 1073–1095.

Karaoğlu, Ö., Selçuk, A. S., and Gudmundsson, A. (2017). Tectonic Controls on the Karlıova Triple junction (Turkey): Implications for Tectonic Inversion and the Initiation of Volcanism. *Tectonophysics* 694, 368–384. doi:10.1016/j.tecto.2016.11.018

King, G. C., Stein, R. S., and Lin, J. (1994). Static Stress Changes and the Triggering of Earthquakes. *Bull. Seismol. Soc. Am.* 84, 935–953.

Kiser, E., Palomeras, I., Levander, A., Zelt, C., Harder, S., Schmandt, B., et al. (2016). Magma Reservoirs from the Upper Crust to the Moho Inferred from High-Resolution Vp and vs Models beneath Mount St. Helens, Washington State, USA. *Geology* 44, 411–414. doi:10.1130/G37591.1

Kürçer, A., and Gökten, Y. E. (2012). "Paleoseismological Three Dimensional Virtual Photography Method; A Case Study: Bağlarkayasi-2010 Trench, Tuz Gölü Fault Zone, Central Anatolia, Turkey," in *Tectonics-Recent Advances*. Editor Sharkov, E. (Rijeka, Croatia: InTech,), 201–228.

Kriswati, E., Meilano, I., Iguchi, M., Abidin, H. Z., and Surono (2019). An Evaluation of the Possibility of Tectonic Triggering of the Sinabung Eruption. *J. Volcanol. Geotherm. Res.* 382, 224–232. doi:10.1016/j.jvolgeores.2018.04.031

Krystopowicz, N. J., Schoenbohm, L. M., Rimando, J., Brocard, G., and Rojay, B. (2020). Tectonic Geomorphology and Plio-Quaternary Structural Evolution of the Tuzgölü Fault Zone, Turkey: Implications for Deformation in the interior of the Central Anatolian Plateau. *Geosphere* 16, 1107–1124. doi:10.1130/GES02175.1

Kürçer, A., and Gökten, Y. E. (2014). Neotectonic-period Characteristics, Seismicity, Geometry and Segmentation of the Tuz Gölü Fault Zone. *Bull.Min.Res.Exp.* 149, 19–68. doi:10.19111/BMRE.94099

Gencalioglu Kuscu, G., and Geneli, F. (2010). Review of post-collisional Volcanism in the Central Anatolian Volcanic Province (Turkey), with Special Reference to the Tepekoy Volcanic Complex. *Int. J. Earth Sci. (Geol Rundsch)* 99, 593–621. doi:10.1007/s00531-009-0504-710.1007/s00531-008-0402-4

Lemarchand, N., and Grasso, J.-R. (2007). Interactions between Earthquakes and Volcano Activity. *Geophys. Res. Lett.* 34, L24303. doi:10.1029/2007gl031438

Males, K., and Gottsmann, J. (2021). Minimum Detectable Mass and Volume Fluxes during Magmatic Recharge at High Prominence Volcanoes: An Application to Erciyes Dağ Volcano (Turkey). *Front. Earth Sci.* 9, 750063. doi:10.3389/feart.2021.750063

Nostro, C., Stein, R. S., Cocco, M., Belardinelli, M. E., and Marzocchi, W. (1998). Two-way Coupling between Vesuvius Eruptions and Southern Apennine Earthquakes, italy, by Elastic Stress Transfer. *J. Geophys. Res.* 103, 24487–24504. doi:10.1029/98JB00902

Perfit, M. R., and Davidson, J. P. (2000). "Plate Tectonics and Volcanism," in *Encyclopedia of Volcanoes*. Editor Sigurdsson, H. San Diego, CA: Academic Press, 89–113.

Pescaroli, G., and Alexander, D. (2018). Understanding Compound, Interconnected, Interacting, and Cascading Risks: A Holistic Framework. *Risk Anal.* 38, 2245–2257. doi:10.1111/risa.13128

Piromallo, C., and Morelli, A. (2003). P Wave Tomography of the Mantle under the Alpine-Mediterranean Area. *J. Geophys. Res.* 108. doi:10.1029/2002JB001757

Roman, D. C., Power, J. A., Moran, S. C., Cashman, K. V., Doukas, M. P., Neal, C. A., et al. (2004). Evidence for dike Emplacement beneath Iliamna Volcano, alaska in 1996. *J. Volcanol. Geotherm. Res.* 130, 265–284. doi:10.1016/S0377-0273(03)00302-0

Ruppert, N. A., Prejean, S., and Hansen, R. A. (2011). Seismic Swarm Associated with the 2008 Eruption of Kasatochi Volcano, Alaska: Earthquake Locations and Source Parameters. *J. Geophys. Res.* 116. doi:10.1029/2010JB007435

Salah, M. K., Şahin, Ş., and Topatan, U. (2014). Crustal Velocity and Vp/Vs Structures beneath Central Anatolia from Local Seismic Tomography. *Arab J. Geosci.* 7, 4101–4118. doi:10.1007/s12517-013-1038-7

Schmitt, A. K., Danišík, M., Aydar, E., Şen, E., Ulusoy, İ., and Lovera, O. M. (2014). Identifying the Volcanic Eruption Depicted in a Neolithic Painting at Çatalhöyük, Central Anatolia, Turkey. *PLoS One* 9, e84711. doi:10.1371/journal.pone.0084711

Şengör, A. M. C., and Zabcı, C. (2019). *The North Anatolian Fault and the north Anatolian Shear Zone*. Switzerland: Springer Nature Switzerland AG 2019, 481–494. doi:10.1007/978-3-030-03515-0_27

Sparks, S. R. J., Sigurdsson, H., and Wilson, L. (1977). Magma Mixing: a Mechanism for Triggering Acid Explosive Eruptions. *Nature* 267, 315–318. doi:10.1038/267315a0

Stein, R. S. (1999). The Role of Stress Transfer in Earthquake Occurrence. *Nature* 402, 605–609. doi:10.1038/45144

Tank, S. B., and Karaş, M. (2020). Unraveling the Electrical Conductivity Structure to Decipher the Hydrothermal System beneath the Mt. Hasan Composite Volcano and its Vicinity, SW Cappadocia, Turkey. *J. Volcano. Geotherm. Res.* 405, 107048. doi:10.1016/j.jvolgeores.2020.107048

Tezel, T., Shibutani, T., and Kaypak, B. (2013). Crustal Thickness of Turkey Determined by Receiver Function. *J. Asian Earth Sci.* 75, 36–45. doi:10.1016/j.jseaes.2013.06.016

Toda, S., Stein, R. S., Sevilgen, V., and Lin, J. (2011). Coulomb 3.3 Graphic-Rich Deformation and Stress-Change Software for Earthquake, Tectonic, and Volcano Research and Teaching—User Guide. *US Geol. Surv. open-file Rep.* 1060, 63.

Toprak, V., and Göncöoğlu, M. C. (1993). Tectonic Control on the Development of the Neogene-Quaternary Central Anatolian Volcanic Province, Turkey. *Geol. J.* 28, 357–369. doi:10.1002/gj.3350280314

Tosun, H., Zorluer, İ., Orhan, A., Seyrek, E., Savaş, H., and Türköz, M. (2007). Seismic hazard and Total Risk Analyses for Large Dams in Euphrates basin, Turkey. *Eng. Geol.* 89, 155–170. doi:10.1016/j.enggeo.2006.10.003

Ulusoy, İ., Diker, C., Şen, E., Aydın, E., Akkaş, E., Gümüş, E., et al. (2020). Surface Expressions of Morphostructural Features at Hasandağ Stratovolcano on DEM Datasets. *Med. Geosc. Rev.* 3, 175–191. doi:10.1007/s42990-020-00044-3

Walter, T. R., and Amelung, F. (2006). Volcano-earthquake Interaction at Mauna Loa Volcano, Hawaii. *J. Geophys. Res.* 111. doi:10.1029/2005JB003861

Walter, T. R., and Amelung, F. (2007). Volcanic Eruptions Following M ≥ 9 Megathrust Earthquakes: Implications for the Sumatra-Andaman Volcanoes. *Geol* 35, 539–542. doi:10.1130/G23429A.1

Walter, T. R., Wang, R., Zimmer, M., Grosser, H., Lühr, B., and Ratdomopurbo, A. (2007). Volcanic Activity Influenced by Tectonic Earthquakes: Static and Dynamic Stress Triggering at Mt. Merapi. *Geophys. Res. Lett.* 34. doi:10.1029/2006GL028710

Wang, C.-Y., Wong, A., Dreger, D. S., and Manga, M. (2006). Liquefaction Limit during Earthquakes and Underground Explosions: Implications on Ground-Motion Attenuation. *Bull. Seismol. Soc. Am.* 96, 355–363. doi:10.1785/0120050019

Wang, J., Xu, C., Freymueller, J. T., Li, Z., and Shen, W. (2014). Sensitivity of Coulomb Stress Change to the Parameters of the Coulomb Failure Model: A Case Study Using the 2008 M W 7.9 Wenchuan Earthquake. *J. Geophys. Res. Solid Earth* 119, 3371–3392. doi:10.1002/2012JB009860

Wells, D. L., and Coppersmith, K. J. (1994). New Empirical Relationships Among Magnitude, Rupture Length, Rupture Width, Rupture Area, and Surface Displacement. *Bull. Seismol. Soc. Am.* 84, 974–1002.

Wilson, L. (1980). Relationships between Pressure, Volatile Content and Ejecta Velocity in Three Types of Volcanic Explosion. *J. Volcanol. Geotherm. Res.* 8, 297–313. doi:10.1016/0377-0273(80)90110-9

Yalcin, A., Gokceoglu, C., and Sönmez, H. (2008). Liquefaction Severity Map for Aksaray City Center (Central Anatolia, Turkey). *Nat. Hazards Earth Syst. Sci.* 8, 641–649. doi:10.5194/nhess-8-641-2008

Young, N. K., and Gottsmann, J. (2015). Shallow Crustal Mechanics from Volumetric Strain Data: Insights from Soufrière Hills Volcano, Montserrat. *J. Geophys. Res. Solid Earth* 120, 1559–1571. doi:10.1002/2014JB011551

Conflict of Interest: The authors declare that the research was conducted in the absence of any commercial or financial relationships that could be construed as a potential conflict of interest.

Publisher's Note: All claims expressed in this article are solely those of the authors and do not necessarily represent those of their affiliated organizations, or those of the publisher, the editors and the reviewers. Any product that may be evaluated in this article, or claim that may be made by its manufacturer, is not guaranteed or endorsed by the publisher.

frontiers in Earth Science

BRIEF RESEARCH REPORT
published: 01 February 2022
doi: 10.3389/feart.2021.775269

Tidal Modulation of Hydrothermal Tremor: Examples From Ischia and Campi Flegrei Volcanoes, Italy

Simona Petrosino[1]*† *and Stéphanie Dumont*[2]†

[1]Istituto Nazionale di Geofisica e Vulcanologia, Sezione di Napoli—Osservatorio Vesuviano, Naples, Italy, [2]Instituto Dom Luiz (IDL), University of Beira Interior, Covilhã, Portugal

Volcano dynamics results from an interplay between internal and external processes spanning different time scales. Unravelling how such processes interact may provide key insights into the mechanisms that may lead to the destabilization of the volcanoes and eruption, a critical information to forecast hazards. Studies dealing with tidal influence on volcanoes fall within this context, yet the cause-effect relationship between tides and eruptions is still poorly understood. In the present study, we investigate the tidal influence on two nearby volcanoes, Ischia and Campi Flegrei (Italy), characterized by intense hydrothermal activity. We analyze the seismic tremor of hydrothermal origin recorded by four seismic stations between January and June 2020 by using Singular Spectrum Analysis. We detect up to five long term tidal periodicities ranging from ~5 to ~29 days. The results indicate that the seismic tremor is modulated by Earth tides at both volcanoes. In addition, differences in phase and amplitude modulation between the response of both hydrothermal systems to tidal forcing reveal specific features related to the tremor source and to properties of the surrounding medium. These phenomena indicate an interplay between solid Earth and the dynamics of these two volcanoes. Similar approaches on hydrothermal systems at volcanoes would contribute to better characterize the hydrothermal circulation and their evolving conditions that may represent a precursor of a new phase of activity.

Keywords: Campi Flegrei, Ischia, seismic tremor, hydrothermal activity, tidal modulation, SSA

OPEN ACCESS

Edited by:
Nico Fournier,
GNS Science, New Zealand

Reviewed by:
Yosuke Aoki,
The University of Tokyo, Japan
Corentin Caudron,
Université libre de Bruxelles, Belgium

***Correspondence:**
Simona Petrosino
simona.petrosino@ingv.it

†*These authors have contributed equally to this work and share first authorship*

Specialty section:
This article was submitted to Volcanology, a section of the journal Frontiers in Earth Science

Received: *13 September 2021*
Accepted: *06 December 2021*
Published: *01 February 2022*

Citation:
Petrosino S and Dumont S (2022) Tidal Modulation of Hydrothermal Tremor: Examples From Ischia and Campi Flegrei Volcanoes, Italy. Front. Earth Sci. 9:775269. doi: 10.3389/feart.2021.775269

INTRODUCTION

Tidal influence has been evidenced at many volcanoes through the analysis of geological, geophysical, and geochemical time-series acquired during unrest and eruptive phases such as earthquake rates, frequency of explosive and/or eruptive events, volcanic tremor, gas, and lava fluxes (Dzurisin, 1980; McNutt and Beavan, 1987; Sottili et al., 2007; Sottili and Palladino, 2012; Girona et al., 2018; Dumont et al., 2020, 2021; Sahoo et al., 2021; Sottili et al., 2021). Some quiescently active volcanoes like Wakamiko Caldera (Japan) and Santorini (Greece), where activity can be reduced to degassing and/or seismicity, seem also to be sensitive to Earth tides (Yakiwara et al., 2013; Contadakis et al., 2017). At open volcanic systems for instance, gas emissions are mainly evacuated through the open conduit. Such passive gas emissions as at Llaima, Villarrica (Chile), and Cotopaxi (Ecuador) volcanoes have shown an oscillating pattern including tidal periodicities (Bredemeyer and Hansteen, 2014; Dinger et al., 2018). More generally, circulation of hydrothermal fluids affects wide areas, taking diverse forms such as fumaroles, diffuse degassing, and inducing rock alteration. This circulation can be

tracked by gas measurements but also by seismic tremor. Monitoring hydrothermal activity at quiescently active volcanoes can provide insights on the dynamics of the underlying magmatic plumbing system (Battaglia et al., 2006; Gottsmann et al., 2007; Miller et al., 2017; Magee et al., 2018; Eichelberger et al., 2020). By studying the interplay between the hydrothermal system and external forcing such as Earth tides, we tackle processes that may lead to the destabilization of the volcanic system and eruption triggering. Actually, by inducing a global mass reorganization on Earth on different time and space scales for both solid and fluid envelopes (Nakiboglu and Lambeck, 1980), solid Earth and ocean tides participate in changing the stress, strain, or pore-fluid pressure conditions that may be critical in dynamical systems such as volcanoes and faults (Jupp et al., 2004; Scholz et al., 2019; Dumont et al., 2022). This is illustrated by studies that have shown a correlation between the onset of volcanic eruptions and the lunar cycle for instance, e.g., Mauk and Johnston (1973); Dzurisin, (1980), or a sensitivity to Earth tides that appears with migration of magma towards the surface or when the systems get closer to a critical state (Berrino and Corrado, 1991; De Lauro et al., 2013; Girona et al., 2018; Miguelsanz et al., 2021). However, such a response of volcanoes to tidal forcing has not been systematically reported, leaving many questions unsolved.

Here, we consider two volcanoes, Ischia island and Campi Flegrei caldera (Italy), characterized by different forms of hydrothermal activity. By analyzing and comparing the hydrothermally generated seismic tremor for two sites located in each volcano, we aim at gaining new insights on the conditions leading volcanic and hydrothermal systems to respond to tidal forces and therefore on those prone to destabilize them. We used time-series of the seismic tremor recorded between January and June 2020. For each site, we calculated the Root Mean Square (RMS) of the signal in the frequency bands recognized as of hydrothermal origin (De Lauro et al., 2013; Chiodini et al., 2017; Falanga et al., 2021). We applied Singular Spectrum Analysis (SSA) to detect any periodicities present in the time-series. We compared them to those extracted in the length-of-day (l.o.d.) to confirm their tidal origin, as l.o.d. represents a measure of the tidal action on the Earth's rotation velocity (Lambeck 2005; Le Mouël et al., 2019). The results indicate that the seismic tremor at both volcanoes is partly modulated by Earth tides; this modulation in phase and amplitude seems to vary with the nature of hydrothermal activity and underlying medium.

Geological Setting

We investigate the tidal influence on two quiescently active coastal volcanoes characterized by intense hydrothermal activity, Ischia island and Campi Flegrei. Both volcanoes belong to the Phlegraean Volcanic District, Southern Italy. The island of Ischia is located in the westernmost part of the Phlegraean Volcanic District representing the subaerial portion of a larger volcanic system. Its activity started around 150 kyr, including eight eruptions over the last 2 kyr and is characterized by both effusive and explosive behaviors (de Vita et al., 2010). The most impacting eruption at Ischia was that of the Green Tuff of Mt. Epomeo, which occurred 55 kyr ago. This eruption caused the collapse of the central sector of the island and was followed by the resurgence of a polygonal block on the northern sector that represents the main source of seismicity on the island. In the last few years, seismicity has been generally low, except for a Mw 3.9 earthquake that occurred on August 21, 2017 along the border of Mt. Epomeo (Trasatti et al., 2019; Cusano et al., 2020a, 2020b). Ischia is affected by significant ground deformation. Presently, a slow subsidence, reflecting a gradual depressurization of the magmatic/hydrothermal system beneath Mt. Epomeo is observed (Ricco et al., 2019). The interactions between volcano-tectonic dynamics, ground deformation, and underground fluid circulation have been recognized as resulting from a complex geothermal system. Deep hot fluids rise from distinct superimposed hydrothermal reservoirs, in the northern and southern part of the island (Di Napoli et al., 2009), with temperatures from 150°C to 270°C and depths ranging from 150 to 1000 m b.s.l. In the shallow aquifer, they mix with meteoric and marine waters after which they rise to the surface along high-permeability pathways, e.g., fractures and faults, inducing surface manifestations such as fumarolic activity and thermal springs. This persistent hydrothermal activity leaves its fingerprints in the background seismic signal (Cusano et al., 2020b; Falanga et al., 2021). Recent studies have shown that the interaction of the circulating fluids within the rock matrix generates self-sustained oscillations observed as seismic tremor in the 1–2 Hz frequency band (Cusano et al., 2020b; Falanga et al., 2021).

The Campi Flegrei caldera, located to the west of the town of Naples, was generated by two major collapses, the Campanian Ignimbrite (~39 kyr), and the Neapolitan Yellow Tuff (~15 kyr). Campi Flegrei is subjected to ground deformation consisting of alternating phases of uplift and subsidence (Isaia et al., 2009; Del Gaudio et al., 2010). This typical activity is known as bradyseism. The deformation is centered in the town of Pozzuoli and gradually decreases towards the caldera margins. The most relevant bradyseismic crises occurred in 1969–1972 and 1982–1984, with a maximum vertical deformation of about 1.8 m. Uplifts are related to both magmatic and hydrothermal sources due to either the pressurization of a magmatic gas reservoir at 3–4 km depth, or caused by repeated CO_2-rich fluid injections from the deeper reservoir into the shallow (~2 km depth) hydrothermal system (Amoruso et al., 2014; Chiodini et al., 2017; Gresse et al., 2017; Petrosino and De Siena, 2021). The hot fluids (mainly H_2O and CO_2) exsolve from a deep magmatic body and then mix with meteoric components in the hydrothermal reservoir (Gresse et al., 2017). A large amount of hot hydrothermal fluids are released at the surface through diffuse degassing and fumaroles as well as boiling mud pools located at the Solfatara crater and Pisciarelli fumarolic field, which are the most thermally active areas of the caldera (Chiodini et al., 2017; Gresse et al., 2017; Young et al., 2020). This hydrothermal activity within Campi Flegrei is concentrated along fault zones, where highly fractured rocks facilitate fluid escape.

Uplift episodes are accompanied by seismic swarms of volcano-tectonic (VT) seismicity (Bellucci Sessa et al., 2021) and, less frequently, by long-period (LP) events (Saccorotti et al., 2007; Cusano et al., 2008). The majority of the

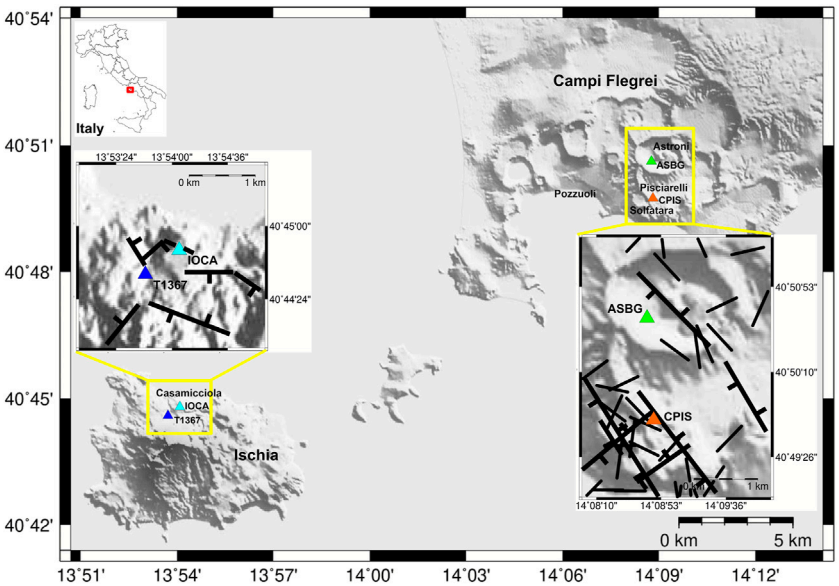

FIGURE 1 | The studied areas (indicated by the red box on the map in the upper left corner) with the location of the seismic stations (triangles). The two insets corresponding to yellow boxes show the fault (black half-tick lines) and fracture distributions (black lines) at Campi Flegrei (Vitale and Isaia, 2014) and Ischia island (Di Giuseppe et al., 2017).

earthquakes are located at shallow depths (up to 4 km b.s.l) beneath the Solfatara-Pozzuoli area. VTs are generated by brittle shear failure mechanisms induced by the pressurization of the hydrothermal system and fluid flow towards the surface (Saccorotti et al., 2007; De Lauro et al., 2016). LPs are caused by the acoustic resonance of cracks filled by a water-gas mixture of hydrothermal origin (Cusano et al., 2008; De Lauro et al., 2012; Falanga and Petrosino, 2012). Geothermal activity is the source of hydrothermal seismic tremor which shares the same frequency content (0.4–1 Hz) as LP events (De Lauro et al., 2013). In addition, at the Pisciarelli fumarolic field, shallow surface degassing and a boiling mud pool generate high frequency (5–15 Hz) tremor (Chiodini et al., 2017), which is only recorded at nearby stations.

The influence of Earth tides at the Campi Flegrei volcanic system has been evidenced on different time scales. Periodicities matching short (semidiurnal, diurnal) to long (fortnightly, monthly) term tidal constituents have been detected in several geophysical data: gravity changes (Berrino and Corrado, 1991), ground deformation (De Lauro et al., 2018; Ricco et al., 2019; Petrosino et al., 2020), ground temperature (Caputo et al., 2020; Cusano et al., 2021), LP and VT earthquake rates and energy (De Lauro et al., 2012; Petrosino et al., 2018), and hydrothermal tremor (De Lauro et al., 2013).

Data and Methods

Seismic data (**Supplementary Figures S1, S2**) were collected at four three-component seismic stations, two (CPIS and ASBG) installed at Campi Flegrei, and two (IOCA and T1367) at Ischia island (**Figure 1**). CPIS, ASBG, and IOCA are equipped with Guralp CMG 40T (60s) broadband seismometers; T1367 with a Lennartz LE-3Dlite (1 Hz) velocimeter. The CPIS station is located at the Pisciarelli site, near a boiling mud pool which is the shallow source of a high-frequency (5–15 Hz) continuous fumarolic tremor (Chiodini et al., 2017). The ASBG station is located inside the natural oasis of the Astroni tuff cone; in this site the instrument records low-frequency (0.4–1 Hz) tremor sourced from the hydrothermal activity in the nearby Solfatara crater (De Lauro et al., 2013). The two seismic stations deployed at Ischia are installed in the northern part, in the Casamicciola town area that was mostly struck by the earthquake of August 21, 2017. Hydrothermal activity at Ischia consists of shallow fluid circulation that generates a seismic tremor whose fundamental mode is centered on the 1–2 Hz band (Cusano et al., 2020a, 2020b; Falanga et al., 2021).

Data were recorded during the first 6 months of 2020 which was a particularly calm period. In fact, on 8 March, Italy started the lockdown period due to the COVID-19 pandemic (Falanga et al., 2021), so the anthropogenic seismic noise was strongly reduced as a consequence of the restrictions imposed to the human activities for containing the pandemic. A preliminary check of the signal gaps due to possible sensor breakdowns was performed; to reduce such gaps, the following intervals were considered for each station:

- CPIS: 1 Jan to 19 Apr (109 days)
- ASBG: 15 Feb to Jun 30, 2020 (136 days)
- IOCA: 1 Jan to Jun 29, 2020 (180 days)
- T1367: 24 Mar to Jun 8, 2020 (75 days)

The seismic tremor of hydrothermal origin was extracted from the raw data by filtering the waveforms in different frequency bands, depending on the stations under consideration: 1–2 Hz band for both Ischia stations, 5–15 Hz for CPIS, and 0.4–1 Hz for

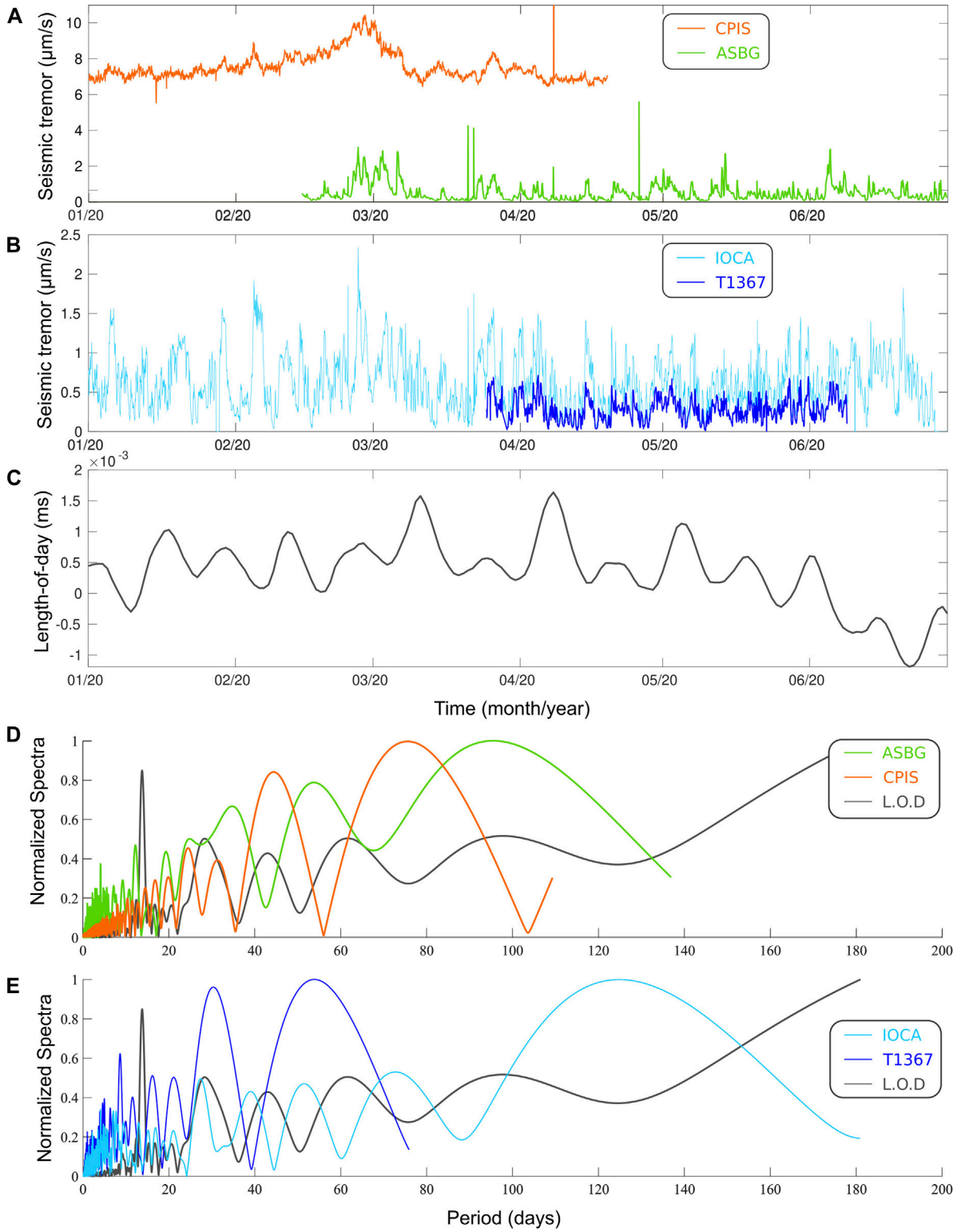

FIGURE 2 | RMS amplitude of the seismic tremor at Campi Flegrei **(A)** and Ischia island **(B)**. Length-of-day (l.o.d) **(C)** and their normalized spectra in the two lower panels **(D–E)**.

ASBG. The frequency bands were chosen on the basis of past studies and correspond to the frequency range in which hydrothermal tremor has been observed (De Lauro et al., 2013; Chiodini et al., 2017; Falanga et al., 2021). Then, we calculated the hourly RMS of the amplitude of the filtered signal hereinafter simply referred to as seismic tremor (De Lauro et al., 2013; Cusano et al., 2020b). As the squared amplitude of a seismic signal is proportional to its energy (Lay and Wallace, 1995), the RMS gives a measure of the energy release. For each station, RMS values were averaged over the three directions of motion.

We also considered the time-series of the length-of-day (l.o.d), a global parameter measured on Earth, that records the Earth's rotation velocity whose short-term variations express the tidal action on Earth (Lambeck, 2005; Le Mouël et al., 2019). We used the daily measurements of l.o.d. from the EOP14C04 dataset covering the 1 January to June 30, 2020 interval and provided by the International Earth Rotation Service (IERS, Paris, France, (https://www.iers.org /IERS /EN /DataProducts /EarthOrientationData /eop.html).

Using a similar approach as Dumont et al. (2020), we applied Singular Spectrum Analysis (SSA) to the seismic tremor and l.o.d time-series. SSA is a non-parametric time-series analysis technique that has been used for a large variety of geophysical datasets (e.g., Bozzo et al., 2010; Lopes et al., 2017; Le Mouël et al., 2019). It allows the decomposition of time-series into a sum of small numbers of components such as slowly varying trend, (pseudo) oscillations, and noise. The algorithm is based on a two-step approach: first, the building of the trajectory matrix based on lagged copies of the original time-series; second, the decomposition using the Singular Value Decomposition (SVD) algorithm. Families of eigenvectors and eigenvalues are then identified through their behavior (pseudo/non-oscillatory) and periods obtained from the Fourier transform, allowing to determine the different components present in the signal. Eigenvalues are ranked in the decreasing order of amplitude (**Supplementary Figure S3**), allowing us to focus on the components contributing the most to the original time-series. These components extracted in the seismic tremor were then compared to those extracted in the l.o.d and the tidal periodicities listed in Ray and Erofeeva (2014), to identify them as tidal constituents. More on SSA method and applications can be found in Golyandina and Zhigljavsky (2013), Bozzo et al. (2010), Lopes et al. (2017), Le Mouël et al. (2019), and Dumont et al. (2020, 2021).

RESULTS

At Campi Flegrei, the seismic tremor was simultaneously recorded at ASBG and CPIS stations over ~2 months. Their variations do not exceed 5 μm/s (**Figure 2A**). Besides, the temporal variations of the seismic tremor amplitude at both stations are relatively different, except late February-early March 2020 when the amplitude of the seismic tremor shows relative higher and sustained values at both sites (**Figure 2A**). These differences are also expressed by their spectral content (**Figure 2D**) that also reflects the different frequency bands used to filter them (**Figure 2D**). On the contrary, at Ischia island (where simultaneous recordings are available over slightly more than 2 months), the seismic tremor variations at IOCA and T1367 sites are much more similar and also smaller, e.g., about half an order than those recorded at Campi Flegrei (**Figures 2B,E**). The seismic tremor measured at T1367 shows lower amplitude variations, that are about half of that at the IOCA station. Over this first half of 2020, the l.o.d variations do not exceed 2 ms, showing a declining trend from late April 2020 (**Figure 2C** and **Supplementary Figure S4**). A first-order comparison of the spectral content of these different time-series suggests that the seismic tremor of IOCA shares more common features with that of the l.o.d. (**Figure 2E**).

We identified trends (**Supplementary Figure S4**) and six to seven oscillating components in each of the seismic tremor and l.o.d. time-series using the main first 15 eigenvalues (**Supplementary Figure S3**). All four seismic tremor time-series are mainly composed by periods of a few days to a few months among which we identified periodicities corresponding to long-term tidal constituents which we later refer to using their Darwin's symbol (**Table 1** and **Supplementary Figure S3**). Thus, we recognized three and five tidal periodicities at the T1367 and IOCA stations located on Ischia island, and four and five for the ASBG and CPIS stations in Campi Flegrei (**Table 1**).

The monthly and fortnightly constituents are common to all sites, although their uncertainties calculated from the half-width of their peaks at half-height do not allow us to discriminate between their lunisolar and lunar origin (MSm/Mm, MSf/Mf). The monthly tidal constituent represents the strongest component after the trend for ASBG and IOCA stations that are the longest time-series with 136 and 180 days, respectively (**Supplementary Figure S3**). This component is better differentiated from the other constituents for ASBG, whereas at IOCA, the contribution of Mm/MSm is of the same order as Mt (**Supplementary Figure S3**). The waveforms of the seismic tremor associated with the Mm/MSm period are locally in phase, i.e., on one hand for IOCA and T1367 stations and on the other hand for CPIS and ASBG (**Figures 3A,B**). For Campi Flegrei, the monthly tidal component clearly appears in quadrature with those extracted in the l.o.d. (**Figures 3A,B**). The waveform corresponding to Mm/MSm for the ASBG station shows a strong attenuation that is not observed at CPIS, the modulation in amplitude of this latter station being closer to those of the l.o.d. Some attenuation seems to also take place at Ischia, with the Mm/MSm component for the T1367 station when compared to that of IOCA.

The fortnightly constituents appear in the first three components for the ASBG and T1367 stations (**Supplementary Figure S3**), as the fifth component for the CPIS station, and in a much lower rank for IOCA, identified as 21st and 22nd eigenvalues. For Campi Flegrei, the fortnightly components extracted in the seismic tremor at CPIS and ASBG both show an amplitude increase, while that of the l.o.d. is rather constant (**Figure 3C**). For Ischia, the Mf/MSf components are in phase for the seismic tremor of T1367 and IOCA, showing slight amplitude variations (**Figure 3D**).

TABLE 1 | Tidal constituents extracted in the l.o.d. and the seismic tremor for four seismic stations: IOCA and T1367 at Ischia island, CPIS and ASBG at Campi Flegrei, and identified using Ray and Erofeeva (2014).

l.o.d	Seismic tremor at Ischia		Seismic tremor at Campi Flegrei		Tidal periodicities (days)	Darwin symbol of tidal constituents
	IOCA (180 days)	T1367 (75 days)	CPIS (109 days)	ASBG (136 days)		
39.0 +/– 5.3 d	—	—	47.4 +/– 13. 2d	40.7 +/– 9.7 d	Semi-annual harmonic (182.6 days)	—
30.1 +/– 3.9 d	29.0 +/– 3.5 d	28.9 +/–9.2 d	27.6 +/– 4.4 d	28.3 +/– 13.7 d	31.8	MSm
27.7 +/– 2.3 d	29.0 +/– 3.5 d	28.9 +/–9.2 d	27.6 +/– 4.4 d	28.3 +/– 13.7 d	27.5	Mm
20.4 +/– 1.4 d	—	—	18.0 +/– 2.3 d	—	Harmonic	
13.7 +/– 0.6 d	12.9 +/– 0.6 d	13.0 +/– 1.5 d	14.1 +/– 1.2 d	12.2 +/– 0.7 d	14.7/13.6	Mf/MSf
9.2 +/– 0.3 d	9.5 +/– 0.4 d	8.7 +/– 0.7 d	10.1 +/– 1.4 d	9.4 +/– 0.5 d	9.1	Mtm
7.0 +/– 0.2 d	7.1 +/– 0.4 d		7.9 +/– 0.4 d	7.2 +/– 0.2 d	7,2	Mt
5.6 +/– 0.2 d	5.4 +/– 0.2 d	—	—	—	5.4	Msp
—	4.1 +/– 0.08 d	4.1 +/– 0.4 d	4.2 +/– 0.1 d	4.1 +/– 0.1 d	Harmonic	—

In the four time-series of seismic tremor, we also extracted the ~9-day tidal periodicity, known by the Darwin's symbol Mtm, at both volcanoes (**Table 1**). The ~7-day tidal periodicity or Mt was detected at all sites except at the T1367 station in Ischia, and that of ~5 days corresponding to Msp tide was only observed at IOCA and in the l.o.d. (**Table 1**). In this table, we also listed a ~4-day period that was extracted in all four seismic tremor time-series (**Figure 3E**). Such periodicity was also detected in co-eruptive geophysical time-series acquired in Cape Verde (Dumont et al., 2021) and might correspond to a harmonic of longer tidal period. An interesting observation of this periodicity resides in the modulation of its amplitude. At Ischia, this ~4-day period shows a decreasing amplitude over the 6 months of observation at the IOCA station. At Campi Flegrei, a similar modulation in amplitude of the seismic tremor is observed but only at ASBG, even if the decrease is much more pronounced. This modulation appears to be opposite to that observed at CPIS, where the amplitude is regularly increasing from January to April, 2020 (**Figure 3E**).

Finally, one can note two additional long periods (~40 and ~18 days) in the seismic tremor recorded at Campi Flegrei, also detected in the l.o.d. Both may represent harmonics of longer tidal periods and in particular those of the solar annual tide.

DISCUSSION

Campi Flegrei

The analysis of the periodicities in the seismic tremor recorded at Campi Flegrei highlights the presence of long-term tidal constituents ranging from ~7 to ~28 days. Our results, together with those from De Lauro et al. (2013), who evidenced semi-diurnal and diurnal components, indicate a broad tidal spectrum of the hydrothermal tremor. Some of the long-term tidal periodicities have also been detected in other geophysical observables, e.g., ground deformation (De Lauro et al., 2018; Ricco et al., 2019; Petrosino et al., 2020) and temperature time-series (Caputo et al., 2020; Cusano et al., 2021) as well as in rates of VT earthquakes (Petrosino et al., 2018), suggesting that these different tides and, in particular, the monthly and fortnightly constituents influence several manifestations of the caldera activity.

The waveforms associated with tidal constituents extracted in the seismic tremor by SSA provide another kind of information. In the examples presented in **Figure 3**, the modulation in amplitude of similar tidal components extracted in ASBG and CPIS time-series varies significantly from site to site, except maybe for the fortnightly constituents (**Figure 3C**). The amplitude at ASBG and CPIS evolves in an opposite manner, accompanied by an attenuation at ASBG which is not observed at CPIS. Such different behavior of the waveforms extracted in the hydrothermal tremor recorded at two nearby stations (<2 km) points towards a local effect. Two factors, the source of the seismic tremor and the site effect, could cause such variations. On one hand, CPIS is located close to the mud pool of the Pisciarelli fumarolic field. It records a tremor whose wavefield is dominated by high frequencies (5–15 Hz) due to the boiling and degassing phenomena at the surface (Chiodini et al., 2017; Gresse et al., 2017). In other words, we are dealing with a high frequency and very localized source of tremor for the CPIS station. On the other hand, the ASBG station is located at a distance of ~1.6 km from the Pisciarelli site and records most exclusively the seismic tremor in a lower frequency band, e.g., 0.4–1 Hz as shown in its Power Spectral Density (**Supplementary Figure S3**; De Lauro et al., 2013; Capuano et al., 2017). The source of this tremor relates to a more complex origin likely due to hydrothermal fluid flow and circulation in the sub-superficial (~2 km of depth) mixing zone of Solfatara (De Lauro et al., 2013; Gresse et al., 2017). Moreover, the results of a recent high-precision gravity survey indicate the presence of a low density body beneath the Astroni volcano where ASBG is located and which was interpreted as a sealed fluid reservoir. This reservoir, which produces no geothermal manifestation at the surface, is likely fed by the Solfatara-Pisciarelli system through a network of faults (Young et al., 2020).

The different responses at CPIS and ASBG can also be due to site effects. There are many geological and geophysical evidences of the heterogeneity of the Campi Flegrei shallow crustal structure. Indeed, differences in seismic velocity and attenuation as well as fracture density (**Figure 1**) characterize

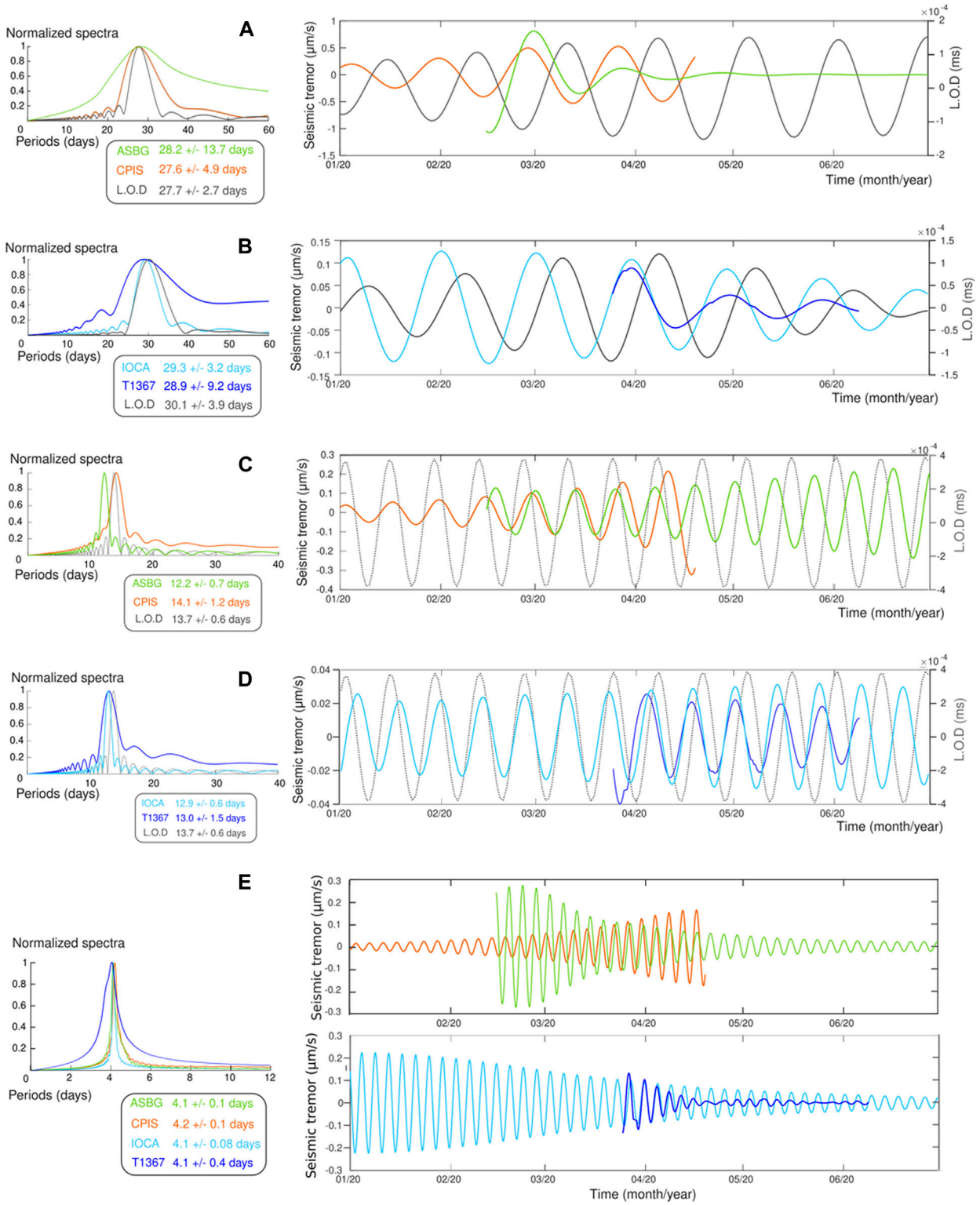

FIGURE 3 | Tidal components extracted in the seismic tremor and l.o.d. time-series for **(A–B)** ~27–31 (Mm/MSm) and **(C–D)** ~13 days (Mf/MSf). Panel **(E)** represents the ~4-day period extracted in all four seismic tremor time-series which likely corresponds to the harmonic of longer-period tides. The normalized spectra are shown on the left side and the corresponding waveforms on the right.

the two sites (De Siena et al., 2010, 2018; Vitale and Isaia, 2014). It is likely that soil and rocks beneath the two stations amplify or act as a damper according to their specific properties, e.g., rheology, porosity, permeability, fracture density. The water-saturation of the host rocks and rock properties vary with tides (Takano et al., 2014; Malagnini et al., 2019) and the seasonal hydrological cycle including rainfall (De Lauro et al., 2018; Ricco et al., 2019; Petrosino et al., 2020, Petrosino et al., 2021). These inherent properties are also highly modified by the hydrothermal activity that induces an alteration of the surrounding layers. Thus, the variations of rock properties of the first kilometers of the crust at ASBG and CPIS sites may significantly impact the wave propagation including that of tidal origin.

Such influence of the site effect on the tidal response of geophysical measurements is in agreement with observations made from the analysis of ground tilt and temperatures time-series (De Lauro et al., 2018; Caputo et al., 2020; Petrosino et al., 2020).

The seismic tremor recorded at Campi Flegrei also shows two additional periodicities (~40 and ~18 days). Interestingly, an ~18-day periodicity was detected in ground tilt and VT occurrence and it was ascribed to the effect of the atmospheric pressure (De Lauro et al., 2018; Petrosino et al., 2018). Furthermore, the availability of long time-series (5 years) of ground temperature recorded at the Pisciarelli site allowed for a finer spectral analysis and revealed spectral components in the range 18.1–19.6 days. Most of these components are related to atmospheric factors, whereas only one was attributed to endogenous processes (Caputo et al., 2020). A similar analysis also evidenced the concomitance of external and internal forcing in modulating the ground temperature time-series in the band 30–50 days (Cusano et al., 2021).

Ischia

Similarly as we obtained for Campi Flegrei, our analysis of the seismic tremor measured at IOCA and T1367 stations reveals tidal components ranging from ~5 to ~29 days (**Table 1**), the higher number of tidal periodicities detected at IOCA being likely due to its longer time record compared with that of T1367. Contrary to Campi Flegrei, the waveforms associated with the tidal periodicities extracted at IOCA and T1367 are in phase and show very similar modulations of their amplitude (**Figure 3**), the amplitude of waveforms extracted for the seismic tremor of the T1367 station shows a light attenuation. Such similar behavior of the two sites suggests that these signals of seismic tremor are similarly first-order modulated by Earth tides, independently of the site of data acquisition. Indeed, the two stations IOCA and T1367 are very close (at a distance of less than 700 m): the seismic and magnetotelluric imaging indicate similar structures beneath them (Capuano et al., 2015; Di Giuseppe et al., 2017) as well as fault density (**Figure 1**, Di Giuseppe et al., 2017; Cusano et al., 2020b). A local amplification effect was indeed detected in the seismic tremor recorded at IOCA in the 1–2 Hz frequency band (Cusano et al., 2020b) and might explain the light difference in the modulation observed in the tidal constituents of IOCA and T1367 (**Figure 3**).

In addition, the seismic signals recorded at both sites are ascribable to the same tremor source related to the fluid flow within the hydrothermal system (Cusano et al., 2020b; Falanga et al., 2021). Past geophysical and geochemical studies have inferred the existence of a deep (>900 m) hydrothermal reservoir feeding a diffuse shallow aquifer (0–200 m of depth) located between the northern coast and the inner part of the island (Di Napoli et al., 2009; Di Giuseppe et al., 2017). Here, meteoric and sea water mix with the ascending deep fluids, causing in turn a pressure build-up in the shallow pipe-like conduits, which originates the hydrothermal seismic tremor. The similar behavior of the waveforms associated with tidal periodicities at IOCA and T1367 is thus consistent with the existence of this common source of tremor.

CONCLUSION

Here we explore the tidal influence on hydrothermal activity at Ischia and Campi Flegrei using seismic tremor data and the SSA technique. By analyzing the seismic tremor at each volcano, we characterize the tidal action on the fluid circulation through the identification of tidal periodicities. We also provide first insights on the response of hydrothermal systems to this external forcing by analyzing the waveforms of tidal constituents extracted by SSA.

At Campi Flegrei, past studies (De Lauro et al., 2013) of tidal modulation of low-frequency hydrothermal tremor were based on simple spectral analysis and focused on semi-diurnal and diurnal tidal constituents. Here, we provide complementary results which contribute in defining the long-period components of the tidal spectrum of both low-frequency and high-frequency tremor. In addition, this study presents the first evidence of tidal modulation of the hydrothermal tremor at Ischia too.

Our results evidence differences between the response of the two hydrothermal systems to tidal forcing. The two sites on Ischia seem to respond more easily and in a more similar manner to solid Earth tides when compared to those in Campi Flegrei. On the opposite side, in the Campi Flegrei caldera, the waveforms associated with tidal periodicities of the hydrothermal tremor show clear site-dependent attenuation likely related to more heterogeneity in the underlying layers.

Evidence of tidal forcing on hydrothermally generated seismic tremor has also been documented in other volcanic environments but mainly submarine ones (Tolstoy et al., 2002; Yakiwara et al., 2013; Meier and Schlindwein, 2018). Interestingly, the modulations of the seismic tremor have been recognized not only during eruptive phases but also in quiescent or unrest volcanoes. Focusing on the tidal influence on hydrothermal circulation of subaerial volcanoes and in particular tracking its temporal variations would provide a new way to monitor the state of the tidal stresses in the volcanic system.

Similar analyses performed on subaerial hydrothermal systems would allow to better explore the causes of the spatial and temporal variations of their response to Earth tides and how sensitive and prompt they are to respond to small environmental changes.

DATA AVAILABILITY STATEMENT

The RMS dataset used for this study can be found in the Zenodo repository https://doi.org/10.5281/zenodo.5502069.

AUTHOR CONTRIBUTIONS

SP conceived the research study and performed the RMS estimate of the seismic tremor time-series. SD performed the SSA analysis. SP and SD contributed to the interpretation of the results and the writing of the manuscript.

FUNDING

Details of all funding sources should be provided, including grant numbers if applicable. Please ensure to add all necessary funding information, as after publication this is no longer possible. SD acknowledges the Fundação para a Ciência e Tecnologia (FCT) and the European Union (UE) for their financial support through the postdoctoral fellowship SFRH/BPD/117714/2016, co-financed by the Ministério da Ciência, Tecnologia e Ensino Superior (MCTES), Fundo Social Europeu (FSE), and Programa Operacional Regional Centro (Centro 2020). This work is part of the projects PTDC/CTA-GEF/6674/2020—RESTLESS and UIDB/50019/2020, Instituto Dom Luiz (IDL) funded by FCT.

ACKNOWLEDGMENTS

The seismic data recorded by the permanent and mobile seismic networks of Ischia and Campi Flegrei were provided by the Istituto Nazionale di Geofisica e Vulcanologia, sezione di Napoli—Osservatorio Vesuviano. **Figure 1** has been drawn by using the software Generic Mapping Tools (Wessel et al., 2013).

SUPPLEMENTARY MATERIAL

The Supplementary Material for this article can be found online at: https://www.frontiersin.org/articles/10.3389/feart.2021.775269/full#supplementary-material

REFERENCES

Amoruso, A., Crescentini, L., and Sabbetta, I. (2014). Paired Deformation Sources of the Campi Flegrei Caldera (Italy) Required by Recent (1980-2010) Deformation History. *J. Geophys. Res. Solid Earth* 119 (2), 858–879. doi:10.1002/2013jb010392

Battaglia, M., Troise, C., Obrizzo, F., Pingue, F., and De Natale, G. (2006). Evidence for Fluid Migration as the Source of Deformation at Campi Flegrei Caldera (Italy). *Geophys. Res. Lett.* 33 (1). doi:10.1029/2005gl024904

Bellucci Sessa, E., Castellano, M., and Ricciolino, P. (2021). GIS Applications in Volcano Monitoring: the Study of Seismic Swarms at the Campi Flegrei Volcanic Complex, Italy. *Adv. Geosci.* 52, 131–144. doi:10.5194/adgeo-52-131-2021

Berrino, G., and Corrado, G. (1991). Tidal Signal in the Recent Dynamics of Campi Flegrei Caldera (Italy). *J. Volcanology Geothermal Res.* 48 (1-2), 93–101. doi:10.1016/0377-0273(91)90035-x

Bozzo, E., Carniel, R., and Fasino, D. (2010). Relationship between Singular Spectrum Analysis and Fourier Analysis: Theory and Application to the Monitoring of Volcanic Activity. *Comput. Math. Appl.* 60 (3), 812–820. doi:10.1016/j.camwa.2010.05.028

Bredemeyer, S., and Hansteen, T. H. (2014). Synchronous Degassing Patterns of the Neighbouring Volcanoes Llaima and Villarrica in South-central Chile: the Influence of Tidal Forces. *Int. J. Earth Sci. (Geol Rundsch)* 103 (7), 1999–2012. doi:10.1007/s00531-014-1029-2

Capuano, P., De Lauro, E., De Martino, S., Falanga, M., and Petrosino, S. (2017). Convolutive Independent Component Analysis for Processing Massive Datasets: a Case Study at Campi Flegrei (Italy). *Nat. Hazards* 86 (2), 417–429. doi:10.1007/s11069-016-2545-0

Capuano, P., De Matteis, R., and Russo, G. (2015). The Structural Setting of the Ischia Island Caldera (Italy): First Evidence from Seismic and Gravity Data. *Bull. Volcanology* 77 (9), 1–10. doi:10.1007/s00445-015-0965-4

Caputo, T., Cusano, P., Petrosino, S., Sansivero, F., and Vilardo, G. (2020). Spectral Analysis of Ground thermal Image Temperatures: what We Are Learning at Solfatara Volcano (Italy). *Adv. Geosci.* 52, 55–65. doi:10.5194/adgeo-52-55-2020

Chiodini, G., Giudicepietro, F., Vandemeulebrouck, J., Aiuppa, A., Caliro, S., De Cesare, W., et al. (2017). Fumarolic Tremor and Geochemical Signals during a Volcanic Unrest. *Geology* 45 (12), 1131–1134. doi:10.1130/g39447.1

Contadakis, M. E., Arabelos, D. N., and Vergos, G. (2017). Testing the Recent Santorini Seismic Activity for Possible Tidal Triggering Effect. *geosociety* 51, 1–17. doi:10.12681/bgsg.11653

Cusano, P., Caputo, T., De Lauro, E., Falanga, M., Petrosino, S., Sansivero, F., et al. (2021). Tracking the Endogenous Dynamics of the Solfatara Volcano (Campi Flegrei, Italy) through the Analysis of Ground Thermal Image Temperatures. *Atmosphere* 12 (8), 940. doi:10.3390/atmos12080940

Cusano, P., Petrosino, S., De Lauro, E., De Martino, S., and Falanga, M. (2020a). Characterization of the Seismic Dynamical State through Joint Analysis of Earthquakes and Seismic Noise: The Example of Ischia Volcanic Island (Italy). *Adv. Geosci.* 52, 19–28. doi:10.5194/adgeo-52-19-2020

Cusano, P., Petrosino, S., De Lauro, E., and Falanga, M. (2020b). The Whisper of the Hydrothermal Seismic Noise at Ischia Island. *J. Volcanology Geothermal Res.* 389, 106693. doi:10.1016/j.jvolgeores.2019.106693

Cusano, P., Petrosino, S., and Saccorotti, G. (2008). Hydrothermal Origin for Sustained Long-Period (LP) Activity at Campi Flegrei Volcanic Complex, Italy. *J. Volcanology Geothermal Res.* 177 (4), 1035–1044. doi:10.1016/j.jvolgeores.2008.07.019

De Lauro, E., De Martino, S., Falanga, M., and Petrosino, S. (2016). Fast Wavefield Decomposition of Volcano-Tectonic Earthquakes into Polarized P and S Waves by Independent Component Analysis. *Tectonophysics* 690, 355–361. doi:10.1016/j.tecto.2016.10.005

De Lauro, E., De Martino, S., Falanga, M., and Petrosino, S. (2013). Synchronization between Tides and Sustained Oscillations of the Hydrothermal System of Campi Flegrei (Italy). *Geochem. Geophys. Geosyst.* 14 (8), 2628–2637. doi:10.1002/ggge.20149

De Lauro, E., Falanga, M., and Petrosino, S. (2012). Study on the Long-Period Source Mechanism at Campi Flegrei (Italy) by a Multi-Parametric Analysis. *Phys. Earth Planet. Interiors* 206-207, 16–30. doi:10.1016/j.pepi.2012.06.006

De Lauro, E., Petrosino, S., Ricco, C., Aquino, I., and Falanga, M. (2018). Medium and Long Period Ground Oscillatory Pattern Inferred by Borehole Tiltmetric Data: New Perspectives for the Campi Flegrei Caldera Crustal Dynamics. *Earth Planet. Sci. Lett.* 504, 21–29. doi:10.1016/j.epsl.2018.09.039

De Siena, L., Del Pezzo, E., and Bianco, F. (2010). Seismic Attenuation Imaging of Campi Flegrei: Evidence of Gas Reservoirs, Hydrothermal Basins, and Feeding Systems. *J. Geophys. Res. Solid Earth* 115 (B9). doi:10.1029/2009jb006938

De Siena, L., Sammarco, C., Cornwell, D. G., La Rocca, M., Bianco, F., Zaccarelli, L., et al. (2018). Ambient Seismic Noise Image of the Structurally Controlled Heat and Fluid Feeder Pathway at Campi Flegrei Caldera. *Geophys. Res. Lett.* 45 (13), 6428–6436. doi:10.1029/2018gl078817

de Vita, S., Sansivero, F., Orsi, G., Marotta, E., and Piochi, M. (2010). Volcanological and Structural Evolution of the Ischia Resurgent Caldera (Italy) over the Past 10 Ky. *Geol. Soc. Am. Spec. Pap.* 464, 193–239. doi:10.1130/2010.2464(10)

Del Gaudio, C., Aquino, I., Ricciardi, G. P., Ricco, C., and Scandone, R. (2010). Unrest Episodes at Campi Flegrei: A Reconstruction of Vertical Ground Movements during 1905-2009. *J. Volcanology Geothermal Res.* 195 (1), 48–56. doi:10.1016/j.jvolgeores.2010.05.014

Di Giuseppe, M. G., Troiano, A., and Carlino, S. (2017). Magnetotelluric Imaging of the Resurgent Caldera on the Island of Ischia (Southern Italy): Inferences for its Structure and Activity. *Bull. Volcanol* 79 (12), 85. doi:10.1007/s00445-017-1170-4

Di Napoli, R., Aiuppa, A., Bellomo, S., Brusca, L., D'Alessandro, W., Candela, E. G., and Valenza, M. (2009). A Model for Ischia Hydrothermal System: Evidences from the Chemistry of thermal Groundwaters. *J. Volcanology Geothermal Res.* 186 (3-4), 133–159. doi:10.1016/j.jvolgeores.2009.06.005

Dinger, F., Bobrowski, N., Warnach, S., Bredemeyer, S., Hidalgo, S., Arellano, S., et al. (2018). Periodicity in the BrO/SO2 Molar Ratios in the Volcanic Gas Plume of Cotopaxi and its Correlation with the Earth Tides during the Eruption in 2015. *Solid Earth* 9 (2), 247–266. doi:10.5194/se-9-247-2018

Dumont, S., Custódio, S., Petrosino, S., Thomas, A., and Sottili, G. (2022). "Tides, Earthquakes and Volcanic Eruptions," in *A Journey through Tides*. Editors M. Green and J. C. Duarte (Elsevier). in revision.

Dumont, S., Le Mouël, J.-L., Courtillot, V., Lopes, F., Sigmundsson, F., Coppola, D., et al. (2020). The Dynamics of a Long-Lasting Effusive Eruption Modulated by Earth Tides. *Earth Planet. Sci. Lett.* 536, 116145. doi:10.1016/j.epsl.2020.116145

Dumont, S., Silveira, G., Custódio, S., Lopes, F., Le Mouël, J.-L., Gouhier, M., et al. (2021). Response of Fogo Volcano (Cape Verde) to Lunisolar Gravitational Forces during the 2014-2015 Eruption. *Phys. Earth Planet. Interiors* 312, 106659. doi:10.1016/j.pepi.2021.106659

Dzurisin, D. (1980). Influence of Fortnightly Earth Tides at Kilauea Volcano, Hawaii. *Geophys. Res. Lett.* 7 (11), 925–928. doi:10.1029/gl007i011p00925

Eichelberger, J., Kiryukhin, A., Mollo, S., Tsuchiya, N., and Villeneuve, M. (2020). Exploring and Modeling the Magma-Hydrothermal Regime. *Geosciences* 10, 234. doi:10.3390/geosciences10060234

Falanga, M., Cusano, P., De Lauro, E., and Petrosino, S. (2021). Picking up the Hydrothermal Whisper at Ischia Island in the Covid-19 Lockdown Quiet. *Sci. Rep.* 11 (1), 1–11. doi:10.1038/s41598-021-88266-9

Falanga, M., and Petrosino, S. (2012). Inferences on the Source of Long-Period Seismicity at Campi Flegrei from Polarization Analysis and Reconstruction of the Asymptotic Dynamics. *Bull. Volcanol* 74 (6), 1537–1551. doi:10.1007/s00445-012-0612-2

Girona, T., Huber, C., and Caudron, C. (2018). Sensitivity to Lunar Cycles Prior to the 2007 Eruption of Ruapehu Volcano. *Sci. Rep.* 8 (1), 1476–1479. doi:10.1038/s41598-018-19307-z

Golyandina, N., and Zhigljavsky, A. (20132013). *Singular Spectrum Analysis for Time Series*. Berlin, Heidelberg: Springer.

Gottsmann, J., Carniel, R., Coppo, N., Wooller, L., Hautmann, S., and Rymer, H. (2007). Oscillations in Hydrothermal Systems as a Source of Periodic Unrest at Caldera Volcanoes: Multiparameter Insights from Nisyros, Greece. *Geophys. Res. Lett.* 34 (7). doi:10.1029/2007gl029594

Gresse, M., Vandemeulebrouck, J., Byrdina, S., Chiodini, G., Revil, A., Johnson, T. C., et al. (2017). Three-Dimensional Electrical Resistivity Tomography of the Solfatara Crater (Italy): Implication for the Multiphase Flow Structure of the Shallow Hydrothermal System. *J. Geophys. Res. Solid Earth* 122 (11), 8749–8768. doi:10.1002/2017jb014389

Isaia, R., Marianelli, P., and Sbrana, A. (2009). Caldera Unrest Prior to Intense Volcanism in Campi Flegrei (Italy) at 4.0 Ka BP: Implications for Caldera Dynamics and Future Eruptive Scenarios. *Geophys. Res. Lett.* 36 (21). doi:10.1029/2009gl040513

Jupp, T. E., Pyle, D. M., Mason, B. G., and Dade, W. B. (2004). A Statistical Model for the Timing of Earthquakes and Volcanic Eruptions Influenced by Periodic Processes. *J. Geophys. Res. Solid Earth* 109 (B2). doi:10.1029/2003jb002584

Lambeck, K. (2005). *The Earth's Variable Rotation: Geophysical Causes and Consequences*. Cambridge University Press.

Lay, T., and Wallace, T. C. (1995). *Modern Global Seismology*. Elsevier.

Le Mouël, J. L., Lopes, F., Courtillot, V., and Gibert, D. (2019). On Forcings of Length of Day Changes: From 9-day to 18.6-year Oscillations. *Phys. Earth Planet. Interiors* 292, 1–11. doi:10.1016/j.pepi.2019.04.006

Lopes, F., Le Mouël, J.-L., and Gibert, D. (2017). The Mantle Rotation Pole Position. A Solar Component. *Comptes Rendus Geosci.* 349 (4), 159–164. doi:10.1016/j.crte.2017.06.001

Magee, C., Stevenson, C. T. E., Ebmeier, S. K., Keir, D., Hammond, J. O. S., Gottsmann, J. H., et al. (2018). Magma Plumbing Systems: a Geophysical Perspective. *J. Pet.* 59 (6), 1217–1251. doi:10.1093/petrology/egy064

Malagnini, L., Dreger, D. S., Bürgmann, R., Munafò, I., and Sebastiani, G. (2019). Modulation of Seismic Attenuation at Parkfield, before and after the 2004 M 6 Earthquake. *J. Geophys. Res. Solid Earth* 124 (6), 5836–5853. doi:10.1029/2019jb017372

Mauk, F. J., and Johnston, M. J. S. (1973). On the Triggering of Volcanic Eruptions by Earth Tides. *J. Geophys. Res* 78 (17), 3356–3362.

McNutt, S. R., and Beavan, R. J. (1987). Eruptions of Pavlof Volcano and Their Possible Modulation by Ocean Load and Tectonic Stresses. *J. Geophys. Res.* 92 (B11), 11509–11523. doi:10.1029/jb092ib11p11509

Meier, M., and Schlindwein, V. (2018). First *In Situ* Seismic Record of Spreading Events at the Ultraslow Spreading Southwest Indian Ridge. *Geophys. Res. Lett.* 45 (19), 10–360. doi:10.1029/2018gl079928

Miguelsanz, L., González, P. J., Tiampo, K. F., and Fernández, J. (2021). Tidal Influence on Seismic Activity during the 2011–2013 El Hierro Volcanic Unrest. *Tectonics* 40 (2), e2020TC006201. doi:10.1029/2020tc006201

Miller, C. A., Le Mével, H., Currenti, G., Williams-Jones, G., and Tikoff, B. (2017). Microgravity changes at the Laguna del Maule volcanic field: Magma-induced stress changes facilitate mass addition. *J. Geophys. Res. Solid Earth* 122 (4), 3179–3196. doi:10.1002/2017jb014048

Nakiboglu, S. M., and Lambeck, K. (1980). Deglaciation Effects on the Rotation of the Earth. *Geophys. J. Int.* 62 (1), 49–58. doi:10.1111/j.1365-246x.1980.tb04843.x

Petrosino, S., Cusano, P., and Madonia, P. (2018). Tidal and Hydrological Periodicities of Seismicity Reveal New Risk Scenarios at Campi Flegrei Caldera. *Sci. Rep.* 8 (1), 13808–13812. doi:10.1038/s41598-018-31760-4

Petrosino, S., and De Siena, L. (2021). Fluid Migrations and Volcanic Earthquakes from Depolarized Ambient Noise. *Nat. Commun.* 12, 6656. doi:10.1038/s41467-021-26954-w

Petrosino, S., Ricco, C., and Aquino, I. (2021). Modulation of Ground Deformation and Earthquakes by Rainfall at Vesuvius and Campi Flegrei (Italy). *Front. Earth Sci.* 9. doi:10.3389/feart.2021.758602

Petrosino, S., Ricco, C., De Lauro, E., Aquino, I., and Falanga, M. (2020). Time Evolution of Medium and Long-Period Ground Tilting at Campi Flegrei Caldera. *Adv. Geosci.* 52, 9–17. doi:10.5194/adgeo-52-9-2020

Ray, R. D., and Erofeeva, S. Y. (2014). Long-period Tidal Variations in the Length of Day. *J. Geophys. Res. Solid Earth* 119 (2), 1498–1509. doi:10.1002/2013jb010830

Ricco, C., Petrosino, S., Aquino, I., Del Gaudio, C., and Falanga, M. (2019). Some Investigations on a Possible Relationship between Ground Deformation and Seismic Activity at Campi Flegrei and Ischia Volcanic Areas (Southern Italy). *Geosciences* 9 (5), 222. doi:10.3390/geosciences905022210.3390/geosciences9050222

Saccorotti, G., Petrosino, S., Bianco, F., Castellano, M., Galluzzo, D., La Rocca, M., et al. (2007). Seismicity Associated with the 2004-2006 Renewed Ground Uplift at Campi Flegrei Caldera, Italy. *Phys. Earth Planet. Interiors* 165 (1-2), 14–24. doi:10.1016/J.PEPI.2007.07.006

Sahoo, S., Senapati, B., Panda, D., Tiwari, D. K., Santosh, M., and Kundu, B. (2021). Tidal triggering of micro-seismicity associated with caldera dynamics in the Juan de Fuca ridge. *J. Volcanology Geothermal Res.* 417, 107319. doi:10.1016/j.jvolgeores.2021.107319

Scholz, C. H., Tan, Y. J., and Albino, F. (2019). The Mechanism of Tidal Triggering of Earthquakes at Mid-ocean Ridges. *Nat. Commun.* 10 (1), 2526–2527. doi:10.1038/s41467-019-10605-2

Sottili, G., Lambert, S., and Palladino, D. M. (2021). Tides and Volcanoes: a Historical Perspective. *Front. Earth Sci.* 9. doi:10.3389/feart.2021.777548

Sottili, G., Martino, S., Palladino, D. M., Paciello, A., and Bozzano, F. (2007). Effects of Tidal Stresses on Volcanic Activity at Mount Etna, Italy. *Geophys. Res. Lett.* 34 (1). doi:10.1029/2006gl028190

Sottili, G., and Palladino, D. M. (2012). Tidal Modulation of Eruptive Activity at Open-Vent Volcanoes: Evidence from Stromboli, Italy. *Terra Nova* 24 (3), 233–237. doi:10.1111/j.1365-3121.2012.01059.x

Takano, T., Nishimura, T., Nakahara, H., Ohta, Y., and Tanaka, S. (2014). Seismic Velocity Changes Caused by the Earth Tide: Ambient Noise Correlation Analyses of Small-Array Data. *Geophys. Res. Lett.* 41 (17), 6131–6136. doi:10.1002/2014gl060690

Tolstoy, M., Vernon, F. L., Orcutt, J. A., and Wyatt, F. K. (2002). Breathing of the Seafloor: Tidal Correlations of Seismicity at Axial Volcano. *Geol* 30 (6), 503–506. doi:10.1130/0091-7613(2002)030<0503:botstc>2.0.co;2

Trasatti, E., Acocella, V., Di Vito, M. A., Del Gaudio, C., Weber, G., Aquino, I., et al. (2019). Magma Degassing as a Source of Long-Term Seismicity at Volcanoes: The Ischia Island (Italy) Case. *Geophys. Res. Lett.* 46 (24), 14421–14429. doi:10.1029/2019gl085371

Vitale, S., and Isaia, R. (2014). Fractures and Faults in Volcanic Rocks (Campi Flegrei, Southern Italy): Insight into Volcano-Tectonic Processes. *Int. J. Earth Sci. (Geol Rundsch)* 103 (3), 801–819. doi:10.1007/s00531-013-0979-0

Wessel, P., Smith, W. H. F., Scharroo, R., Luis, J., and Wobbe, F. (2013). Generic Mapping Tools: Improved Version Released. *EOS Trans. AGU* 94 (45), 409–410. doi:10.1002/2013EO450001

Yakiwara, H., Hirano, S., Miyamachi, H., Takayama, T., Yamazaki, T., Tameguri, T., et al. (2013). Semi-Diurnal Tidal Periodicity Observed by an Ocean Bottom Seismometer Deployed at a Location Very Close to Seafloor Fumaroles in Wakamiko Caldera, Northeast of Sakurajima Volcano (Special Section Sakurajima Special Issue). *Bull. Volcanological Soc. Jpn.* 58 (1), 269–279.

Young, N., Isaia, R., and Gottsmann, J. (2020). Gravimetric Constraints on the Hydrothermal System of the Campi Flegrei Caldera. *J. Geophys. Res. Solid Earth* 125 (7), e2019JB019231. doi:10.1029/2019jb019231

Conflict of Interest: The authors declare that the research was conducted in the absence of any commercial or financial relationships that could be construed as a potential conflict of interest.

Publisher's Note: All claims expressed in this article are solely those of the authors and do not necessarily represent those of their affiliated organizations, or those of the publisher, the editors and the reviewers. Any product that may be evaluated in this article, or claim that may be made by its manufacturer, is not guaranteed or endorsed by the publisher.

frontiers in Earth Science

ORIGINAL RESEARCH
published: 14 March 2022
doi: 10.3389/feart.2022.795760

Gas Monitoring of Volcanic-Hydrothermal Plumes in a Tropical Environment: The Case of La Soufrière de Guadeloupe Unrest Volcano (Lesser Antilles)

Severine Moune[1,2,3], Roberto Moretti[1,2], Arnand Burtin[1], David Edward Jessop[1,2,3], Tristan Didier[1,2], Vincent Robert[1,2], Magali Bonifacie[1,2], Giancarlo Tamburello[4], J-Christophe. Komorowski[1], Patrick Allard[1] and Margaux Buscetti[5]*

[1]CNRS, Institut de Physique Du Globe de Paris, Université de Paris, Paris, France, [2]Observatoire Volcanologique et Sismologique de Guadeloupe, Institut de Physique du Globe de Paris, Gourbeyre, France, [3]CNRS, UMR 6524, Laboratoire Magmas et Volcans, OPGC, Clermont-Ferrand, France, [4]Istituto Nazionale di Geofisica e Vulcanologia, Bologna, Italy, [5]Ecole et Observatoire des Sciences de la Terre, Strasbourg, France

OPEN ACCESS

Edited by:
David M. Pyle, University of Oxford, United Kingdom

Reviewed by:
Marco Neri, National Institute of Geophysics and Volcanology, Italy
Tjarda Roberts, UMR7328 Laboratoire de physique et chimie de l'environnement et de l'Espace (LPC2E), France

***Correspondence:**
Severine Moune
moune@ipgp.fr

Specialty section:
This article was submitted to Volcanology, a section of the journal Frontiers in Earth Science

Received: *15 October 2021*
Accepted: *04 January 2022*
Published: *14 March 2022*

Citation:
Moune S, Moretti R, Burtin A, Jessop DE, Didier T, Robert V, Bonifacie M, Tamburello G, Komorowski J-C, Allard P and Buscetti M (2022) Gas Monitoring of Volcanic-Hydrothermal Plumes in a Tropical Environment: The Case of La Soufrière de Guadeloupe Unrest Volcano (Lesser Antilles). Front. Earth Sci. 10:795760. doi: 10.3389/feart.2022.795760

Fumarolic gas survey of dormant volcanoes in hydrothermal activity is crucial to detect compositional and mass flux changes in gas emissions that are potential precursors of violent phreatic or even magmatic eruptions. Here we report on new data for the chemical compositions (CO_2, H_2S, SO_2) and fluxes of fumarolic gas emissions (97–104°C) from La Soufrière volcano in Guadeloupe (Lesser Antilles) obtained from both mobile MultiGas measurements and permanent MultiGas survey. This paper covers the period 2016–2020, encompassing a period of enhanced hydrothermal unrest including an abrupt seismic energy release (M 4.1) on April 27, 2018. Our dataset reveals fumarolic CO_2/H_2S and SO_2/H_2S gas trends correlated to the evolution of surface activity and to other geochemical and geophysical parameters. We demonstrate that, even under tropical conditions (high humidity and rainfall), MultiGas surveys of low-T fumarolic emissions permit to distinguish deeply sourced signals of volcanic unrest from secondary changes in degassing due to shallow forcing processes such as water-gas-rock interactions in the hydrothermal system and meteorological effects.

Keywords: MultiGas, monitoring, La Soufrière de Guadeloupe, fumaroles, hydrothermal unrest

1 INTRODUCTION

Hydrothermal manifestations at many dormant andesitic volcanoes are commonly sustained by a supply of heat and volatiles from a magma reservoir at depth to the shallow parts of the volcanic system. Through interactions with shallow aquifers and the host rocks this magmatic supply sustains a hydrothermal system beneath and within the edifice and thus hydrothermal manifestations at the surface (e.g., Rye et al., 1992; Hedenquist and Lowenstern, 1994; Rye, 2005). Volcanic-hydrothermal systems can remain in equilibrium as long as the input and output of heat and volatiles compensate each other. Over time, however, they may be disrupted by various processes, such as gradual self-sealing (e.g., Christenson et al., 2010) leading to overpressurization and enhanced gas supply from depth (e.g., de Moor et al., 2016; Christenson et al., 2017) or even the ascent of a magma intrusion (Cashman and Hoblitt, 2004), or instead, by surficial processes, such as sector collapse, leading to their sudden decompression. Depending on the actual process involved, the resulting eruptions can

vary from hydrothermal eruptions to magma-driven explosive events eventually evolving into a magmatic eruption. In most cases, both magma-derived volatiles and hydrothermal fluids are emitted altogether during such eruptive events. Moreover, even hydrothermal eruptions involving no magma emission can be hazardous volcanic events given their sudden occurrence, lack of precursor signals, potentially high intensity and co-associated phenomena such as ash clouds, ballistic ejecta, pyroclastic density currents, partial edifice collapse, outgassing and lahars. The risks from hydrothermal eruptions were further illustrated by the deadly events that happened at Ontake volcano (Japan, 2014; Maeno et al., 2016), White Island (New-Zealand, 2019; Dempsey et al., 2020), Ruapehu volcano (New-Zealand, 2007; Kilgour et al., 2010) and fortunate near-miss disaster at Te Maari, Tongariro (New-Zealand) in 2012 (Procter et al., 2014).

The ability to forecast hydrothermal eruptions depends on their driving mechanism, which will determine the intensity and duration of their precursory signals, but also on the availability of an adequate instrumental monitoring. Sudden events, with limited precursory signals, are rarely predictable but are often of modest size (Barberi et al., 1992; Hurst et al., 2014). Instead, dormant volcanoes with long-lived hydrothermal systems can experience years or decades of unrest, involving a variety of signals, prior to erupting (e.g., Sano et al., 2015; Oikawa et al., 2016). Therefore, detecting the forerunning signals of hydrothermal eruptions requires monitoring the behaviour of volcanic systems on both short and long-time scales. In addition to geophysical monitoring, the survey of hydrothermal gas emissions can provide key warning information because the gas compositions and the gas fluxes are both expected to vary in response to underground processes prior to an eruption (Fischer et al., 1997; Chiodini, 2009; Werner et al., 2013; Allard et al., 2014; de Moor et al., 2016; Moretti et al., 2020a; Girona et al., 2021). However, gas compositions can also be affected by secondary effects linked to scrubbing and other water-gas-rock interactions in the hydrothermal system (Symonds et al., 2001) and meteorological variability at the surface (e.g., Shimoike and Notsu, 2000). Hot magmatic gases infiltrating hydrothermal aquifers become partly depleted in their most water-soluble acid components (SO_2, HCl, HF). Hence, surface fumaroles are correspondingly enriched in less soluble species (CO_2, H_2S, H_2, CH_4, CO) and steam (Symonds et al., 2001). Moreover, the scrubbing of these acid components into aquifers promotes acid alteration of the host rocks, which in turn determines complex chemical reactions and buffering effects during further gas-rock interactions (Moretti and Stefánsson, 2020 and references therein). As a consequence, the original chemical signature of a magma-derived gas supply can be significantly modified, or even almost hidden, in surface fumarolic emissions. These secondary chemical processes are potentially much more important at volcanoes located in tropical environments, where a high rate of rainfall and groundwater infiltration favours extensive gas dilution, scrubbing and water-gas-rock interactions. Meteorological conditions themselves can also influence the composition and flux of volcanic fumaroles in a tropical environment (Faber et al., 2003; Keely et al., 2013). Hence, deciphering the source mechanism of hydrothermal unrest at dormant volcanoes in tropical environments is particularly challenging and requires an adapted geochemical monitoring strategy. Clear unrest signals or even precursors of eruptions were previously detected on such volcanoes, even though contradictory interpretations about the nature of unrest arose in some cases (Symonds et al., 1994; Fischer et al., 1997; Werner et al., 2009; Procter et al., 2014; Allard et al., 2014; Chiodini et al., 2015, 2016; de Moor et al., 2016; Maeno et al., 2016; Moretti et al., 2013, 2017, 2020a; Battaglia et al., 2019; Troise et al., 2019).

Here we focus on La Soufrière of Guadeloupe, an active andesitic volcano of the Lesser Antilles arc, which has been displaying growing fumarolic unrest since 1992 (Komorowski et al., 2005; Villemant et al., 2014). We report new data for the chemical composition and discharge rate of summit fumarolic gas emissions measured with both mobile and permanent multi-sensors (MultiGas) devices during the 2016–2020 period. Our dataset encompasses a sharp peak in activity in April 2018 (Moretti et al., 2020a) and is interpreted in the framework of the multidisciplinary monitoring of La Soufrière conducted by the local volcano observatory (OVSG-IPGP). We find both short-term and long-term changes in the degassing features that can be related to the dynamics of underground processes (gas mixing and water-gas-rock interactions in the hydrothermal system, sulfur deposition and remobilization) and meteorological forcing, as well as geophysical signals (seismicity and deformation).

2 VOLCANOLOGICAL BACKGROUND

La Soufrière de Guadeloupe (16.0446°N, 61.6642°W, 1,467 m, a.s.l., hereby referred to as La Soufrière) is one of the most active and most dangerous volcanoes of the Lesser Antilles island arc (Komorowski et al., 2005). Its summit part consists of an andesitic lava dome, cut by numerous fractures (**Figure 1**), that was emplaced during the last major magmatic eruption in 1530 AD. Since then, intense hydrothermal activity has persisted at La Soufrière, under the forms of fumaroles, steaming ground and hot springs, that occasionally culminated in series of non-magmatic phreatic eruptions and/or hydrothermal explosive eruptions (e.g., Komorowski et al., 2005; Komorowski et al., 2008; Legendre, 2012). The most recent phreatic eruptive sequence, in 1976–1977, ranked amongst the longest and most energetic ones (Le Guern et al., 1980; Feuillard et al., 1983; Hincks et al., 2014). After a decade of post-eruptive quiescence La Soufrière has entered since 1992 a new phase of fumarolic and seismic unrest, whose evolution has previously been described in detail (Allard et al., 1994; Komorowski et al., 2005; Villemant et al., 2014; Rosas-Carbajal et al., 2016; Tamburello et al., 2019; Moretti et al., 2020a; Jessop et al., 2021; Metcalfe et al., 2021).

Persistent hydrothermal activity at La Soufrière is sustained by heat and gas transfer from a 6–7 km deep (b.s.l.) andesitic magma reservoir to shallow aquifers (e.g., Feuillard et al., 1983; Touboul et al., 2007; Allard et al., 2014; Pichavant et al., 2018). Magma-derived gases likely rise through deep fractures in the overlying basement, then interact with the hydrothermal system hosted in a

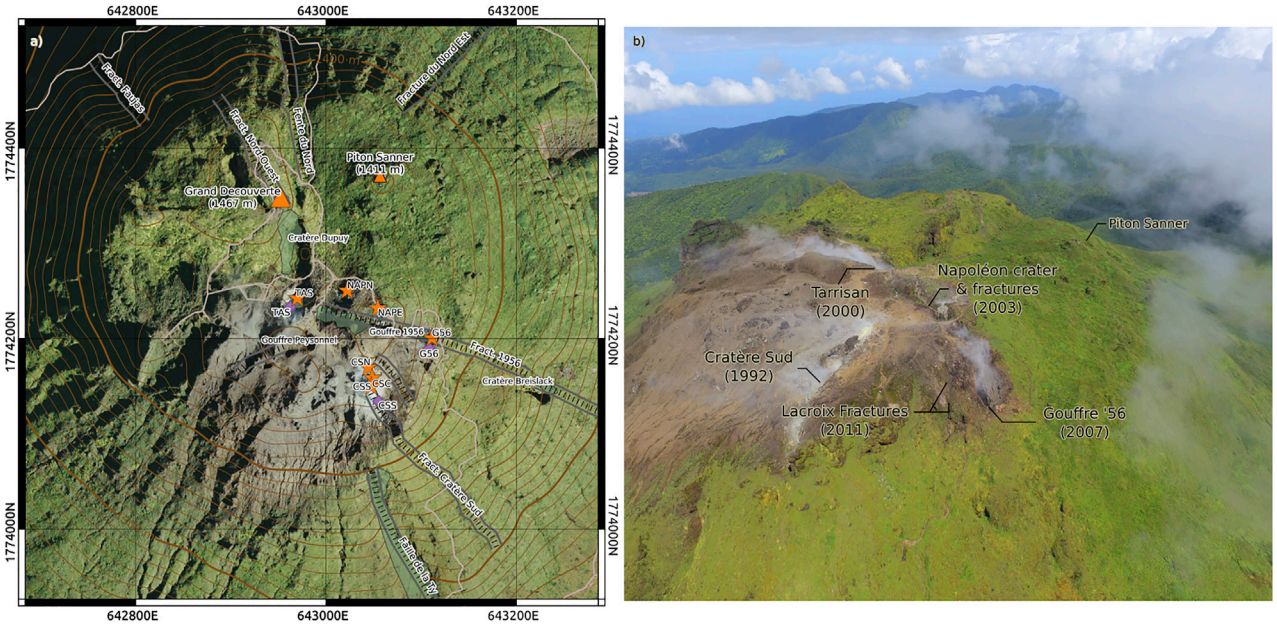

FIGURE 1 | (A) Map of the summit of La Soufrière de Guadeloupe (1467 asl) showing the main geological features/fractures, the location of the fumaroles sampled *via* the MultiGas portable (orange stars: Tarissan, TAS; Cratère Sud-Sud, CSS; Cratère Sud-Centre, CSC; Cratère Sud-Nord, CSN; Gouffre 56, G56; Napoléon Nord, NAPN; Napoléon Est, NAPE) and the location of the three permanent MultiGas stations (purple stars; G56: 643,545 E, 1774499 N; TAS: 643,388 E, 1774541 N; CSS: 643,489 E, 1774441 N). Modified from Jessop et al. (2021). **(B)** Photo of the main active fumaroles with the date of appearance in brackets. Modified from Jessop et al. (2021).

shallower porous and fractured rock body beneath the volcano. Gas mixtures of magma-derived and hydrothermal components then migrate through the most permeable fractures cutting the lava dome to sustain fumarolic activity at the summit. The intense activity of the La Soufrière volcanic-hydrothermal system constitutes a potential threat for several tens of thousands of people living in the immediate surroundings and concern has risen with the increasing degassing unrest over the past 2 decades. This unrest peaked in energy with 1) the highest magnitude felt volcanic-tectonic (VT) event since 1976 (M 4.1 on April 27, 2018; for all characteristics of this event see Moretti et al., 2020a) that was preceded by 350 VTs (2 of which felt) in the previous weeks, 2) horizontal deformation and fracture opening of the lava dome, and 3) gas pulses linked to heating and pressurisation of the hydrothermal system shown by gas geochemistry and consistent with Vp/Vs negative anomalies which determine the rock cracking upon pore pressure build-up in a two-phase fluid (Moretti et al., 2020a; OVSG-IPGP 1999–2021 bulletins). This sequence was interpreted as being due to an enhanced supply of magma-derived gas to the shallow hydrothermal system, whose overpressurization effect could safely be released as the system was sufficiently fractured and opened enough (Moretti et al., 2020a). The total heat output from La Soufrière has recently been re-evaluated at 36.5 MW (Jessop et al., 2021). As most of this thermal release concerns a relatively small area, the heat flux density at La Soufrière (1,366 ± 82 W/m^2) is amongst the highest for volcanoes in hydrothermal activity (Jessop et al., 2021). Concurrent with the accelerating unrest, heat loss through the ground at the summit has also increased from 0.2 ± 0.1 MW in 2010 to 5.7 ± 0.9 MW in 2019–2020 (Jessop et al., 2021), leading to the development and extension of a widespread region of alteration and thermal anomalies. In summary, La Soufrière is a perfect target for improving the understanding of processes controlling volcanic-hydrothermal unrest in a tropical environment.

Since 1992 regular gas sampling and analysis of La Soufrière fumaroles (96°–110°C) has been performed at Cratère Sud (CS), the most active and single accessible vent (Brombach et al., 2000; Allard et al., 2014; Villemant et al., 2014; Moretti et al., 2020a; **Figure 1**). CS hosts three different fumarolic vents: CSS, CSN and CSC (**Figure 1**). Since July 2014, a newly opened vent (Napoléon Nord, NapN; **Figure 1**) has additionally been sampled regularly. Until now CSC and NapN are the only two vents on La Soufrière that have been accessible for gas sampling using Giggenbach bottles (Giggenbach and Goguel, 1989). Fumarolic emissions from the other main vents, such as Gouffre 56 (G56), Tarissan (TAS), Napoleon Est (NapE; **Figure 1**), were more recently measured *in-situ* using MultiGas devices (Aiuppa et al., 2005; Shinohara, 2005). Both G56 and TAS are pit craters with an acid lake present in the latter one. Discrete MultiGas measurements were performed in 2006 and 2012 (Allard et al., 2014) then during three field campaigns between May 2016 and October 2017 (Tamburello et al., 2019). These studies revealed a three-fold increase of the fumarolic gas fluxes between 2012 and 2016, contemporaneous with a widening of fractures cutting the summit lava dome and an increased permeability of the system (e.g., Allard et al., 2014). On the other hand, the compositional variability of the fumaroles observed in

2016–2017 was shown to result from the influence of 1) shallow processes (SO_2 scrubbing and near-surface T-related sulfur precipitation in the ground) related to the circulation of hydrothermal fluids inside the lava dome and 2) widening/closing of fractures cutting the dome (Tamburello et al., 2019). It was argued that current gas emissions from peripheral vents on the summit dome (G56, NapN, NapE; **Figure 1**) were less affected by acid gas scrubbing in the hydrothermal aquifer and thus more representative of the pristine magmatic-hydrothermal gas end-member than more central vents (CS, TAS) (Tamburello et al., 2019). Steam fluxes did not vary significantly since early 2016 (Jessop et al., 2021).

3 METHODS

3.1 MultiGas

3.1.1 Field Measurements

Since 2016 we determined the fumarolic gas compositions on top of La Soufrière by using MultiGas to measure the concentration ratios in air-diluted plumes from the different active vents. This was realized *via* i) monthly measurements with a portable instrument at all vents (orange stars in **Figure 1A**) and ii) a continuous survey with MultiGas stations installed at downwind proximity to the three main vents (CS, TAS and G56; purple diamonds in **Figure 1A**). Fumarolic plumes were pumped at a constant flow rate of 1.0–1.5 l/min through the inlet tube of the instruments, equipped with a PTFE filter (1 μm) and positioned at 0.5–1 m height above the ground (in order to minimize any influence from soil degassing).

All MultiGas instruments used in this study combined a Gascard IR spectrometer for CO_2 determination (calibration range: 0–3,000 ppmv; accuracy: ±2%; resolution: 0.8 ppmv) and City Technology electrochemical sensors for SO_2 (sensor type 3ST/F; calibration range: 0–200 ppm, accuracy: ±2%, resolution: 0.1 ppmv) and H2S (sensor type 2E; range: 0–200 ppm, accuracy: ±5%, resolution: 0.7 ppmv). Atmospheric pressure was recorded by the sensor installed on the CO_2 spectrometer card. All sensors were connected to a Campbell Scientific CR6 datalogger for data capture, acquisition and logging at 1 Hz. Power was provided by a couple of 12 V batteries for the permanent stations and by a Li battery for the portable instrument. All sensors were calibrated in the laboratory using target gases of known concentration every 2 months and before installation. Our portable MultiGas also included a GPS receiver to record its position at 1 Hz and a relative humidity (RH) sensor (Galltec, range: 0–100% RH, accuracy: ± 2%) coupled with a temperature sensor (range: −30 to +70°C, resolution: 0.01°C), both fixed externally, which permit indirect determination of the water vapor concentration in plumes as described by Moussallam et al. (2017). H_2O determination with these external sensors allowed us to minimise the potential influence of steam condensation within the MultiGas inlet tubing. However, due to rapid partial steam condensation in the fumarolic plumes emitted under the tropical conditions on top of La Soufrière, our measured water/gas ratios are unavoidably underestimated by approximately 35% (Gaudin et al., 2016; Jessop et al., 2021).

The three permanent MultiGas stations, installed in 2016–2017, were programmed to measure during four 20-min long sequences per day, with data recorded at 0.33 Hz and transmitted in real-time via Wi-Fi to the 8-km distant volcano observatory (OVSG-IPGP). Calibration of the permanent stations has been tested regularly in the field by measuring the same gas as the portable instrument (the inlets were close together). However, the network had to be partly re-installed after strong hurricanes in September 2017 (Saurel et al., 2020) and repeatedly suffered from the very hostile conditions prevailing on top of La Soufrière, among which the huge rainfall rate of 10 +/− 2 m/year (e.g., Villemant et al., 2014), with RH generally close to 100% (OVSG-IPGP 1999-2021 bulletins; Allard et al., 2014), and a strong corrosion by acid gases. The challenges encountered at the summit of La Soufrière were that the filters were saturated very quickly (within 2–3 weeks) allowing acid water droplets to enter the system and damaging the pump, and sometimes the sensors themselves. The electronic part of the CO_2 IR sensor was more sensitive than the electrochemical ones and the board was damaged more often. As a consequence, large gaps exist in our data set.

With our portable MultiGas, gas concentrations were measured in each plume at 1 Hz during 10–20 min and the data were displayed in real-time on a hand-held tablet connected via Wi-Fi link to the instrument. Furthermore, following previous demonstrations by Allard et al. (2014) and Tamburello et al. (2019), the same instrument was used to determine fumarolic gas fluxes from the three main vents contributing most the gas output and where the fumarolic emissions are strong enough to generate a plume: CS, TAS and G56. We determined these gas fluxes monthly since May 2018. For this, the horizontal and vertical distributions of gas species in the plume cross-sections were measured at two different heights (typically 0.9 and 2 m) during walking traverses orthogonal to the plume direction, a few meters downwind from the vents. Most commonly the fumarolic plumes were flattened to the ground by strong trade winds (up to 14 m/s) and their upper boundary stood at ca. 3–4 m above the ground, with a maximum gas density centred at between ~1.5 and 2 m above the ground (our visual observations; Gaudin et al., 2016; Tamburello et al., 2019). Wind speed was measured with an anemometer at the same height than the MultiGas inlet during all traverses.

Despite many challenges due to ambient meteorological conditions, steam condensation and corrosion by acid gases, we could thus use MultiGas instruments to survey La Soufrière fumarolic gas emissions over the entire summit dome and at a reasonably high frequency. In the case of high (>250°C) temperature fumaroles, MultiGas measurements produce chemical results that are closely similar to direct analyses of direct fumarole sampling via Giggenbach bottles (Aiuppa et al., 2005; Aiuppa et al., 2007), undoubtedly the best technique for a precise determination of vent outlet gas composition. Moretti et al. (2020b) demonstrated that this also applies to low-temperature fumaroles (~100°C) at La Soufrière, despite some minor offset due to secondary phenomena such as gas scrubbing from water droplets in air and diffusive-effusive

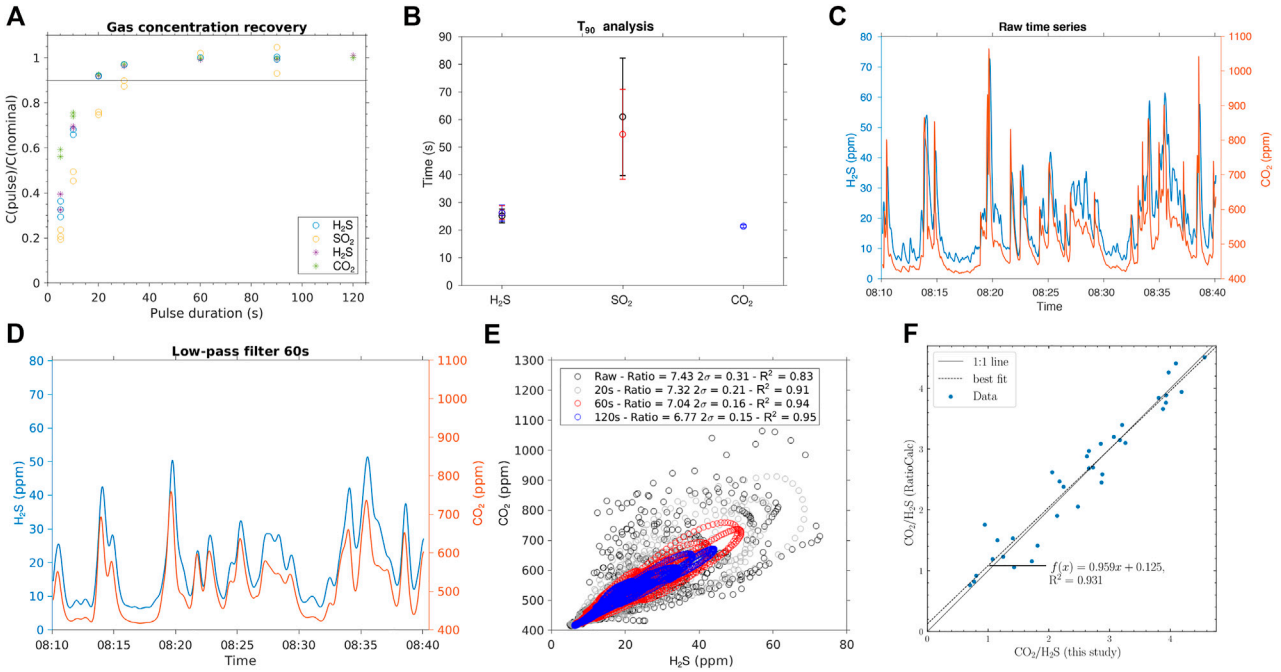

FIGURE 2 | (A,B) t90 behavior of the different sensors (H_2S, SO_2, CO_2). For H_2S, we tested two concentrations (100 and 40 ppm) **(C)** Raw H_2S and CO_2 time series at CS **(D)** Same H_2S and CO_2 time series at CS, but after a 60 s low-pass filter **(E)** The resulting CO_2/H_2S ratios with low-pass filter with various thresholds [raw (i.e., no low pass filter), 20 s low-pass filter, 60 and 120 s low-pass filter]. The gas ratios between non-filtered and filtered dataset are quite similar (<6% of difference) but we improve the R^2 (typically 0.8 to 0.9) and 2σ errors on calculated ratios are decreased by a factor up to ~ two. **(F)** Comparison, for the fumaroles of CS, between the CO_2/H_2S ratios processed in this study and the CO_2/H_2S ratios calculated with the RatioCalc software (Tamburello, 2015). The best fit shows a very good agreement between these two data post-processing.

gradients in the MultiGas inlet pumping line. Finally, because the oxidation of H_2S into SO_2 can be faster under humid (RH > 90%) tropical conditions than in cold and less humid environments, we followed the recommendation by Allard et al. (2014) of analysing fumarolic plumes at La Soufrière at short distance (<20 m) from their source vent. However, in case of G56 and TAS, the plume has already risen few tens of meters from their deep pit crater before arriving at the surface.

3.1.2 Data Processing

MultiGas data were post-processed at the OVSG-IPGP. Gas ratios were derived from linear regression of the concentrations of each component referred to H_2S, this latter being of purely volcanic origin. Such a simple procedure does not require any correction for the atmospheric background in case of CO_2 and H_2O, which are both volcanic and atmospheric components. In order to minimise residuals, we tested two different methods: the commonly used least-square method (e.g., RatioCalc; Tamburello, 2015) and the least-absolute difference method. Both methods were found to yield similar ratios, even though the latter method is known to be less sensitive to outliers (Bloomfield and Steiger, 1983; Dodge, 1997). Following Roberts et al. (2014), we constrained the t90 behaviour (the time required to reach 90% of the final signal following a step change in gas abundance) of our sensors via calibration tests with various gas mixture ratios. Our t90 tests were performed outdoors at the observatory with similar conditions as at the summit (same inlet tubing and high humidity (RH close to ~80% outside the OVSG while at the summit the RH ranges from 80 to 95% during our measurements). Our sensor response is characterised as follows (**Figures 2A,B**): CO_2 (t90 = 21 s), H_2S (t90 = 26 s), H_2 (t90 = 50 s) and SO_2 (t90 = 58 s). We did not test the interference of SO_2 on H_2S since there is little to no SO_2 in La Soufrière gas emissions. However, for a cross-sensitivity typically of order 15% of SO_2 over H_2S (Roberts et al., 2017), we estimated the interference based on mean SO_2 and H_2S measurements in the plume to be about 1%, so that it can considered negligible. Hence, all gas pulses with a duration <26 s for the CO_2/H_2S ratio and <60 s for both SO_2/H_2S and H_2/H_2S ratios are not well-captured by our sensors. In order to overcome this, we applied a low-pass filter at either 26 or 60 s (**Figures 2C,D**) depending on the ratios. The effects of filtering on the gas ratios, and the associated R^2 and errors have been investigated for filters at 20, 60 and 120 s, as shown in **Figure 2E**. The gas ratios in non-filtered and filtered datasets are quite similar (<6% difference) but we improve the R^2 (typically 0.83–0.95) and the 2σ errors on the calculated gas ratios are decreased by a factor up to ~ two (**Figure 2E**).

The dataset filtered using the least-absolute difference method was then cross-correlated to correct the shift between two signals and selected on the basis of several criteria, such as $R^2 > 0.6$ and a CO_2 baseline (background composition) < 490 ppm. Moreover,

TABLE 1 | Molar gas ratios in fumarolic emissions from La Soufrière volcano measured with portable MultiGas in 2017–2020.

Site name	Time	CO_2/H_2S	SO_2/H_2S	H_2O/H_2S
CS (CSN + CSC + CSS)	26/09/17	1.1	—	40.2
—	31/10/17	—	0.032	—
—	23/03/18	2.0	0.173	—
—	02/05/18	2.0	—	—
—	07/06/18	2.5	—	—
—	20/07/18	2.5	—	—
—	24/10/18	2.2	—	—
—	22/11/18	2.2	—	—
—	10/01/19	4.2	—	—
—	09/03/19	4.7	—	—
—	12/04/19	4.0	—	—
—	26/06/19	3.7	—	—
—	03/09/19	3.0	0.074	54.0
—	08/10/19	2.7	0.116	—
—	21/11/19	3.3	—	—
—	20/12/19	3.9	—	—
—	16/01/20	3.1	0.004	—
CSC	09/02/17	2.7	—	—
—	25/07/17	—	—	—
—	19/10/17	1.2	—	—
—	24/11/17	2.2	—	—
—	18/01/18	0.8	—	—
—	07/09/18	2.9	0.019	—
—	22/11/18	2.2	—	—
—	10/01/19	4.6	—	—
—	29/03/19	—	0.009	72.7
—	26/06/19	4.2	—	—
—	03/09/19	2.6	0.082	—
—	08/10/19	2.9	0.11	—
CSN	12/01/17	3.1	—	—
—	09/02/17	2.7	—	—
—	18/01/18	1.8	—	—
—	16/03/18	1.7	—	50.5
—	07/09/18	—	0.031	—
—	22/11/18	2.9	—	—
—	10/01/19	4.1	—	—
—	12/04/19	4.0	0.013	52.3
—	26/06/19	—	0.038	—
—	21/11/19	3.9	0.1	228.9
—	20/12/19	3.2	0.009	—
CSS	12/01/17	3.3	—	—
—	09/02/17	2.1	—	—
—	21/04/17	0.8	—	—
—	16/05/17	0.7	—	32.5
—	19/10/17	1.2	—	40.3
—	09/11/17	1.1	—	—
—	24/11/17	1.4	—	83.3
—	18/01/18	1.4	—	63.6
—	16/03/18	0.9	0.049	—
—	07/06/18	2.5	—	—
—	07/09/18	2.7	0.008	—
—	22/11/18	2.1	—	51.6
—	10/01/19	3.9	—	—
—	12/04/19	3.8	—	—
—	26/06/19	3.9	0.006	68.7
—	21/11/19	3.2	0.015	192.6
G56	12/01/17	3.6	0.024	—
—	09/02/17	2.9	0.016	—
—	11/04/17	0.9	—	22.7
—	21/04/17	0.8	—	25.4
—	16/05/17	0.8	—	—
—	25/07/17	—	—	—
—	26/09/17	—	—	—
—	19/10/17	1.8	—	76.2

(Continued on following page)

TABLE 1 | (*Continued*) Molar gas ratios in fumarolic emissions from La Soufrière volcano measured with portable MultiGas in 2017–2020.

Site name	Time	CO_2/H_2S	SO_2/H_2S	H_2O/H_2S
—	09/11/17	1.4	—	—
—	18/01/18	—	0.023	—
—	02/05/18	1.2	—	—
—	07/06/18	2.6	0.119	—
—	20/07/18	—	—	—
—	07/09/18	2.8	0.098	—
—	24/10/18	2.4	—	—
—	22/11/18	2.7	0.054	—
—	10/01/19	3.5	0.091	—
—	09/03/19	3.7	—	—
—	12/04/19	4.2	—	—
—	26/06/19	4.5	—	—
—	03/09/19	3.4	—	—
—	03/09/19	3.2	0.032	—
—	08/10/19	3.5	0.033	—
—	08/10/19	3.9	—	85.0
—	21/11/19	4.5	—	—
—	21/11/19	4.9	0.045	—
—	20/12/19	3.5	0.039	—
—	16/01/20	3.7	0.041	—
NapE1	12/01/17	3.4	—	—
—	09/02/17	3.8	—	—
—	16/05/17	1.1	—	46.6
—	27/06/17	1.0	—	79.9
—	19/10/17	1.5	—	—
—	18/01/18	—	—	—
—	16/03/18	—	—	—
—	07/06/18	3.0	—	—
—	20/07/18	3.9	—	—
—	07/09/18	—	—	—
—	24/10/18	4.0	—	—
—	22/11/18	3.0	—	—
—	10/01/19	5.2	—	87.9
—	12/04/19	5.1	—	—
—	26/06/19	5.2	—	—
—	03/09/19	4.5	—	—
—	08/10/19	5.0	—	—
—	21/11/19	5.0	—	172.8
—	20/12/19	3.1	—	—
—	16/01/20	4.6	—	—
NapE3	12/01/17	—	—	—
—	27/06/17	1.4	0.009	—
—	07/06/18	4.1	0.114	—
—	24/10/18	5.7	0.104	—
—	22/11/18	4.4	—	—
—	10/01/19	8.2	—	207.5
—	12/04/19	—	—	—
—	26/06/19	5.1	—	—
—	03/09/19	6.7	0.032	—
—	08/10/19	5.5	—	—
—	21/11/19	7.0	0.055	—
—	20/12/19	5.1	0.036	—
—	16/01/20	5.2	0.025	—
NapN	12/01/17	3.6	0.019	—
—	09/02/17	3.4	—	—
—	16/05/17	—	0.007	—
—	27/06/17	0.9	0.015	—
—	25/07/17	1.1	0.006	—
—	19/10/17	1.6	0.018	—
—	31/10/17	—	—	—
—	18/01/18	1.4	0.024	—
—	23/03/18	3.0	0.026	—
—	20/07/18	3.4	0.071	—
—	20/07/18	3.4	0.071	—

(Continued on following page)

TABLE 1 | (*Continued*) Molar gas ratios in fumarolic emissions from La Soufrière volcano measured with portable MultiGas in 2017–2020.

Site name	Time	CO_2/H_2S	SO_2/H_2S	H_2O/H_2S
—	07/09/18	3.6	0.06	—
—	24/10/18	2.9	0.13	—
—	22/11/18	3.4	—	—
—	10/01/19	5.4	0.031	177.5
—	09/03/19	4.6	0.027	—
—	12/04/19	5.2	—	—
—	26/06/19	5.4	—	—
—	14/07/19	—	0.033	—
—	03/09/19	4.7	0.037	—
—	08/10/19	5.1	0.044	—
—	21/11/19	5.4	0.048	277.8
—	20/12/19	4.8	0.025	—
—	16/01/20	5.1	0.047	—
—	12/01/17	5.4	—	—
—	09/02/17	4.3	—	—
—	16/05/17	1.6	—	39.1
—	27/06/17	1.4	—	67.7
—	26/09/17	1.5	—	72.7
—	19/10/17	1.9	—	—
—	09/11/17	2.0	—	67.8
—	18/01/18	1.9	—	—
—	16/03/18	2.0	—	—
—	02/05/18	2.4	—	—
—	07/06/18	4.1	—	—
—	20/07/18	4.3	—	—
—	07/09/18	5.1	—	—
—	24/10/18	4.3	—	—
—	22/11/18	4.3	—	—
—	10/01/19	7.1	—	148.5
—	09/03/19	5.9	—	—
—	12/04/19	6.6	—	157.5
—	26/06/19	6.7	—	181.6
—	03/09/19	5.6	—	83.7
—	08/10/19	5.1	—	—
—	21/11/19	5.3	0.02	—
—	20/12/19	4.0	—	—
—	16/01/20	5.3	—	—

given the low SO_2 content of La Soufrière gases we only post-processed the SO_2/H_2S ratio when the average SO_2 concentration was higher than the resolution of our SO_2 sensor (0.5 ppm). This threshold gives us confidence in our reported SO_2/H_2S ratios. CO_2/H_2S ratios were corrected for the effect of pressure. Some of the gas ratios presented in this paper were processed using the RatioCalc software (Tamburello, 2015) and have previously been reported in Moretti et al. (2020a), Moretti et al. (2020b), Jessop et al. (2021) and Massaro et al. (2021). When re-evaluating these data with our improved processing approach we obtain gas ratios that are in a good agreement with the earlier results (see example for CO_2/H_2S ratio at CS: **Figure 2F**). Gas molar ratios and concentrations (ppm by volume) from our MultiGas-based monitoring of La Soufrière are given in **Tables 1**, **2** and **Figures 3**, **4**, **5**.

For determining the gas fluxes, we first interpolated the measured gas concentrations using a 2D spline function and then computed the integrated concentration amounts (ICAs) over the plume cross-section using RatioCalc (Tamburello, 2015). Tamburello et al. (2019) have shown that more reliable flux determination is obtained by using CO_2 instead of H_2S as the volcanic marker, owing to the more conservative behaviour of CO_2 and the faster response of the IR CO_2 sensor compared to the H_2S chemical sensor. We thus followed this approach and computed CO_2 fluxes by scaling the integrated CO_2 column amount in plume cross-sections with the wind speed measured during each gas survey. The fluxes of other gas species were derived by scaling their average weight ratio to CO_2 with the CO_2 flux. Due to the high atmospheric background of CO_2 and H_2O, each of our walking profiles were started and ended in pure air in order to characterize and subtract the ambient air composition from our recorded data. The reported error on gas fluxes, which is typically of about 40%, includes the uncertainty on the measured average wind speed, usually the main source of error. Steam flux estimates are shown and discussed in Jessop et al. (2021). In this present work we focus on the dry gas fluxes that we measured and calculated in routine at the OVSG-IPGP since May 2018.

3.2 Seismic and Hydrology Properties

3.2.1 Relative Seismic Velocity Changes

Relative seismic velocity changes (dV/V) are deduced from the interferometry of ambient seismic noise correlation functions. It

TABLE 2 | CO_2, H_2S and SO_2 fluxes in tonnes per day, at La Soufrière in 2018–2020, computed from CO_2 ICAs and gas moral ratios (**Table 1**). Dry gas flux is calculated as the sum of CO_2, H_2S and CO_2. Wind speeds used for gas flux calculation are indicated. The sensors heights above the ground during the MultiGas traverses were always the same (90 cm and 2 m).

Location	Date	Plume speed	CO_2/H_2S	ICA CO_2	Flux CO_2	Flux H_2S	Flux SO_2	Dry flux
		(m/s)	molar	(ppm/m^2)	t/day	t/day	t/j	t/day
CS (CSN + CSS + CSC)	02/05/18	3.7	2.0	6,300	3.59	1.36	—	4.9
—	07/06/18	3.4	2.5	8,704	4.60	1.42	—	6.0
—	20/07/18	4.4	2.5	2,970	2.03	0.63	—	2.7
—	24/10/18	1.8	2.2	3,716	1.04	0.37	—	1.4
—	22/11/18	3.5	2.2	6,319	3.42	1.22	—	4.6
—	10/01/19	3.3	4.2	9,460	4.86	0.89	—	5.7
—	09/03/19	3.6	4.7	5,107	2.86	0.47	—	3.3
—	12/04/19	3.7	4.0	6,273	3.61	0.70	—	4.3
—	26/06/19	3.9	3.7	6,587	4.00	0.83	—	4.8
—	03/09/19	4.2	3.0	7,238	4.73	1.22	—	5.9
—	08/10/19	4.1	2.7	5,742	3.66	1.05	0.23	4.9
—	21/11/19	2.2	3.3	5,393	1.85	0.43	—	2.3
—	20/12/19	3.2	3.9	4,292	2.14	0.42	—	2.6
—	16/01/20	5.5	3.1	7,573	6.48	1.60	0.01	8.1
G56	02/05/18	4.7	1.2	2,390	1.76	1.13	—	2.9
—	07/06/18	3.8	2.6	3,514	2.08	0.63	0.14	2.8
—	20/07/18	—	—	—	—	—	—	—
—	07/09/18	3.2	2.8	4,007	1.99	0.55	0.10	2.6
—	24/10/18	3.7	2.4	2,427	1.40	0.45	—	1.9
—	22/11/18	5.0	2.7	4,066	3.19	0.91	0.09	4.2
—	10/01/19	3.5	4.2	9,460	4.86	0.89	—	5.7
—	09/03/19	5.5	3.5	2,205	1.89	0.41	0.07	2.4
—	12/04/19	8.3	4.2	2,261	2.92	0.53	—	3.5
—	26/06/19	6.5	4.5	1978	2.00	0.34	—	2.3
—	03/09/19	7.7	3.2	1,279	1.53	0.37	—	1.9
—	08/10/19	8.1	3.5	2,734	3.44	0.75	0.05	4.2
—	21/11/19	2.2	4.9	2075	0.71	0.11	0.01	0.8
—	20/12/19	4.2	3.5	2,839	1.85	0.41	0.03	2.3
—	16/01/20	10.1	3.7	786	1.24	0.26	0.02	1.5
TAS	02/05/18	3.3	2.4	6,205	3.22	1.04	—	4.3
—	07/06/18	3.4	2.5	8,704	4.60	1.42	—	6.0
—	20/07/18	3.6	4.3	4,643	2.60	0.47	—	3.1
—	07/09/18	3.3	5.1	4,950	2.54	0.39	—	2.9
—	24/10/18	1.8	4.3	5,994	1.68	0.30	—	2.0
—	22/11/18	4.6	4.3	6,650	4.80	0.87	—	5.7
—	10/01/19	3.3	7.1	5,829	2.99	0.33	—	3.3
—	09/03/19	3.8	5.9	4,330	2.56	0.34	—	2.9
—	12/04/19	4.2	6.6	6,151	4.02	0.47	—	4.5
—	26/06/19	3.8	6.7	4,472	2.64	0.31	—	2.9
—	03/09/19	5.1	5.6	3,468	2.75	0.38	—	3.1
—	08/10/19	4.3	5.1	3,540	2.37	0.36	—	2.7
—	21/11/19	2.7	5.3	1748	0.73	0.11	0.004	0.8
—	20/12/19	3.7	4.0	3,653	2.10	0.41	—	2.5
—	16/01/20	5.2	5.3	3,226	2.61	0.38	—	3.0
Total (CS + G56 + TAS)	02/05/18	—	—	14,895	8.57	3.53	0.00	12.1
—	07/06/18	—	—	20,922	11.28	3.47	0.14	14.9
—	20/07/18	—	—	7,613	4.63	1.11	0.00	5.7[b]
—	07/09/18	—	—	8,957	4.53	0.94	0.10	5.6[b]
—	24/10/18	—	—	12,137	4.11	1.13	0.00	5.2[a]
—	22/11/18	—	—	17,035	11.41	3.00	0.09	14.5
—	10/01/19	—	—	24,749	12.70	2.11	0.00	14.8
—	09/03/19	—	—	11,642	7.30	1.21	0.07	8.6
—	12/04/19	—	—	14,685	10.55	1.70	0.00	12.2
—	26/06/19	—	—	13,037	8.64	1.48	0.00	10.1
—	03/09/19	—	—	11,985	9.01	1.96	0.00	11.0
—	08/10/19	—	—	12,016	9.47	2.16	0.28	11.9
—	21/11/19	—	—	9,216	3.29	0.65	0.01	4.2[a]
—	20/12/19	—	—	10,784	6.09	1.24	0.03	7.4
—	16/01/20	—	—	11,585	10.32	2.24	0.03	12.6

[a]*Underestimated fluxes due to weak winds, the plume being not flattened to the ground during our walking traverses.*
[b]*Total fluxes calculated only with two vents (not reported in the* ***Figure 3*** *or included in calculation).*

is widely used to monitor the rock properties and fracturation state of a medium through time (Snieder et al., 2002; Nakahara et al., 2007; Wegler and Sens-Schönfelder, 2007; Brenguier et al., 2008a; Gassenmeier et al., 2016). On active volcanoes, dV/V is a proxy of inflation/deflation at depth and could reveal precursory signals of future eruptions (Brenguier et al., 2008b). At shallow depths (<500 m), seismic velocity changes are influenced by environmental forcing. Several studies have explored the potential use of dV/V to monitor the hydrology of medium (Sens-Schönfelder and Wegler, 2006; Lecocq et al., 2017; Clements and Denolle, 2018; Illien et al., 2021). Groundwater level changes modify the water saturation in the medium and modify the seismic velocity. This variation can range from less than 1% up to 10%. Comparing a reference groundwater level, representing for instance the average level at a hydrological season scale, and a reference state of the medium seismic properties, given by an average noise correlation function over a long time period, a higher (lower) groundwater level will produce a decrease (increase) of seismic velocity. This decrease (increase) of seismic velocity produces slight modifications in the medium Green's function by dilating (compressing) the coda waveform of a noise correlation function (Hadziioannou et al., 2009; Sens-Schönfelder and Wegler 2011). To properly interpret the dV/V at shallow depths, we must consider a possible influence of groundwater level changes, especially in a tropical environment with high cumulative rainfall (>8 m/year), such as in La Soufrière.

In this study, the seismic velocity changes are processed from the continuous seismic signal recorded by the OVSG permanent array. Noise correlation functions are computed at a daily scale for each station couple and seismic components. The daily relative velocity changes (dV/V) are deduced from a stretching technique and with a reference Green's function averaged over more than 3 years (e.g., Sens-Schönfelder and Wegler 2011). Finally, to better reflect the changes at the dome, we use all dV/V records and we spatialise them using a region of +/− 500 m around the Tarissan pit. The spatialization is an equivalent to a weighted mean by the length of the ray path crossing the region of interest. This observed relative velocity changes (dV/V obs.) are shown in **Figure 4**.

3.2.2 Groundwater Level Modelling

Having an estimate of the groundwater level at La Soufrière is not possible since no monitored borehole is available. However, in order to obtain at a first order an estimate of groundwater fluctuations, we use an alternative approach to quantify the dynamics of the aquifer. Groundwater is known to be tightly linked to rainfall. Since the dome is the top part of a large watershed no other contributor than rainfall is expected. Water advection due to hydrothermal circulation is only a minor contributor. We thus reconstruct the groundwater level through time with rainfall records according to Akasaka and Nakanishi (2000). In such a model, the aquifer is described by Darcy's law and the drainage is proportional to the height of the groundwater table. At a time t_i, the groundwater level results from the convolution of rainfall with an exponential function and aquifer parameters according to the expression

$$GWL(t_i) = GWL_0 - \sum_{n=0}^{i} \frac{p(t_n)}{\phi} e^{\frac{-(t_i - t_n)}{\tau}}, \quad (1)$$

where GWL_0 is the asymptotic groundwater level, φ the connected porosity, τ the drainage characteristic time and p (tn) the rainfall at time tn. Rainfall input for the hydrological model is estimated from an average of three rain gauges all located at la Soufrière (Sanner (16.04497°N, 61.66272°W, 1,076 m) and Savane à Mulets (16.038540°N, 61.665190°W, 1,139 m) managed by OVSG, and Citerne (16.03270°N, 61.65583°W, 1,076 m) managed by Meteo-France).

To estimate the aquifer parameters (GWL0, φ and τ), we chose to model the groundwater level following **Eq. 1** and we fit a linear relation with the monthly observed level of the Tarissan lake. In such an approach, we assume that the Tarissan lake level is a direct proxy of the aquifer level, a first order equivalent to monitored borehole. This assumption being a drastic constraint for the modelling of the groundwater level, we also convert the absolute variation of the groundwater level to a relative level, which can be interpreted as an anomaly of groundwater content in the medium. The normalization stage is defined by an average groundwater level GWLyear, corresponding to the mean level for the year 2018, and a range of fluctuation ΔGWLyear, corresponding to the difference of extreme values of the same year. We end with an equivalent of an anomaly of groundwater level dGWL/GWL defined as

$$\frac{dGWL}{GWL}(t_i) = \frac{GWL(t_i) - GWL_{year}}{\Delta GWL_{year}}, \quad (2)$$

The asymptotic level is discarded by the term GWLyear and the connected porosity by ΔGWLyear. The final signal for groundwater anomaly is given in **Figure 4**. A negative anomaly will reflect a lower level of the groundwater with respect to the average and a positive anomaly an excess of water in the aquifer. The only parameter to invert is the drainage characteristic time and is estimated to be 40 days. This value is coherent with the results from hydrologeogical tracing by Bigot et al. (1994) that pointed to a fracture-dominated groundwater transport at the scale of the entire dome.

Finally, we use the groundwater anomaly to calculate the induced relative velocity fluctuation (dV/V calc; Sens-Schönfelder and Wegler, 2011) and we compare with the observed relative velocity changes (dV/V obs). Most of the time the calculated and observed dV/V are showing coherent fluctuations implying that velocity changes at sub-surface are driven by the aquifer dynamics. Nevertheless, some discrepancies are observed, like after the April 2018 M.4 earthquake where an important velocity drop is noticed. This drop explained by the damaging of the sub-surface following the solicitation of the seismic waves after the main shock. Such an observation has been widely documented for other context (e.g., Brenguier et al., 2008a; Takagi and Okada, 2012). Other periods of discrepancies could be related to geochemical signals and are discussed in the following sections.

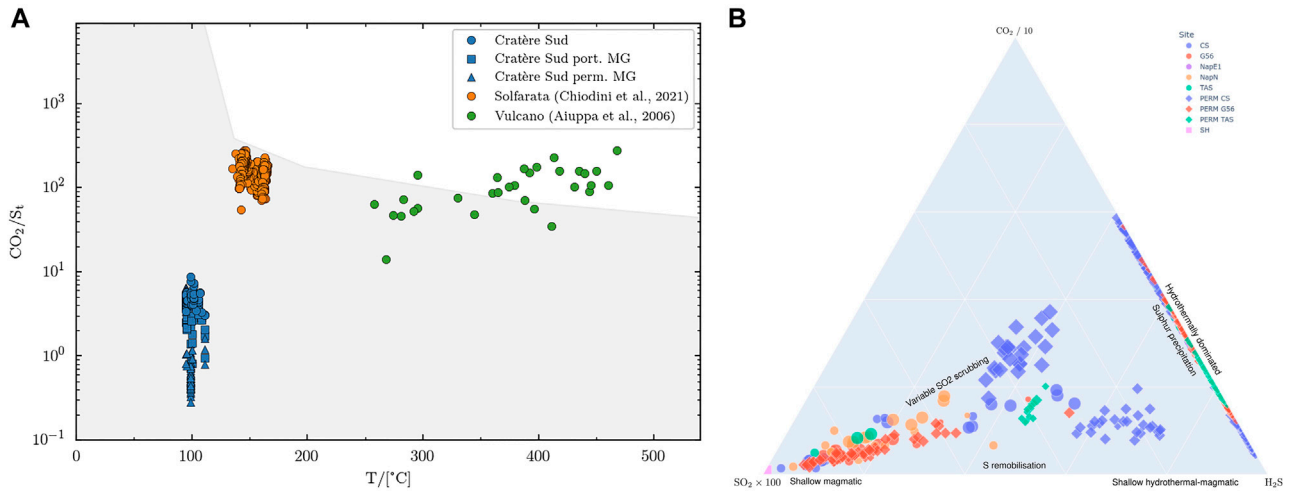

FIGURE 3 | (A) Temperature vs. CO_2/St (St = H_2S) gas ratios for La Soufrière at Cratère Sud fumaroles (CS). Both MultiGas settings are shown: orange dots for portable MultiGas, green dots for permanent MultiGas, while the blue ones correspond to the Giggenbach bottle results. The grey shaded area represents the temperature dependence of CO_2/St gas ratios in published analyses of volcanic arc gases (Aiuppa et al., 2017) while the other data correspond to Vulcano and Solfatara low-temperature fumarolic emissions obtained by Giggenbach bottles. **(B)** Ternary plot of CO_2/10-H_2S-SO_2*100 of La Soufrière emissions measured by MultiGas (permanent and portable) representing the proposition of each species. Maximum concentrations for CO_2, H_2S and SO_2 for each measurement are shown. Colors are different by site, circles represent portable MultiGas, squares permanent MultiGas, and the size of the symbol indicates the period of interest (P1 and P3 having smallest and biggest symbols, respectively). The Montserrat-type magmatic end-member is shown as a square symbol.

Details of the seismic, extensometry and temperature networks and methods are available in Jacob et al. (2005), Tamburello et al. (2019), Moretti et al. (2020a), Jessop et al. (2021). Seismic data are distributed by IPGP on the public access Volobsis server (http://volobsis.ipgp.fr) and the Data center (http://datacenter.ipgp.fr). Rainfall data from Sanner and Savane à Mulets as well as the Tarissan lake level are available on request from OVSG.

4 RESULTS

4.1 Gas Compositions

Our nearly 4-year long surveys of La Soufrière gas emissions with both portable and permanent MultiGas show a wide temporal variability in gas compositions (**Figures 3**, **4**). However, for a same vent at a given date both portable and permanent MultiGas provide consistent compositions (**Figures 3**, **4**), except for small differences observed at CS. The latter simply result from the fact that few portable measurements were performed during the lifespan of the permanent station at CS and, moreover, not always at the same CSS vent monitored by the permanent MultiGas station. On the other hand, the temporal variability in gas compositions revealed by our MultiGas measurements at CS is also confirmed by the data obtained from direct fumarole sampling via Giggenbach bottles over the same timeframe (**Figures 3**, **4**), even though the chemical variability from the bottles is narrower. One can observe a minor offset between these two techniques, mainly due to secondary effects in the MultiGas inlet line (Moretti et al., 2020b). This offset is minimized from Dec. 2019, since when very high exit vent emission velocities were observed (see IPGP-OVSG 1999–2021 Bulletins).

Over the studied period, both MultiGAS setups reveal CO_2/H_2S ratios varying over an order of magnitude, from <0.5 to >6, and SO_2/H_2S varying from 0 to ~0.25 (**Table 1**; **Figures 3**, **4**). The CS fumarole temperatures varied from 93 to 107°C (**Figures 3**, **4**), which is typical of hydrothermally-dominated emissions (Giggenbach, 1995; Aiuppa et al., 2017; **Figure 3A**). However, the observed large compositional variations of La Soufrière fumaroles also indicate a magmatic influence (compositions richer in SO_2 in such ternary diagram; Giggenbach, 1996; Stix et de Moor, 2018; Moretti et al., 2020a; **Figure 3B**). After steam, CO_2 and H_2S are the predominant species in the fumarolic gases and hence contribute most of the total dry gas flux (**Table 2**). Taking SO_2 fluxes also into account, we find that the total dry gas flux has diminished roughly by a factor of two from 2016 (~19 ± 2 tons/day) to 2020 (11 ± 3 tons/day; **Table 2**, **Figure 4**). We actually observe a decrease in gas flux at all the main vents in this period (**Table 2**). The lowest values measured in October 2018 and November 2019 may simply be biased by the very weak winds that prevailed on occasion of these two measurements, as the low wind did not allow us to catch the whole volcanic plume during our walking traverses.

4.2 Meteorological Forcing and Geophysical Signals

The normalised water table level ranges from −0.8 to 0.9, with its lowest peaks occurring during dry seasons and its highest values observed during an abnormal rainy period in May 2017 and

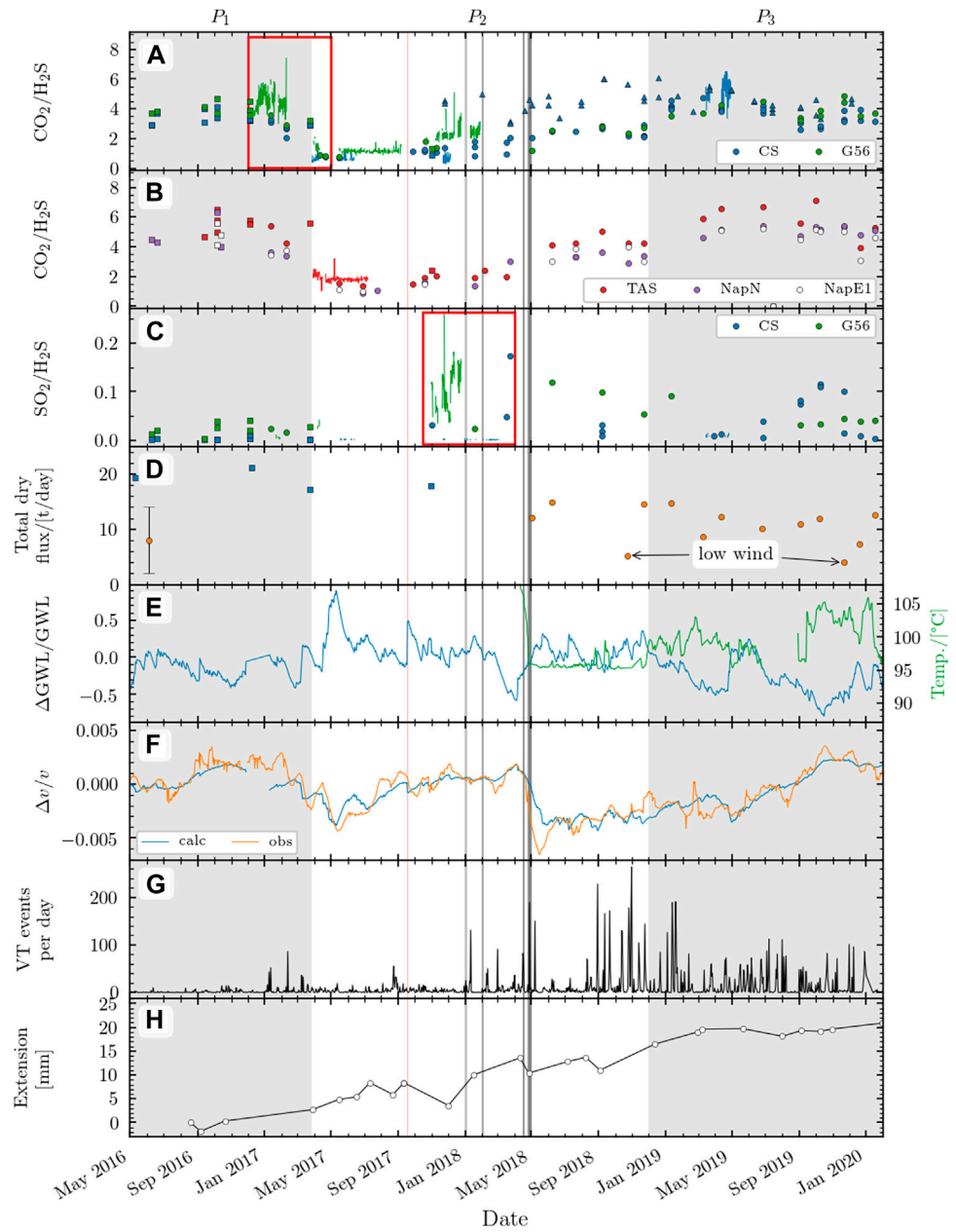

FIGURE 4 | Time series of volcano monitoring for La Soufrière since 2016. **(A–D)** MultiGas data: **(A,B)** Molar CO_2/H_2S ratios for four main fumarolic vents, **(C)** Molar SO_2/H_2S ratios only for CS and G56, **(D)** Total dry gas fluxes (CO_2 +SO_2+ H_2S fluxes at CS, G56 and TAS). MultiGas square data are from Tamburello et al. (2019). **(E)** Groundwater table level (m) along with temperature (°C) **(F)** Relative velocity fluctuations dV/V, observed and calculated. **(G)** Seismic activity showing volcanic tectonic (VTs) counts per day. **(H)** extensometry data for NAP1 (m). Three different periods (P1, P2, P3) of chemical variations are identified. Major VTs are marked in grey and Maria hurricane in red line. Both red insets are periods focused in **Figure 5**.

Hurricane Maria in Sept. 2017 (**Figure 4**). The fumarole temperature seems to be anti-correlated with the variation of the normalised water-table level, with higher temperature when the water table level lowers. Major fluctuations of the observed and calculated dV/V ratios are shown in **Figure 4**. These fluctuations are almost identical for both curves, meaning that the dV/V variations are mostly controlled by the normalised table water level variation (dGWL/GWL; **Figure 4**). Despite the overall background nominal control on the dV/V behaviour by external forcing, some differences between calculated and observed dV/V can be identified, such as after the April 2018 M.4 earthquake where a important velocity drop is noticed. This drop is explained by the damaging of the sub-surface following the solicitation of the seismic waves after the main shock. Such an observation has been widely documented for other contexts (e.g., Brenguier et al., 2008a; Takagi and Okada, 2012). Other periods of discrepancies

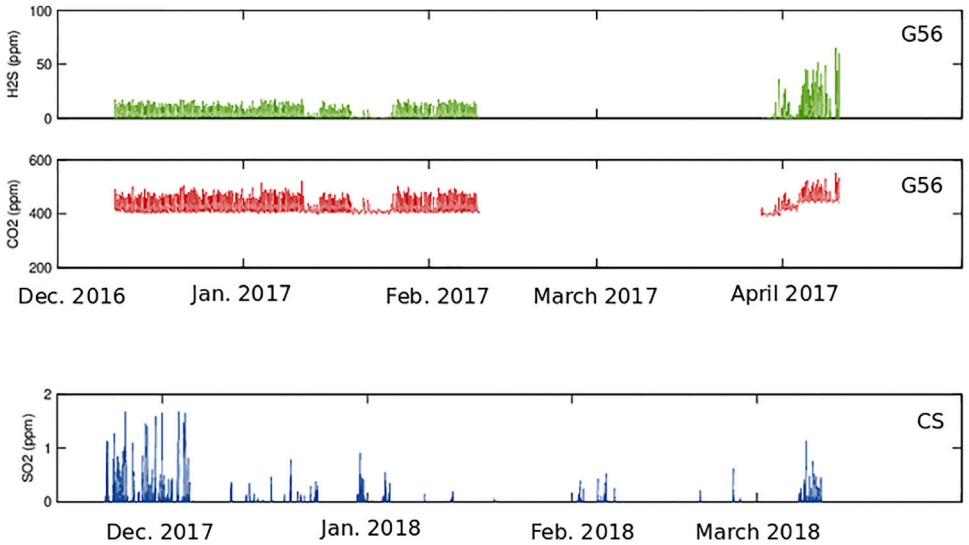

FIGURE 5 | Inset focusing on SO_2, H_2S and CO_2 concentrations of the MultiGas permanent stations during the transition between P1 and P2 (between December 01, 2016 and May 01, 2017), and during P2 (between November 15, 2017 and April 01, 2018) which encompasses the highest peak of activity on La Soufrière since 1976. Note that during P2, the H_2S sensor of the permanent station at CS was saturated.

(late March 2017, late February 2018 and December 2019; **Figure 4**) could be related to geochemical signals and are discussed in the following sections. These differences underline the need of internal forcing to explain the dV/V variability.

The increase in the occurrence of VT seismicity is positively correlated to the general tendency of increased opening of almost all fractures in the active fumarolic zones since May 2017 as determined with one-dimensional extensometry measurements (Moretti et al., 2020a; OVSG-IPGP 1999–2021 bulletins). Gouffre Napoleon (NAP1) is the site affected by the largest extension (~20 mm in 3 years) and is shown in **Figure 4**. However, the periods from mid-2016 to mid 2017 and since Jan. 2019 are marked by much lower extension rates (**Figure 4**, bottom panel).

4.3 Temporal Variability

We identify three distinct periods in our 2016–2020 data set during which gas emissions from all vents followed a similar general trend (cf. shaded regions in **Figure 4**). These periods are defined as P1 (March 2016–April 2017), P2 (April 2017–December 2018) and P3 (December 2018–January 2020).

The P1 period was characterised by high CO_2/H_2S (~4 at CS and G56; ~5 at TAS, NAPN and NAPE1) and low SO_2/H_2S (<~0.015 at all sites), followed by a drastic decrease in the CO_2/H_2S ratio. This rapid and abrupt decrease occurred in late March 2017 and was observed simultaneously at all vents (**Figure 4**). During this period the dry gas fluxes were high and stable at all sites (CS: 7+/−1.5 t/d; G56: 6+/−2.7 t/d; TAS: 6+/−2 t/d; **Table2**; **Figure 3**; Tamburello et al., 2019). A gap in measurements between April and October 2017 makes it impossible to assess any change in gas flux. The water table level remained mostly below the reference level (range: −0.43 to 0.16; average: −0.15) and the fluctuation in observed dV/V ratios are well reproduced by the model (dV/V cal., **Figure 4**). However, by late March 2017 a significant negative dV/V anomaly occurred; this cannot be explained by external forcing (**Figure 4**). Overall the occurrence of VT seismicity was relatively low during the P1 period and the lowest of the entire 2016–2020 period of analysis. In the same time the extensometry survey showed little to no opening or closure of the active faults on top of the dome (OVSG-IPGP 1999–2021 bulletins, **Figure 4**). However, a change in extension rate became observed from late March 2017, especially at NAP1 (**Figure 4**). In January, February and March 2017, small seismic swarms also started to occur.

The P2 period was instead characterised by low CO_2/H_2S (~1 at CS and G56; ~2 at TAS, NAPN and NAPE1) and low SO_2/H_2S (<~0.015 at all sites) ratios, followed by a strong chemical perturbation from November 2017. This chemical perturbation occurred months before the four seismic swarms of January 2018 (70 events), February 2018 (30 events, 1 felt), mid-April (140 events, 1 felt) and late April 2018 (180 events, 2 felt) (**Figure 4**; Moretti et al., 2020a). During the latter swarm, La Soufrière reached its highest level of release of seismic energy on April 27, 2018 with the largest felt volcanic-tectonic (VT) earthquake (M_L 4.1) since the last eruption in 1976 (Moretti et al., 2020a). The perturbation is first characterised by an increase of both CO_2/H_2S and SO_2/H_2S at G56 (permanent station at the beginning of Nov. 2017; **Figure 4**). During this period, chemical ratios involving H_2S from the permanent station could not be estimated at CS because the H_2S sensors became saturated. Instead, relatively high SO_2 concentrations (almost up to 2 ppm) were measured by the permanent station at CS at the end of Nov. 2017 and also in March-April 2018 (**Figure 5** and Moretti et al., 2020a). Trends from the permanent stations are coherent with the portable measurements, showing a similar maximum SO_2/H_2S ratio (0.18) at G56 in November 2017 then at CS in March 2018. This ratio was the highest ever measured at La Soufrière since the

start of MultiGas measurements in 2012 (**Figure 5** and Moretti et al., 2020a), implying a factor 2 increase in SO_2. With such an increase of SO_2, the geochemical composition of gas at CS and G56 but also the emissions of TAS and NapN, acquired in March 2018, shifted towards a typical andesitic magmatic end-member (**Figure 3B**). A small but significant increase in CO_2/H_2S was simultaneously observed at NAPN, and this ratio also increased significantly at NAPE1 and TAS 1 month later. From June to December 2018 there was a continuous decrease of the SO_2/H_2S ratio and a small increase of the CO_2/H_2S ratio all over the dome. Gas flux measurements from MultiGas traverses were not performed successfully from November 2017 to May 2018, making it difficult to infer any quantitative flux change during this major event. However, a noticeable decrease of the dry gas fluxes occurred after the major earthquake, by a factor up to ~2 compared to 2016–2017 values (CS: 4.2 ± 1.8 t/d; G56 2.4 ± 1.4 t/d; TAS: 4 ± 1.6 t/d); **Table 2**; **Figure 4**), and Jessop et al. (2021) noticed, via Pitot tube measurements, that gas fluxes dropped by a factor 3 concurrent with this event. The anomalously low fluxes in October 2018 reflect partial plume analysis, as the low wind did not allow us to catch the whole volcanic plume during our walking traverses. The water table level stood mostly above the reference level (range: −0.59 to 0.9; average: 0.07), with the highest level by early May and the lowest one in April 2018 (**Figure 4**). In Sept. 2017, Hurricane Maria induced a sudden rise of the water table. The fluctuations in observed dV/V ratios are well reproduced by the model (dV/V cal., **Figure 4**) during P2. However, two negative and one positive dV/V anomalies occurred before and after the major VT events (late February and mid-May 2018) and in December 2019. These anomalies cannot be explained by variations in the normalised water table level (**Figure 4**). However, notable increases in seismic rate, in number of VTs (**Figure 4**) and especially in released seismic energy with felt VT earthquakes are observed (Moretti et al., 2020a). These events marked the onset of seismic swarms. Moreover, during P2 almost all fractures of the dome showed opening at a higher rate (Moretti et al., 2020a; OVSG-IPGP 1999–2021 Bulletins; **Figure 4**). However, a reversal of this trend occurred between March and April 2018, implying a slight closure of the active fumarolic zones on top of the dome (**Figure 4**; Moretti et al., 2020a).

The P_3 period is characterised by P1-type high CO_2/H_2S (~4 at CS and G56; ~5 at TAS, NAPN and NAPE1) ratios and low SO_2/H_2S ratio (<~0.02 at all the sites), with the exception of few data points higher SO_2/H_2S ratios up to 0.11. CO_2/H_2S ratios remained quite constant over 2019 and similar to those during P1. While remaining low, the SO_2/H_2S displayed some fluctuations from September to December 2019. In January 2019, both CO_2 and H_2S fluxes had decreased from 14.1 t/d in P2 to 10.5 t/d in P3 and then remained relatively constant all over the dome until January 2020 (**Table 2**; **Figure 4**). Low flux in November 2019 is again an artefact due an extremely too low wind speed that prevented reliable plume analysis. The water table level stood mainly below the reference level (range: −0.8 to 0.25; average: −0.28; **Figure 4**), with the lowest peak in 3 years occurring between September and December 2019. No anomaly was noticed between the observed and calculated dV/V values. This period is also marked by recurrent seismic VT swarms that started markedly in September 2018 and continued throughout 2019 (**Figure 4**). From September 2018 until Jan. 2020, 49 swarms with tens to hundreds of VTs developed at shallow depth beneath the dome (**Figure 4**, OVSG-IPGP 1999-2021 bulletins). They constitute an unprecedented rate of seismicity VT but of very low energy. On the other hand, the stability observed in MultiGAS data is also consistent with a low extension rate on most summit fractures, as observed also during P1. These features during P3 indicate that, in that period, the magmatic-hydrothermal system of La Soufrière had recovered the P1 conditions that prevailed before the April 2018 unrest crisis, except for the VT activity.

5 DISCUSSION

5.1 Chemical Controls on Gas Composition at La Soufrière de Guadeloupe

Figure 3A shows the temperature dependence of the CO_2/S_t ratios in La Soufrière's hydrothermal gases at the CS vent, with S_t being here represented by H_2S. It has been shown that volcanic gases exhibit a general exponential trend of decreasing CO_2/S_t ratios with increasing temperature (Aiuppa et al., 2017). The CO_2/S_t signature of typical hydrothermal fluids is generally more scattered and higher (up to 100,000) than that of magmatic gases essentially because of sulfur scrubbing by hydrothermal reactions (Symonds et al., 2001). However, even though La Soufrière fumarolic gases are thermally defined as hydrothermal (T < 250°C; Giggenbach, 1987; Aiuppa et al., 2017), our dataset shows that they are characterized by quite low CO_2/S_t ratios evolving in a narrow range. This may indicate that they are less affected by scrubbing effects than other low-temperature fumarole emissions at other volcanoes (Aiuppa et al., 2017), such as Vulcano (Aiuppa et al., 2006) and Solfatara of Campi Flegrei (Chiodini et al., 2021) for instance (**Figure 3A**).

Figure 3B shows the measured fumarole compositions of La Soufrière in a CO_2-SO_2-H_2S ternary diagram. The high-temperature (720°C) SO_2-rich gas collected in 1996 from the extruding andesite lava dome of Soufrière Hills on nearby Montserrat island (Hammouya et al., 1998) is taken as a reliable proxy for the andesitic magmatic end-member at La Soufrière and is also shown in **Figure 3B**. Fumarolic gas emissions at La Soufrière display quite large compositional variations between a purely hydrothermal end-member and a mixed hydrothermal-magmatic shallow pole (**Figure 3B**; Giggenbach, 1987; Stix and deMoor, 2018). Specifically, the fumarolic gases display large variations in SO_2/H_2S ratio at relatively steady CO_2/H_2S ratio, along a trend that extends from the SO_2-rich Montserrat-type magmatic end-member towards strongly SO_2-depleted samples (**Figure 3B**). Such a trend is best accounted for by variable SO_2 scrubbing in the hydrothermal liquid water (Tamburello et al., 2019). In the most SO_2 depleted gas emissions, an impoverishment of H_2S is also observed, suggesting a variable but significant loss of H_2S in the volcanic ground prior to gas emission at the surface (Tamburello et al., 2019).

SO_2 scrubbing in liquid water phase is a common process at volcanoes with hydrothermal systems. Because of the very high sulfur reactivity, particularly in hydrothermal environments where sulfur is partitioned between interacting gas, liquid and solid phases, few essential processes can be used to describe how magma-derived SO_2 is efficiently removed from the gas phase during gas-water interactions. The following dissociation reactions (Giggenbach, 1980):

$$4SO_2 + 4H_2O \Leftrightarrow H_2S + 3H_2SO_4 \quad (3)$$

$$3SO_2 + 2H_2O \Leftrightarrow S + 2H_2SO_4 \quad (4)$$

Subtract SO_2 into the hydrothermal liquid, leading to surface gas emissions essentially composed of CO_2 and H_2S besides water vapour. Besides, metastable precipitation of elemental sulfur within the volcanic ground through the gaseous reactions.

$$SO_2 + 2H_2S \Leftrightarrow 3S + 2H_2O \quad (5)$$

and

$$2H_2S + O_2 \Leftrightarrow 2S + 2H_2O \quad (6)$$

can deplete low-temperature volcanic gas in both H_2S and SO_2.

Specific depletion of H_2S that is degassed from a magma or deeper hydrothermal fluids may occur by forming sulfuric acid, H_2SO_4, because of oxidation by atmospheric oxygen in a steam-heated environment. According to

$$H_2S + 2O_2 \Leftrightarrow H_2SO_4 \quad (7)$$

This is one main mechanism (together with pyrite wet oxidation) that produces so-called acid-sulfate waters, which like at La Soufrière react quickly with host rocks to give advanced argillic alteration parageneses (Heap et al., 2021) dominated by kaolinite and alunite, as well as gypsum, opal, and hydrated iron oxides (Steiner, 1977). H_2S partial pressure, hence concentration, in such hydrothermal environments is then buffered by such parageneses via coexisting pyrite, an unspecified Fe-Al-silicate [indicated as (FeO), such as chlorite or epidote and the corresponding Al-silicate in its protonated, Fe-free form, (H_2O) *via* (Giggenbach, 1980; Giggenbach, 1987):

$$2H_2S_{(g)} + [FeO] \Leftrightarrow FeS_{2(pyrite)} + H_{2(g)} + [H_2O] \quad (8)$$

Which can be turned into a gas-solid proxy reaction (Moretti et al., 2013, 2017; 2020a) by considering a shallow or even superficial gas-water-rock interactions involving ferrous iron in the wet volcanic ground:

$$2H_2S_{(g)} + FeO_{(rock)} \Leftrightarrow FeS_{2(pyrite)} + H_{2(g)} + H_2O_{(g,l)} \quad (9)$$

Minor thermally and/or redox-driven fluctuations of the hydrothermal system may thus be accommodated by reaction such as (**Eqs 5, 8, 9**), which can either consume or remobilise sulfur from solid phases to restore equilibrium. In particular, sulphur accumulated in hydrothermal systems can be occasionally remobilised from the previously sealed hydrothermal system (Giggenbach, 1987) which can thus explain part of the fluctuation in C/S_t that ratios we measured at La Soufrière (**Figure 3B**), such as observed for instance at Ruapehu volcano (Christenson et al., 2010). Besides, lowest measured ratios may reflect prolonged and enhanced hydrolysis of either crystalline S (**Eq. (5)**) or pyrite (**Eqs 8, 9**) associated with significant water-rock ratios in the shallow system.

Figure 3B also provides more detailed insight into the spatial and temporal variations in gas composition. Gas emissions from NapE1 and TAS are systematically the most affected by SO_2 scrubbing, which is coherent with the fact that TAS emissions arise from an acid crater lake (Tamburello et al., 2019) and with the low temperature of nearby NapE1 fumarole (40–60°C). SO_2 scrubbing effect is more variable over time in the case of gas emissions from CS and, to a lesser extent, G56 and NapN. As a matter of fact, the extent of SO_2 scrubbing, sulfur precipitation or instead, of remobilisation processes, depend not only on temperature but also on external factors, such as rainfalls and the dynamics of the water table level, which may induce some cycling behavior. Looking at temporal variations, two main features appear in **Figure 3B**: 1) the data points for G56 in Nov. 2017 and for CS, NapN and TAS in March 2018 plot the closest to the andesitic magmatic end-member, in agreement with the inferred magmatic gas pulse in that period (see **section 5.3**; Moretti et al., 2020b); and 2) the data for the period P3, especially at CS, show higher CO_2/H_2S and lower SO_2/H_2S ratios than during P2, indicating extensive sulfur loss in the hydrothermal system (see **section 5.3**). Thereafter, using additional information from geophysical signals, we attempt to better decipher the different processes determining the gas compositional variability observed during our nearly 4-year long survey.

5.2 Gas-Water-Rock Reactions and the Role of Permeability

At La Soufrière, native sulfur deposits are widespread at all active fumarolic vents whereas abundant pyrite (FeS_2) is produced in the shallow volcanic ground as well as in the La Soufrière host-rock (Saläun et al., 2011) by gas interaction with ferrous iron oxides in the wet rocks. Thus, both gas-water-rock reactions in the shallow volcanic ground and sulfur precipitation through gas reaction and oxidation at the surface deplete sulfur in the fumarolic gas phases, leading to an increased CO_2/St (essentially CO_2/H_2S) ratio. A dominant buffering process by these reactions may indeed account for the high and stable CO_2/H_2S ratios during the period P1. As these interactions proceed, S deposits accumulate underground and S-rich sealing processes promote the gradual development of impermeable layers. Sealing by precipitation, in the host-rock voids, of silica dissolved in hydrothermal fluids can also lead to reduced permeabilities in different regions of the hydrothermal system (e.g., Komorowski et al., 1997, 2008, 2010; Boudon et al., 1998). Opal (i.e., hydrothermal silica) was identified in the non-juvenile fragments of the ash produced by explosions during the 1976–1977 eruption of La Soufrière (Feuillard et al., 1983; Salaün et al., 2011; Heap et al., 2021; Inostroza et al., sub-judice). Hence, continuous degassing at depth, verified by a high total dry gas flux at the surface (**Figure 4**), progressively leads to impermeable sealing at the hydrothermal system-host-

rock interface, only allowing concentrated gas escape through preferential drains. For instance, this can explain the lack of thermal ground anomalies around the Cratère Sud (CS) despite a high gas flux and extensive surface sulfur deposition at this most active central vent (Jessop et al., 2021).

The drastic decrease of CO_2/H_2S ratio that occurred in late March 2017 all over the dome, along with the negative anomaly of dV/V, cannot be explained by external forcing (i.e., variation of the table water level; **Figure 4**). These simultaneous changes in two different volcanic parameters are better accounted for by increasing gas accumulation in the vapour-saturated seal of the shallow hydrothermal system at a few hundred meters depth. This interpretation is supported by the dramatic decrease of density in La Soufrière dome on late March 2017 as detected by muon imagery (Le Gonidec et al., 2019). Such a broad decrease of density was explained by an increased vapour/liquid ratio in the shallow hydrothermal system due to a rise in thermal input (Le Gonidec et al., 2019). At that time, the gas exit temperature at CS rose during 3 days (29th–31st of March 2017) from 98.1 to 99.3°C. Higher steam production due to this heat input may have generated an overpressure, flushing the hot fluids in fractures within the lava dome and in the first hundred of meters below (Le Gonidec et al., 2019). This phenomenon likely provoked an increase of pore pressure, inducing hydro-fracturing in the hydrothermal system that likely propagated through the overlying sealed caps and caused an increase of the permeability of the seal region (decreasing dV/V). An expected consequence of these processes is the remobilization of hydrothermal sulfur deposits (S and sulfate) that would have triggered an increase in H_2S degassing and a decrease in CO_2/H_2S ratio, such as observed in our MultiGas dataset (**Figures 4**, **5**). Such a scenario is consistent with the higher number of VTs recorded since January 2017, that indicate the pressure increased in the sismogenic zone until triggering rock fracturing and with extensometric observations that show that the rate of fracture opening increased by late March 2017. Permeability modulations related to hydrothermal convective circulation and involving cycles of clogging and reopening of the dome fractures, transferring heat from deep aquifers to shallower ones, were already proposed by Zlotnicki et al. (1992) as a possible source mechanism for triggering recurrent explosions during the 1976–1977 phreatic eruption crisis.

Le Gonidec et al. (2019) proposed that this destabilisation of the hydrothermal system originated at relatively shallow depth beneath the G56 vent. However, we show here that the sharp gas compositional change by late 2017 occurred at the same time at all active vents on La Soufrière lava dome. Therefore, we rather infer a wider and deeper source destabilisation of the hydrothermal system, triggering an increased ascent of hot fluids through the whole dome. This is further supported by 1) the overall gas chemistry obtained from Giggenbach bottles at both CS and NapN (OVSG-IPGP 1999–2021 bulletins) and 2) the spatial extension of increased ground heating all over the dome (Jessop et al., 2021).

5.3 Detecting Gas Unrest Signals

The changes in CO_2/H_2S and SO_2/H_2S during the period P2, from Nov. 2017 until June 2018, demonstrate a pressure increase in the hydrothermal system. Moretti et al. (2020a) showed that the total S- and increase SO_2 content of gas emissions at the summit CS fumarole resulted from an enhanced influx of magma-derived gas from depth that heated (by 30–40°C) and pressurised by about 60 bar) the La Soufrière hydrothermal system. This increase in pressure and temperature occurred over only 15 days (Moretti et al., 2020a). Whereas gas variations in late March 2017 during P1 had affected all the vents, the different times observed for the increase in SO_2/H_2S and CO_2/H_2S (from November 2017 to March 2017 and from Nov. 2017 to June 2018, respectively) at the different vents during P2 indicate a differing proportion of magmatic versus hydrothermal fluids at each vent. The fact that these changes occurred first at G56, where SO_2 scrubbing has less influence than at the more central vents of CS, NapN, TAS and NapE1 (**Figure 3B**), confirms that gas emissions at G56 are more pristine where they allow monitoring of a deeply sourced unrest at La Soufrière (Tamburello et al., 2019). On the other hand, the delayed signals at CS and then NapN, TAS and NapE1 indicate that these sites are more efficiently buffered by hydrothermal aquifers that promote scrubbing of the soluble acid sulfur-rich gases. Progressive release of a magmatic gas pulse during the period from November 2017 to March 2018 is clearly evidenced by the shift of our data points towards the andesitic magmatic end-member (**Figure 3B**). Finally, it is noteworthy that the two negative dV/V anomalies, as well as the differences between the calculated and observed dV/V values, indicate that the compositional gas changes observed at the surface during P2 were not related to any external forcing.

The entire volcanic system was strongly perturbed by the major M4.1 earthquake on April 27, 2018, and these effects have persisted for several months afterwards. From June to December 2018 we observed both a continuous decrease of SO_2/H_2S ratio and a small increase of CO_2/H_2S ratio all over the dome, along with a lowering of the dry gas fluxes by a factor up to ~2 compared to 2016–2017 values. In December 2018 the positive dV/V anomaly and the difference between the calculated and observed dV/V values suggest a renewed sealing of the system, in agreement with the lower gas flux and lower opening rate of the dome fractures, that returned to levels similar as those during P1.

In December 2018, the summit fumaroles recovered background compositions similar to those in P1, suggesting that the volcanic/hydrothermal system was no longer disturbed. Indeed, the subsequent period P3 (Dec. 2018 to Jan. 2020) displays high CO_2/H_2S and low SO_2/H_2S ratios similar to P1. This return to background compositions is also confirmed by the composition of gases routinely sampling with Giggenbach bottles, not only for the C/S ratio (**Figure 4**) but also for CO_2/CH_4 and He/CH_4 ratios which are sensitive indicators of magma-derived gas input (OVSG-IPGP 1999-2021 bulletins). We thus infer that during the post-unrest period P3 gas transfer was reduced and sulfur loss was re-initiated in the hydrothermal system as evidenced by the high CO_2/H_2S and low SO_2/H_2S ratios. S loss was even more marked at CS (**Figures 3B**, **4**) where extensive sulfur deposition was also observed during P3. However, we outline that since September 2018 recurrent seismic swarms of very low-magnitude but with tens to hundreds of VTs developed at shallow depth beneath the

dome (OVSG-IPGP 1999-2021 bulletins). These VT swarms became more and more frequent, suggesting the alternance of fluid accumulation and release in an increasingly sealed hydrothermal system. The fractured state of the dome allowed the fluid pressure to be released naturally, thereby limiting the risk of a hydrothermal eruption. However, this may not be always the case in future, further highlighting how the permeability of the volcanic system can vary on short spatio-temporal scales and how it determines the probability of a hydrothermal eruption at La Soufrière (e.g., Zlotnicki et al., 1992; Le Gonidec et al., 2019).

5.4 External Forcing

10 +/− 2 m of rain falls annually at the summit of La Soufrière (e.g., Villemant et al., 2014). Extensive fracturation of the lava dome strongly favours the infiltration of up to 30% of meteoric water into the ground and the shallow hydrothermal system (Moretti et al., 2021 and refs. therein). At first sight, our dataset does not show clear compositional changes of fumarolic gases in response to seasonal or/and meteorological variations, contrary to previous observations (e.g., Faber et al., 2003; Keely et al., 2013). In fact, an increase of the normalised water table level seems to have no impact on the gas composition and/or the gas fluxes measured with MultiGas, even during its highest peak in May 2017 or during its sudden increase as a result of the passage of hurricane Maria (September 2017; **Figure 4**), when 440 mm of rainfall in 24 h were recorded by the OVSG rain gauge in Savane à Mulets (Moretti et al., 2021). On the other hand, the gas ratios seem to be more influenced when the normalised water table level decreases. The period P3, unaffected by internal forcing, was characterized by the lowest water table level observed between 2016 and January 2020, which makes it ideal to constrain the effect of external forcing on our MultiGas results. During the lowest water table level (−0.8; September to December 2019), SO_2 concentrations and so SO_2/H_2S ratio increased significantly (**Figure 4**). Even though the corresponding data points moved towards the SO_2-rich magmatic end-member in **Figure 3B**, these higher SO_2 concentrations can be simply explained by lower SO_2 scrubbing in the hydrothermal aquifer. However, no similar signal was observed during another period of low water table level in February to May 2019 (−0.5). Thus, our study reveals a complex situation in which enhanced SO_2/H_2S ratio may track internal forcing related to a magma-derived gas supply, such as observed during P2, but can also result from a lower water table level due to the rainfall regime, i.e., external forcing, such as observed during P3. In April 2018, just before the major earthquake, the water table was also at low level but the difference in calculated and observed dV/V confirmed that an internal forcing process was occurring. Moreover, a low water table level in April 2018 might have amplified the SO_2 signal generated by the influx of magma-derived gas and heat. Hence, while rainy periods do not seem to affect our MultiGas measurements, we find that extended dry periods may amplify relatively the magmatic signal normally hidden and supressed by scrubbing in the hydrothermal system. Hence, for monitoring purposes, it is of prime importance to combine the survey of both geochemical and geophysical parameters in order to have the ability to discriminate the respective influence of internal and external forcing upon volcanic gas compositions and fluxes.

6 CONCLUSION

Our MultiGas monitoring of the degassing activity of La Soufrière in Guadeloupe in 2016–2020, especially with the CO_2/H_2S and SO_2/H_2S trends, provides insight into the temporal and spatial influence of fracturing, permeability and underground hydrothermal fluid circulation upon fumarolic gas compositions. Our data allowed us to 1) track change in the permeability of the dome, which can be modified by internal forcing due to either superficial processes or deep processes, and 2) detect a pulse of magma-derived gas and heat prior to a strong volcano-seismic unrest in April 2018. Moreover, our study highlights the importance of combining MultiGas measurements with other geochemical and geophysical monitoring if one wishes to be able to discriminate external forcing (e.g., rainfall-related) influences from underground processes, the latter being either primary (mixing of magma-derived and hydrothermal fluids) or secondary (fluid-rock alterations, scrubbing, fluid condensation, sulfur deposition and remobilisation). While rainy periods do not seem to affect MultiGas survey, we find that drier periods may trigger or amplify SO_2-rich magmatic signal usually hidden by the hydrothermal system. Our study thus demonstrates that MultiGas surveys are a useful tool for volcano monitoring even under tropical environment. However, the regular change of filters is necessary (every 2 weeks) to prevent the water to enter and damage the system. A new MultiGas architecture could be developed removing the pump, as already suggested in Moretti et al. (2020b), which is the most sensitive part of the system.

The pressurisation of La Soufrière hydrothermal system in April 2018 might have caused a phreatic eruption if the fracturing state of the summit dome had not allowed spontaneous release of the excess pressure (Moretti et al., 2020a). Therefore, surveying the permeability degree of the volcanic system or, reciprocally, its sealing extent is a key approach to assess the probability of an eruption. Our study shows that even without enhanced magmatic gas input, such as in March 2017, sealing effects and the clogging of fractures in a volcanic/hydrothermal system can lead to pressure increase in deep aquifers, generating volcano-tectonic seismic swarms and possibly a phreatic eruption without any change in the magma recharge zone at depth. Our results underscore the necessity to continue MultiGas monitoring at La Soufrière in order to improve our capability to detect and accurately interpret multiparameter monitoring data as eruption precursors.

DATA AVAILABILITY STATEMENT

Details of the seismic, extensometry and temperature networks and methods are available in Jacob et al. (2005), Tamburello et al. (2019), Moretti et al. (2020a), Jessop et al. (2021). Seismic data are distributed by IPGP on the public access Volobsis server (http://volobsis.ipgp.fr) and the Data center (http://datacenter.ipgp.fr). Rainfall data from Sanner and Savane à Mulets as well as the Tarissan lake level are available on request from OVSG. Gas ratios and concentrations from the MultiGas-based monitoring of La Soufrière de Guadeloupe are also available on request from OVSG.

AUTHOR CONTRIBUTIONS

SM acquired the MultiGas measurements, processed and analyzed all the data, wrote the draft of the manuscript and drafted the figures. SM, TD, VR, MBo, DJ, RM, J-CK, and GT undertook fieldwork, installation of permanent stations, calibration and repair of the different instruments. AB, VR, and SM realised the additional calibration tests to obtain the characteristics of the sensors (e.g., t90). AB and MBu during an internship with SM, wrote the codes to post-process the data. AB processed and analyzed the data for the meteorological and geophyiscal parameters. AB and DJ helped with the figures. SM, RM, MBo, AB, VR, and DJ had intense discussions about the geochemical dataset about La Soufrière de Guadeloupe. PA and J-CK provided an extensive reading of the ms. All authors discussed the data, wrote and revised the manuscript and the figures.

FUNDING

General funding to the Observatoires Volcanologiques et Sismologiques (OVS), the INSU-CNRS for funding provided by Service National d'Observation en Volcanologie (SNOV), a Tellus-Aleas project to SM (2014- Investigation of the hydrothermal system of La Soufrière volcano, Guadeloupe) and the Ministère pour la Transition Ecologiques et Solidaires (MTES) for financial support. This work has been supported by the ClerVolc (UCA-LMV) and the AO-IPGP 2018 project "Depth to surface propagation of fluid-related anomalies at La Soufrière de Guadeloupe volcano (FWI): timing and implication for volcanic unrest" (coord. RM), the project "Vers la Plateforme Régionale de Surveillance Tellurique du futur" (PREST) co-funded by INTERREG Caraïbes V for the European Regional Development Fund, and the European Union's Horizon 2020 research and innovation programme, under grant agreement No 731070 (EUROVOLC project).

ACKNOWLEDGMENTS

We thank both reviewers to have read thoroughly the ms. The authors thank the OVSG-IPGP team for logistical support and constant help with data collection and repair. We thank IPGP for general funding the installation of the initial permanent MultiGAS stations and for recurrent funding to the Observatoires Volcanologiques et Sismologiques (OVS IPGP), the INSU-CNRS for funding provided by Service National d'Observation en Volcanologie (SNOV), a Tellus-Aleas projects to SM (2020, Insights into the dynamics of the active hydrothermal system of La Soufrière de Guadeloupe from past eruptions) and to RM (2021, Progress in volcanic UNREST science: filtering hydrothermal chemical signals and tracking the magmatic source), and the Ministère pour la Transition Ecologique et Solidaire (MTES) for financial support. We are grateful to the Parc National de Guadeloupe for allowing us to undertake research and obtain geological samples. This study contributes to the IdEx Université de Paris ANR-18-IDEX-0001 and is Laboratory of excellence ClerVolc contribution number 512.

REFERENCES

Aiuppa, A., Federico, C., and Giudice, G., (2006). Hydrothermal Buffering of the SO_2/H_2S Ratio in Volcanic Gases: Evidence from La Fossa Crater Fumarolic Field, Vulcano Island. *Geophys. Res. Lett.* 33. doi:10.1029/2006gl027730

Aiuppa, A., Federico, C., Giudice, G., and Gurrieri, S. (2005). Chemical Mapping of a Fumarolic Field: La Fossa Crater, Vulcano Island (Aeolian Islands, Italy). *Geophys. Res. Lett.* (13), 32. doi:10.1029/2005gl023207

Aiuppa, A., Fischer, T. P., Plank, T., Robidoux, P., and Di Napoli, R. (2017). Along-arc, Inter-arc and Arc-To-Arc Variations in Volcanic Gas CO 2/S T Ratios Reveal Dual Source of Carbon in Arc Volcanism. *Earth-Science Rev.* 168, 24–47. doi:10.1016/j.earscirev.2017.03.005

Aiuppa, A., Moretti, R., Federico, C., Giudice, G., Gurrieri, S., Liuzzo, M., et al. (2007). Forecasting Etna Eruptions by Real-Time Observation of Volcanic Gas Composition. *Geol* 35, 1115–1118. doi:10.1130/G24149A10.1130/g24149a.1

Akasaka, C., and Nakanishi, S. (2000). "Correction of Background Gravity Changes Due to Precipitation: Oguni Geothermal Field, Japan," in *Proceedings World Geothermal Congress*, 2471–2475.

Allard, P., Aiuppa, A., Beauducel, F., Gaudin, D., di Napoli, R., Calabrese, S., et al. (2014). Steam and Gas Emission Rate from La Soufriere Volcano, Guadeloupe (Lesser Antilles): Implications for the Magmatic Supply during Degassing Unrest. *Chem. Geology.* 384, 76–93. doi:10.1016/j.chemgeo.2014.06.019

Allard, P., Carbonnelle, J., Métrich, N., Loyer, H., and Zettwoog, P. (1994). Sulphur Output and Magma Degassing Budget of Stromboli Volcano. *Nature* 368, 326–330. doi:10.1038/368326a0

Barberi, F., Bertagnini, A., Landi, P., and Principe, C. (1992). A Review on Phreatic Eruptions and Their Precursors. *J. volcanology geothermal Res.* 52 (4), 231–246. doi:10.1016/0377-0273(92)90046-g

Battaglia, J., Hidalgo, S., Bernard, B., Steele, A., Arellano, S., and Acuña, K. (2019). Autopsy of an Eruptive Phase of Tungurahua Volcano (Ecuador) through Coupling of Seismo-Acoustic and SO2 Recordings with Ash Characteristics. *Earth Planet. Sci. Lett.* 511, 223–232. doi:10.1016/j.epsl.2019.01.042

Bigot, S., Roucou, P., Moron, V., Camberlin, P., and Fontaine, B. (1994). *Présentation d'un fichier de précipitations mensuelles en points de grille sur la zone tropicale africaine et sud-américaine (1951–1990)* Ateliers de Modélisation de l'Atmosphére, 435–442.

Bloomfield, P., and Steiger, W. L. (1983). *Least Absolute Deviations: Theory, Applications, and Algorithms*. Boston: Birkhäuser, 349.

Boudon, G., Villemant, B., Komorowski, J.-C., Ildefonse, P., and Semet, M. P. (1998). The Hydrothermal System at Soufriere Hills Volcano, Montserrat (West Indies): Characterization and Role in the On-Going Eruption. *Geophys. Res. Lett.* 25, 3693–3696. doi:10.1029/98gl00985

Brenguier, F., Campillo, M., Hadziioannou, C., Shapiro, N. M., Nadeau, R. M., and Larose, E. (2008a). Postseismic Relaxation along the San Andreas Fault at Parkfield from Continuous Seismological Observations. *Science* 321, 1478–1481. doi:10.1126/science.1160943

Brenguier, F., Shapiro, N. M., Campillo, M., Ferrazzini, V., Duputel, Z., Coutant, O., et al. (2008b). Towards Forecasting Volcanic Eruptions Using Seismic Noise. *Nat. Geosci* 1, 126–130. doi:10.1038/ngeo104

Brombach, T., Marini, L., and Hunziker, J. C. (2000). Geochemistry of the thermal Springs and Fumaroles of Basse-Terre Island, Guadeloupe, Lesser Antilles. *Bull. Volcanol.* 61, 477–490. doi:10.1007/PL00008913

Cashman, K. V., and Hoblitt, R. P. (2004). Magmatic Precursors to the 18 May 1980 Eruption of Mount St. Helens, USA. *Geol* 32 (2), 141–144. doi:10.1130/g20078.1

Chiodini, G., Paonita, A., Aiuppa, A., Costa, A., Caliro, S., De Martino, P., et al. (2016). Magmas Near the Critical Degassing Pressure Drive Volcanic Unrest towards a Critical State. *Nat. Commun.* 7 (1), 13712–13719. doi:10.1038/ncomms13712

Chiodini, G., Caliro, S., Avino, R., Bini, G., Giudicepietro, F., De Cesare, W., et al. (2021). Hydrothermal Pressure-Temperature Control on CO2 Emissions and Seismicity at Campi Flegrei (Italy). *J. Volcanology Geothermal Res.* 414, 107245. doi:10.1016/j.jvolgeores.2021.107245

Chiodini, G. (2009). CO2/CH4 Ratio in Fumaroles a Powerful Tool to Detect Magma Degassing Episodes at Quiescent Volcanoes. *Geophys. Res. Lett.* (2), 36. doi:10.1029/2008gl036347

Chiodini, G., Vandemeulebrouck, J., Caliro, S., D'Auria, L., De Martino, P., Mangiacapra, A., et al. (2015). Evidence of thermal-driven Processes Triggering the 2005-2014 Unrest at Campi Flegrei Caldera. *Earth Planet. Sci. Lett.* 414, 58–67. doi:10.1016/j.epsl.2015.01.012

Christenson, B. W., Reyes, A. G., Young, R., Moebis, A., Sherburn, S., Cole-Baker, J., et al. (2010). Cyclic Processes and Factors Leading to Phreatic Eruption Events: Insights from the 25 September 2007 Eruption through Ruapehu Crater Lake, New Zealand. *J. Volcanology Geothermal Res.* 191 (1-2), 15–32. doi:10.1016/j.jvolgeores.2010.01.008

Christenson, B. W., White, S., Britten, K., and Scott, B. J. (2017). Hydrological Evolution and Chemical Structure of a Hyper-Acidic spring-lake System on Whakaari/White Island, NZ. *J. Volcanology Geothermal Res.* 346, 180–211. doi:10.1016/j.jvolgeores.2017.06.017

Clements, T., and Denolle, M. A. (2018). Tracking Groundwater Levels Using the Ambient Seismic Field. *Geophys. Res. Lett.* 45 (13), 6459–6465. doi:10.1029/2018GL077706

de Moor, J. M., Aiuppa, A., Pacheco, J., Avard, G., Kern, C., Liuzzo, M., et al. (2016). Short-period Volcanic Gas Precursors to Phreatic Eruptions: Insights from Poás Volcano, Costa Rica. *Earth Planet. Sci. Lett.* 442, 218–227. doi:10.1016/j.epsl.2016.02.056

Dempsey, D. E., Cronin, S. J., Mei, S., and Kempa-Liehr, A. W. (2020). Automatic Precursor Recognition and Real-Time Forecasting of Sudden Explosive Volcanic Eruptions at Whakaari, New Zealand. *Nat. Commun.* 11, 3562. doi:10.1038/s41467-020-17375-2

Dodge, Y. (1997). LAD Regression for Detecting Outliers in Response and Explanatory Variables. *J. Multivariate Anal.* 61, 144–158. doi:10.1006/jmva.1997.1666

Faber, E., Morán, C., Poggenburg, J., Garzón, G., and Teschner, M. (2003). Continuous Gas Monitoring at Galeras Volcano, Colombia: First Evidence. *J. volcanology geothermal Res.* 125 (1-2), 13–23. doi:10.1016/s0377-0273(03)00086-6

Feuillard, M., Allegre, C. J., Brandeis, G., Gaulon, R., Le Mouel, J. L., Mercier, J. C., et al. (1983). The 1975-1977 crisis of la Soufriere de Guadeloupe (F.W.I): A still-born magmatic eruption. *J. Volcanology Geothermal Res.* 16, 317–334. doi:10.1016/0377-0273(83)90036-7

Fischer, T. P., Sturchio, N. C., Stix, J., Arehart, G. B., Counce, D., and Williams, S. N. (1997). The Chemical and Isotopic Composition of Fumarolic Gases and spring Discharges from Galeras Volcano, Colombia. *J. Volcanol. Geoth. Res* 77 (1–4), 229–253. doi:10.1016/s0377-0273(96)00096-0

Gassenmeier, M., Sens-Schönfelder, C., Eulenfeld, T., Bartsch, M., Victor, P., Tilmann, F., et al. (2016). Field Observations of Seismic Velocity Changes Caused by Shaking-Induced Damage and Healing Due to Mesoscopic Nonlinearity. *Geophys. J. Int.* 204 (3), 1490–1502. doi:10.1093/gji/ggv529

Gaudin, D., Beauducel, F., Coutant, O., Delacourt, C., Richon, P., de Chabalier, J.-B., et al. (2016). Mass and Heat Flux Balance of La Soufrière Volcano (Guadeloupe) from Aerial Infrared thermal Imaging. *J. Volcanol. Geoth. Res.* 320, 107–116. doi:10.1016/j.jvolgeores.2016.04.007

Giggenbach, W. F. (1996). "Chemical Composition of Volcanic Gases," in *Monitoring and Mitigation of Volcano Hazards*. Editors R. Scarpa and R. I. Tilling (Berlin, Heidelberg: Springer Berlin Heidelberg), 221–256. doi:10.1007/978-3-642-80087-0_7

Giggenbach, W. F. (1980). Geothermal Gas Equilibria. *Geochimica et Cosmochimica Acta* 44, 2021–2032. doi:10.1016/0016-7037(80)90200-8

Giggenbach, W. F., and Goguel, R. L. (1989). *Methods for the Collection and Analysis of Geothermal and Volcanic Water and Gas Samples*.

Giggenbach, W. F. (1987). Redox Processes Governing the Chemistry of Fumarolic Gas Discharges from White Island, New Zealand. *Appl. Geochem.* 2 (2), 143–161. doi:10.1016/0883-2927(87)90030-8

Giggenbach, W. F. (1995). Variations in the Chemical and Isotopic Composition of Fluids Discharged from the Taupo Volcanic Zone, New Zealand. *J. Volcanology Geothermal Res.* 68 (1-3), 89–116. doi:10.1016/0377-0273(95)00009-j

Girona, T., Realmuto, V., and Lundgren, P. (2021). Large-scale thermal Unrest of Volcanoes for Years Prior to Eruption. *Nat. Geosci.* 14, 238–241. doi:10.1038/s41561-021-00705-4

Hadziioannou, C., Larose, E., Coutant, O., Roux, P., and Campillo, M. (2009). Stability of Monitoring Weak Changes in Multiply Scattering media with Ambient Noise Correlation: Laboratory Experiments. *The J. Acoust. Soc. America* 125 (6), 3688–3695. doi:10.1121/1.3125345

Hammouya, G., Allard, P., Jean-Baptiste, P., Parello, F., Semet, M. P., and Young, S. R. (1998). Pre- and Syn-Eruptive Geochemistry of Volcanic Gases from Soufriere Hills of Montserrat, West Indies. *Geophys. Res. Lett.* 25, 3685–3688. doi:10.1029/98gl02321

Heap, M. J., Baumann, T. S., Rosas-Carbajal, M., Komorowski, J. C., Gilg, H. A., Villeneuve, M., et al. (2021). Alteration-Induced Volcano Instability at La Soufrière de Guadeloupe (Eastern Caribbean). *J. Geophys. Res. Solid Earth* 126 (8), e2021JB022514. doi:10.1029/2021jb022514

Hedenquist, J. W., and Lowenstern, J. B. (1994). The Role of Magmas in the Formation of Hydrothermal Ore Deposits. *Nature* 370 (6490), 519–527. doi:10.1038/370519a0

Hincks, T. K., Komorowski, J.-C., Sparks, S. R., and Aspinall, W. P. (2014). Retrospective Analysis of Uncertain Eruption Precursors at La Soufrière Volcano, Guadeloupe, 1975-77: Volcanic hazard Assessment Using a Bayesian Belief Network Approach. *J. Appl. Volcanol.* 3, 1–26. doi:10.1186/2191-5040-3-3

Hurst, T., Jolly, A. D., and Sherburn, S. (2014). Precursory Characteristics of the Seismicity before the 6 August 2012 Eruption of Tongariro Volcano, North Island, New Zealand. *J. Volcanology Geothermal Res.* 286, 294–302. doi:10.1016/j.jvolgeores.2014.03.004

Illien, L., Andermann, C., Sens-Schönfelder, C., Cook, K. L., Baidya, K. P., Adhikari, L. B., et al. (2021). Subsurface Moisture Regulates Himalayan Groundwater Storage and Discharge. *AGU Adv.* 2, e2021AV000398. doi:10.1029/2021AV000398

Inostroza, M., Moune, S., Moretti, R., Bonifacie, M., Robert, V., Burtin, A., et al. *Submitted to JVGR, Decoding Water-Rock Interaction and Volatile Input at La Soufriere Volcano (Guadeloupe) by Using Major and Trace Element Time-Series Analyses in Condensed Gases*.

Jacob, T., Beauducel, F., Hammouya, G., David, J. G., and Komorowski, J. C. (2005). "Ten Years of Extensometry at Soufrière of Guadeloupe: New Constraints on the Hydrothermal System," in *Soufrière Hills Volcano -Ten Years on International Workshop* (Seismic Research Unit, University of West Indies).

Jessop, D., Moune, S., Moretti, R., Gibert, D., Komorowski, J. C., Robert, V., et al. (2021). A multi-decadal view of the heat and mass budget of a volcano in unrest: La Soufrière de Guadeloupe (French West Indies). *Bull. Volcanology* 83 (16), 1–19. doi:10.1007/s00445-021-01439-2

Kilgour, G., Manville, V., Della Pasqua, F., Graettinger, A., Hodgson, K. A., and Jolly, G. E. (2010). The 25 September 2007 Eruption of Mount Ruapehu, New Zealand: Directed Ballistics, Surtseyan Jets, and Ice-Slurry Lahars. *J. Volcanology Geothermal Res.* 191 (1-2), 1–14. doi:10.1016/j.jvolgeores.2009.10.015

Komorowski, J.-C., Boudon, G., Semet, M., Beauducel, F., Anténor-Habazac, C., Bazin, S., et al. (2005). "Guadeloupe," in *Volcanic Hazard Atlas of the {Lesser Antilles}*. Editors J. M. Lindsay, R. E. A. Robertson, J. B. Shepherd, and S. Ali, 65–102.

Komorowski, J-C., Hoblitt, R. P., and Sheridan, M. F. (1997). " Silicification and Brecciation Microtextures of the Mt. St. Helens'1980 Cryptodome-Country Rock Interface: Implications for Hydrothermal Fluid Processes, Precursory Seismicity, and Eruptive Style," in" *Volcanic Activity and the Environment (abstracts), International Association of Volcanology and Chemistry of the Earth's Interior, General Assembly* Puerto Vallarta, Mexico, 76.

Komorowski, J.-C., Legendre, Y., Caron, B., and Boudon, G. (2008). Reconstruction and Analysis of Sub-plinian Tephra Dispersal during the 1530 A.D. Soufrière (Guadeloupe) Eruption: Implications for Scenario Definition and Hazards Assessment. *J. Volcanology Geothermal Res.* 178, 491–515. doi:10.1016/j.jvolgeores.2007.11.022

Komorowski, J.-C., Legendre, Y., Christopher, T., Bernstein, M., Stewart, R., Joseph, E., et al. (2010). Insights into Processes and Deposits of Hazardous Vulcanian Explosions at Soufrière Hills Volcano during 2008 and 2009 (Montserrat, West Indies). *Geophys. Res. Lett.* 37, a–n. doi:10.1029/2010GL042558

Le Gonidec, Y., Rosas-Carbajal, M., Bremond d'Ars, J. d., Carlus, B., Ianigro, J.-C., Kergosien, B., et al. (2019). Abrupt Changes of Hydrothermal Activity in a Lava Dome Detected by Combined Seismic and Muon Monitoring. *Sci. Rep.* 9, 3079. doi:10.1038/s41598-019-39606-3

Le Guern, F., Bernard, A., and Chevrier, R. M. (1980). Soufrière of guadeloupe 1976-1977 Eruption - Mass and Energy Transfer and Volcanic Health Hazards. *Bull. Volcanol* 43 (3), 577–593. doi:10.1007/bf02597694

Lecocq, T., Longuevergne, L., Pedersen, H. A., Brenguier, F., and Stammler, K. (2017). Monitoring Ground Water Storage at Mesoscale Using Seismic Noise: 30 Years of Continuous Observation and Thermo-Elastic and Hydrological Modeling. *Sci. Rep.* 7 (1), 1–16. doi:10.1038/s41598-017-14468-9

Legendre, Y. (2012). *Reconstruction de l'histoire éruptive et scenarii éruptifs àLaSoufriere de Guadeloupe : vers un mode intégralde fonctionnement du volcan .(French)[A high resolution reconstruction of the eruptive past and definition of eruptive scenario at La Soufriere of Guadeloupe]*. Ph .D.thesis. Paris.

Maeno, F., Nakada, S., Oikawa, T., Yoshimoto, M., Komori, J., Ishizuka, Y., et al. (2016). Reconstruction of a Phreatic Eruption on 27 September 2014 at Ontake Volcano, central Japan, Based on Proximal Pyroclastic Density Current and Fallout Deposits. *Earth Planet. Sp* 68, 82. doi:10.1186/s40623-016-0449-6

Massaro, S., Dioguardi, F., Sandri, L., Tamburello, G., Selva, J., Moune, S., et al. (2021). Testing Gas Dispersion Modelling at La Soufrière Volcano (Gudeloupe, Lesser Antilles). *JVGR* 417, 107312. doi:10.1016/j.jvolgeores.2021.107312

Metcalfe, A., Moune, S., Komorowski, J.-C., Kilgour, G., Jessop, D. E., Moretti, R., et al. (2021). Magmatic Processes at La Soufrière de Guadeloupe: Insights From Crystal Studies and Diffusion Timescales for Eruption Onset. *Front. Earth Sci.* 9, 617294. doi:10.3389/feart.2021.617294

Moretti, R., Arienzo, I., Civetta, L., Orsi, G., and Papale, P. (2013). Multiple Magma Degassing Sources at an Explosive Volcano. *Earth Planet. Sci. Lett.* 367, 95–104. doi:10.1016/j.epsl.2013.02.013

Moretti, R., De Natale, G., and Troise, C. (2017). A Geochemical and Geophysical Reappraisal to the Significance of the Recent Unrest at Campi Flegrei Caldera (Southern Italy). *Geochem. Geophys. Geosyst.* 18, 1244–1269. doi:10.1002/2016GC006569

Moretti, R., Komorowski, J.-C., Ucciani, G., Moune, S., Jessop, D., de Chabalier, J.-B., et al. (2020a). The 2018 Unrest Phase at La Soufrière of Guadeloupe (French West Indies) Andesitic Volcano: Scrutiny of a Failed but Prodromal Phreatic Eruption. *J. Volcanology Geothermal Res.* 393, 106769. doi:10.1016/j.jvolgeores.2020.106769

Moretti, R., Moune, S., Jessop, D., Glynn, C., Robert, V., and Deroussi, S. (2021). The Basse-Terre Island of Guadeloupe (Eastern Caribbean, France) and its Volcanic-Hydrothermal Geodiversity: A Case Study of Challenges, Perspectives, and New Paradigms for Resilience and Sustainability on Volcanic Islands. *Geosciences* 11 (11), 454. doi:10.3390/geosciences11110454

Moretti, R., Moune, S., Robert, V., Jessop, D. E., Didier, T., Bonifacie, M., et al. (2020b). Intercomparison of geochemical techniques at La Soufrière de Guadeloupe (FWI) volcano: their advantages and their limits over a long-standing unrest. *Ijg* 139 (3), 398–412. doi:10.3301/ijg.2020.13

Moretti, R., and Stefánsson, A. (2020). Volcanic and Geothermal Redox Engines. *Elem. Int. Mag. Mineralogy, Geochem. Petrol.* 16 (3), 179–184. doi:10.2138/gselements.16.3.179

Moussallam, Y., Peters, N., Masias, P., Apaza, F., Barnie, T., Ian Schipper, C., et al. (2017). Magmatic Gas Percolation through the Old Lava Dome of El Misti Volcano. *Bull. Volcanol.* 79, 46. doi:10.1007/s00445-017-1129-5

Nakahara, H., Wegler, U., and Shiomi, K. (2007). "Detection of Temporal Changes in Subsurface Structures with the Passive Image Interferometry: Application to the 2005 Fukuoka-Ken Seiho-Oki Earthquake," in *Seismological Society of Japan, Fall Meeting* (Sendai, Japan.

Oikawa, T., Yoshimoto, M., Nakada, S., Maeno, F., Komori, J., Shimano, T., et al. (2016). Reconstruction of the 2014 Eruption Sequence of Ontake Volcano from Recorded Images and Interviews. *Earth, Planets and Space* 68 (1), 1–13. doi:10.1186/s40623-016-0458-5

Ovsg-Ipgp (1999-2021). *Monthly reports on the activity of La Soufrière de Guadeloupe and on regional seismicity*. Gourbeyre, Guadeloupe. http://www.ipgp.fr/fr/ovsg/bulletins-mensuels-de-lovsg.

Pichavant, M., Poussineau, S., Lesne, P., Solaro, C., and Bourdier, J.-L. (2018). Experimental Parametrization of Magma Mixing: Application to the Ad 1530 Eruption of La Soufrière, Guadeloupe (Lesser Antilles). *J. Pet.* 59, 257–282. doi:10.1093/petrology/egy030

Procter, J. N., Cronin, S. J., Zernack, A. V., Lube, G., Stewart, R. B., Nemeth, K., et al. (2014). Debris Flow Evolution and the Activation of an Explosive Hydrothermal System; Te Maari, Tongariro, New Zealand. *J. Volcanology Geothermal Res.* 286, 303–316. doi:10.1016/j.jvolgeores.2014.07.006

Roberts, T. J., Lurton, T., Giudice, G., Liuzzo, M., Aiuppa, A., Coltelli, M., et al. (2017). Validation of a Novel Multi-Gas Sensor for Volcanic HCl Alongside H2S and SO2 at Mt. Etna. *Bull. Volcanol* 79, 36. doi:10.1007/s00445-017-1114-z

Roberts, T. J., Saffell, J. R., Oppenheimer, C., and Lurton, T. (2014). Electrochemical Sensors Applied to Pollution Monitoring: Measurement Error and Gas Ratio Bias - A Volcano Plume Case Study. *J. volcanology geothermal Res.* 281, 85–96. doi:10.1016/j.jvolgeores.2014.02.023

Rosas-Carbajal, M., Komorowski, J.-C., Nicollin, F., and Gibert, D. (2016). Volcano Electrical Tomography Unveils Edifice Collapse hazard Linked to Hydrothermal System Structure and Dynamics. *Sci. Rep.* 6, 29899. doi:10.1038/srep29899

Rye, R. O. (2005). A Review of the Stable-Isotope Geochemistry of Sulfate Minerals in Selected Igneous Environments and Related Hydrothermal Systems. *Chem. Geology.* 215 (1-4), 5–36. doi:10.1016/j.chemgeo.2004.06.034

Rye, R. O., Bethke, P. M., and Wasserman, M. D. (1992). The Stable Isotope Geochemistry of Acid Sulfate Alteration. *Econ. Geology.* 87 (2), 225–262. doi:10.2113/gsecongeo.87.2.225

Salaün, A., Villemant, B., Gérard, M., Komorowski, J-C., and Michel, A. (2011). Hydrothermal Alteration in Andesitic Volcanoes : a Study of Trace Element Redistribution in Active and Paleohydrothermal Systems of Guadeloupe (Lesser Antilles). *Jour of Geochemical Exploration* 111, 59–83. doi:10.1016/j.gexplo.2011.06.004

Sano, Y., Kagoshima, T., Takahata, N., Nishio, Y., Roulleau, E., Pinti, D. L., et al. (2015). Ten-year Helium Anomaly Prior to the 2014 Mt Ontake Eruption. *Sci. Rep.* 5, 13069. doi:10.1038/srep13069

Saurel, J.-M., Corbeau, J., Deroussi, S., Didier, T., Lemarchand, A., Moune, S., et al. (2020). Building a Natural-Hazard-Resilient High-Quality Seismic Network: How WI Network Sustained Hurricanes Maria and Irma. *Seismological Res. Lett.* 92, 77–84. doi:10.1785/0220200270

Sens-Schönfelder, C., and Wegler, U. (2006). Passive Image Interferometry and Seasonal Variations of Seismic Velocities at Merapi Volcano, Indonesia. *Geophys. Res. Lett.* 33 (21), 1029–1033. doi:10.1029/2006GL027797

Sens-Schönfelder, C., and Wegler, U. (2011). Passive Image Interferometry for Monitoring Crustal Changes with Ambient Seismic Noise. *Comp. Rend. Geosci.* 343 (89), 639–651.

Shimoike, Y., and Notsu, K. (2000). Continuous Chemical Monitoring of Volcanic Gas in Izu-Oshima Volcano, Japan. *J. Volcanology Geothermal Res.* 101 (3), 211–221. doi:10.1016/s0377-0273(00)00178-5

Shinohara, H. (2005). A New Technique to Estimate Volcanic Gas Composition: Plume Measurements with a Portable Multi-Sensor System. *J. Volcanology Geothermal Res.* 143, 319–333. doi:10.1016/j.jvolgeores.2004.12.004

Snieder, R., Grêt, A., Douma, H., and Scales, J. (2002). Coda Wave Interferometry for Estimating Nonlinear Behavior in Seismic Velocity. *Science* 295, 2253–2255. doi:10.1126/science.1070015

Steiner, A. (1977). The Wairakei Geothermal Area, North Island, New Zealand. *N. Z. Geol. Surv. Bull.* 90, 136.

Stix, J., and de Moor, J. M. (2018). Understanding and Forecasting Phreatic Eruptions Driven by Magmatic Degassing. *Earth Planets Space* 70, 83. doi:10.1186/s40623-018-0855-z

Symonds, R. B., Gerlach, T. M., and Reed, M. H. (2001). Magmatic Gas Scrubbing: Implications for Volcano Monitoring. *J. Volcanology Geothermal Res.* 108, 303–341. doi:10.1016/S0377-0273(00)00292-4

Symonds, R. B., Rose, W. I., Bluth, G. J. S., and Gerlach, T. M. (1994). Chapter 1. VOLCANIC-GAS STUDIES: METHODS, RESULTS, and APPLICATIONS. *Rev. Miner. Geochem.* 30, 1–66. doi:10.1515/9781501509674-007

Takagi, R., and Okada, T. (2012). Temporal Change in Shear Velocity and Polarization Anisotropy Related to the 2011 M9.0 Tohoku-Oki Earthquake Examined Using KiK-Net Vertical Array Data. *Geophys. Res. Lett.* 39, a–n. doi:10.1029/2012GL051342

Tamburello, G., Moune, S., Allard, P., Venugopal, S., Robert, V., Rosas-Carbajal, M., et al. (2019). Spatio-Temporal Relationships between Fumarolic Activity, Hydrothermal Fluid Circulation and Geophysical Signals at an Arc Volcano in Degassing Unrest: La Soufrière of Guadeloupe (French West Indies). *Geosciences* 9, 480. doi:10.3390/geosciences9110480

Tamburello, G. (2015). Ratiocalc: Software for Processing Data from Multicomponent Volcanic Gas Analyzers. *Comput. Geosciences* 82, 63–67. doi:10.1016/j.cageo.2015.05.004

Touboul, M., Bourdon, B., Villemant, B., Boudon, G., and Joron, J. L. (2007). 238 U–230 Th–226 Ra Disequilibria in Andesitic Lavas of the Last Magmatic Eruption of Guadeloupe Soufriere, French Antilles: Processes and Timescales of Magma Differentiation. *Chem. Geol.* 246 (3), 181–206. doi:10.1016/j.chemgeo.2007.09.009

Troise, C., De Natale, G., Schiavone, R., Somma, R., and Moretti, R. (2019). The Campi Flegrei Caldera Unrest: Discriminating Magma Intrusions from Hydrothermal Effects and Implications for Possible Evolution. *Earth-science Rev.* 188, 108–122. doi:10.1016/j.earscirev.2018.11.007

Villemant, B., Komorowski, J. C., Dessert, C., Michel, A., Crispi, O., Hammouya, G., et al. (2014). Evidence for a New Shallow Magma Intrusion at La Soufrière of Guadeloupe (Lesser Antilles). *J. Volcanology Geothermal Res.* 285, 247–277. doi:10.1016/j.jvolgeores.2014.08.002

Wegler, U., and Sens-Schönfelder, C. (2007). Fault Zone Monitoring with Passive Image Interferometry. *Geophys. J. Int.* 168, 1029–1033. doi:10.1111/j.1365–246X.2006.03284.x

Werner, C., Evans, W. C., Poland, M., Tucker, D. S., and Doukas, M. P. (2009). Long-term Changes in Quiescent Degassing at Mount Baker Volcano, Washington, USA; Evidence for a Stalled Intrusion in 1975 and Connection to a Deep Magma Source. *J. Volcanology Geothermal Res.* 186, 379–386. doi:10.1016/j.jvolgeores.2009.07.006

Werner, C., Kelly, P. J., Doukas, M., Lopez, T., Pfeffer, M., McGimsey, R., et al. (2013). Degassing of CO2, SO2, and H2S Associated with the 2009 Eruption of Redoubt Volcano, Alaska. *J. Volcanology Geothermal Res.* 259, 270–284. doi:10.1016/j.jvolgeores.2012.04.012

Zlotnicki, J., Boudon, G., and Le Mouël, J.-L. (1992). The Volcanic Activity of La Soufrière of Guadeloupe (Lesser Antilles): Structural and Tectonic Implications. *J. Volcanology Geothermal Res.* 49, 91–104. doi:10.1016/0377-0273(92)90006-Y

Conflict of Interest: The authors declare that the research was conducted in the absence of any commercial or financial relationships that could be construed as a potential conflict of interest.

frontiers | Frontiers in Earth Science

ORIGINAL RESEARCH
published: 12 April 2022
doi: 10.3389/feart.2022.788294

External Surface Water Influence on Explosive Eruption Dynamics, With Implications for Stratospheric Sulfur Delivery and Volcano-Climate Feedback

Colin R. Rowell [1], A. Mark Jellinek [1], Sahand Hajimirza [2] and Thomas J. Aubry [3,4]*

[1]Department of Earth, Ocean, and Atmospheric Sciences, University of British Columbia, Vancouver, BC, Canada, [2]Department of Earth, Environmental, and Planetary Sciences, Rice University, Houston, TX, United States, [3]Department of Geography, University of Cambridge, Cambridge, United Kingdom, [4]Sidney Sussex College, Cambridge, United Kingdom

Explosive volcanic eruptions can inject sulfur dioxide (SO_2) into the stratosphere to form aerosol particles that modify Earth's radiation balance and drive surface cooling. Eruptions involving interactions with shallow layers (≤500 m) of surface water and ice modify the eruption dynamics that govern the delivery of SO_2 to the stratosphere. External surface water controls the evolution of explosive eruptions in two ways that are poorly understood: 1) by modulating the hydrostatic pressure within the conduit and at the vent, and 2) through the ingestion and mixing of external water, which governs fine ash production and eruption column buoyancy flux. To make progress, we couple one-dimensional models of conduit flow and atmospheric column rise through a novel "magma-water interaction" model that simulates the occurrence, extent and consequences of water entrainment depending on the depth of a surface water layer. We explore the effects of hydrostatic pressure on magma ascent in the conduit and gas decompression at the vent, and the conditions for which water entrainment drives fine ash production by quench fragmentation, eruption column collapse, or outright failure of the jet to breach the water surface. We show that the efficiency of water entrainment into the jet is the predominant control on jet behavior. For an increase in water depth of 50–100 m, the critical magma mass eruption rate required for eruption columns to reach the tropopause increases by an order of magnitude. Finally, we estimate that enhanced emission of fine ash leads to up to a 2-fold increase in the mass flux of particles $< 125\,\mu$m to spreading umbrella clouds, together with up to a 10-fold increase in water mass flux, conditions that can enhance the removal of SO_2 via chemical scavenging and ash sedimentation. On average, compared to purely magmatic eruptions, we suggest that hydrovolcanic eruptions will be characterized by reduced climate forcing. Our results suggest one possible mechanism for volcano-climate feedback: temporal changes with climate in surface distributions of water and ice may modify the relative global frequency or dominance of hydrovolcanic eruption processes, modulating, in turn, global patterns in volcano-climate forcing.

Keywords: external forcing, magma-water interactions, explosive eruption, 1-D plume model, stratospheric sulfur input, climate feedback, 1-d conduit flow model, hydrovolcanism

OPEN ACCESS

Edited by:
Stéphanie Dumont,
University of Beira Interior, Portugal

Reviewed by:
Magnus Tumi Gudmundsson,
University of Iceland, Iceland
Stephen Self,
University of California, Berkeley, United States
Ingo Sonder,
University at Buffalo, United States

****Correspondence:***
Colin R. Rowell
crowell@eoas.ubc.ca

Specialty section:
This article was submitted to Volcanology, a section of the journal Frontiers in Earth Science

Received: *02 October 2021*
Accepted: *21 February 2022*
Published: *12 April 2022*

Citation:
Rowell CR, Jellinek AM, Hajimirza S and Aubry TJ (2022) External Surface Water Influence on Explosive Eruption Dynamics, With Implications for Stratospheric Sulfur Delivery and Volcano-Climate Feedback. Front. Earth Sci. 10:788294. doi: 10.3389/feart.2022.788294

1 INTRODUCTION

Volcanic SO_2 injected into the stratosphere forms sulfate aerosols that persist for 1–3 years, affect Earth's radiation balance and produce one of the strongest natural surface climate cooling mechanisms (Timmreck, 2012; Sigl et al., 2015; Kremser et al., 2016). Although the direct radiative forcing from volcanic aerosols typically acts over annual to decadal timescales (Robock, 2000), the last decade of research has shown that the climate impacts of eruptions are not restricted to discrete and intermittent cooling events with durations of a few years. For example, volcanic emission from small to moderate eruptions and passive degassing provide background concentrations of sulfate aerosols, resulting in a near-continuous negative (cooling) forcing to the planetary surface (Solomon et al., 2011; Schmidt et al., 2012; Santer et al., 2014). Furthermore, a growing body of evidence suggests that volcanic forcing from aerosols can also drive non-linear climate responses on multidecadal to millennial timescales (Zhong et al., 2011; Schleussner and Feulner, 2013; Zanchettin et al., 2013; Santer et al., 2014; Baldini et al., 2015; Toohey et al., 2016; Soreghan et al., 2019; Mann et al., 2021). The strength of aerosol climate forcing depends strongly on the SO_2 mass flux to the stratosphere (e.g., Marshall et al. (2019)), which is governed by the eruption magnitude and eruption column height (the altitude at which gas and ash are dispersed as a neutrally buoyant cloud) relative to the tropopause (Aubry et al., 2019; Krishnamohan et al., 2019; Marshall et al., 2019; Aubry et al., 2021b). In addition to the injection height of SO_2, the chemistry and microphysics governing aerosol formation and stratospheric residence time are also critical controls on the climate effects of eruptions (Timmreck, 2012; Kremser et al., 2016; LeGrande et al., 2016; Zhu et al., 2020; Staunton-Sykes et al., 2021). SO_2 is frequently transported together with fine ash and water from the eruption column (e.g., Rose et al., 2001; Joshi and Jones, 2009; Ansmann et al., 2011), where chemical scavenging of SO_2 onto ash surfaces (Rose, 1977; Schmauss and Keppler, 2014) and physical incorporation into hydrometeors (Rose et al., 1995; Textor et al., 2003) can scrub SO_2 from the eruption column. Water transported by the eruption cloud can enhance nucleation and growth rates of aerosol particles (LeGrande et al., 2016), and ash particles provide sites for aerosol nucleation or direct uptake of SO_2 (Zhu et al., 2020). Consequently, the presence of water and fine ash influences resulting aerosol formation rates, particle sizes, optical properties, and residence times, which are key parameters governing climate forcing (Kremser et al., 2016). Constraining the climate impacts of volcanic eruptions therefore requires understanding of eruption transport processes governing injection height, as well as the quantities of fine ash and water in eruption columns and clouds.

Climate-forcing related to eruptions is sensitive to the environmental conditions of eruptions as well as global eruption frequency-magnitude distributions, both of which can evolve with global climate warming or cooling. For example, sustained anthropogenic climate change will drive an increase in the strength of tropospheric density stratification and tropopause height, and alter stratospheric circulation. These atmospheric changes are expected to reduce the stratospheric delivery of SO_2 in moderate-magnitude eruptions (Aubry et al., 2016, 2019), while exacerbating the radiative effects of relatively rare, large-magnitude eruptions (e.g., Pinatubo 1991) (Aubry et al., 2021b). Other potential mechanisms for climatic influence on volcanism include eruption triggering by extreme rainfall events (e.g., Elsworth et al., 2004; Capra, 2006; Farquharson and Amelung, 2020) or changes to ocean stratification (Fasullo et al., 2017). Glacial-interglacial cycles also influence rates and locations of global volcanism: The advance and retreat of ice sheets and thickening and thinning of mountain glaciers can inhibit or enhance, respectively, melt generation, dike formation, eruption rates and eruption frequency (Jull and McKenzie, 1996; Jellinek et al., 2004; Huybers and Langmuir, 2009; Watt et al., 2013; Baldini et al., 2015; Cooper et al., 2018). For example, Huybers and Langmuir (2009) correlated observed spikes in atmospheric CO_2 with inferred increases in the rate of volcanism following the Last Glacial Maximum, and proposed a glaciovolcanic-CO_2 feedback, where enhanced rates of volcanism and CO_2 outgassing contribute to additional warming and ice sheet loss. Increases in both sea level and in the occurrence and extents of freshwater lakes and ponds with deglaciation are also likely to increase the frequency of direct interactions of erupting magma with surface water. Crucially, the implications of potentially enhanced magma-water interaction (MWI) for volcano-climate forcing remain largely unexplored.

Explosive volcanic eruptions involving interactions of magma with external surface water or ice (termed hereafter *hydrovolcanic eruptions*) evolve as a result of thermophysical and chemical processes that are wholly distinct from those of "dry" magmatic eruptions (those in which the main component of water present is that exsolved from the melt) (Self and Sparks, 1978; Houghton et al., 2015). **Figure 1** shows a summary of hydrovolcanic eruption processes affecting the transport and stratospheric delivery of SO_2 as compared with purely magmatic eruptions. The presence of external surface water influences eruption dynamics and evolution through two primary controls: 1) a modulation of hydrostatic pressure at the vent and within the erupting conduit, and 2) through effects of the entrainment and thermal and mechanical mixing of water into an erupting gas-pyroclast mixture on the mass, momentum, particle and enthalpy fluxes that ultimately drive column rise (Woods, 2010; Wohletz et al., 2013; Smellie and Edwards, 2016; Cas and Simmons, 2018). Increased hydrostatic pressure can, for example, reduce eruption explosivity by suppressing bubble nucleation and growth in the conduit, reducing magma decompression and ascent rates, and potentially preventing magmatic fragmentation (Smellie and Edwards, 2016; Cas and Simmons, 2018; Manga et al., 2018). In contrast, secondary fragmentation and ash production can be relatively enhanced as a result of the actions of large thermal stresses arising through the rapid transfer of heat from hot pyroclasts to entrained surface water (Gonnermann, 2015; van Otterloo et al., 2015; Zimanowski et al., 2015). Heat consumption by the vaporization of entrained external water results in a loss (or redistribution) of the thermal buoyancy delivered by the eruption at the vent, which may be recovered via condensation higher in the plume where temperatures are colder (Koyaguchi and Woods, 1996).

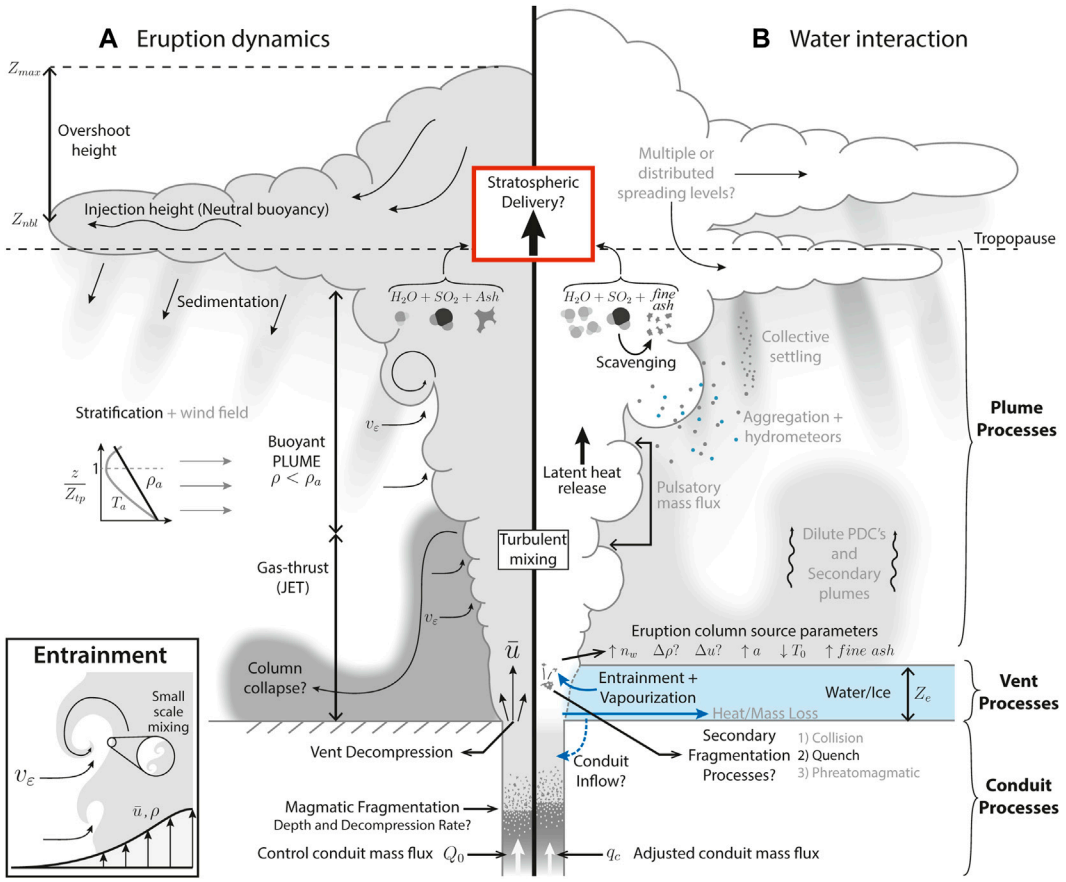

FIGURE 1 | Summary of eruption processes from conduit to atmospheric dispersal. See text for a description of processes and their relevance for SO_2 transport. See **Table 1** for a complete description of symbols. **(A)** Dynamical processes during a sustained, "dry" Plinian eruption. Inset: illustration of the entrainment process. **(B)** Summary of processes influenced by surface water interaction during a hydrovolcanic eruption. Processes in lighter gray text are those not considered in this study, but which are relevant to hydrovolcanic eruptions processes and may play a role in stratospheric delivery of SO_2.

The extent to which water is mixed into the erupting jet and the efficiency of heat transfer between hot pyroclasts and this ingested water control the eruption column source parameters (e.g. bulk temperature, density, velocity, and column radius) (Koyaguchi and Woods, 1996; Mastin, 2007b), as well as the intensity of secondary fragmentation and ash production that governs the ultimate particle size distribution (PSD - we refer to total particle size distributions throughout unless otherwise stated) (Mastin, 2007a; van Otterloo et al., 2015). The character of the PSD governs the rates of particle aggregation and sedimentation, as well as the available particle surface area (Bonadonna et al., 1998; Brown et al., 2012; Girault et al., 2014). In particular, increased water content, ash surface area, and relatively colder temperatures in the rising eruption column provide conditions that enhance chemical scavenging of SO_2 during transport and dispersal relative to dry eruptions (Schmauss and Keppler, 2014). For example, Textor et al. (2003) simulate dynamical, chemical, and microphysical processes occurring in a dry Plinian eruption and estimate that the percent of SO_2 erupted at the vent that is ultimately injected into the stratosphere was $\gtrsim$ 80%. However, in marked contrast, for the glaciovolcanic eruption of Grimsvötn in 2011, Sigmarsson et al. (2013) estimate that approximately 50% of the exsolved sulfur gas was dispersed to the atmosphere, with much of the remainder lost to scavenging by ash particles or external surface water. As another provocative example, the recent powerful and water-rich eruption of Hunga Tonga-Hunga Ha'apai injected an eruption cloud to at least 30–35 km above sea level. Despite a cloud height comparable to the 1991 eruption of Mt. Pinatubo (Bluth et al., 1997), preliminary analyses have suggested stratospheric loading of SO_2 for the recent eruption is likely comparatively negligible. The exact cause for this discrepancy between apparent eruption magnitude and SO_2 output for Hunga Tonga-Hunga Ha'apai relative to Mt. Pinatubo is currently undetermined, but the water-rich nature of the eruption is one possible cause.

Magma-water interactions (MWI) and their effects throughout an eruptive phase are maximized in persistent deep layers of water where significant entrainment can occur over the time of column rise. In subglacial or subaqueous environments where water availability is limited by, say, ice melting and melt-water drainage (e.g., Gudmundsson et al.,

2012; Magnússon et al., 2012), build-up of insulating volcanic tephra (e.g., Fee et al., 2020), or by simply the finite volume of a reservoir (e.g., Gudmundsson et al., 2014), water access to the volcanic vent can decline during an eruption, causing the extent of MWI to evolve, in turn. With declining water layer depths, eruptions styles may progress from an initial suppression of explosive behavior, to collapsing jets, to buoyant plumes of increasing height (Koyaguchi and Woods, 1996; Mastin, 2007b; Van Eaton et al., 2012; Wohletz et al., 2013; Manga et al., 2018). This evolution is important to recognize: the degree to which an erupting magma interacts with surface water can exert critical control over the ultimate delivery of ash, water, and SO_2 into the troposphere and stratosphere (Rose et al., 1995). Although observational, experimental, and numerical studies have individually investigated processes relevant to hydrovolcanic eruptions, it is critical to assess their behavior as a system to reveal controls on the ultimate fate of erupted ash and gas.

To make critical progress in understanding the extent to which surface water governs the character and magnitude of volcano-climate forcing, it is necessary to examine syn-eruptive processes that determine the transport and ultimate fate of volcanic SO_2. In particular:

1) How do hydrostatic pressure, water entrainment, and MWI affect the coupled dynamics of gas exsolution and magma fragmentation in the subterranean conduit, heat transfer from pyroclasts to external water, secondary production of fine ash, and transport of ash, water, and SO_2 in the eruption column?
2) To what extent can MWI processes and their control on eruption source conditions be quantitatively linked to the observable thickness or abundance of a surface water layer?
3) What are the critical relationships among water mass fraction at the eruption column source and mass fluxes of SO_2, fine ash, and water to the stratosphere?

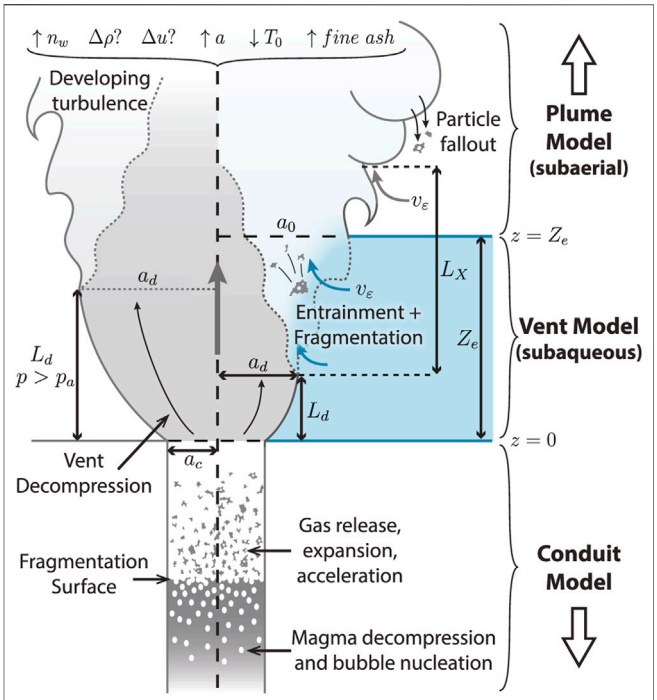

FIGURE 2 | Schematic summary of coupled model, highlighting geometry of the vent and MWI region. The left and right sides are divided between a control scenario with no external water and a scenario with a shallow water layer, respectively. In the hydrovolcanic case, decompression of the erupting jet of gas and pyroclasts is suppressed relative to the dry control scenario (indicated by decompression length L_d and radius a_d), and initiation of turbulent mixing with external water results in water entrainment and quench fragmentation. In the water layer scenario shown here, water depth Z_e is greater than the decompression length L_d but less than the height at which large entraining eddies are fully developed, $L_d + L_X$. See **Table 1** and **Sections 2.2**, **2.3**, and **2.4** for a complete description of symbols and processes.

In this study, we address these questions using coupled conduit-plume 1D numerical simulations of sustained, sub-Plinian to Plinian hydrovolcanic eruptions with rhyolitic magma compositions. We estimate the sensitivity of the efficiency of stratospheric SO_2 injection to the presence of water layers up to 500 m deep. The model approach consists of three coupled components (see **Figures 1**, **2**): 1) a 1D conduit model simulating magma ascent and fragmentation (Hajimirza et al., 2019), which we modify with an arbitrary hydrostatic pressure boundary condition applied at the vent; 2) a novel near-field "vent" model simulating decompression of the initial gas-pyroclast mixture, water entrainment, and quench fragmentation as a function of surface water depth Z_e; and 3) a modified version of the 1D eruption column model from Degruyter and Bonadonna (2012), incorporating a particle size distribution with sedimentation following Girault et al. (2014). We focus our analysis on the main factors affecting overall column rise (e.g., magma ascent and fragmentation, MWI and eruption column source parameters, and resulting column gravitational stability, height, and sedimentation) and environmental conditions for vertical SO_2 transport (e.g., temperature, water mass fluxes, and mass and surface area of ash particles). In considering only column height, entrainment of water mass, and particle loss, we neglect a number of issues that will enter into more complete future treatments of an SO_2 delivery efficiency: 1) a thermodynamic control in the conduit on the SO_2 solubility behaviour below the fragmentation depth; 2) the coupled microphysics and kinetics of SO_2 scavenging by ash particles sedimenting from the column and overlying umbrella cloud through various mechanisms (Rose, 1977; Bursik et al., 1992; Durant et al., 2009; Niemeier et al., 2009; Carazzo and Jellinek, 2012; Manzella et al., 2015); and 3) the kinetics of sulfur aerosol nucleation and growth (Kremser et al., 2016) with or without ash (Zhu et al., 2020). As a consequence of ignoring the above effects, our study does not address: 1) effects on the amount of sulfur gas exsolved from the melt (e.g. possibly reduced SO_2 exsolution due to hydrostatic pressure); 2) scavenging and sedimentation of sulfur species during eruption and column ascent (i.e., we assume 100% of exsolved sulfur is transported along with the column and is delivered to the final buoyancy level or is carried downwards with column collapse); 3) the formation, dispersal, atmospheric lifetime, and radiative effects of sulfate

aerosols following co-injection of SO_2, ash, and water into the spreading eruption cloud. However, we discuss the implications of co-injection of SO_2 with enhanced quantities of fine ash and water in **Section 4**.

2 METHODS

2.1 A Model of Sustained, Explosive Hydrovolcanism

Our focus is on sustained eruptions with sufficient momentum and buoyancy fluxes at the column source, which we will define carefully below, to inject SO_2 into the stratosphere. Consequently we restrict our analysis and modelling efforts to a class of powerful eruptions driven by magmatic vesiculation and fragmentation in the conduit, where the gas-pyroclast mixture is modified by the entrainment and mixing of external water that is primarily confined to the surface environment. This approach is motivated by observations of pyroclast textures and particle size distributions from several hydrovolcanic eruptions, including the 25 ka Oruanui and 1.8 ka Taupo eruptions, New Zealand (Self and Sparks, 1978; Wilson and Walker, 1985), the 2500 BP Hverfjall Fires eruption (Liu et al., 2017), the 10^{th} century eruption of Eldgjá Volcano, Iceland (Moreland, 2017; Moreland et al., 2019), the 1875 eruption of Askja Volcano, Iceland (Self and Sparks, 1978; Carey et al., 2009), and the 2011 eruption of Grímsvötn (Liu et al., 2015). Whereas airfall deposits from dry phases of each of these eruptions have total PSDs and porosities typical of Plinian events (Cas and Wright, 1987; Fisher and Schmincke, 2012), PSDs from wet eruption phases are relatively fines-enriched. Observations of PSDs, pyroclast textures and vesicularities from these events lead to the interpretation that melts fragmenting inside the conduit produce approximately similar PSDs that are modified, in turn, through a "secondary" episode of fragmentation related to the quenching of the gas-pyroclast mixture within overlying surface water layers (Liu, 2016; Aravena et al., 2018; Houghton and Carey, 2019; Moreland et al., 2019). In principle, PSDs can also be modified through effects of groundwater infiltration through the conduit walls, which can be enhanced with an overlying water layer as has been suggested on the basis of field observations (Barberi et al., 1989; Houghton and Carey, 2019). However, numerical simulations of Aravena et al. (2018) demonstrate that the extent of groundwater infiltration from 100 to 300 m-thick aquifers perched at or above the fragmentation depth depends on the magma mass eruption rate (MER). Crucially, for MER $\gtrsim 5 \times 10^6$ kg/s, which is typical of the sustained explosive eruptions and rhyolitic magma composition on which we focus, Aravena et al. (2018, Supplementary Material) find that water infiltration into the conduit flow is largely restricted to less than about 5–6 *wt%* for rhyolitic magmas. In addition, their calculations suggest that conduit failure or collapse is likely favored where ingested water mass fractions in the conduit exceed about 5 *wt%*. Aravena et al. (2018) further suggest this condition may by an explanation for why phreatomagmatic activity associated with direct interaction of un-fragmented melt with external water is more commonly dominant in eruptions with relatively low MER, a result consistent with field observations (Walker, 1981; Houghton and Wilson, 1989; Cole et al., 1995; Houghton and Carey, 2019; Moreland et al., 2019); for completeness we include eruptions with MER as low as 5.5×10^5 kg/s, however we note that the above assumptions are likely less valid for these low values.

Taking these observations and inferences into consideration in our modelling approach, we assume that secondary fragmentation from MWI is driven predominantly by quench fragmentation (also known as thermal granulation) (van Otterloo et al., 2015), as opposed to phreatomagmatic fragmentation by molten-fuel-coolant interaction (Büttner et al., 2002). Following Jones et al. (2019), Hajimirza et al. (2022) the MWI model is based on the physics of water entrainment for a subaqueous jet as well as the energetics of quench fragmentation. We do not consider classes of hydrovolcanic events driven primarily by episodic molten-fuel coolant interactions (Wohletz et al., 2013; Houghton et al., 2015; Zimanowski et al., 2015). We focus on eruptive phases in a sub-Plinian to Plinian to Phreatoplinian continuum under established classification schemes (Walker, 1973; Self and Sparks, 1978). Furthermore, we model only the sustained, steady-state phases of these events. **Figure 2** shows a conceptual overview of the problem definition and model setup in the near-vent region where an erupting jet emerges from the volcanic vent and encounters a shallow (≤ 500 m) water layer (see **Supplementary Material Section S1** and **Supplementary Figure S1** for a detailed overview of the model internal workflow and solver methods). On the basis of arguments from Aravena et al. (2018) for eruptions with MER $\gtrsim 10^6$ kg/s, we do not consider water infiltration into the shallow conduit and assume MWI occurs only within the overlying water layer. We include further discussion on this assumption and sample calculations of the effects of water infiltration into the conduit in **Section 4.4**. This study is not an exhaustive coverage over the full range of hydrovolcanic events, but rather is a first attempt at characterizing the broad behavior of an important end-member of sustained hydrovolcanic eruption for which 1) primary magmatic fragmentation is the dominant driving mechanism, 2) fuel-coolant interactions play at most a minor role in the momentum and energy budgets, and 3) substantial stratospheric injection of SO_2 is a likely outcome.

2.2 1D Conduit Model

We use the one dimensional conduit model of Hajimirza et al. (2021) and integrate flow properties over the cross-sectional area of the conduit. We assume a vertical cylindrical conduit with radius a_c and depth z (for a complete description of mathematical symbols and nomenclature, see **Table 1**). The conduit radius is fixed except near the surface, where flaring near the vent is possible to enforce mass conservation for a choked flow at the vent (Gonnermann and Manga, 2013). We assume the flow is steady - i.e., the duration of magma ascent is much shorter than the duration of Plinian eruptions (Mastin and Ghiorso, 2000). The magma is a mixture of rhyolitic melt (76% SiO_2) and H_2O bubbles that exsolve continuously during ascent because H_2O solubility is proportional to the square root of pressure. We also

TABLE 1 | List of variables and subscript nomenclature.

Variable	Description	Units
a	Radius of conduit or plume	m
A	Cross-sectional area of conduit or plume	m^2
B	Entrainment weighting for αRT scenario	-
C	Heat capacity	J/(kg K)
c	Sound speed	m/s
c_{H_2O}	Concentration of water dissolved in melt	wt%
D_0	Power law exponent for initial particle size distribution	-
E_s	Particle fracture surface energy	J/m^2
$\dot{E}$	Energy flux	J/s
ΔE_{ss}	Specific fragmentation energy (per mass of melt)	J/(kg m)
F_{fric}	Frictional pressure loss	Pa/m
f	Friction factor	-
g	Gravitational acceleration	m/s^2
h	Enthalpy	J/kg
h_{vap}	Bulk mixture enthalpy at $T = T_{sat}$ and $x_v = 1$	J/kg
h_{vap}	Bulk mixture enthalpy at $T = T_{sat}$ and $x_v = 0$	J/kg
K	Bulk modulus	Pa
L_d	Decompression length scale	m
L_X	Crossover length scale	m
M	Mach number	-
N_i	Number of particles in size bin i	-
N_ϕ	Number of particle size bins	-
n	Mass fraction	-
n_{ec}	Mass fraction of external water infiltrating the conduit	-
r	Particle radius	m
r_{c1}	Critical particle radius for maximum effective porosity	m
r_{c2}	Critical particle radius for zero effective porosity	m
R_v	Gas constant for water vapor	J/(kg K)
p	Pressure	Pa
p_{choke}	Theoretical gas pressure for a choked vent	Pa
$\dot{p}$	Magma decompression rate	MPa/s
Δp_b	Bubble overpressure	MPa
q	Mass flux	kg/s
q_c	Adjusted conduit mass flux (MER) for hydrovolcanic simulations	kg/s
Q_0	Reference conduit MER for control ($Z_e = 0$) simulations	kg/s
Q_{crit}	Critical MER to reach the tropopause	kg/s
S	Specific surface area of particles	m^2/kg
T	Temperature	K
T_g	Glass transition temperature lower bound	K
ΔT_g	Temperature range for glass transition	K
T_0	Initial magma temperature	K
T_{ref}	Reference temperature for enthalpy calculations	K
T_{sat}	Water saturation temperature	K
u	Vertical velocity (radially averaged)	m/s^2
x_v	Water phase dryness fraction	-
z	Vertical coordinate	m
Z_e	External surface water depth	m
$Z_{e,choke}$	Critical water depth at which hydrostatic pressure exceeds choking pressure	m
Z_{tp}	Height of tropopause	m
Z_{max}	Maximum height of eruption column	m a.v.l.
Z_{nbl}	Neutral buoyancy (spreading) height of eruption column	m a.v.l.
α	Entrainment coefficient	-
α_{RT}	Rayleigh-Taylor entrainment coefficient	-
β	Vent overpressure ratio	-
ζ	Fragmentation energy efficiency	-
η	Magma mixture dynamic viscosity	Pa s
Λ	Particle roughness scaling parameter	-
λ	Water vapor condensation rate	s^{-1}
ρ	Density	kg/m^3
ϕ	Particle sieve size	-
ϕ_μ	Mean ϕ size of quench fragmented particles	-
ϕ_σ	Standard deviation ϕ size of quench fragmented particles	-

(Continued on following page)

TABLE 1 | (*Continued*) List of variables and subscript nomenclature.

Variable	Description	Units
χ	Volume fraction	-
χ_i	Porosity of particle size bin *i*	-
χ_0	Threshold porosity for conduit fragmentation	-
ψ_{SO_2}	Gaussian profile for vertical distribution of SO_2 injection	-
ω	Jet-water interface acceleration for Rayleigh-Taylor entrainment	-
Subscripts		
–	Bulk mixture (no subscript for material property)	
a	Dry air phase	
b	Bubble gas properties in pyroclasts	
c	Property of mixture in the conduit or vent	
d	Property after vent decompression	
e	Property of external water (MWI model) or air (plume model)	
f	"Final" value, or next iteration step	
i	Particle size bin *i*	
l	Liquid water phase	
m	Magma phase (excluding bubbles)	
s	"Solids" phase (melt + bubbles)	
v	Water vapor phase	
w	Total water phase in conduit or plume (liquid + vapor)	
0	Initial value	

assume crystals are only present as a dilute suspension of uniformly distributed sub-micron scale microphenocrysts that enable a 1D approximation of heterogeneous bubble nucleation (Shea, 2017). This simplified picture also leads to assumptions that the presence of microphenocrysts has negligible effects on magma density and rheology. Thus, below the level of fragmentation we define magma as a mixture of silicate melt and H_2O bubbles, and we assume the melt phase is incompressible (Massol and Koyaguchi, 2005). The flow transitions discontinuously above the level of fragmentation to a dilute mixture of continuous H_2O vapor with suspended fragments of vesicular pyroclasts. For model purposes, we treat water as the only magmatic volatile: SO_2 (and other gases) do not contribute to the thermodynamic state of the magma and are carried within the mixture passively. We use the term "gas" interchangeably with water vapor throughout unless otherwise stated.

We assume the relative velocity between the melt/pyroclast and bubble/gas phases to be negligible below and above the fragmentation level. Below fragmentation, bubbles are entrained in the very viscous melt and the magma rises as a foam (e.g., Mastin and Ghiorso, 2000; Gonnermann and Manga, 2007). Above fragmentation, a real volcanic flow will experience complex phenomena including solid/gas phase separation and sound wave dispersion, as well as buoyancy effects including the excitation of compaction and porosity waves (e.g., Bercovici and Michaut, 2010; Michaut et al., 2013). Such dynamics are important for degassing and can modify fragmentation processes in one-dimensional conduit models. However, their inclusion is practically challenging and the effect of resulting fluctuations in MER on the height and gravitational stability of steady-state plumes is ultimately small in comparison to controls arising through parameterizations for water and air entrainment. For simplicity and to retain a focus on the effect of entrainment and MWI on plume height and SO_2 delivery to the stratosphere, we neglect these dynamics and apply the common pseudo-gas approximation for fully-coupled gas and particle flow (Wilson et al., 1980; Mastin and Ghiorso, 2000). The properties of the magma mixture (melt and bubbles or gas and pyroclasts) are, consequently, the volumetric average of the two phases. We also assume the conduit flow to be isothermal (Colucci et al., 2014) because heat loss to conduit walls is negligible over the time scale of rise through the depth z (Mastin and Ghiorso, 2000). The latent heat flux consumed through the exsolution of H_2O with magma ascent helps to enforce this condition, although the effect is very small.

With these assumptions and simplifications, conservation of mass and momentum for the ascending magma are (Wilson et al., 1980; Mastin and Ghiorso, 2000)

$$\frac{\partial(\rho u A)}{\partial z} = 0, \tag{1}$$

and

$$\rho u \frac{\partial u}{\partial z} = -\frac{\partial p}{\partial z} - \rho g - F_{\text{fric}}, \tag{2}$$

respectively. Here u is magma ascent rate and $A = \pi a_c^2$ is the conduit cross sectional area. The bulk magma density is

$$\rho = \chi_v \rho_{\text{v}} + (1 - \chi_v)\rho_{\text{m}}, \tag{3}$$

where χ_v is the volume fraction of bubbles, and ρ_{v} and $\rho_{\text{m}} = 2{,}400\ \text{kg/m}^3$ are gas and melt densities respectively. The frictional pressure loss $F_{\text{fric}} = \rho u^2 f / a_c$ where f is a friction factor. Below the fragmentation depth $f = 16/\text{Re} + f_0$ and above the fragmentation depth $f = f_0$. Here, the Reynolds number $\text{Re} = 2\rho u a/\eta$, where η is the viscosity of the mixture. The reference friction factor $f_0 = 0.0025$ depends on the conduit wall roughness (Mastin and Ghiorso, 2000). By

substituting **Eqs. 1** and **2** and defining the isothermal mixture sound speed

$$\left(\frac{\partial \rho}{\partial p}\right)_{T_0} = c^2, \tag{4}$$

we obtain (Gonnermann and Manga, 2013; Hajimirza et al., 2021)

$$-\frac{\partial p}{\partial z} = \frac{\rho g + F_{\text{fric}} - \frac{\rho u^2}{A}\frac{\partial A}{\partial z}}{1 - M^2}, \tag{5}$$

where the Mach number $M = u/c$. Below the fragmentation depth the sound speed of the mixture $c = (K/\rho)^{1/2}$, where K is the bulk modulus of the mixture given by:

$$\frac{1}{K} = \frac{\chi_v}{K_{\text{v}}} + \frac{1 - \chi_v}{K_{\text{m}}}. \tag{6}$$

Above the fragmentation depth, the bulk modulus of the gas phase K_{v} is calculated for the mixture temperature from the equation of state for water (Holloway, 1977).

The conduit model includes treatments for water vapor exsolution from the melt and subsequent bubble growth from Hajimirza et al. (2021). At a given depth below fragmentation, heterogeneous bubble nucleation on crystal nanolites occurs with a specified critical supersaturation, and growth is by the diffusion of water from the melt. Above the fragmentation depth the bubble volume and number density are fixed, although vapor can continue to exsolve and escape from pyroclasts into the surrounding free vapor by permeable flow. We employ a fixed porosity threshold of 75% as a fragmentation condition, which is consistent with measurements and analyses of pumice permeabilities and vesicle size distributions that show that PSDs follow power laws comparable to those of pore-scale microstructures in erupted pumice (Kaminski and Jaupart, 1998; Rust and Cashman, 2011). We consequently do not fix a PSD in the conduit and assume only that fragmentation proceeds to small enough length scales such that gas escape from connected pores in the entrained pyroclasts is sufficient to ensure that pore-scale pressures are equivalent to the free gas in the conduit at the vent (Rust and Cashman, 2011).

Assuming negligible gas escape or water infiltration through conduit walls, the primary effect of overlying surface water or ice is to modify the pressure boundary condition at the volcanic vent. Above magmatic fragmentation, the gas-pyroclast mixture fluidizes, accelerates, and decompresses towards the conduit exit. If the flow speed remains below the mixture sound speed c, then the vent exit pressure p_c must balance the ambient pressure above the vent p_e, which is determined by water depth:

$$p_e = \rho_e g Z_e + p_{atmo}. \tag{7}$$

Here ρ_e is the density of external water and p_{atmo} is the atmospheric pressure at the water surface. However, if $M \rightarrow 1$, the flow becomes choked, which causes the flow at vent to be overpressured relative to ambient (Gonnermann and Manga, 2013). As a metric for vent overpressure, we introduce the vent overpressure ratio $\beta = p_c/p_e$. To enforce mass conservation for choked flow, either choking must occur at the vent exit of a fixed radius conduit or the conduit radius must flare accordingly (Gonnermann and Manga, 2013). The conduit modelling approach is therefore to seek solutions where the pressure in the conduit flow matches the surface pressure boundary condition (i.e., $\beta \approx 1$), or for which the conduit is choked at (no flaring) or near (with flaring) the vent (i.e., $\beta \gtrsim 1$, $M \approx 1$).

To gain insight into how an ascending magma responds to changes in hydrostatic pressure related to loading by overlying layers of water or ice, it is instructive to compare solutions for eruptions with and without external water, with other independent parameters fixed. To this end we choose a fixed conduit depth $z = 6$ km, an initial magmatic temperature $T_0 =$ 1,123.15 K and a maximal (unexsolved) magmatic water content corresponding to saturation as determined with the method of Liu et al. (2005). We then use an iterative search to find conduit parameters that satisfy either the pressure-balanced or choked conditions. We first allow conduit radius to vary to obtain solutions for a "dry" or subaerial vent where no external water is present and the ambient pressure above the vent is equal to atmospheric ($Z_e = 0$). Subaerial vent simulations were run and suitable conduit radii obtained for a range of "control" MER $10^{5.5} \leq Q_0 \leq 10^9$ kg/s, and we refer to these subaerial vent scenarios as "control" simulations hereafter. For control scenarios, we seek specifically solutions where choking occurs at the vent exit and thus no conduit flaring is required. This calculation provides a reference conduit radius to use in scenarios with a water layer present above the vent, with water depths $0 < Z_e \leq 500$ m. For these hydrovolcanic cases, we then fix the conduit radius to that of the control scenario and find an adjusted conduit MER q_c such that the surface pressure and/or choking boundary conditions are again satisfied. All values of MER referred to herein (i.e., Q_0, q_c) indicate magmatic mass fluxes in the conduit (i.e., excluding external water). See **Supplementary Figure S2** for a visualization of the search process for conduit radius and MER in control and hydrovolcanic cases, respectively. Although we choose MER as our adjusted parameter, other parameter choices are possible, such as the excess pressure of the magma reservoir at the base of the conduit or modification of the vent geometry. To make clear our approach and the consequences of our approximations and simplifications, see **Section 3.1** for example conduit model results.

2.3 Vent and Magma-Water Interaction Model

2.3.1 Initial Particle Size Distribution

The model PSD is specified explicitly at the vent ($z = 0$) using output from the conduit model. We define an initial power-law PSD following Kaminski and Jaupart (1998) and Girault et al. (2014), over the particle size range $-10 \leq \phi_i \leq 8$. The number of particles N_i at size ϕ_i is given by

$$N_i = 2^{\log_2(N_0) + D_0 \phi_i}, \tag{8}$$

where D_0 is the power-law exponent, N_0 is an arbitrary normalization constant, and subscript i indicates a particle size

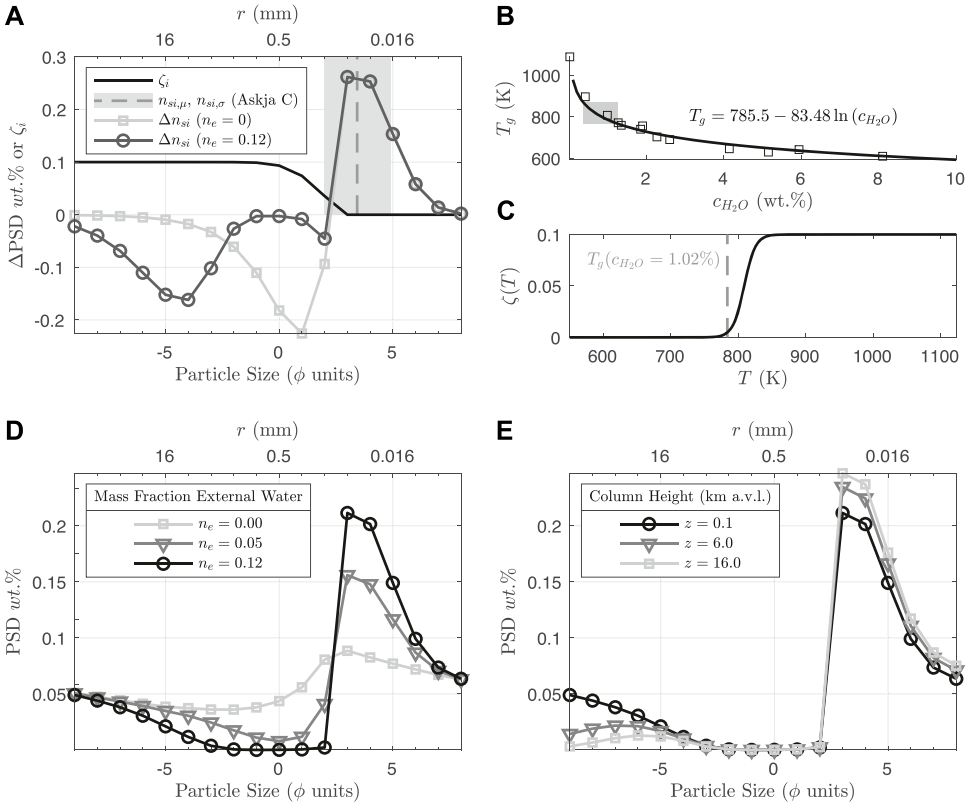

FIGURE 3 | PSD and quench fragmentation model for rhyolitic melt, using a single example simulation with $q = 1.03 \times 10^8$ kg/s, $Z_e = 120$ m, and $\zeta = 0.1$. **(A)** Change in PSD ($\Delta n_{s,i} = -n_{si,0} + n_{si,f}$) from **Eq. 52** at two different mass fractions of entrained external water n_e. The "output" particle sizes of quench fragmentation $n_{si,f}$ are defined from the mean and standard deviation (in ϕ units, shown as the vertical grey dashed line and shaded region, respectively) of the Askja phase C deposit, as reported in Costa et al. (2016). The"input" particle sizes – $n_{si,0}$ (i.e., from which mass is removed to generate the products of quench fragmentation), are a function of available surface area in the PSD coarse fraction (**Equation 49**), and evolve as the total PSD coarse fraction is progressively depleted with increasing n_e (see also panel **(D)**). The solid black line shows ζ_i (**Equation 47**), which defines the size bins for the "coarse" fraction. **(B)** Glass transition temperature T_g data from Dingwell (1998) (squares) and curve fit (black line) as a function of concentration of dissolved water in the melt. The grey shaded rectangle shows the range of values in the *Reference* set of simulations after exit from the vent. **(C)** Fragmentation energy efficiency as a function of temperature (**Equations 45**, **46**) for $T_g = 784$ K. **(D)** Evolution of the total PSD $n_{s,i}$ during quench fragmentation. The initial power law PSD, with no external water, and therefore no quench fragmentation ($n_e = 0$), is shown in light grey, with a reduced mass fraction in the range $\phi \lesssim 2$ arising from the large porosity and consequently low density of these particles (**Eqs. 11**–**13**). The remaining dark grey and black lines show $n_{s,i}$ after quench fragmentation for $n_e = 0.05$ and $n_e = 0.12$, respectively. After sufficient external water is entrained ($n_e \approx 0.12$) to cross T_g, $n_{s,i}$ does not evolve further from quench fragmentation. Note that owing to their larger surface area, particles are preferentially depleted in the mid-size-range ($-3 \lesssim \phi \lesssim 2$). **(E)** Further evolution of $n_{s,i}$ due to particle fallout, after water breach and during subaerial column rise, with preferential fallout of the coarsest fraction ($\phi \lesssim -3$) and additional enriching of fines.

bin. We choose a default value of $D_0 = 2.9$. Each size class is assigned an effective porosity value χ_i on the basis of an effective particle radius according to

$$\chi_i = \chi_0, \quad r_i \geq r_{c1}, \tag{9}$$

$$\chi_i = \chi_0 \left(1 - r_{c2}/r_i\right), \quad r_{c2} \leq r_i \leq r_{c1}, \tag{10}$$

$$\chi_i = 0, \quad r < r_{c2}. \tag{11}$$

Here, $\chi_0 = 0.75$ is the porosity threshold for fragmentation, r_i is the particle radius for bin i, $r_{c1} = 10^{-2}$ m and $r_{c2} = 10^{-4}$ m. Particles of sufficiently small size have, thus, no effective porosity and densities equal to that of the pure melt phase ($\rho_{s,i} = \rho_m$). By contrast, the density of larger particles is a strong function of porosity and bubble gas density (Kaminski and Jaupart, 1998). This approach leads to expressions for particle mass fraction in each size bin, $n_{s,i}$, and the bubble gas mass fraction of each size bin, $n_{b,i}$:

$$\rho_{s,i} = \left(1 - \chi_i\right)\rho_m + \chi_i \rho_v, \tag{12}$$

$$n_{s,i} = \frac{N_i r_i^3 \rho_{s,i}}{\sum_{i=1}^{N_\phi}\left(N_i r_i^3 \rho_{s,i}\right)}, \tag{13}$$

$$n_{b,i} = \frac{\frac{\rho_v \chi_i}{\rho_m\left(1-\chi_i\right)}}{\left(1 + \frac{\rho_v \chi_i}{\rho_m\left(1-\chi_i\right)}\right)}, \tag{14}$$

where subscript s denotes the bulk "solids" phase (melt plus bubbles) and N_ϕ is the number of particle size bins. **Figure 3D** shows the initial PSD for $D = 2.9$, accounting for particle density as a function of porosity (light gray line and square symbols).

2.3.2 Vent Decompression

Figure 2 highlights the geometry and relevant length scales for the MWI model. For an overpressured jet in the near-vent region with $M \geq 1$ (e.g., Ogden et al., 2008), we assume that mixing of the

gas-pyroclast mixture with external water is negligible over a "decompression length scale" L_d where expanding gas prevents pyroclasts inside the jet from interacting with external water (e.g., Kokelaar, 1986). Our decompression model therefore assumes that turbulent entrainment and mixing of external water begins at heights above L_d. For L_d, we use a modified form of the free decompression condition of Woods and Bower (1995) to find the height at which the jet gas pressure plus dynamic pressure is equivalent to external water hydrostatic pressure:

$$p_d + \frac{u_d^2 \rho_d}{2} = \rho_e g (Z_e - L_d) + p_{atmo}, \tag{15}$$

where p is pressure, u_d is the speed after decompression, and ρ is density. Subscripts d and e denote properties of the jet mixture after "decompression" and of "external" water, respectively. Assuming the decompression speed is approximately the mixture sound speed (i.e., $M = 1$ at the expanding shock front) (Ogden et al., 2008) and using the dusty-gas approximation (Woods and Bower, 1995),

$$u_d \approx c_d \approx c_{v,d} \sqrt{\frac{\rho_{v,d}}{\rho_d \chi_{v,d}}} \tag{16}$$

$$= \sqrt{\frac{\rho_v}{\rho_d \chi_{v,d}} \frac{\gamma p_d}{\rho_v}} \tag{17}$$

$$\approx \sqrt{\frac{\gamma p_d}{\rho_d}}, \tag{18}$$

where subscript v denotes the "vapor" phase, the free gas volume fraction $\chi_v \approx 1$, and γ is the ratio of specific heats for the vapor phase. Substituting **Eq. 18** into **Eq. 15** gives

$$p_d = \frac{p_e (L_d)}{1 + \frac{\gamma}{2}}. \tag{19}$$

Assuming that the mixture volume is approximately conserved, the decompression length L_d is proportional to the change in jet radius with decompression:

$$L_d = 2\Delta a = 2 (a_d - a_c), \tag{20}$$

where

$$a_d = \left(\frac{\rho_c u_c a_c^2}{\rho_d c_d} \right)^{1/2}, \tag{21}$$

and

$$\rho_d = \left(\frac{1 - n_v}{\rho_s} + \frac{n_v}{\rho_{v,d}} \right)^{-1}. \tag{22}$$

Here n_v is the jet gas mass fraction, and the subscript c indicates properties in the "conduit" prior to decompression. Momentum and energy are not perfectly conserved after decompression in this formulation as they are in Woods and Bower (1995), because the radially averaged decompression velocity is taken to be the mixture sound speed. However, this approach is consistent with the results of numerical simulations (e.g., Ogden et al., 2008), where excess energy is dissipated via shock formation and related effects of supersonic flow, and radially average velocities after decompression are close to sonic. These equations give a decompression length approximately similar to the Mach disk height relation of Ogden et al. (2008), (see **Supplementary Figure S3** for a comparison), but with the difference that $L_d \to 0$ for $\beta \leq 1$. This is an important distinction since the formal definition of L_d in our model is the height at which the jet overpressure is sufficiently small that turbulent mixing and entrainment can begin. For a pressure-balanced jet ($\beta = 1$), this critical height should be immediately above the vent. We note, however, that due to the rapid pressure change with height in the water column, the mixture will continue to expand and decompress, such that the static estimate of L_d used here is likely a lower bound.

2.3.3 Water Entrainment and Magma-Water Interaction Model

The mixing of water, steam, pyroclasts, and lithic debris in the vent region in explosive hydrovolcanic eruptions is complex and may involve effects of shocks, supersonic flow, film boiling, and multiple fragmentation mechanisms (Wohletz et al., 2013; Houghton and Carey, 2015; van Otterloo et al., 2015) that introduce inherently time-dependent and three-dimensional mechanisms for entrainment and mechanical stirring that are not captured in a one-dimensional steady-state integral model. However, following extensive studies of entrainment and mixing into turbulent plumes (Morton et al., 1956; Linden, 1979; Turner, 1986), a recent complementary analysis of water entrainment into supersonic, submerged gas jets (Zhang et al., 2020) and studies of the bulk energetics of interactions between hot pyroclasts and water (Mastin, 2007a; Dufek et al., 2007; Schmid et al., 2010; Sonder et al., 2011; Dürig et al., 2012; Woodcock et al., 2012; Moitra et al., 2020) we can parameterize these processes to explore effects on total budgets for mass, energy, and buoyancy. Following Morton et al. (1956); Kaminski et al. (2005); Carazzo et al. (2008); Zhang et al. (2020), Hajimirza et al. (2022), we will relate the radial entrainment speed of water or atmosphere to the local rise speed of a jet and prescribe resulting velocity, pressure and temperature fields. We assume the rate of mixing and heat transfer between solid pyroclasts and entrained water to be sufficiently fast that all phases are well-mixed and at equal temperature inside the jet over the timescale of rise through the water column. We discuss consequences of this assumption further in **Section 4**.

We initialize the water entrainment model at height L_d above the vent. Initial conditions for jet velocity, radius, and density are determined after decompression by balancing jet gas pressure with hydrostatic pressure at L_d. Other parameters such as gas mass fraction and temperature are obtained from values at the top of the conduit model, while the PSD and pyroclast porosity and density are determined according to **Section 2.3.1** above. An iterative MATLAB solver integrates solutions to the differential equations for water and particle mass, bulk momentum and energy, and PSD mass fractions from the decompression height to the water surface. The physical properties of entrained water are calculated using the International Association for the Properties of Water and Steam 1995 formulation (Junglas, 2009). To capture the evolution with

height of the mixture energy (enthalpy plus average vertical kinetic and gravitational potential energy), we follow a similar approach to Mastin (2007b). The initial enthalpy of the solid phase at the vent surface h_{s0} is determined from a weighted combination of the enthalpy of exsolved gas bubbles and the specific heat of the melt phase:

$$h_{s0} = h_b\left(p_b, T_0\right)\sum_{i=1}^{N_\phi} n_{s,i}n_{b,i} + C_m\left(T_0 - T_{ref}\right)\sum_{i=1}^{N_\phi}\left(1 - n_{b,i}\right)n_{s,i}. \quad (23)$$

Here h_b (p_b, T_0) is bubble gas enthalpy as a function of pressure and temperature, C_m = 1250 J/(kg K) is the melt heat capacity (assumed constant), and T_{ref} = 274.15 K is a reference temperature. The total mixture enthalpy, h is then

$$h = n_w h_w\left(p, T\right) + \left(1 - n_w\right)h_s, \quad (24)$$

where n_w and h_w are the mass fraction and enthalpy of water (gas and liquid) within the jet mixture. At the decompression length, the total power supplied by the jet is

$$\dot{E}_0 = q_c\left(h_0 + g'L_d + \frac{u_d^2}{2}\right), \quad (25)$$

where q_c is the conduit MER and $g' = g\left(\rho - \rho_e\right)/\rho_e$ is the reduced gravity, and the dot notation over E indicates the time derivative of the system's energy at decompression length L_d.

From an initial value T_0, the bulk temperature of the jet mixture T is calculated at each solver step following Mastin (2007b). Specifically, the enthalpy at each step is compared with two values: the enthalpy h_{vap} that the mixture would have at the water saturation temperature assuming 100% steam (dryness fraction x_v = 1), and h_{liq}, where the water phase is 100% liquid (x_v = 0). For $h > h_{vap}$, the mixture temperature is found using an iterative approach to match the known enthalpy value h. For $h_{liq} < h < h_{vap}$, $T = T_{sat}$ and $x_v = (h - h_{liq})/(h_{vap} - h_{liq})$. We employ a stop condition as dryness fraction reaches $x_{v,crit}$ = 0.02. This condition is justified physically because as the jet water fraction becomes mostly liquid with $x_v \to 0$, the resulting high-density jets always collapse almost immediately after breaching the water surface and are therefore ineffectual at injecting SO_2 into the stratosphere. Conceptually, this condition is equivalent to the case where *at most* only minor quantities of steam breach the water surface, potentially generating steam plumes but carrying negligible quantities of volcanic ash or other volatiles (e.g., Cahalan and Dufek, 2021). We refer to the above ultra-high water fraction scenarios as the "steam plume" regime hereafter. For greater water depths still, the gas jet would entirely condense and fail to breach the water surface (Cahalan and Dufek, 2021). Furthermore, as the vapor fraction approaches zero, steep gradients in density significantly increase problem stiffness and computation time, and we thus discard these results and do not integrate further.

Entrainment of ambient fluid into a jet or plume is driven by both radial pressure variations arising from the relatively fast rise of the jet and local shear across the jet-water interface (see **Figure 1**). Entrainment parameterizations in integral plume models typically assume that the rate of radial inflow of ambient fluid v_ε at any height is proportional to the upflow speed (Morton et al., 1956):

$$v_\varepsilon = \alpha u, \quad (26)$$

where α is an entrainment coefficient of order 0.1. Here we employ a variable entrainment coefficient following Kaminski et al. (2005); Carazzo et al. (2008):

$$\alpha = 0.067\,5 + \left(1 - \frac{1}{A}\right)Ri + \frac{a}{2}\frac{d}{dz}\ln\left(A\right), \quad (27)$$

where

$$Ri = \frac{g'a}{u^2} \quad (28)$$

is the local Richardson number that expresses the balance between the momentum and stabilizing buoyancy fluxes at a given height. The shape function $A = A(z)$ depends on the diameter of the jet and Ri at z = 0. This well-established hypothesis for ambient fluid entrainment is, however, strictly valid only where turbulence is fully developed. This picture assumes that there is a direct momentum exchange between large entraining eddies that form plume edges and a full spectrum of turbulent overturning motions that mix momentum, heat and mass across the plume radius down to spatial scales limited by either molecular diffusion or dissipation by very fine ash (Lherm and Jellinek, 2019). In general, this condition is established over heights of roughly 5 to 10 vent diameters (i.e. the vent near-field, see also **Figure 2**) and corresponds to a transition from flow as a jet governed by the momentum flux delivered at L_d to flow as a buoyant plume driven by a balance between buoyancy and inertial forces (Carazzo et al., 2006; Saffaraval and Solovitz, 2012). A key issue for the character and magnitude of effects related to MWI is whether and where in the water layer this transition occurs such that water entrainment is fully established.

To constrain this transition height relative to L_D we follow an approach developed in Kotsovinos (2000) to identify the dynamical "crossover height" L_X at which fully turbulent plume rise starts and above which **Eq. 26** holds. Below L_X, the flow evolves predominantly in response to the momentum flux supplied. In this regime, drag related to turbulent instabilities, accelerations, overturning motions and mixing is not established and on dimensional grounds the evolving height of the jet

$$h_{jet} \sim \left(\pi a_d^2 u_d\right)^{1/4} t_{jet}^{1/2}. \quad (29)$$

Above L_X, plume height predominantly governed by a balance between buoyancy and inertial forces is, by contrast,

$$h_{BI} \sim \left(\frac{g'q}{\pi a_d^2}\right)^{1/2} t_{BI}^{3/2}. \quad (30)$$

The transition height L_X occurs where $h_{jet} = h_{BI}$, which corresponds to where the characteristic time scale $t_{jet} = t_{BI}$. After algebra we obtain

$$L_X = \pi^{5/8} u_d^{3/4}\left(\frac{a_d^5 \rho_d}{g'q}\right)^{1/4}. \quad (31)$$

Starting from height $z = L_d$, we assume the thickness a_{mix} of a turbulent mixing layer at the jet boundary develops monotonically over distance L_X:

$$a_{mix} = a\frac{z - L_d}{L_X}; \qquad a_{mix} \le a, \tag{32}$$

above which the radial turbulent mixing is complete and the velocity profile is top-hat or Gaussian, consistent with the assumption of self-similar flow (Morton et al., 1956; Turner, 1986). We then obtain an effective entrainment coefficient, α_{eff}, by scaling the entrainment coefficient based on the volumetric growth of the mixing layer:

$$\alpha_{eff} = \alpha\frac{2aa_{mix} - a_{mix}^2}{a^2}. \tag{33}$$

Using a similar entrainment parameterization to Mastin (2007b) which accounts for the relative density difference of the ambient and entraining fluid, the rate of water entrainment into the jet is

$$\frac{dq_{w,e}}{dz} = 2\pi a\alpha_{eff}u\sqrt{\rho\rho_e}. \tag{34}$$

In a recent study of supersonic air jets intruding 1–400 m deep layers of water from below (Zhang et al., 2020) shows that entrainment and mixing is significantly augmented by buoyancy effects related to the rise of air through layers of relatively dense water. Their results suggest that this mechanism will dominate the mechanics of entrainment for water layer depths exceeding a few hundred meters. This condition is presumably set by the height in the water column at which the overturn time of large entraining eddies related to the rise of buoyant air becomes less than the time scale for water ingestion through shear-induced turbulence (**Eq. 27**). The extent to which this mechanism governs the evolution of rapidly expanding hot volcanic jets erupting through comparably thick layers of water is, however, unclear and particularly so where L_d is of the same order of magnitude as the water depth. For completeness, we compare results obtained from **Eqs. 27–33** with complementary calculations assuming entrainment is partially governed through the buoyancy-driven "Rayleigh-Taylor" entrainment mode of Zhang et al. (2020). Specifically, we define an alternative α_{eff} as a weighted average of the shear-driven and Rayleigh-Taylor entrainment modes:

$$\alpha_{eff} = B\alpha + (1 - B)\alpha_{RT}, \tag{35}$$

where

$$\alpha_{RT} = 4\pi\frac{a_d}{q_c}a\sqrt{\frac{2\rho}{3}\left(3\sigma\rho_e\omega\right)^{1/2}}. \tag{36}$$

Here, α_{RT} is the Rayleight-Taylor coefficient for buoyancy driven entrainment, B is a specified weighting determining the relative contributions of buoyancy effects and shear to the total water entrainment, σ is the surface tension at the water-steam interface, and $\omega \approx (0.3u)^2/(2\pi a)$ is the average radial acceleration of the interface (Zhang et al., 2020). The geometric constant of 0.3 is an approximate scaling for the magnitude of turbulent velocity fluctuations (Cerminara et al., 2016) and ensures that the radial momentum flux carried by the inflow is an order of magnitude smaller than the vertical momentum flux carried by the jet itself. This condition is required for the jet to remain intact and approximately conical, consistent with the results of (Zhang et al., 2020), and for the equations underlying the 1D plume model to hold (Morton et al., 1956). We compare the consequences of different entrainment modes for eruption behavior in **Sections 3.2** and **4.1**.

2.3.4 Quench Fragmentation Model

The process of quench fragmentation of pyroclastic particles of various size during MWI is complex. Driving thermal stresses and stress concentrations arising through interactions with cold water depend on the curvatures of the outer surfaces of pyroclasts, their porosity and surface area-to-volume ratio, and on the spatial distributions and rates of both surface cooling and film boiling. How to capture thoroughly these particle-scale effects and their consequences for the mean particle size distribution in an evolving volcanic jet mixture is unclear and remains a subject of vigorous research (e.g., Wohletz, 1983; Büttner et al., 2002, 2006; Mastin, 2007a; Woodcock et al., 2012; Patel et al., 2013; Liu et al., 2015; van Otterloo et al., 2015; Dürig et al., 2020b; Fitch and Fagents, 2020; Moitra et al., 2020; Hajimirza et al., 2022). However, with a specified magmatic heat flow at the vent, considerations of the surface energy consumed to generate fine ash fragments (Sonder et al., 2011), guided by published experiments along with observational constraints on the hydromagmatic evolution of particle sizes (Costa et al., 2016), provide a way forward that is appropriate for a 1D integral model. **Figure 3** highlights the salient features of the fragmentation model, using the example of a single simulation with $q_c = 1.03 \times 10^8$ kg/s and $Z_e = 120$ m. Sonder et al. (2011) performed lab experiments submerging molten basalt into a fresh water tank to constrain the partitioning of thermal energy lost from the melt between that which is transferred from melt to heat external water and that which is consumed irreversibly through fracturing of the melt to generate new surface area and fine ash. At any height above the vent, the total power delivered to entrained external water from the melt is

$$\Delta\dot{E}_e = (1 - \zeta)\Delta\dot{E}_m, \tag{37}$$

and $\Delta\dot{E}_m$ is the rate of heat loss from the melt phase. The remaining heat loss from the melt i.e. $\zeta\Delta\dot{E}_m$ is the energy consumed by fragmentation. Note that we define fragmentation energy efficiency in the opposite sense to Sonder et al. (2011) such that $\zeta = 1 - \eta$, where η is as defined in that work. The parameter ζ is an empirical fragmentation energy efficiency that gives the fraction of thermal energy lost irreversibly to fragmenting pyroclasts to generate fine ash. Where thermal stresses related to cooling produce no fine ash, $\zeta = 0$ and $\Delta\dot{E}_e = \Delta\dot{E}_m$. Experimentally, Sonder et al. (2011) find $0.05 \lesssim \zeta \lesssim 0.2$ for thermal granulation processes, with typical values of ~ 0.1.

Below, we use **Eq. 37** to define power transfer during each height step of the MWI model. In more detail, entrained water must thermally equilibrate with both pyroclasts and internal water already in the volcanic jet. With both sinks for thermal

energy included, we recast **Eq. 37** to be the total power transferred to entrained water at each height step:

$$\Delta\dot{E}_e = (1-\zeta)\Delta\dot{E}_m + \Delta\dot{E}_w, \tag{38}$$

where $\Delta\dot{E}_w$ is the power supplied for heating external water by heated water already in the volcanic jet. Although this energy sink is very small for typical magma water mass fractions of $\lesssim 5\%$ at the vent height, this contribution to the energy balance in **Eq. 38** evolves to be significant with height in the jet as a result of progressive water entrainment.

Neglecting a comparatively very small contribution from the specific heat of water trapped within the pores of pyroclasts, **Eq. 38** can be recast as an enthalpy change with water entrainment over a height step:

$$-\Delta q_{w,e}\left(h_{w,f} - h_e\right) = (1-\zeta)q_s C_m\left(T_f - T\right) + q_w\left(h_{w,f} - h_w\right), \tag{39}$$

where $\Delta q_{w,e}$ is the mass flux of entrained water, $h_{w,f}$ is the final enthalpy of the water phase after thermal equilibration (i.e., where the jet gas and particles are well-mixed and at the same temperature), h_e is the external water enthalpy, q_w and h_w are the mass fluxes and enthalpy, respectively, of water already equilibrated thermally within the jet. In **Eq. 39**, T_f and T are the unknown final mixture temperature and known initial mixture temperature for the current height step, respectively. To estimate heat transfer to the entrained water phase, we assume that the change in temperature after equilibration $T_f - T$ is sufficiently small at each step that the jet water heat capacity can be approximated as constant for the current step, such that

$$h_{w,f} = h_w + C_w\left(T_f - T\right), \tag{40}$$

where C_w is the water heat capacity at temperature T. Substituting 41 into 40 leads to

$$T_f = \frac{(1-\zeta)q_s C_m T + q_w C_w T - \Delta q_{w,e}\left(h_w - C_w T - h_e\right)}{\left(\Delta q_{w,e} + q_w\right)C_w + (1-\zeta)q_s C_m}. \tag{41}$$

T_f can then be used to estimate heat transfer to entrained water $\Delta h_w = h_{w,f} - h_e$, which is used along with ζ and the PSD to later calculate the specific fragmentation energy, ΔE_{ss}.

Since we assume that the energy consumption during quench fragmentation results from the generation of new surface area (Sonder et al., 2011; Dürig et al., 2012; Fitch and Fagents, 2020; Hajimirza et al., 2022), we calculate the specific surface area at each particle bin size assuming spherical particle geometry:

$$S_i = \frac{3\Lambda}{\rho_i r_i}, \tag{42}$$

where Λ is a scaling parameter accounting for particle roughness, as true particle surface area can potentially exceed that of ideal spherical particles by up to two orders of magnitude (Fitch and Fagents, 2020). We take a default value $\Lambda = 10$, and discuss the effects of different choices for Λ in **Sections 3.2** and **4**. The total surface specific surface area for a given PSD is

$$S = \sum_{i=1}^{N_\phi} S_i n_{s,i}. \tag{43}$$

To simulate the evolution of the PSD by quench fragmentation, we prescribe a representative range of particle sizes produced by thermal granulation based on the fine mode of particle sizes for the phreatomagmatic phase C of the 1875 Askja eruption, as reported in Costa et al. (2016). The resulting "output" PSD, $n_{si,f}$, is a normal probability density function, in ϕ size units, with mean $\phi_\mu = 3.43$ (~ 100 μm) and standard deviation $\phi_\sigma = 1.46$, and is shown in **Figure 3A** (gray shaded region).

The "input" particle sizes (i.e., particles that fragment to produce the fine fraction) are defined according to the available surface area in the coarse fraction ($\phi < \phi_\mu$). We use the output mean, ϕ_μ as a fragmentation cutoff - particles of this size and smaller are assumed to not participate in quench fragmentation, but can participate in heat transfer to water. This allows the definition of an effective fragmentation energy efficiency as a function of particle size (see **Figure 3A**, black line),

$$\zeta_i = \begin{cases} \zeta\dfrac{1-n_{si,f}}{n_{s\phi_\mu,f}} & \phi_i < \phi_\mu \\ 0 & \phi_i \geq \phi_\mu, \end{cases} \tag{44}$$

where $n_{s\phi_\mu,f}$ is the mass fraction of the mean size bin in the output PSD. Fragmentation efficiency thus quickly reduces to zero as particle sizes approach the mean output size. In addition to the above particle size limitation on fragmentation, we also halt fragmentation once the bulk mixture passes below the glass transition temperature. We define the glass transition lower bound for a hydrous rhyolitic melt using an empirical fit to data from Dingwell (1998) (note that **Eq. 45** is a distinct equation from the empirical fit provided in that work):

$$T_g = 785.5 - 83.48\,log\left(c_{H_2O}\right), \tag{45}$$

where c_{H_2O} is the residual concentration (in wt%) of H_2O still dissolved in the melt and obtained from the conduit model (see **Figure 3B**). Since the glass transition occurs over a range of temperatures (Giordano et al., 2005; van Otterloo et al., 2015), we apply the glass transition limit using a smooth-heaviside step function of temperature,

$$hs_{sm} = \left\{1 + exp\left[\frac{-6}{\Delta T_g}\left(T - \left(T_g + \frac{\Delta T_g}{2}\right)\right)\right]\right\}^{-1}, \tag{46}$$

where ΔT_g is the glass transition temperature range, with typical values of ~ 50 K (Giordano et al., 2005). Using hs_{sm} to scale ζ with temperature (**Figure 3C**), **Eq. 44** becomes:

$$\zeta_i = hs_{sm}\begin{cases} \zeta\dfrac{1-n_{si,f}}{n_{s\phi_\mu,f}} & \phi_i < \phi_\mu \\ 0 & \phi_i \geq \phi_\mu, \end{cases} \tag{47}$$

and the effective fragmentation energy efficiency for determining total fragmentation energy from the PSD is

$$\zeta_{eff} = \sum_{i=1}^{N_\phi}(1-n_{bi})n_{s,i}\zeta_i. \tag{48}$$

Note that fracturing and fragmentation can in reality still occur once the bulk temperature cools below T_g, contrary to our assumption here. However, due primarily to a decrease in thermal expansion coefficient below T_g (Bouhifd et al., 2015), we assume that thermal stresses below T_g are insufficient to cause substantial further alteration to the PSD and magmatic energy budget (the PSD is considerably enriched in fine ash already at external water mass fractions sufficient to cool below T_g, see **Figure 3**). See **Supplementary Material Section S2** and **Supplementary Figure S4** for a discussion of the rationale for **Eqs. 46–48** based on thermal stress estimates. The PSD of the coarse particle fraction (i.e., particle sizes that experience mass loss due to quench fragmentation), $n_{si,0}$, is calculated as proportional to available particle surface area in each size bin, modified by the fragmentation efficiency (**Figure 3A**, gray lines):

$$n_{si,0} = \frac{\zeta_i S_i n_{s,i}\,(1 - n_{bi})}{\sum_{i=1}^{N_\phi} \zeta_i S_i n_{s,i}\,(1 - n_{bi})}. \tag{49}$$

Finally, we define the specific fragmentation energy (per mass of pyroclasts in the jet)

$$\Delta E_{ss} = \frac{\zeta_{eff}}{1 - \zeta_{eff}} \frac{\Delta h_w}{q_s} \frac{dq_{w,e}}{dz}, \tag{50}$$

and the change in mass of the pyroclast fraction due to gas release from vesicles on fragmentation

$$\frac{dm_{w,fr}}{dz} = m_s \frac{\Delta E_{ss}}{S_f E_s} \left[\sum_{i=1}^{N_\phi} \frac{n_{bi} n_{s,i}}{1 - n_{bi}} - \sum_{i=1}^{N_\phi} \frac{n_{bi}\left(n_{s,i} + \frac{dw_{s,i}}{dz}\right)}{1 - n_{bi}} \right], \tag{51}$$

where we choose $E_s = 100$ J/m^2 for the particle surface energy for fragmentation (Dürig et al., 2012; Hajimirza et al., 2022). The final system of differential equations for evolution of the PSD, and conservation of water mass, pyroclast mass, momentum, and energy, are respectively

$$\frac{dn_{s,i}}{dz} = \frac{\Delta E_{ss}}{S_f E_s}\left(-n_{si,0} + n_{si,f}\right), \tag{52}$$

$$\frac{dq_w}{dz} = \frac{dq_{w,e}}{dz} + \frac{dq_{w,fr}}{dz}, \tag{53}$$

$$\frac{dq_s}{dz} = -\frac{dq_{w,fr}}{dz}, \tag{54}$$

$$\frac{d}{dz}\left(\rho u^2 a^2\right) = g\left(\rho_w - \rho\right) r^2, \tag{55}$$

$$\frac{d\dot{E}}{dz} = \frac{dq_{w,e}}{dz}\left(g' z + h_w\right) - q_s \Delta E_{ss}. \tag{56}$$

Figure 3D shows the evolution of the total PSD during water entrainment and quench fragmentation in the MWI stage of the model according to **Eq. 52**. The coarse to mid-size fraction of particles ($-3 \lesssim \phi \lesssim 2$) of particles deplete fastest owing to the surface area dependence in **Eq. 49**. For example results of the MWI model, see **Section 3.2**.

2.4 1D Plume Model

For jets that breach the water surface, conditions at $z = Z_e$ are taken as the source parameters for the integral plume model. We use the integral plume model of Degruyter and Bonadonna (2012), modified with the particle fallout parameterization of Girault et al. (2014) to simulate differences in sedimentation in the eruption column as a function of fine ash production. **Figure 3E** shows the total PSD evolution due to particle fallout in the eruption column for a PSD that has been fines-enriched during MWI. The conservation equations for mass of dry air, water vapor, liquid water, and particles are, respectively

$$\frac{d}{dz}\left(\rho_a u a^2 \chi_a\right) = 2 v_\varepsilon a \rho_{a,e}\, \chi_{a,e}, \tag{57}$$

$$\frac{d}{dz}\left(\rho_v u a^2 \chi_v\right) = 2 v_\varepsilon a \rho_{v,e} \chi_{v,e} - \lambda \rho_v a^2 \chi_v, \tag{58}$$

$$\frac{d}{dz}\left(\rho_l u a^2 \chi_l\right) = \lambda \rho_v a^2 \chi_v, \tag{59}$$

$$\frac{d}{dz}\left(\rho_{s,i} u a^2 \chi_{si}\right) = -\xi \frac{q_s n_{s,i} u_{\phi,i}}{au}, \tag{60}$$

where v_ε is the entrainment velocity, subscript a denotes properties for dry air, $\lambda = 10^{-2}$ s^{-1} is a constant condensation rate (Glaze et al., 1997), $u_{\phi,i}$ are particle settling velocities following Bonadonna et al. (1998), and $\xi = 0.27$ is the particle fallout probability. The equations for vertical momentum and energy are, respectively:

$$\frac{d}{dz}\left(\rho u^2 a^2\right) = g\left(\rho_e - \rho\right) a^2 - w \frac{d\left(\rho u r^2\right)}{dz} + u \sum_{i=1}^{N_\phi} \frac{dq_{s,i}}{dz}, \tag{61}$$

$$\frac{d}{dz}\left(\rho C T u a^2\right) = C_e T_e \rho_e a u_\varepsilon - \rho u a^2 g + L \frac{d}{dz}\left(\rho_l u a^2 \phi_l\right) + C_s T \sum_{i=1}^{N_\phi} \frac{dq_{s,i}}{dz}, \tag{62}$$

where C_s and C_e are the heat capacities of particles and air, respectively, T_e is the ambient air temperature, and L is the latent heat of condensation of water vapor. Note that the plume model retains the capability for simulating cross-winds as in Degruyter and Bonadonna (2012), but we show here only the vertical component of the momentum equation as we do not consider wind effects (wind fields are set to zero in atmospheric profiles). For further details on the plume model, we refer the reader to Degruyter and Bonadonna (2012, 2013), and to Girault et al. (2014) for the particle fallout details.

2.5 Simulation Scenarios

The conduit, MWI, and plume models are solved in series, with the conduit model providing source conditions for the MWI model, and the MWI model, in turn, providing source conditions for the plume model. As described above, our model approach is to simulate eruptions across a parameter space with $10^{5.5} \leq Q_0 \leq 10^9$ kg/s and $0 \leq Z_e \leq 500$ m. In **Table 2** we define the *Reference* scenario which employs default values as described above for the various model parameters. Specifically, the *Reference* scenario uses a water entrainment scheme that includes both decompression and cross-over length scalings, and default fragmentation parameters $\Lambda = 10$, $\zeta = 0.1$, $D = 2.9$. The atmospheric profile used in the *Reference* scenario is obtained

TABLE 2 | List of simulations sets highlighting varied model parameters: Atmospheric profile, external water temperature T_e, decompression length switch, crossover length switch, entrainment equation, PSD power-law exponent D, particle roughness scale Λ, and fragmentation energy efficiency ζ.

Name	Atmosphere	T_e (K)	use L_d?	use L_X?	α Equation	D	Λ	ζ
Reference	Iceland	274	Yes	Yes	28	2.9	10	0.1
Low-Lat	Ecuador	294	Yes	Yes	28	2.9	10	0.1
No-L_d	Iceland	274	No	Yes	28	2.9	10	0.1
No-L_X	Iceland	274	Yes	No	28	2.9	10	0.1
No-L_d-No-L_X	Iceland	274	No	No	28	2.9	10	0.1
αRT	Iceland	274	Yes	No	36	2.9	10	0.1
High-Λ	Iceland	274	Yes	Yes	28	2.9	25	0.1
High-ζ	Iceland	274	Yes	Yes	28	2.9	10	0.2
Low-ζ	Iceland	274	Yes	Yes	28	2.9	10	0.05
High-D	Iceland	274	Yes	Yes	28	3.2	10	0.1

from ERA reanalysis data for the 2011 eruption of Grímsvötn Volcano (Hersbach et al., 2020; Aubry et al., 2021a), and we use a vent altitude of 1700 m above sea level. Note that we are not attempting to reproduce precise conditions for that eruption, but rather use this as a representative environmental condition for a high-latitude subglacial or sublacustrine eruption. To explore the effects of various model assumptions and parameter choices, we carried out nine additional simulation scenarios in addition to the *Reference* scenario, with each varying a single model parameter and performed over the same parameter space for MER and water depth. The second scenario we define, *Low-Lat*, uses an ERA reanalysis atmospheric profile for the 2014 eruption of Tungarahua Volcano with vent altitude 0 m a.s.l. as a representative atmosphere for a low-latitude submarine setting, keeping other parameters the same as the *Reference* scenario (see **Supplementary Figure S5** for a comparison of atmospheric profiles used in the *Reference* and *Low-Lat* scenarios). Additional scenarios are broadly categorized into those with differing water entrainment assumptions and those with different fragmentation parameters relative to the *Reference* scenario. Entrainment scenarios include those without one or both of the decompression and crossover length scalings (*No-L_d*, *No-L_X*, and *No-L_d-No-L_X*), and a scenario with the Rayleigh-Taylor entrainment scheme of **Eq. 35** (*αRT*). Additional fragmentation scenarios include one with a higher particle roughness (*High-Λ*), higher and lower fragmentation energy efficiencies (*High-ζ* and *Low-ζ*), and a higher initial PSD power-law exponent (*High-D*). We highlight the effects of different entrainment scenarios in **Section 3.2**, and discuss the consequences of different parameter choices for these scenarios in **Section 4**.

3 RESULTS

3.1 Conduit Flow: Effects of an External Water Layer

An external water layer modifies the hydrostatic pressure in the conduit, which affects water saturation and exsolution, and in turn, magma decompression rate and fragmentation conditions (Cas and Simmons, 2018). In **Figure 4**, we compare conduit model output for control (Z_e = 0 m, red lines) and hydrovolcanic (Z_e = 400 m, blue lines) simulations for $Q_0 \sim 1.6 \times 10^8$ kg/s. In the dry scenario, gas exsolution begins with an initial bubble nucleation event at a depth of 5.5 km below the vent (panel (e)). Above the first nucleation event, gas exsolution continues, driving increasing magma buoyancy, ascent and decompression rates. A sharp increase in exsolution and bubble growth near z = 1.3 km drives the gas volume fraction above the fragmentation threshold of 75% (panel (d)). At this depth, fragmentation occurs and the flow becomes a fluidized mixture of gas and suspended pyroclasts. Above this fragmentation depth, the flow accelerates to the mixture sound speed near the vent and becomes choked (panel (b)). At the vent the choked flow has a significant overpressure with $\beta \approx 11$ (panel (a) inset), and erupts to form an explosively decompressing subaerial jet.

Consistent with previous studies of subaqueous eruptions, the higher hydrostatic pressure at the vent in the hydrovolcanic case results in less gas exsolution and bubble growth, and consequently a slower decompression rate in the ascending magma (Cas and Simmons, 2018). Slower exsolution also results in lower total gas exsolution from the magma, and lower gas volume fraction above fragmentation (panel (d)). Above the fragmentation depth in the wet scenario, both the reduced mixture buoyancy related to a lower fraction of free gas and the higher hydrostatic pressure contribute to a reduced acceleration of the mixture, and the flow is subsonic ($M \approx 0.5$, panel (b)) and pressure-balanced ($\beta \approx 1$, panel (a) inset) at the vent. For this water depth and MER, we consequently find no viable conduit solution where the vent is choked (see also **Supplementary Figure S2** for conduit solution search details). Across all model scenarios (see **Table 2**), water depths sufficient to cause this pressure-balanced condition usually lead to a weak jet that does not breach the water surface and/or to a steam plume condition (see **Section 3.3** and **Figure 9** below).

Figure 5 shows select parameters of the conduit model output as a function of MER and water depth, including vent overpressure ratio (panel (a), color field and contours), Mach number at the vent (b), MER adjustment relative to control runs (c), magma decompression rate at fragmentation depth (d), fragmentation depth (e), and the weight percent of residual water content dissolved in the pyroclasts at vent level (f). For the control runs (Z_e = 0), the vent is always overpressured and choked, with $\beta \to 45$ for the largest values of MER. Overpressure declines rapidly with

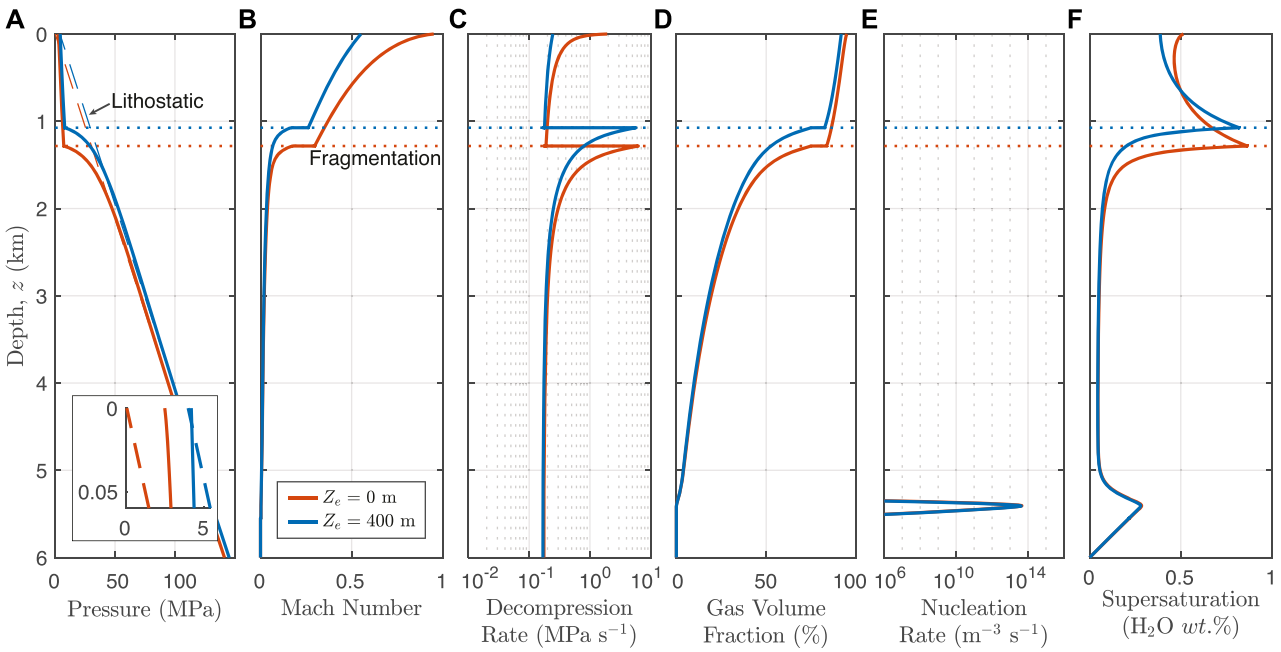

FIGURE 4 | Example conduit model output from the *Reference* set (see **Table 2**) versus depth below the vent for a pair of simulations: red lines show a "dry" control run with a_c = 53.8 m, Z_e = 0, and Q_0 = 1.6 × 10^8 kg/s. Blue lines show a hydrovolcanic scenario with a_c = 53.8 m, Z_e = 400 m, and q_c = 1.53 × 10^8 kg/s (blue lines). **(A)** Magma pressure. Inset: pressure in the top 60 m of the conduit (same units as panel **(A)** axes), highlighting the vent overpressure of the control run versus the pressure-balanced vent of the hydrovolcanic run. **(B)** Mach number. **(C)** Decompression rate. **(D)** Gas Volume Fraction. **(E)** Bubble Nucleation Rate. **(F)** Supersaturation of dissolved water (i.e., difference between dissolved water c_{H_2O} and water solubility).

increasing water depth until choking at the vent is impossible and the gas-pyroclast mixture enters the water layer as a pressure balanced, subsonic jet (solid blue line in panels (a),(c),(d)). We find that the largest water depth for which choking is possible is typically equal to about five vent radii. For example, for Q_0 = 10^7 kg/s, conduit radius a_c = 20 m, and the choking threshold depth occurs at ~100 m, whereas this threshold increases to ~220 m for Q_0 = 10^8 kg/s and a_c = 45.5 m. For depths greater than the choking limit, the Mach number falls off rapidly to values of 0.5 and 0.1 for depths equal to about 10 and 30 vent radii, respectively. For sufficiently large water depths and small MER, we find no conduit solutions in which fragmentation occurs (blue region, panel (a) top-left). As introduced in **Section 2.2**, for hydrovolcanic runs we adjust the MER relative to control runs to match the vent boundary condition. **Figure 5C** shows the ratio of adjusted MER to control MER, q_c/Q_0, which for control simulations is always equal to 1 by definition. The adjustment is minor (no more than about 10%) and positive in most cases where vent choking is maintained. For water depths greater than the choking threshold, q_c begins to decrease, reaching values as low as 20–30% of Q_0 for low MER and large water depths. This trend is, however, not universal: for low MER, a strong second nucleation event occurs near the fragmentation depth and leads to relatively larger values of released gas and consequently greater MER until water depths of about 150–200 m (panels (c) and (f), lower-left corner).

Figure 5D shows the peak magma decompression rate $\dot{p}$ at the fragmentation depth. Where the choking condition holds, peak decompression rate ranges between about 4 and 7 MPa/s and varies with MER, but for all depths greater than about five vent radii, decompression rate decreases, falling to values well below 3 MPa/s for depths greater than about 15–20 vent radii. The blue dashed line in panel (d) shows the maximum water depth for which peak bubble overpressure $\Delta p_b = p_b - p_m$ (i.e., the difference between the gas pressure inside bubbles and pressure in the ascending magma *at the fragmentation depth*) is equal to 5 MPa, which is an approximate low bound for the tensile strength of the magma (Cas and Simmons, 2018). Our fragmentation criterion allows fragmentation regardless of peak decompression rate or bubble overpressures, so long as sufficient vapor exsolution occurs to reach a porosity of 75%. However, the decrease in both maximum decompression rate and maximum bubble overpressure with increasing water depth has important implications if alternative criteria for magma fragmentation are considered, which we discuss further in **Section 4.3**. Fragmentation depth (panel (e)) is governed by decompression and gas exsolution rates and decreases with both increasing MER and increasing hydrostatic pressure, reaching about 500 m at its shallowest for the largest values of MER and water depth. As shown in **Figure 5F**, we find that for $Q_0 \lesssim 3 \times 10^6$ kg/s and $Ze \lesssim$ 150–200 m, a second nucleation event in the conduit near fragmentation results in a notably higher total gas exsolution from pyroclasts (a difference of up to about 0.5 wt%). Higher total gas exsolution increases the free gas mass fraction at the vent, which in turn slightly boosts vent overpressure and adjusted MER. Importantly for our results, enhanced gas

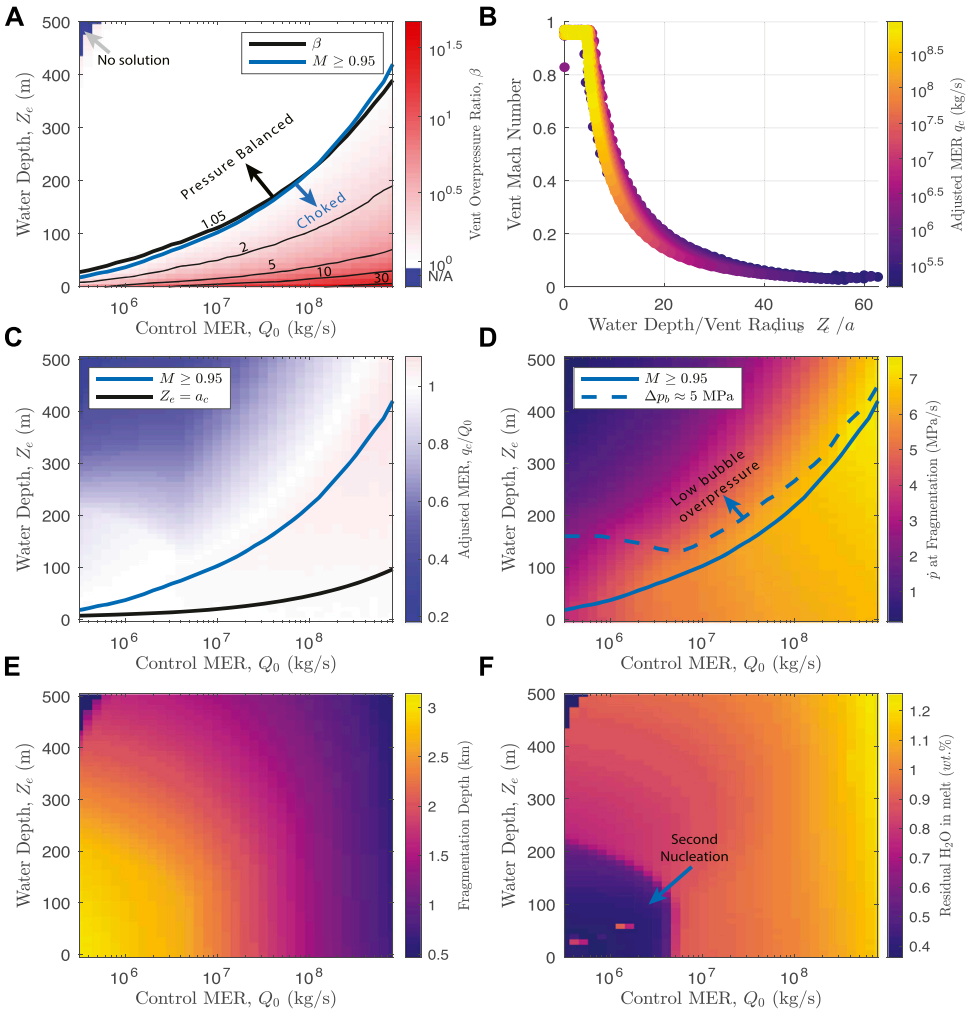

FIGURE 5 | Conduit model output as a function of control MER, Q_0, and external water depth, Z_e. **(A)** Vent overpressure β. The blue line in panels **(A,C,D)** denotes the tolerance threshold for Mach number (M = 0.95), and the red line is the (approximately coincident) vent overpressure threshold, β = 1.05. The vent is choked and overpressured for water depths less than this. The blue region in the top left (high Z_e and low Q_0 are failed simulations - no viable conduit solutions were found in this region. **(B)** Vent Mach number. **(C)** Mass eruption rate adjustment for fixed conduit radius, relative to the control case for Z_e = 0. **(D)** Maximum decompression rate recorded at fragmentation (χ_0 = 0.75). The dashed blue line highlights the maximum water depth for which peak bubble overpressure is at least 5 MPa, which is an approximate low bound for bubble wall rupture (Cas and Simmons, 2018). **(E)** Fragmentation depth. **(F)** Residual dissolved water in pyroclasts at the vent, highlighting a strong second nucleation event for low MER and water depths less than about 200 m.

exsolution alters the glass transition temperature according to **Eq. 45**, with consequences for quench fragmentation during MWI that we discuss below.

3.2 Magma-Water Interaction Model and the Effects of Water Entrainment

Figure 6 shows MWI model results for four simulation scenarios with different water entrainment parameterizations: the *Reference* scenario (blue) with scalings for both decompression length (L_d, **Eqs. 14–20**) and crossover length (L_X, **Eqs. 29–33**), no crossover length scaling (*No-*L_X, red), no decompression length (*No-*L_d, purple), and with the weighted Rayleigh-Taylor entrainment coefficient in **Eqs. 35** and **36** (αRT, light blue). In the simulation shown (q_c = 1.03 × 10^8 kg/s, and Z_e = 120 m), the jet in the *Reference* scenario begins entraining water after decompression at a height of about 55 m above the vent. In contrast to a sub-aerial jet, the gas jet is buoyant in sub-aqueous settings and accelerates towards the water surface (panel (a)). Bulk temperature (panel (b)) decreases with water entrainment, and bulk density (panel (c)) decreases from both an increase in the vapor mass fraction (panel (d), solid lines) and decompression as the jet moves upwards in the water column. New ash surface area is produced through quench fragmentation (panel (e)), proportional to the mass of water ingested. This process proceeds until the mixture cools below the glass transition at a height of about 105 m above the vent (marked with circle symbols in panels (b) and (e)), after which no additional ash surface area is generated. The effective entrainment coefficient (panel (f)), scaled by L_X (**Eq. 31**), grows approximately linearly

from an initial value of zero according to **Eq. 33**, resulting in a continuous increase in the rate of water ingestion. In the *No-L_X* scenario, the entrainment coefficient is equal to that given by **Eq. 27**. Here, the entrained mass of water rises much more sharply with height and causes the mixture to reach the glass transition by around 10 m of above the decompression length L_D. Furthermore, in these calculations water vapor saturation is reached after only 25 m of rise. Above water saturation, the liquid water fraction in the jet increases rapidly with height (panel (d), dashed lines). The concomitant increase in density reduces jet acceleration relative to the *Reference*, until breach of the water surface occurs. In the *No-L_d* scenario, the entrainment coefficient initiates at a value of zero as in the *Reference*, but entrainment begins from $z = 0$ rather than $z = L_d$. The crossover length $L_T = 230$ m is greater than water depth for this event, and consequently the entrainment rate increases over the full height of the water layer (see **Eqs. 32** and **33**), reaching a larger maximum value at the water surface ($\alpha = 0.076$ versus $\alpha = 0.04$ in the *Reference*). The bulk mixture temperature for the *No-L_d* scenario reaches the saturation temperature at a height of 80 m, and ultimately a similar total mass of entrained water to the *No-L_X* scenario on reaching the water surface (about 45 wt%). The *αRT* scenario uses a weighted combination of entrainment coefficients driven by buoyancy and turbulent shear. Buoyancy-driven entrainment in **Eq. 36** is approximately proportional to the surface area to volume ratio of the plume, i.e., $\alpha_{RT} \propto a^2/q_c$. For the relatively large MER shown here, q_c dominates in the above ratio resulting in a low value of α_{RT}, and the weighted α_{eff} is consequently a middle value between the *Reference* and *No-L_X* scenarios. We further discuss the consequences of these water entrainment scenarios in **Sections 3.3** and **4.1**.

For a specified fragmentation efficiency ζ, the production of ash surface area from quench fragmentation increases with the extent of water entrainment, which increases with water depth (see **Eq. 38**). Quench fragmentation proceeds rapidly compared with the timescale for the jet to cross the water layer (**Figures 3D**, **6E**). In the model, the primary limit for fine ash production is, thus, the height at which water entrainment causes the mixture temperature to become less than the glass transition temperature. For $C_m = 1250$ J/(kg K) and $T_0 = 1123$ K, this condition is met where $n_e \gtrsim 0.12$. However, even with this imposed temperature limit for quench fragmentation, **Figure 3D** shows that the PSD is substantially enriched in fine ash for this mass fraction of entrained water. For an initial PSD exponent of $D = 2.9$ (**Figure 3D**, light grey line), the mass fraction of ash particles less than 120 μm ($\phi \leq 3$) is about 45%, while it is 80% after the glass transition is passed (**Figure 3D**, black line). Therefore in the absence of the glass transition limit, coarse particles could be fully depleted. In **Section 4** we further discuss the consequences of our choice of fragmentation model and the associated key parameters: initial PSD, particle roughness, fragmentation energy efficiency, and glass transition temperature.

3.3 Effects of the Water Layer on Column Rise

Figure 7 shows eruption column model results for two example simulations with $Q_0 = 10^7$ kg/s: a control simulation ($Z_e = 0$ m), and a hydrovolcanic case with $Z_e = 70$ m. Dashed grey lines show parameters of the ambient atmosphere. The control scenario (in red) inherits conditions directly from sub-aerial vent decompression: bulk density (panel (a)) is determined by the mass fractions of pyroclasts and magmatic vapor (shown in panels (e) and (f), respectively), velocity (panel (b)) is equal to the mixture sound speed, and the bulk temperature is equal to the initial value in the conduit (panel (d)). The jet cools rapidly with entrainment of ambient air and condensation of water vapor begins shortly above the vent, though the liquid mass fraction remains below 1% (panel (f), dashed lines). The jet becomes buoyant (density less than ambient atmosphere) within a few hundred meters of the vent, becomes negatively buoyant above the neutral buoyancy height of about 9 km above the vent (Z_{nbl}), and rises to a maximum overshoot height $Z_{\max}$ of over 12 km. In contrast, the hydrovolcanic simulation emerges at the water vapor saturation temperature, $T_{sat} = 367\,K$, with a total water mass fraction of 46% (near the threshold for gravitational collapse). Acceleration through the water layer results in a higher initial velocity relative to the control simulation (see **Figure 6A**), and the high mass fraction of water vapor gives the initial jet a relatively low density. However, due to the low temperature and increasing density from condensation, the hydrovolcanic jet generates buoyancy much more slowly than in the control case, becoming buoyant relative to ambient 3 km above the vent. The reduction in total buoyancy flux results in maximum height and neutral buoyancy level approximately 1.5 km and 700 m less than the control case, respectively.

To demonstrate behavior of the coupled system, **Figure 8** shows values of controlling parameters in the conduit, vent, and column model components for *Reference* simulations with $Q_0 = 10^8$ kg/s and varying water depths $0 \leq Z_e \leq 300$ m. **Figure 8A** compares the eruption column maximum height and level of neutral buoyancy (in km above sea level) against tropopause and vent altitudes. Panels (b) through (e) highlight parameters of the conduit including adjusted MER q_c, fragmentation depth Z_{frag}, vent overpressure β, and vent Mach number M. Panels (f) through (i) show output of the MWI model. Panel (f) shows the scalings for decompression L_d and crossover length L_X, and panel (g) shows the maximum value of the effective entrainment coefficient over the height of the water layer (as determined by **Eqs. 27** and **33**, see **Figure 6F**). Panels (h) and (i) show jet radius and velocity, respectively, at two different heights: after decompression $z = L_d$ and at the water surface level $z = Z_e$ (water surface level also corresponds to the eruption column source height as shown in **Figure 2**). Finally, panels (j) and (k) show the water mass fractions (vapor and liquid) and temperature for the eruption column source (i.e. $z = Z_e$). In all panels in **Figure 8**, vertical dashed lines show the threshold water depths for four important behavior regimes: 1) the height at which water depth and decompression length are equivalent $L_d = Z_e$, 2) the water depth above which the subaerial eruption column collapses before reaching a level of neutral buoyancy, 3) transition at the vent between a pressure balanced jet at high Z_e and one that is overpressured and choked ($\beta \gtrsim 1.05$, $M \gtrsim 0.95$) at lower Z_e, and 4) the depth above which the water dryness fraction $x_v \lesssim 0.05$, where at most minor quantities of steam breach the water surface

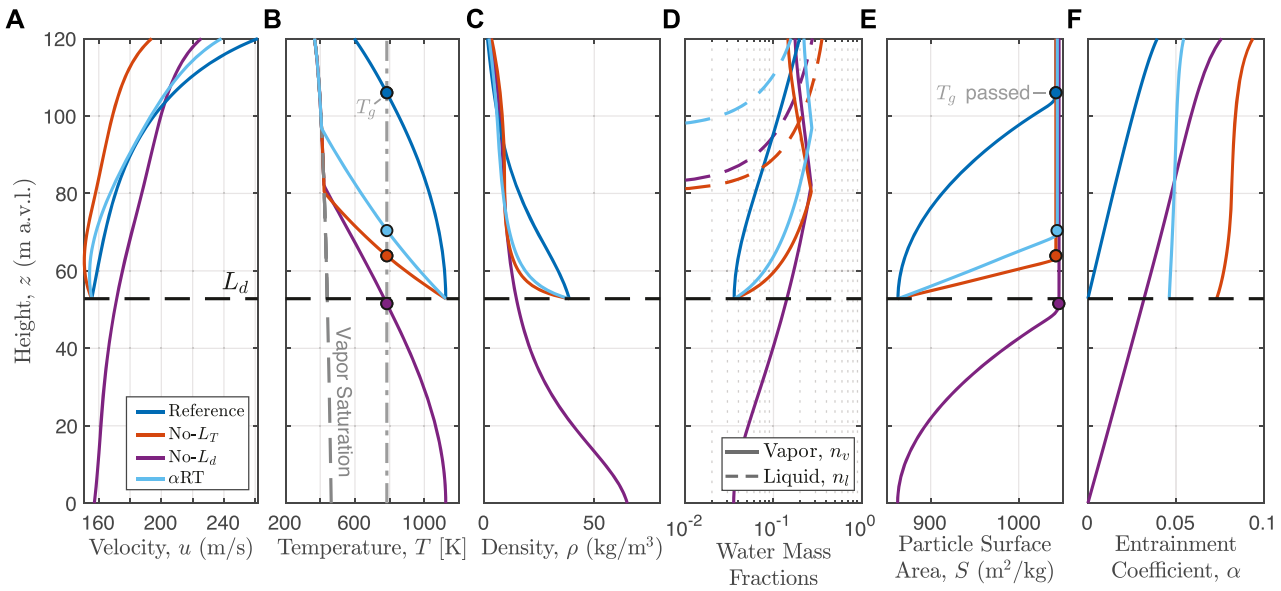

FIGURE 6 | Example MWI model parameters versus position in the water layer above the vent for a single simulation at $q_c = 1.03 \times 10^8$ kg/s, and $Z_e = 120$ m. Four different water entrainment scenarios are shown: the *Reference* scenario using an entrainment condition modified by both decompression and crossover length scales (blue), a scenario with no scaling for turbulent mixing length (*no-*L_X, red), a scenario with no decompression length scale, where entrainment initiates immediately at the vent (*no-*L_σ, purple), and a scenario using the weight Rayleigh-Taylor entrainment mode of **Eq. 35** (αRT scenario, light blue). **(A)** Vertical velocity. **(B)** Jet mixture temperature. **(C)** Jet bulk density. **(D)** Jet water liquid and vapor mass fractions. **(E)** Specific surface area of pyroclasts. **(F)** Local entrainment coefficient. Colored circles in **(B,E)** highlight the crossing of the glass transition temperature.

(the "steam plume" condition as introduced in **Section 2.3.3**). The decompression length L_d defines the lower limit for water entrainment to start, and decreases with increasing hydrostatic pressure. For water depths in excess of L_D (panel (f)), water begins to entrain and mix into the jet, whereas our decompression length scaling prevents water ingestion for shallower depths (panel (g)). As the water mass fraction increases above about 30%, the water saturation temperature is reached and the column source includes liquid water (panel (j)), increasing its density. Consequently, jet velocity (panel (i)) decreases for greater water depths, and combined with reduced heat content in the particle fraction to generate buoyancy (panel (k)), it becomes impossible for the jet to undergo a buoyancy reversal, and gravitational collapse occurs (panel (a)). Since the vent maintains the choked and overpressured condition until depths greater than the collapse threshold, the collapse condition for the subaerial column is not significantly influenced by changes in conduit conditions with increasing water depth, and is primarily determined by the mass fraction of entrained external water. At the upper limit for water entrainment, once the water mass fraction reaches ~ 0.7, the heat budget of the pyroclasts is largely exhausted and most of the plume water ($\gtrsim$ 95% by mass) is in liquid form, resulting in steam plume conditions where the a dense pyroclast jet collapses within at most ~1 km above the water surface.

Figure 9A shows total plume water mass fraction at the base of the subaerial eruption column as a function of MER and water depth for the *Reference* scenario. For comparison, the vent radius is marked in purple. The hatched light gray region highlights conditions for which stable buoyant plumes form, whereas collapse occurs for all simulations outside this region. At slightly lower water depths than the collapse threshold and for MER $\gtrsim 10^6$ kg/s, buoyant plumes breach the tropopause (tropopause height $Z_{tp} \approx 8.6$ km a.s.l. for the high latitude atmosphere used in the *Reference* scenario). The critical conduit MER for stratospheric injection, Q_{crit}, is highly sensitive to water depth. For example, the MER required for a buoyant column to reach the tropopause for a water depth of 150 m is over 10 times that for a water depth of 50 m, and nearly 100 times that for a subaerial vent. This is driven primarily by the shift of the column collapse condition with increasing water depth (see also **Figure 10**). A notable feature is that for MER $\gtrsim 10^{8.3}$, the column collapses for the control case with no external water, but becomes a buoyant column for entrained water mass fractions up to ~ 30%. In addition, low MER eruptions are able to support higher mass fractions of external water without collapse (e.g. $n_w \approx 45\%$ for $q_c = 10^7$ kg/s versus $n_w \approx 35\%$ for $q_c = 10^8$ kg/s). The relative buoyancy of low MER columns is caused by more efficient entrainment of air at smaller jet radii, as well as entrainment of atmospheric humidity and condensation and latent heat release in the plume. We note that condensation of atmospheric moisture has a more significant impact on buoyancy for smaller MER in the condensation parameterization used here (Glaze et al., 1997; Aubry and Jellinek, 2018). The solid blue line in **Figure 9A** marks the threshold where weak steam plumes may form, or fail to breach the water surface entirely for greater depths still. In the *Reference* scenario, the steam plume threshold is approximately coincident with the water depth limit for choked and overpressured vents. This limiting condition is a consequence

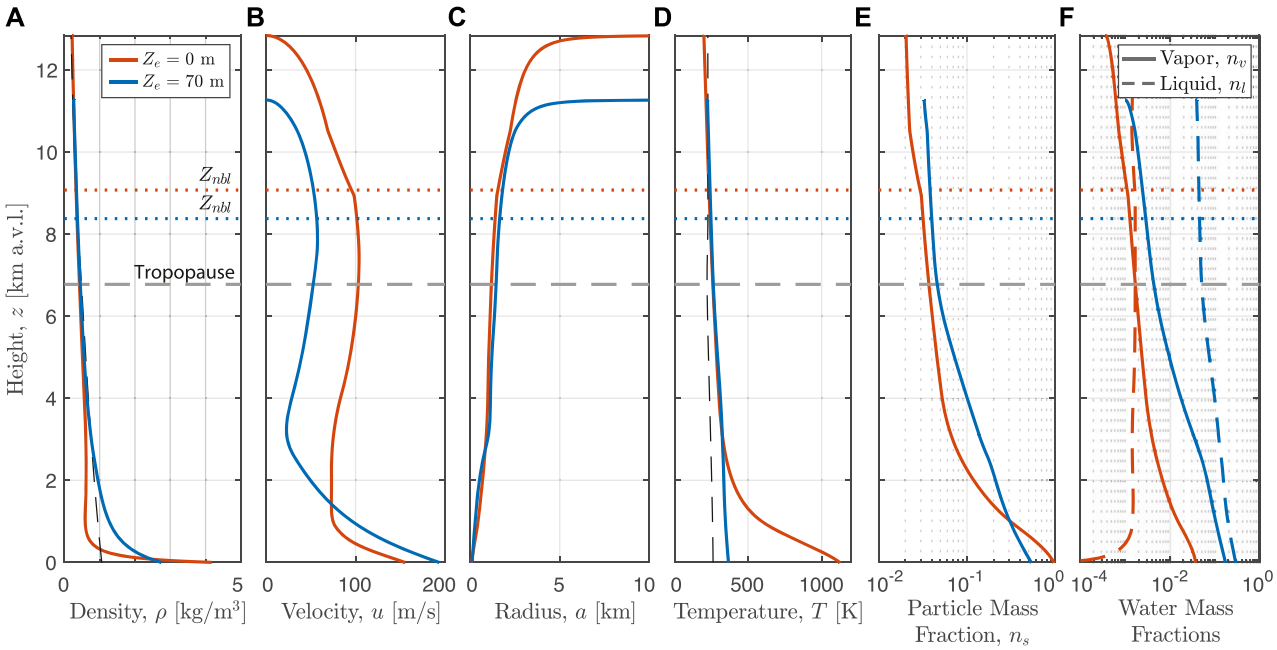

FIGURE 7 | Example plume model output from the *Reference* set (see **Table 2**) versus height above the vent for a pair of simulations: red lines show a "dry" control run with a_c = 20.0 m, Z_e = 0, and Q_0 = 1.00 × 10^7 kg/s. Blue lines show a hydrovolcanic scenario with a_c = 20.0 m, Z_e = 70 m, and q_c = 1.01 × 10^7 kg/s (blue lines). **(A)** Bulk density. **(B)** Vertical velocity. **(C)** Column Radius. **(D)** Bulk temperature. **(E)** Particle mass fraction. **(F)** Water liquid and vapor mass fractions. Horizontal dotted lines show the level of neutral buoyancy for each case, and the horizontal dashed gray line shows the height of the tropopause (note y-axis is kilometers above vent level).

of greater entrainment efficiency near the choking limit; Since $L_d \rightarrow 0$ as $\beta \rightarrow 1$, and entrainment rate grows over the height of the water column until $z = L_d + L_X$, maximum water entrainment rates are favored for pressure-balanced jets. However, the choking and steam plume limits need not be coincident, as shown in **Figure 9B**.

Figure 9B shows the threshold water depths for failed plumes (dashed lines) and stratospheric injections (solid lines), for a subset of the simulation scenarios (see **Table 2**). The black lines in panel (b) are for the *Reference* scenario with high latitude (Iceland) atmosphere (corresponding to the solid blue line for steam plumes and solid black line for stratospheric injection in panel (a)). Blue lines show the scenario for low latitude (Equador) atmosphere (*Low-Lat*). Neglecting the effects of wind, atmospheric humidity, stratification, and tropopause height are the primary drivers of differences between these two scenarios, particularly affecting the low values of Q_{crit} for water depths less than about 60 m. The remaining lines in **Figure 9B** show the results of the different entrainment scenarios in the MWI model as shown in **Figure 6** and **Table 2**. With the exception of the αRT scenario, these alternative scenarios for water entrainment lead to more rapid mixing of the jet with external water, thereby reducing the maximum depth of water through which the jet can penetrate and increasing the critical MER required to reach the tropopause. For the αRT scenario, the dependence of the entrainment coefficient on jet surface area to volume ratio (see **Eq. 36**) causes the collapse and steam plume conditions to occur at shallow water depths compared to *Reference* scenario for $Q_0 \lesssim 10^7$. In contrast as $Q_0 \rightarrow 10^8$, collapse conditions still occur for shallower water depths than the *Reference*, but the steam plume condition occurs at greater depths. For large MER, jet radius expands rapidly as the jet rises in the water column due to both decompression and an increase in steam volume fraction. As a consequence, α_{RT} decreases with height in the water column, reducing water entrainment rate and delaying the point at which the steam plume condition is reached. Critically, for all entrainment scenarios considered here, and regardless of the choice of atmospheric profile, we find that only the largest eruptions with $Q_0 \sim 10^9$ kg/s breach the tropopause for water depths greater than about 200 m.

Figure 10 shows example results of eruption column height at both high latitude (*Reference* scenario, left column) and low latitude (*Low-Lat*, right column). Panels (a), (b) show column heights at varying water depth for three control values of MER, and (c), (d) show heights for varying MER at three fixed values of water depth. Solid lines show maximum column height, dashed lines show neutral buoyancy height, open circles show thresholds for column collapse, and closed circles show the threshold for steam plumes. The dominant effect of added external water on column height is to drive column collapse, which is consistent with the results of previous integral models of hydrovolcanic columns (e.g., Koyaguchi and Woods, 1996; Mastin, 2007b). Panels (a) and (b) show that for buoyant plumes, column height is essentially unchanged for water depth below decompression length, while for greater depths there is a 10–25% decrease in column height. For relatively low water depths and low MER, the release of latent heat drives increased column height, particularly from entrained atmospheric moisture in a humid atmosphere (e.g., panel (b)

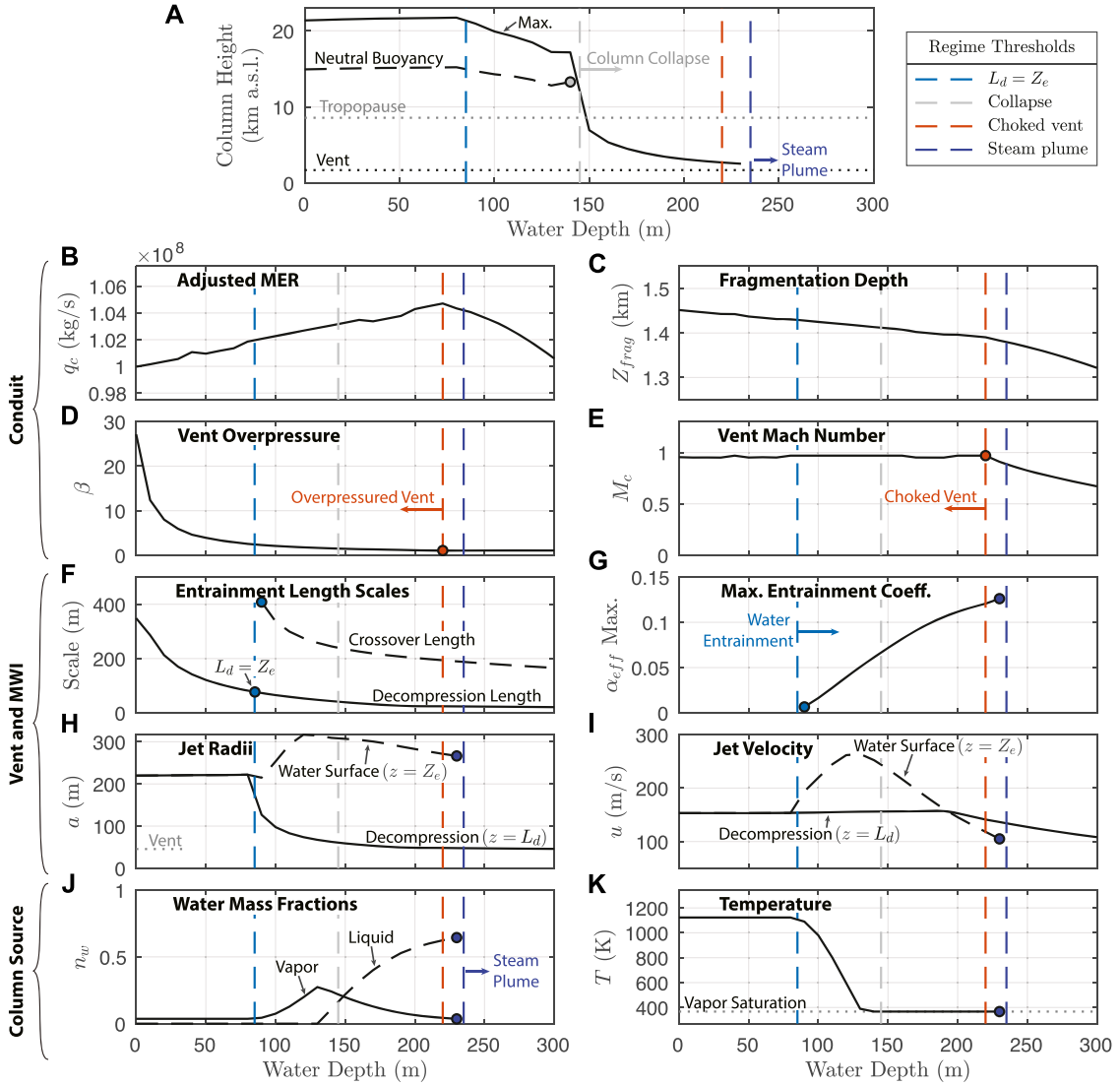

FIGURE 8 | Output of the coupled model (conduit, vent, and column) *Reference* scenario for $Q_0 = 10^8$ kg/s and a range of water depths. Behavior thresholds for decompression length, column collapse, vent choking, and steam plumes corresponding to regimes in **Figure 9A** are marked with vertical dashed lines. **(A)** Eruption column maximum height and neutral buoyancy height above sea level, shown with vent and tropopause altitude. Conduit results: **(B)** adjusted conduit MER q_c; **(C)** depth of fragmentation surface; vent **(D)** overpressure β and **(E)** Mach number M. MWI model results: **(F)** decompression L_d and crossover L_X length scales; **(G)** maximum value of the entrainment coefficient in the water layer; **(H)** radius of the vent and jet after initial decompression (at $z = L_d$) and at the water surface ($z = Z_e$) **(J)** velocity of the jet after initial decompression (at $z = L_d$) and at the water surface ($z = Z_e$). Column source conditions: **(J)** vapor and liquid water mass fractions **(K)** bulk mixture temperature.

for Z_e = 20 m and $Q_0 = 10^6$ kg/s). However, for the high latitude atmosphere this is largely offset by the decreases in total height resulting from changes to column source parameters (e.g., panel (a) for Z_e = 70 m and $Q_0 = 10^7$ kg/s, see **Figure 8**). Therefore in most cases, we find that both maximum height and neutral buoyancy levels of plumes decrease relative to the control simulations for increasing water depth. For buoyant plume scenarios with non-zero mass fraction of external water ($Z_e > L_d$), neutral buoyancy levels are typically reduced by 10–25%. Panels (c) and (d) show that increasing water depth narrows the range of MER for which buoyant columns may form. For example, at only 100 m of water depth, buoyant columns are restricted to MER between about 3×10^7 and 2×10^8 kg/s for the reference scenario, and an even narrower range for the low latitude atmosphere. Water depths greater than about 200–250 m result in either column collapse or failed plume conditions in our *Reference* simulations, except for very large MER ~ 10^9 kg/s.

3.4 Evolution of Particle Surface Area With Fragmentation and Sedimentation

Figure 11A shows particle specific surface area S (surface area per unit mass of particles - a metric for fine ash production) at the water surface after MWI, as a function of the concentration of

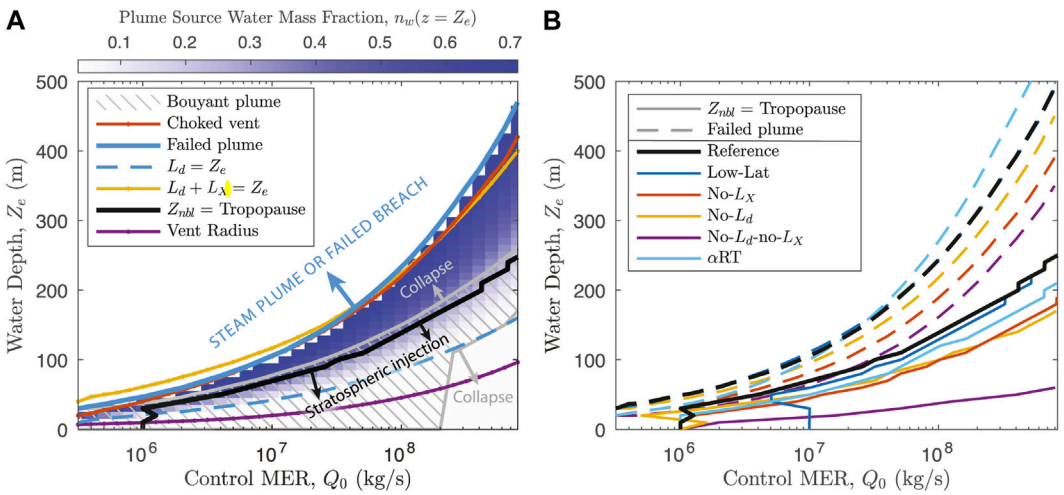

FIGURE 9 | (A) Plume source water mass fraction as a function of MER and water depth, with overlaid thresholds for behavior of the coupled conduit-plume system. The red line marks the threshold for which the vent is choked and overpressured, with pressure-balanced, subsonic jets occurring at deeper depths. The decompression length is equal to water depth at the blue dashed line, which is the depth above which water entrainment begins. Buoyant columns occur within the grey hatched region, with column collapse elsewhere. The steam plume threshold is marked by the solid blue line - failed plumes with only negligibly small amounts of steam reach the water surface for depths greater than this (indicated by the blue arrow). Finally, the solid black line marks the water depth above which bouyant columns breach the tropopause. **(B)** Variation in the critical MER to reach the tropopause (solid lines) and maximum water depth before plume failure (i.e. the steam plume condition, dashed lines) for different simulation scenarios (see **Table 2**). Black lines are for the *Reference* scenario (high latitude atmosphere), while blue lines are for the low latitude atmosphere. The remaining colors are for the four scenarios with different water entrainment parameterizations: no mixing length (*No-*L_X, red), no decompression length (*No-*L_d, yellow), neither mixing length nor decompression length (*No-*L_X*-no-*L_X, purple), and the weighted Rayleigh-Taylor entrainment mode (*αRT*, light blue).

residual water dissolved in the melt, c_{H_2O}. Symbol size represents MER for all panels in **Figure 11** and colors denote the mass fraction of entrained external water. The upper limit of S following quench fragmentation is determined in the model primarily by the glass transition temperature, T_g. Simulations with high rates of exsolution in the conduit (particularly those with strong second bubble nucleation events near the fragmentation depth, see **Figure 5F**) result in lower c_{H_2O} and higher T_g (see **Eq. 45** and **Figure 3B**) upon entering the water layer. Higher T_g in turn reduces the total thermal energy available for production of fine ash during quench fragmentation, and these events have PSD's with consequently lower particle surface area. Since total gas exsolution is inversely correlated with Q_0 in our conduit model, values of S after quench fragmentation increase with increasing Q_0, as shown by symbol size in **Figure 11A**.

Figure 11B shows S at both column source (i.e., water surface $z = Z_e$, grey symbols) and at maximum column height ($z = Z_{max}$, blue symbols) as a function of the water mass fraction at the plume source. In both panels (b) and (c), circles show buoyant plumes that do not breach the tropopause, 'x' symbols show collapsing columns, and diamonds show plumes that are both buoyant and of sufficient magnitude to breach the tropopause at the height of neutral buoyancy Z_{nbl}. Considering first values of S at the eruption column source (grey symbols, panel (b)), the sharp plateau in S above $n_w \approx 0.15$ in panel (b) is a result of cooling below the glass transition temperature, marked with a vertical blue bar (see also **Figure 6E**). For entrained water mass fractions greater than this, quench fragmentation halts and S remains approximately constant at a value determined primarily by the glass transition and the size of particles produced by quench fragmentation (see **Section 2.3.4** and **Figure 3**).

Blue symbols in panel (b) highlight the effects of sedimentation on ash surface area over the rise of the subaerial eruption column. The PSD is further enriched in fine ash following fallout of coarse particles, and S consequently increases with height of the eruption column. Furthermore, because the local rate of particle loss from the edges of entraining eddies is proportional to the ratio of particle fall speeds to the mixture rise speed according to **Eq. 60**, buoyant plumes with low MER, rise velocities, and radii have the largest increase in S during column rise. For collapsing columns ('x' symbols), S increases proportional to maximum height prior to collapse. Owing to a combination of fines enrichment from quench fragmentation and enhanced sedimentation due to reduced column rise speeds, all buoyant hydrovolcanic plumes (circle and diamond symbols) increase in particle specific surface area at their maximum height with increasing mass fraction of water.

The combined effects of quench fragmentation followed by sedimentation in the rising column influence both total retained mass of ash in the eruption cloud and the surface area per unit mass of particles. **Figure 11C** shows the fraction of total erupted particle mass remaining in the column at its maximum rise height, again as a function of water mass at the column source; symbols are as in panel (b), with colors showing S at maximum column height. Small

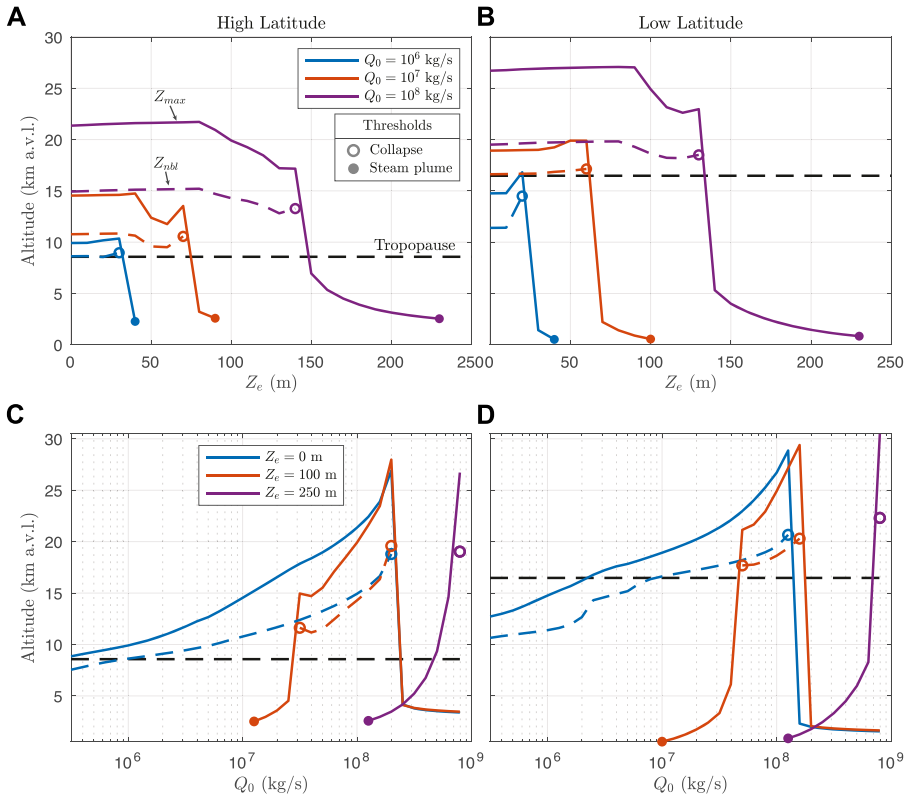

FIGURE 10 | Eruption column height (above vent level) versus **(A,B)** surface water depth for three control values of MER and **(C,D)** MER for three fixed values of water depth. Left column plots **(A,C)** are for high latitude and right column **(B,D)** for low latitude atmospheres. For all plots, solid lines denote maximum column height, Z_{max}, dashed lines are height of neutral buoyancy, Z_{nbl}, open circles indicate threshold values for column collapse, and closed circles indicate threshold values for steam plumes at the water surface.

eruptions that do not reach the tropopause (circle symbols) lose the greatest portion of their particle mass to sedimentation, while collapsing columns retain mass up to their (relatively much lower) maximum height before collapsing entirely. Of note, however, are the subset of eruptions that are both buoyant and of sufficiently high magnitude to breach the tropopause (highlighted with an arrow in panel (c)). With increasing water mass fractions, such events not only retain a greater portion of their initial pyroclast mass relative to control runs, but also have a more fines-enriched PSD in the spreading cloud as measured by the *S* parameter. Provided they generate buoyant eruption columns, the above results highlight the greater total flux of ash surface area to the spreading cloud for hydrovolcanic scenarios, with important implications for chemical and microphysical interactions with SO_2.

4 DISCUSSION

Here for the first time, we link the dynamics of magma flow in a volcanic conduit to the turbulent rise of an overlying subaerial eruption column for a submerged volcanic vent, using a model which governs water mixing into a gas-pyroclast jet and the coupled energetics of quench fragmentation. In marked contrast to previous studies which parameterize the mass fraction of external water ingested into the subaerial eruption column source (e.g., Koyaguchi and Woods, 1996; Mastin, 2007b; Van Eaton et al., 2012), we interrogate eruption dynamics that evolve with magma-water interactions that depend explicitly on the depth of an external water layer. Integral conduit and eruption column models of "dry" eruptions are well established in previous studies (Gonnermann and Manga, 2007; Michieli Vitturi and Aravena, 2021; Woods, 2010). Consequently, here we focus on effects of a water layer on the mechanical couplings among the conduit, vent and eruption column model components and their consequences for column rise and gravitational stability. We identify critical water depth conditions where column heights exceed the tropopause, explore sensitivities of these results to parameterizations for water entrainment and quench fragmentation, and compare results to observations of hydrovolcanic eruptions. We address, in particular, how key parameters in the fragmentation model influence the fragmentation energy budget and govern the production of particle surface area (ash). In addition to modulating the rise of a hydrovolcanic eruption column, the extent of ash production potentially affects also the SO_2 absorption and the heterogeneous nucleation and growth of sulfur aerosols. Thus, we conclude by

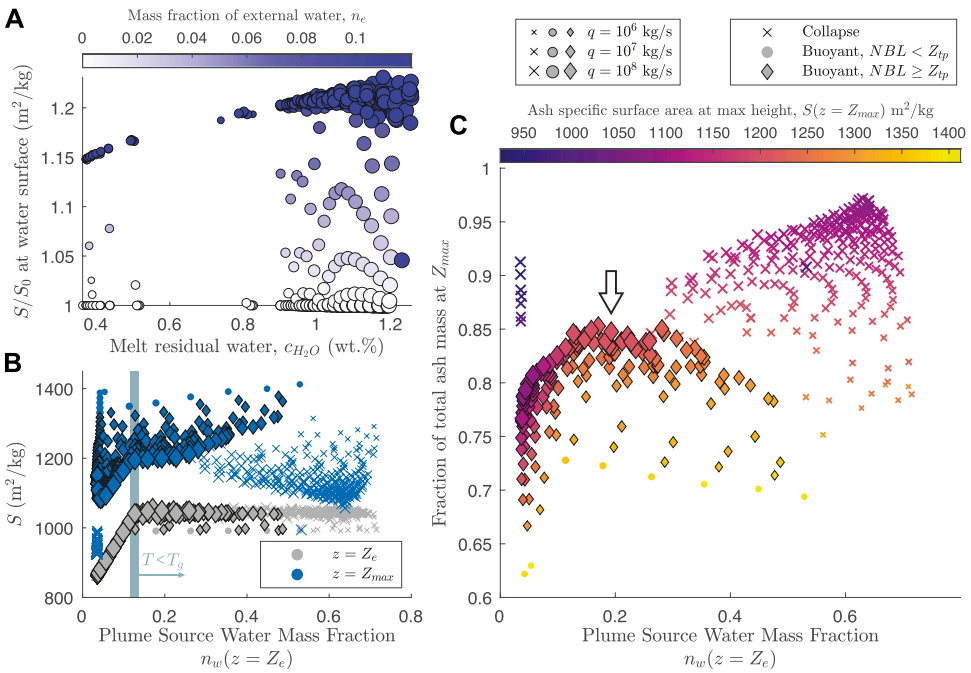

FIGURE 11 | Effects of MWI and sedimentation on particle specific surface area S. **(A)** Specific surface area, S, immediately after the jet breaches the water surface ($Z = Z_e$), as a function of c_{H_2O}, the water mass fraction still dissolved in the melt after conduit exit. Symbols are sized according to MER at the vent and colored according to the mass fraction of entrained external water. The dissolved water content controls the glass transition temperature, T_g, which in turn is the primary limiting factor in the model for how much surface area can be generated during quench fragmentation. **(B)** S at two different heights in the eruption column: at column source, immediately after MWI ($Z = Z_e$, grey symbols), and at the column maximum height ($z = Z_{max}$, blue symbols) as a function of water mass fraction at column source. Symbol sizes as in **(A)**. An 'x' denotes a collapsing column, a filled circle denotes a column that is buoyant but with Neutral Buoyancy Level (NBL) below the tropopause, and diamonds are columns that are buoyant with NBL at or above the tropopause. Evolution from grey to blue symbols is a result of sedimentation over the rise height of the column. The approximate water mass fraction above which the pyroclasts cool below the glass transition temperature T_g is marked with a vertical blue bar. **(C)** Fraction of particle mass remaining in the column at its maximum rise height as a function of column source water mass fraction. Symbols are sized by MER as in **(A,B)**, and colored according to the value of S at maximum column height. Symbol shapes as in **(B)**. The arrow highlights the subset of simulations with NBL above the tropopause and where the column retains increased (relative to "dry" runs) particle mass and specific surface area.

discussing the co-injection across the tropopause of ash, SO_2, and water in hydrovolcanic eruption clouds and implications for chemistry, microphysics, and associated climate impacts.

4.1 Water Entrainment and Mixing Efficiency Governs Eruption Column Buoyancy

For a given MER, the model parameter that exerts the greatest control on atmospheric injection height and mass loading of fine ash and water is the effective water entrainment coefficient α_{eff}. For a given water depth, the height above the vent at which water entrainment effectively begins and the rate at which water ingestion occurs govern the total mass of external water introduced into the column. The resulting water budget controls, in turn, the total thermal energy transfer from the melt to heat external water and supply the irreversible work to fragment pyroclasts to produce ash. The extent and rate of water entrainment therefore governs the conditions for column collapse or buoyant rise, the extent of fine ash production by quench fragmentation, and the depth at which water vapor is largely exhausted and the pyroclastic jet transitions to a weak steam plume. To make clear the insight gained through our considering the controls on the entrainment mechanics that govern column evolution, we will discuss in detail the behavior of our different entrainment scenarios. For comparison, we introduce natural examples of eruptive phases that involve interaction with water layers at various depths.

Except in the special case where the column does not decompress on exiting the vent, the decompression length L_D acts to reduce the fraction of the water column height where entrainment can occur. Below the crossover length L_X, where turbulent buoyant plume rise starts, the evolving local rate of entrainment is less than the steady-state value above L_X. These expectations are broadly consistent with Saffaraval et al. (2012) who demonstrate that for overpressured jets, entrainment was 30–60% less efficient at axial distances less than about five vent diameters and vent overpressures up to about 3 atm. In more detail, over the decompression length L_D water entrainment is impossible by definition and none occurs where $L_D > Z_e$. In contrast, for $L_D \leq Z_e$ water ingestion is possible and enhanced for (shallow) water depths greater than around 2 vent radii because

increases in hydrostatic pressure suppress decompression (**Figure 8F**). Consequently, with no decompression scaling (*No-L_d* scenario), whereas the threshold depth for steam plumes is, for example, not significantly affected because the decompression length is very small at these depths (see **Figure 8F**), the threshold water depth for column collapse and stratospheric injection decreases by ~20–30% (see **Figure 9B**).

The mechanism of decompression length inhibiting water entrainment in our model can be related to observations of real eruptions in shallow water layers. For example, the 2016–2017 eruption of Bogoslof volcano featured both transient explosions and sustained plumes emerging from vents typically in water depths of 5–100 m (Lyons et al., 2019). Lyons et al. (2019) interpreted acoustic signals of transient events at Bogoslof to result from explosive expansion of large bubbles of magmatic gas, which limited the direct interaction of external water with the erupting fragmented mixture. Deposits from these events in the near-vent region suggested that little or no condensed water was present during emplacement of pyroclastic surges, and Waythomas et al. (2020) interpreted this to mean that any water present was entirely in vapor form, further suggesting that these explosive events were drier than is typical of "Surtseyan"-type activity. The requirement for low liquid water content in pyroclastic surges at Bogoslof, combined with the observations of Lyons et al. (2019), suggests either a highly efficient mixing process and complete vaporization (possibly driven by molten-fuel-coolant explosions (Wohletz et al., 2013)), or limited ingestion of external water by explosive expansion of magmatic gas in a shallow water setting. Whereas events in our model with water depths less than L_d result in no incorporation of external water, we suggest this regime is analogous to real events similar to those of Bogoslof where water depths are comparable to or less than length scales for gas decompression, resulting in *limited* (though likely non-zero) amounts of external water incorporated into the eruption column. An overpressured vent is required for this event to occur, which is possible for either a steady eruption with choked vent flow, or for transient explosions originating in the shallow conduit. In our simulations, pyroclasts cool to the water saturation temperature around water mass fractions of 30–35% assuming that mixing and heat transfer are complete, at which point the liquid water content rises dramatically. This is therefore a likely upper bound for the mass fraction of external water in these relatively dry events at Bogoslof.

The crossover length scale L_X governs where in the water layer column rise transitions from that of a pure jet to a turbulent buoyant plume. At and above this transition, entrainment by turbulent motions is fully developed (see **Eq. 27**). The crossover length is most sensitive to jet radius and velocity after decompression (see **Eq. 31**). The column rise speed changes little over L_D so long as the conduit remains choked. However, the jet radius after decompression decreases rapidly with increasing hydrostatic pressure and decreasing vent overpressure, and for deep water L_X approaches a value less than half of that for a subaerial jet (see **Figure 8** panels (d), (f), and (h)). As L_X decreases with increasing water depth, α_{eff} increases more rapidly with height above the vent (see **Eqs. 32** and **33**) and the jet entrains external water at slightly greater rates for deeper water layers. However, more important remains the total height over which water entrainment occurs. Without considering the crossover length scale (*No-L_X* scenario), entrainment sufficient to cause column collapse or steam plumes occurs within only a few tens of meters of where entrainment starts, even for very large MER (see **Figure 9B**). Because of the progressive increase of α_{eff} with height in scenarios that include the L_X scaling, removing it in the *No-L_X* scenario has a greater impact on the threshold for steam plumes than for the column collapse condition, relative to the *No-L_d* scenario.

By definition, the *No-L_d-No-L_X* scenario has entrainment at rates corresponding to those for fully developed turbulence in subaerial jets (e.g., Morton et al., 1956; Carazzo et al., 2008), and even for the largest MER leads to ingestion of water masses sufficient to overwhelm jets that would otherwise lead to stratospheric injections. For example at $Q_0 \approx 10^9$ kg/s stratospheric injection is prevented at water depths greater than about 60 m, compared to a limit of 250 m in the *Reference* scenario (see **Figure 9B**). The entrainment rates and collapse conditions in the *No-L_d-No-L_X* scenario are therefore likely inconsistent with real hydrovolcanic eruptions. For example the ~24,000 BP Oruanui hydrovolcanic eruption in New Zealand had estimated magma mass fluxes of 10^8–10^9 kg/s and is recognized for its remarkably wide dispersal of airfall deposits (Wilson, 2001). This eruption emerged through Lake Taupo, which in modern times has water depths averaging about 150 m, and is believed to have had depths of at least 100 m at the time of the eruption (Nelson and Lister, 1995). These inferences are consistent with little water entrainment and mixing in the near-field and reinforce the importance of considering L_d and L_X in the evolution of buoyant subaerial columns from submerged volcanic jets.

The isothermal, single-phase experiments of Zhang et al. (2020) show that fully developed turbulence with steady-state entrainment in subaqueous, supersonic jets occurs at a distance from the vent greater than about ten vent diameters, with comparatively inefficient and transient entrainment modes dominating closer to the jet source. For such subaqeuous jets, both turbulent shear and buoyancy effects contribute to the development of large turbulent eddies that injest surrounding water. For comparison with the typical shear-driven entrainment condition used in our *Reference* scenario and to highlight potential variability in the entrainment mechanisms of real sub-aqueous volcanic jets, we parameterize buoyancy-driven entrainment in the *αRT* scenario using a slightly modified form of the "Rayleigh-Taylor" entrainment coefficient of Zhang et al. (2020) in **Eqs. 35** and **36**. Differences between the *αRT* and *Reference* scenarios (see light blue and black lines in **Figure 9B**, respectively) are governed by the $\alpha \propto a^2/q_c$ dependence of **Eq. 36**. For $Q_0 \lesssim 10^7$, the ratio of jet cross-sectional area to mass flux a^2/q_c is relatively large, resulting in large entrainment rates comparable to those for fully developed plumes (i.e. *No-L_d-noL_X* scenario) and consequently shallow water depths for the column collapse and steam-plume conditions. For $Q_0 \gg 10^7$ kg/s, as entrained water is vaporized jet density initially decreases, resulting in enhanced Rayleigh-

Taylor entrainment and column collapse for slightly shallower depths than the *Reference* scenario. However, for larger water depths where the jet cools to the water saturation temperature, entrained water remains liquid, jet density increases and radius decreases (see **Figure 8**, panels (h) and (j)). As a result, q_c dominates in **Eq. 36** for water depths much greater than the threshold for collapse, and entrainment rates are suppressed. The reduced entrainment rates for large MER and deep water layers, in turn, prevent total exhaustion of the particle heat budget such that, in contrast to other scenarios, the steam plume condition occurs for pressure-balanced jets much deeper than the limit for vent choking (see **Figure 9B**). As a final remark here, we reiterate that the mechanics of water entrainment exert the greatest control over column rise. Our results underscore, however, that this process is poorly understood and is a key avenue for future work on hydrovolcanism. As implemented, the shear-driven and buoyancy-driven modes govern water ingestion for very different MER-water depth conditions. Whereas it is straightforward to embrace both contributions parametrically through the effective entrainment coefficient given by **Eq. 35**, there are no observational or experimental constraints on how best to characterize the relative contributions of each mode. Furthermore, how the underlying dynamics and their couplings are modified by local MFCI as well as particle inertial and buoyancy effects, as well as the character and thermal mixing properties of MWI, are unknown.

Conditions leading to gravitational collapse in our model (water mass fractions ≳30–40 wt%) are consistent with those in previous integral plume models of wet eruption columns (Koyaguchi and Woods, 1996; Mastin, 2007b). Our results are further consistent with observations that buoyant, ash-laden subaerial eruption columns are rarely observed for water depths greater than about 100 m (Mastin and Witter, 2000). However, a challenge with interpretation of integral plume models is that they predict sharp boundaries between behavioral regimes (i.e., collapse or no collapse), whereas real eruptions have gradual transitions between behaviors. Columns that are either fully buoyant or completely collapsing are now understood to be end member behaviors, with eruption columns undergoing partial collapse and simultaneous rise of buoyant central columns and secondary plumes from pyroclastic density currents being commonplace (Neri et al., 2002; Gilchrist and Jellinek, 2021). Indeed, hydrovolcanic eruptions are noted for highly dispersive eruption columns with multiple spreading levels (Carazzo and Jellinek, 2013; Houghton and Carey, 2015), owing to complex cloud microphysical processes including latent heat exchange and hydrometeor formation (Van Eaton et al., 2012, 2015), wet particle aggregation (Brown et al., 2012; Telling et al., 2013; Van Eaton et al., 2015), or collective settling and diffusive convection (Carazzo and Jellinek, 2012, 2013). The thresholds shown in **Figure 9**, including for column collapse, stratospheric injection, vent choking, and plume failure are best interpreted as gradual transitions between likely behavioral regimes. Similarly, the condition for steam plumes represents a transitional regime where jets of liquid water, ash and steam can still breach the water surface and may produce water-rich plumes driven by moist convection, but the vast majority of water and particle mass collapses immediately at the surface or does not breach it at all (see **Figure 8A**). As an example of this regime, the eruption of South Sarigan Volcano in 2010 occurred in water depths of 180–350 m, and produced a column up to 12 km in height during its peak phase. However, satellite observations showed that the plume was very short-lived and consisted primarily of water, with only minimal ash fallout or aerosols detected (McGimsey et al., 2010; Global Volcanism Program, 2013; Green et al., 2013).

A final consideration for the development of buoyancy in the subaerial eruption column is the effect of thermal disequilibrium. To validate the assumption of thermal equilibrium in an integral model, Koyaguchi and Woods (1996) assumed timescales for heat transfer between particles and entrained water of order 1 s or less, which is reasonable for particle diameters less than about 1 mm, and also requires the column to be well-mixed. For the range of water depths considered here, typical timescales for the jet to penetrate the water surface are about 0.1–5 s (assuming choked flow at the vent). Our MWI model therefore assumes entrainment and heat transfer occur on timescales < 0.1 s, and further assumes that internal turbulent mixing of the jet mixture with entrained water is complete on these timescales. If disequilibrium heat transfer or incomplete mixing are considered, entrained water may not vaporize fully over the timescale of rise through the water column, even for jets with bulk pyroclast temperatures well above the water saturation temperature. In turn, the subaerial jet would host domains of varying fractions of liquid water and vapor, resulting in heterogeneous density distributions in the early stages of the eruption column. Such effects are beyond the capability of a 1D integral model and could further contribute to partial column collapse or particle shedding events, with consequently reduced mass flux of particles and gas in the rising column. An additional consequence of incomplete mechanical and thermal mixing is that the column may retain a hot core of particles that do not supply thermal energy to entrained external water to drive quench fragmentation, which is consistent with observations of pyroclast textures and particle sizes (e.g., Moreland, 2017). Our assumed complete mixing and parameterized fragmentation efficiency thus probably provides an upper bound to the extent of quench fragmentation and ash production.

4.2 Trade-Offs Among Thermal Energy Budget, Particle Loss, Particle Surface Roughness, and Fragmentation Efficiency

Our fragmentation model aims to capture the essential energy and mass budget characteristics of quench fragmentation derived from observational and experimental constraints on the glass transition temperature T_g (Dingwell, 1998), the fragmentation energy efficiency ζ (Sonder et al., 2011), particle roughness Λ (Zimanowski and Büttner, 2003; Fitch and Fagents, 2020), the initial PSD power-law exponent D (e.g., Girault et al., 2014), and measured hydrovolcanic particle sizes (Costa et al., 2016). Here we focus on the consequences of varying Λ, ζ, and D for

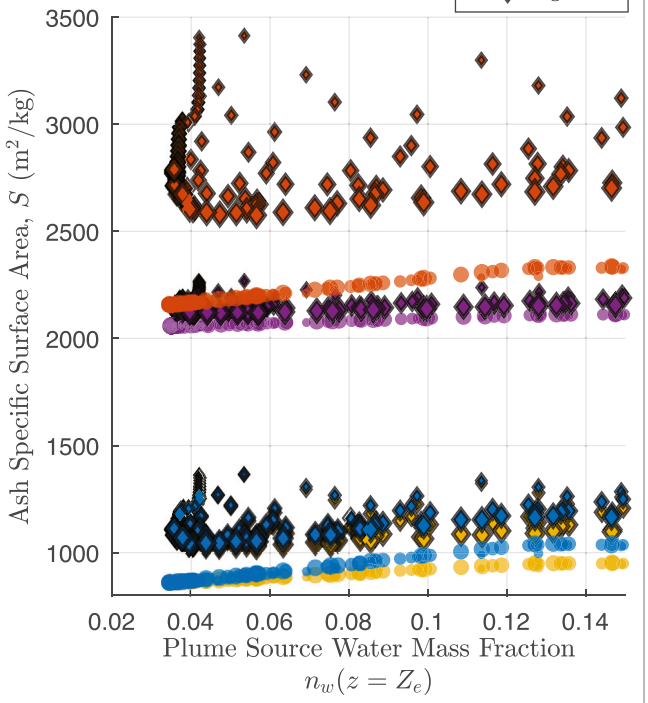

FIGURE 12 | Pyroclast specific surface area as a function of water mass fraction at the water surface (circles) and height of neutral buoyancy (diamonds) for scenarios with different fragmentation properties. The *Reference* scenario is shown in blue. Reducing the fragmentation energy efficiency to $\zeta = 0.05$ (*Low*-ζ scenario, yellow symbols) reduces the amount of energy consumed to generate surface area per unit mass of entrained water, resulting in a smaller increase in S during MWI relative to the *Reference* scenario. Conversely, a high initial value of the PSD power-law exponent, $D = 3.2$ (*High-D* scenario, purple symbols), concentrates initial particle mass in the fine fraction. Because of the fixed particle sizes for output from quench fragmentation used here (see **Figure 3**), there is relatively little particle mass available to fragment for the creation of new surface area and the relative change in S with water entrainment is small. Finally, increasing the particle roughness scale, $\Lambda = 25$ (*High*-Λ scenario, red symbols), results in initially high particle surface area, but also a greater energy requirement to generate new particles of a given size. This scenario results in the highest absolute changes in particle surface area after quench fragmentation and sedimentation, but a smaller relative change than for the *Reference* scenario.

production of fine ash. For reference, we refer to **Section 3.4** and **Figure 11B**, which plots *Reference* scenario particle specific surface area at two heights - column source and maximum column height - as a function of column water mass fraction at the water surface. These same data for the *Reference* scenario (i.e., gray and blue diamond symbols in **Figure 11B**) are again plotted in **Figure 12** in blue (now circles and diamonds for values at the column source and maximum height, respectively), together with results of scenarios with alternative fragmentation model parameters (see **Table 2**). As in **Figure 11B**, MER is represented by symbol size. As described in **Section 3.4**, cooling below the glass transition temperature limits the generation of additional ash surface area for total mass fractions of water $n_w \gtrsim 0.15$. First examining the *Reference* scenario ($\zeta = 0.1$, $\Lambda = 10$, $D = 2.9$, and mean output particle size, $\phi_\mu = 3.4$; blue symbols in **Figure 12**), this mechanical limit results in approximately a 20% increase in ash specific surface area S at the base of the eruption column, and a 10–15% increase in S at the spreading height, relative to control scenarios. As discussed in **Section 3.4**, coarse particle fallout is relatively enhanced for low-MER events which have small radii and lower column rise speeds when compared with larger MER. As a consequence, sedimentation in low-MER ($\ll 10^7$ kg/s) columns exerts a stronger control on particle surface area than does quench fragmentation in our simulations, whereas the two mechanisms are comparable in magnitude for larger eruptions.

Red symbols in **Figure 12** show the *High*-Λ scenario, where the particle roughness scale Λ is increased from 10 to 25 and other input parameters are held constant. Similar to Fitch and Fagents (2020), Λ has the largest influence on total ash surface area. Increasing Λ to 25 results in a proportional increase in initial surface area; the minimum value of S for the *Reference* scenario with no entrained external water is 860 m^2/kg, and is 2,160 m^2/kg for the *High*-Λ scenario. However, the energy requirement to generate particles of a given size also increases proportionally. Since the fragmentation energy budget per unit mass of pyroclasts is approximately the same as in the *Reference* scenario (determined by magma heat capacity, fragmentation energy efficiency, and the glass transition temperature), the amount of total surface area generated during MWI is similar to the *Reference* scenario, but the proportional increase in S resulting from MWI is less than 10% relative to the control simulations. Comparing change in surface area resulting from water entrainment and quench fragmentation (red circles) with that resulting from sedimentation (difference between circles and diamonds), the effects of sedimentation in this case exert a much stronger control on ash surface area in the eruption cloud than does MWI. High particle roughness scenarios thus have the greatest total ash surface area in the eruption cloud, but a relatively modest change compared to control simulations with no external water.

The fragmentation energy efficiency ζ governs the relative partitioning of irreversible thermal energy loss from the melt between that used to heat and vaporize water and that consumed by fragmentation and production of particle surface area. Choosing a low value for the fragmentation energy efficiency, $\zeta = 0.05$ (*Low*-ζ scenario, yellow symbols in **Figure 12**), reduces the energy consumed by fragmentation per unit mass of entrained water, resulting in overall less ash production before the glass transition limit is reached. This scenario has both the lowest total particle surface area after quench fragmentation and a modest change relative to control scenarios of 5–10%. The high fragmentation energy efficiency scenario with $\zeta = 0.15$ (*High*-ζ scenario, data not shown) has an effect of similar magnitude but opposite sign on specific surface area S compared with the *Low*-ζ scenario. S after sedimentation in the eruption column, however, is very similar to that for the *Reference* scenario, and we consequently do not show those results in **Figure 12**.

The initial PSD, governed by *D*, determines the relative weight of particles towards fine or coarse fractions prior to MWI. Since we fix the particle sizes produced by quench fragmentation to values based on the phreatomagmatic phase C of the Askja 1875 eruption (see **Section 2.3.4** and **Figure 3**), an initial PSD already enriched in these particle sizes will not change significantly in our MWI model, and consequently little fragmentation energy will be consumed. The *High-D* scenario with $D = 3.2$ (purple symbols in **Figure 12**), results in very high initial particle surface area (~ 2050 m^2/kg) but only minor changes to the PSD and *S* from MWI and sedimentation (the highest values of *S* at the maximum plume height are ~ 2200 m^2/kg). Consequently, the strongest control on production of ash surface in this scenario is the minimum particle size that can be produced during quench fragmentation.

The results of the various fragmentation scenarios above reveal an important trade-off among particle size distribution, particle roughness, and the consumption of fracture surface energy during quench fragmentation. The primary effect of the glass transition limit and fragmentation energy efficiency is to determine the energy budget for fragmentation, whereas particle roughness and surface energy limit the mass of fine particles that can be produced within a given energy budget. The initial PSD, in turn, determines the mass of "coarse" particles available with which to generate new fine ash. The mass in this coarse fraction is dependent on the choice of particle sizes that fragment during quenching, and the preferred sizes of particles produced. Our simple mechanical energy balance model relies on a prescribed initial PSD and on a perfect conversion of fragmentation energy to the plastic work of brittle fragmentation. For a given ζ, the approach provides a crude and probably lower bound that should be applied cautiously. Whereas we fix the particle sizes generated by quench fragmentation to those of a known deposit, modal particle sizes from quench fragmentation vary as a function of melt properties and cooling rates (van Otterloo et al., 2015), as well as bubble size distributions (Liu et al., 2015). Our model further assumes that quench fragmentation is a brittle failure process limited in extent by rapid cooling below the glass transition temperature (e.g., Mastin, 2007a; van Otterloo et al., 2015). This limit constrains failure to occur only in conditions in which the melt phase can accumulate elastic thermal stresses in excess of a yield stress. This approach neglects, for example, potentially important time-dependent effects related to the growth of thermal stress gradients and stress concentrations, which can arise with additional cooling (Woodcock et al., 2012; van Otterloo et al., 2015), and evolve depending on the character of the water boiling regime at the melt-water interface (Moitra et al., 2020). The cessation of quench fragmentation with decreasing particle temperature is probably more gradual in real eruptions than in our model (see **Supplementary Material Section S2** and **Supplementary Figure S4** for additional discussion of thermal stresses during quench fragmentation). Despite these complexities, together with consideration of the entrained masses of water in hydrovolcanic eruption columns, these constraints allow estimation of the total mass and surface area of fine ash delivered to the spreading levels of buoyant hydrovolcanic eruption clouds.

4.3 Water Layer Depth, Volatile Saturation and Fragmentation in the Conduit, and Vent Choking

The additional hydrostatic pressure with a water layer overlying the vent influences the results of our coupled model in two primary ways: 1) it modulates the extent to which a vent is choked and overpressured, and 2) it controls the total amount of gas exsolved from the melt (Smellie and Edwards, 2016; Cas and Simmons, 2018; Manga et al., 2018), which, in turn, influences both the magma ascent rate and the quench fragmentation process. For water depths near the collapse threshold, magma flow at the vent is choked and overpressured (see **Figure 8** panels (a), (d), and (e), and **Figure 9A**). Consequently, the column collapse condition is not heavily influenced by changes in conduit conditions with increasing water depth, and is primarily determined by the mass fraction of entrained external water. However, for water depths sufficient to suppress vent overpressure, $L_d \rightarrow 0$ and L_X approaches its minimum value. Entrainment consequently starts near the vent and ingestion rates are typically faster overall for pressure-balanced jets, which is broadly consistent with experimental comparisons of overpressured and pressure-balanced jets (Saffaraval and Solovitz, 2012). This condition leads to the tendency for the steam plume regime to coincide with the water depth limit for choking (**Figure 9A**). However, as discussed in **Section 4.1**, the choking and steam plume conditions need not coincide if entrainment rates are either very high (e.g., *No-L_d-noL_X* scenario), or very low (e.g., αRT scenario for $Q_0 \geq 10^8$ kg/s). Therefore buoyant columns are most likely for subaqueous eruptions that are choked and overpressured at the vent as opposed to pressure-balanced, but this is not a strict requirement and depends on the dynamics of decompression and water entrainment near the vent, as well as the conditions for choking (for example the mixture sound speed).

Comparing total exsolution for small and large water depths (**Figure 5F**), differences in vapor exsolution in the conduit model control the glass transition temperature (**Figure 3B**), which, in turn, governs the heat budget available for ash production during the quench fragmentation (**Figure 11A**). This effect is most apparent when considering events with a second nucleation event occurring in the conduit model for low MER (**Figure 5F**). Specifically, diffusion rate of vapor leaving the melt is sensitive to bubble number density, so a second nucleation event near fragmentation enhances exsolution rate above fragmentation, leading to the sharp change in total exsolution shown in **Figure 5F**. Simulations with a strong second nucleation in the conduit result in distinctly different production of ash surface area during quench fragmentation (**Figure 11A** for $c_{H_2O} < 0.6$ wt%). As we will show in **Section 4.5** below, the influence of this process on the dispersed mass of fine ash is apparent in our model even at the spreading height of the eruption cloud.

For primary brittle fragmentation and explosive volcanism to occur during magma ascent in the conduit (i.e. without the influence of external water), either gas overpressure in bubbles must exceed the tensile strength of the melt, or the rate of magma ascent must be sufficiently high to exceed the critical strain rate for brittle failure of the melt (Papale, 1999; Gonnermann, 2015). As described in **Section 3.1**, both maximum decompression rate and maximum bubble overpressure (as recorded at the fragmentation depth) decrease with increasing hydrostatic pressure in our conduit model. In **Figure 5D**, we show that for water depths of about 200 m or greater, the maximum bubble overpressure Δp_b in our model falls below values likely to cause rupture of bubble walls. Were bubble overpressure used as the fragmentation criteria in our conduit model, fragmentation could in principle still occur, albeit at shallower depths in the conduit, but becomes increasingly less likely with increasing water depth (Campagnola et al., 2016; Cas and Simmons, 2018). For example, Manga et al. (2018) used a strain-rate fragmentation criterion to estimate that for the 2012 submarine eruption of Havre volcano, magmatically-driven brittle fragmentation in the conduit could only have occurred if the vent were shallower than about 290 m. It is worth noting that brittle fragmentation mechanisms in general, particularly those driven by water interaction, are not precluded at such depths, though explosive expansion of steam is suppressed (Murch et al., 2019; Dürig et al., 2020a). Critically, increasing thicknesses of water or ice will increasingly suppress the conditions for which sustained brittle or explosive fragmentation may drive gas jets or plumes, particularly those capable of reaching tens of kilometers into the atmosphere.

4.4 Sensitivity: Water Infiltration Into the Shallow Conduit

As highlighted in **Section 2.1**, our coupled conduit-vent-plume model scenarios do not include the effect of water infiltration into the shallow conduit. However, some ingress of groundwater into the conduit is likely in many circumstances. Accordingly, we show sample calculations and simulations to explore potential effects on eruption column behavior in our MWI and plume models. Existing models of magma-water interaction (MWI) in the shallow conduit (i.e., above the level of fragmentation) (Starostin et al., 2005; Aravena et al., 2018) have highlighted that the increased gas content resulting from vaporization of external water leads to an increase in vent velocity, vent overpressure, and mass eruption rate (MER), and reduced eruption temperatures. Of greatest importance for the purposes of this study are the extent to which water infiltration into the shallow conduit may influence the behavior regimes highlighted in **Section 3.3** and **Figure 9**, thereby influencing the conditions for stratospheric injection. In particular, added water in the conduit will increase the gas pressure at the vent, and therefore deepen the critical water depth at which vent choking and overpressure are suppressed. Here we perform a sensitivity analysis for changes to the choking condition arising from the infiltration of external water into the conduit, and resulting effects on water entrainment, plume rise, and stratospheric injection in our model. We do not consider cases where the conduit geometry is modified by failure or erosion during MWI, and we also do not include the effects of fragmentation resulting from water infiltration into the conduit prior to eruption (i.e. additional energy consumed through mechanical modifications to the grain size distribution).

For a choked conduit flow ($M = 1$) the theoretical pressure at the vent can be approximated as (Koyaguchi, 2005)

$$p_{choke} \approx \sqrt{n_v R_v T}\ \frac{q}{A_c} \approx \rho c^2, \tag{63}$$

where $c = \sqrt{n_v R_v T}$ is a simplified expression for the pseudo-gas sound speed (Woods and Bower, 1995), R_v is the specific gas constant for water vapor, T is the mixture temperature, and $A_c = \pi a_c^2$ is the conduit cross-sectional area. **Eq. 63** is in excellent agreement with our conduit simulations with choked vents, whereas simulations in which hydrostatic pressure exceeds p_{choke} are pressure-balanced ($\beta \approx 1$, $M < 1$) at the vent (see **Supplementary Figure S6**). Considering **Eq. 63** and neglecting any changes to the conduit geometry or magmatic mass flux, the addition of external water into the conduit will have the dual effect of increasing the gas mass fraction n_v (provided the water is all vaporized), and decreasing the mixture temperature T. From the results of Aravena et al. (2018), mass fractions of external water infiltrating into the conduit n_{ec} greater than about 5 *wt%* are not favored for rhyolitic compositions and will tend to lead to conduit failure. Here for completeness, we consider mass fractions $0 \leq n_{ec} \leq 0.15$, at which values all of the water is in the vapor phase after mixing (pressures in the regimes presented here are generally well below the critical point for water). To calculate the mixture temperature after infiltration and mixing of external water into the conduit, we calculate water properties for groundwater assuming an average depth of 100 m below the rock surface (accounting for hydrostatic pressure from external water) and at temperature $T_{ec} = 274.15$ K using the IAPWS-95 Standard (Junglas, 2009). For simplicity we assume constant latent heat of vaporization L_{ec} and heat capacities for water C_l and vapor C_v (for example, typical average values are 1.85×10^6 J/kg, 4.22×10^3 $\mathrm{Jkg^{-1}K^{-1}}$, 2.23×10^3 $\mathrm{Jkg^{-1}K^{-1}}$, respectively, for temperature ranges between T_{ec} and magmatic temperature T_0), and magma $C_m = 1{,}250$ $\mathrm{Jkg^{-1}K^{-1}}$. The approximate energy balance following thermal mixing of external water into the conduit is

$$\begin{aligned} 0 \approx\ & (1 - n_v) C_m (T - T_0) + n_0' C_v (T - T_0) \\ & + n_{ec} [C_l (T_{sat} - T_e c) + L_{ec} + C_v (T - T_{sat})], \end{aligned} \tag{64}$$

where $n_0' = n_0 (1 - n_{ec})$ is the adjusted mass fraction of initial magmatic water vapor after mixing with external water, and $n_v = n_{ec} + n_0'$ is the total water vapor mass fraction after mixing. Solving **Eq. 64** for the final temperature T gives

$$T \approx \frac{T_0 C_B - n_{ec} C_l (T_{sat} - T_{ec}) - n_{ec} (L_{ec} + C_v T_{sat})}{C_B + n_{ec} C_v}, \tag{65}$$

where $C_B = (1 - n_0') C_m + n_0' C_v$. **Eqs. 63** and **65** can be used to calculate the theoretical pressure for a choked vent p_{choke} (q_0, n_{ec}), assuming vent radii equal to those of the control simulations with no external water (see **Section 2.5**). Where p_{choke} is less than ambient hydrostatic pressure, the vent pressure can be assumed

equal to the hydrostatic pressure, resulting in a pressure-balanced jet with $M < 1$. Mixture density, sound speed, vent velocity, and particle volume fraction are then calculated from corresponding water equations of state and magmatic properties using the above estimated pressure and temperature. See **Supplementary Material Section S3** and **Supplementary Figures S6, S7** for a comparison of model results with these theoretical relationships.

To demonstrate the effect of water infiltration into the conduit on the MWI and eruption column models, **Figure 13** shows a series of model simulations in which we calculate the vent condition from the above relations (i.e., without running the conduit model, but using a sound speed corresponding to **Eq. 6** and running the MWI and plume models from the calculated vent condition). We use a fixed magmatic mass flux of $q_0 = 2 \times 10^7$ kg/s, $0 \leq n_{ec} \leq 0.15$ (see also **Supplementary Figure S7**), and vary water depths from 0 to 300 m ($Z_e/a_c \approx 12$). Panel (a) shows the critical water depth at which hydrostatic pressure exceeds the vent choking pressure, resulting in a transition to a pressure-balanced jet. Values of n_{ec} corresponding to the simulations shown in panels (b)-(e) are highlighted with blue and gray circles. For $n_{ec} = 0.15$, the water depth limit for choking is more than doubled (from 130 to 267 m) relative to the case with no external water in the conduit. Panels (b), (c), and (d) show subaerial eruption column source parameters after breach of the water surface for varying water depth Z_e and conduit water fractions n_{ec}, and panel (e) shows the eruption column height. Panel (b) shows the total mass fractions of vapor and liquid water (external and magmatic). Importantly, the water depth at which liquid water dominates the jet (the steam plume condition) differs only by about 20 m between scenarios. Panel (c) shows column source temperature, highlighting the change in decompression length and onset of mixing with surface water that results from increased gas pressure at the vent. Panel (d) shows the increase in jet velocity, driven by changes in the mixture sounds speed and jet density as it travels through the water column. Panel (e) shows the maximum plume height and level of neutral buoyancy, which decrease by up to about 3 and 1.7 km respectively with $n_{ec} = 0.15$. The water depth threshold for column collapse is increased by up to about 40 m relative to scenarios with no external water in the conduit. The critical result of the above analysis is that despite a doubling of the depth threshold for vent choking highlighted in panel (a), infiltration of external water into the conduit changes the behavior thresholds of the eruption column passing through a surface water later by a comparatively small amount of tens of meters. An important caveat to this discussion is that these simulations do not include the potential for highly energetic and impulsive releases of energy driven by fuel-coolant interaction, or related changes in the magmatic mass flux and vent geometry that may arise from an influx of external water.

4.5 Stratospheric Injection in Hydrovolcanic Eruptions and Implications for Sulfate Aerosol Lifecycle

Radiative forcing by sulphate aerosols is governed by the total mass of injected sulfur dioxide, the height, season, and latitude of injection, and the chemical and microphysical processes that determine the resulting aerosol particle size distribution (Timmreck, 2012; Lacis, 2015; Kremser et al., 2016; Marshall et al., 2019; Toohey et al., 2019). The injection height relative to tropopause height is critical for determining the mass of stratospheric sulfur burden. However, the total mass and size distribution characteristics of fine ash as well as high water content in hydrovolcanic eruptions are also likely to play a role in the life cycle of sulfur aerosols. For example, LeGrande et al. (2016) showed that the coincident injection of SO_2 with high concentrations of water can shorten the characteristic timescale for conversion of SO_2 to aerosol from weeks to days, enhancing aerosol radiative forcing in the earliest weeks after an eruption. Chemical scavenging of SO_2 onto ash surfaces is a potentially important source of SO_2 removal both during eruption column rise and in the days and weeks following an eruption (Rose, 1977; Schmauss and Keppler, 2014; Zhu et al., 2020). Experimental results from Schmauss and Keppler (2014) demonstrated that SO_2 absorption onto ash particle surfaces is most efficient where volcanic plumes are cool, SO_2 is dilute, and ash surface areas are high - all conditions that are likely to be enhanced in hydrovolcanic eruption columns relative to purely magmatic cases. Zhu et al. (2020) reported that persistent fine ash particles dispersed along with SO_2 from the 2014 eruption of Kelut Volcano contributed to enhanced nucleation of aerosol particles onto ash surfaces and aerosol particles sizes up to 10 times that of typical background stratospheric aerosol. Critically, chemical uptake of SO_2 onto ash surfaces increased the rate of sulfur removal by sedimentation by 43% in the first 2 months following the eruption. Finally, enhanced stratospheric loading of water can directly produce a positive radiative forcing in the troposphere, potentially counteracting the cooling effects of sulfur aerosols (Joshi and Jones, 2009).

Figure 14 shows estimates for the flux of SO_2, fine ash, and water to the tropopause for simulations with two different atmospheric profiles (*Reference*, top row of panels and *Low-Lat*, bottom row). Panels (a) and (b) show the estimated fraction of SO_2 delivered to or above the tropopause, where we approximate the vertical distribution of the SO_2 cloud $\psi_{SO_2}(z)$ as a Gaussian profile of thickness proportional to (and centered on) injection height Z_{nbl} (Aubry et al., 2019):

$$\psi_{SO_2} = \exp\left(\frac{-(z - Z_{nbl})^2}{(0.108\,(Z_{nbl} - Z_e))^2}\right) \tag{66}$$

The estimated fraction of SO_2 delivered to the stratosphere is the fraction of the integrated area of **Eq. 66** that lies above the tropopause. Events with injection heights close to the tropopause ($Q_0 \approx 3 \times 10^6$ kg/s and $Q_0 \approx 3 \times 10^7$ kg/s in the high and low latitude atmospheres, respectively) show reduced efficiency of stratospheric delivery of SO_2 for water depths that surpass the decompression length (and therefore non-zero quantities of external water are entrained). The exceptions are columns in the low-latitude atmosphere with minor quantities of entrained water ($n_w \approx 0.15$), which have increased column heights relative to control scenarios (see **Figure 10B**). Panels (b) and (c) show the ratio of fine ash mass flux (particle diameter $< 125\,\mu$m) at the maximum plume height relative to control simulations. We find that events with sufficient entrained water to pass the glass transition (and thus maximize production of fine ash in our

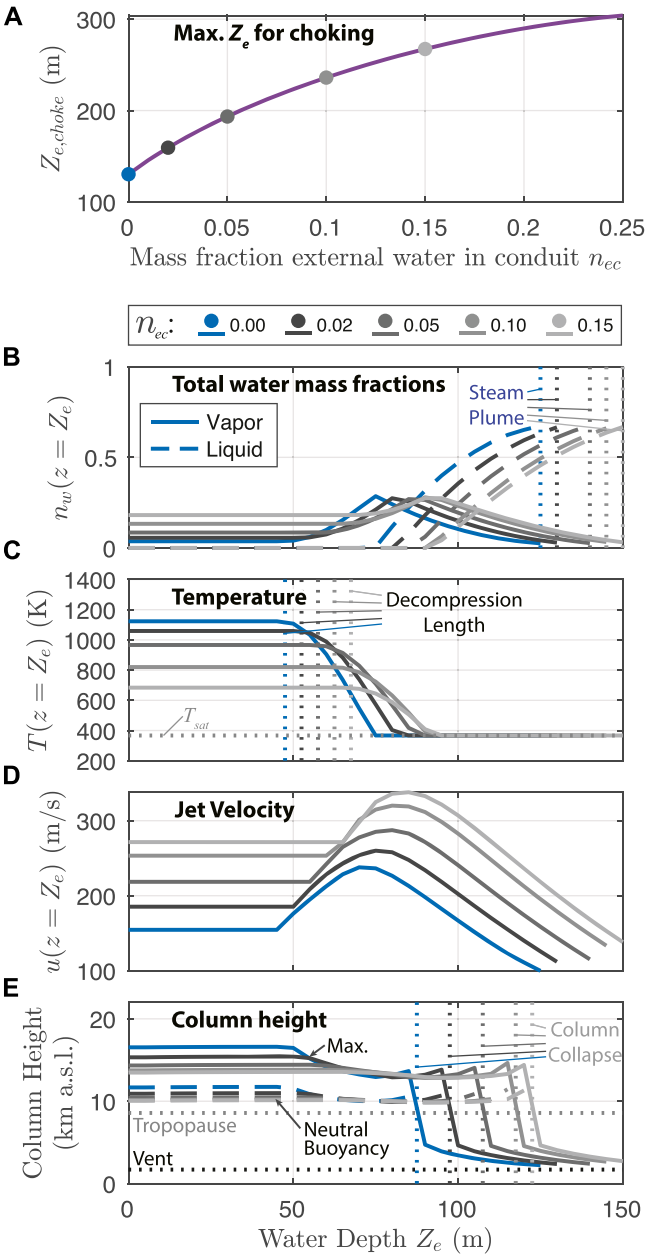

FIGURE 13 | Sensitivity analysis for infiltration of a prescribed mass fraction of external water infiltrating into the conduit n_{ec}. Simulations use a magmatic mass flux of 2×10^7 kg/s, and all other parameters including atmospheric profiles are held fixed relative to the *Reference* scenario. Vent conditions are calculated according to **Eqs. 63** and **65**. **(A)** Critical surface water depth at which hydrostatic pressure exceeds vent choking pressure (**Eq. 63**) as a function of water infiltration into the conduit. Circles highlight the values of n_{ec} used in the simulations shown for panels **(B–E)**. Panels **(B–D)** show parameters at the subaerial eruption column source after breach of the water surface ($z = Z_e$). **(B)** Total mass fractions of liquid and vapor water phases. Vertical dotted lines show the water depth threshold for steam plumes for each of the conduit water scenarios. **(C)** Jet mixture temperature. Vertical dotted lines show the threshold at which decompression length scale L_d is equal to water depth Z_e. **(D)** Jet vertical velocity. **(E)** Maximum eruption column height (solid lines) and level of neutral buoyancy (dashed lines). Vertical dotted lines show the water depth threshold for column collapse.

model) deliver a fine ash mass flux approximately 2-fold that of the control simulations. For low MER simulations with a second nucleation event in the conduit ($Q_0 \lesssim 4 \times 10^6$ kg/s), and consequently relatively less fine ash production, the mass flux of fine ash delivered is approximately 1.5 times that of the control cases. Finally, panels (e) and (f) show the ratio of water mass flux at maximum plume height compared to control scenarios. Buoyant hydrovolcanic plumes that breach the tropopause carry water mass fluxes of up to 10 times that of control simulations. Low-latitude eruption columns in humid

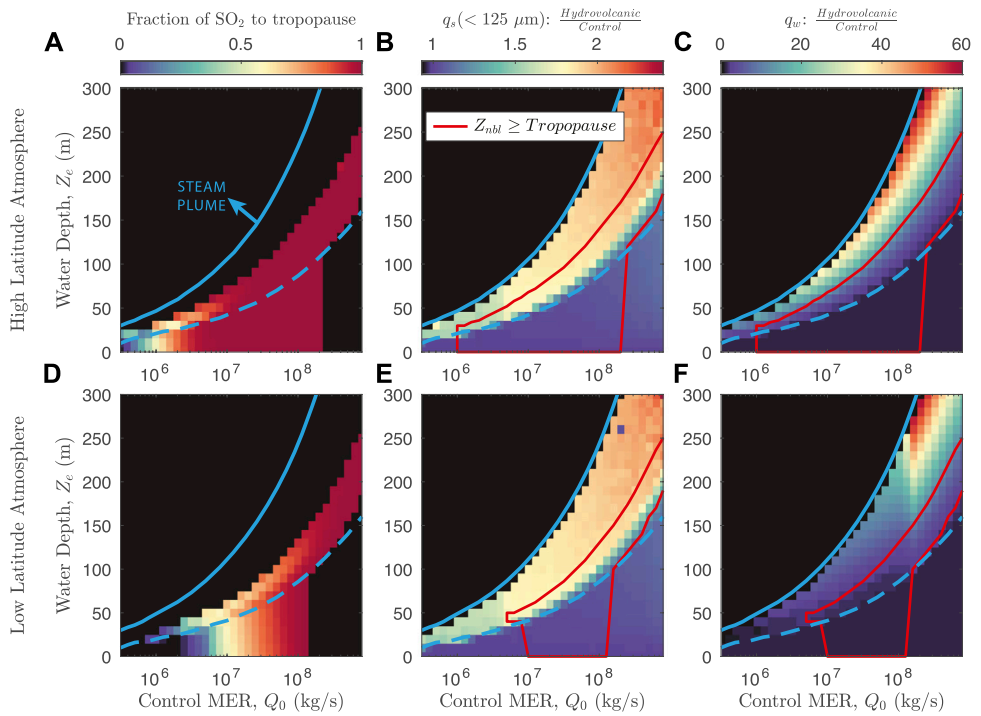

FIGURE 14 | Estimated fraction of SO_2, fine ash mass flux, and water mass flux to the stratosphere. **(A)** Estimated fraction of outgassed SO_2 injected above the tropopause assuming a Gaussian injection profile centered about the height of neutral buoyancy (**Equ. 66**), as a function of control MER Q_0 and water depth Z_e. In all panels, the dashed blue line is threshold water depth for water entrainment (decompression length equal to water depth, $L_d = Z_e$), and the solid blue line is the threshold depth for steam plumes (see **Figure 9**). Black regions indicate column collapse. **(B)** Fine ash mass flux to the eruption column maximum height as a ratio of hydrovolcanic ($Z_e > 0$) to control ($Z_e = 0$) simulations, for particle diameters less than 125 μm. Red line outlines simulations with buoyant plumes at spreading heights at or above the tropopause. **(C)** Water mass flux to the eruption column maximum height as a ratio of hydrovolcanic ($Z_e > 0$) to control ($Z_e = 0$) simulations. Black regions indicate the steam plume regime in panels **(B,C,E,F)**. Panels **(A–C)** are for with a high latitude (Iceland) atmospheric profile (*Reference* scenario). Panels **(D–F)** are the same as **(A–C)**, respectively, but for the low latitude (Equador) atmosphere (*Low-lat* scenario).

atmospheres entrain a greater mass of atmospheric moisture, such that this ratio is somewhat less for the *Low-Lat* scenario, with typical values of 2–7 times that of control simulations.

In summary, we find that incorporation of high mass fractions of external water in eruption columns acts to reduce eruption column height or induce gravitational collapse, while also enhancing conditions for chemical scavenging of SO_2 into ash and hydrometeors, including initially colder temperatures, high available ash surface area, and abundant water. For SO_2 that does reach the stratosphere, results of LeGrande et al. (2016) and Zhu et al. (2020) suggest that the presence of water and fine ash enhance aerosol reaction rates and sedimentation. Our results imply that in the absence of an explicit functional dependence on the change in PSD related to MWI, the SO_2 delivery efficiency given by **Eq. 66** is at best an upper bound where eruptions interact with water layers deeper than about 50 m. On the basis of results presented here, we suggest that hydrovolcanic eruption processes will on average act to reduce the climate impacts of volcanic aerosols. However, the evaluation of stratospheric sulfur loading in volcanic eruptions requires further analysis, particularly of microphysical processes not included in our model. For example, moist convection in water saturated air may enhance lofting of secondary plumes even for collapsing columns, potentially delivering SO_2 to the stratosphere following dynamics similar to thunderstorms (Joshi and Jones, 2009; Van Eaton et al., 2012; Houghton and Carey, 2015). Alternatively, formation of hydrometeors (graupel, hail, or liquid water droplets) and aggregation of ash particles can lead to sedimentation of fine ash and water at much higher rates than predicted by particle settling time alone (Brown et al., 2012; Van Eaton et al., 2015), and column buoyancy and sedimentation processes can be further modified by interaction with atmospheric cross-winds (Girault et al., 2016). If sedimentation occurs faster than the timescales for chemical scavenging of SO_2 onto ash surfaces, this can lead to early separation of ash and gas phases, as was observed for the 2011 eruption of Grímsvötn Volcano (Prata et al., 2017). However, if the timescale for SO_2 scavenging is fast relative to particle fallout time as a result of say, high particle surface area and cold column temperature (Schmauss and Keppler, 2014), then aggregation-enhanced particle settling could act to efficiently remove scavenged SO_2 from the eruption column. For example, despite the observed separation of ash and gas clouds in the Grímsvötn eruption, Sigmarsson et al. (2013) estimated that approximately 30% of outgassed SO_2 was scavenged by ash particles and subsequently removed from the eruption cloud, with an additional 10% lost directly to the

subglacial lake (16 and 5% of the total magmatic sulfur budget, respectively).

4.6 Implications of Hydrovolcanism for Volcano-Climate Feedback

We have discussed coupled processes in hydrovolcanic eruptions which suggest that the stratospheric sulfate aerosol climate impacts of hydrovolcanic eruptions are likely to be reduced relative to dry eruptions. This hypothesis, in turn, suggests the potential for a largely unrecognized mechanism for volcano-climate feedback, where changes to the relative extent or frequency of hydrovolcanism resulting from evolving climatic conditions (glacial-interglacial cycles, for example) in turn modulate volcanic aerosol forcing. This feedback mechanism potentially acts concurrently to the effect of changing stress fields on the crust as a result of ice sheet advance and retreat, referred to as the 'unloading effect' in Cooper et al. (2018). Regional to global-scale changes in the occurrence of hydrovolcanism could for example arise from enhanced eruption rates in glaciated regions during glacial unloading (e.g., Jellinek et al., 2004; Albino et al., 2010; Sigmundsson et al., 2010). Huybers and Langmuir (2009) suggest that globally enhanced rates of volcanism would lead to an amplifying feedback where outgassing of volcanic carbon contributed to additional warming. This hypothesis was based on the assumption that time-averaged radiative forcing of volcanic CO_2 is stronger (over century to millennial timescales) than that of short-lived aerosol cooling events. However, the potential for climate impacts on multi-decadal to millennial timescales (Zhong et al., 2011; Baldini et al., 2015; Soreghan et al., 2019; Mann et al., 2021) challenges this view, and there is open debate on whether (or under what climate conditions and/or timescales) the effects of global volcanism drive net climate cooling or warming (Baldini et al., 2015; Lee and Dee, 2019; Soreghan et al., 2019). For example, Baldini et al. (2015) suggest that large volcanic sulphate injections during the Last Glacial Maximum drove hemispherically asymmetric temperature shifts and millennial-scale cooling feedbacks. A change in the relative global frequency of hydrovolcanism is one potential mechanism for steering the volcanic climate control in one direction or another over these timescales. In particular, the outgassing of volcanic CO_2 is likely less affected by surface MWI than is SO_2, since CO_2 exsolves at initially greater crustal depths (Wallace et al., 2015) than SO_2 and its climate impacts are insensitive to injection height or co-emission with ash and water. On timescales of centuries to millennia, this process could in principle modulate the global importance for climate forcing of volcanic sulfate aerosols relative to volcanic carbon and therefore alter the character (e.g. amplifying or stabilizing) of volcano-climate feedbacks resulting from glacial unloading. The extent to which hydrovolcanism modulates global volcano-climate forcing remains an open question, and likely depends critically on both eruption rates and the surface distribution and thickness of ice sheets overlying volcanic regions, and the resulting frequency and intensity of hydrovolcanic processes.

4.7 Emerging Constraints and Knowledge Gaps for Silicic Hydrovolcanic Eruptions

The primary research goal of this study is to highlight external water controls on the climate impacts of hydrovolcanic eruptions. In attempting to address this central question, we have highlighted connections among magmatic heat budget, mixing efficiency with external water, and the extent of quench fragmentation which are relevant to general aspects of hydrovolcanic eruptions. First, we show that the combined effects of gas decompression and the monotonic development of turbulence in the overlying eruption column reduce the height over which water entrainment and mixing can occur and the overall rate of entrainment relative to subaerial jets and plumes. Indeed, a key finding is that without this mechanical modulation and regardless of the predominant mechanism for water entrainment, water mass fractions sufficient to exhaust the pyroclast heat budget are ingested in relatively shallow water depths of tens of meters for even very large eruptions (see the No-L_d-No-L_X scenario in **Figure 9B**). Second, we include fragmentation in the energy conservation scheme to quantify a relationship between the amount of entrained external water and the extent of quench fragmentation. Assuming the fragmentation energy efficiency of Sonder et al. (2011) is broadly applicable, extensive fines-enrichment of the total PSD can occur for relatively modest mass fractions of entrained external water ($n_e \approx 0.12$, see **Figure 3**). Taken together, these two insights highlight two classes of question for further research into coupled hydrovolcanic processes: 1) What are the quantitative connections among hydrostatic-pressure influenced volatile exsolution, pyroclast vesicularity and permeability, glass transition temperature, and particle size distributions following magmatic fragmentation? How do the above connections modulate the mechanisms and products of fragmentation resulting from water entrainment and thermal mixing? 2) What are the predominant mechanisms governing the entrainment and mechanical and thermal mixing of external water into hot eruption columns? In particular, under what conditions is the erupting mixture particularly affected by the additional intrusion of water into the conduit through permeable wall rock (e.g. Barberi et al., 1989; Aravena et al., 2018)? Where and at what spatial scales, eruption stages, or flow regimes do processes such as molten-fuel coolant interactions (e.g., Zimanowski and Büttner, 2003) dominate? Under what conditions can energetic fuel-coolant interactions or lofting from secondary plumes following column collapse enhance stratospheric delivery of sulfur dioxide relative to mechanisms presented here?

4.8 Summary

We present a novel coupled integral model of conduit and eruption column dynamics for hydrovolcanic eruptions. We

have simulated steady phases of explosive eruptions through a shallow water layer ($Z_e \lesssim 500$ m) overlying the volcanic vent, including the effects of gas exsolution and magma ascent in the conduit, water entrainment and quench fragmentation, and eruption column rise and particle fallout. Based on our model results and arguments in **Sections 4.1–4.5**, in addition to findings of previous studies, we summarize key effects of changes in hydrostatic pressure and direct MWI on steady explosive eruption processes:

1) Increasing hydrostatic pressure with water depth reduces vent overpressure and the likelihood for choking in the conduit. These effects limit the magnitude of explosive decompression and reduce vent velocities. Choked vents do not occur in our simulations for water depths greater than about five vent diameters.
2) Increasing hydrostatic pressure with water depth reduces gas exsolution and decompression rates in the conduit, decreasing the total fraction of gas that is exsolved on eruption at the vent, and potentially limiting the conditions for magmatically-driven fragmentation (e.g., bubble overpressure).
3) The total mass of entrained water increases with water depth, driving a decrease in eruption column heights. Column collapse occurs for water mass fractions greater than about 30%.
4) There is a range of water mass fractions (10–15%) in the starting subaerial jet in which plumes heights are increased relative to dry control scenarios as a result of high vapor mass fractions and the release of latent height with condensation. However, we find that plume heights are increased only in moist, low-latitude atmospheres and for a very narrow range of water depths.
5) The critical mass eruption rate required for eruption columns to reach the tropopause is sensitive to increasing water depth and is governed primarily by the column collapse condition. For water depths greater than about 200 m, only the largest eruptions (MER ~ 10^9 kg/s) reach the tropopause, independent of the eruption latitude.
6) As water depth exceeds the limit for which overpressured vents occur ($Z_e \gtrsim 5$ vent diameters in our *Reference* scenario), the magmatic heat budget becomes exhausted, gas phases condense, and water in the jet approaches 100% liquid. Such events may still generate subaerial jets and steam plumes, but are unlikely to inject significant quantities of SO_2 or ash into the stratosphere. We find that hydrostatic pressures sufficient to suppress choking in the vent are similar to those for which minimal steam ($\lesssim 5$ wt% of the jet water phase) breaches the surface of the external water layer.
7) Fine ash production by quench fragmentation leads to an approximately 2-fold increase in the mass flux of fine ash ($< 125\ \mu$m) delivered to buoyant eruption clouds in our *Reference* scenario. Entrained external water increases mass flux of water to the spreading cloud by up to 10-fold.
8) The total ash surface area available for chemical absorption of SO_2 systematically increases in hydrovolcanic scenarios relative to control cases. However, the total surface area generated is sensitive to processes governing particle fallout and to the physics of quench fragmentation (e.g., particle roughness and surface fracture energy, and the fraction of thermal energy consumed for fragmenting particles). We suggest that the high water and fine ash content and colder temperature of hydrovolcanic columns provide conditions that enhance scavenging of SO_2 by ash and hydrometeors relative to subaerial eruptions (Schmauss and Keppler, 2014).

The above results are consistent with expectations for conduit ascent in submarine and subglacial eruptions (Wallace et al., 2015; Smellie and Edwards, 2016), and for the rise of hydrovolcanic eruption columns in the atmosphere (Koyaguchi and Woods, 1996; Mastin, 2007b). Furthermore, increasing water depths or ice thicknesses beyond threshold conditions for choked flows at the vent will lead to governing physical processes not included in our model that further act to reduce or prevent stratospheric injections of ash and volatiles (e.g. Gudmundsson et al., 2004; Manga et al., 2018). On the basis of these arguments, we hypothesize that hydrovolcanic eruptions will, *on average*, tend towards reduced stratospheric loading and residence times of sulfate aerosols relative to purely magmatic eruptions. To the extent that volcanic aerosol radiative forcing is governed by the stratospheric load and injection altitude of SO_2, H_2O, and ash, hydrovolcanism will reduce the overall climate impact. Thus, depending on the distributions of water and ice sheets on the Earth's surface, hydrovolcanism could, in principle, modulate putative volcano-climate feedbacks associated with large scale glacial unloading and associated changes in crustal stress regimes (e.g. Jellinek et al., 2004; Huybers and Langmuir, 2009; Sigmundsson et al., 2010; Cooper et al., 2018). In particular, crustal loading or unloading of water and ice may influence volcano-climate forcing both by locally altering eruption frequency as well as the extent to which eruptions are dominated by MWI processes. Evaluating the climate impacts of hydrovolcanic eruptions relative to purely magmatic eruptions requires further detailed analysis of the interplay between the coupled processes of conduit ascent and gas exsolution, fragmentation mechanisms, and the fluid dynamics, microphysics, and chemistry of transport and dispersal of SO_2, ash, and water in eruption columns.

DATA AVAILABILITY STATEMENT

Complete model output for each of the simulation scenarios presented here (see **Table 2**) are available at https://doi.org/10.6084/m9.figshare.19243230.v1.

AUTHOR CONTRIBUTIONS

CR was the primary study author, and performed the bulk of code development for the coupled model, including novel components. CR performed data analysis and the bulk of manuscript writing. AJ was the primary investigator and holder of funding sources, and

provided physical insight for the development of model equations and extensive discussion and review of the study results, interpretations, and manuscript writing. SH is the author of the conduit model and provided relevant code with modifications necessary for this study, and provided code examples and physical insight for the development of the water-entrainment model, and authored the conduit model components of the manuscript methods section. TA provided code for the eruption column model and analysis for estimates of stratospheric injection of sulfur dioxide, and provided advice and oversight of data analysis related to eruption column components of the study.

FUNDING

CR and AJ were funded through an NSERC Discovery Grant to AJ. SH was supported by NSF Grant EAR-1348072 to Helge Gonnermann. TA acknowledges support from the European Union's Horizon 2020 research and innovation program under the Marie Sklodowska-Curie grant agreement No. 835939, and from the Sidney Sussex college through a Junior Research Fellowship.

ACKNOWLEDGMENTS

This research benefited from conversations and insight provided by Josef Dufek, Erin Fitch, Helge Gonnermann, Gary Glatzmaier and Thomas Jones. We would like to thank Ingo Sonder, Magnús T. Guðmundsson, and Steve Self for their thoughtful reviews and comments, which greatly improved the manuscript.

SUPPLEMENTARY MATERIAL

The Supplementary Material for this article can be found online at: https://www.frontiersin.org/articles/10.3389/feart.2022.788294/full#supplementary-material

REFERENCES

Albino, F., Pinel, V., and Sigmundsson, F. (2010). Influence of Surface Load Variations on Eruption Likelihood: Application to Two Icelandic Subglacial Volcanoes, Grímsvötn and Katla. *Geophys. J. Int.* 181, 1510–1524. doi:10.1111/j.1365-246X.2010.04603.x

Ansmann, A., Tesche, M., Seifert, P., Groß, S., Freudenthaler, V., Apituley, A., et al. (2011). Ash and fine-mode Particle Mass Profiles from EARLINET-AERONET Observations over central Europe after the Eruptions of the Eyjafjallajökull Volcano in 2010. *J. Geophys. Res. Atmospheres* 116, D00U02. doi:10.1029/2010JD015567

Aravena, A., Vitturi, M. d. M., Cioni, R., and Neri, A. (2018). Physical Constraints for Effective Magma-Water Interaction along Volcanic Conduits during Silicic Explosive Eruptions. *Geology* 46, 867–870. doi:10.1130/G45065.1

Aubry, T. J., Cerminara, M., and Jellinek, A. M. (2019). Impacts of Climate Change on Volcanic Stratospheric Injections: Comparison of 1-D and 3-D Plume Model Projections. *Geophys. Res. Lett.* 46. doi:10.1029/2019GL083975

Aubry, T. J., Engwell, S., Bonadonna, C., Carazzo, G., Scollo, S., Van Eaton, A. R., et al. (2021a). The Independent Volcanic Eruption Source Parameter Archive (IVESPA, Version 1.0): A New Observational Database to Support Explosive Eruptive Column Model Validation and Development. *J. Volcanology Geothermal Res.* 417, 107295. doi:10.1016/j.jvolgeores.2021.107295

Aubry, T. J., Jellinek, A. M., Degruyter, W., Bonadonna, C., Radić, V., Clyne, M., et al. (2016). Impact of Global Warming on the Rise of Volcanic Plumes and Implications for Future Volcanic Aerosol Forcing. *J. Geophys. Res. Atmospheres* 121, 2016JD025405. doi:10.1002/2016JD025405

Aubry, T. J., and Jellinek, A. M. (2018). New Insights on Entrainment and Condensation in Volcanic Plumes: Constraints from Independent Observations of Explosive Eruptions and Implications for Assessing Their Impacts. *Earth Planet. Sci. Lett.* 490, 132–142. doi:10.1016/j.epsl.2018.03.028

Aubry, T. J., Staunton-Sykes, J., Marshall, L. R., Haywood, J., Abraham, N. L., and Schmidt, A. (2021b). Climate Change Modulates the Stratospheric Volcanic Sulfate Aerosol Lifecycle and Radiative Forcing from Tropical Eruptions. *Nat. Commun.* 12, 4708. doi:10.1038/s41467-021-24943-7

Baldini, J. U. L., Brown, R. J., and McElwaine, J. N. (2015). Was Millennial Scale Climate Change during the Last Glacial Triggered by Explosive Volcanism? *Scientific Rep.* 5, 17442. doi:10.1038/srep17442

Barberi, F., Cioni, R., Rosi, M., Santacroce, R., Sbrana, A., and Vecci, R. (1989). Magmatic and Phreatomagmatic Phases in Explosive Eruptions of Vesuvius as Deduced by Grain-Size and Component Analysis of the Pyroclastic Deposits. *J. Volcanology Geothermal Res.* 38, 287–307. doi:10.1016/0377-0273(89)90044-9

Bercovici, D., and Michaut, C. (2010). Two-phase Dynamics of Volcanic Eruptions: Compaction, Compression and the Conditions for Choking. *Geophys. J. Int.* 182, 843–864. doi:10.1111/j.1365-246X.2010.04674.x

Bluth, G. J. S., Rose, W. I., Sprod, I. E., and Krueger, A. J. (1997). Stratospheric Loading of Sulfur from Explosive Volcanic Eruptions. *J. Geology.* 105, 671–684. doi:10.1086/515972

Bonadonna, C., Ernst, G. G. J., and Sparks, R. S. J. (1998). Thickness Variations and Volume Estimates of Tephra Fall Deposits: The Importance of Particle Reynolds Number. *J. Volcanology Geothermal Res.* 81, 173–187. doi:10.1016/S0377-0273(98)00007-9

Bouhifd, M. A., Whittington, A. G., and Richet, P. (2015). Densities and Volumes of Hydrous Silicate Melts: New Measurements and Predictions. *Chem. Geology.* 418, 40–50. doi:10.1016/j.chemgeo.2015.01.012

Brown, R. J., Bonadonna, C., and Durant, A. J. (2012). A Review of Volcanic Ash Aggregation. *Phys. Chem. Earth, Parts A/B/C* 45-46, 65–78. doi:10.1016/j.pce.2011.11.001

Bursik, M. I., Sparks, R. S. J., Gilbert, J. S., and Carey, S. N. (1992). Sedimentation of Tephra by Volcanic Plumes: I. Theory and its Comparison with a Study of the Fogo A Plinian deposit, Sao Miguel (Azores). *Bull. Volcanology* 54, 329–344. doi:10.1007/BF00301486

Büttner, R., Dellino, P., Raue, H., Sonder, I., and Zimanowski, B. (2006). Stress-induced Brittle Fragmentation of Magmatic Melts: Theory and Experiments. *J. Geophys. Res. Solid Earth* 111. doi:10.1029/2005JB003958

Büttner, R., Dellino, P., Volpe, L. L., Lorenz, V., and Zimanowski, B. (2002). Thermohydraulic Explosions in Phreatomagmatic Eruptions as Evidenced by the Comparison between Pyroclasts and Products from Molten Fuel Coolant Interaction Experiments. *J. Geophys. Res. Solid Earth* 107, ECV 5–1–ECV 5–14. doi:10.1029/2001JB000511

Cahalan, R. C., and Dufek, J. (2021). Explosive Submarine Eruptions: The Role of Condensable Gas Jets in Underwater Eruptions. *J. Geophys. Res. Solid Earth* 126, e2020JB020969. doi:10.1029/2020JB020969

Campagnola, S., Romano, C., Mastin, L. G., and Vona, A. (2016). Confort 15 Model of Conduit Dynamics: Applications to Pantelleria Green Tuff and Etna 122 BC Eruptions. *Contrib. Mineralogy Petrology* 171, 60. doi:10.1007/s00410-016-1265-5

Capra, L. (2006). Abrupt Climatic Changes as Triggering Mechanisms of Massive Volcanic Collapses. *J. Volcanology Geothermal Res.* 155, 329–333. doi:10.1016/j.jvolgeores.2006.04.009

Carazzo, G., and Jellinek, A. M. (2012). A New View of the Dynamics, Stability and Longevity of Volcanic Clouds. *Earth Planet. Sci. Lett.* 325 (326), 39–51. doi:10.1016/j.epsl.2012.01.025

Carazzo, G., and Jellinek, A. M. (2013). Particle Sedimentation and Diffusive Convection in Volcanic Ash-Clouds. *J. Geophys. Res. Solid Earth* 118, 1420–1437. doi:10.1002/jgrb.50155

Carazzo, G., Kaminski, E., and Tait, S. (2008). On the Rise of Turbulent Plumes: Quantitative Effects of Variable Entrainment for Submarine Hydrothermal Vents, Terrestrial and Extra Terrestrial Explosive Volcanism. *J GEOPHYSICAL RESEARCH* 113, B09201. doi:10.1029/2007jb005458

Carazzo, G., Kaminski, E., and Tait, S. (2006). The Route to Self-Similarity in Turbulent Jets and Plumes. *J. Fluid Mech.* 547, 137–148. doi:10.1017/S002211200500683X

Carey, R. J., Houghton, B. F., and Thordarson, T. (2009). Abrupt Shifts between Wet and Dry Phases of the 1875 Eruption of Askja Volcano: Microscopic Evidence for Macroscopic Dynamics. *J. Volcanology Geothermal Res.* 184, 256–270. doi:10.1016/j.jvolgeores.2009.04.003

Cas, R. A. F., and Simmons, J. M. (2018). Why Deep-Water Eruptions Are So Different from Subaerial Eruptions. *Front. Earth Sci.* 6. doi:10.3389/feart.2018.00198

Cas, R., and Wright, J. (1987). *Volcanic Successions Modern and Ancient: A Geological Approach to Processes, Products and Successions*. Springer Science & Business Media.

Cerminara, M., Esposti Ongaro, T., and Berselli, L. C. (2016). ASHEE-1.0: A Compressible, Equilibrium–Eulerian Model for Volcanic Ash Plumes. *Geoscientific Model. Development* 9, 697–730. doi:10.5194/gmd-9-697-2016

Cole, P. D., Queiroz, G., Wallenstein, N., Gaspar, J. L., Duncan, A. M., and Guest, J. E. (1995). An Historic Subplinian/phreatomagmatic Eruption: The 1630 AD Eruption of Furnas Volcano, Sã˜O Miguel, Azores. *J. Volcanology Geothermal Res.* 69, 117–135. doi:10.1016/0377-0273(95)00033-X

Colucci, S., de' Michieli Vitturi, M., Neri, A., and Palladino, D. M. (2014). An Integrated Model of Magma Chamber, Conduit and Column for the Analysis of Sustained Explosive Eruptions. *Earth Planet. Sci. Lett.* 404, 98–110. doi:10.1016/j.epsl.2014.07.034

Cooper, C. L., Swindles, G. T., Savov, I. P., Schmidt, A., and Bacon, K. L. (2018). Evaluating the Relationship between Climate Change and Volcanism. *Earth-Science Rev.* 177, 238–247. doi:10.1016/j.earscirev.2017.11.009

Costa, A., Pioli, L., and Bonadonna, C. (2016). Assessing Tephra Total Grain-Size Distribution: Insights from Field Data Analysis. *Earth Planet. Sci. Lett.* 443, 90–107. doi:10.1016/j.epsl.2016.02.040

[Dataset] Global Volcanism Program (2013). *South Sarigan Seamount (284193)*.

de' Michieli Vitturi, M., and Aravena, Á. (2021). "Chapter 6 - Numerical Modeling of Magma Ascent Dynamics," in *Forecasting and Planning for Volcanic Hazards, Risks, and Disasters*. Editor P. Papale (Elsevier), 239–284. doi:10.1016/B978-0-12-818082-2.00006-8

Degruyter, W., and Bonadonna, C. (2013). Impact of Wind on the Condition for Column Collapse of Volcanic Plumes. *Earth Planet. Sci. Lett.* 377–378, 218–226. doi:10.1016/j.epsl.2013.06.041

Degruyter, W., and Bonadonna, C. (2012). Improving on Mass Flow Rate Estimates of Volcanic Eruptions. *Geophys. Res. Lett.* 39. doi:10.1029/2012GL052566

Dingwell, D. B. (1998). The Glass Transition in Hydrous Granitic Melts. *Phys. Earth Planet. Interiors* 107, 1–8. doi:10.1016/S0031-9201(97)00119-2

Dufek, J., Manga, M., and Staedter, M. (2007). Littoral Blasts: Pumice-Water Heat Transfer and the Conditions for Steam Explosions when Pyroclastic Flows Enter the Ocean. *J. Geophys. Res. Solid Earth* 112, B11201. doi:10.1029/2006JB004910

Durant, A. J., Rose, W. I., Sarna-Wojcicki, A. M., Carey, S., and Volentik, A. C. M. (2009). Hydrometeor-enhanced Tephra Sedimentation: Constraints from the 18 May 1980 Eruption of Mount St. Helens. *J. Geophys. Res. Solid Earth* 114. doi:10.1029/2008JB005756

Dürig, T., Sonder, I., Zimanowski, B., Beyrichen, H., and Büttner, R. (2012). Generation of Volcanic Ash by Basaltic Volcanism. *J. Geophys. Res. Solid Earth* 117. doi:10.1029/2011JB008628

Dürig, T., White, J. D. L., Murch, A. P., Zimanowski, B., Büttner, R., Mele, D., et al. (2020a). Deep-sea Eruptions Boosted by Induced Fuel–Coolant Explosions. *Nat. Geosci.* 13, 498–503. doi:10.1038/s41561-020-0603-4

Dürig, T., White, J. D. L., Zimanowski, B., Büttner, R., Murch, A., and Carey, R. J. (2020b). Deep-sea Fragmentation Style of Havre Revealed by Dendrogrammatic Analyses of Particle Morphometry. *Bull. Volcanology* 82, 67. doi:10.1007/s00445-020-01408-1

Elsworth, D., Voight, B., Thompson, G., and Young, S. (2004). Thermal-hydrologic Mechanism for Rainfall-Triggered Collapse of Lava Domes. *Geology* 32, 969–972. doi:10.1130/G20730.1

Farquharson, J. I., and Amelung, F. (2020). Extreme Rainfall Triggered the 2018 Rift Eruption at Kīlauea Volcano. *Nature* 580, 491–495. doi:10.1038/s41586-020-2172-5

Fasullo, J. T., Tomas, R., Stevenson, S., Otto-Bliesner, B., Brady, E., and Wahl, E. (2017). The Amplifying Influence of Increased Ocean Stratification on a Future Year without a Summer. *Nat. Commun.* 8, 1236. doi:10.1038/s41467-017-01302-z

Fee, D., Lyons, J., Haney, M., Wech, A., Waythomas, C., Diefenbach, A. K., et al. (2020). Seismo-acoustic Evidence for Vent Drying during Shallow Submarine Eruptions at Bogoslof Volcano, Alaska. *Bull. Volcanology* 82, 2. doi:10.1007/s00445-019-1326-5

Fisher, R. V., and Schmincke, H.-U. (2012). *Pyroclastic Rocks*. Springer Science & Business Media.

Fitch, E. P., and Fagents, S. A. (2020). Using the Characteristics of Rootless Cone Deposits to Estimate the Energetics of Explosive Lava–Water Interactions. *Bull. Volcanology* 82, 83. doi:10.1007/s00445-020-01422-3

Gilchrist, J. T., and Jellinek, A. M. (2021). Sediment Waves and the Gravitational Stability of Volcanic Jets. *Bull. Volcanology* 83, 64. doi:10.1007/s00445-021-01472-1

Giordano, D., Nichols, A. R. L., and Dingwell, D. B. (2005). Glass Transition Temperatures of Natural Hydrous Melts: A Relationship with Shear Viscosity and Implications for the Welding Process. *J. Volcanology Geothermal Res.* 142, 105–118. doi:10.1016/j.jvolgeores.2004.10.015

Girault, F., Carazzo, G., Tait, S., Ferrucci, F., and Kaminski, É. (2014). The Effect of Total Grain-Size Distribution on the Dynamics of Turbulent Volcanic Plumes. *Earth Planet. Sci. Lett.* 394, 124–134. doi:10.1016/j.epsl.2014.03.021

Girault, F., Carazzo, G., Tait, S., and Kaminski, E. (2016). Combined Effects of Total Grain-Size Distribution and Crosswind on the Rise of Eruptive Volcanic Columns. *J. Volcanology Geothermal Res.* 326, 103–113. doi:10.1016/j.jvolgeores.2015.11.007

Glaze, L. S., Baloga, S. M., and Wilson, L. (1997). Transport of Atmospheric Water Vapor by Volcanic Eruption Columns. *J. Geophys. Res. Atmospheres* 102, 6099–6108. doi:10.1029/96JD03125

Gonnermann, H. M. (2015). Magma Fragmentation. *Annu. Rev. Earth Planet. Sci.* 43, 431–458. doi:10.1146/annurev-earth-060614-105206

Gonnermann, H. M., and Manga, M. (2013). "Dynamics of Magma Ascent in the Volcanic Conduit," in *Modeling Volcanic Processes: The Physics and Mathematics of Volcanism*. Editors R. M. C. Lopes, S. A. Fagents, and T. K. P. Gregg (Cambridge: Cambridge University Press), 55–84. doi:10.1017/CBO9781139021562.004

Gonnermann, H. M., and Manga, M. (2007). The Fluid Mechanics inside a Volcano. *Annu. Rev. Fluid Mech.* 39, 321–356. doi:10.1146/annurev.fluid.39.050905.110207

Green, D. N., Evers, L. G., Fee, D., Matoza, R. S., Snellen, M., Smets, P., et al. (2013). Hydroacoustic, Infrasonic and Seismic Monitoring of the Submarine Eruptive Activity and Sub-aerial Plume Generation at South Sarigan, May 2010. *J. Volcanology Geothermal Res.* 257, 31–43. doi:10.1016/j.jvolgeores.2013.03.006

Gudmundsson, M. T., Pálsson, F., Thordarson, T., Hoskuldsson, A., Larsen, G., Hognadottir, T., et al. (2014). Water/magma Mass Fractions in Phreatomagmatic Eruption Plumes - Constraints from the Grímsvötn 2011 Eruption. *AGU Fall Meet. Abstr.* 11, V11B–V4718.

Gudmundsson, M. T., Sigmundsson, F., Björnsson, H., and Högnadóttir, T. (2004). The 1996 Eruption at Gjálp, Vatnajökull Ice Cap, Iceland: Efficiency of Heat Transfer, Ice Deformation and Subglacial Water Pressure. *Bull. Volcanology* 66, 46–65. doi:10.1007/s00445-003-0295-9

Gudmundsson, M. T., Thordarson, T., Höskuldsson, Á., Larsen, G., Björnsson, H., Prata, F. J., et al. (2012). Ash Generation and Distribution from the April-May 2010 Eruption of Eyjafjallajökull, Iceland. *Scientific Rep.* 2, 572. doi:10.1038/srep00572

Hajimirza, S., Gonnermann, H. M., Gardner, J. E., and Giachetti, T. (2019). Predicting Homogeneous Bubble Nucleation in Rhyolite. *J. Geophys. Res. Solid Earth* 124, 2395–2416. doi:10.1029/2018JB015891

Hajimirza, S., Gonnermann, H. M., and Gardner, J. E. (2021). Reconciling Bubble Nucleation in Explosive Eruptions with Geospeedometers. *Nat. Commun.* 12, 283. doi:10.1038/s41467-020-20541-1

Hajimirza, S., Jones, T. J., Moreland, W. M., Gonnermann, H. M., and Thordarson, T. R. (2022). Impacts of Climate Change on Volcanic Stratospheric Injections:

Comparison of 1-D and 3-D Plume Model Projections. *Geochem. Geophys. Geosystems* 23, e2021GC010160. doi:10.1029/2021GC010160

Hersbach, H., Bell, B., Berrisford, P., Hirahara, S., Horányi, A., Muñoz-Sabater, J., et al. (2020). The ERA5 Global Reanalysis. *Q. J. R. Meteorol. Soc.* 146, 1999–2049. doi:10.1002/qj.3803

Holloway, J. R. (1977). "Fugacity and Activity of Molecular Species in Supercritical Fluids," in *Thermodynamics in Geology*. Editor D. G. Fraser (Dordrecht: Springer Netherlands), NATO Advanced Study Institutes Series), 161–181. doi:10.1007/978-94-010-1252-2_9

Houghton, B., and Carey, R. J. (2015). "Chapter 34 - Pyroclastic Fall Deposits," in *The Encyclopedia of Volcanoes*. Editor H. Sigurdsson. Second Edition (Amsterdam: Academic Press), 599–616. doi:10.1016/B978-0-12-385938-9.00034-1

Houghton, B. F., and Carey, R. J. (2019). Physical Constraints for Effective Magma-Water Interaction along Volcanic Conduits Silicic Explosive Eruptions: COMMENT. *Geology* 47, e461. doi:10.1130/G46200Y.110.1130/g46033c.1

Houghton, B. F., and Wilson, C. J. N. (1989). A Vesicularity index for Pyroclastic Deposits. *Bull. Volcanology* 51, 451–462. doi:10.1007/BF01078811

Houghton, B., White, J. D. L., and Van Eaton, A. R. (2015). "Chapter 30 - Phreatomagmatic and Related Eruption Styles," in *The Encyclopedia of Volcanoes*. Editor H. Sigurdsson. Second Edition (Amsterdam: Academic Press), 537–552. doi:10.1016/B978-0-12-385938-9.00030-4

Huybers, P., and Langmuir, C. (2009). Feedback between Deglaciation, Volcanism, and Atmospheric CO2. *Earth Planet. Sci. Lett.* 286, 479–491. doi:10.1016/j.epsl.2009.07.014

Jellinek, A. M., Manga, M., and Saar, M. O. (2004). Did Melting Glaciers Cause Volcanic Eruptions in Eastern California? Probing the Mechanics of dike Formation. *J. Geophys. Res. Solid Earth* 109. doi:10.1029/2004JB002978

Jones, T., Gonnermann, H., Moreland, W., and Thordarson, T. (2019). Quantifying Water Entrainment in Volcanic Jets. *Geophys. Res. Abstr.* 21, 1.

Joshi, M. M., and Jones, G. S. (2009). The Climatic Effects of the Direct Injection of Water Vapour into the Stratosphere by Large Volcanic Eruptions. *Atmos. Chem. Phys.* 9 (16), 6109–6118. doi:10.5194/acp-9-6109-2009

Jull, M., and McKenzie, D. (1996). The Effect of Deglaciation on Mantle Melting beneath Iceland. *J. Geophys. Res. Solid Earth* 101, 21815–21828. doi:10.1029/96JB01308

Junglas, P. (2009). Implementation of the IAPWS-95 Standard for Use in Thermodynamics Lectures. *Int. J. Eng. Education* 25, 3–10.

Kaminski, E., and Jaupart, C. (1998). The Size Distribution of Pyroclasts and the Fragmentation Sequence in Explosive Volcanic Eruptions. *J. Geophys. Res. Solid Earth* 103, 29759–29779. doi:10.1029/98JB02795

Kaminski, E., Tait, S., and Carazzo, G. (2005). Turbulent Entrainment in Jets with Arbitrary Buoyancy. *J. Fluid Mech.* 526, 361–376. doi:10.1017/S0022112004003209

Kokelaar, P. (1986). Magma-water Interactions in Subaqueous and Emergent Basaltic. *Bull. Volcanology* 48, 275–289. doi:10.1007/BF01081756

Kotsovinos, N. E. (2000). Axisymmetric Submerged Intrusion in Stratified Fluid. *J. Hydraulic Eng.* 126, 466–456. doi:10.1061/(ASCE)0733-942910.1061/(asce)0733-9429(2000)126:6(446)

Koyaguchi, T. (2005). An Analytical Study for 1-dimensional Steady Flow in Volcanic Conduits. *J. Volcanology Geothermal Res.* 143, 29–52. doi:10.1016/j.jvolgeores.2004.09.009

Koyaguchi, T., and Woods, A. W. (1996). On the Formation of Eruption Columns Following Explosive Mixing of Magma and Surface-Water. *J. Geophys. Res. Solid Earth* 101, 5561–5574. doi:10.1029/95JB01687

Kremser, S., Thomason, L. W., von Hobe, M., Hermann, M., Deshler, T., Timmreck, C., et al. (2016). Stratospheric Aerosol-Observations, Processes, and Impact on Climate: Stratospheric Aerosol. *Rev. Geophys.* 54, 278–335. doi:10.1002/2015RG000511

Krishnamohan, K.-P. S.-P., Bala, G., Cao, L., Duan, L., and Caldeira, K. (2019). Climate System Response to Stratospheric Sulfate Aerosols: Sensitivity to Altitude of Aerosol Layer. *Earth Syst. Dyn.* 10, 885–900. doi:10.5194/esd-10-885-2019

Lacis, A. (2015). Volcanic Aerosol Radiative Properties. *Past Glob. Change Mag.* 23, 50–51. doi:10.22498/pages.23.2.50

Lee, C.-T., and Dee, S. (2019). Does Volcanism Cause Warming or Cooling? *Geology* 47, 687–688. doi:10.1130/focus072019.1

LeGrande, A. N., Tsigaridis, K., and Bauer, S. E. (2016). Role of Atmospheric Chemistry in the Climate Impacts of Stratospheric Volcanic Injections. *Nat. Geosci.* 9, 652–655. doi:10.1038/ngeo2771

Lherm, V., and Jellinek, A. M. (2019). Experimental Constraints on the Distinct Effects of Ash, Lapilli, and Larger Pyroclasts on Entrainment and Mixing in Volcanic Plumes. *Bull. Volcanology* 81, 73. doi:10.1007/s00445-019-1329-2

Linden, P. F. (1979). Mixing in Stratified Fluids. *Geophys. Astrophysical Fluid Dyn.* 13, 3–23. doi:10.1080/03091927908243758

Liu, E. J., Cashman, K. V., Rust, A. C., and Gislason, S. R. (2015). The Role of Bubbles in Generating fine Ash during Hydromagmatic Eruptions. *Geology* 43, 239–242. doi:10.1130/G36336.1

Liu, E. J., Cashman, K. V., Rust, A. C., and Höskuldsson, A. (2017). Contrasting Mechanisms of Magma Fragmentation during Coeval Magmatic and Hydromagmatic Activity: The Hverfjall Fires Fissure Eruption, Iceland. *Bull. Volcanology* 79, 68. doi:10.1007/s00445-017-1150-8

Liu, E. J. (2016). *The Generation of Volcanic Ash during Basaltic Hydromagmatic Eruptions : From Fragmentation to Resuspension*. Ph.D. thesis. Bristol, England: University of Bristol.

Liu, Y., Zhang, Y., and Behrens, H. (2005). Solubility of H2O in Rhyolitic Melts at Low Pressures and a New Empirical Model for Mixed H2O–CO2 Solubility in Rhyolitic Melts. *J. Volcanology Geothermal Res.* 143, 219–235. doi:10.1016/j.jvolgeores.2004.09.019

Lyons, J. J., Haney, M. M., Fee, D., Wech, A. G., and Waythomas, C. F. (2019). Infrasound from Giant Bubbles during Explosive Submarine Eruptions. *Nat. Geosci.* 12, 952–958. doi:10.1038/s41561-019-0461-0

Magnússon, E., Gudmundsson, M. T., Roberts, M. J., Sigurðsson, G., Höskuldsson, F., and Oddsson, B. (2012). Ice-volcano Interactions during the 2010 Eyjafjallajökull Eruption, as Revealed by Airborne Imaging Radar. *J. Geophys. Res. Solid Earth* 117. doi:10.1029/2012JB009250

Manga, M., Fauria, K. E., Lin, C., Mitchell, S. J., Jones, M., Conway, C. E., et al. (2018). The Pumice Raft-Forming 2012 Havre Submarine Eruption Was Effusive. *Earth Planet. Sci. Lett.* 489, 49–58. doi:10.1016/j.epsl.2018.02.025

Mann, M. E., Steinman, B. A., Brouillette, D. J., and Miller, S. K. (2021). Multidecadal Climate Oscillations during the Past Millennium Driven by Volcanic Forcing. *Science* 371, 1014–1019. doi:10.1126/science.abc5810

Manzella, I., Bonadonna, C., Phillips, J. C., and Monnard, H. (2015). The Role of Gravitational Instabilities in Deposition of Volcanic Ash. *Geology* 43, 211–214. doi:10.1130/G36252.1

Marshall, L., Johnson, J. S., Mann, G. W., Lee, L., Dhomse, S. S., Regayre, L., et al. (2019). Exploring How Eruption Source Parameters Affect Volcanic Radiative Forcing Using Statistical Emulation. *J. Geophys. Res. Atmospheres* 124, 964–985. doi:10.1029/2018JD028675

Massol, H., and Koyaguchi, T. (2005). The Effect of Magma Flow on Nucleation of Gas Bubbles in a Volcanic Conduit. *J. Volcanology Geothermal Res.* 143, 69–88. doi:10.1016/j.jvolgeores.2004.09.011

Mastin, L. G. (2007b). A User-Friendly One-Dimensional Model for Wet Volcanic Plumes. *Geochem. Geophys. Geosystems* 8. doi:10.1029/2006GC001455

Mastin, L. G. (2007a). Generation of fine Hydromagmatic Ash by Growth and Disintegration of Glassy Rinds. *J. Geophys. Res. Solid Earth* 112. doi:10.1029/2005JB003883

Mastin, L. G., and Ghiorso, M. S. (2000). *A Numerical Program for Steady-State Flow of Magma-Gas Mixtures through Vertical Eruptive Conduits*. Tech. rep. Washington, DC: Department of the Interior.

Mastin, L. G., and Witter, J. B. (2000). The Hazards of Eruptions through Lakes and Seawater. *J. Volcanology Geothermal Res.* 97, 195–214. doi:10.1016/S0377-0273(99)00174-2

McGimsey, R. G., Neal, C. A., Searcy, C. K., Camacho, J. T., Aydlett, W. B., Embley, R. W., et al. (2010). *The May 2010 Submarine Eruption from South Sarigan Seamount, Northern Mariana Islands 2010, T11E–07 07M*.

Michaut, C., Ricard, Y., Bercovici, D., and Sparks, R. S. J. (2013). Eruption Cyclicity at Silicic Volcanoes Potentially Caused by Magmatic Gas Waves. *Nat. Geosci.* 6, 856–860. doi:10.1038/ngeo1928

Moitra, P., Sonder, I., and Valentine, G. A. (2020). The Role of External Water on Rapid Cooling and Fragmentation of Magma. *Earth Planet. Sci. Lett.* 537, 116194. doi:10.1016/j.epsl.2020.116194

Moreland, W. (2017). *Explosive Activity in Flood Lava Eruptions: A Case Study of the 10th Century Eldgjá Eruption, Iceland*. Ph.D. thesis. Reykjavík, Iceland:

University of Iceland, School of Engineering and Natural Sciences, Faculty of Earth Sciences.

Moreland, W. M., Thordarson, T., Houghton, B. F., and Larsen, G. (2019). Driving Mechanisms of Subaerial and Subglacial Explosive Episodes during the 10th century Eldgjá Fissure Eruption, Southern Iceland. *Volcanica* 2, 129–150. doi:10.30909/vol.02.02.129150

Morton, B. R., Taylor, G. I., and Turner, J. S. (1956). Turbulent Gravitational Convection from Maintained and Instantaneous Sources. *Proc. R. Soc. Lond. Ser. A. Math. Phys. Sci.* 234, 1–23. doi:10.1098/rspa.1956.0011

Murch, A. P., White, J. D. L., and Carey, R. J. (2019). Characteristics and Deposit Stratigraphy of Submarine-Erupted Silicic Ash, Havre Volcano, Kermadec Arc, New Zealand. *Front. Earth Sci.* 7, 1. doi:10.3389/feart.2019.00001

Nelson, C. S., and Lister, G. S. (1995). Surficial Bottom Sediments of Lake Taupo, New Zealand: Texture, Composition, Provenance, and Sedimentation Rates. *New Zealand J. Geology. Geophys.* 38, 61–79. doi:10.1080/00288306.1995.9514639

Neri, A., Di Muro, A., and Rosi, M. (2002). Mass Partition during Collapsing and Transitional Columns by Using Numerical Simulations. *J. Volcanology Geothermal Res.* 115, 1–18. doi:10.1016/S0377-0273(01)00304-3

Niemeier, U., Timmreck, C., Graf, H.-F., Kinne, S., Rast, S., and Self, S. (2009). Initial Fate of fine Ash and Sulfur from Large Volcanic Eruptions. *Atmos. Chem. Phys.* 9, 9043–9057. doi:10.5194/acp-9-9043-2009

Ogden, D. E., Wohletz, K. H., Glatzmaier, G. A., and Brodsky, E. E. (2008). Numerical Simulations of Volcanic Jets: Importance of Vent Overpressure. *J. Geophys. Res. Solid Earth* 113, B02204. doi:10.1029/2007JB005133

Papale, P. (1999). Strain-induced Magma Fragmentation in Explosive Eruptions. *Nature* 397, 425–428. doi:10.1038/17109

Patel, A., Manga, M., Carey, R. J., and Degruyter, W. (2013). Effects of thermal Quenching on Mechanical Properties of Pyroclasts. *J. Volcanology Geothermal Res.* 258, 24–30. doi:10.1016/j.jvolgeores.2013.04.001

Prata, F., Woodhouse, M., Huppert, H. E., Prata, A., Thordarson, T., and Carn, S. (2017). Atmospheric Processes Affecting the Separation of Volcanic Ash and SO2 in Volcanic Eruptions: Inferences from the May 2011 Grímsvötn Eruption. *Atmos. Chem. Phys.* 17, 10709–10732. doi:10.5194/acp-17-10709-2017

Robock, A. (2000). Volcanic Eruptions and Climate. *Rev. Geophys.* 38, 191–219. doi:10.1029/1998RG000054

Rose, W. I., Bluth, G. J. S., Schneider, D. J., Ernst, G. G. J., Riley, C. M., Henderson, L. J., et al. (2001). Observations of Volcanic Clouds in Their First Few Days of Atmospheric Residence: The 1992 Eruptions of Crater Peak, Mount Spurr Volcano, Alaska. *J. Geology.* 109, 677–694. doi:10.1086/323189

Rose, W. I., Delene, D. J., Schneider, D. J., Bluth, G. J. S., Krueger, A. J., Sprod, I., et al. (1995). Ice in the 1994 Rabaul Eruption Cloud: Implications for Volcano hazard and Atmospheric Effects. *Nature* 375, 477–479. doi:10.1038/375477a0

Rose, W. I. (1977). Scavenging of Volcanic Aerosol by Ash: Atmospheric and Volcanologic Implications. *Geology* 5, 621–624. doi:10.1130/0091-7613(1977)5<621:SOVABA>2.0.CO;2

Rust, A. C., and Cashman, K. V. (2011). Permeability Controls on Expansion and Size Distributions of Pyroclasts. *J. Geophys. Res. Solid Earth* 116. doi:10.1029/2011JB008494

Saffaraval, F., and Solovitz, S. A. (2012). Near-exit Flow Physics of a Moderately Overpressured Jet. *Phys. Fluids* 24, 086101. doi:10.1063/1.4745005

Saffaraval, F., Solovitz, S. A., Ogden, D. E., and Mastin, L. G. (2012). Impact of Reduced Near-Field Entrainment of Overpressured Volcanic Jets on Plume Development. *J. Geophys. Res. Solid Earth* 117. doi:10.1029/2011JB008862

Santer, B. D., Bonfils, C., Painter, J. F., Zelinka, M. D., Mears, C., Solomon, S., et al. (2014). Volcanic Contribution to Decadal Changes in Tropospheric Temperature. *Nat. Geosci.* 7, 185–189. doi:10.1038/ngeo2098

Schleussner, C. F., and Feulner, G. (2013). A Volcanically Triggered Regime Shift in the Subpolar North Atlantic Ocean as a Possible Origin of the Little Ice Age. *Clim. Past* 9, 1321–1330. doi:10.5194/cp-9-1321-2013

Schmauss, D., and Keppler, H. (2014). Adsorption of Sulfur Dioxide on Volcanic Ashes. *Am. Mineral.* 99, 1085–1094. doi:10.2138/am.2014.4656

Schmid, A., Sonder, I., Seegelken, R., Zimanowski, B., Büttner, R., Gudmundsson, M. T., et al. (2010). Experiments on the Heat Discharge at the Dynamic Magma-Water-Interface. *Geophys. Res. Lett.* 37. doi:10.1029/2010GL044963

Schmidt, A., Carslaw, K. S., Mann, G. W., Rap, A., Pringle, K. J., Spracklen, D. V., et al. (2012). Importance of Tropospheric Volcanic Aerosol for Indirect Radiative Forcing of Climate. *Atmos. Chem. Phys.* 12, 7321–7339. doi:10.5194/acp-12-7321-2012

Self, S., and Sparks, R. S. J. (1978). Characteristics of Widespread Pyroclastic Deposits Formed by the Interaction of Silicic Magma and Water. *Bull. Volcanologique* 41, 196. doi:10.1007/BF02597223

Shea, T. (2017). Bubble Nucleation in Magmas: A Dominantly Heterogeneous Process? *J. Volcanology Geothermal Res.* 343, 155–170. doi:10.1016/j.jvolgeores.2017.06.025

Sigl, M., Winstrup, M., McConnell, J. R., Welten, K. C., Plunkett, G., Ludlow, F., et al. (2015). Timing and Climate Forcing of Volcanic Eruptions for the Past 2,500 Years. *Nature* 523, 543–549. doi:10.1038/nature14565

Sigmarsson, O., Haddadi, B., Carn, S., Moune, S., Gudnason, J., Yang, K., et al. (2013). The Sulfur Budget of the 2011 Grímsvötn Eruption, Iceland. *Geophys. Res. Lett.* 40, 6095–6100. doi:10.1002/2013GL057760

Sigmundsson, F., Pinel, V., Lund, B., Albino, F., Pagli, C., Geirsson, H., et al. (2010). Climate Effects on Volcanism: Influence on Magmatic Systems of Loading and Unloading from Ice Mass Variations, with Examples from Iceland. *Philosophical Trans. R. Soc. A: Math. Phys. Eng. Sci.* 368, 2519–2534. doi:10.1098/rsta.2010.0042

Smellie, J. L., and Edwards, B. R. (2016). *Glaciovolcanism on Earth and Mars*. Cambridge University Press.

Solomon, S., Daniel, J. S., Neely, R. R., Vernier, J.-P., Dutton, E. G., and Thomason, L. W. (2011). The Persistently Variable "Background" Stratospheric Aerosol Layer and Global Climate Change. *Science* 333, 866–870. doi:10.1126/science.1206027

Sonder, I., Schmid, A., Seegelken, R., Zimanowski, B., and Büttner, R. (2011). Heat Source or Heat Sink: What Dominates Behavior of Non-explosive Magma-Water Interaction? *J. Geophys. Res. Solid Earth* 116. doi:10.1029/2011JB008280

Soreghan, G. S., Soreghan, M. J., and Heavens, N. G. (2019). Explosive Volcanism as a Key Driver of the Late Paleozoic Ice Age. *Geology* 47, 600–604. doi:10.1130/G46349.1

Starostin, A. B., Barmin, A. A., and Melnik, O. E. (2005). A Transient Model for Explosive and Phreatomagmatic Eruptions. *J. Volcanology Geothermal Res.* 143, 133–151. doi:10.1016/j.jvolgeores.2004.09.014

Staunton-Sykes, J., Aubry, T. J., Shin, Y. M., Weber, J., Marshall, L. R., Luke Abraham, N., et al. (2021). Co-emission of Volcanic Sulfur and Halogens Amplifies Volcanic Effective Radiative Forcing. *Atmos. Chem. Phys.* 21, 9009–9029. doi:10.5194/acp-21-9009-2021

Telling, J., Dufek, J., and Shaikh, A. (2013). Ash Aggregation in Explosive Volcanic Eruptions. *Geophys. Res. Lett.* 40, 2355–2360. doi:10.1002/grl.50376

Textor, C., Graf, H.-F., Herzog, M., and Oberhuber, J. M. (2003). Injection of Gases into the Stratosphere by Explosive Volcanic Eruptions. *J. Geophys. Res. Atmospheres* 108, 4606. doi:10.1029/2002JD002987

Timmreck, C. (2012). Modeling the Climatic Effects of Large Explosive Volcanic Eruptions. *Wiley Interdiscip. Rev. Clim. Change* 3, 545–564. doi:10.1002/wcc.192

Toohey, M., Krüger, K., Schmidt, H., Timmreck, C., Sigl, M., Stoffel, M., et al. (2019). Disproportionately strong Climate Forcing from Extratropical Explosive Volcanic Eruptions. *Nat. Geosci.* 12, 100. doi:10.1038/s41561-018-0286-2

Toohey, M., Krüger, K., Sigl, M., Stordal, F., and Svensen, H. (2016). Climatic and Societal Impacts of a Volcanic Double Event at the Dawn of the Middle Ages. *Climatic Change* 136, 401–412. doi:10.1007/s10584-016-1648-7

Turner, J. S. (1986). Turbulent Entrainment: The Development of the Entrainment assumption, and its Application to Geophysical Flows. *J. Fluid Mech.* 173, 431–471. doi:10.1017/S0022112086001222

Van Eaton, A. R., Herzog, M., Wilson, C. J. N., and McGregor, J. (2012). Ascent Dynamics of Large Phreatomagmatic Eruption Clouds: The Role of Microphysics. *J. Geophys. Res. Solid Earth* 117, B03203. doi:10.1029/2011JB008892

Van Eaton, A. R., Mastin, L. G., Herzog, M., Schwaiger, H. F., Schneider, D. J., Wallace, K. L., et al. (2015). Hail Formation Triggers Rapid Ash Aggregation in Volcanic Plumes. *Nat. Commun.* 6, 7860. doi:10.1038/ncomms8860

van Otterloo, J., Cas, R. A. F., and Scutter, C. R. (2015). The Fracture Behaviour of Volcanic Glass and Relevance to Quench Fragmentation during Formation of Hyaloclastite and Phreatomagmatism. *Earth-Science Rev.* 151, 79–116. doi:10.1016/j.earscirev.2015.10.003

Walker, G. P. L. (1981). Characteristics of Two Phreatoplinian Ashes, and Their Water-Flushed Origin. *J. Volcanology Geothermal Res.* 9, 395–407. doi:10.1016/0377-0273(81)90046-9

Walker, G. P. L. (1973). Explosive Volcanic Eruptions — a New Classification Scheme. *Geologische Rundschau* 62, 431–446. doi:10.1007/BF01840108

Wallace, P. J., Plank, T., Edmonds, M., and Hauri, E. H. (2015). "Chapter 7 - Volatiles in Magmas," in *The Encyclopedia of Volcanoes*. Editor H. Sigurdsson. Second Edition (Amsterdam: Academic Press), 163–183. doi:10.1016/B978-0-12-385938-9.00007-9

Watt, S. F. L., Pyle, D. M., and Mather, T. A. (2013). The Volcanic Response to Deglaciation: Evidence from Glaciated Arcs and a Reassessment of Global Eruption Records. *Earth-Science Rev.* 122, 77–102. doi:10.1016/j.earscirev.2013.03.007

Waythomas, C. F., Angeli, K., and Wessels, R. L. (2020). Evolution of the Submarine–Subaerial Edifice of Bogoslof Volcano, Alaska, during its 2016–2017 Eruption Based on Analysis of Satellite Imagery. *Bull. Volcanology* 82, 21. doi:10.1007/s00445-020-1363-0

Wilson, C. J. N. (2001). The 26.5ka Oruanui Eruption, New Zealand: An Introduction and Overview. *J. Volcanology Geothermal Res.* 112, 133–174. doi:10.1016/S0377-0273(01)00239-6

Wilson, C. J. N., and Walker, G. P. L. (1985). The Taupo Eruption, New Zealand I. General Aspects. *Philosophical Trans. R. Soc. Lond. Ser. A, Math. Phys. Sci.* 314, 199–228. doi:10.1098/rsta.1985.0019

Wilson, L., Sparks, R. S. J., and Walker, G. P. L. (1980). Explosive Volcanic Eruptions — IV. The Control of Magma Properties and Conduit Geometry on Eruption Column Behaviour. *Geophys. J. Int.* 63, 117–148. doi:10.1111/j.1365-246X.1980.tb02613.x

Wohletz, K. (1983). Mechanisms of Hydrovolcanic Pyroclast Formation: Grain-Size, Scanning Electron Microscopy, and Experimental Studies. *J. Volcanology Geothermal Res.* 17, 31–63. doi:10.1016/0377-0273(83)90061-6

Wohletz, K., Zimanowski, B., and Büttner, R. (2013). "Magma–water Interactions," in *Modeling Volcanic Processes: The Physics and Mathematics of Volcanism* (Cambridge: Cambridge University Press). doi:10.1017/CBO9781139021562.011

Woodcock, D. C., Gilbert, J. S., and Lane, S. J. (2012). Particle-water Heat Transfer during Explosive Volcanic Eruptions. *J. Geophys. ResearchSolid Earth* 117. doi:10.1029/2012JB009240

Woods, A. W., and Bower, S. M. (1995). The Decompression of Volcanic Jets in a Crater during Explosive Volcanic Eruptions. *Earth Planet. Sci. Lett.* 131, 189–205. doi:10.1016/0012-821X(95)00012-2

Woods, A. W. (2010). Turbulent Plumes in Nature. *Annu. Rev. Fluid Mech.* 42, 391–412. doi:10.1146/annurev-fluid-121108-145430

Zanchettin, D., Timmreck, C., Bothe, O., Lorenz, S. J., Hegerl, G., Graf, H.-F., et al. (2013). Delayed winter Warming: A Robust Decadal Response to strong Tropical Volcanic Eruptions? *Geophys. Res. Lett.* 40, 204–209. doi:10.1029/2012GL054403

Zhang, X., Li, S., Yu, D., Yang, B., and Wang, N. (2020). The Evolution of Interfaces for Underwater Supersonic Gas Jets. *Water* 12, 488. doi:10.3390/w12020488

Zhong, Y., Miller, G. H., Otto-Bliesner, B. L., Holland, M. M., Bailey, D. A., Schneider, D. P., et al. (2011). Centennial-scale Climate Change from Decadally-Paced Explosive Volcanism: A Coupled Sea Ice-Ocean Mechanism. *Clim. Dyn.* 37, 2373–2387. doi:10.1007/s00382-010-0967-z

Zhu, Y., Toon, O. B., Jensen, E. J., Bardeen, C. G., Mills, M. J., Tolbert, M. A., et al. (2020). Persisting Volcanic Ash Particles Impact Stratospheric SO 2 Lifetime and Aerosol Optical Properties. *Nat. Commun.* 11, 4526. doi:10.1038/s41467-020-18352-5

Zimanowski, B., Büttner, R., Dellino, P., White, J. D. L., and Wohletz, K. H. (2015). "Chapter 26 - Magma–Water Interaction and Phreatomagmatic Fragmentation," in *The Encyclopedia of Volcanoes*. Editor H. Sigurdsson. Second Edition (Amsterdam: Academic Press), 473–484. doi:10.1016/B978-0-12-385938-9.00026-2

Zimanowski, B., and Büttner, R. (2003). "Phreatomagmatic Explosions in Subaqueous Volcanism," in *Geophysical Monograph Series*. Editors J. D. L. White, J. L. Smellie, and D. A. Clague (Washington, D. C.: American Geophysical Union), 51–60. doi:10.1029/140GM03

Conflict of Interest: The authors declare that the research was conducted in the absence of any commercial or financial relationships that could be construed as a potential conflict of interest.

Publisher's Note: All claims expressed in this article are solely those of the authors and do not necessarily represent those of their affiliated organizations, or those of the publisher, the editors and the reviewers. Any product that may be evaluated in this article, or claim that may be made by its manufacturer, is not guaranteed or endorsed by the publisher.

frontiers | Frontiers in Earth Science

ORIGINAL RESEARCH
published: 29 April 2022
doi: 10.3389/feart.2022.868569

The Impact of Ice Caps on the Mechanical Stability of Magmatic Systems: Implications for Forecasting on Human Timescales

Lilian C. Lucas[1], *John A. Albright*[1], *Patricia M. Gregg*[1]* *and Yan Zhan*[1,2]

[1]*Department of Geology, University of Illinois at Urbana-Champaign, Urbana, IL, United States,* [2]*Earth and Planets Laboratory, Carnegie Institution for Science, Washington, DC, United States*

Monitoring the activity of subglacial volcanoes along the Aleutian Arc in Alaska is important to the safety of local populations, as well as air traffic flying through the region. However, observations of volcanic unrest are limited by accessibility and resources, particularly at glacier-covered systems, making investigations of their stability challenging. Westdahl Peak, a subglacial volcano on Unimak Island in the Aleutian Arc has experienced significant unrest and uplift since its most recent VEI three eruption in 1991-1992. Given the magnitude of observed uplift, previous investigations suggested the potential for eruption by 2010, but no such event has occurred. One hypothesis to explain this prolonged unrest is that the 1-km thick glacier may increase the stability of the magma system. However, the impact of ice caps and glaciers on the short-term stability of volcanoes is not well understood. In this study, thermomechanical finite element models are used to evaluate how the stability of a glaciated volcano is impacted by variations in ice cap thickness, magma chamber depth, geometry, magma flux rate, and seasonal changes in ice cover thickness. Our numerical experiments indicate that the presence of an ice cap (1–3 km thick) increases the average repose interval for a magma system. Among models with different magma chamber geometries, depths, and flux rates, the greatest increases in repose interval are observed in prolate systems where the increase is up to 57% for a chamber located at 5 km-depth. Spherical and oblate also experience smaller, yet significant, increases in repose interval. Additionally, the percentage increase in repose interval is not impacted by variations in magma flux rate for a given ice cap thickness and magma chamber geometry. However, flux rates do influence the timing of eruptions when the system is experiencing seasonal variations in ice thickness. Our results show that systems with low flux rates are more likely to fail when the ice thickness is at its lowest. The numerical estimates further suggest that the ice cap on Westdahl Peak, which is ~1 km, may slightly increase the stability of the magma system. In general, given flux rates and magma chamber geometries estimated for the Westdahl system, the repose interval can increase by ~7 years due to the Westdahl glacier. This increase is small on a geologic scale but is significant on human time scales and the impact of glaciers must be considered in future forecasting efforts.

Keywords: volcano, subglacial, flux rate, westdahl, seasonality, viscoelastic, finite element method

OPEN ACCESS

Edited by:
Simona Petrosino, Istituto Nazionale di Geofisica e Vulcanologia, Italy

Reviewed by:
Luis E. Lara, Servicio Nacional de Geología y Minería de Chile (SERNAGEOMIN), Chile
Lucia Capra, National Autonomous University of Mexico, Mexico

***Correspondence:**
Patricia M. Gregg
pgregg@illinois.edu

Specialty section:
This article was submitted to Volcanology, a section of the journal Frontiers in Earth Science

Received: *02 February 2022*
Accepted: *13 April 2022*
Published: *29 April 2022*

Citation:
Lucas LC, Albright JA, Gregg PM and Zhan Y (2022) The Impact of Ice Caps on the Mechanical Stability of Magmatic Systems: Implications for Forecasting on Human Timescales. Front. Earth Sci. 10:868569. doi: 10.3389/feart.2022.868569

INTRODUCTION

Constraining the impact of glaciation on magma system stability is critical for evaluating potential hazards and the eruption potential of active volcanoes located in high latitudes. Previous studies have investigated the effects of deglaciation on magma systems through elastic axisymmetric models, and conclude that a decrease in surface load pressure may either enhance or inhibit conditions for dike initiation dependent upon magma chamber geometry and depth (Albino et al., 2010; Sigmundsson et al., 2010). In particular, these studies evaluate how decreasing surface loads impact both the pressure within the magma chamber and the threshold conditions for tensile failure and dike initiation in the host rock. Albino et al. (2010) apply their models to Grímsvötn and Katla Volcanoes in Iceland. Both applications conclude that surface load variations, such as jökulhlaups (large lake water discharge events) and annual snow cover melting, may enhance the potential for dike initiation and/or eruption when the magma chamber is already near failure. Additionally, recent numerical studies have shown that viscoelastic effects in the host rock impact the timing and conditions for failure of long-lived magma systems (Del Negro et al., 2009; Gregg et al., 2012; Cabaniss et al., 2018; Zhan and Gregg, 2019). However, the combined effects of both viscosity and ice cap loading have not yet been studied. It is therefore critical to investigate the roles that viscoelasticity and long-term stress accumulation play in glaciated systems.

In this study, we run a series of numerical simulations to investigate the impact of ice caps on the stability and eruption potential of long-lived magma systems. Viscoelastic, temperature-dependent models are developed to evaluate the overall effect of ice caps on magma systems. Particular care is taken to assess the effect of variables such as ice cap thickness, magma chamber size, geometry, and the flux of new material into the magma system. Finally, we apply our generic model to Westdahl Volcano, a caldera system on Unimak Island in the Aleutian Arc of Alaska (**Figure 1**). Westdahl is covered by ~1 km of ice and has an active magma chamber at a depth of ~7.2 km (Gong, 2015). Since its last eruption, in 1991-1992, Westdahl has experienced significant and ongoing inflation that previous studies interpreted as an indication of imminent eruption (Lu et al., 2004). However, no eruption has occurred despite continuing inflation well past the time scale considered in these studies. One potential explanation for this lack of eruption is that the mechanical loading of the ice cap is prolonging the magma reservoir's stability. In applying our generic model, we investigate the contribution of Westdahl's ice cap to the mechanical stress state of the volcano and the ongoing likelihood of eruption.

METHODS

Building upon previous models (Grosfils, 2007; Gregg et al., 2012; Albright et al., 2019), we use COMSOL Multiphysics 5.5 to create viscoelastic finite element models that incorporate temperature-dependent rheology (**Figure 2**). In these models, ice caps of various thicknesses are then implemented to simulate glaciated volcanoes. In a 50 by 25 km, two-dimensional model space, the magma reservoir is constructed as a pressurized elliptical void along a central axis of rotational symmetry. Roller boundaries are implemented on the right lateral and bottom walls. A layer with variable thickness is included to simulate an ice cap covering the volcano. The rock and ice domains are gravitationally loaded to impose an initial lithostatic stress.

In this study, we use a generalized Maxwell model to describe a viscoelastic rheology whose relaxation time, τ, is given by:

$$\tau = \left(\frac{\eta}{G_{0td}u_1}\right) * \left(\frac{3K_{td} + G_{0td}}{3K_{td} + G_{0td}u_0}\right) \quad (1)$$

In **Eq (1)**, the shear modulus, G_{0td}, is the instantaneous elastic response of the material when under pressure. The time dependent viscous response is represented by η (Gregg et al.,

FIGURE 1 | Map of Aleutian Arc, Alaska with glaciated volcanoes represented with yellow circles. Glaciated volcanoes from left to right are Gareloi, Takawangha, Moffett, Vsevidof, Recheschnoi, Makushin, Westdahl, Shishaldin, Isanotski, Dutton, Veniaminof, and Spurr.

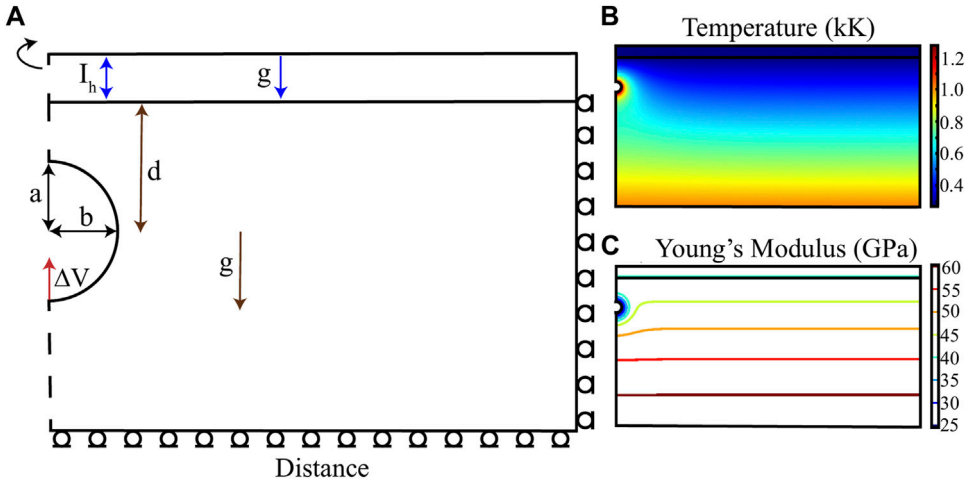

FIGURE 2 | Finite element model setup. **(A)** Schematic diagram of model geometry and boundary conditions. The left boundary has rotational symmetry while roller conditions are implemented along the bottom and top boundaries. The model space is divided into a variable-thickness layer of ice on top of a 50 by 25 km domain representing the magmatic system host rock. The magma chamber is simulated as a pressurized elliptical void along the rotational boundary, while the labels indicate different parameter values used in this study and the gravitational loading incorporated into both model domains. Depth to center is indicated by "d"; however, some experiments use the depth to the crest of the magma chamber as indicated in the text. **(B)** Heat transfer module is incorporated in the model, and rock near the magma chamber (1,000°C) experiences higher temperatures. Temperature gradient of the Earth is also represented in the models as 30°C/km. **(C)** Temperature-dependent Young's Modulus is defined in the models to make them viscoelastic, therefore temperature- and time-dependent.

TABLE 1 | Model parameters.

Parameter	Description	Value
a, b	Magma chamber radius, m	1000, 1500, 2000, 2500, 3000, 3500, 4000, 4500, 5000
C_p	Heat Capacity, J/(g*°C)	1×10^{-5}
ΔV	Flux rate, m^3/yr	1×10^5, 5×10^5, 1×10^6, 2.4×10^6, 5×10^6, 6.7×10^6, 1×10^7, 5×10^7
d	Depth to center of magma chamber, m	2000, 3000, 4000, 5000, 6000, 7000, 8000, 9000
G_0	Shear Modulus of rock, Pa	2×10^{10}
G_i	Shear Modulus of ice, Pa	2×10^{10}
g	Gravity, m/s^2	9.8
η_i	Viscosity of ice, Pa*s	2×10^{13}
η_r	Viscosity of rock, Pa*s	2×10^{16}
ih	Ice thickness, m	0, 1000, 2000, 3000
K	Bulk Modulus, Pa	3.333×10^{10}
k	Thermal Conductivity, W/(m*K)	3
μ_1	Fractional Shear	0.5
N_i	Bulk Modulus, Pa	9.8029×10^8
ν	Poisson Ratio	0.25
ρi	Density of ice, g/m^3	916000
ρ_r	Density of rock, g/m^3	2700000
T_{grad}	Temperature Gradient, °C/m	0.03
Tm	Magma chamber temperature°C	100

2012). K_{td} is the bulk modulus, and u_0 and u_1 are the fractional moduli (see **Table 1**).

The COMSOL solid mechanics and heat transfer modules are used to implement both time- and temperature-dependence within the viscoelastic model space. **Eq (2)** represents the temperature-dependent host rock viscosity:

$$\eta = A_D e^{\frac{E_a}{R_{gas}T}} \quad (2)$$

where A_D is the Dorn parameter, E_a is activation energy, R_{gas} is the gas constant, and T is temperature. Our model also incorporates a geothermal gradient of 30°C/km as well as a constant magma chamber temperature of 1,000°C, which is appropriate for a basaltic magma system.

Throughout the modeling process, we measure the change in repose interval of the magma systems in response to changing parameters including different thicknesses of ice, magma chamber geometries, magma chamber depths, and magma flux rates. Repose interval is defined as the time period for the tensile stress along the reservoir wall to progress from a state of compression to tension. In this investigation, we focus on

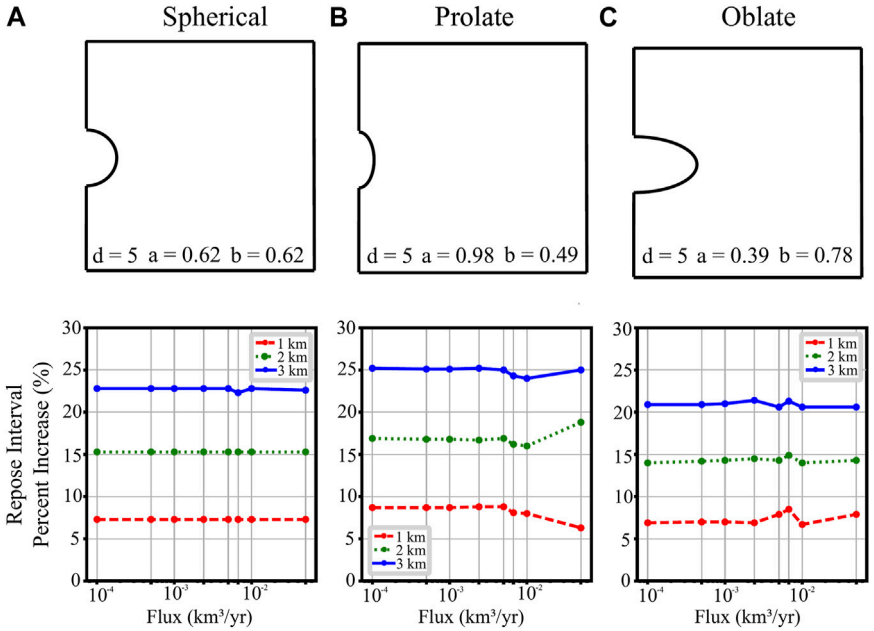

FIGURE 3 | Flux rate versus percent change in the repose intervals of volcanic systems with spherical, prolate, and oblate magma chamber geometries. **(A)** In the spherical case, a magma chamber with radius ~0.62 and 5 km depth to center is modeled. Flux rates range from 0.0001-0.05 km^3/yr and percent changes due to an ice cap thickness of 1, 2, and 3 km are represented by the dashed red line, dotted green line, and solid blue line respectively. **(B)** A prolate chamber with depth of 5 km, horizontal radius of ~0.49 km, and vertical radius of ~0.98 km is modeled. **(C)** An oblate chamber with ~0.78 km horizontal radius, ~0.39 km vertical radius, and depth of 5 km is used.

tensile failure along the reservoir boundary as a proxy for dike initiation and eruption, as opposed to shear failure in the surrounding host rock, which has also been shown to potentially catalyze eruptions (Gregg et al., 2012). Tensile rupture of the chamber and the onset of eruption is assumed to occur when tensile stress becomes positive:

$$\sigma_t > 0 \tag{3}$$

FACTORS CONTROLLING THE HOST ROCK STABILITY IN ICE-COVERED VOLCANOES

A series of numerical experiments are conducted to investigate the impact of ice cap loading on the stability of magma systems. In particular, we examine the relationship between the stability of a magma system replenished by a constant magma flux and the presence an ice cap. The repose interval is defined as the time from the start of new magma injection, which remains constant throughout the simulation, to when tensile failure is observed at the reservoir boundary, as described above. Specifically, repose intervals of magma systems with ice caps of 1–3 km are compared with repose intervals of otherwise identical magma systems without ice to calculate percent change in time to eruption due to the ice cap. We should note that the repose interval described here represents a minimum, and natural systems may have protracted periods with no new magma injection. Results, including both the absolute timescales as well as the percent change in repose for all of the experiments described below can be found in the **Supplementary Material S1**.

Ice Cap Thickness

In general, an additional load above a magma chamber, such as from ice, increases the confining stress along the reservoir wall, making it more difficult for the chamber to rupture (Grosfils, 2007). In all experiments, we found that ice cap thickness increases the repose interval, but different parameters of the magma system affect how much the repose interval is changed relative to an ice-free baseline. In the following sections, we investigate the effects of magma flux (3.2), depth to reservoir crest (3.3), and reservoir geometry (3.4).

Magma Flux

Magma flux is thought to be a primary driver of inflation and ultimately controls the timing of failure for magma systems (Cabaniss et al., 2018). As such, a wide range of fluxes is investigated from 0.0001 to 0.05 km^3/yr (Wilson et al., 2006; Annen, 2009; Gelman et al., 2013). Model results indicate that the percent increase of repose interval due to glacial loading is independent of the flux rate (**Figure 3**). For instance, the repose interval of a spherical chamber at 5 km depth will increase by ~4.8%, independent of varying the flux rate. Similarly, a prolate chamber located at a depth to center of 5 km underneath 3 km of ice, will see an increase in repose of ~23%, regardless of the flux rate (**Figure 3B**). A similar response is observed for chambers with an oblate geometry (**Figure 3C**). Additionally, the timing of tensile failure in systems with identical

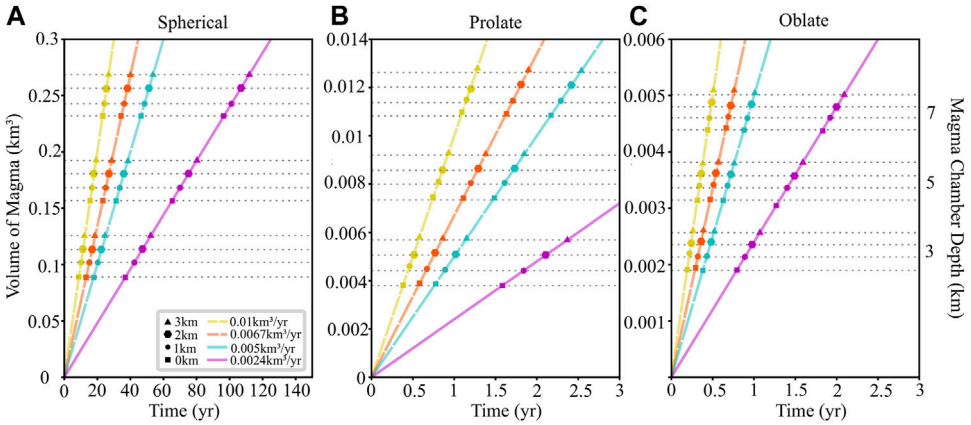

FIGURE 4 | Volume of magma added into the chamber versus time with steady flux rates of 0.0024, 0.005, 0.0067 and 0.01 km^3/yr for **(A)** spherical, **(B)** prolate, and **(C)** oblate chambers. The spherical chamber has a radius of ~0.62 km. The prolate magma chamber has radii of ~0.49 and 0.98 km, and oblate chamber radii are ~0.39 and 0.78 km. Along each linear flux rate line, the times to failure of several different systems are indicated by points. Each magma chamber depth (3, 5 and 7 km) has four points representing the times to failure for each ice cap thickness (0, 1, 2 and 3 km). Tensile failure for systems with identical magma chamber depths and ice cap thicknesses occur at similar volumes, whose average approximations are represented by the horizontal dashed grey lines.

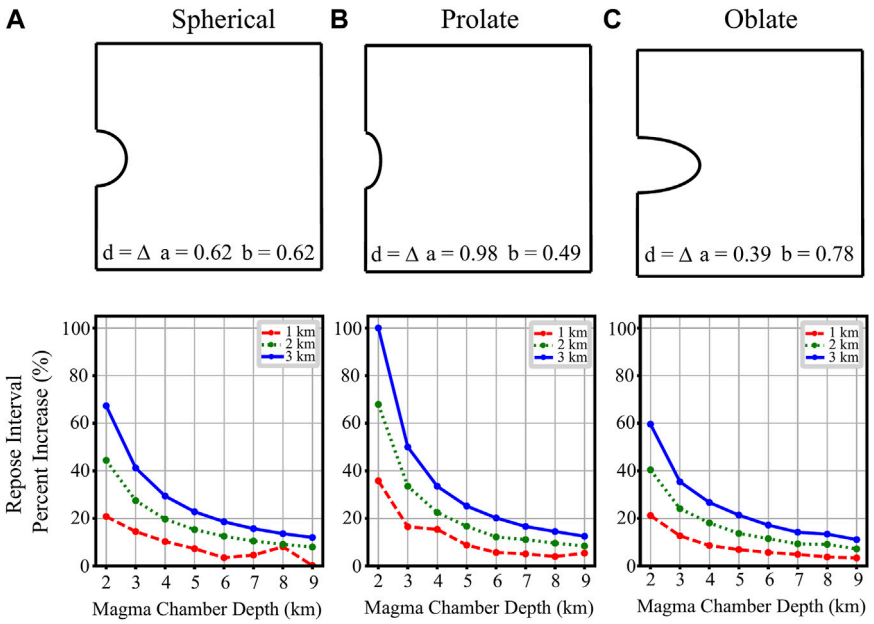

FIGURE 5 | Depth versus percent change in the repose intervals of volcanic systems with spherical, prolate, and oblate magma chamber geometries. The flux remains constant at a rate of 0.0024 km^3/yr. **(A)** Depth to the center of the magma chamber ranges from 2-9 km, and the spherical chamber radius of 0.62 km remains constant. Percent changes due to an ice cap thickness of 1, 2, and 3 km are represented by the dashed red line, dotted green line, and solid blue line respectively. As the depth of the magma chamber increases, the effect of the ice cap on the repose interval percent change generally decreases for each ice cap thickness. This pattern is also found for the magma systems with prolate and oblate magma chambers. **(B)** Depth of magma chamber center versus percent change in the repose interval of a prolate chamber. Depth varies from 2-9 km, but vertical radius and horizontal radius remain constant at ~0.98 and 0.49 km respectively. **(C)** The percent change in repose interval as we vary depth and ice cap thickness is measured in a magma system with an oblate magma chamber. The horizontal radius is set at ~0.78 km while the vertical radius is ~0.39 km, and the depth to the center of the magma chamber ranges from 2-9 km.

depth, shape, and ice cap thickness occurs independent of flux rate for similar volumes of magma added. Although the modeled magma systems indicate an insensitivity to flux rate, their repose intervals are highly dependent on the total magnitude of volume change (**Figure 4**). For each simulation, tensile failure is produced for the same total volume of magma added, regardless of the rate of intrusion, for the flux rates investigated (0.0001–0.05 km^3/yr). For example, tensile failure for a spherical magma chamber with a

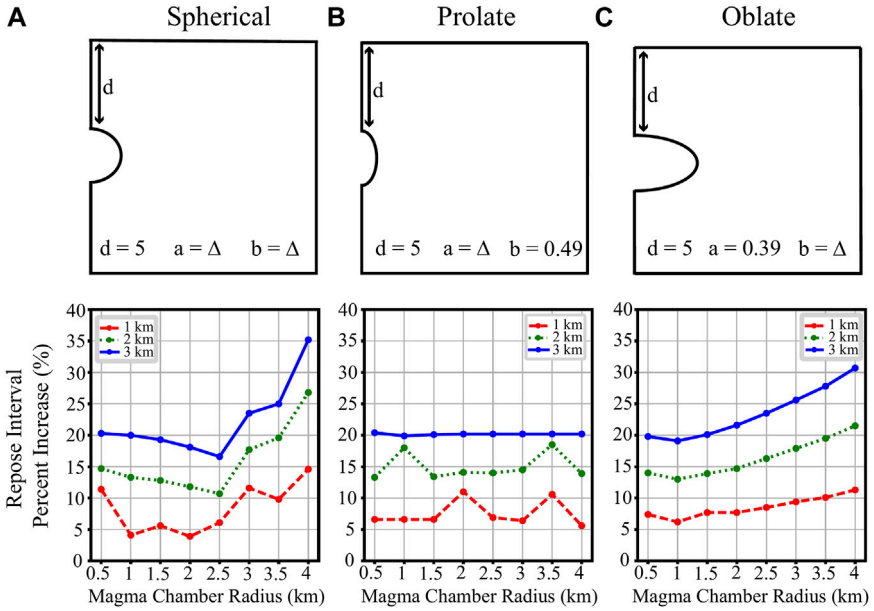

FIGURE 6 | Magma chamber radius versus percent change in repose interval of volcanic systems with spherical, prolate, and oblate magma chamber geometries. In each case, a volcanic system with a depth of 5 km to the crest of the magma chamber and a 0.0024 km^3/year flux rate is modeled. The magma chamber radii change for each of the spherical, prolate and oblate chamber systems. **(A)** In the spherical system, the horizontal and vertical radii are identical lengths and range from 0.5 to 4 km. The percent increase of repose interval from the presence of the glacier slightly decreases when the radius is increased from 0.5 to 2 km length and increases when the radius is increased from 2 to 4 km. **(B)** In the prolate system, the horizontal radius remains ~0.49 km while the vertical radius ranges between 0.5 and 4 km. **(C)** The vertical radius for an oblate magma chamber system is held constant at ~0.39 km while the horizontal radius ranges between 0.5 and 4 km. Repose interval percent change increases as the horizontal radius of an oblate magma chamber is increased in length.

depth of 7 and 1 km of ice will occur when ~0.24 km^3 of magma is added to the chamber (**Figure 4A**).

Magma Chamber Depth

Previous studies have interpreted magma chamber depth to be an influential factor on the stability of a magma system (Albino et al., 2010; Geyer and Bindeman, 2011; Satow et al., 2021). A suite of simulations is run to examine the impact of magma chamber depths to center, ranging from 2-9 km (e.g., Huber et al., 2019; Rasmussen et al., 2019; Kent et al., 2022). Results indicate that the ice cap has a decreased effect on the relative repose interval for deeper magma sources, as is expected given the overall contribution to the surface load. For instance, the repose interval of a system with a spherical chamber at a depth of 2 km will increase by ~55% when loaded with a 3 km ice cap (**Figure 5A**). Identical loading conditions will increase the repose interval by only ~11% for a system with a magma chamber at 9 km depth to center (**Figure 5A**). This effect is greater for non-spherical chambers, with prolate chambers being most sensitive to variations in magma chamber depth (**Figure 5B**). Specifically, a prolate chamber located at 2 km depth beneath 3 km of ice will experience an ~86% increase in its repose interval. Whereas the same chamber at 9 km depth will have an increase in repose of ~12% (**Figure 5B**).

Magma Chamber Geometry

The final parameter we investigate in this study is magma chamber geometry. In accordance with previous studies, we model three simplified magma chamber shapes: spherical, prolate, and oblate (Lisowski, 2007). Starting off, as the radius of a spherical chamber increases, we find glacial loading will ultimately have an increased effect on the repose interval. Our models show that the presence of a 3 km glacier increases the relative repose interval from 17.6% for a chamber with a 0.5 km radius to 34.6% for a chamber with a 4 km radius (**Figure 6A**). Oblate systems experience a similar, but amplified change in relative repose interval as the size of the horizontal radius is increased (**Figure 6C**). For example, a 3 km-thick ice cap will increase the repose interval from 22.3% for a 0.5 km horizontal radius to 103% for a 4 km horizontal radius (**Figure 6C**). Finally, as a prolate chamber becomes more prolate, there is not a significant change in the repose interval given a specific ice cap thickness.

DISCUSSION

The Role of Glaciers in Maintaining Magma System Stability

Previous investigations have focused on the twofold impact of active regional ice cap withdrawal on both the flux of magma into the magma chamber (Sigmundsson et al., 2010) and the threshold conditions for driving tensile failure and dike initiation (Albino et al., 2010). In particular, the removal of ice caps may promote additional melt generation from the mantle source due to decompression, which may increase flux to the crustal magma

system (Sigmundsson et al., 2010). Furthermore, the decreased load from the ice cap withdrawal will reduce confining pressure, promoting tensile failure and the likelihood of dike initiation if a magma system is near failure (Albino et al., 2010). In contrast, this investigation focuses purely on the static, long-term effects of the presence or absence of ice caps and does not consider the dynamic processes of their active removal. Motivated by high latitude, glacially covered systems such as Westdahl Volcano in Alaska, we seek to determine whether the presence of a large glacier or ice cap can account for unexpectedly long repose intervals (Lu et al., 2004).

Our numerical experiments indicate that glaciers modulate eruption timescales. In particular, the additional load from an ice cap increases the confining stress around the magma reservoir, which must subsequently be overcome to initiate tensile failure. For a given reservoir size and shape, this additional stress is dependent only on the thickness of the glacier, requiring a fixed volume change within the reservoir, and by extension time, to reach failure. In most cases, the delay due to ice loading is relatively small compared to the system's baseline repose interval, which is predominantly controlled by the lithostatic stress. However, for shallow reservoirs (<5 km depth to center), an ice cap contributes a greater proportion of the overlying load, and as such has a larger relative impact on the potential repose interval. Regardless, even for deep systems where the relative change in repose interval due to the presence of ice is small, the impact is significant on human timescales and must be considered in future forecasting efforts. For example, a spherical chamber (radius of 0.62 km and flux of 0.0024 km^3/yr) at 9 km depth will experience an increase in repose of ~3 months–~15 years with a 1 km or 3 km-thick ice cap respectively.

The Role of Flux

In many previous numerical modeling studies that use elastic rheology, the main driver of reservoir tensile failure has been the cumulative critical volume change or a critical change in overpressure of the magma reservoir (Grosfils, 2007; Gerbault et al., 2012; Gregg et al., 2012). This effect is somewhat modulated in viscoelastic rheology where the host rock can relax to dissipate some of the reservoir boundary stresses (Gregg et al., 2012; Gregg et al., 2013; Degruyter and Huber, 2014). In our results, however, the viscoelasticity does not appear to play a major role in system stability. If significant viscoelastic relaxation were present, we would expect to see a greater relative change in repose interval at lower fluxes. Specifically, in the time it takes to overcome the additional load of the ice cap, the system would have relaxed even further, requiring yet more volume change. In contrast, we observe a near constant relative change in repose interval, regardless of flux rate (**Figure 3**).

Our numerical results agree with previous studies, which indicate that volcanic unrest on year to decadal timescales mostly behaves in an elastic manner (Zhan and Gregg, 2019). With higher flux rates (>0.05 km^3/yr), repose timescales will be even shorter, bringing the system even closer to the elastic endmember. Alternatively, at lower flux rates (<0.0001 km^3/yr), the likelihood of solidification prior to eruption increases (Annen, 2009). Additionally, on longer timescales there is more time for viscoelastic relaxation to take effect, prolonging stable storage and inhibiting eruption even further.

The existence of an ice cap linearly increases the confining pressure around a magma reservoir, which must then be overcome by changing the volume of magma by a set amount, ΔV_q. The time needed to accumulate this critical volume of magma, in other words the total delay before an eruption (t_d), will therefore vary inversely with the flux rate (q) into the system:

$$t_d = \Delta V_q / q$$

For example, the total volume of magma required for the tensile failure of a volcanic system with a spherical magma chamber at 3 km depth will be ~0.1 km^3 of magma, independent of flux rate (**Figure 4**).

Seasonal Impacts on the Timing of Failure

In understanding the potential effects of loading on the stability of a magma system, previous studies have additionally investigated the effects of a seasonal surface load change. Annual unloading events, such as snow melt represented in numerical models, have suggested that a decrease in a load as thin as 6.5 m may trigger a dike initiation event, if the system is initially near failure conditions (Albino et al., 2010). This effect has been suggested in systems such as Katla Volcano, a subglacial system with annual snow cover, whose last nine major eruptions have been initiated between May and November when the yearly snow had melted (Larsen, 2000).

The results of our study suggest the presence of an annual snow cover increases the repose interval of the volcano, but the strength of this effect is strongly dependent on the thickness of the ice cover and parameters of the magma system. In particular, annual changes in snow and ice thickness at Katla and Westdahl volcanoes are on the order of 6.5 m (Albino et al., 2010; Littell et al., 2018), significantly less than the km-scale ice masses modeled here. Compared to the total overlying load that the magma chamber must overcome in order to reach tensile failure, small seasonal variations are unlikely to play a major role for most systems. However, seasonal ice loss may impact the timing of eruption for systems close to failure.

Using our modeling results above as well as additional simulations with 10 m of ice, we compare the impact of short-term ice thickness variations on the seasonal timing of magma system failure (**Figure 7**). Four end-member models are evaluated to determine the relative impacts of flux-rate and seasonal ice variability on when magma system failure is more likely to occur. In each case, the reservoir failure threshold is interpolated as a sinusoid that alternates yearly between the ice-free and the 1 km ice cap results. For lower seasonality, we assume a linear relationship between ice thickness and the reservoir failure threshold and proportionally reduce the amplitude of the sinusoid.

Our results indicate that low flux rate systems are much more likely to fail when the ice thickness is at its lowest, August - October in the northern hemisphere (**Figure 7**). In these systems ice mass variations impact the failure conditions more than

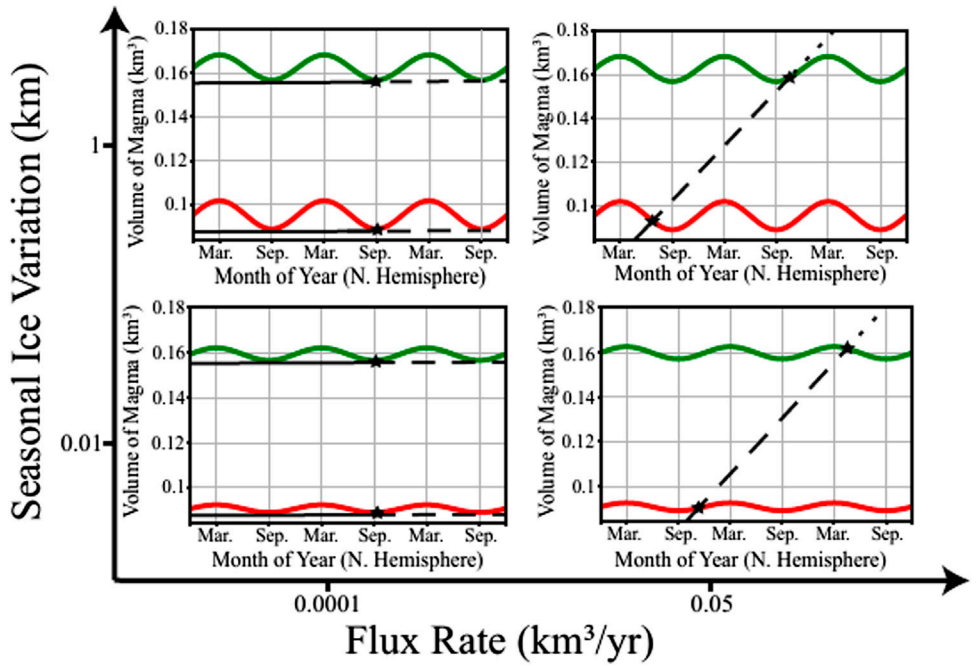

FIGURE 7 | The relationship between flux rate and seasonality on the timing of reservoir tensile failure. Each subplot compares the seasonally varying tensile failure threshold of a 3 km deep (depth to center, red line) and 5 km deep (depth to center, green line) spherical reservoir (radius = 0.62 km) against the continuous volume flux into the magma system (black line). The subplots are arranged within a set of larger axes, determining the amount of seasonal ice variation (10 m vs. 1 km) and the flux rate (0.0001 km^3/yr vs. 0.05 km^3/yr) into the system. In each case, tensile failure occurs at the point where the volume in the magma reservoir first intersects the failure threshold (black stars). The solid, dashed, and dotted black lines indicate an example trajectory of the volume change before the initial rupture of the 3 km deep chamber, before the rupture of the 5 km chamber, and after the rupture of the 5 km chamber, respectively. When flux is low (left subplots), seasonal ice variations outpace the system's long-term accumulation of magma volume, consistently causing failure when ice thickness reaches its minimum. On the other hand, high-flux systems (right subplots) can produce tensile failure in any season, although the distribution may be skewed depending on the magnitude of ice variation.

increasing volume change in the magma reservoir. In contrast, for magma systems with high flux and low seasonal ice variability, the onset of failure is most sensitive to the accumulation of magma, rather than the timing of the lowest level of ice mass, and so can occur at any time of year. Finally, systems with both high magma flux and high-seasonal ice variability display a slight skew in the specific timing of reservoir failure; eruptions are possible at any time, but are more likely to occur during periods of low ice mass.

We should note, however, that our results are entirely based on the stresses within the host rock and do not take into account the pressure changes within the magma reservoirs during ice loss that may also affect the onset of eruptions, such as decompression melting in the magma reservoir (Mora and Tassara, 2019) or hydrologic effects from the influx of meltwater (Albino et al., 2010). Such effects would likely push eruptions to earlier in the warm season.

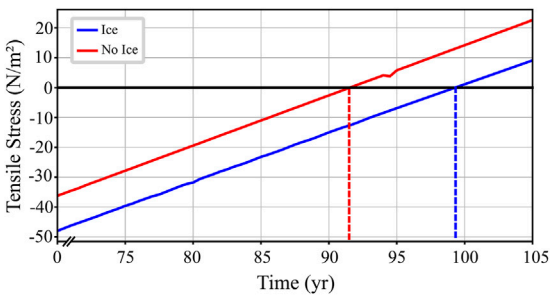

FIGURE 8 | Westdahl tensile stress versus time with and without a 1 km glacier. The figure has been zoomed in to highlight the timing of failure. Failure condition is represented by the black horizontal line and repose intervals are represented by the dotted lines. Depth to reservoir center is 7.2 km, flux rate is 0.0024 km^3/yr, and the radius of the magma chamber is 1.39 km (based on geodetic inversions conducted by Gong, 2015).

Is Westdahl's Protracted Unrest due to Glacial Loading?

Previous investigations of the unrest of Westdahl have observed a prolonged period of surface inflation, but without an accompanying eruption (Lu and Dzurisin, 2014). To evaluate the effect Westdahl's 1 km-thick ice cap has on this long-term stability, we apply our aforementioned numerical modeling approach to replicate conditions at this specific volcano. Based on previous geodetic inversions (Lu and Dzurisin, 2014; Gong, 2015), we simulate a 1.39 km-radius spherical reservoir centered 7.2 km below the ground surface with a flux of 0.0024 km^3/yr, and then compare the system's repose interval with and without an ice cover of 1 km (**Figure 8**).

Based on our numerical results, we find that the presence of the glacier would at most delay the onset of eruption by ~7 years as compared to models of Westdahl with no glacier (99 vs. 92 years from the start of constant inflation). This is significant on monitoring time scales, but relatively small compared to the modeled system's repose interval of ~100 years. However, the true system's absolute repose times will vary as the system geometry and underlying flux rates evolve. Based on our more general results, Westdahl's long-term stability is most likely controlled by the system's relatively deep reservoir (**Figure 5**) and spherical geometry (**Figure 6**). Regardless, future models attempting to forecast Westdahl's unrest need to consider all parameters that may significantly affect the onset of eruption on human time scales, including loading from the ice cap.

Westdahl's 5–10 m seasonal ice variations (Littell et al., 2018) and recent inflation, which has an estimated flux of ~0.0024 km^3/yr (Lu and Dzurisin, 2014), place it as a moderately high flux rate system with low seasonal variability (**Figure 7**). As such, we would expect the timing of eruption from Westdahl to be only moderately sensitive to seasonal ice loss. However, we do not know how close to failure the system is currently, and recent geodetic data have not yet been investigated to update our estimates of the system's flux rate. If the flux into Westdahl's magma reservoir has slowed in recent years while the system remains close to failure, seasonality may ultimately play a larger role than would be expected from this study. Future investigations would benefit from comparing more up-to-date estimates of Westdahl's unrest and its seasonal ice variations, as demonstrated here.

CONCLUSION

In this study, we investigate how the presence or absence of ice caps impacts the stability of volcanic systems on human timescales. Our numerical results indicate that large ice caps and glaciers with thicknesses of 1–3 km can appreciably delay the onset of eruptions on the order of years to decades. In particular, there is a linear relationship between the thickness of an ice cap and the additional reservoir volume change necessary to induce tensile failure. As such, the specific change in repose interval will depend on the underlying flux rate into the system for a given ice thickness. Therefore, when flux rates are low, seasonal variations in the overlying ice cap thickness may be adequate to trigger tensile failure once a system approaches the critical stress threshold. When we apply our findings to the recent unrest at Westdahl Volcano, Alaska, we find that for the previously modeled flux rate of 0.0024 km^3/year, the ~1 km ice cap would delay an eruption by ~7 years. Although the ice cap may greatly increase stability of the volcano, it is unlikely to fully account for the volcano's long periods of non-eruptive inflation. However, the numerical results presented assume constant flux, which may not capture the full dynamics of systems with long periods of quiescence or sudden spikes in flux rate. Moreover, we focus only on the stress conditions related to ice caps and not additional dynamic effects that may occur during their active emplacement or removal. This study establishes basic relationships between ice caps and volcanic reservoir stability, but future works should incorporate more realistic or dynamic parameters.

DATA AVAILABILITY STATEMENT

The original contributions presented in the study are included in the article/**Supplementary Material**, further inquiries can be directed to the corresponding author.

AUTHOR CONTRIBUTIONS

LL led this work as part of her undergraduate research supervised primarily by JA with guidance from PG and YZ. All authors contributed to analyzing the numerical results, drafting figures, and writing the manuscript.

FUNDING

Numerical modeling to investigate magma system stability is funded U.S. National Science Foundation (NSF GRFP-Albright, EAR 2122745 and EAR 1752477–Gregg), NASA (80-NSSC19K-0357–Gregg), and the University of Illinois Department of Geology Summer Undergraduate Research Opportunity Program (Lucas).

ACKNOWLEDGMENTS

The authors would like to thank C. Proistosescu, H. Cabaniss, R. Goldman, and M. Head for helpful conversations that enhanced this investigation.

SUPPLEMENTARY MATERIAL

The Supplementary Material for this article can be found online at: https://www.frontiersin.org/articles/10.3389/feart.2022.868569/full#supplementary-material

REFERENCES

Albino, F., Pinel, V., and Sigmundsson, F. (2010). Influence of Surface Load Variations on Eruption Likelihood: Application to Two Icelandic Subglacial Volcanoes, Grímsvötn and Katla. *Gr ´ ımsv otn*, 1510–1524. doi:10.1111/j.1365-246X.2010.04603.x

Albright, J. A., Gregg, P. M., Lu, Z., and Freymueller, J. T. (2019). Hindcasting Magma Reservoir Stability Preceding the 2008 Eruption of Okmok, Alaska. *Geophys. Res. Lett.* 46, 8801–8808. doi:10.1029/2019GL083395

Annen, C. (2009). From Plutons to Magma Chambers: Thermal Constraints on the Accumulation of Eruptible Silicic Magma in the Upper Crust. *Earth Planet. Sci. Lett.* 284, 409–416. doi:10.1016/j.epsl.2009.05.006

Cabaniss, H. E., Gregg, P. M., and Grosfils, E. B. (2018). The Role of Tectonic Stress in Triggering Large Silicic Caldera Eruptions. *Geophys. Res. Lett.* 45, 3889–3895. doi:10.1029/2018GL077393

Degruyter, W., and Huber, C. (2014). A Model for Eruption Frequency of Upper Crustal Silicic Magma Chambers. *Earth Planet. Sci. Lett.* 403, 117–130. doi:10.1016/j.epsl.2014.06.047

Del Negro, C., Currenti, G., and Scandura, D. (2009). Temperature-dependent Viscoelastic Modeling of Ground Deformation: Application to Etna Volcano during the 1993-1997 Inflation Period. *Phys. Earth Planet. Interiors* 172, 299–309. doi:10.1016/j.pepi.2008.10.019

Gelman, S. E., Gutiérrez, F. J., and Bachmann, O. (2013). On the Longevity of Large Upper Crustal Silicic Magma Reservoirs. *Geology* 41, 759–762. doi:10.1130/G34241.1

Gerbault, M., Cappa, F., and Hassani, R. (2012). Elasto-plastic and Hydromechanical Models of Failure Around an Infinitely Long Magma Chamber. *Geochem. Geophys. Geosyst.* 13, a–n. doi:10.1029/2011GC003917

Geyer, A., and Bindeman, I. (2011). Glacial Influence on Caldera-Forming Eruptions. *J. Volcanol. Geotherm. Res.* 202, 127–142. doi:10.1016/j.jvolgeores.2011.02.001

Gong, W. (2015). Journal of Geophysical Research : Solid Earth. *AGU J. Geophys. Res. Solid Earth* 119, 3678–3699. doi:10.1002/2013JB010641.Received

Gregg, P. M., De Silva, S. L., Grosfils, E. B., and Parmigiani, J. P. (2012). Catastrophic Caldera-Forming Eruptions: Thermomechanics and Implications for Eruption Triggering and Maximum Caldera Dimensions on Earth. *J. Volcanol. Geotherm. Res.* 241-242, 1–12. –242. doi:10.1016/j.jvolgeores.2012.06.009

Gregg, P. M., de Silva, S. L., and Grosfils, E. B. (2013). Thermomechanics of Shallow Magma Chamber Pressurization: Implications for the Assessment of Ground Deformation Data at Active Volcanoes. *Earth Planet. Sci. Lett.* 384, 100–108. doi:10.1016/j.epsl.2013.09.040

Grosfils, E. B. (2007). Magma Reservoir Failure on the Terrestrial Planets: Assessing the Importance of Gravitational Loading in Simple Elastic Models. *J. Volcanol. Geotherm. Res.* 166, 47–75. doi:10.1016/j.jvolgeores.2007.06.007

Huber, C., Townsend, M., Degruyter, W., and Bachmann, O. (2019). Optimal Depth of Subvolcanic Magma Chamber Growth Controlled by Volatiles and Crust Rheology. *Nat. Geosci.* 12, 762–768. doi:10.1038/s41561-019-0415-6

Kent, A., Wieser, P. E., and Till, C. (2022). *Geophysical and Geochemical Constraints on Magma Storage Depths along the Cascade Arc: Knowns and Unknowns*. Goldschmidt.

Larsen, G. (2000). Holocene Eruptions within the Katla Volcanic System, South Iceland: Characteristics and Environmental Impact. *Jökull* 49, 1–28.

Littell, J., McAfee, S., and Hayward, G. (2018). Alaska Snowpack Response to Climate Change: Statewide Snowfall Equivalent and Snowpack Water Scenarios. *Water* 10, 668. doi:10.3390/w10050668

Lu, Z., and Dzurisin, D. (2014). *InSAR Imaging of Aleutian Volcanoes: Monitoring a Volcanic Arc from Space*.

Lu, Z., Rykhus, R., Masterlark, T., and Dean, K. G. (2004). Mapping Recent Lava Flows at Westdahl Volcano, Alaska, Using Radar and Optical Satellite Imagery. *Remote Sens. Environ.* 91, 345–353. doi:10.1016/j.rse.2004.03.015

Lisowski M., (Editor) (2007). *Analytical Volcano Deformation Source Models* (Bath, UK: Springer), 469. doi:10.1007/978-3-540-49302-0

Mora, D., and Tassara, A. (2019). Upper Crustal Decompression Due to Deglaciation-Induced Flexural Unbending and its Role on Post-glacial Volcanism at the Southern Andes. *Geophys. J. Int.* 216, 1549–1559. doi:10.1093/gji/ggy473

Rasmussen, D. J., Plank, T. A., and Roman, D. C. (2019). *The Aleutian Arc through and through: Magmatic Water Content Controls Magma Storage Depth*. New York, NY: Columbia University.

Satow, C., Gudmundsson, A., Gertisser, R., Ramsey, C. B., Bazargan, M., Pyle, D. M., et al. (2021). Eruptive Activity of the Santorini Volcano Controlled by Sea-Level Rise and Fall. *Nat. Geosci.* 14, 586–592. doi:10.1038/s41561-021-00783-4

Sigmundsson, F., Pinel, V., Lund, B., Albino, F., Pagli, C., Geirsson, H., et al. (2010). Climate Effects on Volcanism: Influence on Magmatic Systems of Loading and Unloading from Ice Mass Variations, with Examples from Iceland. *Phil. Trans. R. Soc. A* 368, 2519–2534. doi:10.1098/rsta.2010.0042

Wilson, C. J. N., Blake, S., Charlier, B. L. A., and Sutton, A. N. (2006). The 26·5 Ka Oruanui Eruption, Taupo Volcano, New Zealand: Development, Characteristics and Evacuation of a Large Rhyolitic Magma Body. *J. Pet.* 47, 35–69. doi:10.1093/petrology/egi066

Zhan, Y., and Gregg, P. M. (2019). How Accurately Can We Model Magma Reservoir Failure with Uncertainties in Host Rock Rheology? *J. Geophys. Res. Solid Earth* 124, 8030–8042. doi:10.1029/2019JB018178

Conflict of Interest: The authors declare that the research was conducted in the absence of any commercial or financial relationships that could be construed as a potential conflict of interest.

Publisher's Note: All claims expressed in this article are solely those of the authors and do not necessarily represent those of their affiliated organizations, or those of the publisher, the editors and the reviewers. Any product that may be evaluated in this article, or claim that may be made by its manufacturer, is not guaranteed or endorsed by the publisher.

frontiers | Frontiers in Earth Science

ORIGINAL RESEARCH
published: 31 May 2022
doi: 10.3389/feart.2022.759475

A Data-Based Minimal Model of Episodic Inflation Events at Volcanoes

Damian Walwer[1]*, *Michael Ghil*[2,3] and *Eric Calais*[2,4]

[1]Department of Geosciences, The Pennsylvania State University, University Park, PA, United States, [2]Department of Geosciences, Ecole Normale Supérieure, PSL Research University, Paris, France, [3]Department of Atmospheric and Oceanic Sciences, University of California, Los Angeles, Los Angeles, CA, United States, [4]Institut de Recherche pour le Développement, Observatoire De La Côte D'Azur, Université Côte d'Azur, Géoazur, Nice, France

Space geodetic time series, be they ground-based or space-based, have increased in length and accuracy. These series can now be mined for information on the qualitative dynamics of volcanic systems directly from surface deformation data. Here, we study three volcanoes: Akutan and Okmok that are part of the Aleutian arc, and Piton de la Fournaise on la Reunion Island. All three are continuously monitored by the Global Positioning System (GPS) and exhibit common stair step–shaped inflation cycles sometimes referred to as to as "episodic inflation events". Here we seek to characterize the corresponding dynamical regime of pressure build-up within their plumbing system. To do so, we make use of Multichannel Singular Spectrum Analysis (M-SSA), a data-adaptive, non-parametric time series analysis methodology that allows for 1) the reliable detection and extraction of such patterns even when the corresponding signal lies close to, or even below, the data scatter; and 2) the extraction of information relevant to the underlying qualitative dynamics without a priori assumptions on the underlying physical mechanisms. For our three volcanoes, we find that the inflation cycles resemble the relaxation oscillations of a simple oscillator that involves a nonlinear dissipative mechanism. This finding provides important guidelines for physics-based models of episodic inflation cycles. In fact, the three volcanoes share a plumbing system composed of several interconnected storage bodies. Guided by the qualitative M-SSA–inferred dynamics, we formulate a simple physical model of two magma bodies connected by a conduit in which the viscosity of the fluid varies with temperature or magma crystallization. We show that such a model possesses internal relaxation oscillations similar to those of a simple oscillator. These oscillations correspond to repetitive events with sharp variations in the rate of magma transport and they can account for episodic events of pressure build-up in magma bodies, with no need for a time-dependent magma flux into or out of the system. We also show that the model's number of degrees of freedom is consistent with the amount of information extracted from M-SSA data analysis. The approach presented here relies on the robust statistical analysis of deformation time series to constrain the phenomenology of pressure build-up within a volcanic plumbing system; it provides a novel framework for understanding the dynamics of volcanic systems.

Keywords: episodic inflation events, relaxation oscillations, statistical analysis of time series, magma transport, Hopf bifurcation

OPEN ACCESS

Edited by:
Simona Petrosino, Sezione di Napoli—Osservatorio Vesuviano, Italy

Reviewed by:
Alessandro Bonaccorso, National Institute of Geophysics and Volcanology, Italy
Jeffrey Todd Freymueller, Michigan State University, United States

***Correspondence:**
Damian Walwer
damianwalwer@gmail.com

Specialty section:
This article was submitted to Volcanology, a section of the journal Frontiers in Earth Science

Received: *16 August 2021*
Accepted: *06 May 2022*
Published: *31 May 2022*

Citation:
Walwer D, Ghil M and Calais E (2022) A Data-Based Minimal Model of Episodic Inflation Events at Volcanoes. Front. Earth Sci. 10:759475. doi: 10.3389/feart.2022.759475

1 INTRODUCTION AND MOTIVATION

A large, and rapidly increasing, volume of continuous space geodetic observations is now available from ground-based data using the Global Positioning System (GPS) or from space-based data using Interferometric Satellite Aperture Radar (InSAR). These data sets are particularly dense in areas of volcanic unrest and they show a range of nonlinear temporal evolutions of surface deformation that reflect the dynamics of the underlying magmatic processes and provide information on the way pressure builds up within plumbing systems (Biggs and Pritchard, 2017). These processes may include magma flux into the magmatic plumbing system or out of it (Dvorak and Okamura, 1987; Mériaux and Jaupart, 1995; Parks et al., 2012), crystallization and degassing in melt reservoirs (Tait et al., 1989; Caricchi et al., 2014; Degruyter and Huber, 2014) or hydrothermal circulation driven by the magmatic thermal anomaly (Lu et al., 2010; Hutchison et al., 2016). The resulting surface deformation is sometimes readily visible from geodetic time series (Newman et al., 2006; Feng and Newman, 2009). In other cases, advanced time series analysis techniques have shown that nonlinear deformation caused by magmatic processes can be present during seemingly quiet time intervals where little or no deformation is apparent in the data (Ji and Herring, 2011; Walwer et al., 2016).

A common temporal deformation pattern observed near volcanoes is that of inflation with a decaying rate; see **Figure 1A**. This pattern is often explained by the linear dynamics of magma influx driven by a pressure gradient between a storage reservoir embedded in an elastic medium and a deeper source (Dvorak and Okamura, 1987; Jaupart and Tait, 1990; Lenglin et al., 2008; Pinel et al., 2010). In this case, the characteristic time scale of decay in the inflation rate can be related to physical properties of the plumbing system, such as the volume of the storage zones and their effective bulk modulus.

Other types of inflation patterns, such as successive transient inflation episodes superimposed onto longer-term inflation are also commonly observed; see Biggs and Pritchard (2017) and **Figures 1B,C** here. Such a pattern is sometimes referred to as "episodic inflation events" (Ji et al., 2017). At the Aleutian volcano Akutan, for instance, repeating transient inflation events are superimposed onto a secular linear inflation of the volcano (Walwer et al., 2016; Ji et al., 2017; Xue and Freymueller, 2020). Other volcanoes that exhibit repeating transient inflation events include Okmok (Alaska) and Piton de la Fournaise (La Réunion) (Peltier et al., 2008; Walwer et al., 2016; Xue and Freymueller, 2020).

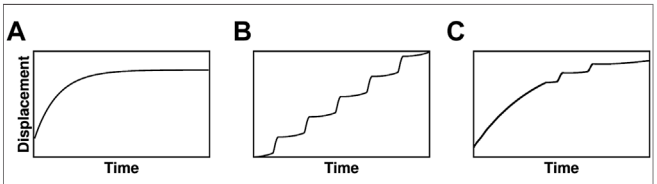

FIGURE 1 | Schematic inflation regimes observed at volcanoes and mentioned within the text. **(A)** Inflation with a monotonically decaying rate often explained by the linear dynamics of pressure build-up within a storage zone through magma supply (e.g., Pinel et al., 2010). **(B)** Regime of successive transient inflation episodes superimposed onto an inflation with constant rate; this regime is referred to as "episodic inflation events" by Ji et al. (2017) and it is observed for example at Akutan volcano. **(C)** Episodic inflation events superimposed onto a longer period inflation with decaying rate (e.g., Walwer et al., 2019).

The amplitude, spatial wavelength, and time scale of these events can vary significantly from one volcano to the other. As a result, these episodic inflation cycles are difficult to relate to a single physical process and are therefore sometimes interpreted as the result of ad hoc time-dependent forcing mechanisms, such as pulses of magma flux, degassing, or heat flux (Biggs et al., 2009; Peltier et al., 2009; Biggs et al., 2010; Xue and Freymueller, 2020). It is also worth noting that—in some cases, such as for the Okmok volcano and Piton de la Fournaise—successive inflation events do precede large eruptions while in other cases, such as at Akutan, they do not (e.g., Ji et al., 2017; Walwer et al., 2019).

Here we seek to extract temporal variability patterns from continuous deformation measurements at volcanoes that experience repetitive inflation events and to mine the available data for qualitative information on their underlying dynamics. To do so, we objectively extract repeating transient inflation signals at three volcanoes—Akutan, Okmok and Piton de la Fournaise—using a data-adaptive statistical methodology, namely Multichannel Singular Spectrum Analysis (M-SSA), applied to continuous GPS time series (Walwer et al., 2016).

These three volcanoes, which display such repetitive inflation events, have the advantage that their plumbing systems are well constrained by independent geochemical, petrological, seismic and geodetic datasets. We illustrate the resemblance of their deformation patterns using phase portrait reconstructions (Guckenheimer and Holmes, 1983; Ghil and Childress, 1987; Jordan and Smith, 2007), which indicate a striking dynamical similarity amongst them. To extract the dynamical features that lead to the observed phase portraits, we use a simple nonlinear oscillator that shares qualitative behavior with the inflation cycles observed at the volcanoes studied herein. This analogy, in turn, provides guidelines that we then use to build a physical model based on the plumbing system of the volcanoes being investigated.

The present paper aims in particular at presenting the connection between statistical analysis of GPS time series and dynamical modeling of volcanoes. The data used and the methods applied are presented in **Section 2**. In **Section 3**, we apply M-SSA to the GPS time series. The similarities in the phase portraits obtained for the three volcanoes are discussed in **Section 4**. The model for pressure build-up through magma flow between connected reservoirs is formulated in **Section 5**. Concluding remarks follow in **Section 6** and we emphasize the consistency between our dynamical modeling approach and the amount of information contained in the geodetic data extracted and analyzed using our M-SSA methodology.

2 DATA AND METHODS

2.1 Three Volcanoes and Their GPS Data Sets

We used position time series from continuous GPS data at stations located on three volcanoes: Akutan (8 stations) and Okmok (5 stations) in Alaska, and Piton de la Fournaise (10

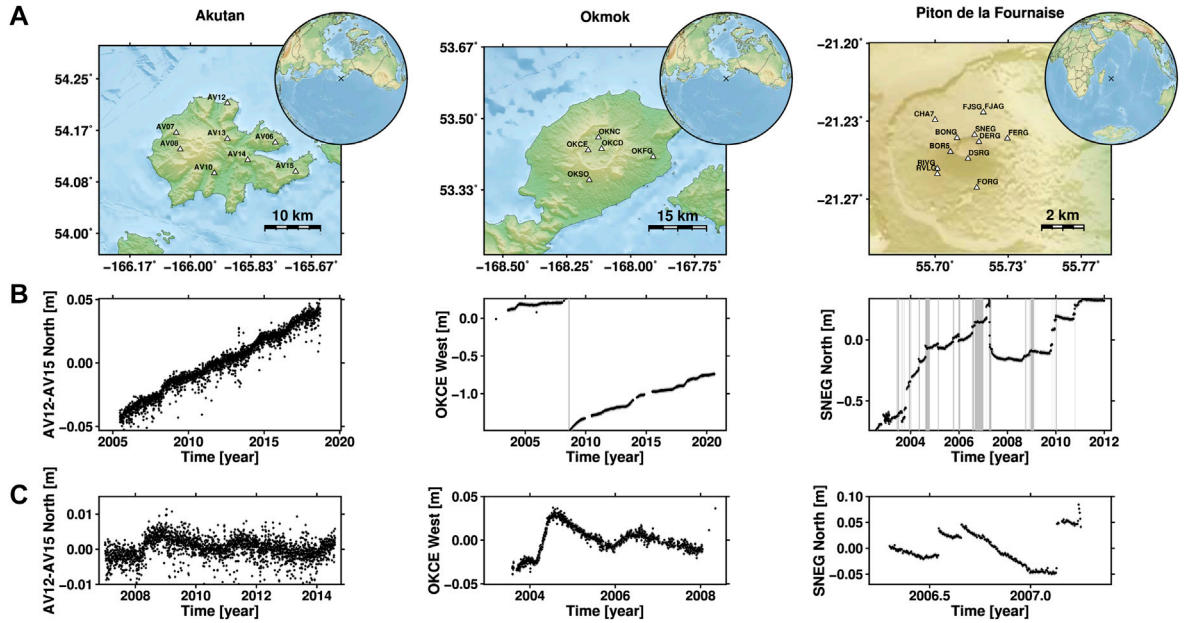

FIGURE 2 | Location map and selected time series of GPS displacement for the three volcanoes used in this study. **(A)**: Maps, with grey triangles showing the GPS sites from which the displacement time series used herein have been extracted; **(B)**: Full time series available, including linear trend; **(C)**: Selected time interval, with linear trend removed. The selected sites and directional components are indicated on the ordinate of the **(B,C)**. For instance, for Akutan, AV12-AV15 North indicates the difference between the northward GPS displacements at sites AV12 and AV15. Grey vertical bars in the middle panels indicate intervals of eruptive activity.

stations) on La Réunion island (**Figure 2**). For Akutan the time series were taken from the Plate Boundary Observatory, pbo.unavco.org; they are expressed with respect to a North American Reference Frame. Time series recorded at Okmok and Piton de le Fournaise (PdF hereafter) were taken from the Nevada Geodetic Laboratory geodesy.unr.edu; they are expressed with respect to a North American reference frame and to the IGS international reference frame (IGS14), respectively (Blewitt et al., 2018). These time series contain the magmatic signals we are interested in, but also components of tectonic deformation, seasonal deformation due to atmospheric and hydrological processes, and GPS measurement noise.

Akutan and Okmok are located close to a subduction system where interseismic tectonic loading produces long-term deformation of the whole plate margin, including the volcanoes. At Akutan, the linear trend that dominates the variance of the time series is probably the result of this tectonic loading combined with a local volcanic inflation caused, for instance, by a constant magma flux into Akutan's plumbing system. Following the approach of DeGrandpre et al. (2017), we remove the tectonic signal by considering the time series of baselines with respect to station AV15, the site farthest away from the volcanic center (**Figure 2**). This site is likely to record mainly tectonic deformation shared across the other Akutan GPS sites and it thus allows us to remove the common tectonic signal while conserving the magmatic signals we are interested in, including a linear volcanic inflation (DeGrandpre et al., 2017; Ji et al., 2017).

At Okmok, the smaller number of continuous GPS stations, together with gaps in the GPS time series at sites far away from the volcanic center, do not allow us to use the baseline approach described above for Akutan. However, volcanic signals at Okmok are of much larger amplitude, and InSAR time series, displayed in Biggs et al. (2010) for example, show that the GPS signals recorded before the 2008 eruption are superimposed onto a longer period signal with inverse exponential shape, characteristic of the dynamics of infilling of a magma reservoir (e.g., Reverso et al., 2014; Walwer et al., 2019). We therefore consider that the signals starting in 2003, before the 2008 eruption, mainly reflect volcanic deformation.

The PdF corresponds to an active hot spot within the Somalian tectonic plate; hence, no signal of tectonic loading is expected to be present in the deformation time series. Flank instability was associated with the 2007 co-eruptive and post-eruptive deformation events, but our study focuses on the signals preceding the 2007 eruption (Tridon et al., 2016; Poland et al., 2017).

2.2 Basic Ingredients of the M-SSA Analysis

In order to isolate the displacements associated with the activity of the volcanic systems from other geophysical signals—such as seasonal oscillations of atmospheric or hydrological origin—and from the GPS measurement noise, we filtered the position time series using M-SSA. M-SSA is a data-adaptive, non-parametric method that simultaneously exploits the spatial and temporal correlations associated with time evolving data sets (Ghil et al., 2002; Groth and Ghil, 2015; Alessio, 2016; Walwer et al., 2016). Apart from unraveling signals of different origins and signals from noise, M-SSA helps extract information about the underlying qualitative dynamics from the time series. The

connection between M-SSA results of statistical time series analysis and dynamical systems behavior has been the subject of considerable research (Broomhead and King, 1986; Vautard and Ghil, 1989); it is exploited in **Section 4.1** and **Section 6.1** of the present paper.

M-SSA decomposes a set of D time series into modes of spatio-temporal variability that correspond to nonlinear trends, oscillations, or noise. These modes are derived from the eigenvectors of the covariance matrix:

$$\mathbf{C} = \frac{1}{(N - M + 1)}\mathbf{X}^{\mathrm{t}}\,\mathbf{X}. \tag{1}$$

Here, $\mathbf{C}$ is computed from the ensemble of M lagged copies of the D time series composing the data sets and forming the columns of matrix $\mathbf{X}$. This matrix, referred to as the "trajectory matrix," provides a useful connection between M-SSA analysis and dynamical systems theory (Ghil et al., 2002) that is further exploited in **Section 4.1**.

The maximum period of the modes that can be extracted using the M-SSA is roughly $M\tau_s$, where τ_s is the sampling interval of the time series. Here we used $\tau_s = 1$ day for the three GPS data sets analyzed for Akutan, Okmok, and PdF. The choice of M depends on the characteristics of the analyzed time series and the period of the signal one wants to extract.

The decomposition of the covariance matrix $\mathbf{C}$ given by

$$\mathbf{\Lambda} = \mathbf{E}^{\mathrm{t}}\,\mathbf{C}\,\mathbf{E} \tag{2}$$

yields the $D \times M$ real eigenvalues that are the diagonal elements of $\mathbf{\Lambda}$ and the eigenvectors that appear as the columns of $\mathbf{E}$. Signals that are strongly correlated in space and time in a given data set are captured as the modes with the largest eigenvalues. Here, we expect these modes to be signals of magmatic origin.

The projection of the time series and their lagged copies contained in the trajectory matrix $\mathbf{X}$ upon the eigenvectors gives the principal components (PCs) that form the columns of the matrix

$$\mathbf{A} = \mathbf{X}\,\mathbf{E}. \tag{3}$$

The PCs are time series that represent the temporal behavior of the extracted modes. The variance of the data set described by each PC is given by the corresponding eigenvalue. The PCs can be seen as a sparse representation of the time-dependent patterns shared across a set of time series. They are a convenient tool for 1) visualizing the temporal shapes of the modes extracted by the M-SSA, and 2) identifying which modes may correspond to magmatic signals and which ones are more likely to represent either noise or geophysical signals of non-magmatic origin, such as seasonal oscillations caused by hydrological loads.

Once the modes corresponding to the magmatic deformation are identified, one can reconstruct the corresponding signal by projecting the PCs onto a set $\mathcal{K} \subset \{1, \ldots, DM\}$ of the eigenvectors:

$$\mathbf{R} = \mathbf{A}\,\mathbf{K}\,\mathbf{E}^{\mathrm{t}} = \mathbf{X}\mathbf{E}\mathbf{K}\mathbf{E}^{\mathrm{t}}. \tag{4}$$

This subset corresponds to the signal of interest, and $\mathbf{K}$ is a diagonal matrix of size $DM \times DM$ whose elements K_{kk} are 1 if $k \in \mathcal{K}$ and 0 otherwise. The reconstructed components, called RCs hereafter, provide the appropriate visualization of the signal after filtering out non-magmatic components and the lower-variance noise (Ghil et al., 2002; Alessio, 2016, and references therein). The RCs can also be used to represent the corresponding spatial deformation patterns at GPS in map view, for instance for selected time intervals (Walwer et al., 2016).

3 M-SSA EXTRACTION OF EPISODIC INFLATION EVENTS

3.1 Applying M-SSA to the GPS Data Sets

We performed the M-SSA analysis on GPS time series recorded at the three volcanoes under study, for time intervals that contain the same number of cycles for each volcano, i.e., three episodes of inflation Having the same number of episodic inflation events for the three volcanoes allows us to consistently compare and discuss the statistical information obtained, as well as the dynamics inferred therefrom.

Before applying M-SSA we removed the linear part of the time series that accounts for a large portion of the data variance. Removing the linear trend before applying M-SSA is commonly done to focus the analysis on the nonlinear part of the volcanic signal; see Walwer et al. (2016). Linear trends represent, in all likelihood, longer-term inflation upon which the nonlinear volcanic signal we are interested in is superimposed. While the time series analysis presented here focuses on the nonlinear signals, we do not preclude that the inflation trends play a role in the observed dynamics.

The connection between the extracted nonlinear signals and the long-term inflations is explained in **Section 5.2** and discussed in **Section 6.1** as well. Examples of detrended time series plotted over the selected time intervals are displayed in the **Figure 2C**. At Okmok and PdF, the last inflation episode—the few points ending the bottom time series in **Figures 2** – precedes a large co-eruptive deflation event.

The main input parameter for the M-SSA analysis is the maximum lag $M\tau_s$ used to compute the entries of the covariance matrix $\mathbf{C}$ in **Eq. 1**. Because the duration of the magmatic inflation events is different amongst the three volcanoes, the selected value of $M\tau_s$ also differs for each data set. We use $M\tau_s$ = 400 days for Akutan, $M\tau_s$ = 150 days for Okmok, and $M\tau_s$ = 30 days for PdF. The singular spectra—i.e., the normalized eigenvalues ranked in decreasing order—are displayed in **Figure 3** together with the first 6 PCs. The relative variance captured by these PCs is given by the associated normalized eigenvalues, so that, for example, PC 1 at Akutan, Okmok and PdF describes respectively 5, 60 and 25% of the variance of the corresponding data set. **Table 1** contains a summary of the characteristics of the data sets analyzed herein, together with the M-SSA input parameters and results.

3.2 Mode Selection for the Volcanic Signals

We select the modes associated with magmatic signals based on their large variance and on two additional criteria. First, we search for temporal patterns that consist of relatively short inflations

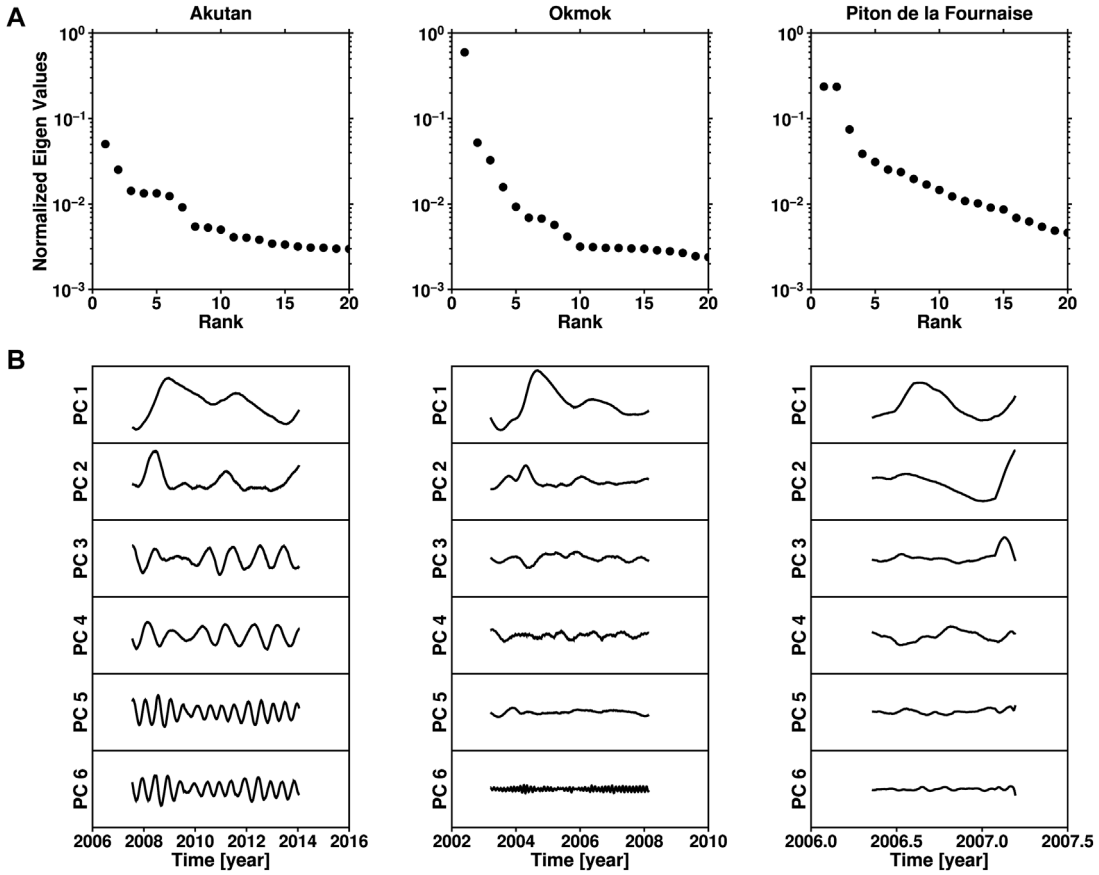

FIGURE 3 | M-SSA analysis applied to the time series recorded at Akutan, Okmok and Piton de la Fournaise (PdF). The **(A)** show the normalized eigenvalues of the GPS position time series. **(B)** show the 6 leading PCs resulting from the M-SSA analysis applied to these three volcanoes.

followed by longer intervals of rest or small-amplitude deformation. Because we detrended the time series before applying M-SSA, such a pattern corresponds to the PCs in **Figure 3** that reflect intervals of increase in displacement, followed by a decrease in displacement. Second, we use the selected mode to reconstruct the corresponding nonlinear signals using **Eq. 4**, together with the extracted linear trend to represent the associated displacements in map view in order to check that the reconstructed spatial pattern is qualitatively consistent with volcanic inflation, i.e., radial displacements centered on the active crater that decay in amplitude with distance (**Figure 4**). The final check on the number of M-SSA modes S retained at each volcano relies on the consistency of the temporal and spatial pattern of the reconstructed displacements.

There is always a part of arbitrary decision when choosing the modes to reconstruct a given signal. The impact of this educated guesswork can be minimized by applying significance tests to specifically determine which modes are likely to be associated with colored noise, as opposed to a true geophysical signal. Varying the window size M within a reasonable range around the chosen values can constitute such a test. For the data sets at hand, we found that it does not affect the results of our analysis.

More sophisticated tests rely on the formulation of a null hypothesis against which the M-SSA results can be tested (Groth and Ghil, 2015). Such a test was performed for Akutan volcano by Walwer et al. (2016); we did not find it necessary to perform it for Okmok and PdF here, since the corresponding magmatic signals there are of much greater amplitude and readily visible in the data. Also, we observed that the reconstructed signal at the latter two volcanoes leads to spatial and temporal patterns that are quite consistent with the expectation of magmatic inflation–deflation events.

A key aspect of the M-SSA analysis, as further discussed in **Section 6.1**, is that the number of modes S used to reconstruct the signals is an output of the analysis itself. In the following, we provide details on how the leading modes were chosen in order to reconstruct the deformation signal for each volcano.

3.2.1 Akutan

Walwer et al. (2016) applied M-SSA to the Akutan GPS time series and the details provided there on the choice of the M-SSA parameters are not repeated here. The left panels of **Figure 3** show the first 20 eigenvalues and the first 6 PCs obtained. One can clearly distinguish two groups of PCs: PCs 3–6 display oscillations with either an annual (PCs 3-4) or a semi-annual

TABLE 1 | Summary of the M-SSA parameters and of the results of the analysis, along with the characteristics of the deformation observed at the volcanoes investigated.

Volcanoes	Akutan	Okmok	PdF
Time series characteristics and M-SSA parameters			
Selected time interval	2007–2014.6	2003–2008.3	2006.3–2007.2
Number of data points N	2,777	1954	347
Number of GPS stations used n	8	2	6
Number of time series $D = 3n$	24	6	18
Window size M	400	150	30
Number of modes retained S	2	2	3
Signal-to-noise ratio	≃ 7%	≃ 60%	≃ 55%
Embedding phase plane			
Phase plane abscissa	PC 1	PC 1	PCs 1 + 2
Phase plane ordinate	PC 2	PC 2	PC 3
Spatio-temporal characteristics of the volcanic deformation			
Duration of inflation events (month)	≃ 12	≃ 6	≃ 0.3
Cycle duration (month)	≃ 36	~ 24	~ 6
Displacements (mm)	≃ 1–10	≃ 25–50	≃ 50–100
Deformation wavelength (km)	≃ 10	≃ 10	≃ 2
Structures causing the deformation	Chambers —	Chambers —	Chambers Dykes and Sills
Main references			
Geochemistry/Petrology	—	Larsen et al. (2013)	Famin et al. (2009)
Seismology	Syracuse et al. (2015)	—	Battaglia et al. (2005)
Geodesy	Walwer et al. (2016) DeGrandpre et al. (2017) Ji et al. (2017)	Biggs et al. (2010) Walwer et al. (2019) Xue et al. (2020)	Peltier et al. (2008) Peltier et al. (2009) —

(PCs 5-6) period, while the combination of PCs 1-2 corresponds to a nonlinear trend that may include longer periods. PC 1 has an M-shape and captures the "skeleton" of the nonlinear trend associated with magmatic deformation, while PC 2 accounts for high-rate deformation that is correlated with the time intervals over which PC 1 displays an increase in displacement.

It follows that the best combination to use for reconstructing a spatially consistent volcanic signal is the combination of PCs 1 and 2. These two modes together account for roughly 7% of the detrended time series total variance. The corresponding spatial patterns for selected episodes of inflation, as well as an example of a M-SSA reconstructed time series that includes also the linear trend, are displayed in **Figure 4**. As expected, they show a clear radial displacement centered on the summit of the volcanic edifice, typical of a magmatic process.

3.2.2 Okmok

The singular spectrum at Okmok is displayed in the middle column of panels in **Figure 3**, along with the first six PCs. The first eigenvalue stands clearly above the rest of the spectrum and captures about 60% of the total variance. The associated PC has an M-shape very similar to PC 1 extracted at Akutan and, in the same way, captures the "skeleton" of the nonlinear temporal pattern of magmatic deformation.

The second PC, while accounting only for ~6% of the detrended time series variance, captures a signal correlated with the first PCs and is needed to properly reconstruct the signal shown in **Figure 4**. We note here the striking similarities between the first two PCs at Akutan and Okmok, obtained without any a priori assumptions. These phenomenological similarities reflect, with some likelihood, a similarity between the dynamics underlying the two magmatic systems; see **Section 4.1** below.

3.2.3 Piton de la Fournaise (PdF)

The singular spectrum for PdF in the right column of **Figure 3** shows that the first two modes account for roughly 45% of the detrended time series total variance. As for PC 1 at Akutan and Okmok, these first two modes combined describe the "skeleton" of the nonlinear magmatic deformation pattern. The third eigenvalue stands also slightly above the rest of the modes, capturing about 10% of the total variance. The associated third PC has a peak that occurs simultaneously with the second episode of increase in displacement, as reflected by PCs 1 and 2. As for the PC 2 at Akutan and Okmok, PC 3 at PdF further emphasizes the asymmetry between the inflation episodes and the episodes of rest or small-amplitude deformation.

We selected, therefore, these first three modes to reconstruct the nonlinear volcanic signal at PdF (right panels in **Figure 4**). The reconstructed spatial patterns of displacement are more asymmetric than at Akutan or Okmok. This asymmetry is, most likely, a result of melt pressurization of shallow structures, such as dykes or sills, at PdF, instead of the deeper

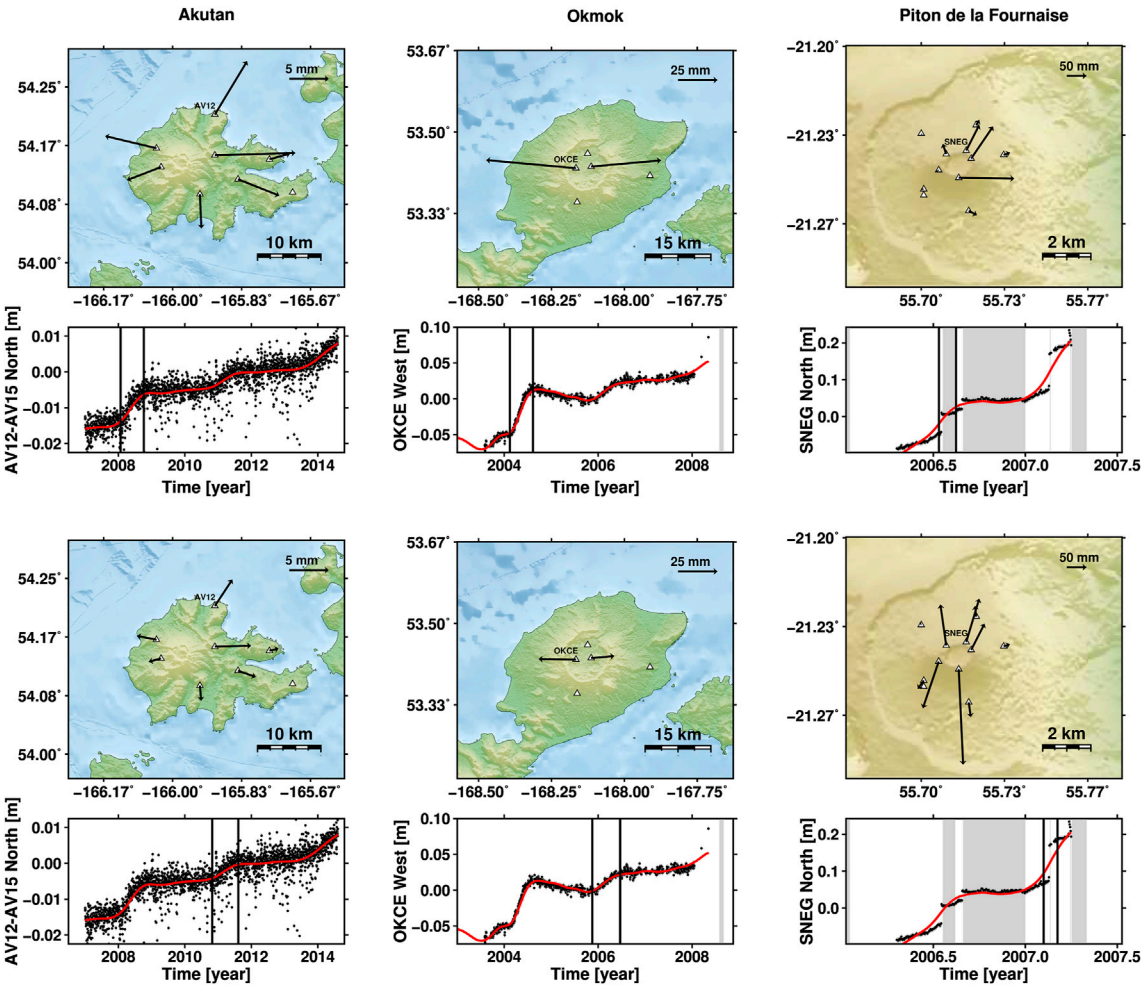

FIGURE 4 | Spatial and temporal pattern of horizontal displacements at the three volcanoes. The two maps for each volcano show the total horizontal displacements (black arrows) during a selected episode of inflation; these episodes are indicated by the two vertical black lines on the time series corresponding to the map. The panels with the selected GPS time series display black dots for the raw GPS data points and a heavy red line for the sum of the corresponding M-SSA nonlinear volcanic signal reconstruction and linear trend. The GPS receivers associated with the plotted time series are labeled on the maps, as in **Figure 2**.

magma reservoirs present at the other two volcanoes (Peltier et al., 2008).

4 SIMILARITIES IN DYNAMICAL BEHAVIOR

4.1 Phase Portrait Reconstruction

To gain insight into the dynamics described by the filtered time series considered above, we now introduce a nonlinear relaxation oscillator whose solutions share certain key features with the behavior of all three volcanoes under study. The repetitive character of the transient inflation episodes studied herein motivates the use of an oscillator to provide phenomenological insights into mechanisms that may drive the cyclic behavior of interest.

Our highly idealized oscillator is not meant to explain the detailed physics of the natural processes at play. But it does help identify features that lead to the qualitative dynamical behavior observed in the data. These features, in turn, will serve as constraints for designing a physical model for the observed oscillations, as described in **Section 5.2** below.

In order to identify the proper design features for our oscillator, we first compute phase portraits for the three volcanoes by plotting the PCs identified as magmatic signals in a phase plane (Packard et al., 1980; Roux et al., 1980; Takens, 1981; Gualandi et al., 2020). Such phase portraits show the evolution of a dynamical system as trajectories that contribute to a geometric representation of the system's dynamics. In phase space, stationary solutions appear as fixed points and periodic ones as closed trajectories, called limit cycles (Guckenheimer and Holmes, 1983; Jordan and Smith, 2007). These representations highlight, in particular, how the dynamics of a system that is out of equilibrium is organized around equilibrium states (Ghil and Childress, 1987; Deremble et al., 2009). The goal here is to extract qualitative features of the magmatic systems' dynamics.

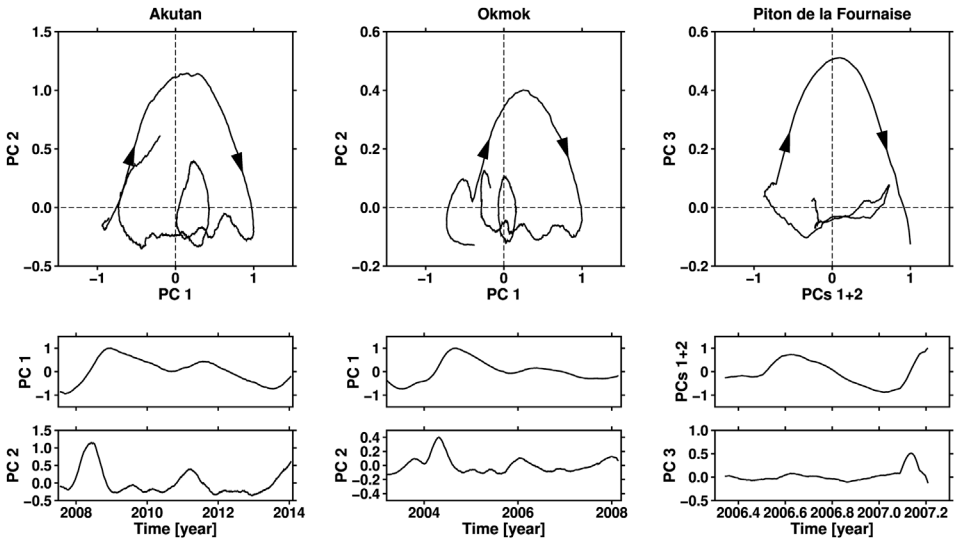

FIGURE 5 | Phase portrait reconstructions that reflect the dynamics of the three volcanic systems under study. The **(A)** are the actual phase portraits, while the **(B)** below each phase portrait show the two PCs (for Akutan and Okmok) or three PCs (for PdF) used to reconstruct the trajectories in the phase plane.

The use of M-SSA to reconstruct phase portraits is inspired by the work of Broomhead and King (1986) and exploits several advantages of the M-SSA algorithm. First, the M-SSA results are obtained without a priori information on the dynamics that produced the volcanic signals. This is not necessarily the case for other signal processing techniques that use functions with predetermined temporal or spatial shapes to extract geophysical signals, and hence rely—sometimes implicitly—on assumptions about the underlying dynamics. Second, the connection between M-SSA and the qualitative dynamical study of physical systems is supported by theoretical, experimental, and observational work (Packard et al., 1980; Mañé, 1981; Takens, 1981; Broomhead and King, 1986; Vautard and Ghil, 1989). M-SSA can be seen as a particular formulation of the so-called "method of delays" that integrates observational time series into an embedding space through the construction of a trajectory matrix such as the matrix **X** introduced in **Section 2.2**. We refer the reader to Ghil et al. (2002) and (Alessio, 2016, Ch. 12) for comprehensive reviews of the connection between M-SSA and the dynamical study of natural systems from observational time series.

Reconstructed phase portraits for the three volcanoes are shown in **Figure 5**. The trajectories form almost closed orbits, typical of oscillatory behavior, with slight spiraling in and out. The striking similarities in the phase space structure of the trajectories drawn in **Figure 5** between the three volcanoes indicate a dynamical similarity between them for the time intervals studied herein. A feature common to the phase portraits is that the trajectories are highly asymmetric about the horizontal line. This asymmetry is caused by PC 2 for Akutan and Okmok, and PC 3 for PdF. The latter PCs emphasize the relatively fast inflation episodes and further enhance the asymmetry between the deformation during the fast inflation events compared with the following, slower time intervals.

Note that the phase portraits in **Figure 5** that we reconstructed from the GPS time series correspond to a particular perspective on the phase space and the volcanoes' dynamics. Alternative views of phase space trajectories can be constructed and may include, for example, the longer-period inflations that were initially removed but contain also information on the dynamics. The perspective we choose to display in **Figure 5**, however, contains the features we wish to focus on and serves well the line of reasoning presented in the following sections.

4.2 A Simple Conceptual Model

The phase portraits in **Figure 5** indicate that further insight into the nature of the observed oscillations will be provided by formulating and analyzing a simple, nonlinear oscillatory model. The purpose of such a conceptual model is only to reproduce the first-order qualitative features of the phase portraits. As explained in the previous subsection, these phase portraits provide only one particular perspective upon the volcanic systems' dynamics. Thus, the following conceptual model aims to replicate only the first-order features apparent from this perspective in order to gain basic insights into the dynamics associated with it. The choice of the model presented below is somewhat arbitrary and mainly motivated by its relative simplicity. Still, this exercise will help us formulate constraints relevant to the more detailed physical models described in **Section 5.2**.

Our conceptual model is governed by the following system of two coupled ordinary differential equations:

$$\dot{x} = y, \tag{5a}$$

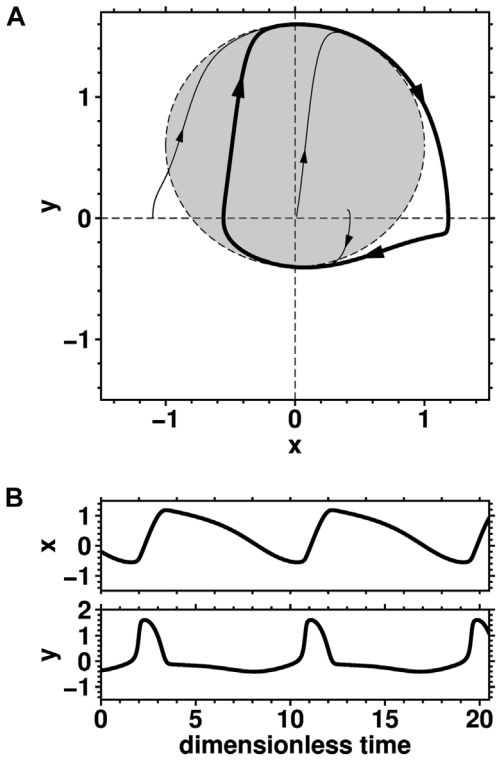

FIGURE 6 | Nonlinear oscillation of the idealized model governed by **Eqs 5a**, **5b**, for $\mu = 10$ and $y_0 = -0.6$. **(A)**: Phase portrait in the (x, y)-plane, with $y = \dot{x}$; **(B,C)**: The associated time series representing, respectively, $x(t)$ and $y(t)$. In **(A)**, the closed trajectory (heavy solid line) is the limit cycle. The light solid lines are typical trajectories converging to the limit cycle from the interior and the exterior of this cycle. The shaded area is the one where damping is negative, i.e., $\kappa > 0$ in **Eq. 7**. Arrows indicate the direction of motion on the limit cycle and on the trajectories that converge onto it.

$$\dot{y} = -\mu\left[x^2 + (y + y_0)^2 - 1\right]y - x; \tag{5b}$$

here x and its time derivative y are the system's two coupled variables, while μ and y_0 are independent parameters; see for example Jordan and Smith (2007). Both the dependent variables x, y and the independent variable t here are dimensionless.

The model governed by **Eqs 5a**, **5b** contains the possibility of oscillatory solutions, as is the case for the following much simpler system that would be obtained, for instance, by setting $\mu = 0$ in **Eq. 5b**

$$\dot{x} = y, \ \dot{y} = -x. \tag{6}$$

Whether this ability to oscillate is realized for the system (**Eqs 5a**, **5b**) depends on the model parameter values, as we shall see below. The simpler system (**Eq. 6**) is (a) linear, and (b) it is conservative, while system (**Eqs 5a**, **5b**) is neither. The nonlinearity in **Eqs 5a**, **5b** results from the form of the damping coefficient

$$\kappa = \kappa(\mu, y_0) \equiv -\mu\left[x^2 + (y + y_0)^2 - 1\right]. \tag{7}$$

The cases where $\kappa < 0$ and of $\kappa > 0$ are referred to as positive and negative damping, respectively.

For simplicity, let us assume that $y_0^2 < 1$. In this case, the regime into which the system evolves is controled by the value of μ. For $\mu < 0$, $\kappa < 0$ in **Eq. 7** as long as $x^2 + y^2$ is small enough and this regime has exactly one fixed point, i.e., one steady-state solution at the origin. This fixed point is linearly stable for the dissipative situation characterized by $\mu < 0$. Linear stability means that, for any initial state sufficiently close to the origin, the system will spontaneously evolve towards the latter.

For $\mu = \kappa = 0$, as in system (**Eq. 6**), there exist an infinite number of concentric, perfectly circular trajectories. When $\mu > 0$, κ becomes positive, as long as x and y are located in the grey area of **Figure 6**, which contains the origin. This positive damping causes the origin to become unstable, and so the system's trajectories spiral out, until they enter a region in which κ changes sign and thus limits further increase of the $x^2 + y^2$ distance from the origin. As a result, only a single closed trajectory exists, due to the damping. This trajectory is typically not circular, due to the nonlinearity, as illustrated by the one in **Figure 6**, computed for $\mu = 10$.

The change in the dynamics of a nonlinear deterministic system from a unique stable fixed point to a stable closed orbit—such as the one seen in **Figure 6**—is called a Hopf bifurcation and the closed orbit itself is called a limit cycle (Guckenheimer and Holmes, 1983; Ghil and Childress, 1987; Jordan and Smith, 2007). The particular type of nonlinear oscillations that involve sawtooth-type behavior, as opposed to the sinusoidal oscillations of **Eq. 6**, with rapid escape from a no-longer stable fixed point followed by slow relaxation back to it, are called relaxation oscillations (Van der Pol, 1926; Ghil and Childress, 1987; Grasman, 2011; Ghil, 2019). In fact, the limit cycle in **Figure 6** is precisely of the relaxation-oscillation type: not only is its shape not circular, but the velocities along it are nonuniform. This nonuniformity is highlighted by the changes in the slope of the $x(t)$ and $y(t)$ curves in the lower panels of **Figure 6**.

A first-order feature noticeable in **Figure 6** that is common to the GPS observations at the three volcanoes studied here and is likewise present in the simple system governed by **Eqs 5a**, **5b** is the alternation of intervals of fast increase in the observed quantities, followed by intervals with slower variations. For the three volcanoes, this correspond to relatively short and rapid inflation episodes, followed by longer intervals of small-amplitude deformation. This observed behavior is analogous to the fast increase in $x(t)$, followed by its slower decrease, in the conceptual model.

We argue that, at the volcanoes being studied herein, these common patterns can be modeled as resulting from asymmetric oscillations similar to the ones in the conceptual model of **Eqs 5a**, **5b**. This inference is also supported by the closed orbits of the phase portraits in **Figures 5**, **6**. Pursuing this line of thought, one might suspect that the observed magmatic regime of the three volcanoes can be modeled as resulting from the loss of stability of an equilibrium point that is causing a Hopf bifurcation such as in the nonlinear oscillator of **Eqs 5a**, **5b**.

Another important constraint we can extract from this analogy is that the "skeleton" of the dynamics—i.e., the main temporal pattern according to which these volcanic systems evolve—can be modeled by considering the interaction of merely two variables, like the two degree of freedom x and $\dot{x} = y$ of our conceptual model. This point is further discussed in **Section 6.1** and supported by the statistical results obtained by M-SSA in **Section 3**.

Dynamical similarity does not necessarily imply physical similarity (Barenblatt, 2003). In the following section, however, we present a more complete physical model that shares some of the dynamical features described above, such as Hopf bifurcation, and provides new insights into the behavior of the three volcanoes studied herein.

5 MAGMA FLOW BETWEEN CONNECTED STORAGE ZONES

We start this section by presenting evidence—for the three volcanoes studied herein—on a plumbing system composed of interconnected storage bodies fed by a deeper source. These storage bodies are either magma chambers or, as in the case of PdF, shallow networks of dykes and sills. The presence of interacting storage bodies is a key feature of the model presented in **Section 5.2** below. This model aims to explain recurrent inflation events as reflecting an oscillatory regime caused by loss of stability of an equilibrium state in a manner that recalls the Hopf bifurcation in the conceptual model of **Section 4.2**.

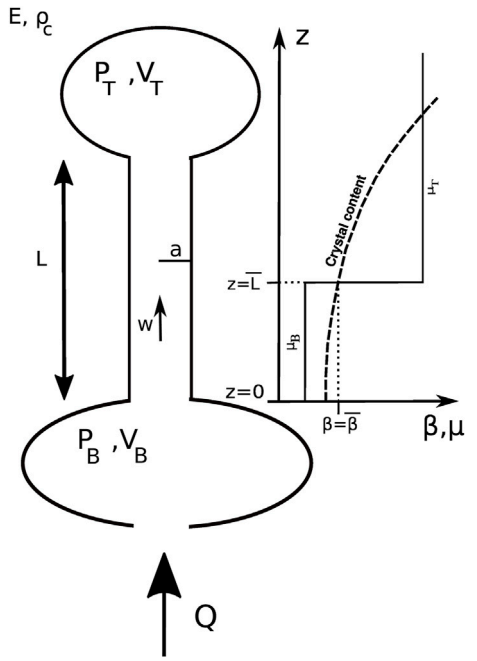

FIGURE 7 | Schematic representation of the components of the physical model described in **Section 5.2**, including the key associated variables and parameters. Two reservoirs with volumes V_B and V_T, for bottom (B) and top (T), respectively, contain magma at pressures P_B and P_T. They are fed by magma from a deeper source region with constant flux Q. The pipe linking the two reservoirs has radius a and length L, and the magma flows through it at velocity w. Inside the pipe, the crystal concentration β per volume reaches the value $\bar{\beta}$ when $z = \bar{L}$. Above $\bar{L}$ the viscosity increases from μ_B to μ_T.

5.1 Evidence for Connected Storage Zones of Magma

5.1.1 Akutan

The analysis of seismicity at Akutan volcano by Syracuse et al. (2015) highlights the elements that compose Akutan's plumbing system. The precise location of seismic events shows that earthquakes beneath Akutan are clustered at depths that range between the near surface and roughly 30 km. Crustal seismic tomography shows a low-velocity zone located at depths of 7.5–10 km below the eastern flank of Akutan's caldera (Syracuse et al., 2015). Interestingly, this low-velocity region seems to indicate the presence of storage zones that are distinct from the detected source of deformation located through geodetic data inversions around 4 km depth (Ji et al., 2017).

Moreover, part of the earthquakes occurring between 2003 and 2009 are low-frequency events (LFEs) at depths ranging from 10 to 27 km. LFEs are often interpreted as reflecting fluid transport in general, for instance episodes of magma transport (Power et al., 2004; Shapiro et al., 2018). They may indicate that a source supplies a part of the shallow plumbing system located around 7–10 km depth, which may in turn feed shallower storage zones. The latter could include, for example, the one detected by Ji et al. (2017) and located around 4 km depth (Syracuse et al., 2015).

Overall, seismic and geodetic observations at Akutan volcano point towards a plumbing system in which a deep reservoir supplies shallower melt bodies (Syracuse et al., 2015; DeGrandpre et al., 2017). This interpretation is also supported by the recent tomographic study of Koulakov et al. (2021), which provides a detailed imaging of Akutan's plumbing system; see their **Figure 8**. Discrete inflation events, such as the ones displayed in **Figure 4** herein, together with LFE occurrences, reflect discrete episodes of increase in the rate of shallow reservoir outflux (DeGrandpre et al., 2017).

5.1.2 Okmok

Different types of observations also indicate that Okmok's plumbing system is composed of several melt storage zones, as briefly reviewed by Walwer et al. (2019). For instance, Larsen et al. (2013) found that the geochemistry and petrology of cones and vents created during the 1997 and 2008 eruptions implies melt sources coming from storage zones at distinct depths. In particular, more mafic material erupted during the 1997 eruption than in 2008, leading Larsen et al. (2013) to propose a deep storage body that feeds shallower reservoirs, inside which the magma evolution may vary from one eruption to the next.

Geodetic data sets also highlight the complexity of Okmok's plumbing system. The spatial deformation pattern observed by GPS shows that both the 2008 source of precursory

inflation—which occurred just before the eruption—and the source of the co-eruptive deflation are shallower and horizontally shifted from the source of the 1997 and 2008 deformation episodes (Freymueller and Kaufman, 2010). Xue et al. (2020) modeled the post-eruptive deformation in 2008 as resulting from the pressurization of a shallow sill fed by a deeper Mogi source. Moreover, InSAR time series from 1997 to 2008 recorded at Okmok reveal two successive episodes of inflation with a decreasing rate: one from 1997 to 2002 and then another one from 2002 to 2008; see Biggs et al. (2010), **Figure 7** and Walwer et al. (2019), **Figure 2**. Walwer et al. (2019) interpreted this deformation sequence as reflecting interactions between two magma bodies.

A schematic plumbing system for Okmok, inferred from a combination of geodetic, geochemical, and petrological data, is depicted in Larsen et al. (2013), their Figure 14). It indicates that several shallow melt bodies are connected to a deeper, mid-crustal magma reservoir that is itself supplied with basaltic magma from greater depths.

5.1.3 Piton de la Fournaise (PdF)

Peltier et al. (2009) reviewed geochemical and petrological data from PdF and showed that several types of lavas erupted during its recent activity. Minerals in some lava bodies crystallized in a shallow storage zone located at roughly 2 km depth (Famin et al., 2009). Melt inclusions in materials from the 2005 eruptions show that the crystallization of olivine occurred at shallow depths of 0–2.5 km (Famin et al., 2009). The maximum estimated depth for the entrapment of melt inclusions is consistent with the estimated depth of the source of deformation determined from geodetic measurements, as well as with the source of most earthquakes located between 200 m and 2.5 km below the surface (Peltier et al., 2009). According to Peltier et al. (2008), the corresponding reservoir is likely to be connected to a shallow network of dykes and sills that regularly get pressurized and produce episodic inflation events, such as the ones displayed in **Figure 4** herein.

The geochemistry of the lava from the 1998 eruption shows that it underwent fractionation, which indicates a deeper origin and is consistent with seismic events in 2005 and 2008 located at depths of around 7.5 km (Battaglia et al., 2005; Boivin and Bachèlery, 2009). Battaglia et al. (2005) describe a seismic swarm migrating from 7.5 km to the surface before the March 1998 eruption.

All together, the observations summarized above show that the PdF plumbing system contains at least two reservoirs. One corresponds to the source of surface inter-eruptive deformation and is located at a depth of about 2 km. It supplies an overlying network of dikes and sills generating the episodic inflation events such as the ones displayed in **Figure 4**, together with eruptive activity. A second reservoir corresponds to a source of deeper seismicity at about 7.5 km depth. A schematic representation of the PdF plumbing system is proposed in Famin et al. (2009), **Figure 8**.

5.2 A Model of Interacting Storage Zones

5.2.1 Basic Geophysical Insights

In **Section 4.1**, we showed that a nonlinear oscillator captures key features of the qualitative dynamics of the three volcanoes studied herein. We then described evidence for connected magma storage bodies—whether magma reservoirs or a reservoir connected to a shallow network of dykes and sills—for all three volcanoes. We now present a more detailed physical model that builds upon these findings and produces relaxations oscillations similar to the observed ones.

Before formally describing the model, let us first provide some basic insights into the mechanisms at play. Our model treats magma transport as driven by pressure variations between two storage bodies, a shallower and a deeper one. This scheme is typical of models often used for magma plumbing systems (Lenglin et al., 2008; Pinel et al., 2010; Reverso et al., 2014). Here, however—depending on the characteristics of the plumbing system being modeled, as described in **Section 5.1**—these two bodies correspond either to lower and upper crustal magma bodies or to two relatively shallow magma bodies, the latter being more appropriate for the PdF plumbing.

In our case, the deeper storage is fed from below at a constant rate, so that the transient inflation events described above are not a result of ad hoc variations in the overall magma flux, contrary to most other approaches. As magma flows from the deeper storage body into the shallower one, it undergoes decompression-induced crystallization that leads to a viscosity increase in the connecting conduit. The resulting larger viscosity lowers the efficiency of the hydraulic connection between the two storage bodies, which eventually cancels out the pressure gradient driving the flow.

As the deeper storage zone keeps being supplied from below at a constant rate, its pressure continues to build up. Under such circumstances, the viscosity-dependent velocity of the magma flow connecting the two storage zones can exhibit a sudden pulse to reduce the pressure gradient and bring the system closer to its equilibrium state of equal pressure between the two storage zones.

When the proper conditions are met, this phenomenon repeats, so that pressure in the top storage zone builds up in a staircase manner, i.e., with transient episodic increases in pressure. This pressure build-up regime is of the relaxation oscillation type, and thus dynamically similar to the one presented in **Section 4.2**, which also explains the occurrence of sharp pressure variations between the storage zones that alternate with more gradual variations. We argue that these transient increases in pressure in the uppermost storage zone are the cause of the episodic inflation events described in **Section 3.2**.

5.2.2 Mathematical Model Formulation

A schematic representation of our model is displayed in **Figure 7** and the associated variables and parameters are summarized in **Table 1**. Formally, a hydraulic connection of length L and radius a links two storage bodies of volumes V_T and V_B, with pressures P_T and P_B. Subscripts B and T refer to bottom and top, respectively. The bottom body is fed with from below with constant magma flux Q.

The magma rises through the conduit between the two storage bodies with an horizontally averaged vertical velocity w. Doing so, the magma viscosity changes. Several mechanisms can lead to this; here we assume that viscosity increases as a result of

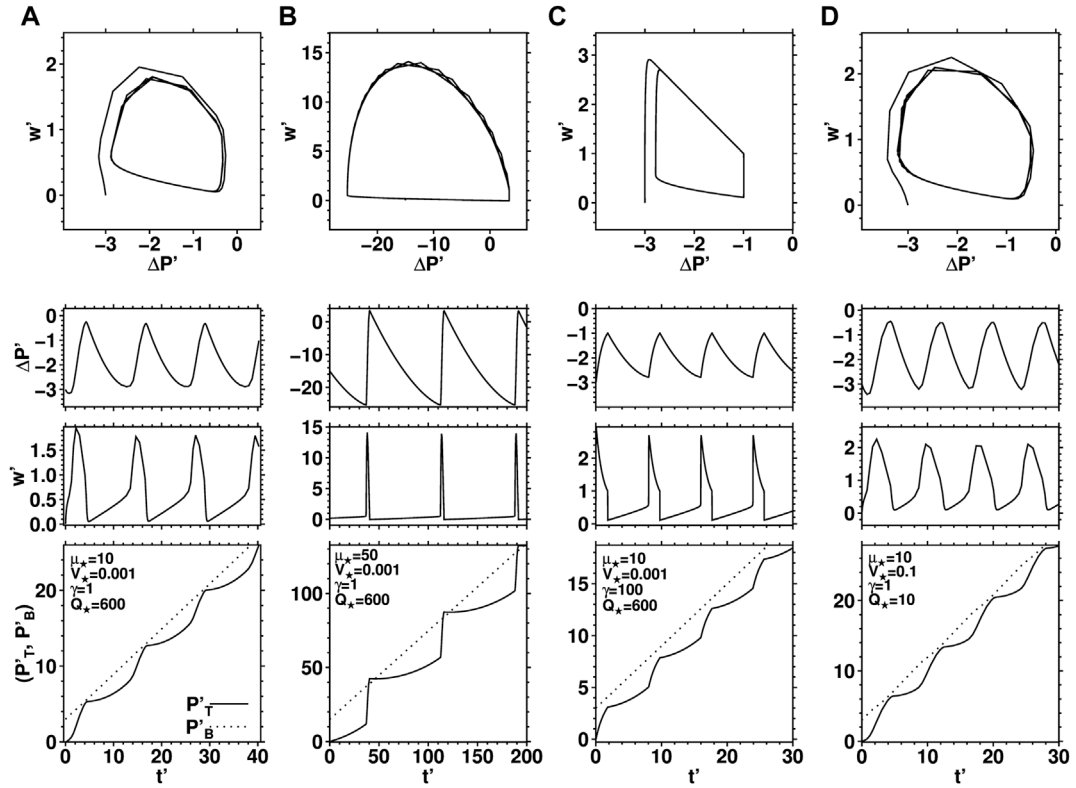

FIGURE 8 | Nonlinear pressure oscillation of the idealized physical model governed by **Eqs 9a**, **9b**. Top panels represent the phase portraits of the simulation in the $(\Delta P', w')$ plane. Subsequent panels represent, from top to bottom: Time series of $\Delta P'(t')$; time series of $w'(t')$; and time series of $P'_B(t')$ (dotted) and $P'_T(t')$ (solid). The model solutions were computed using the following sets of parameters: **(A)** $(\mu_\star, V_\star, \gamma, Q_\star) = (10, 0.001, 1, 600)$; **(B)** $(\mu, V_\star, \gamma, Q_\star) = (50, 0.001, 1, 600)$; **(C)** $(\mu_\star, V_\star, \gamma, Q_\star) = (10, 0.001, 100, 600)$; **(D)** $(\mu_\star, V_\star, \gamma, Q_\star) = (10, 0.1, 1, 10)$. All variables and parameters are expressed in dimensionless form.

decompression-induced crystallization, as described by Blundy and Cashman (2001) for instance. This mechanism is motivated by the observations at Okmok and PdF, where Larsen et al. (2013) and Famin et al. (2009) have described evidence of crystallization and degassing during magma ascent. We follow Barmin et al. (2002) and consider that, along the conduit, the viscosity is given by a step function and switches from the constant value μ_B to the constant value μ_T when the crystal content β per volume reaches the threshold value $\bar{\beta}$ (**Figure 7**).

The model presented here builds upon the insights of Whitehead and Helfrich (1991) and Barmin et al. (2002) on velocity-dependent viscosity in magmas; further details on its derivation are provided by Walwer et al. (2019) and in **Supplementary Appendix SB** of the present paper as well. The resulting system of equations

$$\begin{aligned}
&\frac{\mathrm{d}P_B}{\mathrm{d}t} = Q - w\frac{E\pi a^2}{V_B},\\
&\frac{\mathrm{d}P_T}{\mathrm{d}t} = w\frac{E\pi a^2}{V_T},\\
&\frac{\mathrm{d}w}{\mathrm{d}t} = \begin{cases} -\dfrac{1}{L\rho}\left((P_T - P_B) + \rho g L\right) - \dfrac{8w(\mu_B - \mu_T)\bar{L}}{a^2 L} - \dfrac{8w\mu_B}{a^2} & \text{for} \quad w \le \bar{w}, \quad \text{and}\\ -\dfrac{1}{L\rho}\left((P_T - P_B) + \rho g L\right) - \dfrac{8w\mu_B}{a^2} & \text{for} \quad w > \bar{w} \end{cases}
\end{aligned} \tag{8}$$

governs the joint temporal evolution of the bottom and top pressures, P_B and P_T, as well as of the vertical velocity w. It is derived from the coupling between the horizontally averaged vertical magma momentum equation, elastic deformation induced by volume changes in the magma bodies that have a bulk modulus equals to E, and the chemical kinetics of magma crystallization that relates the rate of decompression, proportional to w, to the viscosity through crystal content β. System (**Eq. 8**) reduces to the linear dynamics of reservoir pressure variations commonly used to model observed volcanic inflation or co-eruptive subsidence with decaying exponential shape when no change in viscosity occurs in the conduit (e.g., Dvorak and Okamura, 1987; Reverso et al., 2014).

The derivation of system (**Eq. 8**) follows the Whitehead and Helfrich (1991) approach and relies on the introduction of the length scale $\bar{L}$ that corresponds to the height above which enough crystallization occurs in order for the viscosity to transition from μ_B to μ_T (**Figure 7**). A key point is that $\bar{L}$ depends on the decompression rate and therefore on the vertical magma velocity w, thus conferring a nonlinear character to system **Eq. 8**. The velocity scale $\bar{w}$ is obtained by posing $L = \bar{L}$ in such a way that, if $w > \bar{w}$, the decompression rate is too high for significant crystallization to occur and the magma exhibits no change in

viscosity; hence the two forms taken by dw/dt in (**Eq. 8**) depend upon the value of w.

The study of system (**Eq. 8**) can be simplified by expressing it in a nondimensional form and by considering the pressure difference $\Delta P = P_T - P_B$ rather than P_T and P_B individually. The model leads to the following dimensionless set of ordinary differential equations, in which all dimensionless variables are denoted by a prime and govern the time evolution of the dimensionless pressure difference $\Delta P' = P'_T - P'_B$ and of the vertical magma velocity w':

$$\frac{\mathrm{d}\Delta P'}{\mathrm{d}t'} = -V_\star Q_\star + (1 + V_\star)w', \tag{9a}$$

$$\frac{\mathrm{d}w'}{\mathrm{d}t'} = \gamma\left(g\left(w'\right)w' - \Delta P'\right), \tag{9b}$$

where

$$g\left(w'\right) = \begin{cases} \left(\mu_\star - 1\right)w' - \mu_\star & \text{for} \quad w' \le 1, \quad \text{and} \\ -1 \quad \text{for} \quad w' > 1. \end{cases} \tag{10}$$

The scales used to transform the system (**Eqs 9a**, **9b**) to the nondimensional version are:

$$w = \bar{w}w', \quad \bar{w} = \frac{(36\pi n_{ch})^{1/3}\bar{\beta}^{2/3}\chi L}{\Delta\beta}, \tag{11a}$$

$$t = \bar{t}t', \quad \bar{t} = \frac{8\rho\mu_B L V_\mathrm{T}}{E\pi a^4}, \tag{11b}$$

$$\Delta P = \bar{p}\Delta P' = \bar{p}\left(P'_T - P'_B\right), \quad \bar{p} = \frac{L\rho 8\mu_\mathrm{T}\bar{w}}{a^2}, \tag{11c}$$

$$Q = \bar{Q}Q_\star, \quad \bar{Q} = \pi\bar{w}a^2. \tag{11d}$$

The velocity scale $\bar{w}$ is the threshold below which crystal content increases significantly, hence resulting in a viscosity change; see Barmin et al. (2002), Walwer et al. (2019) and **Supplementary Appendix SB** herein. The time scale $\bar{t}$ is the characteristic time derived from a linear hydraulic model of pressure balance between two reservoirs (Pinel et al., 2010), while $\bar{p}$ is the viscous pressure scale that arises from the steady-state, horizontally averaged vertical momentum conservation (Jaupart and Tait, 1990; Whitehead and Helfrich, 1991).

5.2.3 Conditions for Pressure Oscillations

The four dimensionless parameters that control the dynamic behavior of the system are:

$$\mu_\star = \frac{\mu_\mathrm{T}}{\mu_\mathrm{B}}, \quad V_\star = \frac{V_\mathrm{T}}{V_\mathrm{B}}, \quad \gamma = \left(8\mu_\mathrm{B}\right)^2\frac{\rho L V_\mathrm{B}}{E\pi a^6}, \quad Q_\star = \frac{Q}{\bar{w}\pi a^2}, \tag{12}$$

where ρ is the magma density, E an elasticity coefficient linking the volume variation with the pressure variation inside the magma reservoirs, and μ_B and μ_T the viscosity in the lower and the upper parts of the conduit, respectively (Whitehead and Helfrich, 1991; Walwer et al., 2019).

Note the similar relationship between variables x and y in the conceptual model (**Eqs 5a**, **5b**), with $\dot{x} \propto y$ and $\dot{y} \propto -x$, and the variables $\Delta P'$ and w' in the physical model governed by **Eqs 9a**, **9b**, with $(\Delta P') \propto w'$ and $\dot{w}' \propto -\Delta P'$. Moreover, the nonlinear function $g\,(w')$ in **Eq. 9b** plays a role analogous to the nonlinear damping $\kappa(y)$ in (**Eq. 5b**). As a result, the physical model (**Eqs 9a**, **9b**) also contains the possibility of oscillatory solutions arising from the stability loss of the equilibrium state. This situation is met when:

$$\mu_\star > 2 \tag{13}$$

and when the magma flux $Q_\star$ satisfies the following two-sided inequality

$$\frac{V_\star + 1}{V_\star} > Q_\star > \frac{1}{2}\frac{(V_\star + 1)\mu_\star}{V_\star\left(\mu_\star - 1\right)} \tag{14}$$

These two inequalities imply that the pressure oscillations can only arise when 1) the magma undergoes a large enough change in viscosity as it flows from the bottom magma body to the top one; and 2) the magma flux feeding the system is also bounded in magnitude according to **Eq. 14**. The inequalities **Eq. 14** constitute one of the key insights provided by our modeling approach and show how the history and the rate at which the magma enters the plumbing system can affect its dynamics. If the magma flux is too low or too high no sustained oscillations of magma pressure within the storage zones are possible. This result is further discussed in the **Section 6.2** in relation to observations at Akutan, Okmok and PdF.

Phase portraits of the physical model in the relaxation oscillation regime are displayed in **Figure 8** for the four sets of the dimensionless parameters defined in **Eq. 12**; each set of parameters corresponds to the panels in one of the figure's columns (a)–(d). The trajectories asymptote in each case to closed orbits, as for the phase portraits derived from the data in **Figure 5** and those of the conceptual model in **Figure 6**.

The sawtooth-shaped oscillations of $\Delta P'(t')$ in **Figure 8** resemble the oscillations of $x(t)$ in **Figure 6**. The $\Delta P'(t')$ oscillations reflect pulses of magma flow velocity increase $w'(t')$ in the connecting pipe that are analogous to the $\dot{x} = y\,(t)$ pulses in **Figure 6**. While $P'_B\,(t')$ increases linearly (dotted lines in the bottom row of panels in **Figure 8**), due to the constant flux $Q_\star$, these $w'(t')$ pulses cause sharp periodic pressure variations of $\Delta P'(t')$ (middle row of panels in **Figure 8**). As a result, $P'_T\,(t') = P'_B\,(t') + \Delta P'\,(t')$ in the top storage zone (solid line in the bottom panels) exhibits the staircase-shaped pattern in the bottom panels of **Figure 8**.

The latter temporal patterns are a simplified, purely periodic version of the more irregular patterns observed at the three volcanoes in **Figure 4**. Both the model and the observations show episodes of fast and short pressure increases, followed by episodes of longer and slower pressure decreases. We also note, in the top row of panels of **Figure 8**, that the amplitude of the oscillations only depends on the system's parameter values and not on the initial state from which they arise. This independence of initial state seems to also characterize the observations in **Figure 4**, as far as the limited data sets allow such inferences to be made.

Finally, the degree of asymmetry, the period, and the amplitude of the pressure oscillations in the physical model are also controlled by the dimensionless parameters $\mu_\star$, γ, $V_\star$ and $Q_\star$). Panels in columns (a)–(d) of **Figure 8** show model

results for a range of parameter values. We observe that the larger the viscosity ratio $\mu_\star$, the longer the period of the oscillation and the larger their amplitude; see **Figures 8B** vs. **Figure 8A**.

Parameter γ mainly controls the asymmetry of the oscillations, with larger values of γ creating sharper variations of pressure; see **Figures 8C** vs. **Figure 8A**. Note that when the ratio $V_\star = V_T/V_B$ varies, the flux $Q_\star$ has to be adjusted to satisfy the two-sided inequality (**Eq. 14**), so that the system generates pulses of pressure increase; see **Figures 8D** vs. **Figure 8A**. The quantitative implications of the physical model in this section, in particular inequalities (**Eq. 14**), are discussed in **Section 6.2** and **Section 6.3**.

6 DISCUSSION

6.1 M-SSA, Parsimonious Modeling, and the Dynamics of Volcanic Systems

In **Section 2**, we used multichannel singular spectrum analysis (M-SSA) of GPS time series to characterize the qualitative dynamics of three volcanic systems: Akutan, Okmok and Piton de la Fournaise (PdF); see **Figures 2–5**. We then showed in **Section 4** that a highly idealized conceptual model governed by **Eqs 5a**, **5b** can explain the common qualitative dynamics of these three volcanic systems; see **Figure 6**.

The basic features of the conceptual model and the similarities between the phase portraits in **Figures 5**, **6** helped us formulate in **Section 5** a still fairly simple physical model of a magmatic system with two storage bodies connected by a conduit in which magma flows with a time-dependent viscosity. Both the conceptual model of **Section 4.2** and the physical model of **Section 5.2** possess only 2 variables, often referred to in the physical sciences as two degrees of freedom.

An important aspect of our statistical time series analysis is that the number of leading modes S retained to construct the volcanic deformation signal displayed in **Figure 4** and the phase portrait in **Figure 5** is quite small, namely $2 \leq S \leq 3$. From the perspective of extracting information about the dynamics of natural systems using M-SSA, the number of modes S retained to reconstruct the signals of interest has been referred to as the statistical dimension of the system (Vautard and Ghil, 1989).

This S corresponds to an upper bound on the number of degrees of freedom required for a parsimonious description of the underlying dynamics within the accuracy of the data. It accounts for the amount of information contained in the observations, which is limited by the noise and the discrete sampling (Broomhead and King, 1986; Vautard and Ghil, 1989). Another important limitation of the information available on volcanic systems is the fact that geophysical observations are often indirect measurements of the systems under study and constitute therewith only indirect constraints on the quantities we are interested in. In the present case, geodetic data sets provide indirect information about pressure evolution inside volcanic plumbing systems.

Vautard and Ghil (1989) showed that the value of S used to reconstruct an observed signal is not unique and depends on the data quality as well as on the key M-SSA parameters: the number of data points N in each time series, the number D of time series or "channels," and the window length M. These authors showed that increasing M or the signal-to-noise ratio tends to increase S. Because of the characteristics of the data sets used here, M and the signal-to-noise ratio are indeed different for each volcano, as described in **Table 1**. Still, a common feature of the three M-SSA analyses is that the volcanic signal reconstructions result in using a very small number of modes S.

Together, the small number S of leading modes needed to describe the deformation signal, and the two degrees of freedom of the conceptual model that capture the key features of the data sets, suggest that the number of variables needed to describe the dynamical state of the volcanic systems studied here during the time interval under consideration and within the accuracy of the data is also quite small (Farmer et al., 1983; Broomhead and King, 1986; Vautard and Ghil, 1989). Two interpretations can be proposed to explain this striking result. First, the observations themselves, i.e., the time-dependent deformation data, only provide limited information on the mechanism leading to the observed signal. Second, although volcanic systems a priori possess a large number of degrees of freedom, the qualitative nature of the oscillatory phenomenon observed herein reflects a form of self-organization that requires only the interaction of a few variables to generate the "skeleton" of the observed dynamics (Guckenheimer and Holmes, 1983; Carr, 2012). In any case, reduced dynamical systems, be they simple conceptual models or more detailed physical models of an idealized plumbing system, provide useful frameworks to model the observations presented here.

The temporal pattern of deformation observed herein at three volcanoes can thus be explained by a parsimonious nonlinear model of magma body interaction with velocity-dependent magma viscosity in the rising magma. The connection between a data-adaptive time series analysis method and a parsimonious physical model provides an interesting guideline for understanding and modeling volcanic episodic inflation events. Whether or not the specific proposed mechanism, i.e., viscosity variation through decompression-induced crystallization, is the most appropriate one remains to be established. But it seems fairly clear that physical models capable of explaining deformation observations should possess a Hopf bifurcation from a fixed point to a limit cycle that gives rise to asymmetric, sawtooth-shaped oscillations.

It is worth mentioning here that models involving other physical mechanisms with qualitatively different viscosity profiles can display similar behavior (e.g., Whitehead and Helfrich, 1991; Walwer et al., 2019). Altogether, these models show that the key ingredient from which of relaxation oscillations of magma pressure arise is the nonlinear coupling between the flow velocity and the flow resistance. This is somewhat analogous to the phenomenon of velocity-weakening of friction that can lead, in similar ways, to the oscillatory behavior of systems with frictional interfaces (e.g., Gu and Wong, 1994; Marone, 1998).

The present work could thus stimulate new research to determine to which extent volcanic inflation cycles may lie—for a given set of parameter values—in a stable oscillatory regime or, to the contrary, be subject to an instability that, in turn,

TABLE 2 | List of main variables and parameters described in the main text and appearing in the proposed physical model of **Section 5.2**.

Description	Symbols	Values
Variables		
Pressure in the top magma chamber	P_T	1–10 MPa
Pressure in the bottom magma chamber	P_B	1–10 MPa
Horizontally averaged vertical velocity	w	0, – ,1 m/s
Difference of overpressures	$\Delta P = P_T - P_B$	1–10 MPa
Volume concentration of crystals	β	0, – ,1
Geometrical parameters		
Conduit length	L	0.1–10 km
Conduit radius	a	1–10 m
Magma properties		
Kinematic viscosity	μ	1–100 Pa s
Density	ρ	2,800, – ,3,000 kg m^{-3}
Critical volume concentration of crystals	$\bar{\beta}$	0.7
Crystal growth rate	χ	$\simeq 10^{-12}$ m/s
Number density of crystals	n	$\simeq 10^{14}$ m^{-3}
Storage zones properties		
Volume of the top storage zone	V_T	10^{-5}–1 km^3
Volume of the bottom storage zone	V_B	10^{-5}–1 km^3
Feeding volumetric flux	Q	$\simeq 10^6$ m^3/year
Effective bulk modulus	E	$\simeq 10^9$Pa
Scales		
Velocity scale—$\bar{w}$	$(36\pi n_{ch})^{1/3}\bar{\beta}^{2/3}\chi L/\Delta\beta$	$\simeq 10^{-4}$ m/s
Time scale	$8\rho\mu_B L V_T/(E\pi a^4)$	—
Pressure scale	$L\rho 8\mu_H \bar{w}/a^2$	—
Volumetrix flux scale	$(\pi\bar{w}a^2)$	—
Important dimensionless parameters		
Constant dimensionless volumetric flux of magma	$Q_\star = Q/(\bar{w}\pi a^2)$	—
Proportional to the vertical acceleration dw/dt	$\gamma = (\frac{8\mu_B}{a^2})^2 \frac{\rho L V_T}{E\pi a^2}$	—
Volume ratio between the two magma chambers	$V_\star = V_B/V_T$	—
Viscosity ratio	$\mu_\star = \mu_T/\mu_B$	—

may lead to eruptive behavior, as observed at PdF and Okmok in 2007 and 2008, respectively (Larsen et al., 2013; Rivet et al., 2014). Being able to distinguish between these two regimes also hints at the possibility of understanding the eruptive potential of such volcanoes by monitoring possible transitions from the oscillatory to the runaway regime.

6.2 Long-Term Inflation Trend and the Flux of Magma Entering the Plumbing System

The long-term inflation trend reflects the temporal pattern of magma supply from depth into the plumbing system modeled here. The model of **Figure 7** implies that the pressure oscillations giving rise to the episodic inflation events are sustained only when the volumetric flux of magma Q feeding the system is bounded by the values expressed in inequality (**Eq. 14**). At Akutan, the linear long-term trend suggests that Q is constant, which may explain why the episodic inflation events are sustained over time and repeat regularly. The same is true for PdF, where inflation events occur frequently from 2004 to 2007; see again **Figure 2**.

A key difference between Akutan and PdF, however, is that the amplitude and time interval between successive events are relatively similar for the former, while for the latter they exhibit more variations, as well as small eruptive events (**Figure 2**). The dynamical regime observed in the GPS time series may be qualified as more chaotic for Pdf in opposition to the seemingly regular occurrences of transient inflation events observed at Akutan.

At Okmok, the episodic inflation events preceding the 2008 eruption occurred at the end of an inflation episode with a decaying rate that started in 2002 (Biggs et al., 2010; Walwer et al., 2019). We infer that the magma flux was too large at the beginning of this inflation episode to produce sustained pressure

oscillations and only dropped into the proper range, given by (**Eq. 14**), afterwards (Walwer et al., 2019).

Quantitative estimates of the volumetric flux of magma supply into the plumbing system for all three volcanoes are on the order of $Q \sim 10^6$ m^3/year (Peltier et al., 2008; Fournier et al., 2009; Xue and Freymueller, 2020). At Okmok, this value corresponds to the estimated volumetric flux before the occurrence of the inflation events studied here (Fournier et al., 2009, Figure 12). A corresponding value for the dimensionless flux that intervenes in the model governed by **Eqs 9a**, **9b** is $Q_\star \simeq 500$ (**Table 2**). From inequality **Eq. 14**, this implies that the volume ratio $V_\star$ is on the order of 10^{-3} for the three volcanoes. At Akutan, estimated values for the volume of the storage bodies are in the range $10^{-5} - 1$ km^3 (DeGrandpre et al., 2017, Tables 4 and 6). At PdF, the shallow structure causes the deformation to arise from a network of dykes and sills that most likely have significantly smaller volume than the deeper reservoir connected to it. Hence, $V_\star \simeq 0.001$, i.e., the bottom storage zone V_B, quite plausibly, has a volume that is roughly 1,000 times larger than the uppermost body's volume V_T.

6.3 Temporal and Spatial Patterns of the Volcanic Deformation

A substantial difference between the volcanoes studied here consists in their characteristic time scales and deformation wavelengths (**Table 1**). Akutan and Okmok deformed over a distance of roughly 10 km with a delay between two inflation events of around 2 and 3 years, respectively. The events at PdF have noticeably smaller spatial wavelengths, of about 2 km, and the delay between successive events is of a few days (**Table 1**). The spatial deformation pattern at PdF also shows azimuthal asymmetries during inflation events (**Figure 4**), probably caused by the pressurization of small shallow structures such as dykes and sills, as described above, that are connected to the surface and produce co-occurring eruptive activity (Peltier et al., 2008; Famin et al., 2009).

Deformation cycles of shorter duration thus correlate with smaller deformation wavelength, an observation consistent with model (**Eqs 9a**, **9b**) presented in **Section 5.2**. The spatial deformation wavelength is a function of both size and depth of the structures producing the observed GPS displacements. The time scale used to render **Eqs 9a**, **9b** dimensionless is proportional to the volume V_T of the shallow storage body (**Table 2**). All else being equal, the smaller the volume V_T, the smaller the time scale and the shorter the duration of the episodic inflation events. Overall, the simple and parsimonious model governed by **Eqs 9a**, **9b** can account for the spectrum of observed time scales and deformation scales at Akutan, Okmok, and PdF.

7 CONCLUSION

Our paper strongly suggests that mechanisms resulting from 1) the presence of two or more magma bodies and 2) the mere dependence of the magma's flow resistance on temperature or crystallisation in the conduit between these bodies can explain key features of the observed recurrent inflation episodes in rather diverse volcanoes. The presence of these two key ingredients in many active volcanic systems suggests that our model may apply fairly broadly, beyond the three examples used here.

A more complete explanation of the currently available information in the geodetic and geochemical evidence will require, of course, more detailed modeling and, possibly, additional observations. At this stage, though, it does not appear that external forcing by time-dependent magma inflow is essential for the explanation of the most salient aspects of the alternation of rapid inflation with longer episodes of relatively low level of deformation.

The phenomenological approach presented herein starts with the statistical analysis of geodetic time series and ends with the construction of a relatively simple physical model of volcanic plumbing systems. The connection between the observational data and the physical model is provided by the study of a simple nonlinear oscillator's capturing key features of the observations.

This approach can be applied to help understand a wide range of observed temporal patterns of deformation. It is, therefore, not restricted to the type of behavior studied herein. The two relatively simple models presented, conceptual (**Section 4.2**) and physical (**Section 5.2**), can be seen as a contribution to a hierarchy of models with increasing complexity—from the very simplest conceptual models to high-resolution, three-dimensional ones—that share important features and thus can provide more and more details on the phenomena under study. A model hierarchy of this kind is fairly common in other areas of the geosciences, such as the climate sciences (Schneider and Dickinson, 1974; Ghil et al., 2001; Held, 2005; Ghil, 2019).

DATA AVAILABILITY STATEMENT

Publicly available datasets were analyzed in this study. This data can be found here: www.earthscope.org geodesy.unr.edu.

AUTHOR CONTRIBUTIONS

DW, MG, and EC designed the study. DW conducted the data analysis and the model studies. All authors discussed the results and implications and commented on the manuscript at all stages.

FUNDING

This research was supported by a doctoral grant from PSL Research University (DW), and by research Grant No. 9AD01274 from the INSU/CNRS program Programme National de Télédétection Spatiale (PNTS) (EC). The present paper is TiPES contribution #128; this project has received funding from the European Union's Horizon 2020 research and innovation programme under Grant Agreement No. 820970.

ACKNOWLEDGMENTS

We are grateful to Claude Jaupart for insightful discussions. It is a pleasure to thank Andreas Groth for sharing his M-SSA codes and for helping us with certain aspects of practically implementing the M-SSA methodology. DW thanks Pascal Richet for his thoughtful comments and corrections on the first version of the manuscript. It is a pleasure to acknowledge two reviewers as well as Valerio Acocella for constructive and insightful comments and suggestions on the paper's originally submitted manuscript. EC acknowledges support from the Institut Universitaire de France. This work uses data products provided by the Plate Boundary Observatory operated by UNAVCO for EarthScope (www.earthscope.org) and by the Nevada Geodetic Laboratory (geodesy.unr.edu).

SUPPLEMENTARY MATERIAL

The Supplementary Material for this article can be found online at: https://www.frontiersin.org/articles/10.3389/feart.2022.759475/full#supplementary-material

REFERENCES

Alessio, S. M. (2016). "Singular Spectrum Analysis (SSA)," in *Singular Spectrum Analysiss (SSA)* (Berlin, Germany: Springer), 537–571. Ch. 12. doi:10.1007/978-3-319-25468-5_12

Barenblatt, G. I. (2003). *Scaling, Vol. 34*. Cambridge: Cambridge University Press.

Barmin, A., Melnik, O., and Sparks, R. S. J. (2002). Periodic Behavior in Lava Dome Eruptions. *Earth Planet. Sci. Lett.* 199, 173–184. doi:10.1016/s0012-821x(02)00557-5

Battaglia, J., Ferrazzini, V., Staudacher, T., Aki, K., and Cheminée, J.-L. (2005). Pre-eruptive migration of earthquakes at the Piton de la Fournaise volcano (Réunion Island). *Geophys. J. Int.* 161, 549–558. doi:10.1111/j.1365-246x.2005.02606.x

Biggs, J., Anthony, E. Y., and Ebinger, C. J. (2009). Multiple Inflation and Deflation Events at Kenyan Volcanoes, East African Rift. *Geology* 37, 979–982. doi:10.1130/g30133a.1

Biggs, J., Lu, Z., Fournier, T., and Freymueller, J. T. (2010). Magma Flux at Okmok Volcano, Alaska, from a Joint Inversion of Continuous GPS, Campaign GPS, and Interferometric Synthetic Aperture Radar. *J. Geophys. Res.* 115. doi:10.1029/2010JB007577

Biggs, J., and Pritchard, M. E. (2017). Global Volcano Monitoring: what Does it Mean when Volcanoes Deform? *Elements* 13, 17–22. doi:10.2113/gselements.13.1.17

Blewitt, G., Hammond, W. C., and Kreemer, C. (2018). Harnessing the Gps Data Explosion for Interdisciplinary Science. *Eos* 99. doi:10.1029/2018eo104623

Blundy, J., and Cashman, K. (2001). Ascent-driven Crystallisation of Dacite Magmas at Mount St Helens, 1980-1986. *Contrib. Mineral. Pet.* 140, 631–650. doi:10.1007/s004100000219

Boivin, P., and Bachèlery, P. (2009). Petrology of 1977 to 1998 eruptions of Piton de la Fournaise, La Réunion Island. *J. Volcanol. Geotherm. Res.* 184, 109–125. doi:10.1016/j.jvolgeores.2009.01.012

Broomhead, D. S., and King, G. P. (1986). Extracting Qualitative Dynamics from Experimental Data. *Phys. D. Nonlinear Phenom.* 20, 217–236. doi:10.1016/0167-2789(86)90031-X

Caricchi, L., Biggs, J., Annen, C., and Ebmeier, S. (2014). The Influence of Cooling, Crystallisation and Re-melting on the Interpretation of Geodetic Signals in Volcanic Systems. *Earth Planet. Sci. Lett.* 388, 166–174. doi:10.1016/j.epsl.2013.12.002

Carr, J. (2012). *Applications of Centre Manifold Theory, Vol. 35*. Berlin, Germany: Springer Science & Business Media.

DeGrandpre, K., Wang, T., Lu, Z., and Freymueller, J. T. (2017). Episodic Inflation and Complex Surface Deformation of Akutan Volcano, alaska Revealed from Gps Time-Series. *J. Volcanol. Geotherm. Res.* 347, 337–359. doi:10.1016/j.jvolgeores.2017.10.003

Degruyter, W., and Huber, C. (2014). A Model for Eruption Frequency of Upper Crustal Silicic Magma Chambers. *Earth Planet. Sci. Lett.* 403, 117–130.

Deremble, B., D'Andrea, F., and Ghil, M. (2009). Fixed Points, Stable Manifolds, Weather Regimes, and Their Predictability. *Chaos* 19, 043109. doi:10.1063/1.3230497

Dvorak, J. J., and Okamura, A. T. (1987). A Hydraulic Model to Explain Variations in Summit Tilt Rate at Kilauea and Mauna Loa Volcanoes. *U. S. Geol. Surv. Prof. Pap.* 1350, 1281–1296.

Famin, V., Welsch, B., Okumura, S., Bachelery, P., and Nakashima, S. (2009). Three differentiation stages of a single magma at piton de la fournaise volcano (reunion hot spot). *Geochem. Geophys. Geosystems* 10. doi:10.1029/2008gc002015

Farmer, J. D., Ott, E., and Yorke, J. A. (1983). The Dimension of Chaotic Attractors. *Phys. D. Nonlinear Phenom.* 7, 153–180. doi:10.1016/0167-2789(83)90125-2

Feng, L., and Newman, A. V. (2009). Constraints on Continued Episodic Inflation at Long Valley Caldera, Based on Seismic and Geodetic Observations. *J. Geophys. Res.* 114, 6240. doi:10.1029/2008JB006240

Fournier, T., Freymueller, J., and Cervelli, P. (2009). Tracking Magma Volume Recovery at Okmok Volcano Using GPS and an Unscented Kalman Filter. *J. Geophys. Res.* 114, 5837. doi:10.1029/2008JB005837

Freymueller, J. T., and Kaufman, A. M. (2010). Changes in the Magma System during the 2008 Eruption of Okmok Volcano, Alaska, Based on GPS Measurements. *J. Geophys. Res.* 115, 7716. doi:10.1029/2010JB007716

Ghil, M. (2019). A Century of Nonlinearity in the Geosciences. *Earth Space Sci.* 6, 1007–1042. doi:10.1029/2019ea000599

Ghil, M., Allen, M. R., Dettinger, M. D., Ide, K., Kondrashov, D., Mann, M. E., et al. (2002). Advanced Spectral Methods for Climatic Time Series. *Rev. Geophys.* 40, 3–1. doi:10.1029/2000rg000092

Ghil, M., and Childress, S. (1987). *Topics in Geophysical Fluid Dynamics: Atmospheric Dynamics, Dynamo Theory, and Climate Dynamics, Vol. 60 of Applied Mathematical Sciences*. Berlin, Germany: Springer Science & Business Media, reissued as eBook 2012.

Ghil, M., Ma, T., and Wang, S. (2001). Structural Bifurcation of 2-d Incompressible Flows. *Indiana Univ. Math. J.* 50, 159–180. doi:10.1512/iumj.2001.50.2183

Grasman, J. (2011). "Relaxation Oscillations," in *Mathematics of Complexity and Dynamical Systems*. Editor R. A. Meyers (Berlin, Germany: Springer Science & Business Media), 1475–1488.

Groth, A., and Ghil, M. (2015). Monte Carlo Singular Spectrum Analysis (SSA) Revisited: Detecting Oscillator Clusters in Multivariate Datasets. *J. Clim.* 28, 7873–7893. doi:10.1175/jcli-d-15-0100.1

Gu, Y., and Wong, T.-f. (1994). "Nonlinear Dynamics of the Transition from Stable Sliding to Cyclic-Stick-Slip in Rock," in *Nonlinear Dynamics and Predictability of Geophysical Phenomena, Geophysical Monograph. Vol. 83, American Geophysical Union* (Hoboken, NJ, USA: Wiley Online Library), Vol. 83, 15.

Gualandi, A., Avouac, J. P., Michel, S., and Faranda, D. (2020). The Predictable Chaos of Slow Earthquakes. *Sci. Adv.* 6, eaaz5548. doi:10.1126/sciadv.aaz5548

Guckenheimer, J., and Holmes, P. J. (1983). *Nonlinear Oscillations, Dynamical Systems, and Bifurcations of Vector Fields, Vol. 42 of Applied Mathematical Sciences*. Berlin, Germany: Springer Science & Business Media.

Held, I. M. (2005). The Gap between Simulation and Understanding in Climate Modeling. *Bull. Amer. Meteor. Soc.* 86, 1609–1614. doi:10.1175/bams-86-11-1609

Huppert, H. E., and Woods, A. W. (2002). The Role of Volatiles in Magma Chamber Dynamics. *Nature* 420, 493–495. doi:10.1038/nature01211

Hutchison, W., Biggs, J., Mather, T. A., Pyle, D. M., Lewi, E., Yirgu, G., et al. (2016). Causes of Unrest at Silicic Calderas in the East African Rift: New Constraints from InSAR and Soil-Gas Chemistry at Aluto Volcano, Ethiopia. *Geochem. Geophys. Geosyst.* 17, 3008–3030. doi:10.1002/2016GC006395

Jaupart, C., and Tait, S. (1990). Chapter 8. Dynamics of Eruptive Phenomena. *Rev. Mineralogy Geochem.* 24, 213–238. doi:10.1515/9781501508769-012

Ji, K. H., and Herring, T. A. (2011). Transient Signal Detection Using GPS Measurements: Transient Inflation at Akutan Volcano, Alaska, during Early 2008. *Geophys. Res. Lett.* 38, a–n. doi:10.1029/2011GL046904

Ji, K. H., Yun, S.-H., and Rim, H. (2017). Episodic Inflation Events at Akutan Volcano, alaska, during 2005-2017. *Geophys. Res. Lett.* 44, 8268. doi:10.1002/2017gl074626

Jordan, D. W., and Smith, P. (2007). *Nonlinear Ordinary Differential Equations – an Introduction for Scientists and Engineers*. Oxford; New York: Oxford University Press.

Koulakov, I., Komzeleva, V., Smirnov, S. Z., and Bortnikova, S. B. (2021). Magma-fluid Interactions beneath Akutan Volcano in the Aleutian Arc Based on the Results of Local Earthquake Tomography. *J. Geophys. Res. Solid Earth* 126, e2020JB021192. doi:10.1029/2020jb021192

Larsen, J. F., Śliwiński, M. G., Nye, C., Cameron, C., and Schaefer, J. R. (2013). The 2008 Eruption of Okmok Volcano, Alaska: Petrological and Geochemical Constraints on the Subsurface Magma Plumbing System. *J. Volcanol. Geotherm. Res.* 264, 85–106. doi:10.1016/j.jvolgeores.2013.07.003

Lengliné, O., Marsan, D., Got, J.-L., Pinel, V., Ferrazzini, V., and Okubo, P. G. (2008). Seismicity and Deformation Induced by Magma Accumulation at Three Basaltic Volcanoes. *J. Geophys. Res.* 113, 5937. doi:10.1029/2008JB005937

Lu, Z., Dzurisin, D., Biggs, J., Wicks, C., and McNutt, S. (2010). Ground Surface Deformation Patterns, Magma Supply, and Magma Storage at Okmok Volcano, Alaska, from InSAR Analysis: 1. Intereruption Deformation, 1997–2008. *J. Geophys. Res. Solid Earth* 115.

Mañé, R. (1981). "On the Dimension of the Compact Invariant Sets of Certain Non-linear Maps," in *Dynamical Systems and Turbulence, Warwick 1980* (Berlin, Germany: Springer), 230–242.

Marone, C. (1998). Laboratory-derived Friction Laws and Their Application to Seismic Faulting. *Annu. Rev. Earth Planet. Sci.* 26, 643–696. doi:10.1146/annurev.earth.26.1.643

Mériaux, C., and Jaupart, C. (1995). Simple Fluid Dynamic Models of Volcanic Rift Zones. *Earth Planet. Sci. Lett.* 136, 223–240.

Newman, A. V., Dixon, T. H., and Gourmelen, N. (2006). A Four-Dimensional Viscoelastic Deformation Model for Long Valley Caldera, California, between 1995 and 2000. *J. Volcanol. Geotherm. Res.* 150, 244–269. doi:10.1016/j.jvolgeores.2005.07.017

Packard, N. H., Crutchfield, J. P., Farmer, J. D., and Shaw, R. S. (1980). Geometry from a Time Series. *Phys. Rev. Lett.* 45, 712–716. doi:10.1103/PhysRevLett.45.712

Parks, M. M., Biggs, J., England, P., Mather, T. A., Nomikou, P., Palamartchouk, K., et al. (2012). Evolution of Santorini Volcano Dominated by Episodic and Rapid Fluxes of Melt from Depth. *Nat. Geosci.* 5, 749–754. doi:10.1038/ngeo1562

Peltier, A., Bachèlery, P., and Staudacher, T. (2009). Magma transport and storage at piton de la fournaise (la réunion) between 1972 and 2007: A review of geophysical and geochemical data. *J. Volcanol. Geotherm. Res.* 184, 93–108.

Peltier, A., Famin, V., Bachèlery, P., Cayol, V., Fukushima, Y., and Staudacher, T. (2008). Cyclic magma storages and transfers at Piton de La Fournaise volcano (La Réunion hotspot) inferred from deformation and geochemical data. *Earth Planet. Sci. Lett.* 270, 180–188. doi:10.1016/j.epsl.2008.02.042

Pinel, V., Jaupart, C., and Albino, F. (2010). On the Relationship between Cycles of Eruptive Activity and Growth of a Volcanic Edifice. *J. Volcanol. Geotherm. Res.* 194, 150–164. doi:10.1016/j.jvolgeores.2010.05.006

Poland, M. P., Peltier, A., Bonforte, A., and Puglisi, G. (2017). The spectrum of persistent volcanic flank instability: A review and proposed framework based on Kilauea, Piton de la Fournaise, and Etna. *J. Volcanol. Geotherm. Res.* 339, 63–80. doi:10.1016/j.jvolgeores.2017.05.004

Power, J., Stihler, S., White, R., and Moran, S. (2004). Observations of Deep Long-Period (DLP) Seismic Events beneath Aleutian Arc Volcanoes; 1989–2002. *J. Volcanol. Geotherm. Res.* 138, 243–266. doi:10.1016/j.jvolgeores.2004.07.005

Reverso, T., Vandemeulebrouck, J., Jouanne, F., Pinel, V., Villemin, T., Sturkell, E., et al. (2014). A Two-Magma Chamber Model as a Source of Deformation at Grímsvötn Volcano, Iceland. *J. Geophys. Res. Solid Earth* 119, 4666–4683. doi:10.1002/2013jb010569

Rivet, D., Brenguier, F., Clarke, D., Shapiro, N. M., and Peltier, A. (2014). Long-term dynamics of Piton de la Fournaise volcano from 13 years of seismic velocity change measurements and GPS observations. *J. Geophys. Res. Solid Earth* 119, 7654–7666. doi:10.1002/2014JB011307

Roux, J. C., Rossi, A., Bachelart, S., and Vidal, C. (1980). Representation of a Strange Attractor from an Experimental Study of Chemical Turbulence. *Phys. Lett. A* 77, 391–393. doi:10.1016/0375-9601(80)90519-8

Schneider, S. H., and Dickinson, R. E. (1974). Climate Modeling. *Rev. Geophys.* 12, 447–493. doi:10.1029/rg012i003p00447

Shapiro, N. M., Campillo, M., Kaminski, E., Vilotte, J.-P., and Jaupart, C. (2018). Low-frequency Earthquakes and Pore Pressure Transients in Subduction Zones. *Geophys. Res. Lett.* 45, 11–083. doi:10.1029/2018gl079893

Syracuse, E. M., Maceira, M., Zhang, H., and Thurber, C. (2015). Seismicity and Structure of Akutan and Makushin Volcanoes, alaska, Using Joint Body and Surface Wave Tomography. *J. Geophys. Res. Solid Earth* 120, 1036–1052.

Tait, S., Jaupart, C., and Vergniolle, S. (1989). Pressure, Gas Content and Eruption Periodicity of a Shallow, Crystallising Magma Chamber. *Earth Planet. Sci. Lett.* 92, 107–123. doi:10.1016/0012-821x(89)90025-3

Takens, F. (1981). "Detecting Strange Attractors in Turbulence," in *Dynamical Systems and Turbulence, Warwick 1980* (Berlin, Germany: Springer), 366–381. doi:10.1007/bfb0091924

Tridon, M., Cayol, V., Froger, J. L., Augier, A., and Bachèlery, P. (2016). Inversion of coeval shear and normal stress of piton de la fournaise flank displacement. *J. Geophys. Res. Solid Earth* 121, 7846–7866. doi:10.1002/2016jb013330

Van der Pol, B. (1926). LXXXVIII. On "Relaxation-Oscillations". *Lond. Edinb. Dublin Philosophical Mag. J. Sci.* 2, 978–992. doi:10.1080/14786442608564127

Vautard, R., and Ghil, M. (1989). Singular Spectrum Analysis in Nonlinear Dynamics, with Applications to Paleoclimatic Time Series. *Phys. D. Nonlinear Phenom.* 35, 395–424. doi:10.1016/0167-2789(89)90077-8

Walwer, D., Calais, E., and Ghil, M. (2016). Data-adaptive Detection of Transient Deformation in Geodetic Networks. *J. Geophys. Res. Solid Earth* 121, 2129–2152. doi:10.1002/2015JB012424

Walwer, D., Ghil, M., and Calais, E. (2019). Oscillatory Nature of the Okmok Volcano's Deformation. *Earth Planet. Sci. Lett.* 506, 76–86. doi:10.1016/j.epsl.2018.10.033

Whitehead, J. A., and Helfrich, K. R. (1991). Instability of Flow with Temperature-dependent Viscosity: A Model of Magma Dynamics. *J. Geophys. Res.* 96, 4145–4155. doi:10.1029/90jb02342

Xue, X., Freymueller, J., and Lu, Z. (2020). Modeling the Posteruptive Deformation at Okmok Based on the Gps and Insar Time Series: Changes in the Shallow Magma Storage System. *J. Geophys. Res. Solid Earth* 125, e2019JB017801. doi:10.1029/2019jb017801

Xue, X., and Freymueller, J. T. (2020). A 25-year History of Volcano Magma Supply in the East Central Aleutian Arc, alaska. *Geophys. Res. Lett.* 47, e2020GL088388. doi:10.1029/2020gl088388

Conflict of Interest: The authors declare that the research was conducted in the absence of any commercial or financial relationships that could be construed as a potential conflict of interest.

Publisher's Note: All claims expressed in this article are solely those of the authors and do not necessarily represent those of their affiliated organizations, or those of the publisher, the editors and the reviewers. Any product that may be evaluated in this article, or claim that may be made by its manufacturer, is not guaranteed or endorsed by the publisher.

frontiers | Frontiers in Earth Science

PERSPECTIVE
published: 08 June 2022
doi: 10.3389/feart.2022.845511

On the Link Between Global Volcanic Activity and Global Mean Sea Level

Stéphanie Dumont[1]*, *Simona Petrosino*[2] *and Maria C. Neves*[3]

[1]Instituto Dom Luiz (IDL), Universidade da Beira Interior, Covilhã, Portugal, [2]Istituto Nazionale di Geofisica e Vulcanologia, Sezione di Napoli—Osservatorio Vesuviano, Napoli, Italy, [3]Instituto Dom Luiz (IDL), Universidade do Algarve, Faro, Portugal

Studying a large number of volcanic eruptions is a way to decipher general characteristics related to volcano dynamics but also on external forcing influencing it, such as solid Earth and ocean tides. Many studies have tackled this tidal influence on the onset of volcanic eruptions and more generally, on volcanic activity. However, the interplay between this quasi-permanent forcing and volcanic systems is still poorly understood. With the present study, we propose to consider a global viewpoint to address this interaction. We analyzed the number of monthly volcanic eruptions and the global mean sea level between 1880 and 2009 using the Singular Spectrum Analysis time-series analysis technique to evaluate the existence of common periodicities. We found multi-decadal components of similar periodicities present in both time-series which we link to those already recognized in the polar motion. Its multi-decadal variations result in a mass reorganization in the oceans whose associated stress changes may impact processes generating volcanic eruptions worldwide. Our results show the influence of global processes on volcanic activity and open many questions to further investigate these multi-scale interactions.

Keywords: external forcing, volcanic activity, global mean sea level, solid Earth and ocean tides, eruption triggering, interaction external/internal processes, singular spectrum analysis, polar motion

OPEN ACCESS

Edited by:
Agust Gudmundsson,
University of London, United Kingdom

Reviewed by:
Vladimir G. Kossobokov,
Institute of Earthquake Prediction Theory and Mathematical Geophysics (RAS), Russia

***Correspondence:**
Stéphanie Dumont
sdumont@segal.ubi.pt

Specialty section:
This article was submitted to Volcanology, a section of the journal Frontiers in Earth Science

Received: *29 December 2021*
Accepted: *13 April 2022*
Published: *08 June 2022*

Citation:
Dumont S, Petrosino S and Neves MC (2022) On the Link Between Global Volcanic Activity and Global Mean Sea Level. Front. Earth Sci. 10:845511. doi: 10.3389/feart.2022.845511

INTRODUCTION

The triggering of volcanic eruptions represents the ultimate stage of a series of non-linear physico-chemical processes. Although the conditions that make a volcano ready to enter in eruption are still elusive, deciphering those that participate in the destabilization of metastable systems could provide new insights on the processes leading to eruption triggering. Knowledge of how volcanic systems work has been mainly gained from studies on individual volcanoes first based on specific methodologies and more and more on multi-method approaches (e.g., McNutt, 1996; Newhall and Punongbayan, 1996; Battaglia et al., 2006; Dzurisin, 2006; Sigmundsson et al., 2015; Gudmundsson et al., 2016). Despite of the high variability of volcanoes illustrated in particular by their eruptive activity, internal structure, or chemical composition, common processes drive volcanic activity (Cashman and Biggs, 2014). Studies on a large number of volcanoes have allowed to provide more constraints on global processes controlling their dynamics and evolution as for instance, the magnitude-frequency relationship of large explosive eruptions (e.g., Deligne et al., 2010), the link between deformation and eruption (e.g., Biggs et al., 2014), as well as the role of external forcing on the eruption triggering such as tectonic earthquakes (Seropian et al., 2021), the sea level and climate variations (e.g., Laskar et al., 2004; Mason et al., 2004; Kutterolf et al., 2013; Satow et al., 2021) and Earth tides (Mauk and Jonhston, 1973).

Actually, the variations of the sea level, climate and Earth tides are all related, taking part of a global dynamics as pieces of a giant puzzle. The Liouville-Euler equations link the redistribution of

mass at Earth's surface, and in particular that of the fluid envelopes to the movement of the Earth's rotation axis through a system of linear equations and excitation functions (Lambeck, 2005; Lopes et al., 2021). These movements take place at different time scales ranging from a few days to at least 18.6 years, as revealed by the study of the length-of-day variations, a global parameter whose fluctuations on short-term capture the mass redistribution on Earth through their impact on Earth's rotation velocity (Le Mouël et al., 2019). The revolution of the Earth around the Sun and the variations of the Earth's rotation axis that are associated with seasons and Milankovitch cycles modulate this force and mass movements and interfere with those induced by plate tectonics, ocean and atmospheric currents (e.g., Lambeck, 2005; Le Mouël et al., 2021a,b; Zaccagnino et al., 2020).

The idea of tidal influence on volcanic activity has persisted over the last century (e.g., Jaggar et al., 1924; McNutt and Beavan, 1987; Emter 1997; Sottili et al., 2021). Statistical approaches have shown that the onset of volcanic eruptions at global scale (e.g., Mauk and Johnston, 1973) as well as at local scale (e.g., Johnston and Mauk, 1972; Filson et al., 1973; Golombek and Carr, 1978; Dzurizin, 1980; Martin and Rose, 1981) could be related to the Moon and in particular, its alignment with the Earth and the Sun, known as the fortnightly cycle. Similar observations of preferred periods for eruption onsets have been made with ocean tides for submarine, coastal and insular volcanic systems (e.g., McNutt and Beavan, 1987; McNutt, 1999; Mason et al., 2004; Tolstoy, 2015). In coastal environment, the tidal deformation coupled with the ocean loading, which corresponds to the movement of surface water mass, induce variations in the compressional stresses that can promote squeezing out magma (e.g., McNutt and Beavan, 1987; McNutt, 1999). At time scales of hundreds of thousands years, pronounced sea level variations related to ice melting and more generally long-period climatic and astronomical variations have also been associated with pulses of volcanic activity, e.g., Mason et al. (2004); Andrew and Gudmundsson (2007); Pagli and Sigmundsson (2008); Kutterolf et al. (2013); Watt et al. (2013); Satow et al. (2021); Sottili et al. (2021).

The influence of solid Earth and ocean tides has also been suggested on shorter time scales through periodic behavior detected in various physical parameters measured at volcanoes, e.g., seismic tremor, earthquake rate, gas fluxes. Actually, tidal constituents have been identified at volcanoes independently of their phases of activity including quiescence, unrest and eruptions (e.g., Jaggar et al., 1924; McNutt and Beavan, 1981, 1984; Shimozuru, 1987; Leandro and Alvarado 1988; Rydelek et al., 1988; Caltabanio et al., 1994; Kasahara et al., 2001; Custódio et al., 2003; López et al., 2006; Roult et al., 2012; Sottili and Palladino, 2012; Yakiwara et al., 2013; Bredemeyer and Hesteen, 2014; Conde et al., 2014; Contadakis et al., 2017; Dinger et al., 2018; Girona et al., 2018; Patrick et al., 2019; Dumont et al., 2020, 2021; İçhedef et al., 2020; Miguelsanz et al., 2021). Most of these parameters express the transfer of fluids, either melt or/and hydrothermal fluids, from deeper layers towards and at the Earth's surface. At the quiescent and hydrothermally active caldera of Campi Flegrei (Italy), studies have demonstrated that tidal modulation can take place according to a complex coupling mechanism that affects both crustal structure and hydrothermal fluids (e.g., Bottiglieri et al., 2010; De Lauro et al., 2012, 2013, 2018; Petrosino et al., 2018, 2020; Ricco et al., 2019; Caputo et al., 2020; Cusano et al., 2021; Petrosino and Dumont, 2022). At erupting volcanoes, increase in explosions or seismic activity as well as second-order variations of geophysical time-series were also attributed to tides (e.g., Mauk and Kienle, 1973; Golombek and Carr, 1978; Martin and Rose, 1981; Jentzsch et al., 2001; Williams-Jones et al., 2001; Dumont et al., 2020, 2021).

Despite all these observations, not all volcanoes show a sensitivity to solid Earth and ocean tides, and the cause-effect relationship is still elusive (e.g., Sparks, 1981; Neuberg, 2000). Actually, past studies have mainly focused either on short or very-long time scales, from hours to a few years on one hand, or over several kyr on the other hand. However, the interaction between tidally-generated movements and volcanic systems is expected to occur on all time scales on which this external forcing acts. Therefore, should we not expect a possible response of volcanoes at all these time-scales?

We address these questions by exploring the link between ocean tides and volcanoes from a global viewpoint over a ~130 years time interval. Oceans as all fluid and solid envelopes on Earth respond to external forcing induced by lunisolar tidal potential. They participate in a significant redistribution of mass through ocean loading, and therefore stresses at Earth's surface over different time scales. Considering that most volcanoes lie near, within or beneath the oceans (**Figure 1**), we can raise the question of whether the tidally-induced ocean movements and therefore stresses can participate in changing the dynamical systems and so the destabilization of volcanoes on decadal timescales. This is what we tackle with this paper, by analyzing the common periodicities which may exist in the number of worldwide volcanic eruptions and the global mean sea level using the Singular Spectrum Analysis (SSA) technique.

INVESTIGATING THE LINK BETWEEN THE GLOBAL MEAN SEA LEVEL AND WORLDWIDE VOLCANIC ACTIVITY

Data and Method

We considered volcanic eruptions worldwide reported by the Smithsonian Institution through the Global Volcanism Program (2013) spanning a 129-year period from 1 January 1880 to 31 December 2009. This data series counts 3,781 confirmed eruptions with known Volcanic Explosivity Index (VEI, Newhall and Self, 1982), associated to 514 volcanic systems (**Figure 1C**). We built a number of volcanic eruptions (NVE) using a median filter with a 12-months sliding window applied to the number of monthly eruptive events (**Figure 1A**). We performed a similar analysis for eruptions with VEI≥2 to test the stability of our results with respect to the catalog completeness. We also classified these volcanic systems according to their environment, i.e. continental, insular or

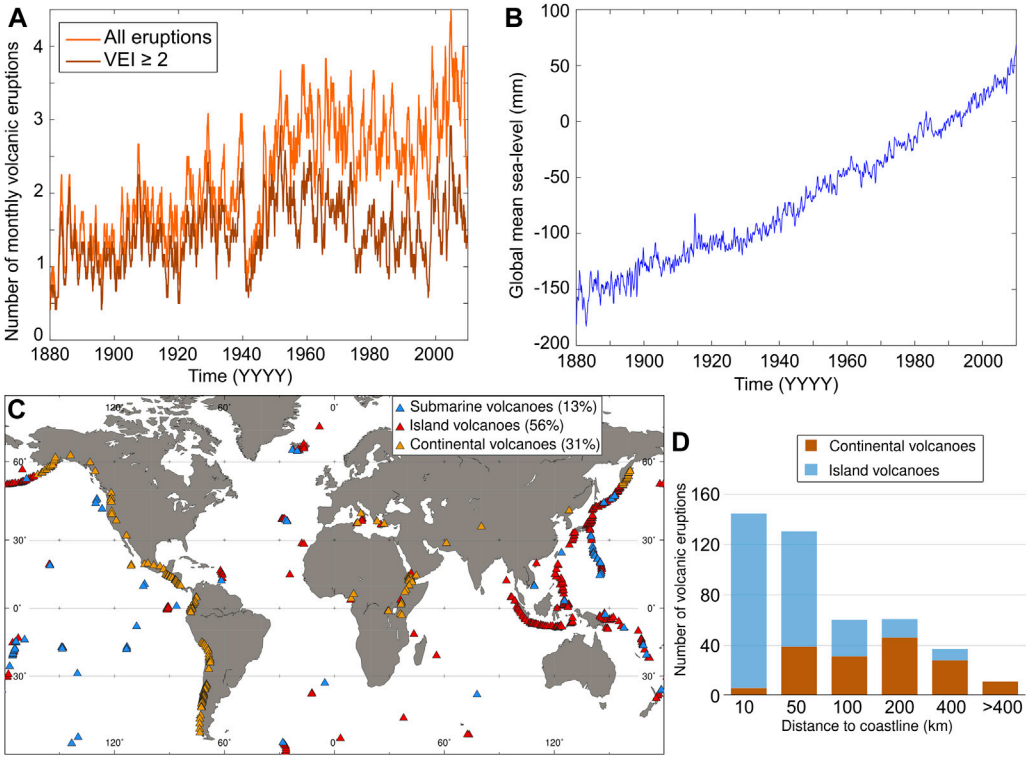

FIGURE 1 | Global volcanic activity and global mean sea level from 1880 to 2009. **(A)** Curves showing the number of confirmed monthly volcanic eruptions since 1 January 1880 to 31 December 2009 for all and VEI≥2 eruptions (Global Volcanism Program, 2013). These eruptions are associated with 514 volcanic systems shown in **(C)**. The color of the triangles corresponds to submarine (blue), island (red) or continental (orange) volcanic systems whose proportions are indicated in the top inset **(C)**. **(B)** Curve of the global mean sea level from January 1880 to December 2009 after Church and White (2006). **(D)** Histogram showing the distance to the coastline for the 161 continental and 284 island volcanoes (total: 445).

submarine, and for the first two settings, we calculated their distance to the coastline (**Figures 1C,D**, **Supplementary Figure S1**).

We used the reconstruction of the Global Mean Sea Level (GMSL) by Church and White (2006). The GMSL time-series is derived from data acquired from both worldwide-distributed tide gauges and different altimeter satellites. It has a monthly-sampling which was only corrected for Glacial Isostatic Adjustment (**Figure 1B**).

We analyzed both time-series, e.g. that of volcanic eruptions and that of GMSL, using SSA. This technique has been widely applied on various geophysical data sets (Carniel et al., 2006; Bozzo et al., 2010; Lopes et al., 2021; Dumont et al., 2020, 2021; Petrosino and Dumont, 2022), including sea level (Le Mouël et al., 2021a,b). This time-series analysis technique allows to decompose any time-series into a sum of physical components corresponding to slowly-varying components such as trend, regular and modulated oscillations and noise (e.g., Golyandina and Zhigljavsky, 2013). First, the cross-lagged correlation matrix was built from embedded vectors of lengths adapted to each time-series [561 for GMSL, 2,682 for NVE (all eruptions) and 1,416 for NVE (VEI≥2)]. Then, the singular value decomposition was applied resulting in eigenvectors and eigenvalues that were identified as non- or pseudo-oscillatory components and whose periods were estimated using Fourier Transform. We only considered the first five eigenvalues which are the strongest components of the original signal (**Supplementary Figure S2**).

Results

The number of reported volcanic eruptions increases over the whole time interval (**Figure 1A**), which does not represent a global increase of volcanic activity on Earth but rather more systematic reports on eruptions around the world over the 20th century. A significant drop appears, around 1940, due to the second world war, followed by a sharp increase up to ~1950–1960. Then, the period ~1960- late 1990 was characterized by a slow decrease of volcanic activity which preceded a strong increase that culminated around 2005. Very similar variations are observed for VEI≥2 eruptions. Over the 1880–2009 period, the variations of the GMSL (**Figure 1B**) appear more regular, with a global increase of ~2 cm punctuated by shorter variations of low amplitude (<0.5 cm).

Three of the first five eigenvalues of the NVE (all eruptions and VEI≥2) appear to be very similar, and within uncertainties, to those detected in the GMSL (**Figure 2** and **Supplementary Figures S2, S3**). They are characterized by a period of 52.5 years, 37.9 ± 8.9 years and 19.8 ± 2.2 years (56.9 ± 20.4 years,

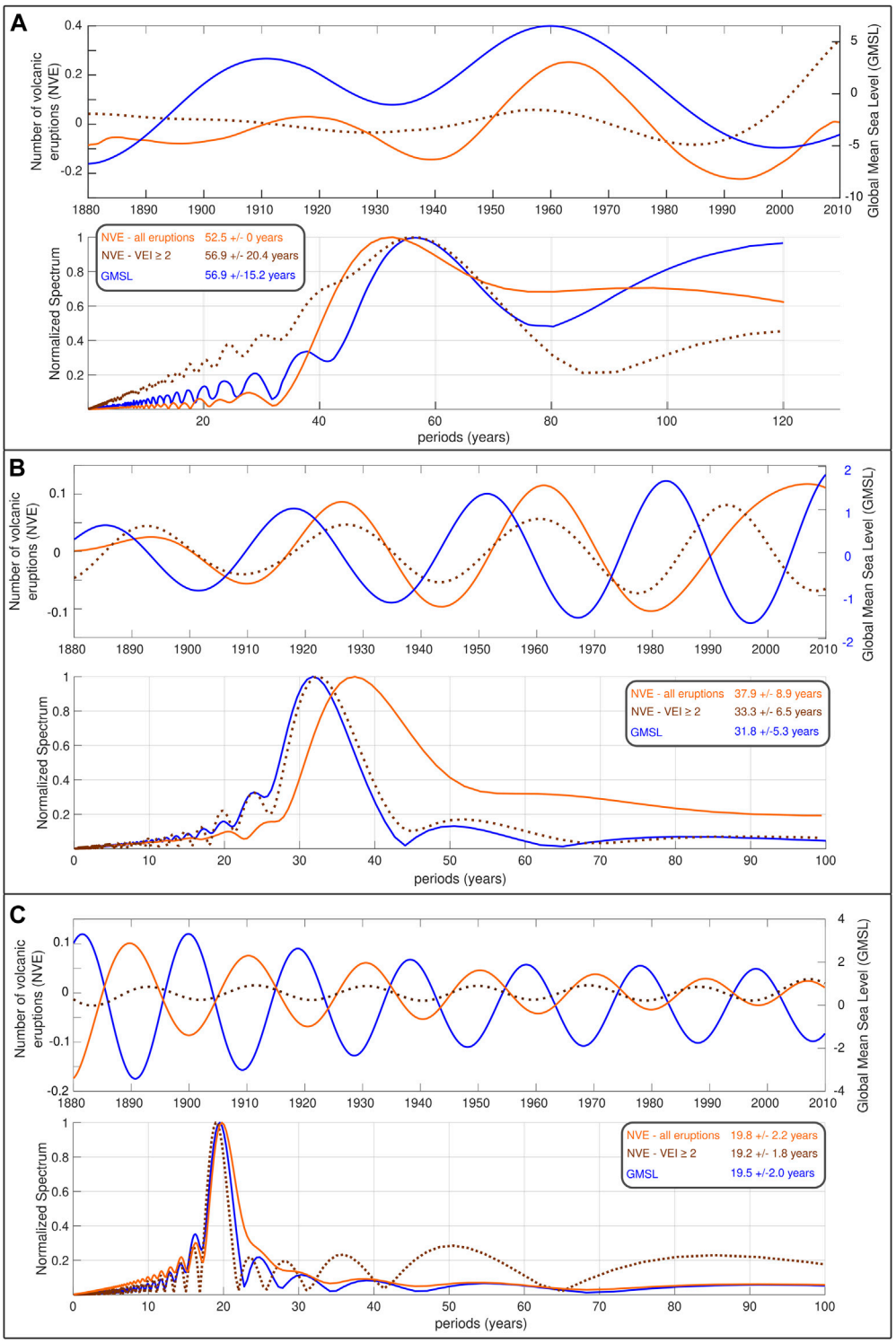

FIGURE 2 | Examples of common long-period components extracted using SSA in the global mean sea level (blue) and volcanism (orange for all eruptions and dotted brown for VEI≥2 eruptions) with that of **(A)** ~50–60, **(B)**~30, and **(C)** ~20 years.

33.3 ± 6.5 years and 19.2 ± 1.8 years for VEI≥2). The corresponding periods extracted in the GMSL are of 56.9 ± 15.2 years, 31.8 ± 5.3 years and 19.5 ± 2 years. To further investigate their link, we compare their waveforms (**Figure 2**). The first periodicity of ~50–60 years appears in phase for the NVE and GSML although the uncertainties are relatively

significant. Thus, when the global mean sea level is high, the volcanic activity is also globally high on Earth. For the ~20-year components, the NVE and GMSL appear in phase opposition, while for the ~30 years a phase delay is detected between GMSL variations and volcanic activity. In the NVE, we also found a component of ~85 years (~90 years for VEI≥2) that is not well resolved due to the duration of the time interval considered. Although not found in the GMSL analyzed in this paper, previous studies of sea level data have found a similar cycle of ~90 years, known also as the Gleissberg cycle (cf. Gleissberg, 1939; Le Mouël et al., 2021b).

DISCUSSION

Our analysis, performed for both the whole eruption catalog and VEI≥2 eruptions, shows the existence of consistent multi-decadal periodicities not only for low and non-explosive eruptions but also for explosive-dominated phenomena as already suggested for sulfur rich tropical eruptions (Ammann and Nadeau, 2003), and despite a catalog completeness which has kept improving over the 20th century (Siebert et al., 2015). Although some of the uncertainties are significant, very comparable periodicities were found in the GMSL. These different periodicities form the larger contributions in each time-series representing more than 90% of the original signals, once considered together with the trend (**Supplementary Figures S2, S3, S4**). Moreover, a specific link between these multi-decadal components extracted in the NVE and GMSL is observed (in phase, phase shifted/opposition). All together, these results lead us to consider that these multi-decadal periodicities in the NVE and GMSL time-series are related.

Most volcanic eruptions considered in this study, e.g. ~70%, occur on volcanoes located either on islands or sea floor, indicating a prime link of spatial order between volcanic systems and oceans, knowing that the submarine eruptions are by far underestimated (**Figures 1C,D**). Moreover, for volcanoes situated on continents or islands, about 54% of them are located within 50 km to the coast (**Figure 1D**, **Supplementary Figure S1**). Water, which is ubiquitous on Earth, is not only present at Earth's surface but also as groundwater, penetrating beneath the islands and far into the continents. Water also accumulates within intraplate regions (e.g., Gleeson et al., 2016; Craig et al., 2017; MacMillan et al., 2019; Jasechko et al., 2020). All fluid layers redistribute water masses from the microscopic scale through pore-fluid pressures to the global scale via their loading, by oscillating at periods ranging from few hours to multi-decades in response to tidal forces and pole motion (e.g., Lambeck, 2005; MacMillan et al., 2019; Le Mouël et al., 2021b; Lopes et al., 2021). These two different ways by which water can interfere with dynamical systems have not only been suggested for volcanoes, but also for fault systems where tidal stresses may enhance the long-term tectonic loads (Thomas et al., 2009; Neves et al., 2015; Ide et al., 2016). Considering that both faults and volcanoes share some commonalities in their driving processes, we believe that taking into account their response to external forcing could improve understanding of how this interplay works.

Past studies spotted that long periods (>6 months) of the hydrological cycle can influence eruption onsets at volcanoes located nearby the coast (e.g., McNutt and Beavan, 1987; McNutt, 1999). This idea seems to be confirmed by our study and the work of Mason et al. (2004) based on worldwide catalog of eruptions who showed a correlation between eruption rates and annual sea level variations. Besides, it is well known that bathymetry and boundary effects associated with coastlines have a major impact on the local amplitudes of semi-diurnal, spring, and neap tides (**Supplementary Figure S5**). Likewise, sea level variations over longer time scales, like the ones highlighted in this study, have different amplitudes and larger loading depending on geographic location. As long periods of hydrological loading redistribute more water masses than shorter periods, it could explain why long periods and multi-decadal periodicities would have more impact on unstable and dynamical systems.

Detecting these decadal periodicities in both time-series suggests as well that they relate to a global phenomenon. Although the way these processes take place and interfere is still puzzling, we note that four similar multi-decadal periods were detected in the fluctuations of the pole motion, being of 21.6, 31.5, 57.3 and 92.2 years (e.g., Lopes et al., 2021). Yet, any movement of the Earth's rotation axis is accompanied by mass movements according to Liouville-Euler equations (Lambeck, 2005; Lopes et al., 2021). This may be illustrated by the late Pleistocene deglaciation, the concomitant sea level changes and a secular drift present in the pole motion (Nakiboglu and Lambeck, 1980). This is what we observe through the common periodicities extracted in the GMSL and the pole motion (Lopes et al., 2021). We interpret the presence of these decadal periodicities in the NVE as a consequence of this global mass redistribution operating at similar time scales. The water masses transported over these decadal periods induce pressure changes on crust that adds to the local stresses, leading to a slow destabilization of magma plumbing systems. In fact, the decadal cycles extracted in the NVE do not properly trigger one eruption every ~50 or ~20 years as evidenced by the amplitude of the waveforms extracted by SSA (**Figure 2**), although they participate to the triggering process. Complementary approaches will be necessary for better understanding this link, as for instance, numerical modeling to investigate how tidal stresses can destabilize magma chambers and fault systems (McNutt and Beaven, 1987; Ide et al., 2016; Jonhson et al., 2017; Scholz, 2019). Moreover, the impact of the fluctuations of the Earth's rotation axis on volcanic eruptions was also suggested locally and regionally (Kutterolf et al., 2013; Lambert and Sottili, 2019).

CONCLUDING REMARKS AND FUTURE PERSPECTIVES

Our study leads us to suggest that movements affecting globally our planet over a wide range of time scales, e.g., lunisolar gravitational forces, pole motion, may contribute to the dynamics of volcanic systems. These considerations and results raise also some more questions as for instance, are volcanoes sensitive to all or just some of these periodicities and what may

explain these differences? Could this forcing be viewed as a background variation participating in the regular dynamics of magma plumbing systems? We think that these decadal variations together with short and very long periodicities deserve to be more explored and investigated as they might reveal global conditions and space-time patterns favorable to eruption triggering.

These results represent an avenue to explore how the mass redistribution acting at global scale participates in the processes leading to the triggering of volcanic eruptions as already suggested by Mason et al. (2004) or Sottili et al. (2021). Deciphering the link between global and local scale is critical to understand how external forcing acts on different time scales and how it can disrupt dynamical systems like volcanoes. We think that assessing these processes at multiple scales will allow to provide more constraints on the parameters and conditions that make volcanoes sensitive to small environmental changes (e.g. Canon-Tapia, 2014; Caricchi et al., 2021).

Singular Spectrum Analysis, in addition to be a robust time-series analysis technique that has been applied to a large variety of Earth sciences data, allows to extract trends and periodic components without an a priori model, which has some advantages when analyzing signals integrated at various time scales such as tides and whose modulation may vary over time as in case of seismic tremor in a highly heterogeneous medium (e.g., Petrosino and Dumont, 2022). Similar analyses could provide new insights on studied processes, including cause-effect relationships between parameters as well as what makes some volcanoes sensitive to quasi-permanent external forcing and why (e.g., Dumont et al., 2021). All active volcanoes do not respond to solid Earth and ocean tides (e.g., Neuberg, 2000) and that sensitivity may be related to inherent properties of volcanoes, their location on Earth or the plate boundaries conditions (e.g., Mauk and Johnston, 1973; Dzurisin, 1980; Dumont et al., 2021). Many studies have also reported an increase of the sensitivity to tidal forcing when plumbing systems are approaching a critical state coinciding for some volcanoes to pre-eruptive periods (e.g., Filson et al., 1973; Berrino and Corrado, 1991; De Lauro et al., 2013; Girona et al., 2018; Miguelsanz et al., 2021). More systematics observations are required to unravel these critical conditions.

Technique plays an important role in the road to findings, but data, as all the ingredients in a recipe, play an equally fundamental role. The data availability and quality are of great importance to advance in the comprehension of the interplay between external and internal processes at volcanoes. The role of volcano observatories and initiatives such WOVOdat (Newhall et al., 2017) or the Global Volcanism Program (2013) have been primordial to tackle these questions and many others. Revisiting past volcanic activity together with recent volcanic events, from global to local scale using time-series analysis, may help to advance in this direction.

DATA AVAILABILITY STATEMENT

Publicly available datasets were analyzed in this study. The list of worldwide volcanic eruptions is from the Global Volcanism Program, Smithsonian Institution (Global Volcanism Program, 2013): https://volcano.si.edu/. The global mean sea-level data from Church and White (2006) is accessible here: https://www.psmsl.org/products/reconstructions/church.php.

AUTHOR CONTRIBUTIONS

SD contributed to conceptualization, data analysis and led the writing of the original draft. SD and MN made the figures. All authors contributed to the writing, review and editing of the paper.

FUNDING

This work was performed through the fellowship SFRH/BPD/117714/2016 funded by the Fundação para a Ciência e Tecnologia (FCT) and the European Union, co-financed by the Ministério da Ciência, Tecnologia e Ensino Superior (MCTES), Fundo Social Europeu (FSE), and Programa Operacional Regional Centro (POR-Centro, Centro 2020); in the framework of the project SHAZAM (PTDC/CTA-GEO/31475/2017—POCI-01-0145-FEDER-031475), co-financed by the FCT through national and FEDER funds through the Programa Operacional Competitividade e Internacionalização—COMPETE 2020, as well as projects financed by the financed by the FCT, I.P/MCTES through national funds (PIDDAC), RESTLESS (PTDC/CTA-GEF/6674/2020), the Instituto Dom Luiz (IDL, UIDB/50019/2020) and the Colaboratório para as Geociências (PTDC/GEO-GEO/1123/2014).

ACKNOWLEDGMENTS

SD ackowledges F. Lopes for stimulating discussions which were critical. The authors thank the reviewer whose comments contributed to improve the manuscript.

SUPPLEMENTARY MATERIAL

The Supplementary Material for this article can be found online at: https://www.frontiersin.org/articles/10.3389/feart.2022.845511/full#supplementary-material

REFERENCES

Ammann, C. M., and Naveau, P. (2003). Statistical Analysis of Tropical Explosive Volcanism Occurrences over the Last 6 Centuries. *Geophys. Res. Lett.* 30 (5), 1210. doi:10.1029/2002gl016388

Andrew, R. E., and Gudmundsson, A. (2007). Distribution, Structure, and Formation of Holocene Lava Shields in Iceland. *J. Volcanol. Geotherm. Res.* 168 (1-4), 137–154. doi:10.1016/j.jvolgeores.2007.08.011

Battaglia, M., Troise, C., Obrizzo, F., Pingue, F., and De Natale, G. (2006). Evidence for Fluid Migration as the Source of Deformation at Campi Flegrei Caldera (Italy). *Geophys. Res. Lett.* 33 (1), L01307. doi:10.1029/2005gl024904

Berrino, G., and Corrado, G. (1991). Tidal Signal in the Recent Dynamics of Campi Flegrei Caldera (Italy). *J. Volcanol. Geotherm. Res.* 48 (1-2), 93–101. doi:10.1016/0377-0273(91)90035-x

Biggs, J., Ebmeier, S. K., Aspinall, W. P., Lu, Z., Pritchard, M. E., Sparks, R. S., et al. (2014). Global Link between Deformation and Volcanic Eruption Quantified by Satellite Imagery. *Nat. Commun.* 5 (1), 3471–3477. doi:10.1038/ncomms4471

Bottiglieri, M., Falanga, M., Tammaro, U., De Martino, P., Obrizzo, F., Godano, C., et al. (2010). Characterization of GPS Time Series at the Neapolitan Volcanic Area by Statistical Analysis. *J. Geophys. Res. Solid Earth* 115 (B10), B10416. doi:10.1029/2009jb006594

Bozzo, E., Carniel, R., and Fasino, D. (2010). Relationship between Singular Spectrum Analysis and Fourier Analysis: Theory and Application to the Monitoring of Volcanic Activity. *Comput. Math. Appl.* 60 (3), 812–820. doi:10.1016/j.camwa.2010.05.028

Bredemeyer, S., and Hansteen, T. H. (2014). Synchronous Degassing Patterns of the Neighbouring Volcanoes Llaima and Villarrica in South-Central Chile: the Influence of Tidal Forces. *Int. J. Earth Sci. Geol. Rundsch)* 103 (7), 1999–2012. doi:10.1007/s00531-014-1029-2

Caltabiano, T., Romano, R., and Budetta, G. (1994). SO2flux Measurements at Mount Etna (Sicily). *J. Geophys. Res.* 99 (D6), 12809. doi:10.1029/94jd00224

Cañón-Tapia, E. (2014). Volcanic Eruption Triggers: A Hierarchical Classification. *Earth-Science Rev.* 129, 100–119. doi:10.1016/j.earscirev.2013.11.011

Caputo, T., Cusano, P., Petrosino, S., Sansivero, F., and Vilardo, G. (2020). Spectral Analysis of Ground Thermal Image Temperatures: what We Are Learning at Solfatara Volcano (Italy). *Adv. Geosci.* 52, 55–65. doi:10.5194/adgeo-52-55-2020

Caricchi, L., Townsend, M., Rivalta, E., and Namiki, A. (2021). The Build-Up and Triggers of Volcanic Eruptions. *Nat. Rev. Earth Environ.* 2, 458–476. doi:10.1038/s43017-021-00174-8

Carniel, R., Barazza, F., Tárraga, M., and Ortiz, R. (2006). On the Singular Values Decoupling in the Singular Spectrum Analysis of Volcanic Tremor at Stromboli. *Nat. Hazards Earth Syst. Sci.* 6 (6), 903–909. doi:10.5194/nhess-6-903-2006

Cashman, K., and Biggs, J. (2014). Common Processes at Unique Volcanoesâ€"a Volcanological Conundrum. *Front. Earth Sci.* 2, 28. doi:10.3389/feart.2014.00028

Church, J. A., and White, N. J. (2006). A 20th Century Acceleration in Global Sea-level Rise. *Geophys. Res. Lett.* 33 (1), L01602. doi:10.1029/2005gl024826

Conde, V., Bredemeyer, S., Duarte, E., Pacheco, J. F., Miranda, S., Galle, B., et al. (2014). SO2 Degassing from Turrialba Volcano Linked to Seismic Signatures during the Period 2008-2012. *Int. J. Earth Sci. Geol. Rundsch)* 103 (7), 1983–1998. doi:10.1007/s00531-013-0958-5

Contadakis, M. E., Arabelos, D. N., and Vergos, G. (2017). Testing the Recent Santorini Seismic Activity for Possible Tidal Triggering Effect. *geosociety* 51, 1–17. doi:10.12681/bgsg.11653

Craig, T. J., Chanard, K., and Calais, E. (2017). Hydrologically-driven Crustal Stresses and Seismicity in the New Madrid Seismic Zone. *Nat. Commun.* 8 (1), 2143–2211. doi:10.1038/s41467-017-01696-w

Cusano, P., Caputo, T., De Lauro, E., Falanga, M., Petrosino, S., Sansivero, F., et al. (2021). Tracking the Endogenous Dynamics of the Solfatara Volcano (Campi Flegrei, Italy) through the Analysis of Ground Thermal Image Temperatures. *Atmosphere* 12 (8), 940.

Custodio, S. I., Fonseca, J. F., d'Oreye, N. F., Faria, B. V., and Bandomo, Z. (2003). Tidal Modulation of Seismic Noise and Volcanic Tremor. *Geophys. Res. Lett.* 30 (15), 1816. doi:10.1029/2003gl016991

De Lauro, E., De Martino, S., Falanga, M., and Petrosino, S. (2013). Synchronization between Tides and Sustained Oscillations of the Hydrothermal System of Campi Flegrei (Italy). *Geochem. Geophys. Geosyst.* 14 (8), 2628–2637. doi:10.1002/ggge.20149

De Lauro, E., Falanga, M., and Petrosino, S. (2012). Study on the Long-Period Source Mechanism at Campi Flegrei (Italy) by a Multi-Parametric Analysis. *Phys. Earth Planet. Interiors* 206, 16–30.

De Lauro, E., Petrosino, S., Ricco, C., Aquino, I., and Falanga, M. (2018). Medium and Long Period Ground Oscillatory Pattern Inferred by Borehole Tiltmetric Data: New Perspectives for the Campi Flegrei Caldera Crustal Dynamics. *Earth Planet. Sci. Lett.* 504, 21–29. doi:10.1016/j.epsl.2018.09.039

Deligne, N. I., Coles, S. G., and Sparks, R. S. J. (2010). Recurrence Rates of Large Explosive Volcanic Eruptions. *J. Geophys. Res. Solid Earth* 115 (B6), B06203. doi:10.1029/2009jb006554

Dinger, F., Bobrowski, N., Warnach, S., Bredemeyer, S., Hidalgo, S., Arellano, S., et al. (2018). Periodicity in the BrO/SO₂ Molar Ratios in the Volcanic Gas Plume of Cotopaxi and its Correlation with the Earth Tides during the Eruption in 2015. *Solid earth.* 9 (2), 247–266. doi:10.5194/se-9-247-2018

Dumont, S., Le Mouël, J.-L., Courtillot, V., Lopes, F., Sigmundsson, F., Coppola, D., et al. (2020). The Dynamics of a Long-Lasting Effusive Eruption Modulated by Earth Tides. *Earth Planet. Sci. Lett.* 536, 116145. doi:10.1016/j.epsl.2020.116145

Dumont, S., Silveira, G., Custódio, S., Lopes, F., Le Mouël, J.-L., Gouhier, M., et al. (2021). Response of Fogo Volcano (Cape Verde) to Lunisolar Gravitational Forces during the 2014-2015 Eruption. *Phys. Earth Planet. Interiors* 312, 106659. doi:10.1016/j.pepi.2021.106659

Dzurisin, D. (1980). Influence of Fortnightly Earth Tides at Kilauea Volcano, Hawaii. *Geophys. Res. Lett.* 7 (11), 925–928. doi:10.1029/gl007i011p00925

Dzurisin, D. (2006). *Volcano Deformation: New Geodetic Monitoring Techniques*. Berlin: Springer Science & Business Media.

Emter, D. (1997). *Tidal Triggering of Earthquakes and Volcanic Events*. Berlin, Heidelberg: Tidal phenomena, 293–309.

Filson, J., Simkin, T., and Leu, L.-k. (1973). Seismicity of a Caldera Collapse: Galapagos Islands 1968. *J. Geophys. Res.* 78 (35), 8591–8622. doi:10.1029/jb078i035p08591

Girona, T., Huber, C., and Caudron, C. (2018). Sensitivity to Lunar Cycles Prior to the 2007 Eruption of Ruapehu Volcano. *Sci. Rep.* 8 (1), 1476. doi:10.1038/s41598-018-19307-z

Gleeson, T., Befus, K. M., Jasechko, S., Luijendijk, E., and Cardenas, M. B. (2016). The Global Volume and Distribution of Modern Groundwater. *Nat. Geosci.* 9 (2), 161–167. doi:10.1038/ngeo2590

Gleissberg, W. (1939). A Long-Periodic Fluctuation of the Sun-Spot Numbers. *Observatory* 62, 158–159.

Global Volcanism Program (2013). in *Volcanoes of the World, V. 4.9.2 (15 Dec 2020)*. Editor E Venzke (United States: Smithsonian Institution). doi:10.5479/si.GVP.VOTW4-2013

Golombek, M. P., and Carr, M. J. (1978). Tidal Triggering of Seismic and Volcanic Phenomena during the 1879–1880 Eruption of Islas Quemadas Volcano in El Salvador, Central America. *J. Volcanol. Geotherm. Res.* 3 (3–4), 299–307. doi:10.1016/0377-0273(78)90040-9

Golyandina, N., and Zhigljavsky, A. (20132013). *Singular Spectrum Analysis for Time Series*. Berlin, Heidelberg: Springer.

Gudmundsson, M. T., Jónsdóttir, K., Hooper, A., Holohan, E. P., Halldórsson, S. A., Ófeigsson, B. G., et al. (2016). Gradual Caldera Collapse at Bárdarbunga Volcano, Iceland, Regulated by Lateral Magma Outflow. *Science* 353 (6296), aaf8988. doi:10.1126/science.aaf8988

İçhedef, M., Giammanco, S., Neri, M., Catalano, R., Immé, G., Morelli, D., et al. (2020). In Soil Radon Anomalies and Volcanic Activity on Mt. Etna (Italy). *J. Environ. Radioact.* 218, 106267. doi:10.1016/j.jenvrad.2020.106267

Ide, S., Yabe, S., and Tanaka, Y. (2016). Earthquake Potential Revealed by Tidal Influence on Earthquake Size-Frequency Statistics. *Nat. Geosci.* 9 (11), 834–837. doi:10.1038/ngeo2796

Jaggar, T. A., Finch, R. H., and Emerson, O. H. (1924). The Lava Tide, Seasonal Tilt, and the Volcanic Cycle. *Mon. Wea. Rev.* 52 (3), 142–145. doi:10.1175/1520-0493(1924)52<142:tltsta>2.0.co;2

Jasechko, S., Perrone, D., Seybold, H., Fan, Y., and Kirchner, J. W. (2020). Groundwater Level Observations in 250,000 Coastal US Wells Reveal Scope

of Potential Seawater Intrusion. *Nat. Commun.* 11 (1), 3229–9. doi:10.1038/s41467-020-17038-2

Jentzsch, G., Haase, O., Kroner, C., and Winter, U. (2001). Mayon Volcano, Philippines: Some Insights into Stress Balance. *J. Volcanol. Geotherm. Res.* 109 (1-3), 205–217. doi:10.1016/s0377-0273(00)00312-7

Johnson, C. W., Fu, Y., and Bürgmann, R. (2017). Stress Models of The Annual Hydrospheric, Atmospheric, Thermal, and Tidal Loading Cycles on California Faults: Perturbation of Background Stress and Changes in Seismicity. *J. Geophys. Res.: Solid Earth* 122 (12), 10-605.

Johnston, M. J. S., and Mauk, F. J. (1972). Earth Tides and the Triggering of Eruptions from Mt Stromboli, Italy. *Nature* 239 (5370), 266–267. doi:10.1038/239266b0

Kasahara, J., Nakao, S., and Koketsu, K. (2001). Tidal Influence on the 2000 Miyake Jima Eruption and its Implications for Hydrothermal Activity and Volcanism. *Proc. Jpn. Acad. Ser. B Phys. Biol. Sci.* 77 (6), 98–103. doi:10.2183/pjab.77.98

Kutterolf, S., Jegen, M., Mitrovica, J. X., Kwasnitschka, T., Freundt, A., and Huybers, P. J. (2013). A Detection of Milankovitch Frequencies in Global Volcanic Activity. *Geology* 41 (2), 227–230. doi:10.1130/g33419.1

Lambeck, K. (2005). *The Earth's Variable Rotation: Geophysical Causes and Consequences*. Cambridge: Cambridge University Press.

Lambert, S., and Sottili, G. (2019). Is There an Influence of the Pole Tide on Volcanism? Insights from Mount Etna Recent Activity. *Geophys. Res. Lett.* 46 (23), 13730–13736. doi:10.1029/2019gl085525

Laskar, J., Robutel, P., Joutel, F., Gastineau, M., Correia, A. C. M., and Levrard, B. (2004). A Long-Term Numerical Solution for the Insolation Quantities of the Earth. *A&A* 428 (1), 261–285. doi:10.1051/0004-6361:20041335

Le Mouël, J. L., Lopes, F., and Courtillot, V. (2021a). A Strong Link between Variations in Sea-Ice Extent and Global Atmospheric Pressure? *The Cryosphere Discussions*, 1–28. doi:10.5194/tc-2021-216

Le Mouël, J. L., Lopes, F., Courtillot, V., and Gibert, D. (2019). On Forcings of Length of Day Changes: From 9-day to 18.6-year Oscillations. *Phys. Earth Planet. Interiors* 292, 1–11. doi:10.1016/j.pepi.2019.04.006

Le Mouël, J. L., Lopes, F., and Courtillot, V. (2021b). Sea-Level Change at the Brest (France) Tide Gauge and the Markowitz Component of Earth's Rotation. *J. Coast. Res* 37 (4), 683–690. doi:10.2112/JCOASTRES-D-20-00110.1

Leandro, C. E., and Alvarado, G. E. (1988). Influencia de las mareas lunisolares sobre el comportamiento del volcán Arenal, Costa Rica. *Bol. Obs. Vulcanol. Arenal* 1 (2), 44–56.

Lopes, F., Le Mouël, J. L., Courtillot, V., and Gibert, D. (2021). On the Shoulders of Laplace. *Phys. Earth Planet. Interiors* 316, 106693. doi:10.1016/j.pepi.2021.106693

López, D. L., Bundschuh, J., Soto, G. J., Fernández, J. F., and Alvarado, G. E. (2006). Chemical Evolution of Thermal Springs at Arenal Volcano, Costa Rica: Effect of Volcanic Activity, Precipitation, Seismic Activity, and Earth Tides. *J. Volcanol. Geotherm. Res.* 157 (1-3), 166–181. doi:10.1016/j.jvolgeores.2006.03.049

Martin, D. P., and Rose, W. I., Jr (1981). Behavioral Patterns of Fuego Volcano, Guatemala. *J. Volcanol. Geotherm. Res.* 10 (1-3), 67–81.

Mason, B. G., Pyle, D. M., Dade, W. B., and Jupp, T. (2004). Seasonality of Volcanic Eruptions. *J. Geophys. Res. Solid Earth* 109 (B4), B04206. doi:10.1029/2002jb002293

Mauk, F. J., and Johnston, M. J. S. (1973). On the Triggering of Volcanic Eruptions by Earth Tides. *J. Geophys. Res.* 78 (17), 3356–3362. doi:10.1029/jb078i017p03356

Mauk, F. J., and Kienle, J. (1973). Microearthquakes at St. Augustine Volcano, Alaska, Triggered by Earth Tides. *Science* 182 (4110), 386–389. doi:10.1126/science.182.4110.386

McMillan, T. C., Rau, G. C., Timms, W. A., and Andersen, M. S. (2019). Utilizing the Impact of Earth and Atmospheric Tides on Groundwater Systems: A Review Reveals the Future Potential. *Rev. Geophys.* 57 (2), 281–315. doi:10.1029/2018rg000630

McNutt, S. R., and Beavan, R. J. (1987). Eruptions of Pavlof Volcano and Their Possible Modulation by Ocean Load and Tectonic Stresses. *J. Geophys. Res.* 92 (B11), 11509–11523. doi:10.1029/jb092ib11p11509

McNutt, S. R., and Beavan, R. J. (1984). Patterns of Earthquakes and the Effect of Solid Earth and Ocean Load Tides at Mount St. Helens Prior to the May 18, 1980, Eruption. *J. Geophys. Res.* 89 (B5), 3075–3086. doi:10.1029/jb089ib05p03075

McNutt, S. R., and Beavan, R. J. (1981). Volcanic Earthquakes at Pavlof Volcano Correlated with the Solid Earth Tide. *Nature* 294 (5842), 615–618. doi:10.1038/294615a0

McNutt, S. R. (1999). "Eruptions of Pavlof Volcano, Alaska, and Their Possible Modulation by Ocean Load and Tectonic Stresses: Re-evaluation of the Hypothesis Based on New Data from 1984-1998," in *Seismicity Patterns, Their Statistical Significance and Physical Meaning* (Basel: Birkhäuser), 701–712. doi:10.1007/978-3-0348-8677-2_23

McNutt, S. R. (1996). Seismic Monitoring and Eruption Forecasting of Volcanoes: a Review of the State-Of-The-Art and Case Histories. *Monit. Mitig. volcano hazards*, 99–146. doi:10.1007/978-3-642-80087-0_3

Miguelsanz, L., González, P. J., Tiampo, K. F., and Fernández, J. (2021). Tidal Influence on Seismic Activity during the 2011–2013 El Hierro Volcanic Unrest. *Tectonics* 40 (2), e2020TC006201. doi:10.1029/2020tc006201

Nakiboglu, S. M., and Lambeck, K. (1980). Deglaciation Effects on the Rotation of the Earth. *Geophys. J. Int.* 62 (1), 49–58. doi:10.1111/j.1365-246x.1980.tb04843.x

Neuberg, J. (2000). External Modulation of Volcanic Activity. *Geophys. J. Int.* 142 (1), 232–240. doi:10.1046/j.1365-246x.2000.00161.x

Neves, M. C., Cabral, J., Luttrell, K., Figueiredo, P., Rockwell, T., and Sandwell, D. (2015). The Effect of Sea Level Changes on Fault Reactivation Potential in Portugal. *Tectonophysics* 658, 206–220. doi:10.1016/j.tecto.2015.07.023

Newhall, C. G., Costa, F., Ratdomopurbo, A., Venezky, D. Y., Widiwijayanti, C., Win, N. T. Z., et al. (2017). WOVOdat–An Online, Growing Library of Worldwide Volcanic Unrest. *J. Volcanol. Geotherm. Res.* 345, 184–199. doi:10.1016/j.jvolgeores.2017.08.003

C. G. Newhall and R. Punongbayan (Editors) (1996). *Fire and Mud: Eruptions and Lahars of Mount Pinatubo, Philippines* (Quezon City: Philippine Institute of Volcanology and Seismology), 1126.

Newhall, C. G., and Self, S. (1982). The Volcanic Explosivity Index (VEI) an Estimate of Explosive Magnitude for Historical Volcanism. *J. Geophys. Res.* 87 (C2), 1231–1238. doi:10.1029/jc087ic02p01231

Pagli, C., and Sigmundsson, F. (2008). Will Present Day Glacier Retreat Increase Volcanic Activity? Stress Induced by Recent Glacier Retreat and its Effect on Magmatism at the Vatnajökull Ice Cap, Iceland. *Geophys. Res. Lett.* 35 (9), L09304. doi:10.1029/2008gl033510

Patrick, M., Swanson, D., and Orr, T. (2019). A Review of Controls on Lava Lake Level: Insights from Halema ʻuma ʻu Crater, Kīlauea Volcano. *Bull. Volcanol.* 81 (3), 13. doi:10.1007/s00445-019-1268-y

Petrosino, S., Cusano, P., and Madonia, P. (2018). Tidal and Hydrological Periodicities of Seismicity Reveal New Risk Scenarios at Campi Flegrei Caldera. *Sci. Rep.* 8 (1), 13808–13812. doi:10.1038/s41598-018-31760-4

Petrosino, S., and Dumont, S. (2022). Tidal Modulation of Hydrothermal Tremor: Examples from Ischia and Campi Flegrei Volcanoes. *Front. Earth Sci.* 9, 775269. doi:10.3389/feart.2021.775269

Petrosino, S., Ricco, C., De Lauro, E., Aquino, I., and Falanga, M. (2020). Time Evolution of Medium and Long-Period Ground Tilting at Campi Flegrei Caldera. *Adv. Geosci.* 52, 9–17. doi:10.5194/adgeo-52-9-2020

Ricco, C., Petrosino, S., Aquino, I., Del Gaudio, C., and Falanga, M. (2019). Some Investigations on a Possible Relationship between Ground Deformation and Seismic Activity at Campi Flegrei and Ischia Volcanic Areas (Southern Italy). *Geosciences* 9 (5), 222. doi:10.3390/geosciences9050222

Roult, G., Peltier, A., Taisne, B., Staudacher, T., Ferrazzini, V., and Di Muro, A. (2012). A new comprehensive classification of the Piton de la Fournaise activity spanning the 1985-2010 period. Search and analysis of short-term precursors from a broad-band seismological station. *J. Volcanol. Geotherm. Res.* 241-242, 78–104. doi:10.1016/j.jvolgeores.2012.06.012

Rydelek, P. A., Davis, P. M., and Koyanagi, R. Y. (1988). Tidal Triggering of Earthquake Swarms at Kilauea Volcano, Hawaii. *J. Geophys. Res.* 93 (B5), 4401–4411. doi:10.1029/jb093ib05p04401

Satow, C., Gudmundsson, A., Gertisser, R., Ramsey, C. B., Bazargan, M., Pyle, D. M., et al. (2021). Eruptive Activity of the Santorini Volcano Controlled by Sea-Level Rise and Fall. *Nat. Geosci.* 14, 586–592. doi:10.1038/s41561-021-00783-4

Scholz, C. H., Tan, Y. J., and Albino, F. (2019). The Mechanism of Tidal Triggering of Earthquakes at Mid-Ocean Ridges. *Nat. Commun.* 10 (1), 1-7.

Seropian, G., Kennedy, B. M., Walter, T. R., Ichihara, M., and Jolly, A. D. (2021). A Review Framework of How Earthquakes Trigger Volcanic Eruptions. *Nat. Commun.* 12 (1), 1004–1013. doi:10.1038/s41467-021-21166-8

Shimozuru, D. (1987). Tidal Effects on Hawaiian Volcanism. *Volcanism Hawaii* 2, 1337–1343.

Siebert, L., Cottrell, E., Venzke, E., and Andrews, B. (2015). Earth's Volcanoes and Their Eruptions: an Overview. *Encycl. volcanoes*, 239–255. doi:10.1016/b978-0-12-385938-9.00012-2

Sigmundsson, F., Hooper, A., Hreinsdóttir, S., Vogfjörd, K. S., Ófeigsson, B. G., Heimisson, E. R., et al. (2015). Segmented Lateral Dyke Growth in a Rifting Event at Bárðarbunga Volcanic System, Iceland. *Nature* 517 (7533), 191–195. doi:10.1038/nature14111

Sottili, G., Lambert, S., and Palladino, D. M. (2021). Tides and Volcanoes: A Historical Perspective. *Front. Earth Sci.* 9, 777548. doi:10.3389/feart.2021.777548

Sottili, G., and Palladino, D. M. (2012). Tidal Modulation of Eruptive Activity at Open-Vent Volcanoes: Evidence from Stromboli, Italy. *Terra nova.* 24 (3), 233–237. doi:10.1111/j.1365-3121.2012.01059.x

Sparks, R. S. J. (1981). Triggering of Volcanic Eruptions by Earth Tides. *Nature* 290 (5806), 448.

Thomas, A. M., Nadeau, R. M., and Bürgmann, R. (2009). Tremor-tide Correlations and Near-Lithostatic Pore Pressure on the Deep San Andreas Fault. *Nature* 462 (7276), 1048–1051. doi:10.1038/nature08654

Tolstoy, M. (2015). Mid-ocean Ridge Eruptions as a Climate Valve. *Geophys. Res. Lett.* 42 (5), 1346–1351. doi:10.1002/2014gl063015

Watt, S. F. L., Pyle, D. M., and Mather, T. A. (2013). The Volcanic Response to Deglaciation: Evidence from Glaciated Arcs and a Reassessment of Global Eruption Records. *Earth-Science Rev.* 122, 77–102. doi:10.1016/j.earscirev.2013.03.007

Williams-Jones, G., Stix, J., Heiligmann, M., Barquero, J., Fernandez, E., and Gonzalez, E. D. (2001). A Model of Degassing and Seismicity at Arenal Volcano, Costa Rica. *J. Volcanol. Geotherm. Res.* 108 (1-4), 121–139. doi:10.1016/s0377-0273(00)00281-x

Yakiwara, H., Hirano, S., Miyamachi, H., Takayama, T., Yamazaki, T., Tameguri, T., et al. (2013). Semi-Diurnal Tidal Periodicity Observed by an Ocean Bottom Seismometer Deployed at a Location Very Close to Seafloor Fumaroles in Wakamiko Caldera, Northeast of Sakurajima Volcano. *Bull. Volcanol. Soc. Jpn.* 58 (1), 269–279. doi:10.18940/kazan.58.1_269

Zaccagnino, D., Vespe, F., and Doglioni, C. (2020). Tidal Modulation of Plate Motions. *Earth-Science Rev.* 205, 103179. doi:10.1016/j.earscirev.2020.103179

Conflict of Interest: The authors declare that the research was conducted in the absence of any commercial or financial relationships that could be construed as a potential conflict of interest.

Publisher's Note: All claims expressed in this article are solely those of the authors and do not necessarily represent those of their affiliated organizations, or those of the publisher, the editors and the reviewers. Any product that may be evaluated in this article, or claim that may be made by its manufacturer, is not guaranteed or endorsed by the publisher.

frontiers | Frontiers in Earth Science

REVIEW
published: 08 July 2022
doi: 10.3389/feart.2022.871951

Cryospheric Impacts on Volcano-Magmatic Systems

Benjamin R. Edwards[1]*, *James K. Russell*[2] *and Meagen Pollock*[3]

[1]Department of Earth Sciences, Dickinson College, Carlisle, PA, United States, [2]Earth, Ocean, and Atmospheric Sciences, University of British Columbia, Vancouver, BC, Canada, [3]Department of Earth Sciences, College of Wooster, Wooster, OH, United States

In contrast to water and air, ice is the most dynamic enveloping medium and unique environment for volcanic eruptions. While all three environments influence volcanic activity and eruption products, the cryospheric eruption environment is unique because: 1) it supports rapid changes between those environments (i.e. subglacial, subaqueous, subaerial), 2) it promotes a wide range of eruption styles within a single eruption cycle (explosive, effusive), 3) it creates unique edifice-scale morphologies and deposits, and 4) it can modulate the timing and rates of magmatism. The distinctive products of cryospheric eruptions offer a robust means of tracking paleoclimate changes at the local, regional and global scale. We provide a framework for understanding the influence of the cryosphere on glaciovolcanic systems, landforms and deposits.

Keywords: cryosphere, glaciovolcanism, tuya, glaciers, lithofacies, paleo-environment

OPEN ACCESS

Edited by:
Simona Petrosino, Istituto Nazionale di Geofisica e Vulcanologia—Sezione di Napoli—Osservatorio Vesuviano, Italy

Reviewed by:
Ilya Bindeman, University of Oregon, United States
Alina Shevchenko, GFZ German Research Centre for Geosciences, Germany

***Correspondence:**
Benjamin R. Edwards
edwardsb@dickinson.edu

Specialty section:
This article was submitted to Volcanology, a section of the journal Frontiers in Earth Science

Received: *08 February 2022*
Accepted: *09 June 2022*
Published: *08 July 2022*

Citation:
Edwards BR, Russell JK and Pollock M (2022) Cryospheric Impacts on Volcano-Magmatic Systems. Front. Earth Sci. 10:871951. doi: 10.3389/feart.2022.871951

INTRODUCTION

Volcanic systems have many ways of recording and responding to variations in their eruptive environments. As early as the 1800s pillow basalts were speculated to form during eruptions of lava in water (*aquatic environment*; cf. Lewis, 1904)—an assumption that was not confirmed by observation until the 1970s (Moore, 1970; Walker, 1992). In the early 1900s, volcanic deposits with abundant palagonite and associated with glacial sediments were suggested to have formed within a *cryospheric environment* (the Palagonite/Mobérg Formation of Iceland: Peacock, 1926; the Tuya Formation in British Columbia, Canada: Kerr, 1948, 1940; Mathews, 1947). In contrast, the first written detailed description of an explosive *subaerial* eruption dates back to at least 79 AD (Pliny the Younger, 2014), and the majority of our observations are from this environment, for which abundant diagnostic criteria exist. For example, deposits of airfall tephra typically drape the entire landscape and lavas flow unimpeded except by local topography.

Forensic volcanological studies are increasingly able to use volcanic stratigraphy to track dynamic changes in environmental conditions attending volcanic eruptions. For example, Russell et al. (2021) mapped variations in the elevations of passages zones preserved in 1.9 Ma glaciovolcanic deposits that recorded transitions from aquatic to subaerial depositional environments. They used these stratigraphic relationships to reconstruct transient fluctuations in the height and depth of the syn-eruption englacial lake that occurred on time-scales of days to weeks to months. Future studies of eruptions and deposits from the cryospheric environment will increasingly be key for reconstructing and tracking changes in Earth's climate that have occurred over the last 3 Ma or more (Smellie and Edwards, 2016; Smellie, 2018).

All three environments (i.e. air, water, ice) dictate styles of eruption, edifice morphologies, and the distribution and nature of volcanic lithofacies. For the purposes of this work, we consider: the *subaerial environment* as dominated by air at Earth's surface under standard conditions (25 C, 0.101

TABLE 1 | Important physical parameters of eruption environment media.

Environment	Subaerial (Air)	Aquatic (Water)	Cryospheric (Ice)
Factor			
Viscosity of Medium	1.81 x 10^{-5} Pa-s	89 x 10^{-5} Pa-s	1 x 10^{12} Pa-s
Density of Medium	1.225 kg m^{-3}	1,020 kg m^{-3}	921 kg m^{-3}
Environmental Vertical Pressure (EVP) Exerted at Vent	~0.1 MPa (at sea level at 25°C)	20–30 MPa (MOR; 2–3 km below sea level) 50 MPa (abyssal plain; 5 km b.s.L.)	~7 MPa (Vatnajökull; 850 m) ~32 MPa (EAIS; 3.5 km)
Potential Change in EVP During Eruption	0	0	7–32 MPa
Potential Change in EVP During System Life Cycle	0	2 MPa (200 m of sea level change max.)	7–32 MPa (full deglaciation)
Thermal Diffusivity	20 x 10^{-6} m^2 s^{-1}	0.14 x 10^{-6} m^2 s^{-1}	1 x 10^{-6} m^2 s^{-1}
Thermal Conductivity	0.025 W m^{-1} K^{-1}	0.6 W m^{-1} K^{-1}	2.2 W m^{-1} K^{-1}
Heat Capacity	1.0 kJ kg^{-1} K^{-1}	4.18 kJ kg^{-1} K^{-1}	2.0 kJ kg^{-1} K^{-1}
h value (heat transfer coefficient)	2.5–500 W m^{-2} K^{-1} [free to forced convection]	100–25,000 W m^{-2} K^{-1}	0
Thermal Energy for Phase Change	0	2.3 x 10^6 kJ m^{-3} (liquid to gas)	0.31 x 10^6 kJ m^{-3} (solid to liquid)
Total Potential Thermal Energy Loss To Convert Environment to Gas at 100°C	0.12 x 10^3 kJ m^{-3}	5,000.0 x 10^3 kJ m^{-3}	5,300.0 x 10^3 kJ m^{-3}

MPa; **Table 1**); the *aquatic environment* as dominated by sea water or freshwater with essentially uniform properties (e.g., Cas and Simmons, 2018; **Table 1**); and the *cryospheric environment* as dominated by glacial ice but also including permafrost and seasonal snow pack (**Figure 1**; Edwards et al., 2020; Curtis and Kyle, 2017). While much of what is reviewed here applies to those parts of the cryosphere, the focus of this contribution is on cryospheric ice. The first two environments (i.e. subaerial/aquatic) are well understood and have been the subject of numerous other reviews (see Cas and Simmons, 2018, for the aquatic environment). Thus, the focus of our work here is summarizing how the cryospheric environment affects volcano-magmatic systems. We provide a framework for understanding the influences of the cryosphere on (glacio) volcanic systems, landforms and deposits in contrast to the other two environments. We have expanded the review of environmental physical properties for subaerial and aqueous environments of Cas and Simmons (2018) to include the cryospheric environment. Our compilation and analysis highlight the unique impacts of the cryosphere on igneous systems, including the potential for: 1) modulating the timing and rates of magmatism, 2) creating unique edifice-scale morphologies, 3) controlling eruption processes, and 4) restricting emplacement and deposition of unique volcanic products.

PHYSICAL CONSTRAINTS IMPOSED BY ERUPTION ENVIRONMENTS

The most obvious physical difference between the subaerial, aquatic and cryospheric environments is the medium into which an eruption occurs: air, water, or ice (and resulting meltwater), respectively. A summary of key physical parameters characteristic of these three environments (**Table 1**) shows that the *cryospheric environment* is the most extreme and the most dynamic. Melting of the enveloping ice can cause rapid changes in eruptive pressure at the vent and melting of ice and heating of meltwater allows for efficient heat transfer and loss from the volcanic system.

The rheological properties of the enveloping media for the three environments are very different. Viscosities vary by at least one order of magnitude (air versus water), and up to 17 orders of magnitude (air versus ice). On the time scales of volcanic eruption, however, the cryospheric environment presents a viscoelastic envelope that can melt and/or flow, or fail brittley. This rheological difference in environment directly controls the distribution of explosive and effusive deposits resulting from glaciovolcanic eruptions. For example, whereas subaerial and aquatic environments allow for relatively unimpeded flow of lavas (e.g., Gregg and Fornari, 1997), cryospheric environments limit the aerial distribution of lavas by imposing physical barriers, even though snow and ice can support the mass of flowing lava over short time-scales (e.g., 24 h or less; Edwards et al., 2012, 2013, 2015). In explosive eruptions, the enveloping media strongly controls the distribution of volcanic ash; large subaerial eruptions can produce global distributions of tephra and water can distribute tephra rafts across ocean basins, while cryospheric environments can, although do not always, restrict ash dispersal because ash frequently ash is deposited in cavities within the ice or in the englacial lake (e.g., Jude-Eton et al., 2012), and transport on the ice surface will be slow. For eruptions through very thin cryosphere, such as snowpack, dispersal may not be restricted at all.

Density differences in the surrounding media translate into substantial differences in environmental vent pressures (EVP). Depending on the depth of water or thickness of overlying ice EVP can be ~2 orders of magnitude higher in aquatic and cryospheric environments than subaerial ones (**Table 1**), which potentially suppresses expansion of volatile phases and subsequently influences fragmentation and the distribution of tephra relative to subaerial environments (cf. Cas and Simmons, 2018). For subaerial and aqueous environments, EVPs are

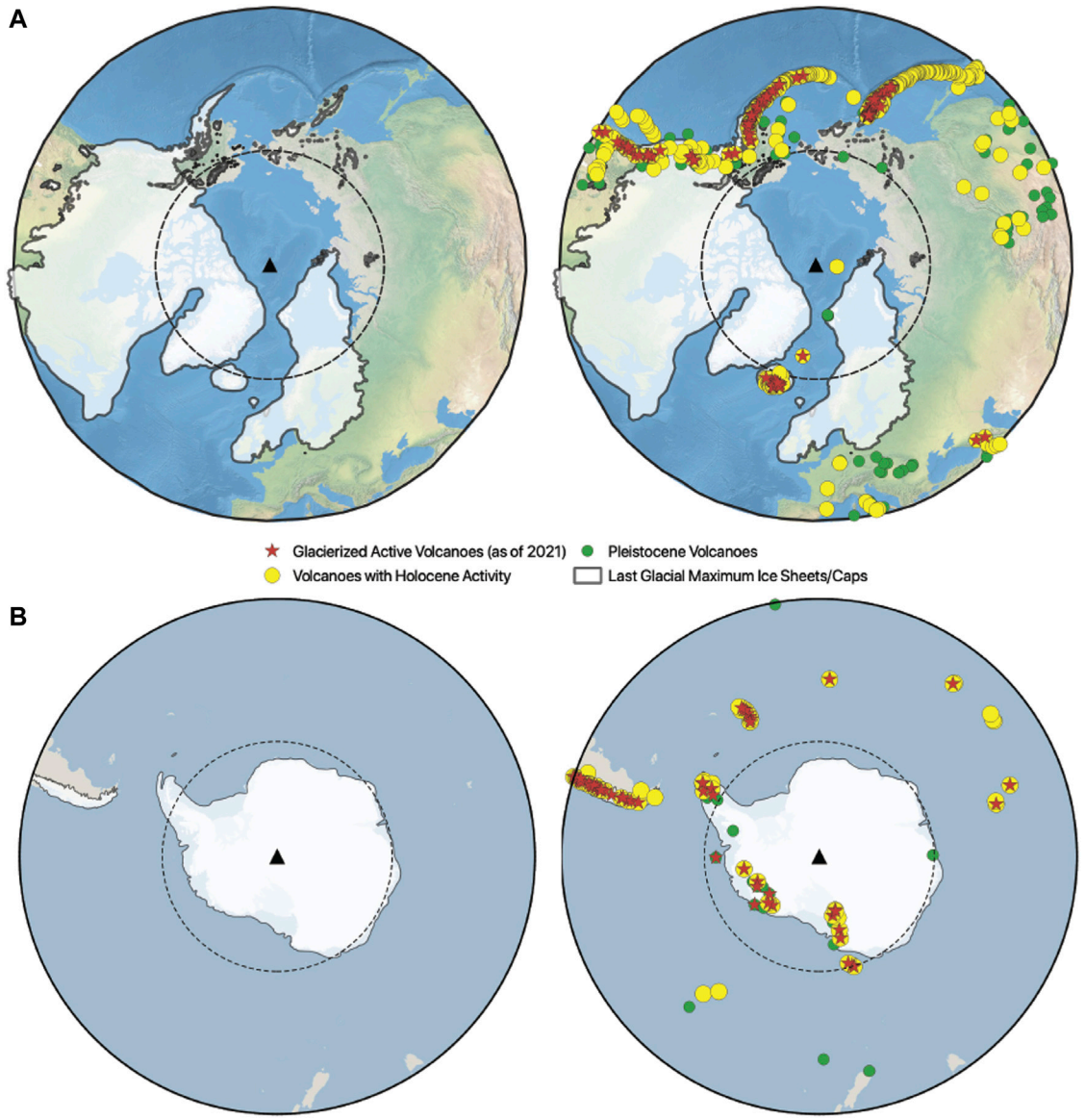

FIGURE 1 | Global maps showing estimates of the extents of ice sheets and ice caps at the Last Glacial Maximum (Gowan, 2019) and distributions of glacierized (Edwards et al., 2020), Holocene and Pleistocene volcanoes (from the Smithsonian Global Volcanism Program). **(A)** Ice conditions and volcanoes from 40° north latitude to the North Pole. **(B)** Ice conditions and volcanoes from 40° south latitude to the South Pole.

essentially static during eruptions while for cryospheric environments EVP can be dynamic and can vary by one to two orders of magnitude during the eruption as the enclosing ice melts and the resulting meltwater drains (**Figure 2**; **Table 1**).

The three environments also dissipate heat in very different ways and with different efficiencies. Conductive heat loss to the enveloping media depends on the associated physical properties. Thermal conductivity (K) reflects the materials' ability to conduct heat in a thermal gradient. Air is the most insulatory (lowest K) and is one order of magnitude lower than water and 2 orders of magnitude less than ice. Thermal diffusivity (κ) values dictate characteristic rates of heat transfer through the media, and values of κ for air are 2 orders of magnitude higher than for water and 1 order higher than for ice (**Table 1**). The lower viscosities of air and water, relative to ice, mean that heat transfer in those environments is likely to be dominated by advective heat transfer. The heat transfer coefficient, which is a simplified proxy for the complexities of advective heat transfer processes, is significantly higher for water than for air (**Table 1**). In the cryospheric environment, meltwater is rapidly produced by melting of the enclosing ice at which point advective heat transfer will dominate.

Heat in the volcanic system is also dissipated by endothermic phase transitions that attend aquatic and cryospheric eruptions. As an example, for an eruption to convert its enveloping medium to a gas phase at 100°C requires 0.12×10^3 kJ m^{-3} for air, 5,000.0

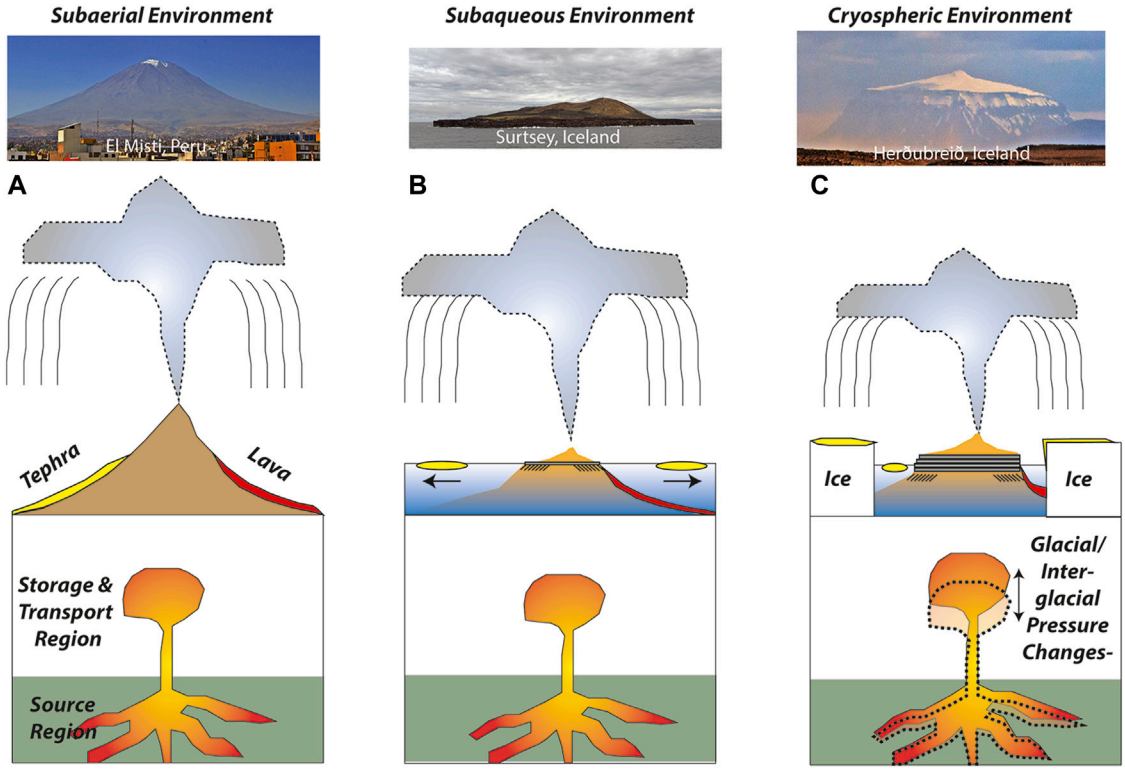

FIGURE 2 | Schematic illustrations of the three eruption environments. **(A)** Subaerial eruptions essentially show no variation, except potentially that associated with changes in barometric pressure. This environment imposes very few constraints on the distributions of pyroclastic deposits and lava effusions. **(B)** Aquatic eruptions can also experience changes in barometric pressure, but those changes are very minor compared to the hydrostatic pressure, which is static in the short-term but which can change as eruption products accumulate at the vent. Deposits of pyroclastic materials can be distributed widely by water transport, and the physical properties of the aqueous environment do not strongly impede the movement of lava effusions. **(C)** Cryospheric eruptions can also experience barometric pressure changes, but again these are minor compared to cryostatic/hydrostatic pressures. For this environment pressure changes have the potential to be dynamic instead of static, as meltwater produced during the eruption can leave the vent area, leading to reductions in pressure on the order of several MPa. Ice is also very capable to limiting the distribution of pyroclastic materials and lava effusions.

$\times 10^3$ kJ m^{-3} for water, and 5,300.0 $\times 10^3$ kJ m^{-3} for ice, including the phase transitions from ice to water, and from water to steam. In the aqueous environment, about half of the required energy is used to heat water from initial temperatures, here assumed to 0°C although they could be as low as −4°C for abyssal marine environments, to phase transition temperatures for the liquid: gas/fluid transition that depend on pressure (i.e. water depth). In cryospheric environments the temperatures in the vent area will be close to the temperature for ice:water phase transition (~0°C); even polar ice is generally at temperatures above −60°C (Cuffey and Paterson, 2010). However, the environmental medium (i.e. ice) can pass through two phase transitions via melting and vaporization, consuming the largest amount of energy per cubic meter of erupted material (**Table 1**). The differences in thermal properties are responsible for many of the macro- and microscopic differences seen in deposits from the water- and ice-dominated eruption environments, relative to subaerial volcanic deposits. As developed below, the physical conditions of the cryosphere, relative to the subaerial and aquatic environments, produce signatory characteristics at volcanoes and in their deposits, which has led to a new subdiscipline known simply as "glaciovolcanism" (Kelman et al., 2002; Smellie, 2009; Edwards et al., 2014; Russell et al., 2014; Smellie and Edwards, 2016)

CRYOSPHERIC IMPACTS ON MAGMA GENERATION AND MIGRATION

The cryosphere (**Figure 3**) perturbs magmatic systems mainly during interstadial and interglacial periods, when ice thickness is changing and influencing lithostatic stress conditions (Andrew and Gudmundsson, 2007; Geyer and Bindeman, 2011). Static ice is no different than any other kind of lithospheric load, although compared to typical sediments or other surficial deposits, ice is about 50–70 percent less dense and is susceptible to higher rates of removal. Land-based accumulation of ice, glaciers and ice sheets operates on time scales of tens of thousands of years based on Pleistocene proxies for global sea level and ocean temperatures (e.g., Lisiecki and Raymo, 2005). However, those same records are interpreted to suggest that deglaciations happen much more rapidly. The Laurentide, Cordilleran and Svennoscandian ice sheets are all thought to have been at least 2 km thick (e.g., Clague and Ward, 2011; Lambeck et al., 2006), while at the Last

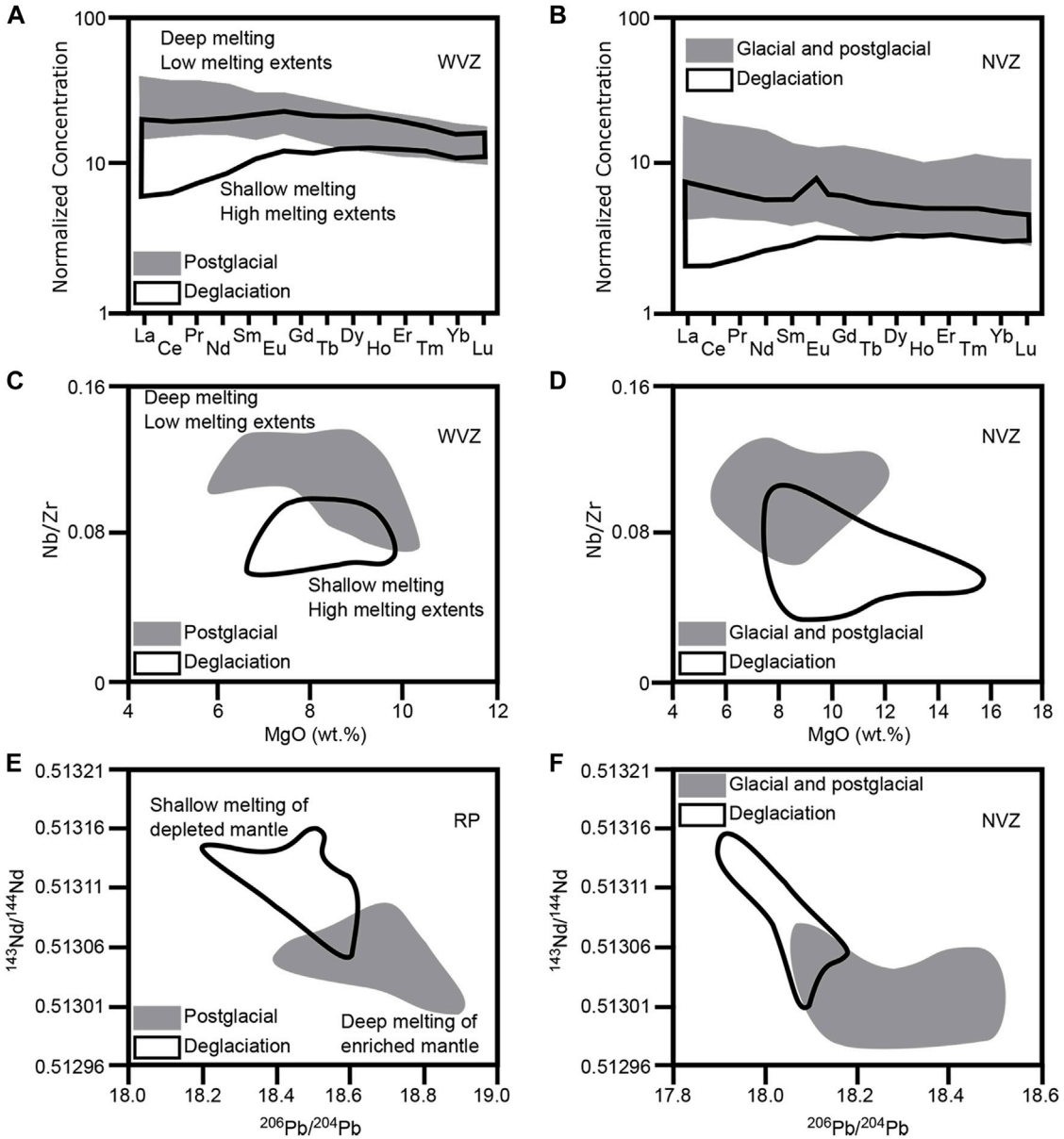

FIGURE 3 | Geochemical trends in lavas erupted during deglaciation compared to isostatic ice conditions. Deglaciation causes increased melting at shallow depths, generating melts that are depleted in Rare Earth Elements (REE), ratios of incompatible elements, and isotopes. **(A,B)** REE normalized to primitive mantle (McDonough and Sun, 1995) for Iceland's Western Volcanic Zone (WVZ; **(A)** and Northern Volcanic Zone (NVZ; **(B)**. **(C,D)** Trace element ratios as a function of MgO (wt %) for the WVZ **(C)** and NVZ **(D)**. **(E,F)** Nd and Pb isotopes for the Reykjanes Peninsula (RP; **(E)** and NVZ **(F)**. Gray fields represent lavas erupted during isostatic ice conditions (glacial and postglacial). Open fields represent lavas erupted during deglaciation. NVZ REE, trace element, and MgO data from Theistareykir from the compilation of Maclennan et al. (2002 and references in their Table 2, excluding picrites) NVZ isotope data from Theistareykir from the compilation of Sims et al. (2013 and references in their Table 1). WVZ REE, trace element, and MgO data from the compilation of Eason et al. (2015 and references in their Figure 4). RP isotope data from Gee et al. (1998).

Glacial Maximum the Icelandic ice sheet was at least 1 km thick on average (Hubbard et al., 2006; Le Breton et al., 2010). Those thicknesses were achieved over a period of ~90 ka suggesting an average accumulation rate of about 0.02 m per year. To generate a similar lithostatic load from sedimentation requires accumulation rates of about 0.01 m per year, or from volcanic activity about 0.009 m per year. In contrast, full destruction of those ice sheets seems to take place in less than 20 ka, and likely closer to 10 ka (Lambeck et al., 2014). Those time-scales suggest ice sheet "erosion" rates about one order of magnitude larger than the accumulation rates (~0.1 m per year). These "ablation rates" are significantly higher than those typically assigned to rates of erosion for most terrestrial environments (e.g., 0.0004 m/yr; Ferrier et al., 2007), or for rates of sea level rise during

deglaciations (e.g., 0.01–0.04 m per year after the Last Glacial Maximum; Lambeck et al., 2006). After some lag time following rapid interglacial sea level rise, high strain rates combine with increased lithospheric loads to induce crustal stress regimes that suppress dike initiation and cause eruptions to cease in marine-dominated environments (Satow et al., 2021). Thus, the characteristic slow loading rate and more rapid unloading rate of ice sheets can also be expected to impact magma source regions in glacial environments by altering the lithospheric stress conditions, influencing the depths and extents of melting, magma transport and storage processes, and pressure and temperature conditions of magma evolution (e.g., crystallization, devolatilization).

For areas where decompression melting is prominent like Iceland, lithospheric unloading has been suggested to change conditions within the mantle melting region and to produce distinctive geochemical signatures (Jull and McKenzie, 1996; Gee et al., 1998; Slater et al., 1998; Maclennan et al., 2002; Sinton et al., 2005; Sims et al., 2013; Eason and Sinton, 2015; Eksinchol et al., 2019). Compared to lavas erupted during isostatic ice conditions, lavas erupted during deglaciation tend to be depleted in radiogenic isotopes and incompatible trace elements (**Figure 3**). Geochemical modeling has shown that the extent of isotopic and incompatible element depletion observed in interglacial lavas cannot be explained by changes in magma chamber processes or mantle source composition (e.g., Maclennan et al., 2002). Instead, the geochemical trends are consistent with increased mantle melting and magma ascent rates from the shallow, isotopically and incompatible element-depleted part of the mantle (Harðarson and Fitton, 1991; Jull and McKenzie, 1996; Slater et al., 1998; Eksinchol et al., 2019). In some locations, the shift in melting conditions is also recorded in major element variations (Eason and Sinton, 2015). An additional impact of deglaciation on major elements, and other parameters controlled by crustal magmatic differentiation processes, can be expected because of the effects of unloading on crustal magma transport (Wilson and Russell, 2020). Rapid deglaciation creates local stress fields favorable for dike propagation, with the potential for erupting variably evolved magmas from a range of crustal depths (Wilson and Russell, 2020).

In volcanic arcs, the effects of glaciation on eruptive chemistry and volcanic output are more likely to be driven by changes in crustal stress and rheological conditions (Geyer and Bindeman, 2011). Several different groups have suggested that hydrothermal alteration weakens host rock and glacial loading and unloading produce changes in the crustal lithosphere stress field that inhibit or drive magma storage and transport (e.g., Jellinek et al., 2004; Geyer and Bindeman, 2011; Praetorius et al., 2016; Rawson et al., 2016; Wilson and Russell, 2020). Over long time-scales crustal loading may impede dyke formation and enhance sill production, while unloading favors dyke formation and enhances magma transport into the eruption region (Gudmundsson, 1986; Sigvaldason et al., 1992; Gee et al., 1998; Glazner et al., 1999; McLeod and Tait, 1999; Jellinek and DePaolo, 2003; Jellinek et al., 2004; Andrew and Gudmundsson, 2007; Albino et al., 2010; Wilson and Russell, 2020). The cyclic loading and unloading of ice ages can lead to "glacial pumping in magma-charged lithosphere" (Edwards and Russell, 2002; Wilson and Russell, 2020). Over short time-scales, the local stress field induced by the overlying ice sheet may interact with dyke orientation to enhance or reduce eruptive activity, thereby influencing crustal magma storage capacity (Hooper et al., 2011). Extended crustal residence times enhance magmatic differentiation by crystallization, assimilation, and mixing processes, thereby recording glaciation-driven events in lava geochemistry (Edwards et al., 2002; Asmerom et al., 2005; Wilson and Russell, 2020).

For magmas that are already close to a state of volatile saturation, rapid changes in lithospheric pressures during interstadial periods and deglaciations are of a magnitude that could drive vesiculation (Bindeman et al., 2010; Geyer and Bindeman, 2011). Sudden load removal caused by volcanic edifice destabilization and catastrophic flank collapse can force the system into a two-phase state, (Capra, 2006; Tormey, 2010; Capra et al., 2015). Rapid gravitational failure and volatile exsolution can potentially trigger an eruption or at the very least increase the eruptibility of the magma (Bindeman et al., 2010; Geyer and Bindeman, 2011; Sparks and Cashman, 2017). Separation of a volatile phase also can change the stability of crystallizing phases, and so the dynamicity of the cryospheric environment has the potential to indirectly alter the liquid line of descent for pre-existing magmas.

CRYOSPHERIC IMPACTS ON VOLCANO MORPHOLOGY

The imprint (**Figure 4**) of the cryospheric eruption environment is most visible and iconic at the edifice scale (**Figure 4**). Entire volcanoes in many parts of the world owe their distinctive morphologies to eruptions within ice while others have a more subtle morphological imprint including: anomalously steep cliffs of ice-dammed (i.e. overthickened) lavas, inverted topography caused by lava emplacement within ice-confined valleys, and characteristic resurfacing and reshaping of edifices due to ice erosion and buttress-destabilization (**Figure 4**). The morphology of tuyas and other cryospherically constrained volcanic edifices has been discussed in detail by several authors (Hickson, 2000; Smellie, 2009, 2018; Pedersen and Grosse, 2014; Russell et al., 2014; Pedersen, 2016), so here we only review the main elements that can be diagnostic of cryospheric environments.

Tuyas, less commonly referred to as "stapi" and "table mountains," are volcanoes whose overall morphology is a direct result of eruptions within confining ice (e.g., Mathews, 1947; Smellie, 2009; Pedersen and Grosse, 2014; Russell et al., 2014). These volcanic landforms have three distinct morphologies: 1) flat-topped platforms comprising laterally continuous, subhorizontal lavas commonly capping subaqueous lava-fed deltas (**Figure 4A**), 3) conical masses comprising palagonitized tephra and intrusions (**Figure 4B**), or 3) elongate ridges of subaqueous tephra and pillow lava (**Figure 4C**). A limited number of compound tuyas have been identified, particularly in British Columbia (**Figure 4D**). There, Kima'Kho tuya features a tephra cone onlapped by a platform of dipping beds of pillow lava breccias capped by horizontal sheets

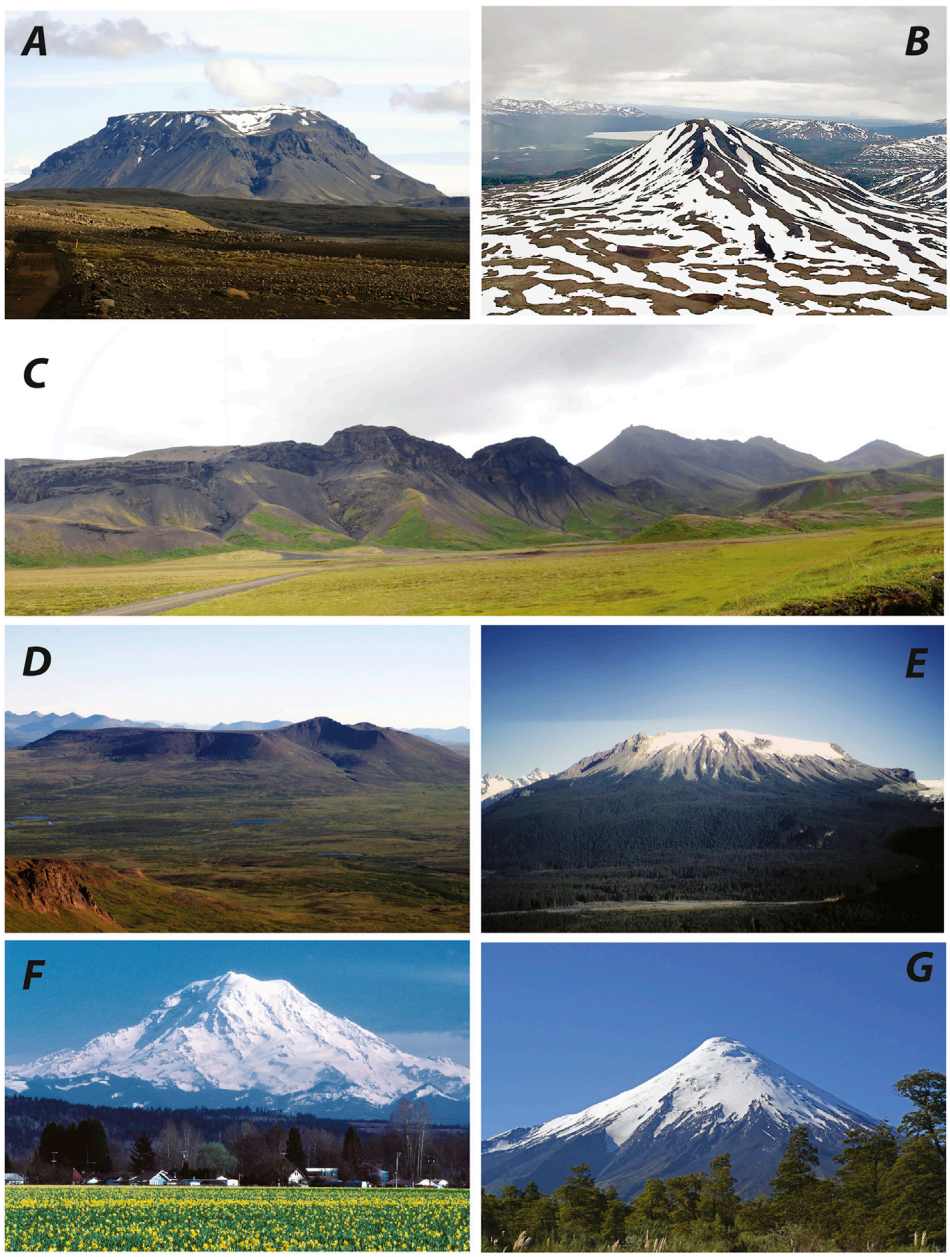

FIGURE 4 | Volcano morphologies diagnostic of cryospheric eruption environments. **(A)** Hlödufell, a flat-topped, basaltic tuya in the Western Volcanic Zone, Iceland. **(B)** South tuya, a conical, basaltic tuya in the Tuya area, British Columbia, Canada. **(C)** Kalfstindar, a basaltic tindar (a.k.a. linear tuya) in the Western Volcanic Zone, Iceland. **(D)** Kima 'Kho tuya, a compound, basaltic tuya on the Kawdy Plateau, British Columbia, Canada. **(E)** Hoodoo Mountain, a long-lived trachyte-phonolite tuya/stratovolcano, Coast Mountains, British Columbia, Canada. **(F)** Mount Rainier, an andesitic stratovolcano in the Cascade volcanic arc, Washington State, U.S.A. (Image courtesy of U.S.G.S. Cascade Volcano Observatory). **(G)** Osorno volcano, a basaltic stratovolcano in the Southern Andean Volcanic Zone, Chile. Unless specifically noted, all images in this and subsequent figures were taken by B. Edwards.

of lava (e.g., Mathews, 1947; Russell et al., 2021). Russell et al. (2014) advocated using the term "tuya" as a generic term to encompass all three morphologies and their combinations, while other authors have more nuanced views (e.g., Smellie, 2009). Recognition of these morphological elements as being unique to the cryospheric eruption environment has been critical for inferring the thicknesses and extents of paleo-ice-sheets on Earth and on Mars (Smellie and Edwards, 2016; Edwards et al., 2020). However, the unexamined assumption that a flat-topped volcano defines a cryospheric environment is problematical especially on not-yet-visited planets. At least in shallow water, the aquatic eruption environment can produce similar morphologies, with the best example being Surtsey volcano, located off the coast of south Iceland.

FIGURE 5 | Effects of ice on the 2010 Eyjafjallajökull eruption, south-central Iceland. Main view is from the north looking at the tephra-covered ice of Gigjökull and the summit of Eyjafjallajökull, with the canyon formed by meltwater and lava in the middle of the image. **(A)** An explosion crater in the summit ice partly filled with tephra. **(B)** An ice 'arch' remnant of an N-channel at the base of Gigjökull through which lava migrated beneath the ice. **(C)** The last stage of lava effusion was a subaerial, blocky lava emplaced into an ice canyon that confined the lava.

Longer-lived volcanoes have the capacity to span glacial-interglacial transitions such that only select morphological elements serve to record cryogenic periods of eruption (**Figures 4E–G**). At Hoodoo Mountain, a volcano in northwestern British Columbia that had eruptions spanning 100 k.y. (Edwards et al., 2002), the prominent cliffs that circumscribe much of the base of the edifice as well as its broad, gently rounded summit that still hosts a small ice-cap form a distinct, squat morphology (**Figure 4E**). Mount Rainier is a Cascade volcano with a morphology that is typical of andesitic stratovolcanos, however, its extended (500 k.y.) eruption history includes periods of ice-confined volcanic eruption which have not created obvious morphological elements reflecting its glaciovolcanic history (**Figure 4F**; Sisson et al., 2014). Detailed work by Lescinsky and Fink (2000), however, identified a number of lava ridges which they established as resulting from lateral impoundment by bounding glaciers. At more mafic long-lived volcanoes like Villarrica and Osorno, in central Chile, fluid lavas largely obscure the morphological influences of the cryogenic environment, where young volcanic cones and lavas are likely built upon older, glaciovolcanic deposits (**Figure 4G**).

CRYOSPHERIC IMPACTS ON VOLCANIC ERUPTIONS

The complex (**Figure 5**) influences of the cryospheric environment on volcanic eruptions has been well documented during several historic eruptions (e.g., 1980 Mount St. Helens, 1996 Gjálp, 2004 Grimsvötn, 2009 Redoubt, 2010 Eyjafjallajökull, 2012–13 Tolbachik; cf. Smellie and Edwards, 2016). Syn-eruption melting of the enclosing ice leads to dynamic pressure changes at the vent and in the environment as coherent icesheet transitions to fracturing and collapsing of the icesheet, and to a rising and falling column of meltwater. Observations on modern eruptions in the cryospheric environment show that the ice melting and formation of ephemeral englacial lakes can be rapid but are areally-limited so that volcanic deposits are largely confined by the enclosing ice (e.g., Jude-Eton et al., 2012; Magnusson et al., 2012; Oddsson, 2016). The linked 2010 Eyjafjallajökull and Fimmvorðuhals eruptions in Iceland are a clear example of this complexity during an essentially single, continuous volcano-magmatic event within the cryosphere (**Figure 5**).

The initial flank eruption of basalt at Fimmvorðuhals from mid-March to mid-April produced lavas that flowed across the top of a 3–5 m snowpack but eventually melted through snowpack to produce ice-confined lavas (Edwards et al., 2012). Locally however, a combination of thicker basal lava breccia and thicker snowpack resulted in several lavas crossing and remaining on top of the snow, even months after the eruption stopped. Just 1 day after the initial eruption ended on 13 April, the eruption shifted to the volcano summit and vented through the ~200 m thick summit glacier and produced at least three explosive craters (Magnusson et al., 2012; **Figure 5B**). One of these eventually enlarged to become the main vent for the eruption and was partly filled with scoria and course tephra. These initial explosive eruptions produced jökulhlaups that predominately passed

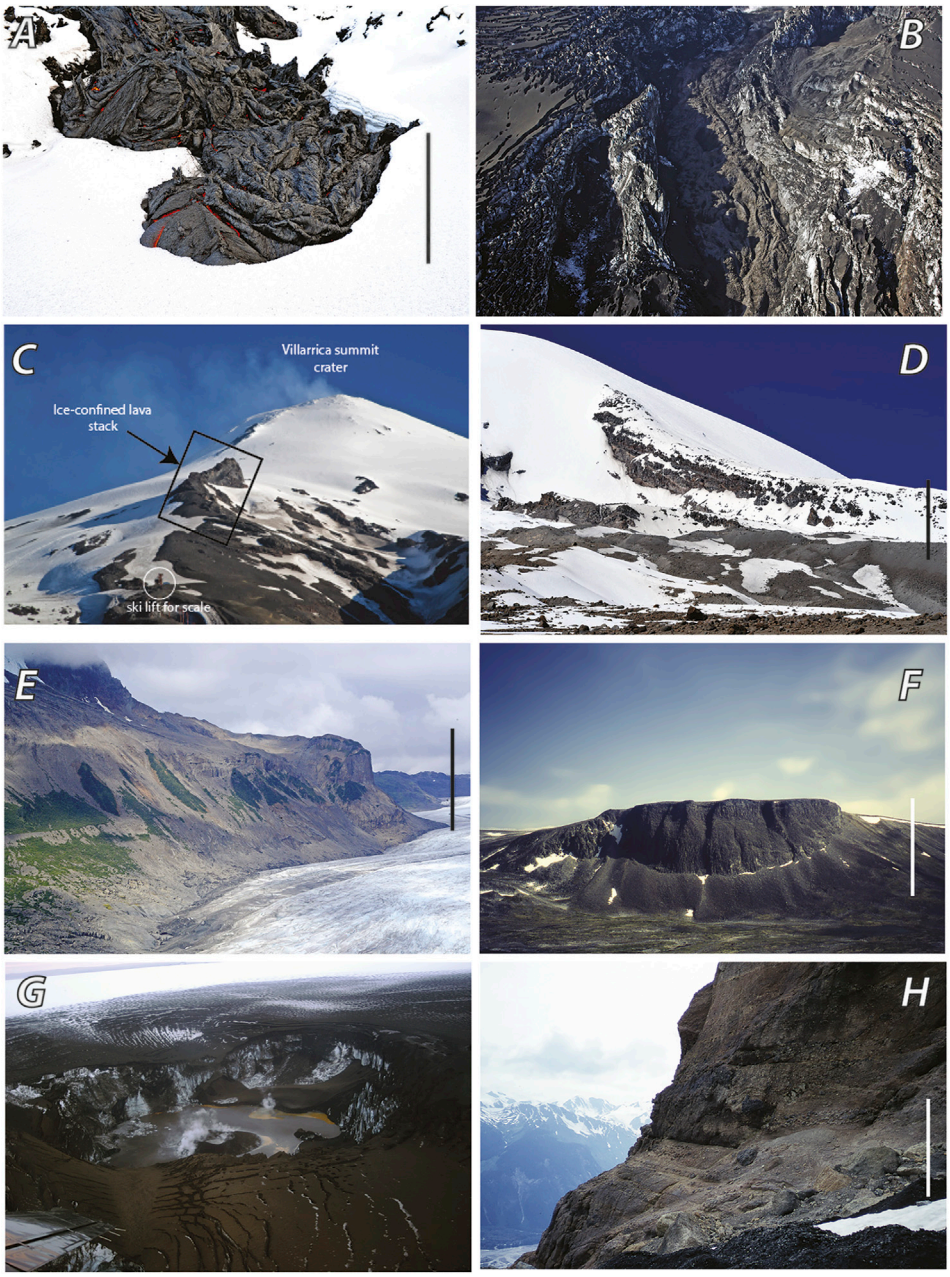

FIGURE 6 | Glaciovolcanic deposits whose structure and character are indicative of emplacement in a cryospheric environment. **(A)** Lava flow emplaced onto of snowpack, which subsequently melted through the snow, Tolbachik, Russia. **(B)** Lava confined within a canyon of ice, Gigjökull, Iceland. **(C)** Stacked lava ridge on the north summit of Villarrica volcano, Chile. **(D)** Stacked lava ridge on the western summit dome, Coropuna volcano, Peru. **(E)** Ice-bounded lava on the northeastern side of Hoodoo Mountain volcano, British Columbia, Canada. **(F)** Ice dammed lava at Llangorse Mountain, northern British Columbia, Canada. **(G)** Eruption site from 2004 Grimsvötn, Iceland, showing tephra covered glacier, englacial lake, and newly produced tephra cone. **(H)** Horizontally-bedded volcaniclastic deposits at 1500 m a.s.l. on the southern flank of Hoodoo Mountain volcano, British Columbia, Canada.

down the north side of the volcano, through Gigjökull, which is the largest outlet glacier on the north side of Eyjafjallajökull. These initial floods likely exploited and enlarged the pre-existing subglacial drainage N- and R-channels. Between 18 April and 4 May, continued summit explosive eruptions were accompanied by lava effusion. The lavas initially flowed beneath the surface of Gigjökull, exploiting the same R- and N-channels that had been enlarged by meltwater (Oddsson et al., 2016; **Figure 5C**). Later "subaerial" lava flowed down a narrow, ice-confined channel through Gigjökull (**Figure 5D**). Distinctive textures of the lava emplaced beneath the ice, including thick outer vitric rinds and highly fractured surfaces, are interpreted to be indicative of an

external "coolant" (Oddsson et al., 2016). This single event produced: 1) proximal and distal tephra airfall deposited on land, neighbouring glaciers, and in the ocean, 2) tephra syn-eruptively entrained and transported by meltwater flowing beneath Gigjökull glacier and by the Markarflöt River, 3) lava emplaced on top of snowpack, 4) lava emplaced within tunnels at the base of Gigjökull, and 5) lava emplaced subaerially within an ice canyon.

Outstanding questions concern how the cryospheric environment impacts magma fragmentation and explosivity. Recent work on eruptions in aqueous (englacial) environments by Rowell et al. (2021) suggests that magma-water interactions can produce more energetic eruption columns. As discussed above, the presence of ice and water can increase rates of heat transfer from the magma (and its fragments) to its environment. The accelerated cooling causes rapid increases in melt viscosity to the point of the glass transition temperature where brittle behaviour dominates over ductile. The thermal stresses within volcanic glass raised by rapid heat extraction provides a means for efficient particle fragmentation. Liquid water trapped within low permeability deposits at high-temperature is easily vaporized causing explosive fragmentation driven by expansion of the gas phase (e.g., Dürig et al., 2020).

CRYOSPHERIC IMPACTS ON VOLCANIC LITHOFACIES

The cryospheric (**Figure 6**) eruption environment exerts a pronounced control on the properties, geometries and distributions of volcanic lithofacies. Salient summaries and descriptions of characteristic glaciovolcanic lithofacies are provided by Smellie (2000), Edwards et al. (2014), Russell et al. (2014), and Smellie and Edwards (2016), as well as, in many deposit-specific studies. Here we limit our discussion to the main elements that are diagnostic of eruptions in the cryosphere (**Figure 6**). These features include anomalous deposit morphologies and properties that reflect confinement, anomalous high rates of cooling (i.e. quenching), and, especially, the presence of a standing body of meltwater in a physiographically implausible location. Most of these deposits show evidence for complicated cooling histories involving variable rates and directions of heat transfer.

Evidence for confinement of the distributions of lavas and volcaniclastic deposits is the signatory of the cryospheric eruption environment. This impoundment can be recorded by deposit geometry, distribution, and other properties. While snow and ice can temporarily support the mass of an overlying lava (**Figure 6A**), heat transfer from the base of the lava eventually leads to the lavas sinking into the cryospheric cover (**Figure 6B**). This has been well documented at historic eruptions in Iceland (Edwards et al., 2012) and in Russia (Edwards et al., 2015). Horizontal to shallowly-dipping sequences of lava perched near the summits of stratovolcanoes have been uniquely interpreted as resulting from ice confinement (Lescinsky and Fink, 2000; **Figures 6C,D**). Impoundment or confinement commonly results in overthickened lavas, which is especially evident for low viscosity lava (i.e., phonolite, basalt, nephelinite, basanite; Harder and Russell, 2007; **Figures 6E,F**) but also found in intermediate composition glaciovolcanic lavas. The extreme case of ice-confined effusive volcanism leads to the formation of lava-dominated tuyas (Kelmen et al., 2002; Wilson et al., 2019; Hodgetts et al., 2021). The key to interpreting these features as having formed in a cryospheric environment depends on there being no logical present-day physiographic explanation for confinement of the flow of lavas.

On a per volume basis most silicate melts release enough heat through cooling to melt about 3–10 times an equivalent volume of ice. Regardless, ice can effectively impede the flow of lava for two main reasons. Firstly, the continuous unimpeded flow of lava would require the volumetric rate of ice melting to match the eruptive flux. Although the heat content of lava is more than sufficient to melt the ice, the time scales of heat transfer from lava to ice are too slow relative to most effusive fluxes. Edwards et al. (2012) showed that lavas can flow onto and across the top of snow or ice with little melting for all but the very slowest-moving flows. This has also been demonstrated experimentally (Edwards et al., 2013), and observed at a number of eruptions (e.g., 1947 Hekla, Einarson, 1949; 2010 Fimmvorðuhals, Edwards et al., 2012; Edwards et al., 2013 Tolbachik, Edwards et al., 2015). Secondly, cooling the fronts and sides of advancing lava causes a reduction in temperature and a marked increase in viscosity causing a decrease in velocity and thickening of the lava front. The cooler lava is an insulator preventing efficient heat transfer from the hot lava interior to ice (Wilson and Russell, 2020). The main difficulty in using "overthickened" lavas as indicators of ice-confinement is that we lack coherent global databases that document the range of thicknesses for lavas associated with subaerial eruption environments.

Volcaniclastic deposits can also show the effects of confinement by their geometry and distributions and, thus, can also be indicative of cryospheric environments. The main features that are likely to be preserved from volcaniclastic/pyroclastic deposits are found proximally. More distal or dispersed deposits that populate the ice surface at the time of eruption are likely to be lost, or to be transported within ice from the eruption site. Deposits that accumulate within the cauldron overlying the vent will have limited distributions (<1 km; **Figure 6G**); they may have subhorizontal bedding even when present topography is steeply sloped (**Figure 6H**) or presumably over-steepened bedding if deposited abutting an ice wall. Either way, the preserved deposits will have geometries that show little thinning with distance from the vent and terminate with anomalous thicknesses and/or geometries (e.g., Smellie, 2000).

Polygonal/columnar jointing is an important volcanological feature that occurs in a wide variety of deposits (e.g., lavas, dykes, and ignimbrites) and provides a record of paleo-cooling history (e.g., Long and Wood, 1986; Goehring and Morris, 2008; **Figure 7**). Cooling-induced joints inform on the transient rates and directions of heat flow; column diameter is inversely proportional to cooling rate and the column orientation (length) indicates heat flow direction.

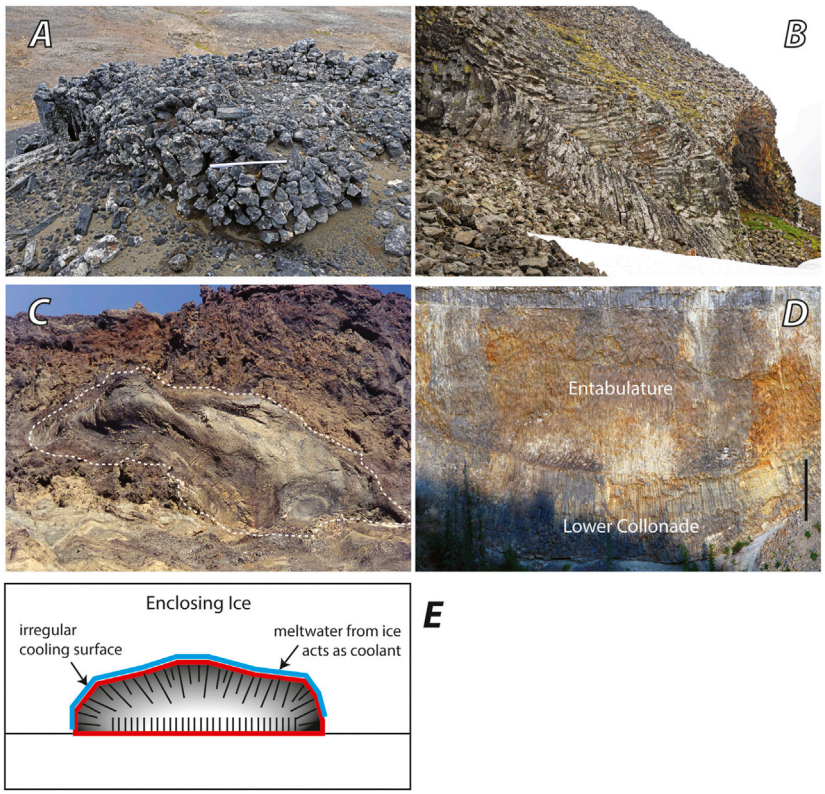

FIGURE 7 | Polygonal jointing examples from glaciovolcanic deposits. **(A)** Anomalously small columnar joints in basaltic lava at Breidravirki tindar, Iceland. **(B)** Highly-jointed mass of trachyte within breccia carapace at Hoodoo Mountain volcano, British Columbia. Jointing is vertical at the contacts between lava and breccia, but is rotated through 90 degrees such that it is horizontal in the middle. **(C)** Radiating joints in ice-confined lava from Mathews Tuya, British Columbia. **(D)** An example of typical polygonal jointing in a subaerial lava from northern British Columbia, with vertical joints in the basal colonnade and irregular joint orientations in the overlying entabulature. **(E)** Schematic drawing illustrating joint orientations in a lava emplaced into ice.

In subaerial environments, cooling columns are commonly well-organized into a lower and upper colonade that are oriented perpendicular to cooling surfaces (i.e., ground, valley walls, and etc.). The colonnades are sometimes separated by an entabulature comprising subvertically-oriented columns with a limited range in sizes (**Figure 7D**). In cryogenic environments, columnar jointing is much more varied and, in many cases, can be diagnostic, or provide supporting evidence, of that environment (e.g., Lescinsky and Fink, 2000; Edwards and Russell, 2002; Lodge and Lescinsky, 2009; Forbes et al., 2014). Lavas cooled in glaciovolcanic settings commonly feature fine-scale columns (cube shaped or small diameter columns; **Figure 7A**) that are indicative of rapid cooling. Column orientations are also commonly diagnostic. In many glaciovolcanic deposits the axes of columns populating the cliff faces of lavas are subhorizontal indicating efficient and sustained heat transfer outwards to a surface that is no longer there (**Figure 7B**). Given the settings and geography of these deposits, at relatively high elevations and/or latitudes, the obvious candidate for the missing confining material is a mass of ice, which explains the anomalous thickness of lava and orientations of columnar joints. In other situations, glaciovolcanic lava masses have radiating and curving clusters of columnar joints (i.e., lobes or channels; **Figure 7C**). Commonly the columns also show a well-organized gradual increase in diameter moving from the exterior surface inwards. The size gradation is a record of relative rates of heat transfer at the moment of columnar joint propagation and shows that heat loss is most efficient on the exterior surface and significantly slower in the interior of the lava mass. The radiating cluster of columns indicates that the exterior surface lava mass was cooling rapidly in all directions and heat was transferred efficiently to an enveloping medium (**Figure 7E**). The sometimes observed inward-curving character of the columns shows how the heat transfer direction changed as the columns propagated inwards from the exterior surface.

Eruptions within ice sheets lead to rapid melting and collapse of the overlying ice and commonly produce an englacial lake whose depth is dictated by the amount and rate of melting, the flux of volcanic material, the rate of sub-ice leakage, and the thickness of the confining ice (e.g., Russell et al., 2021). Eruptions into a standing body of water result in distinctive volcanic lithofacies that can be diagnostic, while not definitive, of the cryospheric environment including: pillow lava, pillow-lava breccias, hyaloclastite, peperitic dykes, lava-fed deltas, and pervasive and variable palagonitization of the deposits (cf. Smellie and Edwards 2016 for summaries and references). Pervasive palagonitization requires abundant vitric material, water and heat. Melting of enclosing ice produces abundant

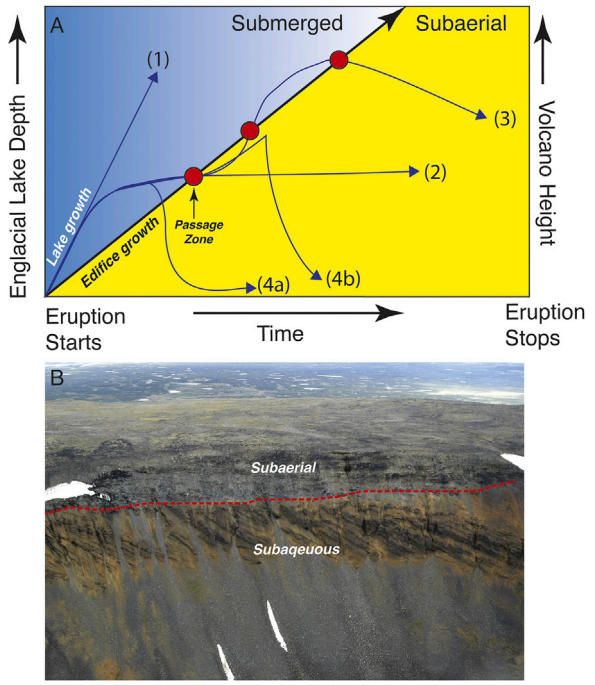

FIGURE 8 | (A) Schematic diagram showing competing rates of growth for an eruption-generated, englacial lake and the growth of the corresponding volcanic edifice. The numbered lines show different paths for the changing lake depth relative to edifice growth: (1) lake depth always outpaces growth of edifice; (2) lake depth initially outpaces edifice but eventually stagnates; (3) relative lake depth and edifice growth repeatedly switch; (4) lake depth initially outpaces edifice growth, then slows allowing edifice to become emergent prior to cataclysmic draining of lake. **(B)** Example of a passage zone from Kima 'Kho tuya, northern British Columbia (Russell et al., 2021).

heated water, and, because the deposits are largely confined to the vent area by enclosing ice, cooling is less efficient. Additionally, dykes are commonly found within palagonitized glaciovolcanic deposits, and their emplacement into the tephra is another source of heat as the dykes cool and solidify, helping to maintain higher temperatures within the tephra pile (e.g., Edwards et al., 2009; Harris Russell, 2022).

Taken individually, most of these lithofacies are not exclusively diagnostic of glaciovoclanism but they clearly demand an aquatic environment and are strong evidence for a standing body of water. The key, as seen at many tuyas, is having multiple lines of evidence for a substantial (deep) standing body of water in situations where there is clearly no obvious means to create and sustain such a lake. Collectively these observations provide the evidence for a cryospheric eruption environment (e.g., Smellie and Edwards, 2016; Smellie, 2018).

DISCUSSION

When compared to subaerial and subaqueous environments, the cryospheric environment is the most dynamic and complex. This is well-illustrated in two examples. Firstly, by an examination of the stability and dynamics of syn-eruptive englacial lakes of melt water formed during glaciovolcanic eruptions (cf. Smellie and Edwards, 2016; Russell et al., 2021). Secondly, by an analysis of how changes in pressure during eruptions can impact vesiculation and vesiculation induced fragmentation.

Dynamic Self-Regulation of Englacial Lakes

The englacial lakes produced during glaciovolcanic eruptions are ephemeral—they rise in depth as they fill with meltwater but are regulated by background leakage via sub-ice drainages systems or susceptible to catastrophical drainage events when water pressures exceed the ice load pressure. Additionally, as englacial lakes form and grow during an eruption they are filling not only with meltwater, but also with a rapidly aggrading volcanic edifice. The competition between inputs of water and volcanic materials can produce a range of conditions that have different consequences for both (**Figure 8A**). For example, some glaciovolcanic pillow ridges (also referred to as "tindar"; see **Figure 4C**) in Iceland and in British Columbia formed during eruptions where the increase in edifice height was much slower than the rise in the enclosing englacial lake such that the edifice was totally emplaced subaqueously (e.g., Pollock et al., 2014; Edwards et al., 2009; **Figure 8A** path 1). A second, relatively common scenario is expressed by the iconic, flat-topped tuya volcanoes that have been studied in detail in Iceland (see **Figure 4A**; e.g., Jones, 1969; Skilling, 2009; Pedersen and Grosse, 2014), British Columbia (Mathews, 1947; Hickson,2000; Moore, 1970; Edwards et al., 2012), and the Antarctic (Smellie, 2009). During these eruptions, the lake surface elevation remains higher than the growing edifice, producing subaqueous facies deposits, until at some point where the edifice becomes emergent and commonly creating a cap of horizontal subaerial lavas (**Figure 8A** path 2). The stratigraphic surface produced when the edifice breaches the lake surface is referred to as a "passage zone" (Jones, 1969). Locally, the competition between water and volcanic materials is clearly demarcated by passage zones (**Figure 8B**). Passage zones are diachronous, stratigraphically-defined surfaces that record subaqueous-subaerial transitions during volcanic eruptions that start subaqueously but later transition to subaerial conditions (e.g., Fuller, 1931; Werner and Schmincke, 1999; Nelson, 1975; Smellie, 2009; Mathews, 1947; Jones, 1969; Smellie and Edwards, 2016; Russell et al., 2021). In the cryospheric environment, passage zone surfaces provide records of the heights and depths of syn-eruptive englacial lakes of meltwater at a specific point in time and space (see detailed review and references in Russell et al., 2021). Thus, they also help document the presence and nature, including minimum thickness, of the enclosing ice sheet. All passage zones are diachronous and, thus, document dynamic changes in lake levels through time (Smellie, 2000; Russell et al., 2014). For example, gradients in passage zone elevations record the rates of rise and fall in englacial lake levels relative to the rates of edifice growth (Russell et al., 2014; **Figure 8A**). Volcanoes having similar morphological features have long been postulated to occur on Mars (Allen, 1979).

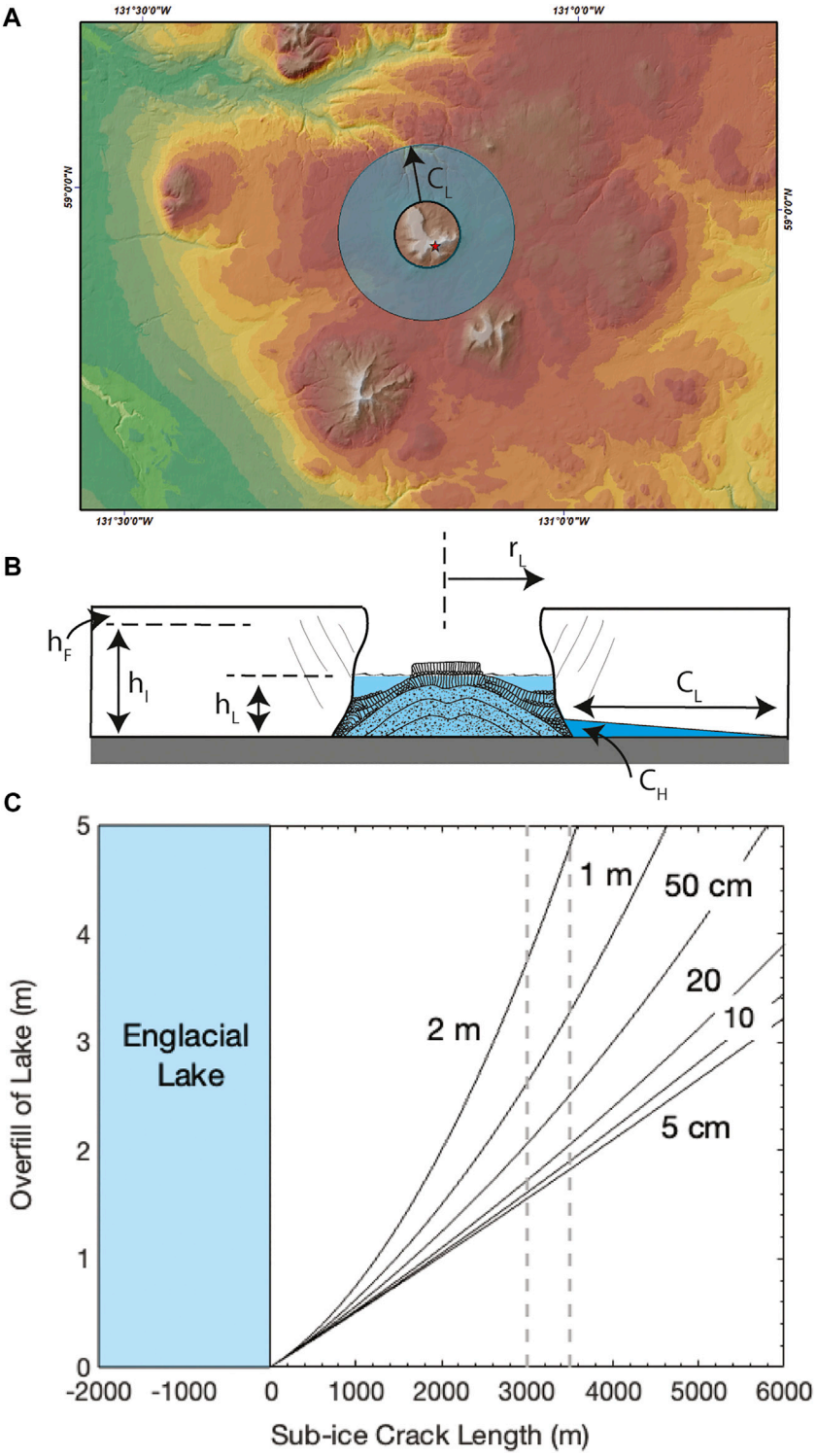

FIGURE 9 | Model for growth and radial propagation of sub-ice crack linked to major drainage systems driven by overfilling of syn-eruptive englacial lake. **(A)** Geometric sketch of model for predicting length (*CL*) of sub-ice wedge-shaped cracks as a function of ice and lake dimensions. **(B)** Model values of crack length versus overfill of lake above an equilibrium depth and contoured for the maximum opening of the crack near the englacial lake. **(C)** The major drainages on the Kawdy plateau surrounding the Kima Kho volcano are less than 3–3.5 km from the vent. The model curves show that very slight rises in lake level would be capable of supporting opening and propagation of sub-ice cracks that intersect those drainages. Conservative initial crack openings of 10–20 cm would find such drainages with only a 1–2 m rise in lake level over its equilibrium height.

In a few cases, the competition between edifice growth and lake deepening is complex, and multiple passages zones can form (**Figure 8A** path 3; e.g., Smellie, 2009; Skilling, 2009; Russell et al., 2014, Russell et al., 2021). A final general path that is less frequently identified is one where, at some point in the eruption, the lake drains catastrophically, which is referred to as a "jökulhlaup." These sudden drainage events are well documented during eruptions at Grimsvötn in Iceland, although not all jökulhlaups originate during or because of volcanic activity (Gudmundsson et al., 2008). Syn-eruptive jökulhlaups have been postulated at volcanoes that were still subaqueous when the drainage event happened (**Figure 8A** path 4a; Hoskuldsson et al., 2006; Owen et al., 2012), as well as for subaerial ones (**Figure 8A** path 4b; Russell et al., 2021).

Russell et al. (2021) recently described a sequence of passage zones within a single glaciovolcanic edifice thereby providing a temporal (relative) record of changes in the depth and volume of the ice-impounded lake during the eruption. Kima' Kho tuya is a highly dissected, large volume (~3.5 km^3; 3 times the volume of Surtsey) basaltic glaciovolcano situated in northwestern British Columbia and covering an area of ~21.0 km^2 (**Figure 9A**). The edifice has a maximum elevation of ~1,957 m above sea level (masl) and a relief of ~490 m above the Kawdy Plateau (~1,460 ± 20 masl). The distribution of volcanic lithofacies indicate that the volcano was enclosed by a >400 m thick glacier and erupted into an ice-confined (englacial) lake having a radius of ~2. The three passage zones ($Pz_{1\text{-}3}$) record the transient levels (i.e. elevation) of the englacial lake caused by syn-eruptive melting of the enclosing ice sheet and subsequent leakage and drainage.

We assume that progressive melting of the enclosing ice sheet resulted in a cylindrical cauldron. The initial (and maximum) lake level attending the explosive phase of eruption is marked by a passage zone situated at 1,800 masl indicating a englacial lake depth of ~340 m. The lake stored a peak water volume of ~2.3 km^3, which also accounts for the submerged volume of the tephra cone (~2.0 km^3). The passage zone is horizontal and extends over 1–2 km (see **Figure 8B**) suggesting a long-lived, stable configuration where lake volume and height were maintained as the eruption transitioned from explosive to effusive. This implies that the increase in water by melting or increase in lake volume by edifice displacement, is balanced by the ambient rates of subglacial drainage for an extended period. Drainage beneath the ice during the initial phase of the eruption must have been limited to allow for storage of meltwater and growth of the englacial lake. However, the fact that the lake level did not rise above 1,800 masl, despite >2 km^3 of surplus meltwater (i.e. over the ~2.3 km^3 stored in the lake), implies a leaky englacial lake system (Russell et al., 2014).

Kima 'Kho tuya formed within the Cordilleran ice sheet at about 1.9 Ma (Edwards et al., 2020; Russell et al., 2021). Ice sheets commonly feature 10s of metres of firn at their surface (Cuffey and Paterson, 2010), which is a more permeable than compacted snow pack but much less so than glacial ice (h_I). In certain situations, firn offers a means of supraglacial draining of meltwater that can modulate englacial lake depth (e.g., Smellie, 2018). However, ice sheets over a certain total thickness (h_T) will never have lake levels high enough to intersect the firn. The maximum volume of meltwater available for the englacial lake (V_L) assuming no loss by subglacial leakage is:

$$V_L = 0.9\,\pi\,(h_I + h_F)\,r_L^2$$

Drainage through the firn requires:

$$V_L \geq \pi\,(h_T - h_F)\,r_L^2$$

implying that supraglacial drainage through the firn can only occur where:

$$h_F \geq 0.1\,h_T$$

Firn thickness (h_F) can vary from 40–120 m in which case firn drainage is limited to ice sheets that have total thicknesses ($h_T = h_I + h_F$) less than 400–1,200 m, and where all of the melt water produced in the eruption is stored and not lost to leakage or syn-eruption evaporation.

One explanation for the apparent long-lived, stable configuration of the initial englacial lake at Kima 'Kho tuya is that, at an elevation of 1,800 masl, the lake depth of 340 m was in hydraulic balance with the ice sheet. Subglacial drainage of meltwater was minimal and controlled by the permeability of the enclosing ice and the nature of the basal interface between the ice sheet and its substrate. In this situation, the water column within the englacial lake exerts pressure at the base of the ice sheet that is less than or equal to the overlying load of the ice.

Evidence presented by Russell and Edwards. (2021) is consistent with a cataclysmic drainage event for the initial englacial lake formed during the eruption. At this tuya the lake refilled and produced two later passage zones, which raises the question of what triggered the jökulhaup. Water pressure in the lake has the capacity to lift the base of the enclosing ice wall and fill any cracks or fissures localized at the basal contact between the ice sheet and its substrate. If the system was near equilibrium or the hydraulic pressure was slightly in excess of the glaciostat, small excursions in lake level could trigger major drainage events. These jökulhaups would be catalyzed by propagation of sub-ice, water-filled cracks that intersect major pre-existing sub-glacial drainage systems. The additional head from "overfilling" of the lake (i.e. > 1,800 masl) needed to support filling of sub-ice cracks that could find and exploit pre-existing major drainages proximal to the Kima Kho volcano (**Figure 9A**) can be estimated by considering a right-angled radial wedge-shaped crack as illustrated (**Figure 9B**) with a total volume (V_c) of:

$$V_c = \frac{1}{2}\pi\,C_H\,\left[C_L^2 + 2\,C_L\,r_L\right]$$

where r_L is the radius of the englacial lake, C_H is the maximum opening of the crack (near the vent), and C_L is the length of the 3-D crack body. The additional volume added to the lake (V_L) that provides the additional head for filling the crack is:

$$V_L = \pi\,\Delta_L r_L^2$$

where Δ_L is the rise in lake level (m). The balance between overfilling of the lake and filling the crack therefore is:

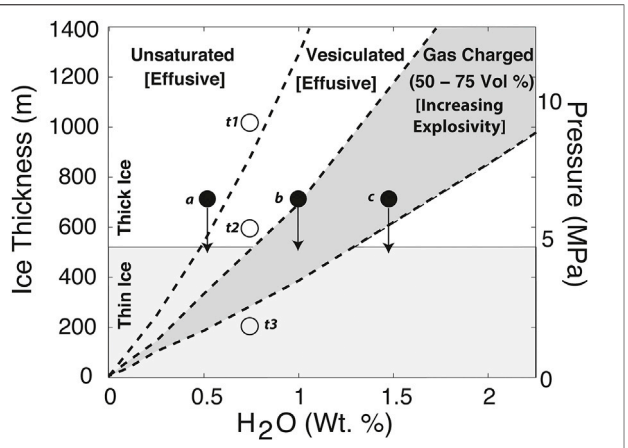

FIGURE 10 | Graph of initial magma water concentrations plotted against Pressure (right axis) and corresponding Ice Thickness (modified from Edwards et al., 2015). Solid circles (black) with arrows show effects and consequences resulting from a 2 MPa pressure drop. Open circles show three different possible emplacement pressures for the same magma.

$$V_L > V_c$$

and as an equality:

$$\pi \, \Delta_L \, r_L^2 = \frac{1}{2} \pi \, C_H \, \left[C_L^2 + 2 \, C_L \, r_L \right]$$

Values of C_L can be solved for from the quadratic expression:

$$C_L^2 + 2 \frac{r_l}{C_H} C_L + \frac{2 \, \Delta_L \, r_L^2}{C_H} = 0$$

which depends on the radius of the englacial lake, the rise in stable lake level, and the initial crack thickness (**Figure 9B**).

This simplified analysis shows that, at least in the landscape near Kima 'Kho tuya, only small volumes of the englacial lake water are needed to produce and fill crack openings (0.1 cm–1 m; **Figure 9C**) that could "find" pre-existing drainage networks (minimum of 3 km at Kima 'Kho; **Figure 9A**), thereby preventing lake overfilling and potentially triggering jökulhaups. This crack propagation process can enable englacial lakes to remain in dynamic equilibrium with their enclosing ice, leading to lake level fluctuations only found in the cryospheric eruption environment.

Dynamic Transitions in Vesiculation and Fragmentation

As illustrated above, the cryospheric eruption environment can produce repeated changes, slow or rapid, in vent conditions due to differences in englacial lake water levels. These changes can also change the state of vesiculation in a magma and lead to shifts from effusive to explosive activity. As for all volcanic eruptions, one of the main controls on explosivity during glaciovolcanic eruptions is the relationship between external pressure and the magma's volatile solubility (**Figure 10**; Owen et al., 2012; Edwards et al., 2014). In general, high glaciostatic/hydrostatic pressures (i.e. thick ice) and "dry" magmas favor effusive eruptions, while lower pressures (i.e. thin ice) and "wet" magmas favor explosive eruptions. Thus, even some "thick" ice eruptions may initially be explosive, which favors high heat transfer efficiencies, rapid melting, and more dangerous jökulhlaups (Gumundsson, 2003). During glaciovolcanic eruptions, the effective pressure is complicated by the nature of the ice "overburden," which melts and fractures as the eruption proceeds. The presence of meltwater also affects eruption style by promoting "quench" fragmentation during effusive eruption, as well as phreatomagmatic explosivity driven by shockwave breakup of the magma followed due to rapid expansion of trapped liquid water being converted to steam. The relative importance of quench, phreatomagmatic, and magmatic fragmentation will ultimately depend on the unique magmatic and glacial conditions for any given eruption, but during eruptions in the cryospheric environment as they be produced repeatedly, leading to complex stratigraphies and grain componentry (e.g., Schopka et al., 2006; Jude-Eton et al., 2012).

Two different aspects of the cryospheric environment have important controls on the state of vesiculation, hence, eruption styles and properties of tephra. Firstly, the waxing and waning of continental ice sheets has occurred over varying time-scales during the Pleistocene (Cuffey and Paterson, 2010). The pre-1 Ma cycles spanned approximately 40 ky, and the more recent post-1 Ma cycles span about 100 ky. These time-scales are shorter than the lifespan of polygenetic glaciovolcanoes (e.g., Hoodoo Mountain; many stratovolcanoes), which means that repeated eruptions from the same edifice will likely not always occur under the same glaciostatic pressures. So, even if the source magmas remain relatively constant in composition with respect to dissolved volatiles, eruptions under different ice conditions will produce deposits with different vesicularities and also potentially different eruption styles. For example, for a magmatic system with 0.75 weight percent dissolved H_2O, a cryospheric eruption during a glacial maxima (~1,000 m of ice) might be effusive (t1, **Figure 10**), while the same eruption during different stages of ice thickening or thinning could be effusive but with a vesiculated magma (t2, **Figure 10**) or explosive (t3, **Figure 10**). Secondly, rapid changes in pressure such as those seen periodically by drainage of englacial lakes in Iceland (e.g., Grimsvötn) are more than sufficient to drive magmatic systems into different eruption states. Given three different magmas each with different concentrations of dissolved H_2O (**Figure 10**, points a, b, c), a 2 MPa drop in pressure due to catastrophic lake drainage can change the magma state from effusive undersaturated to saturated and vesicular (**Figure 10** point a), from effusive vesiculated to highly vesiculated (**Figure 10** point b), or from effusive vesiculated to explosive (**Figure 10** point c).

SUMMARY

Volcanic eruptions within cryospheric environments are controlled by all of the variables and conditions found in subaerial and subaqueous eruption environments save, perhaps, the conditions attending deeper submarine eruptions (Cas and Simmons, 2018). Vent systems can be repeatedly flooded by meltwater, and then drained. Initial stages of eruption are most influenced by environmental confinement but

sustained larger eruptions can evolve to support the more long-distance transport of tephra generally attributed to explosive subaerial eruptions (e.g., Eyjafjallajökull 2010). The unique characteristics of these deposits are key to recognizing their glaciovolcanic origins and provide the means to constrain the syn-eruptive cryospheric environmental conditions (e.g., depth of water, ice thickness). Given the wide-spread distribution of these deposits throughout the Plio-Pleistocene, they remain one of the largest land-based archives available for reconstructing past ice extents, thicknesses and hydrologies on Earth, as well as, other planetary bodies (Smellie and Edwards, 2016; Smellie, 2018; Edwards et al., 2020; Wilson and Russell, 2020). Because the it can change over relatively short time-scales, its englacial lakes can be highly dynamic, and eruptions within the it can transition to subaqueous and subaerial environments repeatedly, the cryospheric environment is the most complex eruption environment for volcano-magmatic systems.

AUTHOR CONTRIBUTIONS

BRE conceptualized the collaborative project. All three authors contributed figures, written text, ideas to the discussion, and participated in preparation of the final manuscript.

FUNDING

Images and concepts presented here are derived from work completed by BRE while funded by the Moraine Foundation, National Geographic Committee for Research and Exploration Grants 9152-12 and 9714-15, U.S. National Science Foundation Petrology and Geochemistry Division EAR grants 1220403 and 0910712, U.S. NSF EAR RAPID grants 1039461 and 1321648. JKR was supported by Discovery grants program of the Natural Sciences and Engineering Research Council of Canada (NSERC). Data and concepts presented here were partly derived from work completed by MP while funded by U.S. National Science Foundation Petrology and Geochemistry Division EAR grant 1220176.

ACKNOWLEDGMENTS

We have benefited by many conversations with too many colleagues to name, but those with J. Smellie, M. Gudmundsson and A. Wilson and two reviewers have been particularly inciteful.

REFERENCES

Albino, F., Pinel, V., and Sigmundsson, F. (2010). Influence of Surface Load Variations on Eruption Likelihood: Application to Two Icelandic Subglacial Volcanoes, Grímsvötn and Katla. *Geophys. J. Int.* 181 (3), 1510–1524.

Andrew, R. E. B., and Gudmundsson, A. (2007). Distribution, Structure, and Formation of Holocene Lava Shields in Iceland. *J. Volcanol. Geotherm. Res.* 168, 137–154. doi:10.1016/j.volgeores.2007.08.01110.1016/j.jvolgeores.2007.08.011

Asmerom, Y., DuFrane, S. A., Mukasa, S. B., Cheng, H., and Edwards, R. L. (2005). Time Scale of Magma Differentiation in Arcs from Protactinium-Radium Isotopic Data. *Geology* 33 (8), 633–636. doi:10.1130/g21638ar.1

Belousov, A., Belousova, M., Edwards, B., Volynets, A., and Melnikov, D. (2015). Overview of the Precursors and Dynamics of the 2012-13 Basaltic Fissure Eruption of Tolbachik Volcano, Kamchatka, Russia. *J. Volcanol. Geotherm. Res.* 299, 19–20. doi:10.1016/j.jvolgeores.2015.04.009

Bindeman, I. N., Leonov, V. L., Izbekov, P. E., Ponomareva, V. V., Watts, K. E., Shipley, N. K., et al. (2010). Large-volume Silicic Volcanism in Kamchatka: Ar-Ar and U-Pb Ages, Isotopic, and Geochemical Characteristics of Major Pre-holocene Caldera-Forming Eruptions. *J. Volcanol. Geotherm. Res.* 189, 57–80. doi:10.1016/j.jvolgeores.2009.10.009

Capra, L., Roverato, M., Groppelli, G., Caballero, L., Sulpizio, R., and Norini, G. (2015). Glacier melting during lava dome growth at Nevado de Toluca volcano (Mexico): Evidences of a major threat before main eruptive phases at ice-caped volcanoes. *J. Volcanol. Geotherm. Res.* 294, 1–10. doi:10.1016/j.jvolgeores.2015.02.005

Capra, L. (2006). Abrupt Climatic Changes as Triggering Mechanisms of Massive Volcanic Collapses. *J. Volcanol. Geotherm. Res.* 155 (3), 329–333. doi:10.1016/j.jvolgeores.2006.04.009

Cas, R. A. F., and Simmons, J. M. (2018). Why Deep-Water Eruptions Are So Different from Subaerial Eruptions. *Front. Earth Sci.* 6. doi:10.3389/feart.2018.00198

Clague, J. J., and Ward, B. (2011). "Quaternary Glaciations–Extent and Chronology: A Closer Look," in *Chapter 44–Pleistocene Glaciation of British Columbia*. Editor J. Ehlers, P. L. Gibbard, and P. D. Hughes (United Kingdom: Elsevier, Developments in Quaternary Sciences Series) 15, 563–573. doi:10.1016/B978-0-444-53447-7.00044-1

Cuffey, K. M., and Paterson, W. S. B. (2010). *The Physics of Glaciers*. 4th Edition. U.S.A. Elsevier, 693p.

Curtis, A., and Kyle, P. (2017). Methods for Mapping and Monitoring Global Glaciovolcanism. *J. Volcanol. Geotherm. Res.* 333-334, 134–144. doi:10.1016/j.jvolgeores.2017.01.017

Dürig, T., White, J. D. L., Murch, A. P., Zimanowski, B., Büttner, R., Mele, D., et al. (2020). Deep-sea Eruptions Boosted by Induced Fuel-Coolant Explosions. *Nat. Geosci.* 13, 498–503.

Eason, D. E., Sinton, J. M., Grönvold, K., and Kurz, M. D. (2015). Effects of Deglaciation on the Petrology and Eruptive History of the Western Volcanic Zone, Iceland. *Bull. Volcanol.* 77, 47. doi:10.1007/s00445-015-0916-0

Edwards, B. R., and Russell, J. K. (2002). Glacial Influences on Morphology and Eruptive Products of Hoodoo Mountain Volcano, Canada. *Geol. Soc. Lond. Spec. Publ.* 202 (1), 179–194. doi:10.1144/gsl.sp.2002.202.01.09

Edwards, B., Russell, J., and Anderson, R. (2002). Subglacial, Phonolitic Volcanism at Hoodoo Mountain Volcano, Northern Canadian Cordillera. *Bull. Volcanol.* 64 (3), 254–272.

Edwards, B. R., Skilling, I. P., Cameron, B., Haynes, C., Lloyd, A., and Hungerford, J. H. D. (2009). Evolution of an Englacial Volcanic Ridge: Pillow Ridge Tindar, Mount Edziza Volcanic Complex, NCVP, British Columbia, Canada. *J. Volcanol. Geotherm. Res.* 185, 251–275. doi:10.1016/j.jvolgeores.2008.11.015

Edwards, B., Magnússon, E., Thordarson, T., Guđmundsson, M. T., Höskuldsson, A., Oddsson, B., et al. (2012). Interactions between Lava and Snow/ice during the 2010 Fimmvörðuháls Eruption, South-Central Iceland. *J. Geophys. Res.* 117, 21. doi:10.1029/2011JB008985

Edwards, B. R., Karson, J., Wysocki, R., Lev, E., Bindeman, I., and Kueppers, U. (2013). Insights on Lava–Ice/snow Interactions from Large-Scale Basaltic Melt Experiments. *Geology* 41 (9), 851–854. doi:10.1130/g34305.1

Edwards, B. R., Belousov, A., and Belousova, M. (2014). Propagation Style Controls Lava-Snow Interactions. *Nat. Commun.* 5, 5666. doi:10.1038/ncomms6666

Edwards, B., Kochtitzky, W., and Battersby, S. (2020). Global Mapping of Future Glaciovolcanism. *Glob. Planet. Change* 195, 103356. doi:10.1016/j.gloplacha.2020.103356

Einarsson, T. (1949). The Flowing Lava: Studies of its Main Physical and Chemical Characteristics. *Soc. Sci. Isl.* 4, 1–70.

Eksinchol, I., Rudge, J. F., and Maclennan, J. (2019). Rate of Melt Ascent beneath Iceland from the Magmatic Response to Deglaciation. *Geochem. Geophys. Geosyst.* 20 (6), 2585–2605. doi:10.1029/2019GC008222

Ferrier, K. L., Kirchner, J. W., and Finkel, R. C. (2007). "Erosion Rates Over Millennial and Decadal Timescales at Caspar Creek and Redwood Creek,

Northern California," in *Proceedings of the Redwood Region Forest Science Symposium: What Does The Future Hold?*. Editor R. B. Standiford, G. A. Giusti, Y. Valachovic, W. J. Zielinski, and M. J. Furniss (Albany, CA: Pacific Southwest Research Station, Forest Service, U.S. Department of Agriculture), 357–358.

Forbes, A. E. S., Blake, S., and Tuffen, H. (2014). Entablature: Fracture Types and Mechanisms. *Bull. Volcanol.* 76. doi:10.1007/s00445-014-0820-z

Fuller, R. E. (1931). The Aqueous Chilling of Basaltic Lava on the Columbia River Plateau. *Amer. J. Sci.* 21, 281–300.

Gee, M. A., Taylor, R. N., Thirlwall, M. F., and Murton, B. J. (1998). Glacioisostacy Controls Chemical and Isotopic Characteristics of Tholeiites from the Reykjanes Peninsula, SW Iceland. *Earth Planet. Sci. Lett.* 164 (1), 1–5. doi:10.1016/s0012-821x(98)00246-5

Geyer, A., and Bindeman, I. (2011). Glacial Influence on Caldera-Forming Eruptions. *J. Volcanol. Geotherm. Res.* 202, 127–142. doi:10.1016/j.jvolgeores.2011.02.001

Glazner, A. F., Manley, C. R., Marron, J. S., and Rojstaczer, S. (1999). Fire or Ice: Anticorrelation of Volcanism and Glaciation in California over the Past 800,000 Years. *Geophys. Res. Lett.* 26 (12), 1759–1762. doi:10.1029/1999gl900333

Goehring, L., and Morris, S. W. (2008). Scaling of Columnar Joints in Basalt. *J. Geophys. Res.* 113, B10203. doi:10.1029/2007JB005018

Gowan, Evan J. (2019). Global Ice Sheet Reconstruction for the Past 80000 Years. *PANGAEA* 12, 1199. doi:10.1594/PANGAEA.905800

Gregg, T. K. P., and Fornari, D. J. (1997). Long Submarine Lava Flows: Observations and Results from Numerical Modeling. *J. Geophys. Res.* 103 (B11), 27517–27531. doi:10.1029/98JB02465

Gudmundsson, M. T., Larsen, G., Höskuldsson, A., and Gylfason, A. G. (2008). Volcanic Hazards in Iceland. *Jökull* 58, 251–268.

Gudmundsson, A. (1986). Mechanical Aspects of Postglacial Volcanism and Tectonics of the Reykjanes Peninsula, Southwest Iceland. *J. Geophys. Res.* 91 (B12), 12711–12721. doi:10.1029/jb091ib12p12711

Gudmundsson, M. T. (2003). in *Subaqueous Explosive Volcanism*. Editors J. D. L. White, J. L. Smellie, and D. A. Clague (United States: American Geophysical Union, Geophysical Monograph Series), 140, 61–72. doi:10.1029/140gm04*Melting of Ice by Magma-Ice-Water Interactions during Subglacial Eruptions as an Indicator of Heat Transfer in Subaqueous Eruptions*

Harðarson, B. S., and Fitton, J. G. (1991). Increased Mantle Melting beneath Snaefellsjökull Volcano during Late Pleistocene Deglaciation. *Nature* 353, 62–64.

Harder, M., and Russell, J. K. (2007). Basanite Glaciovolcanism at Llangorse Mountain, Northern British Columbia, Canada. *Bull. Volcanol.* 69 (3), 329–340. doi:10.1007/s00445-006-0078-1

Harris, M. A., Russell, J. K, Barendregt, J. K., R Porritt, L. A., and Wilson, A. (2022). Explosive Glaciovolcanism at Cracked Mountain Volcano, Garibaldi Volcanic Belt, Canada. *J. Volcanol. Geotherm. Res.* 423, 107477. ISSN 0377-0273. doi:10.1016/j.jvolgeores.2022.107477

Hickson, C. J. (2000). Physical Controls and Resulting Morphological Forms of Quaternary Ice-Contact Volcanoes in Western Canada. *Geomorphology* 32 (3-4), 239–261. doi:10.1016/s0169-555x(99)00099-9

Höskuldsson, A., Sparks, R. S. J., and Carroll, M. R. (2006). Constraints on the Dynamics of Subglacial Basalt Eruptions from Geological and Geochemical Observations at Kverkfjöll, NE Iceland. *Bull. Volcanol.* 68, 689–701.

Hodgetts, A. G. E., McGarvie, D., Tuffen, H., and Simmons, I. C. (2021). The Thórólfsfell Tuya, South Iceland - a New Type of Basaltic Glaciovolcano. *J. Volcanol. Geotherm. Res.* 411, 107175. doi:10.1016/j.volgeores.2021.10717510.1016/j.jvolgeores.2021.107175

Hooper, A., Ófeigsson, B., Sigmundsson, F., Lund, B., Geirsson, H., and Sturkell, E. (2011). Increased Capture of Magma in the Crust Promoted by Ice-Cap Retreat in Iceland. *Nat. Geosci.* 4 (11), 10–1038. doi:10.1038/ngeo1269

Hubbard, A., Sugden, D., Dugmore, A., Norddahl, H., and Pétursson, H. G. (2006). A Modelling Insight into the Icelandic Last Glacial Maximum Ice Sheet. *Quat. Sci. Rev.* 25, 2283–2296. doi:10.1016/j.quascirev.2006.04.001

Jellinek, A. M., and DePaolo, D. J. (2003). A Model for the Origin of Large Silicic Magma Chambers: Precursors of Caldera-Forming Eruptions. *Bull. Volcanol.* 65 (5), 363–381. doi:10.1007/s00445-003-0277-y

Jellinek, A. M., Manga, M., and Saar, M. O. (2004). Did Melting Glaciers Cause Volcanic Eruptions in Eastern California? Probing the Mechanics of Dike Formation. *J. Geophys. Res.* 109. doi:10.1029/2004JB002978

Jones, J. G. (1969). Intraglacial Volcanoes of the Laugarvatn Region, South-West Iceland-I. *Geol. Soc. London Quart. J.* 124, 197–211.

Jude-Eton, T. C., Thordarson, T., Gudmundsson, M. T., and Oddsson, B. (2012). Dynamics, Stratigraphy and Proximal Dispersal of Supraglacial Tephra during the Ice-Confined 2004 Eruption at Grímsvötn Volcano, Iceland. *Bull. Volcanol.* 74, 1057–1082. doi:10.1007/s00445-012-0583-3

Jull, M., and McKenzie, D. (1996). The Effect of Deglaciation on Mantle Melting beneath Iceland. *J. Geophys. Res. Solid Earth* 101 (B10), 2185–21828. doi:10.1029/96jb01308

Kelman, M. C., Russell, J. K., and Hickson, C. J. (2002) *Effusive Intermediate Glaciovolcanism in the Garibaldi Volcanic Belt, Southwestern British Columbia, Canada*. in *Special Publications*. Editors J. L. Smellie and M. G. Chapman (London: Geological Society, London, Special Publications), 202, 195–211. doi:10.1144/gsl.sp.2002.202.01.10

Kerr, F. (1948). *Lower Stikine and Western Iskut River Areas* 246, 94. Ottawa: Geological Survey of Canada Memoir; Canada Department of Mines.

Lambeck, K., Purcell, A., Funder, S., KJaeR, K. H., Larsen, E., and Moller, P. (2006). Constraints on the Late Saalian to Early Middle Weichselian Ice Sheet of Eurasia from Field Data and Rebound Modelling. *Boreas* 35, 539–575. doi:10.1080/03009480600781875

Lambeck, K. H., Rouby, A., Purcell, A., Sun, Y., and Sambridge, M. (2014). Sea Level and Global Ice Volumes from the Last Glacial Maximum to the Holocene. *PNAS* 111, 15296–15303. doi:10.1073/pnas.1411762111

Le Breton, E., Dauteuil, O., and Biessy, G. (2010). Post-glacial Rebound of Iceland during the Holocene. *J. Geol. Soc.* 167, 417–432. doi:10.1144/0016-76492008-126

Lescinsky, D. T., and Fink, J. H. (2000). Lava and Ice Interaction at Stratovolcanoes: Use of Characteristic Features to Determine Past Glacial Extents and Future Volcanic Hazards. *J. Geophys. Res.* 105 (B10), 23711–23726. doi:10.1029/2000jb900214

Lisiecki, L. E., and Raymo, M. E. (2005). A Pliocene-Pleistocene Stack of 57 Globally Distributed Benthic δ18O Records. *Paleoceanography* 20, 17. doi:10.1029/2004PA001071

Lodge, R. W. D., and Lescinsky, D. T. (2009). Fracture Patterns at Lava-Ice Contacts on Kokostick Butte, OR, and Mazama Ridge, Mount Rainier, WA: Implications for Flow Emplacement and Cooling Histories. *J. Volcanol. Geotherm. Res.* 185, 298–310. doi:10.1016/j.jvolgeores.2008.10.010

Long, P. E., and Wood, B. J. (1986). Structures, Textures, and Cooling Histories of Columbia River Basalt Flows. *Geol. Soc. Am. Bull.* 97, 1144–1155. doi:10.1130/0016-7606(1986)97<1144:stacho>2.0.co;2

Maclennan, J., Jull, M., McKenzie, D., Slater, L., and Grönvold, K. (2002). The Link between Volcanism and Deglaciation in Iceland. *Geochem.-Geophys.-Geosyst.* 3 (11), 1–25. doi:10.1029/2001gc000282

Magnússon, E., Gudmundsson, M. T., Roberts, M. J., Sigurðsson, G., Höskuldsson, F., and Oddsson, B. (2012). Ice-volcano Interactions during the 2010 Eyjafjallajökull Eruption, as Revealed by Airborne Imaging Radar. *J. Geophys. Res.* 117, 17. doi:10.1029/2012JB009250

Mathews, W. H. (1947). "Tuyas," Flat-Topped Volcanoes in Northern British Columbia. *Am. J. Sci.* 245 (9), 560–570. doi:10.2475/ajs.245.9.560

McDonough, W. F., and Sun, S.-S. (1995). The Composition of the Earth. *Chem. Geol.* 120 (3-4), 223–253. doi:10.1016/0009-2541(94)00140-4

McLeod, P., and Tait, S. (1999). The Growth of Dykes from Magma Chambers. *J. Volcanol. Geotherm. Res.* 92 (304), 231–245. doi:10.1016/s0377-0273(99)00053-0

Moore, J. G. (1970). Pillow Lava in a Historic Lava Flow from Hualalai Volcano, Hawaii. *J. Geol.* 78 (2), 239–243. doi:10.1086/627506

Nelson, P. H. H. (1975). The James Ross Island Volcanic Group of North-East Graham Land. *Sci. Rep. Br. Antarct. Surv.* 54, 1–64.

Owen, J., Tuffen, H., and McGarvie, D. W. (2012). Explosive Subglacial Rhyolitic Eruptions in Iceland Are Fuelled by High Magmatic H2O and Closed-System Degassing. *Geology* 41, 251–254. doi:10.1130/G33647.1

Peacock, M. A. (1926). The Vulcano-Glacial Palagonite Formation of Iceland. *Geol. Mag.* 63 (9), 385–399. doi:10.1017/s0016756800085137

Pedersen, G. B. M., and Grosse, P. (2014). Morphometry of Subaerial Shield Volcanoes and Glaciovolcanoes from Reykjanes Peninsula, Iceland: Effects of Eruption Environment. *J. Volcanol. Geotherm. Res.* 282, 115–133. doi:10.1016/j.jvolgeores.2014.06.008

Pedersen, G. B. M. (2016). Semi-automatic Classification of Glaciovolcanic Landforms: An Object-Based Mapping Approach Based on Geomorphometry. *J. Volcanol. Geotherm. Res.* doi:10.1016/j.jvolgeores.2015.12.015

Pliny the Younger (2014). *The Complete Works of Pliny the Younger*. Delphi Classics. Book 28.

Pollock, M., Edwards, B., Hauksdóttir, S., Alcorn, R., and Bowman, L. (2014). Geochemical and Lithostratigraphic Constraints on the Formation of Pillow-dominated Tindars from Undirhlíðar Quarry, Reykjanes Peninsula, Southwest Iceland. *Lithos.* 200, 317–333. doi:10.1016/j.lithos.2014.04.023

Praetorius, S., Mix, A., Jensen, B., Froese, D., Milne, G., Wolhowe, M., et al. (2016). Interaction between Climate, Volcanism, and Isostatic Rebound in Southeast Alaska during the Last Deglaciation. *Earth Planet. Sci. Lett.* 452, 79–89. doi:10.1016/j.epsl.2016.07.033

Rawson, H., Pyle, D. M., Mather, T. A., Smith, V. C., Fontijn, K., Lachowycz, S. M., et al. (2016). The Magmatic and Eruptive Response of Arc Volcanoes to Deglaciation: Insights from Southern Chile. *Geology* 44 (4), 251–254. doi:10.1130/g37504.1

Rowell, C. R., Jellinek, A. M., Hajimirza, S., and Aubry, T. J. (2021). External Surface Water Influence on Explosive Eruption Dynamics, with Implications for Stratospheric Sulfur Delivery and Volcano-Climate Feedback. *Volcanology*. doi:10.3389/feart.2022.788294

Russell, J. K., Edwards, B. R., Turnbull, M., and Porritt, L. A. (2021). Englacial Lake Dynamics within a Pleistocene Cordilleran Ice Sheet at Kima' Kho Tuya (British Columbia, Canada). *Quat. Sci. Rev.* 273, 107247. doi:10.1016/j.quascirev.2021.107247

Russell, J. K., Edwards, B. R., Porritt, L., and Ryane, C. (2014). Tuyas: a Descriptive Genetic Classification. *Quat. Sci. Rev.* 87, 70–81. doi:10.1016/j.quascirev.2014.01.001

Satow, C., Gudmundsson, A., Gertisser, R., Ramsey, C. B., Bazargan, M., Pyle, D., et al. (2021). Eruptive Activity of the Santorini Volcano Controlled by Sea-Level Rise and Fall. *Nat. Geosci.* 14, 586–592. doi:10.1038/s41561-021-00783-4

Schopka, H. H., Gudmundsson, M. T., and Tuffen, H. (2006). The Formation of Helgafell, Southwest Iceland, a Monogenetic Subglacial Hyaloclastite Ridge: Sedimentology, Hydrology and Volcano-Ice Interaction. *J. Volcanol. Geotherm. Res.* 152, 359–377. doi:10.1016/j.jvolgeores.2005.11.010

Sigvaldason, G. E., Annertz, K., and Nilsson, M. (1992). Effect of Glacier Loading/deloading on Volcanism: Postglacial Volcanic Production Rate of the Dyngjufjoll Area, Central Iceland. *Bull. Volcanol.* 54 (5), 385–392. doi:10.1007/bf00312320

Sims, K. W. W., Maclennan, J., Blichert-Toft, J., Mervine, E. M., Blusztajn, J., and Grönvold, K. (2013). Short Length Scale Mantle Heterogeneity beneath Iceland Probed by Glacial Modulation of Melting. *Earth Planet. Sci. Lett.* 379, 146–157. doi:10.1016/j.epsl.2013.07.027

Sinton, J., Grönvold, K., and Sæmundsson, K. (2005). Postglacial Eruptive History of the Western Volcanic Zone, Iceland. *Geochem. Geophys. Geosys.* 6, Q12009. doi:10.1029/2005GC001021

Sisson, T. W., Salters, V. J. M., and Larson, P. B. (2014). Petrogenesis of Mount Rainier Andesite: Magma Flux and Geologic Controls on the Contrasting Differentiation Styles at Stratovolcanoes of the Southern Washington Cascades. *Geol. Soc. Am. Bull.* 126 (1-2), 122–144. doi:10.1130/b30852.1

Skilling, I. P. (2009). Subglacial to Emergent Basaltic Volcanism at Hlodufell, South-West Iceland: A History of Ice-Confinement. *J. Volcanol. Geotherm. Res.* 185, 276–289.

Slater, L., Jull, M., McKenzie, D., and Grönvold, K. (1998). Deglaciation Effects on Mantle Melting under Iceland: Results from the Northern Volcanic Zone. *Earth Planet. Sci. Lett.* 164 (1), 151–164. doi:10.1016/s0012-821x(98)00200-3

Smellie, J. L., and Edwards, B. R. (2016). *Glaciovolcanism on Earth and Mars*. Cambridge, UK: Cambridge University Press.

Smellie, J. L. (2000). in *Encyclopedia of Volcanoes*. Editors Haraldur Sigurdsson, Bruce Houghton, Hazel Rymer, John Stix, and Steve McNutt (Amsterdam, Netherlands: Elsevier), 403–418.*Subglacial Eruptions*

Smellie, J. L. (2009) *Terrestrial Sub-ice Volcanism: Landform Morphology, Sequence Characteristics and Environmental Influences, and Implications for Candidate Mars Examples*. in *Preservation of Random Mega-Scale Events on Mars and Earth: Influence on Geologic History*. Editors M. G. Chapman and L. Leszthely (Geol. Soc. Am. Special Papers), 453, 55–76.

Smellie, J. L. (2018). in *Past Glacial Environments (Sediments, Forms and Techniques)*. Editors J. Menzies and J. J. M. van der Meer. 2nd edition (Amsterdam, Netherlands: Elsevier), 335–375. doi:10.1016/b978-0-08-100524-8.00010-5*Glaciovolcanism*

Sparks, R. S. J., and Cashman, K. V. (2017). Dynamic Magma Systems: Implications for Forecasting Volcanic Activity. *Elements* 13 (1), 35–40. doi:10.2113/gselements.13.1.35

Tormey, D. (2010). Managing the Effects of Accelerated Glacial Melting on Volcanic Collapse and Debris Flows: Planchon-Peteroa Volcano, Southern Andes. *Glob. Planet. Change* 74 (2), 82–90. doi:10.1016/j.gloplacha.2010.08.003

Walker, G. P. L. (1992). Morphometric Study of Pillow-Size Spectrum Among Pillow Lavas. *Bull. Volcanol.* 54 (6), 459–474. doi:10.1007/bf00301392

Werner, R., and Schmincke, H.-U. (1999). Englacial vs. Lacustrine Origin of Volcanic Table Mountains: Evidence From Iceland. *Bulletin Volcanol.* 60, 335–354.

Wilson, A. M., and Russell, J. K. (2020). Glacial Pumping of a Magma-Charged Lithosphere: A Model for Glaciovolcanic Causality in Magmatic Arcs. *Earth Planet. Sci. Lett.* 548, 116500. doi:10.1016/j.epsl.2020.116500

Wilson, A. M., Russell, J. K., and Quane, S. L. (2019). The Table, a Flat-Topped Volcano in Southern British Columbia: Revisited. *Am. J. Sci.* 319, 44–73. doi:10.2475/01.2019.02

Conflict of Interest: The authors declare that the research was conducted in the absence of any commercial or financial relationships that could be construed as a potential conflict of interest.

Publisher's Note: All claims expressed in this article are solely those of the authors and do not necessarily represent those of their affiliated organizations, or those of the publisher, the editors and the reviewers. Any product that may be evaluated in this article, or claim that may be made by its manufacturer, is not guaranteed or endorsed by the publisher.

Advantages of publishing in Frontiers

OPEN ACCESS
Articles are free to read for greatest visibility and readership

FAST PUBLICATION
Around 90 days from submission to decision

HIGH QUALITY PEER-REVIEW
Rigorous, collaborative, and constructive peer-review

TRANSPARENT PEER-REVIEW
Editors and reviewers acknowledged by name on published articles

Frontiers
Avenue du Tribunal-Fédéral 34
1005 Lausanne | Switzerland

Visit us: www.frontiersin.org
Contact us: frontiersin.org/about/contact

REPRODUCIBILITY OF RESEARCH
Support open data and methods to enhance research reproducibility

DIGITAL PUBLISHING
Articles designed for optimal readership across devices

FOLLOW US
@frontiersin

IMPACT METRICS
Advanced article metrics track visibility across digital media

EXTENSIVE PROMOTION
Marketing and promotion of impactful research

LOOP RESEARCH NETWORK
Our network increases your article's readership